1-1-2009

Phenomenological studies of hot tearing during solidification of magnesium alloys

Lukas Bichler
Ryerson University

PHENOMENOLOGICAL STUDIES OF HOT TEARING DURING SOLIDIFICATION OF MAGNESIUM ALLOYS

By

Lukas Bichler
B. Eng., Ryerson University, 2003
M.A.Sc., Ryerson University, 2005

A dissertation
presented to Ryerson University
in partial fulfillment of the
requirement for the degree of

Doctor of Philosophy

in the Program of
Mechanical Engineering

Toronto, Ontario, Canada, 2009

Author's Declaration

I hereby declare that I am the sole author of this dissertation.

I authorize Ryerson University to lend this dissertation to other institutions or individuals for the purpose of scholarly research.

_____

Lukas Bichler

I further authorize Ryerson University to reproduce this dissertation by photocopying or by other means, in total or in part, at the request of other institutions or individuals for the purpose of scholarly research.

_____

Lukas Bichler

Abstract

PHENOMENOLOGICAL STUDY OF HOT TEARING DURING SOLIDIFICATION OF MAGNESIUM ALLOYS

Doctor of Philosophy, 2009
Lukas Bichler

Mechanical Engineering
Ryerson University

There is a renewed interest in magnesium alloys in the automotive industry. Magnesium alloys are ~35% lighter than aluminum and ~80% lighter than steel. As a result, incorporation of magnesium alloy castings in new vehicles plays a critical role in reducing the overall vehicle weight and increasing the vehicle's fuel efficiency. Magnesium alloys processed via permanent mold casting (PMC) show a high susceptibility to hot tearing. While several techniques are used to relieve hot tearing (e.g., preheating of molds, grain refinement or elimination of sharp features in part design), the underlying mechanisms responsible for hot tearing remain unclear. In the case of magnesium alloys, limited work has been carried out to advance the fundamental understanding of hot tearing.

This research investigated the influence of alloy microstructure, casting solidification and casting stresses on the onset of hot tearing in AZ91D and AE42 magnesium alloys. A novel approach to determine casting stresses using neutron diffraction was implemented. A custom designed permanent mold was used to manipulate the cooling rate of a casting and ensuing susceptibility to hot tearing.

The results indicate that the mold temperature had a profound influence on the nucleation of hot tears. When the cooling rate of the AZ91D casting reached ~15.1 °C/s (210 °C mold temperature), the fraction of solids development was sufficiently fast to prevent adequate long-range interdendritic feeding of the casting. As a result, shrinkage porosity formed. Shrinkage porosity forming at a location of a stress concentration provided a nucleation site for a hot tear. The stress required to open a shrinkage pore into a hot tear at the stress concentration was ~ 8 – 12 MPa. Increasing the mold temperature to 250 °C decreased the cooling rate, improved interdendritic feeding of the casting, decreased solidification shrinkage and decreased the magnitude of tensile stresses developing

in the casting. In the case of the AE42 alloy, interdendritic feeding of liquid was hindered by the Al_xRE_y intermetallic compounds blocking the interdendritic paths. Further, the presence of acicular $Al_{11}RE_3$ phase pinning the grain boundaries decreased the ductility of the AE42 alloy. As a result, a very slow casting cooling rate (~ 7.7 °C/s) was required to prevent the nucleation of hot tears. For higher cooling rates, hot tears nucleated at locations of stress concentrations and propagated along interdendritic regions and grain boundaries.

Acknowledgement

I am grateful to Professor C. Ravindran, my supervisor, mentor and role-model for his guidance, support, and inspiration throughout my graduate studies. His teachings extended far beyond the textbooks. I have learned much about happiness, prudence and fortitude from him. I am forever thankful for his kindness and willingness to lead me on new paths of life and his unwavering ability to give me hope for future endeavors.

I would like to thank Dr. Dimitry G. Sediako of the Canadian Neutron Beam Centre, National Research Council of Canada, Chalk River, for supervision and guidance in performing neutron diffraction and computer simulation experiments.

Further, I am thankful to Professors Alex McLean and David Naylor for their guidance and valuable discussions throughout the research.

The help, support and friendship of Mr. Alan Machin from the Department of Mechanical and Industrial Engineering, Ryerson University was invaluable for the completion of this thesis.

I sincerely appreciate the assistance of Mr. Christof Heisser, Mr. Matt Proske and Ms. Deepika Gaddam of Magma Foundry Technologies, Ltd., Schaumburg, IL in enabling and carrying out MAGMASOFT® computer simulations. Also, the support of Mr. Ivan Kosi of Meridian Technologies Inc. in providing material support is greatly appreciated.

Further, I would like to thank Mr. Kenneth Lee, Mr. Abdallah Elsayed and Mr. Francesco D'Elia for their help with casting experiments.

In addition, I would like to acknowledge the National Sciences and Engineering Research Council (NSERC) for financial support in the form of a Canada Graduate Scholarship.

I am thankful to Ms. Andrea Gomez and Mr. Neil McFarlane for their help with printing and graphical design of the thesis.

I am grateful to my parents and grandparents for their sacrifice, encouragement and love they provided me with during this long journey. Without their support, completion of this work would not be possible.

Dedication

To my father

Table of Contents

List of Tables

Appendix Tables

List of Figures

Appendix Figures

Nomenclature

Symbol	**Definition**	**Units**
A_g	Constant dependent on grain size and grain dihedral angle	-
a	Composition coefficient of liquid	-
A	Peak amplitude	-
b	Liquid film thickness	[m]
B	Constant background term	-
c	Tortuosity constant of dendritic network	-
C_l	Composition of the liquid at the solid-liquid interface	[wt%]
C_n	Electric charge of a neutron	[C/s]
C_o	Nominal alloy composition	[wt%]
D	Average grain diameter	[m]
DAS	Secondary dendrite arm spacing	[m]
d_{hkil}	Lattice spacing for a family of (*hkil*) planes	[m]
$d_{o\text{-}hkil}$	Lattice spacing for a family of (*hkil*) planes in a stress-free material	[m]
E	Young's modulus	[Pa]
f_{crack}	Factor indicating severity of a hot tear	-
f_l	Fraction of liquid	-
$f_{location}$	Factor indicating the difficulty of cracking at a given casting location	-
f_s	Fraction of solid	-
F_z	Force required to increase film thickness from b_1 to b_2	[N]
G	Shear modulus	[Pa]
h	Planck's constant	[m^2 kg/s]
k	Equilibrium redistribution coefficient	-
L_{SPV}	Length of porous network	[m]
Δl	Relative displacement of two adjacent grains along common interface	[m]
m	Mass	[kg]
m_l	Slope of the liquidus line	-
m_n	Mass of a neutron	[kg]
n	Order of diffraction	-
n^o	Neutron	-
p_r	Reserve of plasticity	[%/°C]
P_s	Effective feeding pressure	[Pa]
q	Heat content	[J]
R	Average grain radius	[m]
S_{pr}	Area between the ε_p and ε_{sh} curves in the brittle temperature range	[%]
$t_{b1\text{-}b2}$	Time required to increase the film thickness from b_1 to b_2	[s]
t_r	Period when mass feeding and stress-relief may occur	[s]

t_v	Period of hot tearing susceptibility	[s]
$t_{ZST-ZDT}$	Vulnerable time interval between ZST and ZDT temperatures	[s]
ΔT_{br}	Brittle temperature range	[°C]
$\dot{T}$	Average cooling rate during solidification of the primary solid phase	[°C/s]
v_{liq}	Liquid metal velocity	[m/s]
v_n	Velocity of a neutron	[m/s]
v_τ	Solidification velocity	[m/s]
V_L	Volume of liquid	[m^3]

Greek Symbols	**Definition**	**Units**
β	Shrinkage factor	-
γ	Liquid film surface tension	[N/m]
γ_{fr}	Effective fracture surface energy	[J]
δ_{ig}	Total intergranular sliding deformation	[m]
ε	Strain	[%]
ε_{hkil}	Strain for (*hkil*) planes	[%]
ε_{sh}	Linear shrinkage/contraction	[%]
$\dot{\varepsilon}_p$	Deformation rate in the solid	[%/s]
$\dot{\varepsilon}^{\max}$	Critical deformation rate to initiate hot tearing	[%/s]
ψ	Microstructure parameter	-
θ_b	Bragg diffraction angle	[°]
ϕ	Angle at which Gaussian function is being evaluated	[°]
ϕ_c	Centre of the fitted peak	[°]
λ	Wavelength	[m]
λ_n	Wavelength of a neutron	[m]
$\overline{\rho}$	Average density	[kg/m^3]
ρ_l	Alloy density at liquidus temperature	[kg/m^3]
ρ_o	Bulk alloy density	[kg/m^3]
ρ_s	Alloy density at solidus temperature	[kg/m^3]
σ_{fr}	Fracture stress	[N/m^2]
σ	Gaussian peak width	[°]
μ_n	Magnetic dipole moment	[J/T]
μ	Dynamic viscosity	[g/cm.s]
ν	Poisson's ratio	-

Elements

Al	Aluminum
Be	Beryllium
Ce	Cerium
Cu	Copper
Fe	Iron
La	Lanthanum
Mg	Magnesium
Mn	Manganese
Nd	Neodymium
Ni	Nickel
Pr	Praseodymium
Si	Silicon
Zn	Zinc
CO_2	Carbon dioxide
SF_6	Sulphur hexafluoride

Acronyms

ANDI	Analytical Neutron Diffraction for Industry
ANOVA	Analysis of Variances
BC	Boundary Condition
BF	Bright Field microscopy
BN	Boron-Nitride coating
BTR	Brittle Temperature Range
CTE	Coefficient of Thermal Expansion
CNBC	Canadian Neutron Beam Centre
DB	Diffracted Beam
DF	Dark Field microscopy
DIC	Differential Interference Contrast
EBSD	Electron Back-Scattered Diffraction
FWHM	Full-Width at Half-Maximum
HCP	Hexagonal Close-Packed
HCS	Hot Cracking Susceptibility index
HPDC	High-Pressure Die-Casting
HTC	Heat Transfer Coefficient
HTI	Hot Tear Index
IC	Initial Condition
LST	Local Solidification Time
LVDT	Linear Variable Differential Transformer
MFT	Magma Foundry Technologies, Inc.
MON	Diffracted neutron beam monitor value
ND	Neutron Diffraction
P/B	Peak-to-Background ratio
PL	Polarized Light
PMC	Permanent Mold Casting
RDG	Rappaz-Drezet-Gremaud hot tearing criterion
RE	Rare Earths
RPM	Revolutions Per Minute
SEM	Scanning Electron Microscope
SM	Stereo Microscopy
UTS	Ultimate Tensile Strength
YS	Yield Strength
ZDT	Zero Ductility Temperature
ZST	Zero Strength Temperature

Chapter 1 – Introduction

There is a renewed interest in magnesium alloys in the automotive industry. Magnesium alloys are ~35% lighter than aluminum alloys and ~80% lighter than steel. As a result, incorporation of magnesium alloy castings in new vehicles may play a critical role in reducing vehicle weight and increasing vehicle fuel efficiency. Also, magnesium alloys show excellent specific properties, castability and recycling potential. However, during part manufacture, magnesium alloys processed via high-pressure die-casting (HPDC) or permanent mold casting (PMC) show high susceptibility to hot tearing.

Hot tears form when a casting is in a semi-solid state and experiences significant thermal and mechanical tensile stresses. Thermal stresses result from a non-uniform temperature distribution leading to non-uniform solidification shrinkage and thermal contraction of a casting upon solidification. Mechanical stresses develop when a casting solidifies within a rigid mold, which limits the casting's solidification shrinkage and thermal contraction.

Reviews of hot tearing theories, evaluation methods and predictive models based on empirical evidence are available in the literature [1, 2, 3, 4]. These and other research investigations identified stress/strain, alloy microstructure and solidification of a given alloy as the key parameters affecting the onset of hot tearing. Theoretical criterion functions based on these three parameters were developed with the aim of predicting the onset of hot tearing [5]. However, experimental validation of these criterion functions remains a challenge. In particular, the currently available methods to evaluate casting stress or strain involve intrusive probes (which alter the casting solidification profile) or indirect estimations. As a result, prediction of the onset of hot tearing is hindered by the absence of accurate and quantitative data about the stress and strain levels required to trigger hot tearing. In the case of the remaining factors (i.e., solidification and microstructure), experiments were carried out for numerous alloys and casting processes.

A classical approach in characterizing casting solidification is based on suitable placement of thermocouple probes in the casting and subsequent thermal analysis [5]. Thus, it is possible to determine the casting's cooling rate, freezing range, phase precipitation kinetics, etc. In addition, information about the material's feeding behavior and mechanical response during solidification may be obtained using the concepts of dendrite coherency temperature (T_{coh}) and rigidity temperature (T_{rig}), along with the zero-ductility-temperature (*ZDT*) and zero-strength-temperature (*ZST*).

The modern approach to casting analysis often involves a numerical computer simulation enabling prediction of fluid flow, microstructure and casting stress evolution. Current state-of-the-art simulation programs are adequate for a limited number of alloys (e.g., steels) and simple geometries, where the solution of the fundamental coupled non-linear governing differential equations can be simplified with suitable assumptions. However, accurate determination of the mechanical response and the onset of hot tearing in shape castings remain difficult for most materials due to incomplete knowledge of the material's thermo-mechanical response (e.g., stresses) at elevated temperatures.

Thermal stresses develop in a casting as a result of temperature gradients causing differential casting contraction during solidification. In addition, when a casting solidifies within a rigid mold, as in the case of HPDC or PMC process, the casting's solidification shrinkage and thermal contraction are hindered by the rigid mold and, consequently, mechanical stresses develop in the material. It is generally accepted [1] that when the combined stress due to the thermal and mechanical loads exceeds the tensile strength of a semi-solid alloy, fragmentation of the dendritic network occurs, leading to the formation of microcracks and subsequent material failure.

The purpose of this research was to develop a novel approach to study and quantify the fundamental mechanisms associated with the onset of hot tearing in AZ91D and AE42 magnesium alloy castings. The elastic residual strain and stress at the onset of hot tearing was measured by neutron diffraction. The alloy microstructure was characterized using optical and scanning electron microscopy. Thermal analysis was performed to provide information about casting solidification and feeding history. In addition, basic computer modeling in MAGMASOFT® simulation software was carried out to obtain additional information about casting filling, temperature, principal stress distribution and heat transfer coefficients. Thus, the fundamental factors associated with the onset of hot tearing were determined without interference with the casting's natural solidification.

In the context of the aforesaid objectives, this research further aimed to:

1. Develop a permanent mold enabling accurate control of hot tearing of alloys.
2. Determine the casting process parameters (e.g., pouring temperature and mold temperature) associated with the onset of hot tearing.
3. Measure the crystallographic texture in castings with distinct degrees of hot tearing using neutron diffraction.
4. Map residual strains across a casting to study the bulk casting deformation.

5. Assess the validity of MAGMASOFT® modeling in predicting the onset of hot tearing.
6. Examine the alloy microstructure and identify additional factors contributing to material failure during solidification.

This dissertation has been structured as follows:

Chapter 2 presents a literature survey that contains a concise review of alloy solidification, mechanical behavior of semi-solid alloys and the current methods for assessing the hot tearing susceptibility of alloys.

Chapter 3 presents the fundamental background to neutron diffraction.

Chapter 4 describes, in detail, the experiments carried out, including permanent mold design, casting practice, neutron diffraction experiments and microscopic evaluation.

In Chapter 5, the experimental results are presented along with a discussion of their significance in relation to hot tearing.

Chapter 6 offers the conclusions arising from this research.

Chapter 7 lists a series of recommendations for future work.

Basic MAGMASOFT® simulations were performed in this research. These simulations were carried out by the software manufacturer using experimental data generated in this research. Thus, the computer simulations were used to obtain additional (i.e., non-essential) information about the casting solidification process. Therefore, discussion of MAGMASOFT® results is presented in Appendix 1.

A flowchart in Figure 1 provides an overview of the scope of this dissertation.

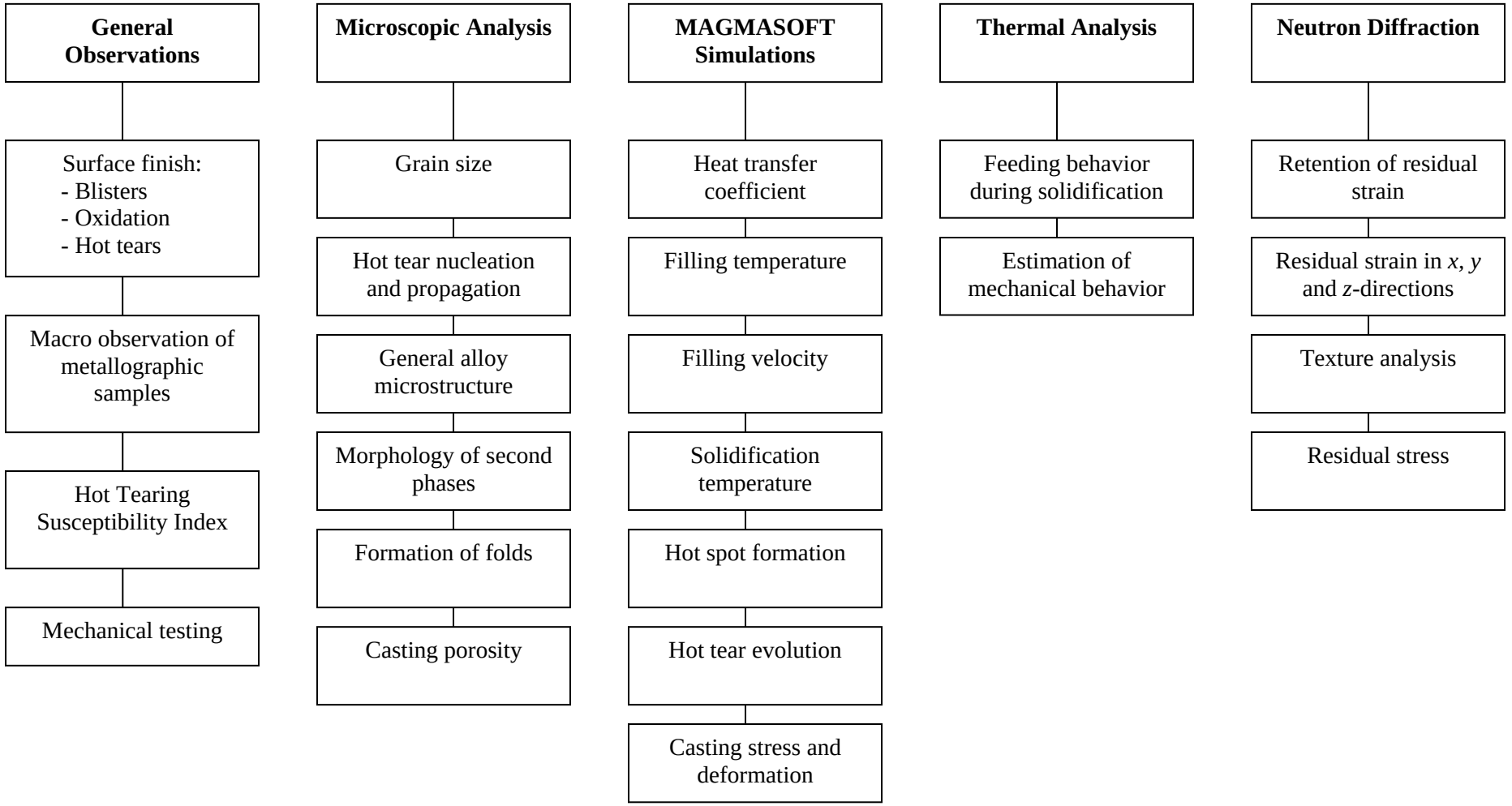

Figure 1: Dissertation overview.

Chapter 2 – Literature Review

In this chapter, a literature review is presented to relate alloy solidification and high-temperature mechanical behavior to hot tearing (Sections 2.1 – 2.2). Experimental methods to assess hot tearing and theoretical models used to predict hot tearing are discussed in Section 2.3.

2.1 Alloy Solidification

For the majority of casting processes currently used in the metalcasting industry, superheated liquid alloy is poured into a mold cavity and allowed to solidify. As the liquid alloy cools below the liquidus (nucleation) temperature, solid agglomerates appear within the melt [1]. For multicomponent alloy systems, the solids typically form dendrites as illustrated in Figure 2 [6]. These dendrites preferentially grow in the direction of temperature or solute concentration gradients at the solid-liquid interface.

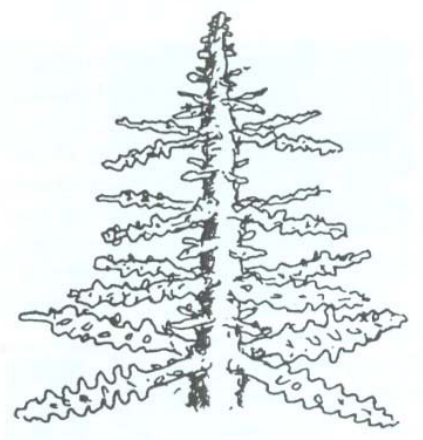

Figure 2: Illustration of a dendrite [6].

As the alloy cools through the freezing range, it can be classified either as a semi-solid slurry or a mush. A slurry is defined as a bulk liquid with suspended solid particles. In contrast, a mush is defined as a solid with liquid phase agglomerated in the interdendritic regions. The fraction of solid, f_s, at which the transition between slurry and mush occurs varies between 0.25 and 0.60, depending on the alloy and the morphology of the solid phase [1].

As a slurry, the alloy cannot sustain any load. As temperature continues to decrease, however, the number and the size of the dendrites increases until they interlock to form a coherent network [7]. Evolution of a

coherent network also influences the feedability of a casting. Thus, the solidification process may be divided into four stages [8, 9, 10, 11]:

1. *Mass feeding*: Both liquid and solid phases are free to move.
2. *Interdendritic feeding*: Liquid phase flows through the developing dendritic network and creates a continuous liquid film on developing grain boundaries. During this stage, the permeability of the solid network remains high and mobile liquid alleviates any developing solidification stresses.
3. *Interdendritic separation of the liquid phase*: With increasing solid fraction and the onset of dendrite coherency, the permeability of the solid network significantly decreases. Eskin *et al*. [1] defined dendrite coherency as the instance during solidification when individual dendrites start to interact with each other: first, by contacting, then by bridging and, finally, by forming a continuous solid skeleton of the primary phase. At the onset of dendrite coherency, the liquid film becomes fragmented and immobilized by surface tension and increasing melt viscosity. As a result, subsequent interdendritic feeding is difficult and casting stresses begin to develop. Also, interdendritic shrinkage pores may nucleate.
4. *Interdendritic bridging and solid feeding*: The alloy further develops strength as dendrites interlock via solid bridges. Since liquid phase exists only as isolated pockets within the casting, feeding of the casting is difficult. At this stage, shrinkage porosity growth and hot tear nucleation are likely.

From these theories, the hot tearing susceptibility of alloys was seen to relate to the morphology of the mush and the (liquid) permeability of the dendritic network. In addition, the mechanical properties (tensile strength and ductility) of the alloy before completion of solidification were seen to impact the onset of hot tearing. To isolate individual contributions and gain a better understanding of the behavior of mushy alloys, numerous tests were developed and are discussed in the following sections.

2.2 Mechanical Behavior of Semi-solid Alloys

In order to accurately investigate the evolution of the mechanical response of an alloy between the liquidus and solidus temperatures, a series of tests must be performed at various temperatures. At each test temperature, the alloy specimen must be isothermal. This requirement has been recognized as a primary impediment to successful evaluation of semi-solid alloy's thermophysical properties, since it is difficult to maintain a constant homogeneous temperature in a sample.

Two approaches to attain the desired test temperature for isothermal tests were reported in the literature: 1) remelting, i.e., heating a solid sample from the room temperature to the desired test temperature; or, 2) solidification, i.e., cooling a liquid alloy to the test temperature. Each approach results in unique alloy microstructure and mechanical properties [1]. For the purpose of understanding casting solidification, the latter approach yields more relevant data.

In general, elevated temperature tensile tests revealed that alloys exhibit ductile behavior until reaching a temperature at which they fail in a brittle-like manner. This temperature is also related to the onset of loss of yield strength. The deterioration of the alloy strength was related to the occurrence of liquid phase at the grain boundaries [7]. Experimental methods to investigate the alloy properties at this instance were developed from modified tensile, shear and compressive tests. However, these unique testing methods enable only comparison of alloys tested under the same conditions.

2.2.1 Tensile Strength of Semi-solid Alloys

Prokhorov and Bochai [12] carried out isothermal tests to study the tensile strength of aluminum alloys at elevated temperatures. A test specimen was placed on a copper support in a furnace, melted and subsequently cooled to a test temperature. The authors reported difficulties with respect to the measurement of strain (elongation) in the semi-solid material due to: 1) poor centering of the sample and the resulting offset of the applied load, and 2) low accuracy of linear displacement measurements at very high operating temperatures. As a result, correction factors were required to compensate for the change of specimen size, orientation and strain measurement during the test.

A typical stress vs. elongation curve reported by Prokhorov and Bochai is schematically presented in Figure 3. The curve shows a gradual decrease of stress beyond the ultimate tensile strength (UTS). Such gradual decrease is not observed during room temperature tensile testing, where a rapid loss of strength and material failure follow necking at the UTS. The gradual decrease of stress was attributed to the presence of semi-solid bridges between fracture surfaces, which transferred applied load even at high strain levels.

The tensile behavior of alloys tested between the liquidus and solidus temperatures was seen to be influenced by the alloy microstructure, composition and solidification characteristics.

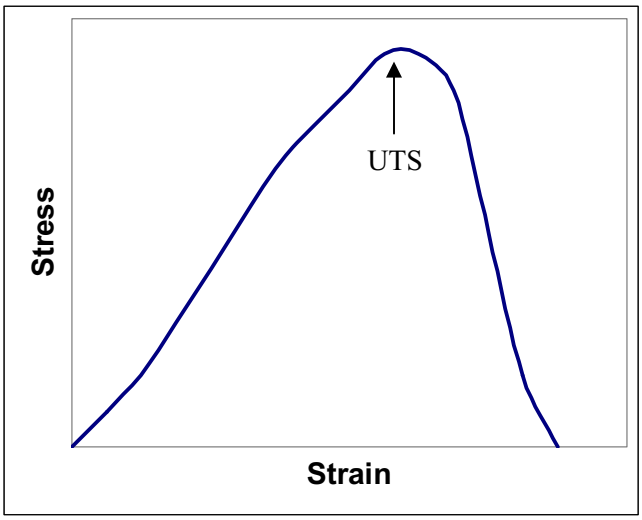

Figure 3: Typical stress vs. strain curve for high temperature tensile test [12].

Metz and Flemings [13] showed that the addition of Ti, Zr or Be grain refiners to aluminum alloys delayed dendrite coherency and associated strength build-up to higher fractions of solid. As a result, relative sliding of dendrites (before coherency) accommodated bulk deformation and only minimal dendrite fragmentation occurred. Novikov [14] confirmed that the semi-solid alloy's strength decreases when a coarse dendritic structure is present. Due to a relatively low number of solid bridges between grains and a small surface area available for load transfer during high temperature deformation, the load bearing capacity of a coarse grained material was poor. Representative results are illustrated in Figure 4.

Metz and Flemings also studied the effect of solute concentration on the mechanical response of various aluminum alloys. They observed that with increasing solute content, the melting temperature of the interdendritic liquid decreased. This enabled grain boundary sliding and loss of strength at lower test temperatures, as illustrated in Figure 5.

In the case of 7064-type Al alloy, Novikov [14] investigated the relation between the alloy composition (Fe:Si ratio) and the semi-solid alloy strength. The concentration threshold for the formation of the low-melting eutectic β-Al_5FeSi shifted to a higher iron and silicon concentrations with increasing Fe:Si ratio. This prevented the formation of thermally stable Si-rich intermetallic compounds at the grain boundaries, which are known to pin the grain boundaries during high temperature deformation. Therefore, the semi-solid strength of the alloy decreased when the Si-rich intermetallics were absent from the grain boundaries [15].

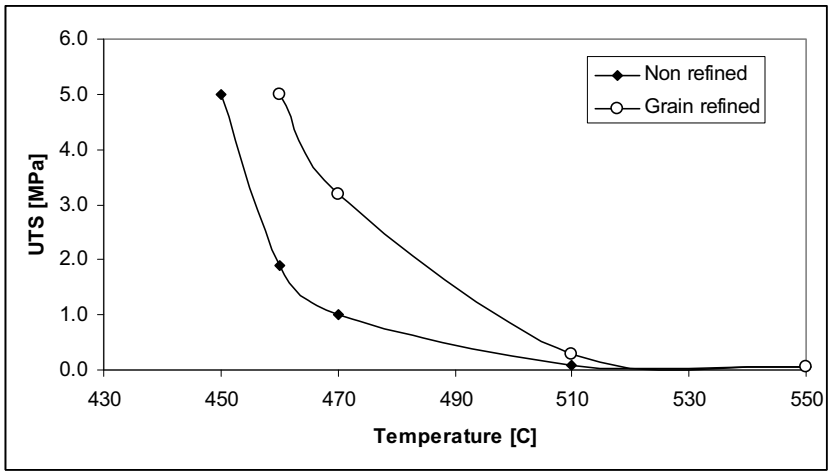

Figure 4: Effect of a grain refiner on the UTS of A585 alloy [14].

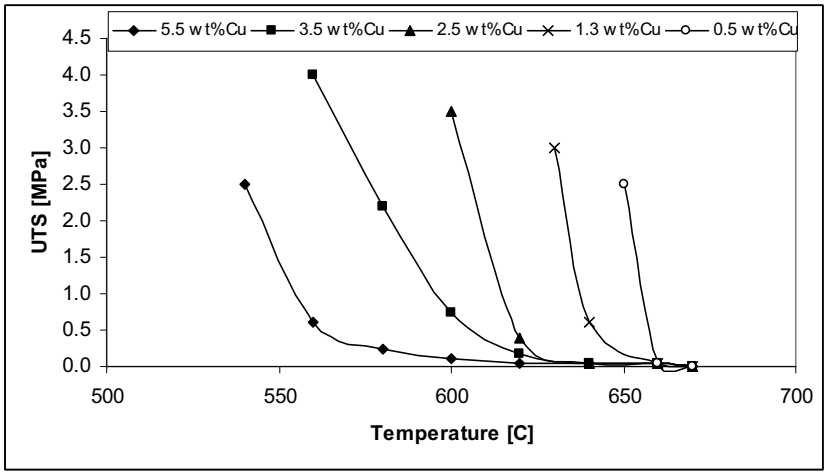

Figure 5: Effect of copper concentration on UTS of Al-Cu alloy [13].

The effect of solute concentration on the semi-solid tensile strength was also related to the amount and distribution of liquid between dendrites. In heavily alloyed systems, coalesced liquid formed large pockets, which decreased the number of solid bridges between adjacent dendrites [16]. As a result, the ability of the dendritic skeleton to transfer and dissipate applied load was low.

Instone *et al*. [17] conducted tensile tests with alloys of different freezing ranges. In a short freezing range alloy, strength developed at ~88 % solid, while in a long freezing range alloy, the corresponding fraction of solid increased to ~95 % solid. This trend was attributed to the formation of eutectic phases in the long freezing range alloy and solute coring effects. With higher solute concentration in the liquid, sliding of grains during deformation was possible and delayed the alloy's strength development [2, 18].

Forest and Bercovici [11] studied the effect of alloy cooling rate on the alloy's tensile strength. Rapid nucleation of primary grains at high cooling rates resulted in finer grain size and enhanced tensile strength. However, the authors also suggested that rapid cooling may accelerate solute segregation, which causes agglomeration of solute-rich low-melting temperature eutectics at the grain boundaries and enables grain boundary sliding during high temperature deformation. They reported that the softening effect, however, was less pronounced than the strengthening effect of the fine grain size.

2.2.2 Ductility of Semi-solid Alloys

Ductility characterizes an alloy's ability to accommodate strain prior to fracture. In permanent mold castings, strains evolve mainly as a result of solidification shrinkage and thermal contraction [1]. Additional strains and stresses may be induced in the material due to additional processing operations, such as drawing of semi-solid material from a mold in direct-chill casting, electromagnetic stirring or deformation of casting material due to application of external pressure during HPDC.

Experimental data on the ductility of aluminum or magnesium alloys in the semi-solid state are seldom reported in the literature. One of the contributing factors is the absence of universally accepted method for measuring ductility of semi-solid alloys. Secondly, the ductility values of alloys typically range between 0.1 – 0.5%. Such small measurement values pose numerous instrumentation challenges. Therefore, the validity of published ductility measurements remains questionable. The available literature reveals that alloy ductility is a strong function of the test temperature, alloy grain structure, cooling rate and composition. A brief explanation of these concepts follows.

Prokhorov and Bochai [12] reported that ductility of a semi-solid alloy depends on the test temperature and follows a U-shaped profile, as schematically illustrated in Figure 6.

The decrease in the fracture strain (ductility) at the onset of the U-shaped profile occurred when low-melting temperature eutectics began to melt. The region designated as "BTR" represents the "Brittle Temperature Range", where an alloy had virtually zero ductility. The slight increase in ductility at temperatures above BTR was related to the local deformation of solid bridges extending between dendrites. Also, grain recrystallization possibly contributed to a marginal increase of alloy ductility at high temperatures [2].

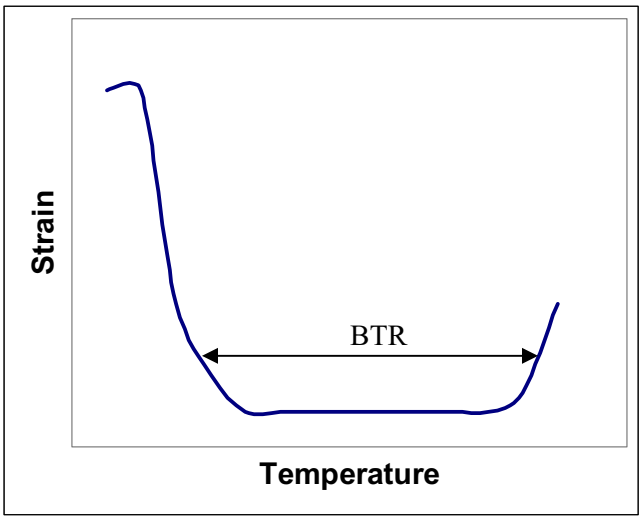

Figure 6: Alloy ductility as a function of temperature [12].

Novikov [14], Singer and Cottrell [19] and Pumphrey and Jennings [20] studied various aspects of deformation mechanisms in semi-solid alloys. With respect to alloy ductility, they concluded that intergranular grain sliding was the primary determinant of material deformation prior to fracture. The total intergranular sliding deformation, δ_{ig}, was related to the number of interfaces between two grains (i.e., the number of solid bridges between dendrites) and the alloy grain diameter via Equation 1 [14]:

$$\delta_{ig} = 0.6\Delta l / D \qquad (1)$$

Where:

Δl = relative displacement of two adjacent grains along common interface

D = average grain diameter

Therefore, it is expected that the semi-solid alloy ductility decreases with an increase in the average grain diameter. This prediction was empirically verified during studies with grain refiners, as observed in Figure 7. Grain growth (from fine equiaxed to coarse columnar) resulted in a decrease of alloy ductility, since columnar grains were not able to rotate or slide and the number of solid bridges was low. Thus, the total deformation in a coarse grained material was lower than in a fine grained material.

In materials subjected to slow cooling, grain growth was slow and homogeneous, resulting in a smooth grain surface. Despite the large grain size, the strain rate was sufficiently low and enabled sliding of grains. Thus, slow deformation rates enabled enhanced alloy ductility [14].

Precipitation of intermetallic compounds was also seen to influence alloy ductility. For example, Mukai *et al*. [21] investigated the effect of lithium on the ductility of AZ31 magnesium alloys. Mg-Li intermetallics formed on the (0001) basal planes of the hexagonal close-packed (HCP) crystals of the alloy matrix. These precipitates acted as barriers to basal dislocation slip, thereby affecting the bulk ductility of the alloy.

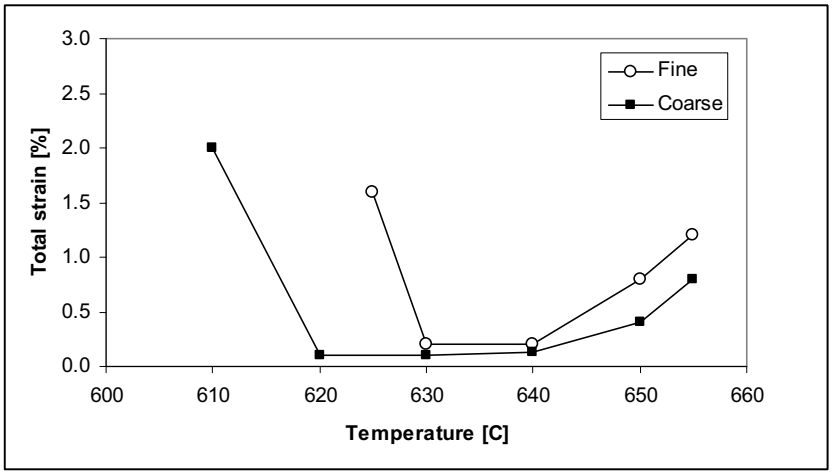

Figure 7: Effect of grain size on the ductility of Al-Cu alloy [1].

The semi-solid strength and ductility of alloys was shown to be of significant importance for the onset of material damage at elevated temperatures. As a result, development of hot tears is expected to be governed by similar factors as those influencing the alloy's elevated temperature mechanical response.

2.3 Hot Tearing

Hot tears are cracks forming in a semi-solid alloy prior to its complete solidification [4]. These cracks may be observed on the casting surface or in the casting interior [22]. Hot tearing has been observed in many engineering materials including steels, aluminum and magnesium alloys.

Formation of hot tears during casting solidification was generally attributed to two factors [5]:

1. When a casting region containing mushy alloy experiences insufficient feeding due to incorrect casting design; and,
2. When the mush zone within the casting experiences tensile loading. Tensile loads evolve in castings due to solidification shrinkage and thermal contraction, imposing a displacement incompatibility with surrounding geometries, such as steel molds, cores, inserts or gates used in intricate casting designs.

The above factors were considered by numerous researchers, who proposed the following theories describing the nucleation and propagation of hot tears:

1. Novikov [14] and Sigworth [4] suggested that hot tears nucleate above the solidus temperature and propagate through interdendritic liquid film.
2. Novikov and Novik [23] and Prokhorov [24] studied the relationship between alloy ductility and hot tearing. The results suggest that at low strain and cooling rates, grain boundary sliding is the main deformation mechanism. Thick eutectic liquid film and grain refinement were seen to delay the onset of hot tearing.
3. Pellini [25] suggested that hot tears nucleate at a casting's hot spot region if the accumulated strain at the hot spot reaches a critical strain value. This value depends on the strain rate and the alloy's cooling rate.
4. Clyne and Davies [9] proposed that the instantaneous strain rate determines the onset of hot tearing, rather than the total strain experienced during solidification. Their theory stipulated that hot tears formed if the casting deformation rate exceeded the deformation rate associated with solidification contraction not compensated by feeding.
5. Williams and Singer [26] and Petterson [27] suggested that hot tears nucleate when stress in the liquid surrounding grains reached a critical level.
6. Fredriksson *et al*. [28] speculated that hot tear formation was caused by supersaturation of vacancies created during the casting solidification process.
7. Monroe and Beckerman [22] suggested that if liquid feeding is not adequate to compensate the casting's solidification shrinkage, shrinkage porosity readily forms and may initiate a hot tear. The shrinkage pores form at high fractions of solid and propagate along the grain boundaries.

As expected from Section 2.1 and Section 2.2, the tensile strength and ductility of semi-solid alloys have a significant impact on the hot tearing susceptibility. Their effect on hot tearing, along with alloy characteristics and processing parameters, is discussed next.

2.3.1 Factors Affecting Hot Tearing

The hot tearing susceptibility of various alloys was observed to be a strong function of the alloy composition. A graph indicating the hot tearing susceptibility as a function of solute concentration is known as the λ-curve. An example of a λ-curve for Al-Mg alloy is presented in Figure 8.

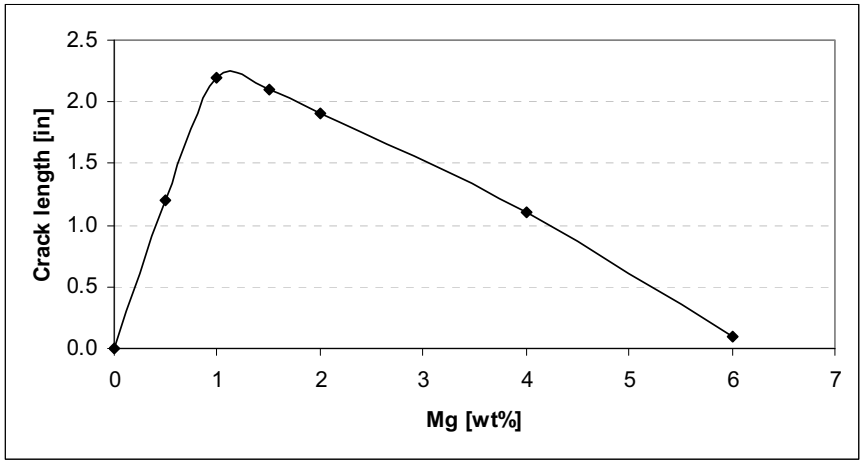

Figure 8: Al-Mg alloy λ-curve [1].

In Figure 8, the initial increase in the crack length (i.e., severity of hot tearing) with increasing solute concentration (from zero to approximately 1 wt%Mg) was related to the widening of the freezing range. The maximum hot tearing susceptibility coincided with the maximum freezing range of the alloy. Subsequent increase of solute concentration resulted in the formation of eutectic microconstituents, which extended interdendritic feeding at late stages of solidification and decreased the alloy's hot tearing susceptibility.

Suyitno *et al*. [29] investigated the hot tearing susceptibility of Al-Cu alloys with varying copper content (in the range of 1 – 3 wt%Cu). Their SEM observations revealed that increasing Cu concentration increased the amount of eutectics on cracked surfaces. They concluded that heavily alloyed systems preferentially fail and propagate hot tears along enriched grain boundaries due to the presence of low melting-temperature eutectics. Further, Suyitno *et al*. suggested that hot tears nucleated at grain triple-junctions, which were the last regions to solidify and contained high fractions of segregated solute.
A similar conclusion was reached by Sun [30], who studied hot cracking during welding of austenitic steels. Sun reported that eutectic liquid segregating at austenitic grain triple-junction boundaries nucleated hot tears.

Cao and Kou [31] studied the effect of various alloying elements on hot tearing in Mg-Al alloys during constrained rod casting. They demonstrated that pure metals, such as pure magnesium or aluminum, were not susceptible to hot tearing, as these metals did not exist as a two-phase mush during solidification. As a result, there was no liquid on the grain boundaries to facilitate grain boundary sliding and interdendritic feeding was not an issue. In the case of highly alloyed magnesium, abundant eutectic interdendritic liquid extended the duration of feeding and possibly healed incipient cracks. For intermediate solute

concentrations, the interdendritic liquid was sufficient to form thin continuous intergranular film along grain boundaries but was not able to heal nucleating hot tears.

Wang *et al*. [32] studied the influence of zinc (Zn) on the hot tearing susceptibility of Mg-9Al-xZn alloys. Their work indicated that the hot tearing susceptibility increased with increasing Zn concentration, since zinc decreased the solidus temperature of the alloy and decreased the solubility of Al in α-Mg phase. Zn was reported to increase the amount of brittle $Mg_{17}Al_{12}$ intermetallic phase on the grain boundaries, thus deteriorating the alloy's ductility [33].

Tang *et al.* [34] studied the effect of calcium (Ca) on the mechanical properties and hot tearing of magnesium alloys. Calcium increased the yield strength and ultimate tensile strength, while alleviating the hot tearing susceptibility of several alloys. This trend was due to the segregation of Ca at the α-Mg grain boundaries and subsequent precipitation of Al_2Ca intermetallic phases. Cao and Kou [33] also studied the effect of Ca on the hot tearing resistance in the Mg-xAl-yCa alloy system and reported a similar trend, as shown in Figure 9.

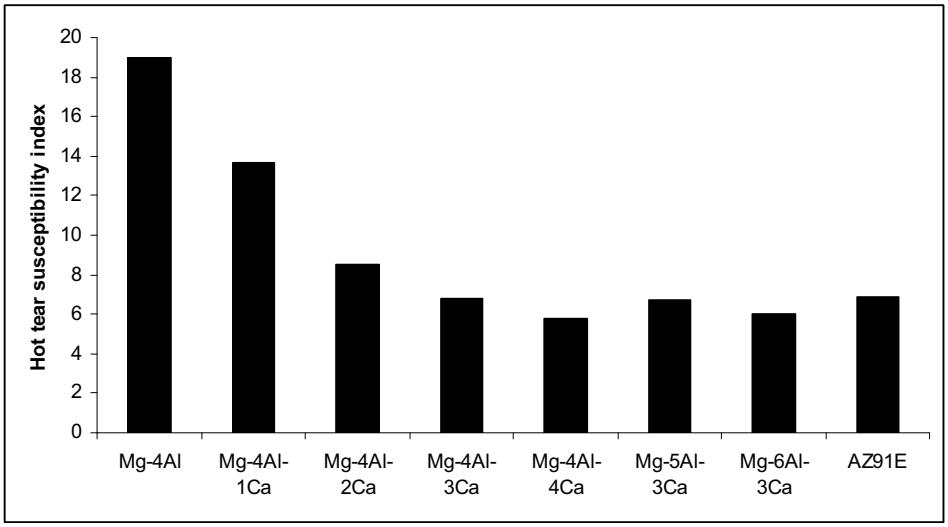

Figure 9: Effect of Al and Ca on hot tearing of Mg-xAl-yCa alloys [34].

Weichao *et al*. [35] showed that the hot tearing tendency of Mg-Al alloys significantly increased with the addition of rare earths (RE), especially in concentrations exceeding 1.2wt%RE. Rare earths caused grain coarsening, which lowered the fracture strain required for hot tear initiation. Further, RE shortened the time when interdendritic channels remained open (due to the precipitation of $Al_{11}RE_3$ intermetallics and their obstruction of interdendritic feeding). Similar results were reported by Pekguleryuz and

Vermette [36] who studied hot tearing of the AE42 (2wt%RE) and AE44 (4wt%RE) alloys cast via the permanent mold casting process.

Datta and Karunakar [37] studied the effect of grain refinement on the hot tearing susceptibility of Al-1wt%Sn alloy. Their results suggest that the addition of titanium-boride (Ti-B) grain refiner decreased the alloy's hot tearing susceptibility. Addition of nickel (Ni) further refined the grains and promoted a peritectic precipitation of Al-Sn-Ni rich phases, which pinned the α-Al grains. However, for all experimental conditions investigated, Datta and Karunakar concluded that grain refinement alone was not capable of completely eliminating hot tears.

2.3.2 Assessment of Hot Tearing

Hot tearing of alloys has been observed by foundrymen for many decades. Several experimental methods have been developed to replicate real-world casting conditions and observe the formation of hot tears [2].

Attempts to quantify the hot tearing susceptibility of alloys were less successful. For example, in order to determine the stress and strain conditions in the alloy during solidification, load cells, LVDT's and push-rods were installed in molds. However, these intrusive probes altered the natural casting solidification profile, thus making the final results questionable.

Theoretical criterion functions based on solidification theories were developed, along with computer models; however, validation of these theoretical criterion functions and computer models was successful only for simple casting geometries and a few alloys (e.g., iron plate castings). To this date, there is no universal formula relating the development of alloy strength to hot tearing [1, 2]. A discussion of the hot tear assessment methods and criterion functions developed to-date is presented next.

2.3.2.1 Ring Mold Test

This method was frequently used to perform qualitative comparison of the hot tearing susceptibilities of alloys. The set-up involved a ring mold, as shown in Figure 10, consisting of a steel core placed concentrically on a flat steel plate. Molten metal was poured into the ring cavity. During solidification, the core resisted the ring's solidification shrinkage and thermal contraction. Consequently, tensile stresses developed in the ring casting and hot tears formed on the ring's outer surface [23]. The frequency and length of observed hot tears was used as an indication of the alloy's hot tearing susceptibility. The limitation of this method was ascribed mainly to the difficulty of controlling the alloy solidification.

This test did not provide any information about the magnitude of stress or strain required for the initiation of hot tears [38].

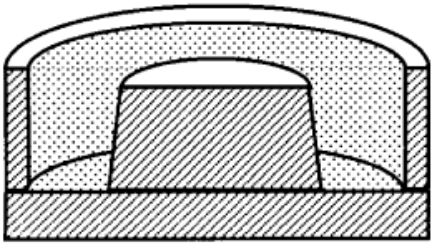

Figure 10: Ring mold [14].

2.3.2.2 Cold Finger Test

This method was developed by Warington and McCartney [39], who placed an internally tapered steel crucible with molten alloy into an open furnace, as illustrated in Figure 11. Subsequently, a water-cooled copper chill with a tapered conical tip was lowered into the molten metal. Upon allowing the metal to solidify, a casting with a 10 mm wall thickness was ejected from the crucible. Hot tears typically formed at the wider sections of the chill. The length of the observed hot tears was used as a measure of an alloy's hot tearing susceptibility, thus allowing relative comparison of various alloys tested by this technique.

2.3.2.3 Dogbone Mold Test

The dogbone mold test involved pouring a molten metal into an open-top mold consisting of a casting bar with two anchors at each end, as illustrated in Figure 12. As the casting bar solidified, its contraction was restricted by the two anchors and consequently tensile stresses developed in the casting bar. The length of hot tears forming in the casting bar was measured and used as an indicator of the hot tearing susceptibility of a given alloy.

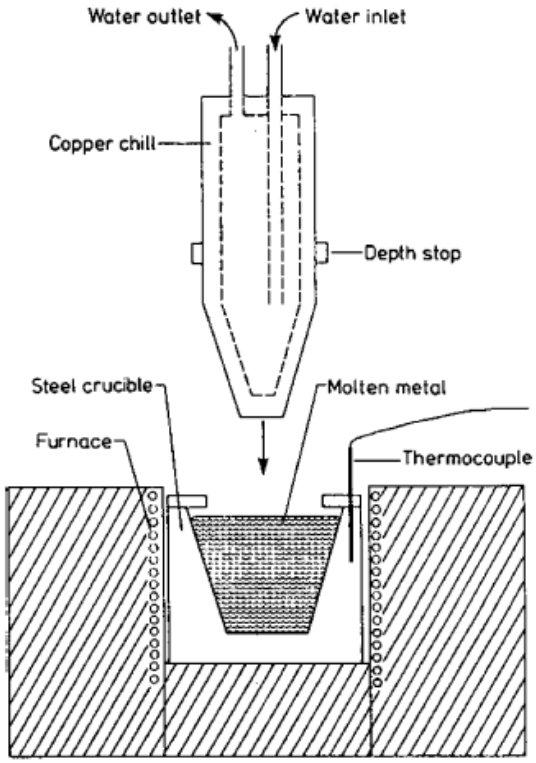

Figure 11: Cold finger test apparatus [39].

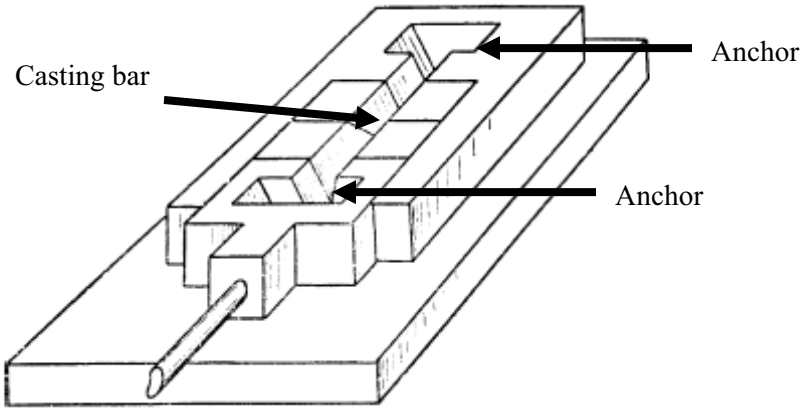

Figure 12: Dogbone mold test apparatus [14].

Novikov and Grushko [40] adopted the dogbone mold setup to a harp-type permanent mold with six bars of different lengths, as shown in Figure 13. As the length of the casting bar increased, its feeding became increasingly difficult and hot tearing of the bar was more likely. A hot tearing susceptibility index was developed based on the longest bar in which hot tears appeared.

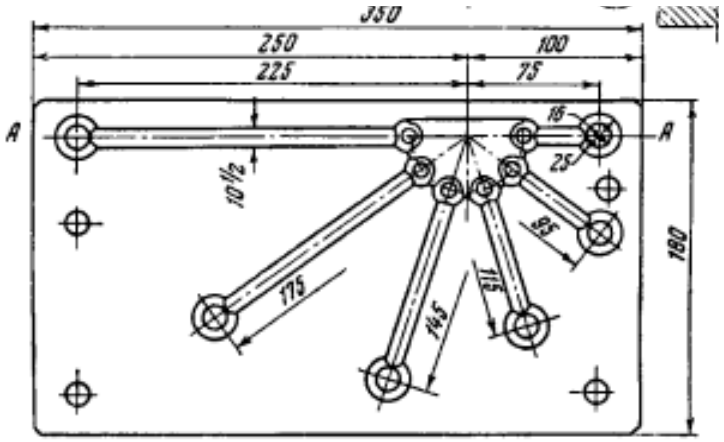

Figure 13: Casting length-type permanent mold (dimensions in 'mm') [40].

Cao and Kou [31] developed yet another variant of the dogbone mold. Instead of changing the length of the casting bars, Cao and Kou varied the diameter, while maintaining the length constant, as seen in Figure 14. A hot tearing susceptibility index was developed using the maximum diameter of a bar with a hot tear.

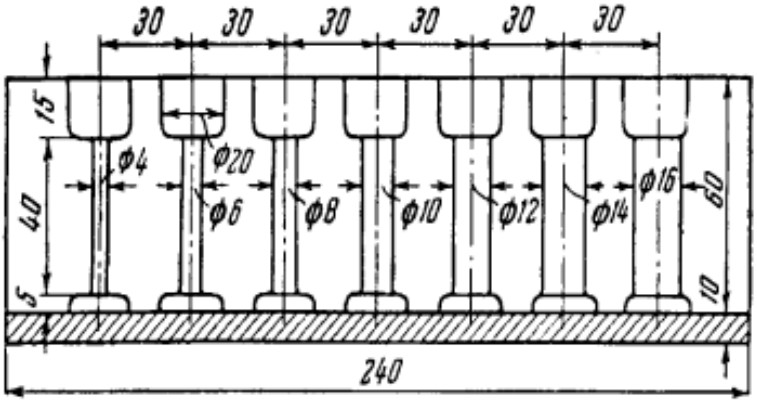

Figure 14: Casting diameter-type permanent mold (dimensions in 'mm') [31].

The experiments with the dogbone-type molds enabled relative comparison of different alloys subjected to various casting process conditions. However, these experiments did not provide quantitative data of the conditions (stress, strain or cooling rate) required for the onset of hot tearing.

2.3.2.4 In-Situ *Test*

Several attempts for *in-situ* observation of hot tear formation were reported in the literature. Pellini [25] used X-ray radiographs to observe hot tearing in Al-Cu alloys and reported that hot tears typically nucleated 5 – 15 °C above the solidus temperatures of the tested alloys.

Davidson *et al*. [41] developed a casting mold with a glass window in order to observe solidification of Al-Cu alloys. Their work revealed that the casting strength developed at about 90% solid fraction and hot tears formed at a solid fraction of 93%. The load associated with the initiation of hot tears was estimated to be 22 kPa. Based on their studies, Davidson *et al*. suggested that for a cavity between grains to open into a tear, one of two conditions must be satisfied: first, the pressure difference due to inhibited feeding of the mushy alloy must significantly increase; or, secondly, individual grains must be mechanically pulled apart. Davidson *et al.*'s work demonstrated that the conditions for the nucleation of hot tears were closely related to the development of the alloy's dendritic structure.

Farup *et al.* [42] observed the formation of hot tears in an organic succinonitrile-acetone, which upon solidification formed dendritic structure similar to that of Al alloys. The solution was placed between two sheets of pyrex glass and allowed to cool. Farup *et al.* identified secondary dendrite arm tips on cracked surfaces, suggesting that hot tears formed as interdendritic cavities in well developed dendritic structures. This observation affirmed the notion that hot tears nucleated at the end of solidification.

2.3.2.5 Hot Tearing Criterion Functions and Predictive Models

There were several attempts to predict the onset of hot tearing *a priori* for a given casting geometry, process parameters and alloy properties. These theoretical models considered stress, strain and feeding as the critical parameters contributing to the initiation of hot tearing.

2.3.2.5.1 Stress-based Criteria

The stress-based criteria of hot tearing suggest that material failure occurs when the induced stress in the material exceeds the alloy's ultimate tensile strength [1]. There were two approaches to estimate the critical (failure) stress in an alloy.

2.3.2.5.1.1 Stress-based Criteria Considering the Bulk Strength of an Alloy

Novikov [14] and Dickhaus *et al*. [43] modeled their criteria to estimate the stress required to pull apart two parallel grain boundaries separated by a liquid film of uniform thickness, b. The model assumed negligible viscosity of the liquid. Also, wetting of the liquid was assumed to be perfect. The fracture stress, σ_{fr}, was calculated as:

$$\sigma_{fr} = 2\gamma / b \tag{2}$$

Where:

γ = liquid film surface tension

The film thickness was related to the average grain diameter, D, and fraction of solid, f_s, via:

$$b = \frac{(1 - f_s)D}{2} \tag{3}$$

This model did not enable accurate modeling of the stresses required for nucleation of hot tears, since it did not consider grain boundary sliding (which has been demonstrated to impact high temperature deformation and hot tearing of alloys). Further, the liquid film thickness between grains is rarely uniform. Therefore, further modification of this approach was attempted by Healy [44], who included the melt dynamic viscosity, μ, and calculated the force, F_z, required to separate spherical grains of radius R, separated by liquid film of thickness b.

$$F_z = \frac{3\pi\mu R^4}{8t_{b1-b2}}\left(\frac{1}{b_1^2} - \frac{1}{b_2^2}\right) \tag{4}$$

Where:

$t_{b1\text{-}b2}$ = time required to increase the film thickness from b_1 to b_2

Lahaie and Bouchard [45] further carried this approach by considering solid fraction, strain, ε, and microstructure parameter, ψ, in their model:

$$\sigma_{fr} = \frac{4\mu}{3b}\left(1 + \left(\frac{f_s^{\psi}}{1 - f_s^{\psi}}\right)\varepsilon\right)^{-1} \tag{5}$$

This equation was applied to equiaxed and columnar grains by adjusting ψ. The ability of Lahaie and Bouchard's model to predict the fracture stress required to trigger hot tearing was strongly dependent on the calculation of fraction of solids. Upon rearrangement, this model did not correctly predict the effect of grain diameter on the expected fracture strength. Also, strain prediction was not accurate, since calculated strain values did not follow the U-shaped dependence of ductility on the temperature, as documented in the literature (viz Section 2.2.2).

2.3.2.5.1.2 Stress-based Criteria Considering the Strength of the Liquid Film between the Grain Boundaries

Stress-based criteria relating the failure of a semi-solid alloy to the presence of a liquid film between grains were proposed by Williams and Singer [26]. The authors argued that the liquid phase present just before completion of solidification was the weakest point in the semi-solid alloy. The fracture stress was defined as:

$$\sigma_{fr} = \sqrt{\frac{8G\gamma_{fr}}{\pi(1-\nu)A_g V_L^{1/2}}} \tag{6}$$

Where:

A_g = constant dependent on grain size and grain dihedral angle

G = shear modulus ν = Poisson's ratio

γ_{fr} = effective fracture surface energy V_L = volume of liquid

The equation was modified based on empirical data as follows to include grain boundary sliding, which is known to affect hot tear growth:

$$\sigma_{fr} = \sqrt{\frac{16\gamma_{fr}G}{\pi(1-\nu)}\left[\frac{1}{0.07D + 0.47AV_L^{1/2} + 0.37D^{1/2}V_L^{1/4}}\right]} \tag{7}$$

Comparison of experimental data and predicted values from Equation 7 is shown in Figure 15. A good correlation between experimental and calculated values of fracture stress was demonstrated for various Sn concentrations in Al-Sn alloys. The effect of the grain size on the fracture stress calculated using the model is shown in Figure 16 and it was observed that the decrease of the grain diameter causes an

increase in the fracture stress. Therefore, this model shows promising results, but its validation for other alloys and a range of cooling rates is yet to be carried out.

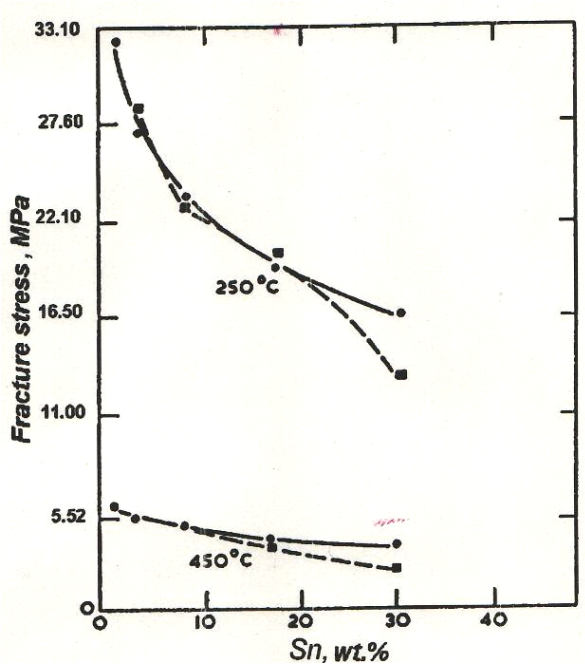

Figure 15: Experimental (solid) and computed (dash) values of fracture stress in Al-Sn alloys [1].

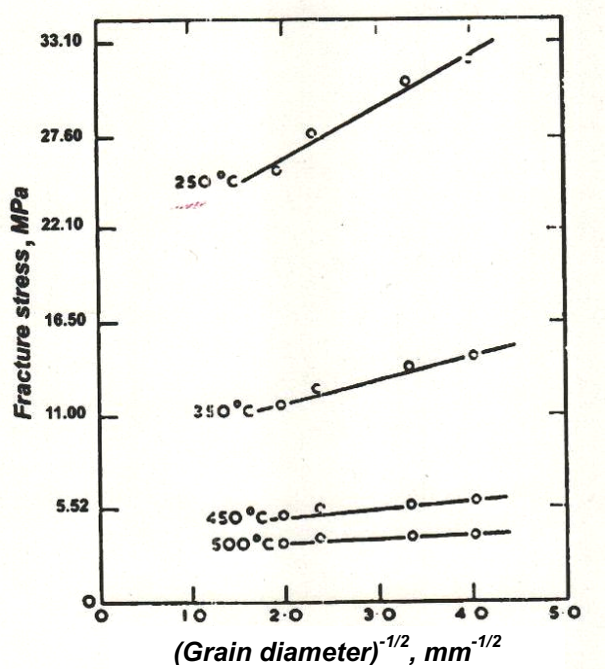

Figure 16: Effect of grain size on the fracture stress of an Al-8.4% Sn alloy [1].

2.3.2.5.2 Strain-based Criteria

Metz and Flemings [13] attempted to relate the onset of hot tearing to the material's deformation. They observed that the fracture shear strain decreased with the increasing strain rate. They explained this phenomenon by assuming formation of solid agglomerates in the melt at the onset of solidification. When the alloy slurry was sheared at a very low rate, the agglomerates rearranged in order to accommodate the imposed strain. At higher strain rates, the rearrangement was more difficult and agglomerate fragmentation occurred. The instance of agglomerate fragmentation was identified as the onset of material plastic damage.

To incorporate strain into a criterion function, Novikov [14] proposed a quantity called the "reserve of plasticity in the solidification range" given by Equation 8. The reserve of plasticity, p_r, was related to S_{pr}, defined as the difference between the average integrated value of the alloy ductility (ε_p) and the linear shrinkage/contraction (ε_{sh}) in the brittle (vulnerable) temperature range (ΔT_{br}), as indicated in Figure 17 [14].

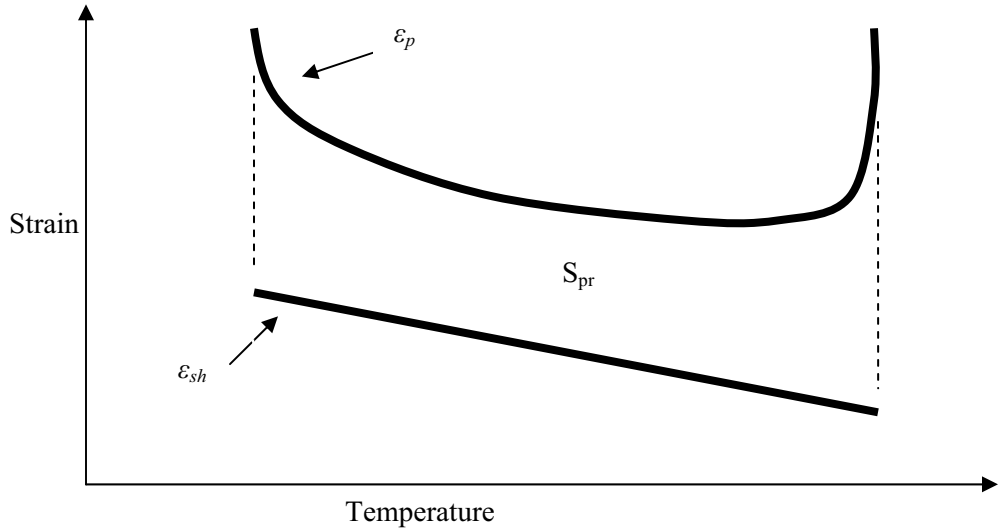

Figure 17: Relationship between ε_p and ε_{sh}.

The reserve of plasticity based on the ε_p and ε_{sh} values was given by:

$$p_r = \frac{S_{pr}}{\Delta T_{br}} \tag{8}$$

Zhao *et al*. [46] tested this model for hot tearing prediction in Al–4.5wt%Cu alloy. They converted the calculated stress to strain required for the formation of a hot tear. This strain was compared to the ductility measurements presented by Magnin *et al*. [47] and reasonable agreement was observed. Zhao *et al.* concluded that hot tears nucleated in the temperature range where the alloy's ductility was lower than the strain induced by solidification shrinkage.

2.3.2.5.3 Strain Rate-based Criteria

Strain gradients develop in geometrically complex castings due to non-homogeneous temperature distribution and subsequent non-homogeneous casting contraction.

The first approach to model evolution of strain gradients during casting solidification was undertaken by Rappaz, Drezet and Gremaud [5]. The RDG criterion considers the limited mush permeability during solidification. At the solidification front, the mush permeability was considered to be high, but decreased deeper in the mushy zone, thus establishing a pressure gradient in the mushy zone. If this pressure gradient exceeded a critical cavitation pressure, a pore nucleated. As a result, the RDG criterion, calculated by solving Equation 9, predicts the appearance (initiation) of interdendritic cavities, which may possibly lead to hot tears. In this regard, the RDG criterion resembles functions developed for the prediction of shrinkage porosity.

$$\frac{d(f_l v_{liq})}{dx} + (1+\beta) f_s \dot{\varepsilon}_p - v_\tau \beta \frac{df_s}{dx} = 0 \qquad (9)$$

Where:

f_l = fraction of liquid

$\dot{\varepsilon}_p$ = deformation rate in the solid

v_{liq} = liquid metal velocity

v_τ = solidification velocity

β = shrinkage factor

By solving Equation 9, a critical deformation rate, $\dot{\varepsilon}^{\max}$, was calculated for the nucleation of a cavity. The hot cracking susceptibility (HCS) was subsequently expressed as Equation 10:

$$HCS = 1/\dot{\varepsilon}^{\max} \qquad (10)$$

Suyitno *et al*. [48] derived a model similar to the RDG criterion. Their function was based on cavity formation due to volume changes caused by localized shrinkage. Further, Suyitno *et al.* included "external' strain rates imposed on the mushy alloy. In their model, a cavity nucleated when a critical cavity dimension was exceeded. Experimental validation of the RDG and Suyitno's criterion functions is in progress.

2.3.2.5.4 Thermal Analysis-based Criteria

These criteria are based on interdendritic feeding and microstructure evolution during solidification. Thus, these functions do not explicitly consider stress or strain conditions in the material during solidification.

Clyne and Davies [9] developed a hot tearing criterion model recognizing the fact that liquid can not move freely during the last stage of solidification. Therefore, strain developing in the alloy at the end of solidification cannot be accommodated by mass feeding and formation of interdendritic porosity is likely. A hot cracking susceptibility index, Equation 11, was formulated as the ratio between the vulnerable time period when cavitation is likely, t_v, and the time available for stress-relief to occur (when mass feeding and liquid feeding are possible), t_r :

$$HCS = \frac{t_v}{t_r} = \frac{t_{99} - t_{90}}{t_{90} - t_{40}} \tag{11}$$

Where:

t_{99} = time at $f_s = 0.99$

t_{90} = time at $f_s = 0.90$

t_{40} = time at $f_s = 0.40$

The use of this criterion remains very limited, as it only indicates the hot tearing tendency of an alloy based on its solidification characteristics. Further, required fractions of solid can be calculated via several models, thereby resulting in different values of HCS for a given alloy.

Thermal analysis was used to develop additional criteria. For example, Niyama [49] stipulated that hot tears nucleate due to the lack of fluid flow through the mushy dendritic structure, since insufficient fluid flow disrupts the continuity of the liquid phase and forms cracks. Feurer [50] used this concept to derive a

criterion function predicting the onset of hot tearing when a critical strain rate is achieved and the liquid can not feed interdendritic regions during deformation. In addition, Feurer included the alloy's composition, solidification conditions, secondary dendrite arm spacing and solidification shrinkage in his model by considering two terms:

1. The maximum volumetric flow rate through the dendritic network (per unit volume), *SPV*, given by Equation 12, and
2. The velocity of volumetric solidification shrinkage, *SRG*, given by Equation 13, which related the density difference between the solid and liquid phases.

$$SPV = \frac{f_l^2 (DAS)^2 P_s}{24\pi c^3 \mu L_{SPV}{}^2} \tag{12}$$

Where:

DAS = secondary dendrite arm spacing
μ = viscosity of liquid melt
P_s = effective feeding pressure
L_{SPV} = length of porous network
c = tortuosity constant

$$SRG = \left(\frac{\partial \ln V}{\partial t} \right) = -\frac{1}{\overline{\rho}} \frac{\partial \overline{\rho}}{\partial t} = \frac{(\rho_o - \rho_s + akC_l)\dot{T} f_l^{(2-k)}}{\overline{\rho}(1-k) m_l C_o} \tag{13}$$

Where:

ρ_o = bulk alloy density
a = composition coefficient of liquid density
ρ_s = alloy density at solidus temperature
C_l = comp. of liquid at the S-L interface
ρ_l = alloy density at liquidus temperature
C_o = nominal alloy comp.
$\overline{\rho}$ = average density
k = equilibrium redistribution coefficient
m_l = slope of the liquidus line
$\dot{T}$ = average cooling rate during solidification of the primary solid phase

The Feurer criterion suggests that hot tearing occurs for conditions when SPV<SRG, as graphically indicated in Figure 18. The difficulties in using this criterion function arise due to estimation of the parameters P_s, L_{SPV} and c in Equation 12; thus, additional research needs to be carried out to accurately quantify these parameters.

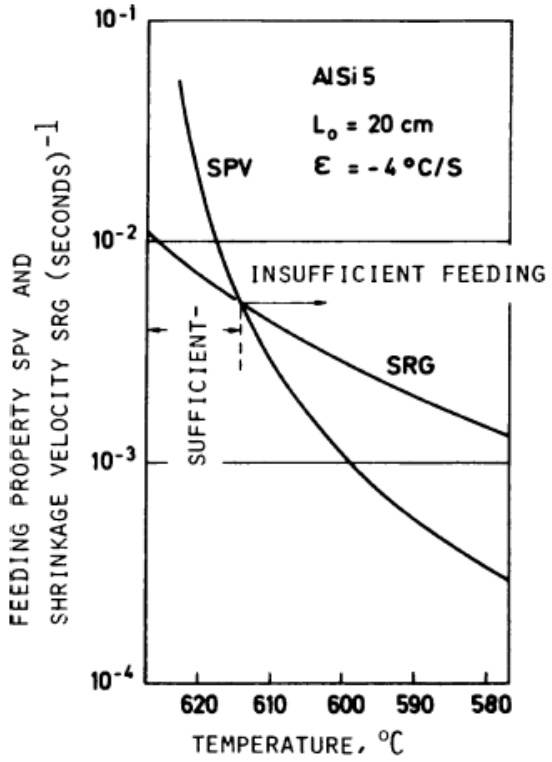

Figure 18: Plot of SPV and SRG obtained from Feurer's hot tearing criterion [50].

2.3.2.6 Software Modeling of Hot Tearing

At the time of writing this dissertation, modeling of hot tearing using commercial simulation software has reached only limited success. Progress has been made for steel castings; however, hot tear prediction in Al or Mg alloys remains difficult.

Schneider and Andersen [51] attempted to use MAGMASOFT® simulation software for analysis of hot tearing susceptibility in steel castings. Their aim was to develop a numerical hot tearing criterion function to indicate casting areas at risk for hot tearing. They included MAGMASOFT's built-in functions to estimate thermal convection and macrosegregation in calculating concentration gradients in a casting.

Their work concluded that prediction of hot tear initiation was very complex and required experimentation to validate MAGMASOFT®'s simulated results. Further, they suggested that prediction of hot tearing must couple stress/strain and heat transfer analyses of the solidifying casting along with macrosegregation phenomena. The stress/strain must provide information about residual stresses and distortions that evolve during solidification and subsequent cooling of the casting. Due to the lack of experimental validation, their modeling yielded only partial results.

Typically, commercially available computer modeling packages, such as MAGMASOFT®, ProCast® or EKK®, enable the user to specify a criterion function for the onset of hot tearing (e.g., one of the criteria discussed in the previous section). However, the resulting predictions are only as accurate as the criteria used.

Chapter Summary

The literature review suggests that hot tearing in alloys is a complex phenomenon. The onset of hot tearing is influenced by stress, strain and solidification conditions. Microstructure evolution (affected by solidification) was seen to play a key role on casting feedability, porosity formation and hot tear nucleation. Criterion functions were developed in an effort to predict the onset of hot tearing. However, many of the functions modeled hot tearing by considering a single factor, thus neglecting interactions from other contributing factors. As a result, conditions required for the onset of hot tearing in many alloys remain unknown. In order to advance the understanding of hot tearing in these alloys, a novel approach to characterize casting stress, strain and solidification is necessary. With this consideration, the current research implemented neutron diffraction experiments to quantify the stress and strain evolving in a casting at the onset of hot tearing. The theory of neutron diffraction is discussed in the following chapter.

Chapter 3 – Theory of Neutron Diffraction

Neutron diffraction (ND) is one of several techniques used to determine the atomic or crystal structure of matter. Neutrons, along with protons and electrons, are the primary constituents of atoms. In order to carry out neutron diffraction analysis, neutrons must be separated from their source atoms and collimated to form a beam. Subsequently, this beam of neutrons is used as a measurement probe.

The advantage of using neutrons as a measurement probe can be attributed to their ability to penetrate furnaces, cryostats, pressure vessels and other testing equipment, so as to determine material properties under precisely controlled environments. Further, the sampling volume used in ND may be up to several cm^3, thus enabling measurement of sample's bulk properties.

The fundamental theory of neutron extraction, laws governing neutron diffraction in a material and finally the use of neutron diffraction to measure residual stresses are outlined in the following sections.

3.1 Neutron Sources

There are several neutron sources available for laboratory-scale diffraction experiments. These sources include radioisotopes, light-ion accelerators and plasma focus generators. These sources, however, provide only medium-grade neutron flux, which is often below that required for meaningful analysis of engineering materials. As a result, the most practical sources of neutrons remain nuclear spallation sources and nuclear reactors. In a nuclear spallation source, such as a synchrotron accelerator, high energy protons hit a target material prompting the emission of neutrons [52].

In a nuclear reactor, neutrons are created in a fission process, which involves the collision of a free neutron (n^0) with a uranium ^{235}U atom. After absorbing the neutron, the new unstable ^{236}U isotope breaks down into two smaller elements and three additional neutrons. Typically, the two elements are ^{141}Ba and ^{92}Kr. This fission process is illustrated schematically in Figure 19. The three new neutrons can either proceed to initiate a new fission reaction (i.e., a chain reaction) with ^{235}U atoms, or they can be absorbed in the moderator of the nuclear reactor.

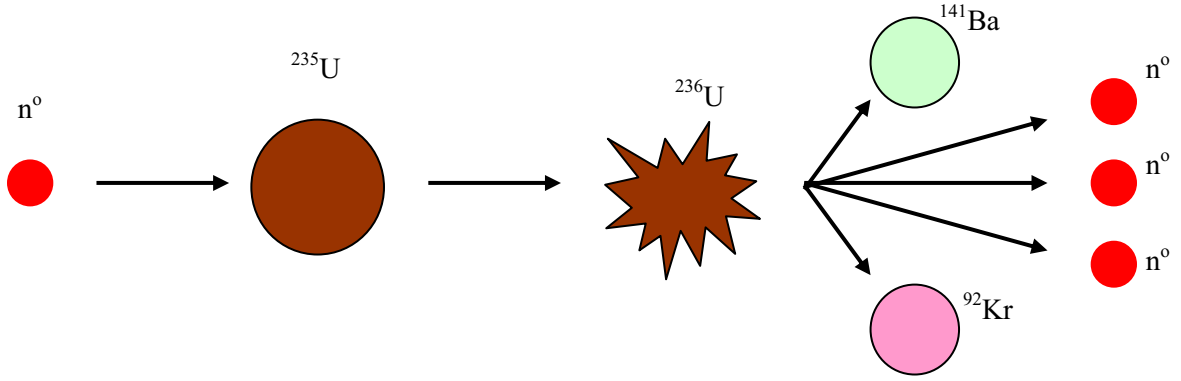

Figure 19: Schematic illustration of a nuclear fission reaction.

Neutrons, like other quantum particles, exhibit wave-particle duality and behave either as particles or as waves. Thus, phenomena of scattering or diffraction may be observed. The basic properties of neutrons are given in Table 1 [52]:

Table 1: Basic properties of a neutron.

Mass, m_n	1.675 x 10^{-27} kg
Electric charge, C_n	0
Spin	½
Magnetic dipole moment, μ_n	-1.913 J/T

As indicated in Table 1, neutrons do not have an electric charge. Consequently, when a neutron encounters a foreign atom, it does not interact with the atom's electron cloud (like X-rays). As a result, only the interference between the neutron and an atom's nucleus may change the neutron's trajectory. Consequently, neutrons are able to penetrate deep into a material. By considering neutrons to behave as waves, the concepts of wave diffraction may be applied to measure residual strains.

3.2 Neutron Diffraction

Neutron diffraction occurs when neutrons are considered to behave as a series of waves, rather than a stream of particles.

The deBroglie wavelength of a neutron beam, λ_n, depends on the neutron's velocity, v_n, and is given by [52]:

$$\lambda_n = \frac{h}{m_n v_n} \tag{14}$$

Where:

m_n = mass of a neutron

h = Planck's constant (6.626068×10^{-34} m^2 kg / s)

In a nuclear reactor, a range of neutron wavelengths are produced at the same time. These "white" neutrons must be channeled into a spectrometer. A schematic representation of a triple-axis spectrometer is presented in Figure 20. The functions of the key spectrometer components are:

1. Monochromator – a disc made of a single crystal used to extract a single wavelength of neutrons from the beam of "white" neutrons.
2. Monochromator shielding drum – absorbs undesirable "white" neutron beam wavelengths and stray radiation emanating from the nuclear reactor.
3. Incident beam collimator – provides a path for a beam of neutrons of a desired wavelength to exit the monochromator shielding drum and interact with the sample.
4. Sample stage.
5. Diffracted beam collimator – provides a path for the diffracted neutron beam to enter the analyzer.
6. Diffracted beam analyzer – measures the angular position and intensity of diffracted neutrons.

When neutron waves encounter diffraction centers (i.e., atoms in a crystal lattice), interference patterns may be produced. These interference patterns are well defined when the order of magnitude of the neutron wavelength is comparable to the spacing of the sample's crystal lattice.

Calculation of elastic strain is carried out using the peak-shift method based on the Bragg's law of diffraction. The law states that in order for diffracted rays to emerge from a test sample and form a well defined pattern, the emerging rays must be in phase with each other and result in constructive interference. Otherwise, the intensity of the diffracted beam is minimal due to destructive interference of individual diffracted rays.

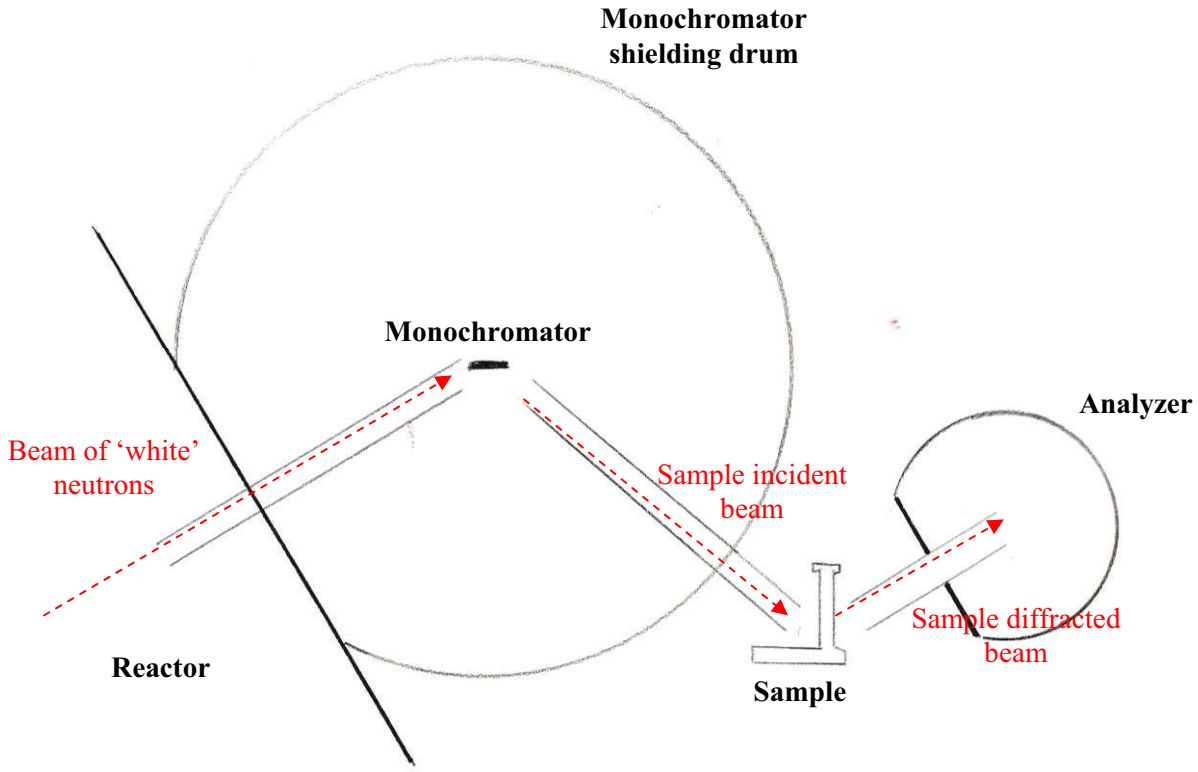

Figure 20: Schematic illustration of a triple-axis spectrometer.

The derivation of Bragg's law considers a monochromatic incident ray of neutrons entering the sample, as shown in Figure 21. The majority of the incident neutrons are transmitted through the sample. However, neutrons which interact with atoms located along certain (*hkil*) crystallographic planes of the sample will form a diffracted ray #1. Similarly, subsequent neutrons may interact with adjacent (*hkil*) planes and form a diffracted ray #2. The spacing between the adjacent (*hkil*) planes is designated as d_{hkil}. The Bragg diffraction angle, θ_b, of ray #1 or ray #2 may be precisely measured with a diffracted beam analyzer.

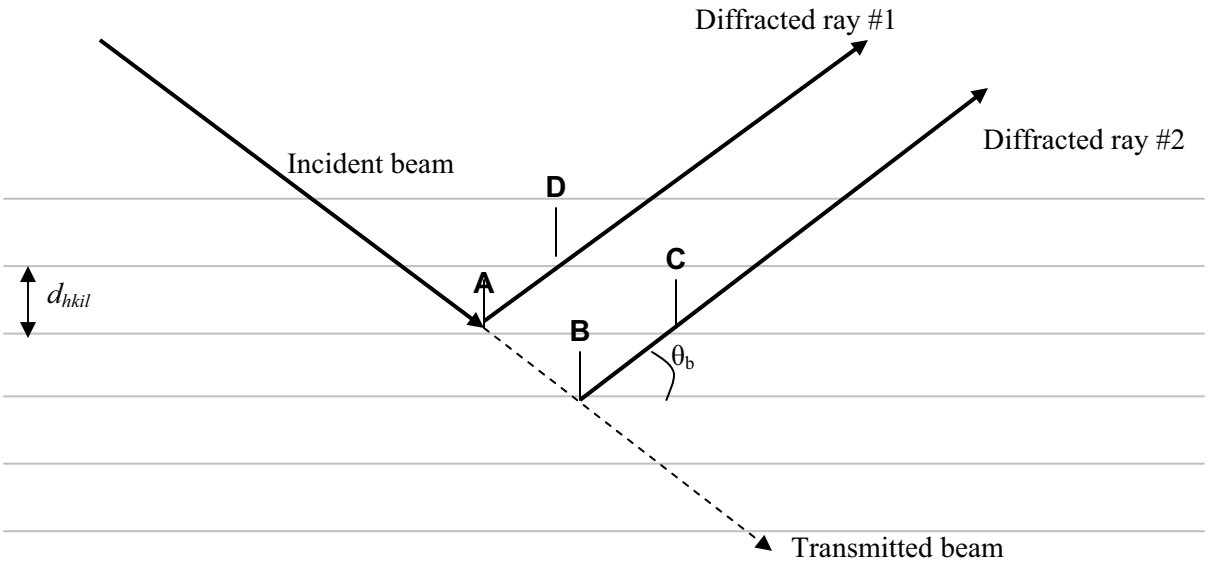

Figure 21: Bragg's diffraction.

Considering the two diffracted rays, there will be a path difference between them, since ray #2 has to travel additional path from A→B and B→C compared to diffracted ray #1. In order to maintain constructive interference between diffracted rays #1 and #2, the path difference must remain an integer multiple of the incident beam wavelength. Thus:

$$(AB + BC) - (AD) = n\lambda \tag{15}$$

Where:

n = integer

From the Pythagorean theorem, the distances in Equation 15 are as follows:

$$AB = BC = \frac{d_{hkil}}{\sin(\theta_b)} \tag{16}$$

$$AC = 2\frac{d_{hkil}}{\tan(\theta_b)} \tag{17}$$

$$AD = AC\cos(\theta_b) = 2\frac{d_{hkil}}{\tan(\theta_b)}\cos(\theta_b) \tag{18}$$

Substituting these expressions in Equation 15 and using identities for sinusoidal functions:

$$n\lambda = \frac{2d_{hkil}}{\sin(\theta_b)} - \frac{2d_{hkil}}{\tan(\theta_b)}\cos(\theta_b) = \frac{2d_{hkil}}{\sin(\theta_b)}(1-\cos^2(\theta_b)) = \frac{2d_{hkil}}{\sin(\theta_b)}\sin^2(\theta_b) \quad (19)$$

Which can be simplified to yield Bragg's law:

$$n\lambda = 2d_{hkil}\sin(\theta_b) \quad (20)$$

Equation 20 describes the fundamental relationship between the neutron beam wavelength, lattice spacing and the angle of diffracted neutrons. In this equation, two of the three parameters are typically known. Therefore, Bragg's law enables the determination of the diffraction angle (e.g., for phase identification), or the neutron beam wavelength (e.g., for wavelength calibration experiments) or the lattice spacing (e.g., for lattice strain measurement). The determination of lattice spacing is the fundamental principle of elastic residual strain measurement in crystalline materials.

3.3 Measurement of Residual Strains and Stresses via Neutron Diffraction

In general, residual stresses evolve in a material due to inhomogeneous deformation. A residual stress is the auto-equilibrating stress that exists in a material at equilibrium or in a material at a constant temperature [53]. Residual stresses can be introduced into materials via several routes: mechanical (e.g., machining, shot peening), thermal (e.g., heat treatment, laser treatment), thermomechanical (e.g., forging, welding) or thermochemical (e.g., carburizing, nitriding) [54].

In casting applications, residual stresses arise due to non-uniform temperature of different parts of a casting during solidification and cooling. To illustrate the development of residual stresses, a stress-lattice, shown in Figure 22, can be used.

The thinner sections of the stress lattice cool faster than the thicker section and begin to thermally contract. This contraction is opposed by the thicker section. Subsequently, tensile stresses develop in the thin sections. At high temperatures, where the yield stress of a material is low, thermal stresses are relieved by plastic deformation. The highest stresses and plastic deformation occur when the temperature difference between faster and slower cooling areas (i.e., thick and thin sections) is at a maximum ($t=t_1$).

As cooling proceeds, the temperature difference between the two casting sections decreases. This initially leads to stress relief (i.e., reduction in tensile stress in the thin sections) and then to a change in the stress state from tensile to compressive. Conversely, in the slower cooling (thick) section, the initially compressive stress may reverse to tensile. Upon cooling to room temperature, $t=t_2$, compressive residual stresses exist in the thin sections and tensile residual stresses in the thick section [55].

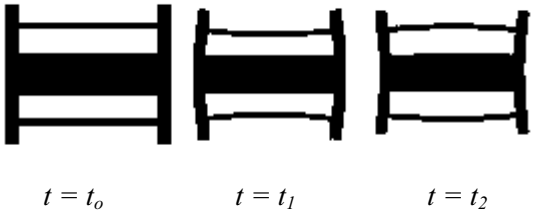

Figure 22: Development of residual stresses in a casting with thin and thick walls [55].

Elastic residual stresses and strains can be measured using neutron diffraction. First, however, elastic residual strains must be measured in a material sample where residual strains were relieved (either by machining, heat treatment, etc.). Determination of lattice spacing in this sample yields the value of the stress-free lattice spacing, $d_{o\text{-}hkil}$.

For classical residual strain measurements, the order of diffraction is typically unity; however, higher order reflections can be also analyzed. The Bragg diffraction angle is directly measured with a diffracted beam analyzer. Hence, the lattice spacing for the sample of interest, d_{hkil}, may be determined from Bragg's law.

When a material is subjected to a tensile load, the lattice spacing increases in the tensile loading direction with respect to its stress-free value. Similarly, the lattice spacing decreases for compressive loads. The strain, ε_{hkil}, experienced by the material's *(hkil)* planes can be expressed using the peak-shift method as:

$$\varepsilon_{hkil} = \frac{d_{hkil} - d_{o-hkil}}{d_{o-hkil}} \tag{21}$$

For an isotropic material, the relationship between stress and strain in orthogonal Cartesian (*x, y,* and *z*) coordinate system is given by the generalized form of Hooke's law [56]:

$$\sigma_\alpha = \frac{E}{1+\nu}\left[\varepsilon_\alpha + \frac{\nu}{1-2\nu}\left(\varepsilon_x + \varepsilon_y + \varepsilon_z\right)\right] \qquad \alpha = (x, y, z) \tag{22}$$

Where:

ε_x = strain in x-direction

ε_y = strain in y-direction

ε_z = strain in z-direction

The value of the elastic constants, i.e., Young's modulus, E, and the Poisson's ratio, ν, can be measured via *in-situ* tensile tests under the neutron beam. When these elastic constants can not be determined *in-situ*, Young's modulus and Poisson's ratio of the bulk material may be used [56]. Single-crystal studies indicate that the error associated with using bulk elastic constants instead of reflection-specific constants is approximately 10% [57].

Measurement of residual strains over a sample is accomplished by translating the sample in the neutron beam.

Chapter Summary

Neutron diffraction is capable of quantifying the elastic residual stresses and strains in a crystalline sample. The measurements are non-destructive and do not interfere with the sample's manufacturing process. As a result, unique data based on the material's bulk properties may be obtained. ND provides direct measurement of physical state of the material. That is, the measured material properties are not approximated or modeled.

Chapter 4 – Experimental Procedure

This chapter presents a detailed description of the experiments carried out in this research. First, the development of the permanent mold to study hot tearing is discussed, followed by a description of casting trials. A description of neutron diffraction experiments is also presented. Alloy microscopy techniques and sample preparation are described. The chapter concludes with a brief description of MAGMASOFT® simulation parameters.

4.1 Permanent Mold Design

The permanent mold was designed with the intent of inducing hot tears in castings. As a result, the mold included features such as sharp corners, casting section thickness transitions and a long casting section with a single feeding channel. All of these features are known to promote the formation of hot tears due to the formation of stress concentrations, deformation (strain) gradients and inhibited casting feeding.

The casting geometry was inspired by the dogbone design (Section 2.3.2.3) currently used in the industry. However, unlike the traditional designs, the current mold had only a single horizontal bar, in order to minimize effects of molten metal mass flow variation during filling. Further, the mold was designed as a single-cavity mold, rather than a centre-split mold with two halves. This feature enhanced the repeatability of casting results, since mold-misalignment, which potentially contributes to the variation of casting stress distribution, was avoided. The casting geometry was designed such that the modulus of the downsprue (V/A) was 1.5 times that of the horizontal bar according to Chvorinov's rule.

In order to avoid entrapment of mold gases in the casting cavity and also to provide an escape path for air in the casting cavity, three vent slots were machined into the face of the mold. These rectangular slots extended from the horizontal cavity to the top surface of the mold, as seen in Figure 23.

The permanent mold was machined from a block of hot-rolled H-13 premium tool steel with dimensions of 415 x 240 x 50 mm. The block was mounted into a CNC milling centre (Dept. of Mechanical and Industrial Engineering, Ryerson University) and milled flat and square. Subsequently, the casting cavity was milled with 12.7 mm (1/2") high speed steel mill. Machining parameters (i.e., feed rate, tool speed and depth of cut) as specified in Reference 58 for the H-13 steel were followed. An isometric view of the mold is shown in Figure 23. The final dimensions of the casting cavity and the mold geometry are indicated in Figure 24 - Figure 27.

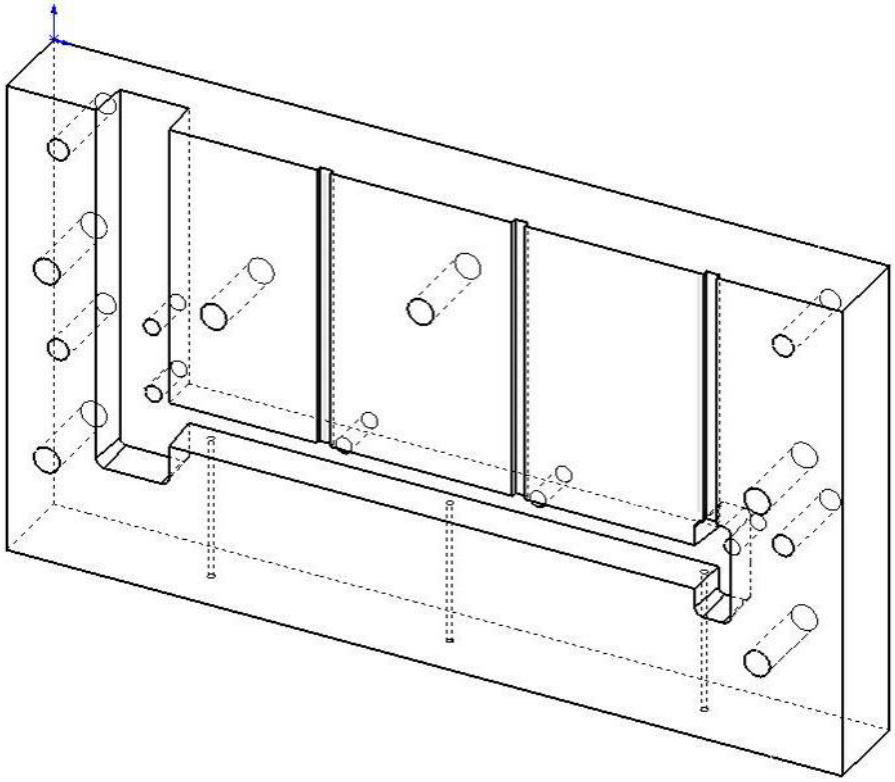

Figure 23: Isometric view of the permanent mold.

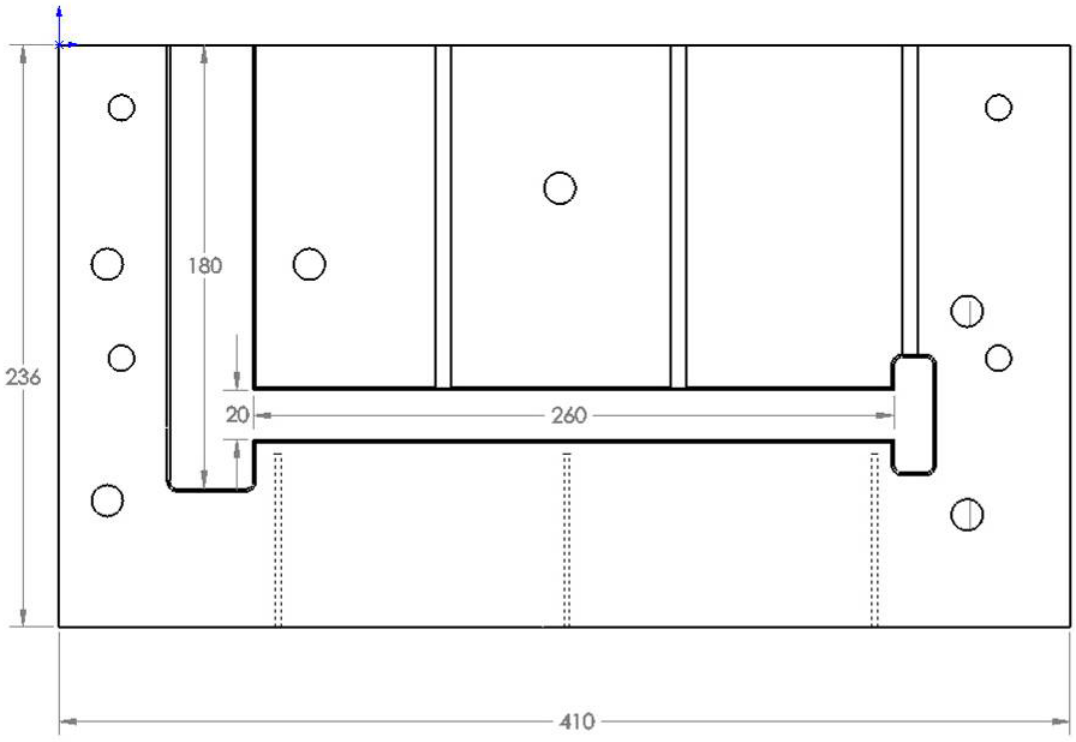

Figure 24: Dimensions of casting cavity (in 'mm').

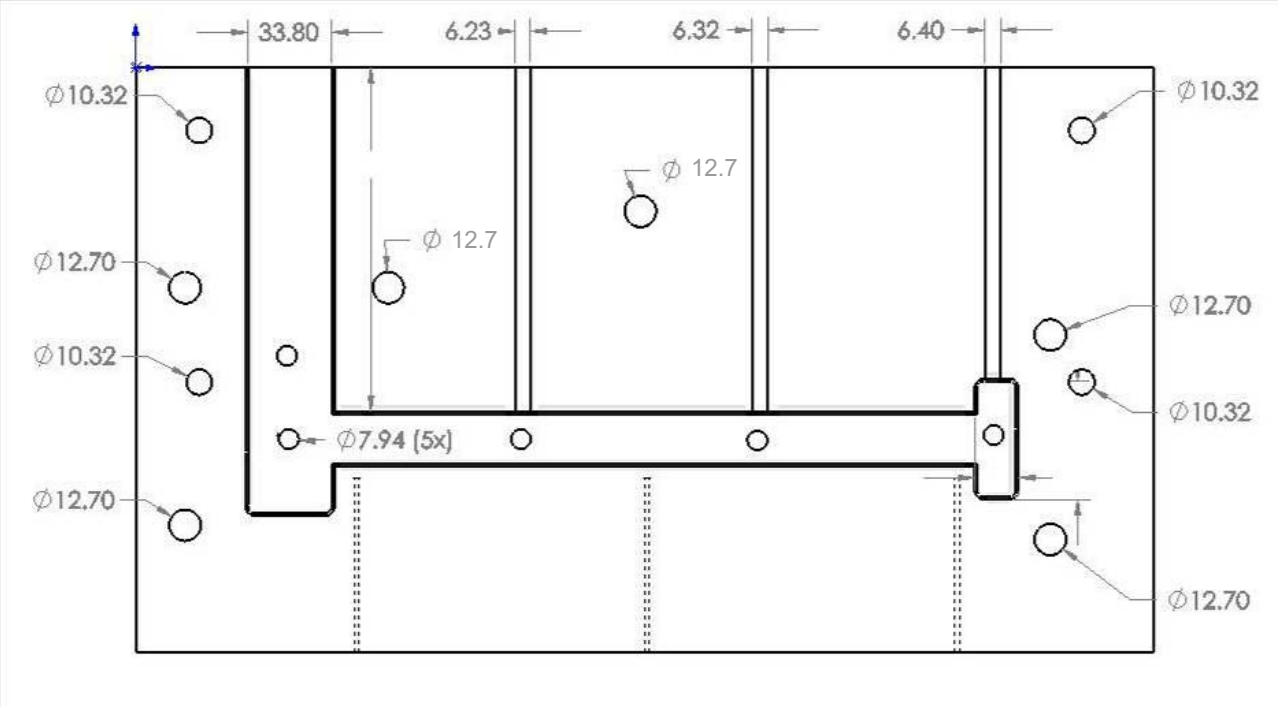

Figure 25: Mold dimensions (in 'mm') - Front view.

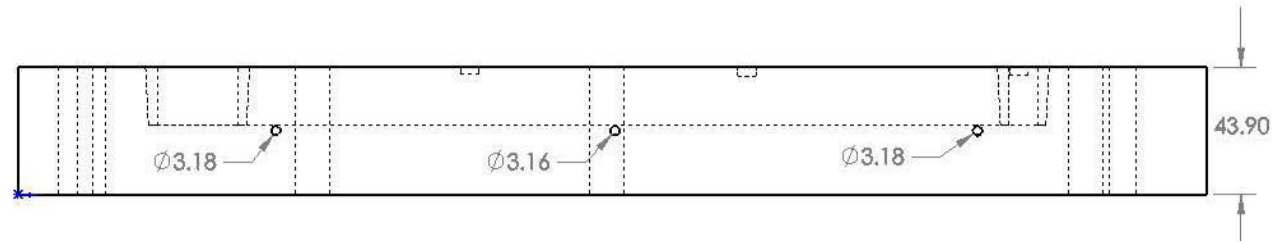

Figure 26: Mold dimensions (in 'mm') - Bottom view.

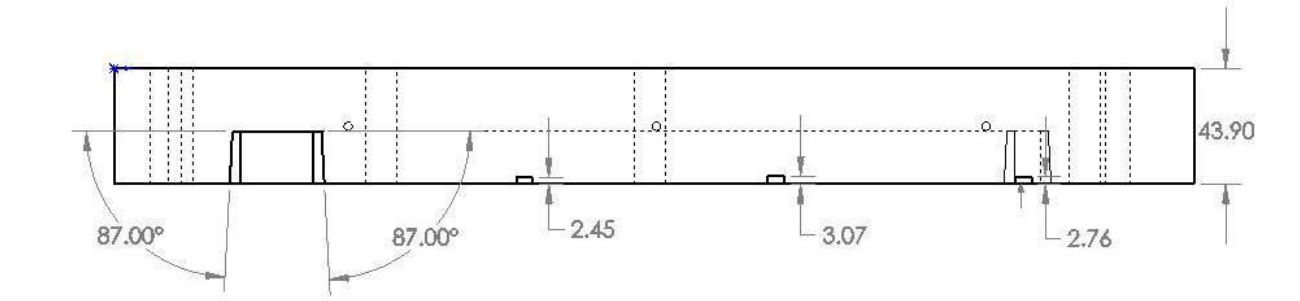

Figure 27: Mold dimensions (in 'mm') - Top view.

Prior to the pour, the mold was opened and five ejector pins (7.9 mm diameter) were inserted into the five ejector pin holes located along the casting cavity. These pins were pushed into the cavity such that the pin heads were flush with the cavity wall. Thus, the ejector pins were concealed and did not interfere with metal flow during mold filling.

In order to eject a casting from the casting cavity, the mold was opened and pushed along sliding bolts to create a 2.5 cm wide gap between the back wall of the mold and the plates with electric heaters located behind the mold. Using 20 cm long nose pliers, a second set of ejector pins was placed through this gap into the ejector pin holes from the back. The second set of pins protruded out of the back side of the mold. Subsequently, the mold was closed, which forced the electric heater plate to push on the protruding pins, which in turn pushed on the pins in contact with the casting and pressed the casting out of the casting cavity. Care was taken to ensure that casting ejection was uniform and casting distortion during ejection was avoided.

4.1.1 Mold Mounting

The H-13 permanent mold was mounted onto a modified Cooper-Chapman pneumatic sand core making machine using 12.2 mm diameter and 20 cm long sliding bolts, as shown in Figure 28. The bolts were screwed 2 cm into the permanent mold. The remainder of the bolt length extended beyond the heating plates, which enabled sliding of the permanent mold in order to insert ejector pins during casting removal.

The Cooper-Chapman molding machine was equipped with twelve 100W electric resistance strip heaters. Six heaters connected in parallel were mounted on either side of the mold. These heaters were tightly secured with bolts against a flat spacer plate, which was in direct contact with the H-13 mold, as shown in Figure 29. The machine was connected to a compressed air line, which powered the pneumatic piston cylinder. Operating this cylinder enabled opening and closing of the mold.

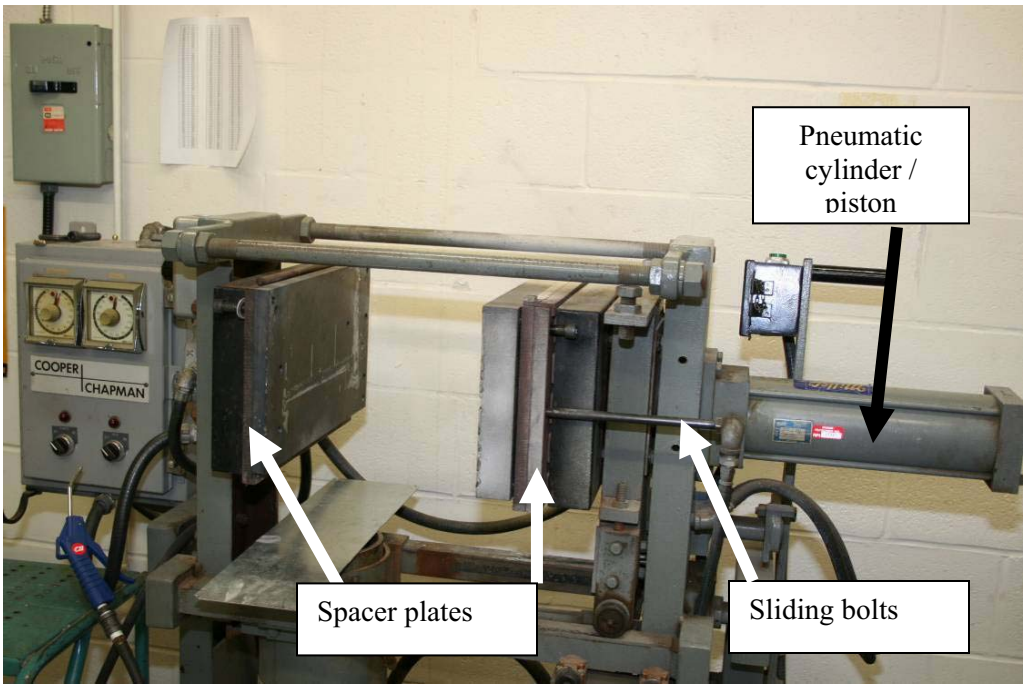

Figure 28: Cooper-Chapman pneumatic sand core-making machine.

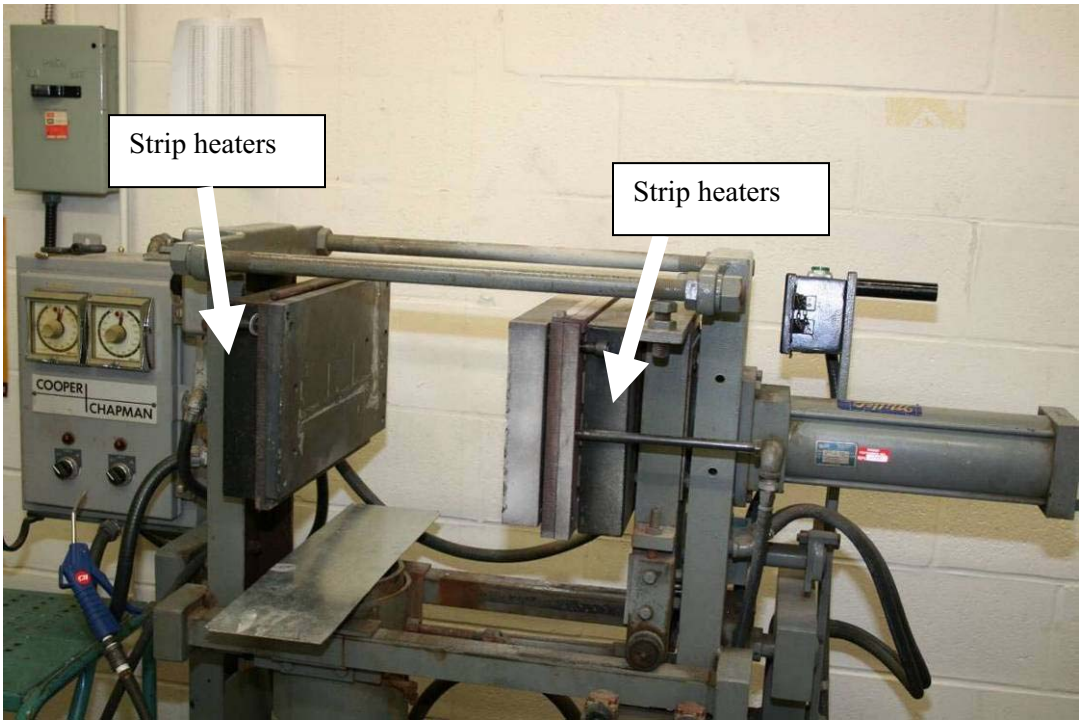

Figure 29: Mold heaters.

4.1.2 Mold Coating

In order to avoid erosion of the H-13 steel mold by molten magnesium during mold filling, the mold cavity was sprayed with Boron-Nitride (BN) coating. The BN coating (supplied by ZYP Chemicals) was applied with a low-pressure high-volume air spray gun onto the mold preheated to 150 °C. The air pressure was set to 275 kPa and the nozzle of the spray gun was adjusted until a conical spray pattern was achieved. The coating was applied in intermittent spray passes from a distance of 25 cm from the face of the mold.

Upon application, the coating was allowed to cure for 24 hours and cool to room temperature. All casting trials were performed with the same coating and re-coating was not necessary.

4.1.3 Casting and Mold Temperature Measurement

Electric power supplied to the mold heating elements was controlled by a bimetallic thermostat. The mold temperature was measured with three in-mold K-type thermocouples. These thermocouples were inserted into holes (3.18 mm diameter and 76.2 mm deep) through the bottom face of the mold (Figure 26). The average temperature reading of these three thermocouples was taken as the average mold temperature.

The mold temperature homogeneity was verified by preheating the mold to 150, 200, 250, 300, 350 and 395 °C and allowing the mold to soak at each temperature for 10 minutes. For this temperature range (150 – 395 °C), the variation of the mold temperature between the three in-mold thermocouples did not exceed ±5 °C. Therefore, prior to each casting trial, the mold was heated and soaked at the desired test temperature for at least 10 minutes.

The mold design enabled the installation of up to six thermocouples to record the casting temperature during solidification. The thermocouples were introduced into the casting cavity via removable spacers, as shown in Figure 30. These six thermocouples were grouped into three pairs. For each pair, one thermocouple recorded the casting temperature at the middle of the casting cross-section (thermocouple "A"). The second thermocouple recorded the casting temperature near the metal-mold interface (thermocouple "B").

Solidification history was primarily collected in order to perform computer modeling in the MAGMASOFT® software. This software required thermal data from two locations in the casting.

Thus, only two of the possible six thermocouples were installed. The first thermocouple was installed 2.75 cm from the 90° junction of the downsprue and the horizontal bar. The second thermocouple was located 12.7 cm from the 90° junction of the downsprue and the horizontal bar. These thermocouples recorded temperatures at the middle of the casting cross section, as shown in Figure 30 (thermocouples "A"). The precise location of the two thermocouples was determined after their installation into the mold and re-checked prior to mold closing. Digital vernier calipers with a measurement resolution of 0.01 mm were used.

The two thermocouples recording the casting temperature were custom made Chromega-Alomega 304 stainless steel sheath 0.50 mm diameter thermocouples (OMEGA - HKMTSS-020E). The thermocouples were tested, calibrated and certified by their manufacturer (OMEGA). The thermocouples were made of "Special Limits of Error Material" and the measurement accuracy was ±1.1 °C for the temperature range 0 – 1250 °C. The response time of the thermocouples was less than 0.25 seconds. The thermocouples were also tested with a FLUKE 814 temperature calibrator prior to their installation in the mold.

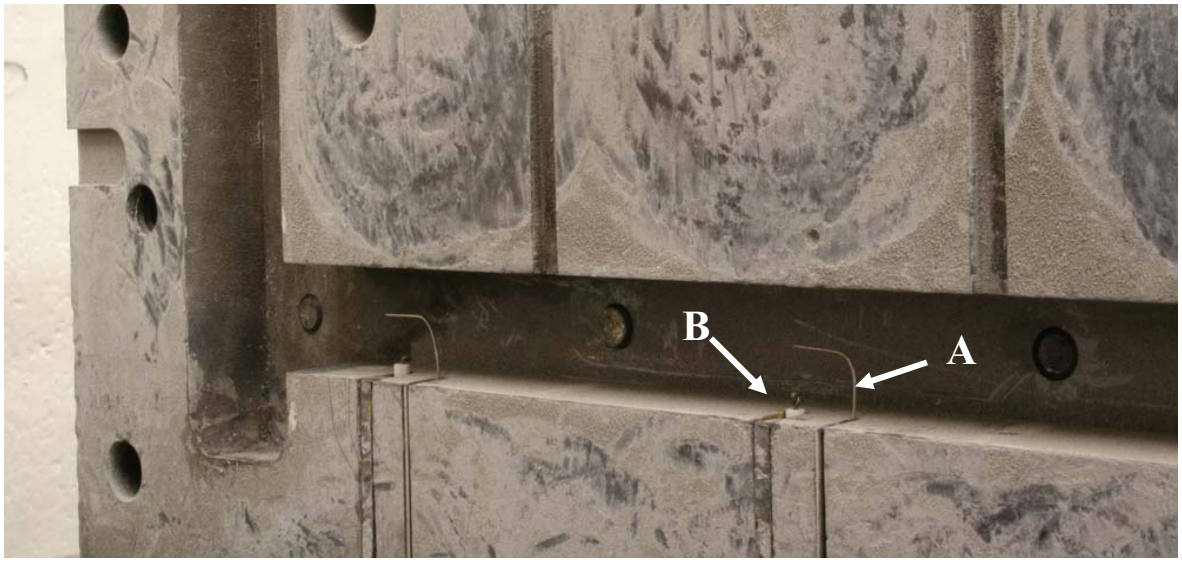

Figure 30: Casting thermocouples.

The three thermocouples used for measuring the mold temperature were also custom made Chromel-Alumel K-Type thermocouples with an exposed junction. These thermocouples consisted of OMEGA TT-K-24-SLE "Special Limits of Error" thermocouple wire, which was fed through a 3.7 mm diameter double-hole ceramic sheath and twisted three times to form an exposed connection. Subsequently the exposed connection was heated with a torch to fuse the Chromel-Alumel wires and form a bead.
The resulting thermocouple probe had a standard measurement error of ±2 °C and a response time of less

than 0.2 seconds. The thermocouples were connected to FLUKE 814 temperature calibrator and tested prior to their installation in the mold. The temperature calibrator was also used to verify the response of the temperature data acquisition system in the temperature range of 20 – 800 °C. Within this temperature range, the maximum discrepancy between the FLUKE 714 temperature calibrator and the temperature recorded by the data acquisition system was 0.1 °C. Thus, the total measurement error for the casting and in-mold thermocouples was ±1.2 °C and ±2.2 °C, respectively.

The FLUKE 714 temperature calibrator was tested, calibrated and certified by the manufacturer (FLUKE Corp.) in August 2006. Based on the manufacturer's certificate, the temperature calibrator was tested in a temperature range from 0 - 1000 °C and the calibration error was within ± 0.5 °C. This accuracy included a compensation of 0.2 °C for a cold junction error.

4.2 Alloy Melting and Casting

The magnesium alloys used in this research were obtained as 10kg ingots from Meridian Technologies, Inc. These ingots were made by Norsk Hydro Magnesium according to ASTM chemical composition specifications for the AZ91D and AE42 alloys. The actual alloy composition obtained from an emission spectrometer is presented in Tables 2 and 3. In the case of the AE42 alloy, chemical analysis verified absence of Si and Fe (these elements constitute deleterious impurities). All castings were made with virgin ingot material (i.e., no recycled alloy was used).

Table 2: Composition of AZ91D alloy.

Mg	Al	Zn	Mn	Si	Cu	Fe	Ni	Be
90.53	8.61	0.60	0.23	0.017	0.003	0.0038	0.0014	0.0012

Table 3: Composition of AE42 alloy.

Mg	Zn	Al	Cu	Mn	Ni	Be	Ce	La	Nd	Pr
93.69	0.01	3.65	0.002	0.36	0.0002	0.0006	1.3875	0.6858	0.4301	0.1407

The ingots were sectioned into ~200 g blocks. These blocks were preheated to 150 °C prior to melting in a custom made 1020 steel crucible. The crucible with preheated ingots was placed into an electric resistance furnace and covered with a steel lid. The crucible lid was fitted with a pipe enabling purging of the crucible with carbon dioxide (CO_2) shielding gas. Carbon dioxide was used due to its adequate

protective ability within the alloy pouring range used in this research [59]. The CO_2 gas flow-rate was maintained at 10 L/hr to ensure adequate melt protection.

The melt temperature was measured with a 6.3 mm diameter stainless sheath K-Type thermocouple probe. First, the melt was superheated above the desired pouring temperature. Then, the crucible was removed from the melting furnace and placed onto a refractory brick. When the melt temperature decreased to 15 °C above the pouring temperature, the molten metal surface was skimmed to remove melt surface oxides. When the temperature decreased to 5 °C above the pouring temperature, the crucible was carried from the furnace area to the mold and the melt was poured into the permanent mold.

4.3 Determination of Hot Tear Onset Conditions

In order to determine the process parameters corresponding to the onset of hot tearing, a series of trial-and-error experiments were performed. The objective was to manipulate the pouring and mold temperatures to produce castings with distinct degrees of hot tearing. This systematic manipulation of the process temperatures enabled the visual determination of the onset conditions for hot tearing in each alloy. An example of the influence of the mold temperature on the hot tearing susceptibility of the AZ91D alloy is presented in Figure 31. For the trial-and-error experiments with the AZ91D alloy, pouring temperatures from 680 – 720 °C and mold temperatures from 140 – 395 °C were investigated.

In case of the AE42 alloy, pouring temperatures below 720 °C resulted in the formation of hot tears for the entire available mold temperature range (room temperature – 395 °C). Therefore, the pouring temperature was systematically increased in order to reduce the casting cooling rate and prevent formation of hot tears. Castings were made at pouring temperatures of 720, 740, 760 and 765 °C and various mold temperatures. Higher pouring temperatures were not investigated, since the protective effectiveness of the CO_2 cover gas significantly decreased above this temperature. In summary, these systematic experiments demonstrated that the onset of hot tearing for the AZ91D alloy occurred at 720 °C pouring temperature between 210 °C and 250 °C mold temperatures. In the case of the AE42 alloy, the onset of hot tearing occurred at 765 °C pouring temperature between 340 °C and 390 °C mold temperatures. For these four casting conditions, three castings were produced at each mold temperature to verify repeatability of the hot tear severity.

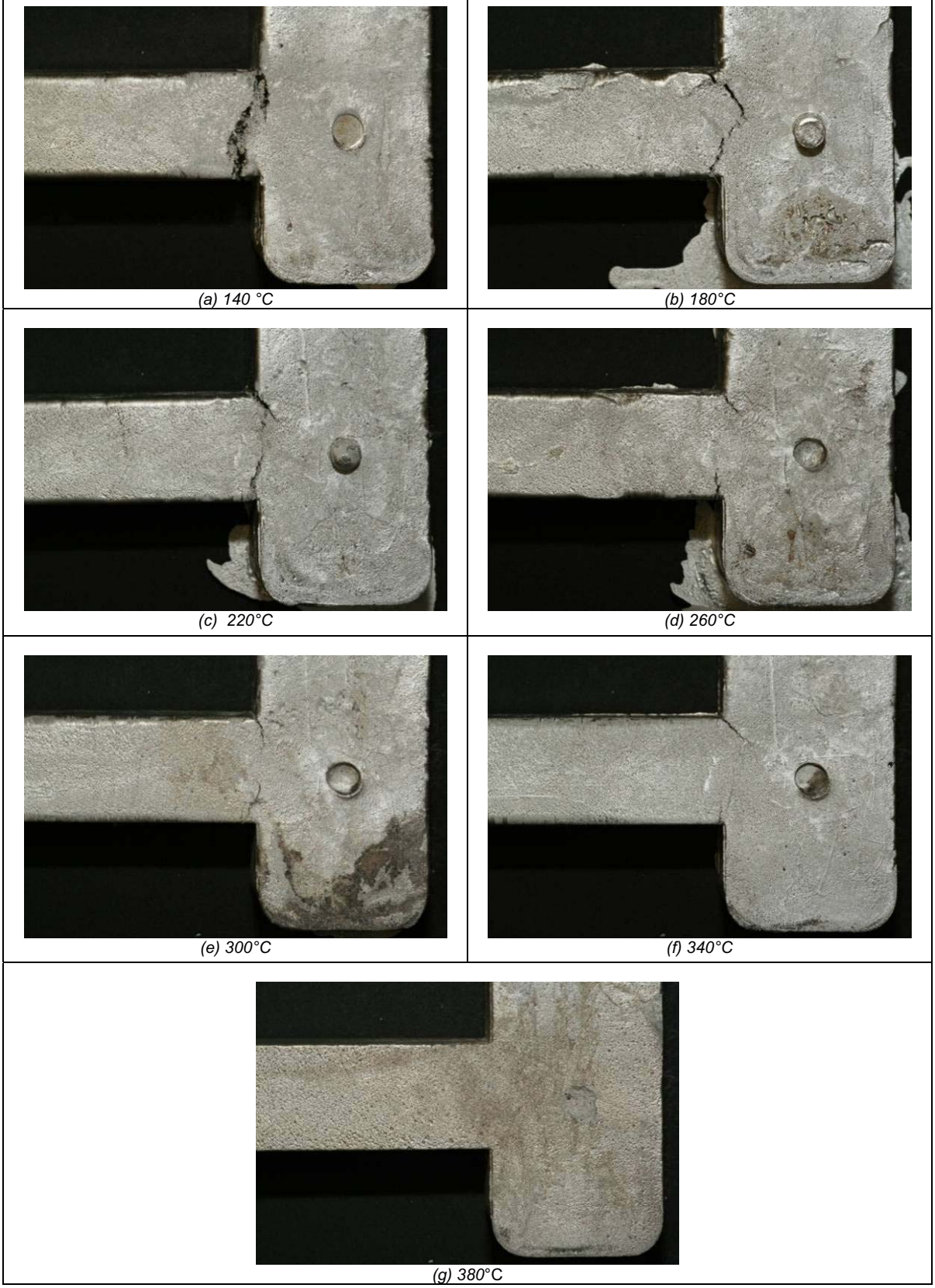

(a) 140 °C

(b) 180°C

(c) 220°C

(d) 260°C

(e) 300°C

(f) 340°C

(g) 380°C

Figure 31: Effect of mold temperature on hot tearing of AZ91D alloy. 700 °C pouring temperature.

In order to determine the hot tearing susceptibility index (HSI) of the AZ91D castings, a methodology suggested by Pekguleryuz and Vermette [36] and Cao and Kou [31] was adopted (Equation 23). The crack length was measured with vernier calipers to the nearest 0.01 mm.

$$HSI = Crack\ length\ [mm] * f_{crack} * f_{location} \quad (23)$$

Where:

f_{crack} = factor indicating severity of the hot tear

$f_{crack} = 1$ for a hairline crack; $f_{crack} = 2$ for a full crack; $f_{crack} = 3$ for broken casting

$f_{location}$ = factor indicating the difficulty of cracking at a given casting location

$f_{location} = 1$ for a crack near downsprue; $f_{location} = 2$ for a crack near the end restraint; $f_{location} = 3$ for a crack near midsection of the casting bar

4.4 Neutron Diffraction

Residual strain measurements were carried out at the Canadian Neutron Beam Centre (Ryerson – CNBC contract #C678). For all strain measurements, the E3 beamline with a triple-axis spectrometer was used. This spectrometer was also used for texture analysis. The details of ND experiments and spectrometer setup follow.

4.4.1 E3 Triple Axis Spectrometer

The spectrometer used in this research was connected to the "E" beamline and the 3rd port hole of the NRU nuclear reactor at Chalk River. A schematic diagram of the E3 spectrometer set-up is given in Figure 20. Actual images of the spectrometer and the specimen stage are shown in Figures 32 and 33, respectively.

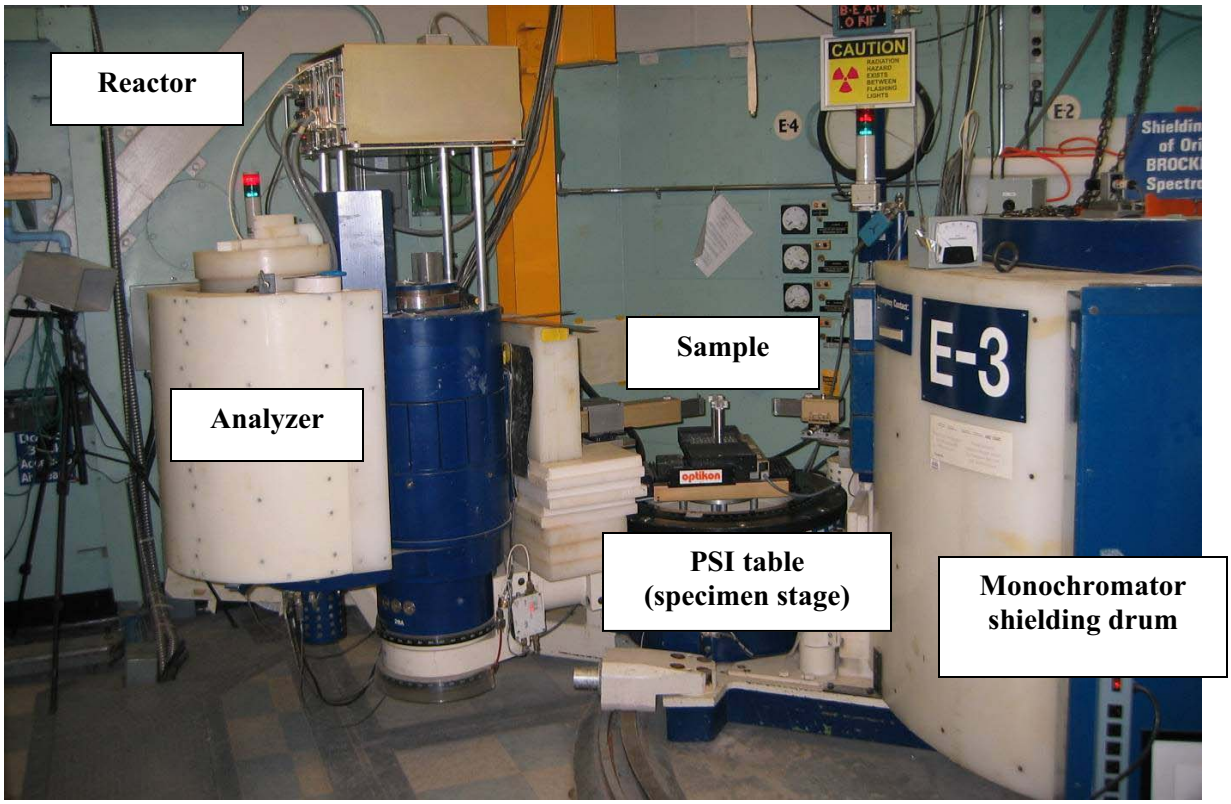

Figure 32: E3 triple-axis spectrometer.

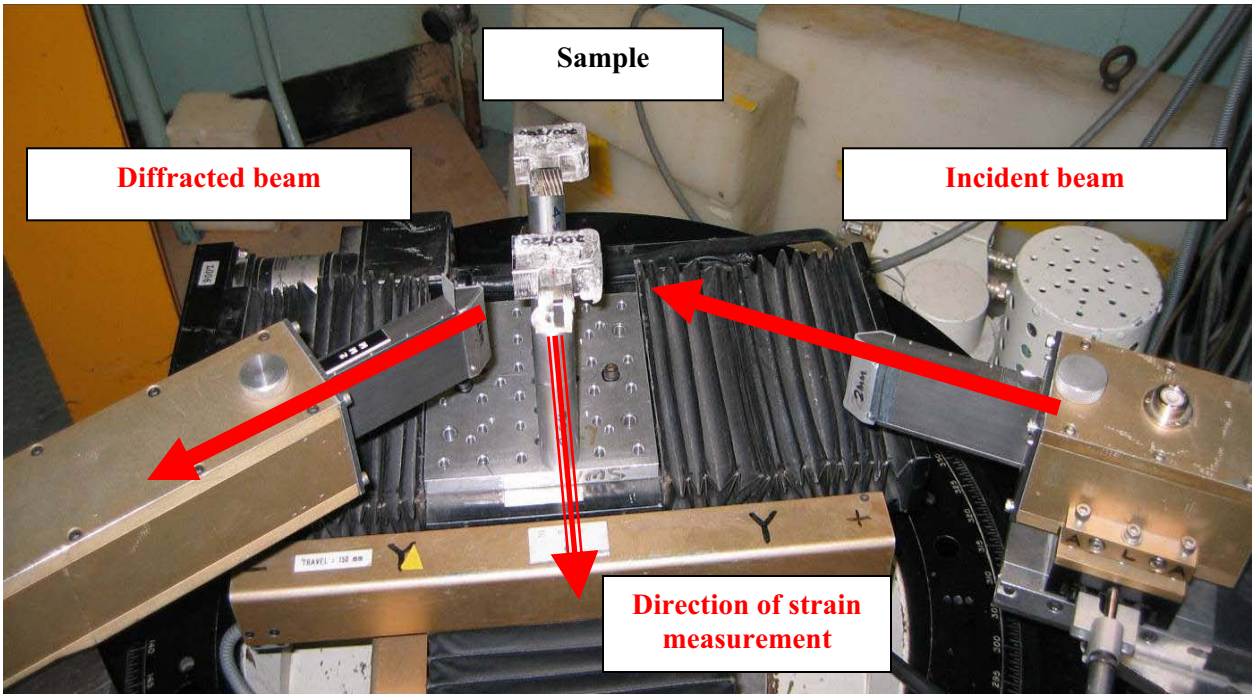

Figure 33: Strain measurement setup.

Prior to conducting strain mapping experiments, the spectrometer was aligned following procedures outlined in Reference 60, under the supervision of NRC staff.

Throughout the research project, two (incident) neutron beam wavelengths were used. Selection of neutron wavelength was achieved by re-orienting a Gallium single-crystal monochromator with respect to the incident neutron white beam from the reactor. Initially, a neutron beam wavelength of ~2.35 Å was used; however, the intensity of the neutron beam at this wavelength was relatively low, resulting in slow counting rates. Therefore, with a view to achieving all required experiments within allotted time, the monochromator was rotated for a neutron beam wavelength of ~1.96 Å, thus providing a higher intensity beam.

The exact wavelength of the incident neutron beam was determined by conducting wavelength calibration tests. In these tests, ultra-high purity silicon and nickel were used. For these elements, the lattice spacing, d_{hkl}, and the Bragg diffraction angle (for a given crystallographic reflection) were known. As a result, the actual wavelength of the incident neutron beam was determined using Bragg's law. In order to enhance measurement accuracy, the wavelength was calibrated using several crystallographic reflections for each element. Table 4 and Table 5 present the results of the neutron beam wavelength calibration experiments. The average wavelength (λ = 1.9488 Å or λ = 2.3713 Å) for a given set of experiments was subsequently used in calculating residual strains in the AZ91D and AE42 castings.

Table 4: Nickel wavelength calibration data.

Plane (hkl)	**Theoretical**		**Actual Bragg Angle (°)**	**Actual Wavelength (Å)**
	d_{hkl}	**Bragg Angle (°)**		
111	2.0345	57.5890	57.2240	1.9485
200	1.7620	67.5830	67.1491	1.9488
220	1.2459	103.7300	102.9255	1.9490
			Average	**1.9488**

Table 5: Silicon wavelength calibration data.

Plane (hkl)	**Theoretical**		**Actual Bragg Angle (°)**	**Actual Wavelength (Å)**
	d_{hkl}	**Bragg Angle (°)**		
111	3.1355	44.0161	44.4357	2.3712
220	1.9201	75.4603	76.2712	2.3714
311	1.6374	91.7070	92.7935	2.3713
			Average	**2.3713**

4.4.2 Shaping of the Neutron Beam

The beam of "white" neutrons entering the spectrometer via a reactor gate traveled through a 5 x 5 cm beam collimator until reaching the monochromator. After diffraction by the monochromator, the beam traveled towards the outer surfaces of the monochromator drum via a 5 x 5 cm incident beam collimator.

Residual strain was measured in the sample at a location where the incident and diffracted beams intersected. As a result, diffraction information was obtained from a volume, rather than a point. To shape the neutron beam, beam width limiter slits were installed in the incident and diffracted beam collimators, resulting in a beam width of 4 mm. The height of the beam was 20 mm.

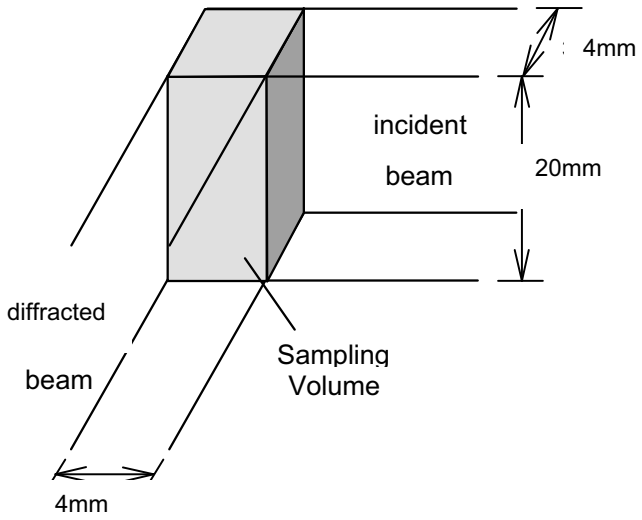

Figure 34: Neutron beam sampling volume.

In the case of strain measurements in the z-direction, ε_z, a beam height limiter was also used. The beam height limiter reduced the sampling volume height from 20 mm to 4 mm.

4.4.3 Selection of Crystallographic Reflections

Magnesium with its hexagonal-close-packed (HCP) crystal structure enables measurement of lattice strains in several crystallographic orientations. For this research, lattice strain was measured for four crystallographic planes (Table 6):

Table 6: Crystallographic reflections of interest.

Plane	Miller indices	Miller-Bravais indices
Basal	(001)	(0001)
Prismatic	(100)	$(10\bar{1}0)$
1st Pyramidal	(101)	$(10\bar{1}1)$
2nd Pyramidal	(102)	$(10\bar{1}2)$

These planes are shown in the HCP crystal in Figure 35 [61]. The Miller-Bravais and Miller indices are used interchangeably in this dissertation.

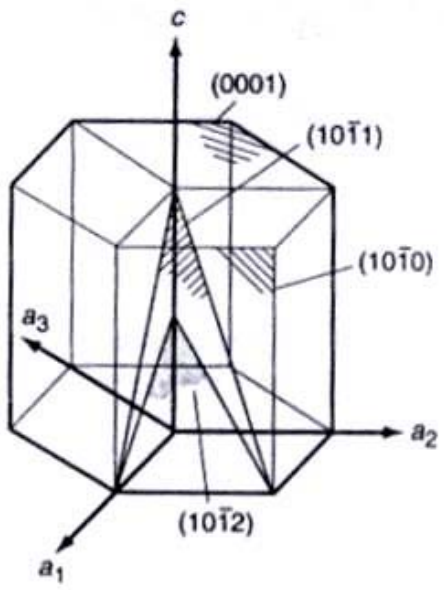

Figure 35: Orientation of planes of interest in an HCP crystal.

While calculating residual stresses from measured residual strain, the elastic constants of bulk AZ91D alloy were used from Reference 61. As per Cullity [57], the bulk elastic constants of a material represent the average elastic constants for all crystallographic reflections. Further, as will be discussed in Section 5.4.5, the AZ91D alloy was polycrystalline and isotropic (texture was absent) for the mold temperature range between 220 – 380 °C. Thus, the use of bulk elastic constants in the calculations was deemed reasonable.

4.4.4 Selection of Samples for Strain Mapping via ND Analysis

Due to the cost of the neutron beam time and limited availability of the E3 spectrometer, judicious selection of samples for neutron diffraction strain measurements was made. For each alloy, strain measurements were performed on two castings:

1. AZ91D alloy (720 °C pouring temperature): one casting made at 210 °C and one made at 250 °C mold temperature.
2. AE42 alloy (765 °C pouring temperature): one casting made at 340 °C and one made at 390 °C mold temperature.

Individual castings were mounted on the sample table (PSI stage) of the spectrometer. The coordinate axes of the spectrometer related to the casting geometry as indicated in Figure 36. All experimental data reported in this dissertation will be presented with respect to this coordinate system.

The castings and their critical regions are shown in Figure 37 - Figure 40. The terms “critical region”, “junction of the horizontal bar and the downsprue” and “critical 90° corner” refer to the area of the casting where hot tears were observed (for example, Figure 37c).

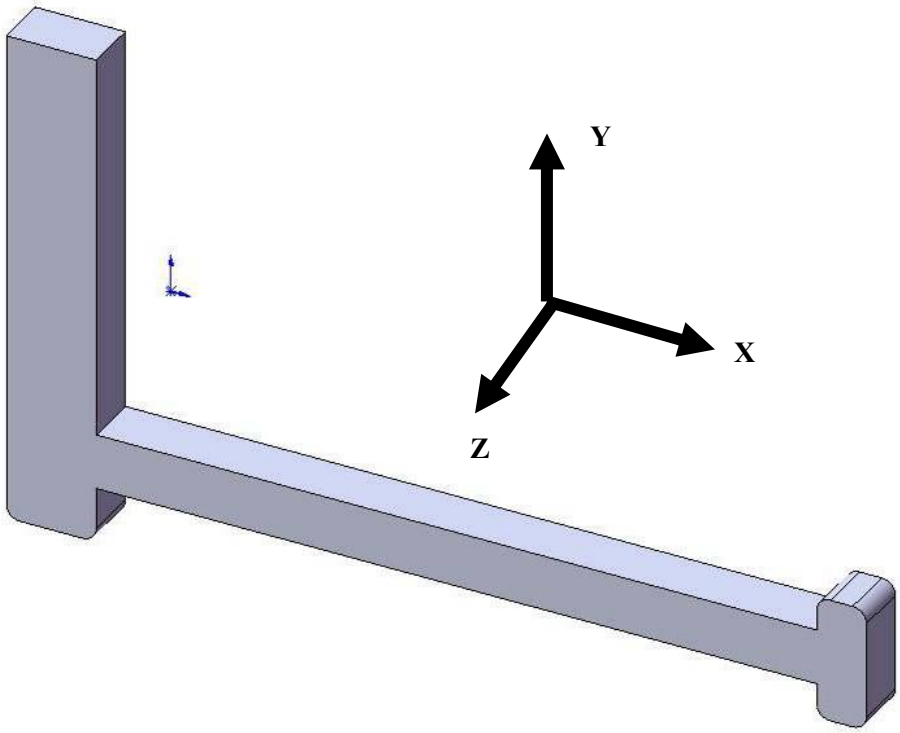

Figure 36: Co-ordinate axes of spectrometer in relation to the casting.

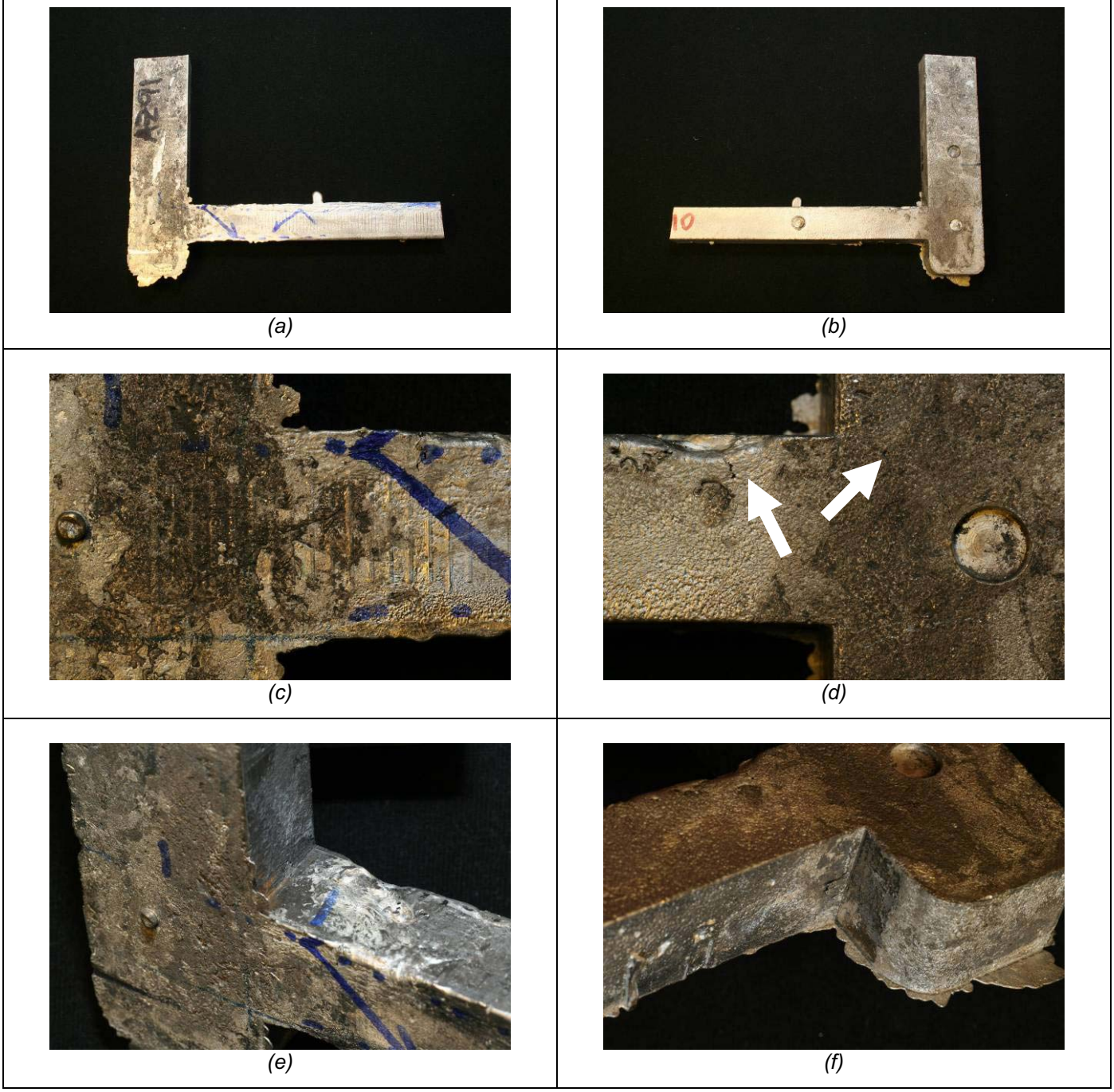

(a) (b)

(c) (d)

(e) (f)

Figure 37: AZ91D alloy casting used for ND analysis; 720 °C pouring temperature and 210 °C mold temperature.

(a) *(b)*

(c) *(d)*

(e) *(f)*

Figure 38: AZ91D alloy casting used for ND analysis; 720 °C pouring temperature and 250 °C mold temperature.

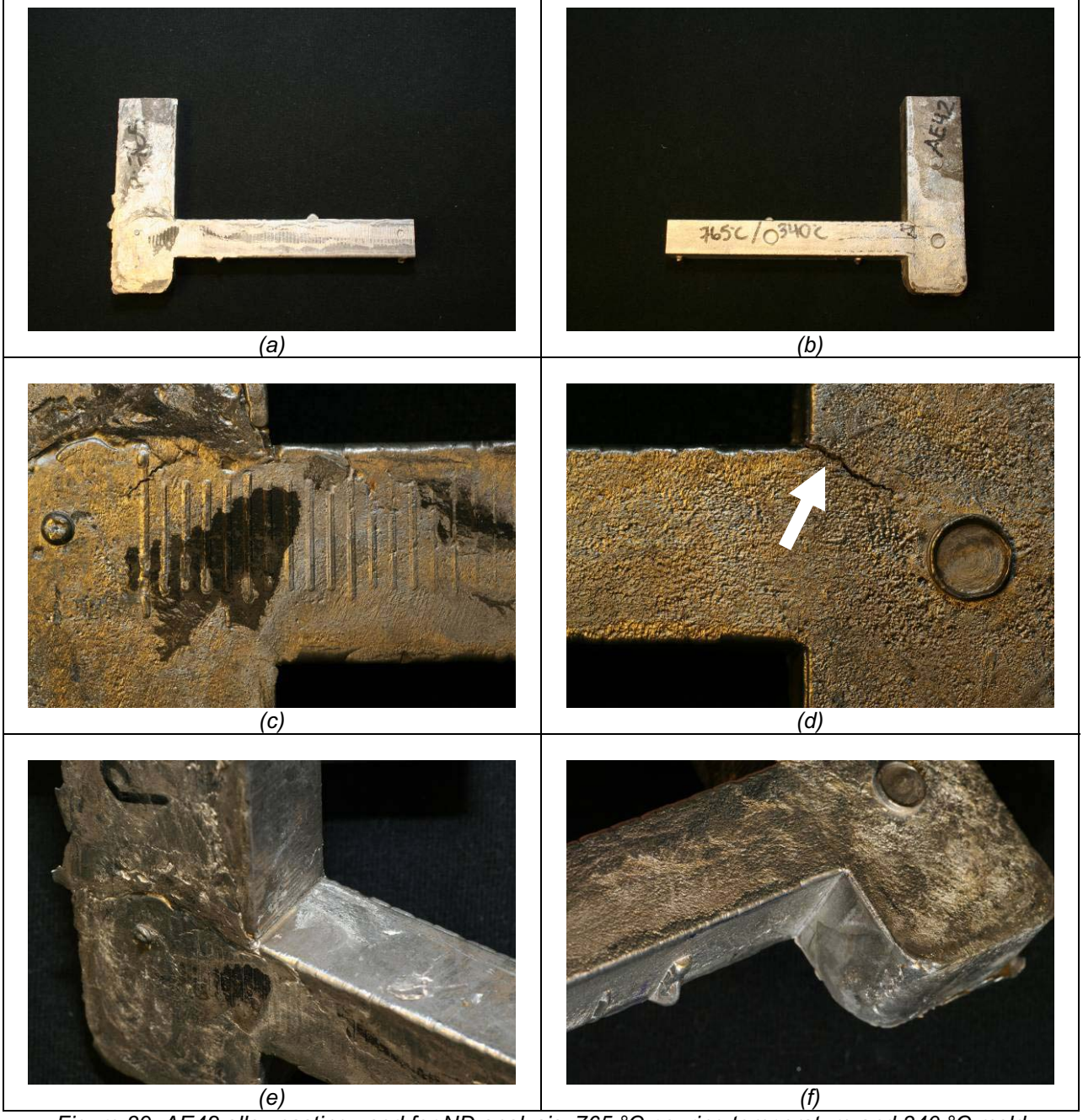

(a) *(b)*

(c) *(d)*

(e) *(f)*

Figure 39: AE42 alloy casting used for ND analysis; 765 °C pouring temperature and 340 °C mold temperature.

(a) *(b)*

(c) *(d)*

(e) *(f)*

Figure 40: AE42 alloy casting used for ND analysis; 765 °C pouring temperature and 390 °C mold temperature.

Residual strain measurements were performed along several linescans on the casting. Before proceeding with defining the location (coordinates) of each linescan, the position of the casting with respect to the neutron beam had to be determined. Therefore, the (*x, y, z*) coordinates of the casting edges were located using a wall-scan feature of the diffractometer computer control software. During a wall-scan, the neutron beam scanned along a specified direction (e.g., *x*-axis) with a beam sampling volume located in the casting. Subsequently, the scan proceeded with measurements out of the casting. When the sampling volume was still within the casting, neutrons were diffracted and received by the diffracted beam analyzer. When the sampling volume moved outside of the casting, neutron diffraction did not take place and the diffracted beam intensity was zero. Using this technique, the coordinates of the casting edges (*x, y* and *z*) were determined to the accuracy of 0.5 mm. This procedure was repeated for every casting.

Once the co-ordinates of the casting surfaces were known, linescans were programmed into a DSCAN file, which controlled the positioning of the sample, along with other diffraction scan parameters (e.g., diffraction angles, sample oscillation, etc.). Four linescans were programmed as follows:

1. *Top edge linescan*: a scan made 4 mm below the surface of the top edge of the horizontal bar.
2. *Centerline linescan*: a scan along the centerline of the horizontal bar.
3. *Bottom edge linescan*: a scan located 4 mm above the surface of the bottom edge of the horizontal bar.
4. *Cross-scan*: a scan perpendicular to the three above (horizontal) linescans, located in the downsprue.

The locations of the linescans are illustrated in Figure 41.

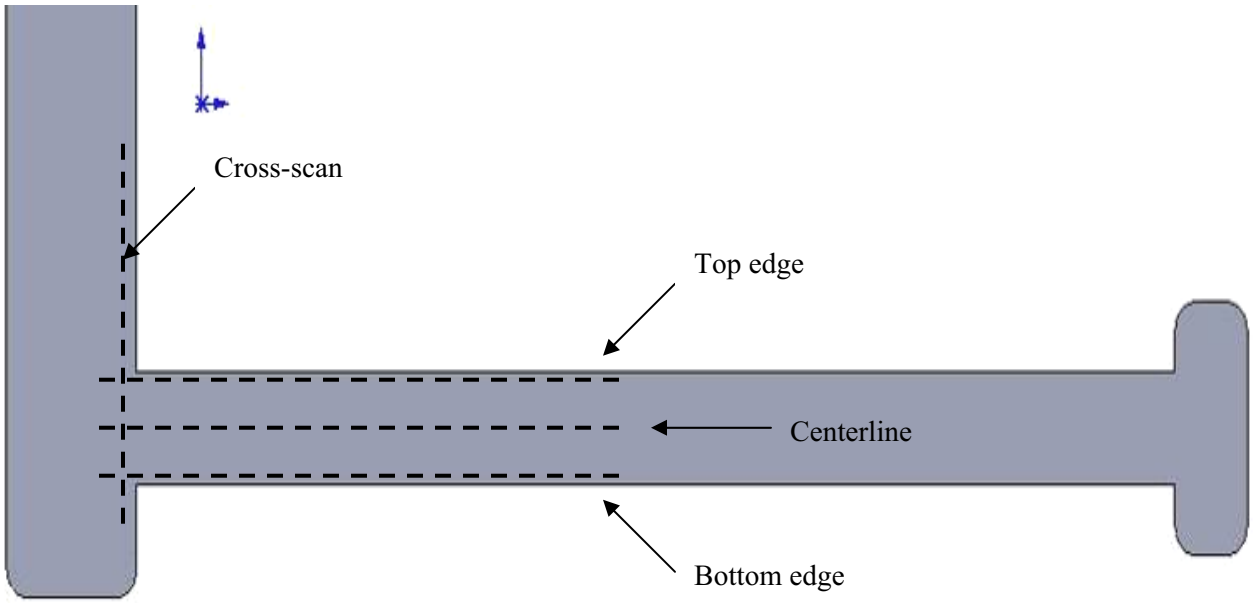

Figure 41: Linescan locations.

The horizontal linescans initiated 10 mm in the sprue and extended 100 mm along the length of the horizontal bar, as indicated in Figure 42.

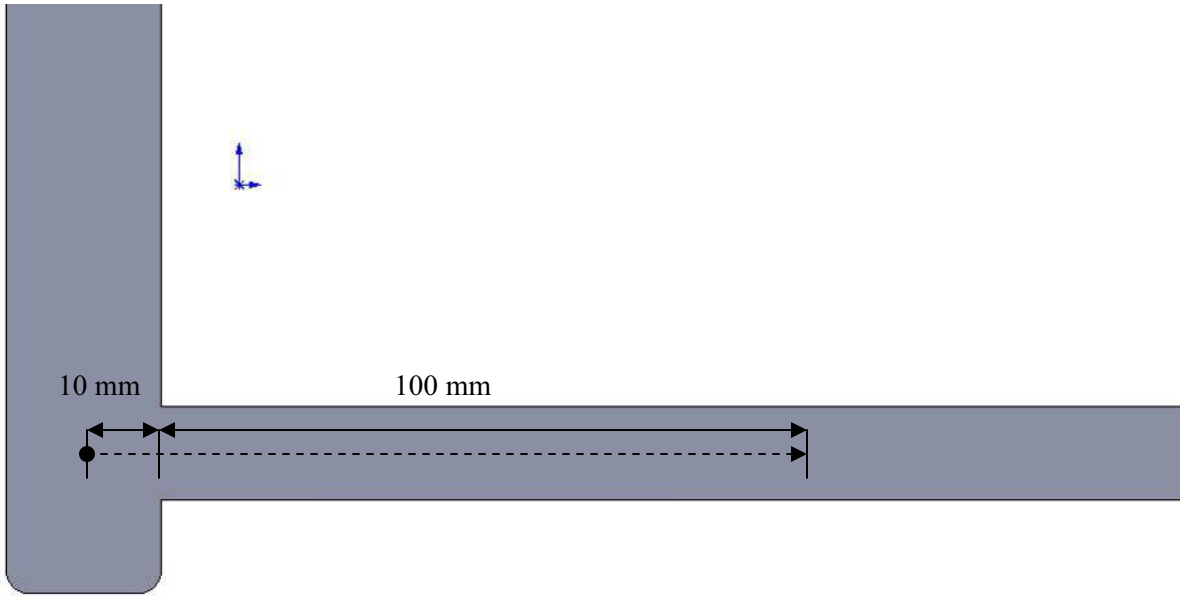

Figure 42: Length of horizontal scans.

In the case of the vertical cross-scan in the downsprue, the scan was located 4 mm from the right edge of the downsprue, as indicated in Figure 43. The scan initiated 10 mm below the bottom edge and continued 60 mm above the top edge of the horizontal bar.

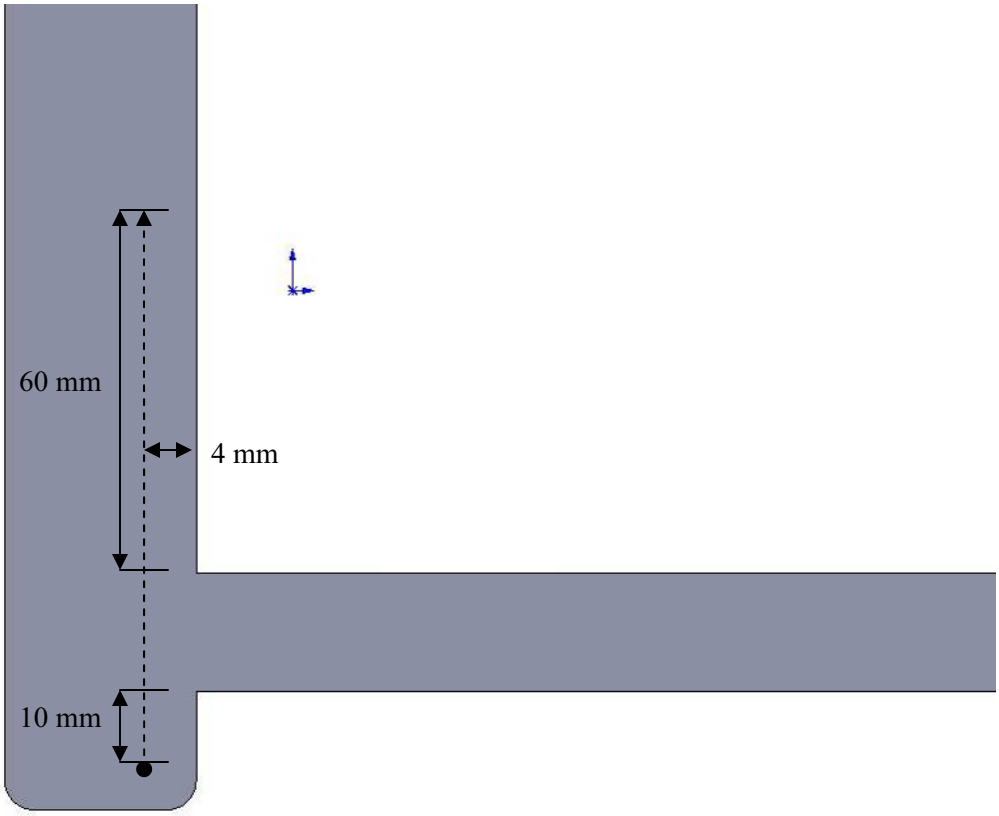

Figure 43: Location of vertical cross-scan.

For selected castings, two linescans were programmed to measure strain in the *z*-direction. The ε_z was measured along the "top edge" and "cross-scan" linescans, as shown in Figure 44. For these scans, beam height limiters were used and strain at the center of the casting (10 mm into the casting thickness) was measured.

Due to the restriction imposed by the cost of neutron beam time and spectrometer availability, it was not feasible to measure strains in the *x, y* and *z*-directions for all samples, linescans and reflections. From preliminary experiments, it was determined that the development of strain in the *x*-direction was significant for the nucleation of hot tears. As a result, ε_x was measured for all castings and all linescans. For the AZ91D castings, it was necessary to evaluate the stress state in the critical region. Thus, strains in the *y* and *z*-directions had to be measured as well. A summary of the strain measurements is presented in Table 7.

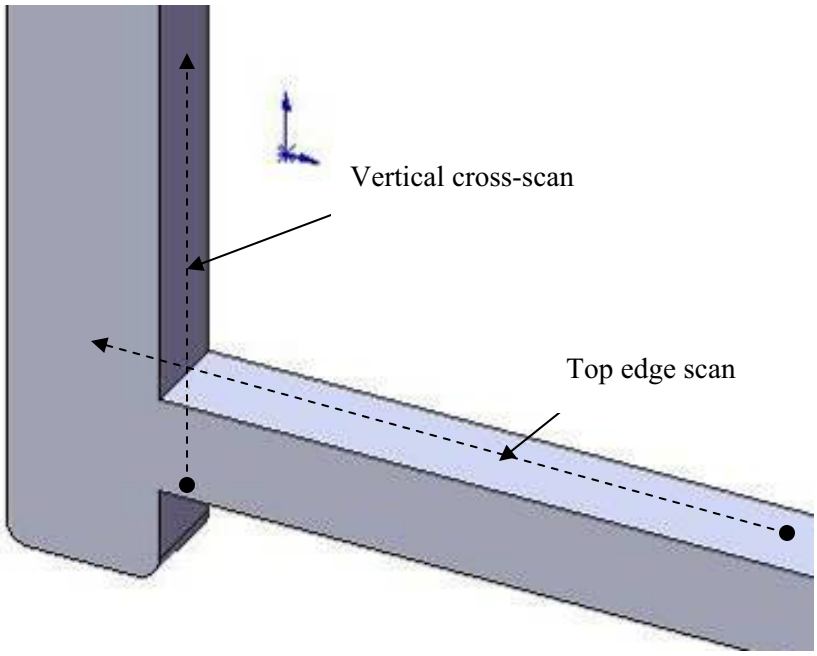

Figure 44: Location of linescans for ε_z.

As can be observed from Table 7, ε_y and ε_z strains were not measured in the AE42 alloy castings. This was justified by considering the fact that the casting cooling rates had to be very low in order to produce an AE42 casting free of hot tears. These slow cooling rates promoted significant grain growth and the resulting alloy (in the as-cast condition) was not practical for industrial applications. Therefore, AE42 strain mapping was limited to the measurement of the ε_x residual strains in the horizontal bar and the sprue.

Table 7: Linescan summary.

Condition	$\boldsymbol{\varepsilon_x}$				$\boldsymbol{\varepsilon_y}$				$\boldsymbol{\varepsilon_z}$			
	TE	**CL**	**BE**	**CS**	**TE**	**CL**	**BE**	**CS**	**TE**	**CL**	**BE**	**CS**
AZ91D 720 - 210	✓	✓	✓	✓	✓			✓	✓			✓
AZ91D 720 - 250	✓	✓	✓	✓	✓			✓	✓			✓
AE42 765 - 340	✓	✓	✓	✓								
AE42 765 - 390	✓	✓	✓	✓								

* TE = Top Edge; CL = Centerline, BE = Bottom Edge, CS = Cross-scan

4.4.5 Selection of Samples for Residual Strain-retention Tests and Texture Analysis

In the preliminary stage of the project, AZ91D castings with distinct degrees of hot tearing were produced. These castings were used as a proof-of-concept for the retention of residual strains in the castings after their ejection from the mold.

These samples were cast at a 700 °C pouring temperature and four mold temperatures: 220, 320, 340 and 380 °C. Linescans along the top edge, centerline, bottom edge and cross-scan were carried out. These samples and the severity of hot tears are shown in Figure 45.

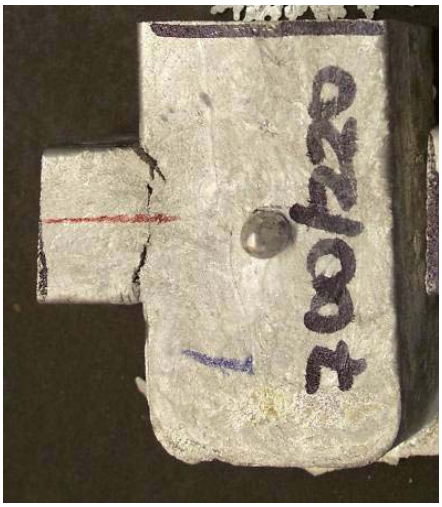

(a) 220 °C mold temperature.

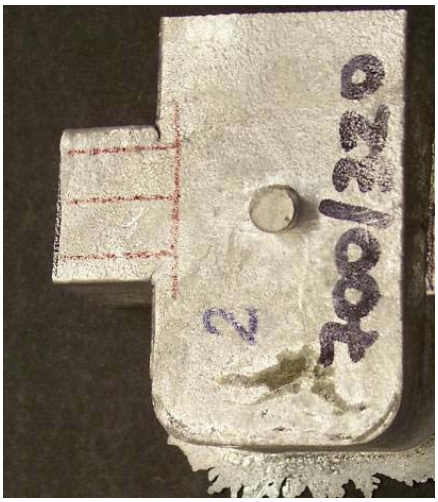

(b) 320 °C mold temperature.

(c) 340 °C mold temperature.

(d) 380 °C mold temperature.

Figure 45: AZ91D samples poured at 700 °C for initial ND analysis.

4.4.6 Stress Free Samples

In order to enable calculation of residual strains using the peak-shift method, stress-free samples of AZ91D and AE42 alloys were obtained. These samples were extracted from the center (i.e., midsection) of the downsprue of the castings, as shown in Figure 46. The stress-free sample had dimensions of 3 x 3 x 20 mm. The sample was located near the pouring cup, thus experiencing free contraction and very slow cooling. Further, by machining the sample to the desired size, any remaining residual stresses were relieved.

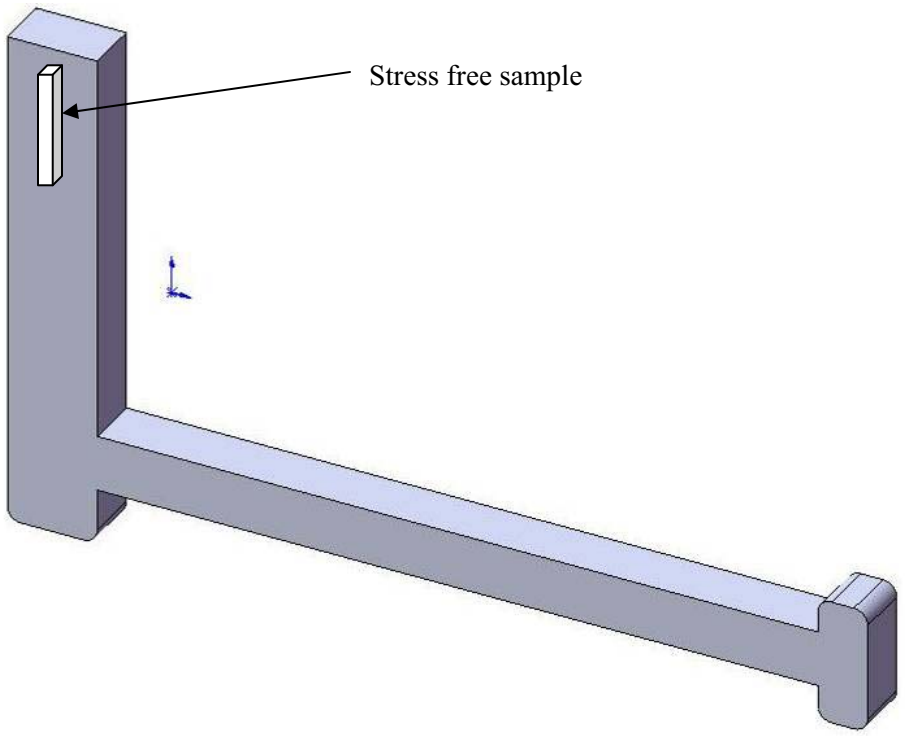

Figure 46: Origin of stress-free sample.

4.4.7 Texture Analysis

The samples described in Section 4.4.5 were also used to investigate possible texture development in the castings. After performing residual strain measurements, the original samples in Figure 45 were sectioned and specimens of 20 x 20 x 15 mm were extracted. The specimens were mounted in an Eulerian cradle placed on the diffractometer sample table, as shown in Figure 47.

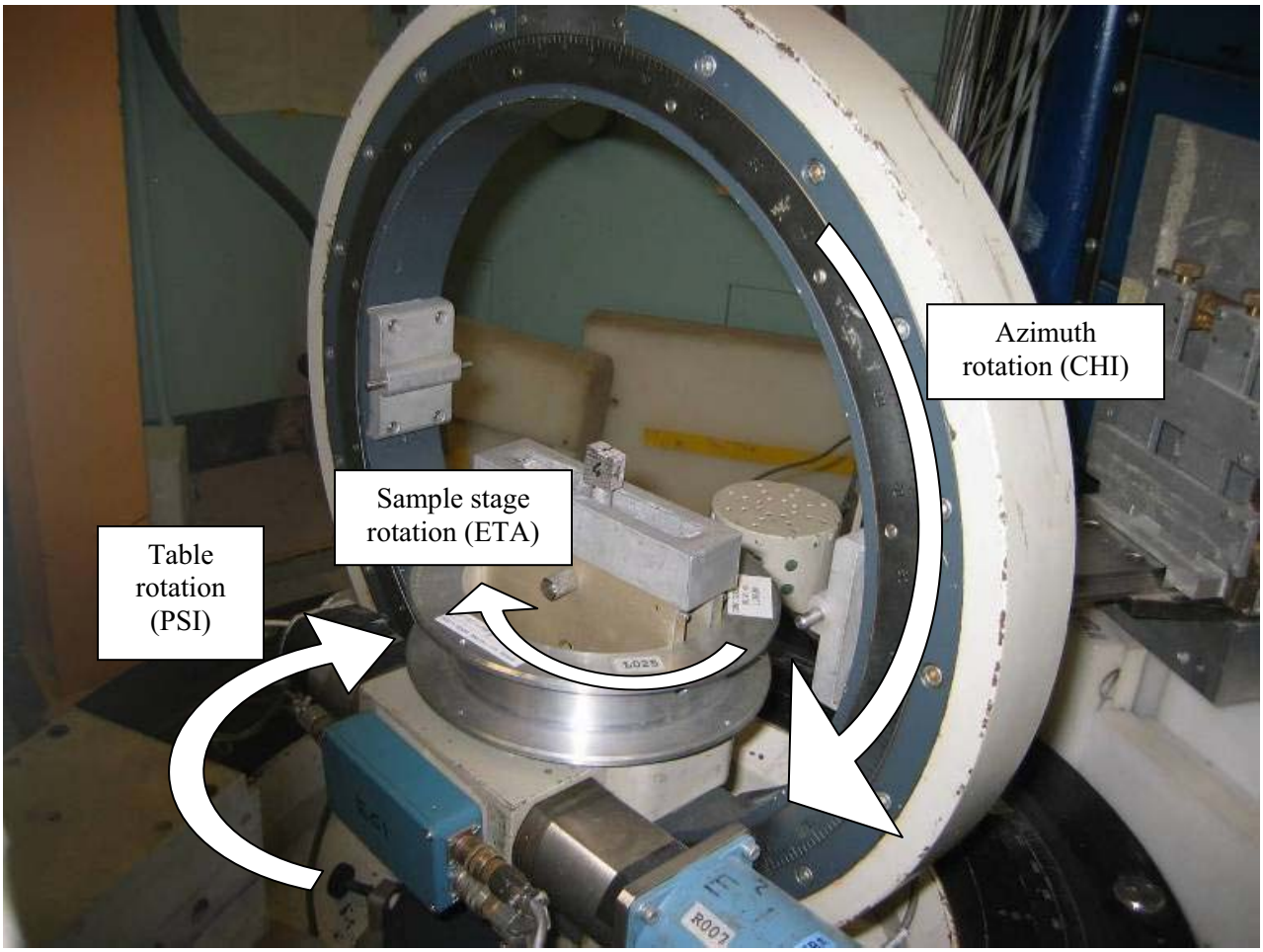

Figure 47: Eulerian cradle for texture analysis.

For crystallographic texture analysis, additional higher order reflections were studied. Specifically, pole figures for $(10\bar{1}0)$, (0001), $(10\bar{1}1)$, $(10\bar{1}2)$, $(20\bar{2}1)$, $(10\bar{1}4)$, $(2\bar{1}\bar{1}2)$, $(20\bar{2}2)$, (0002), $(20\bar{2}0)$ and $(20\bar{2}3)$ reflections were collected. The CHI angle (cradle azimuth) was increased in 30° increments ranging from 0° - 120°. The sample stage oscillation (ETA) was disabled for texture analysis.

In order to generate pole figures from the raw experimental data, POLCON software developed by CNBC staff [62] was used. Within this program, the following user parameters were maintained for all pole figure plots:

1. One smoothing pass was applied to the raw data.
2. Stereographic projection was created.
3. Zero linear contour intervals.

4.4.8 Statistical Treatment of Diffraction Data

In order to enable valid calculation of residual strain from different samples and linescans, statistical analysis of the raw neutron count data was performed. The number of incident neutrons entering the sample was governed by the base monitor (MON) value. The diffracted neutron intensity was calibrated with respect to this monitor value. The counting of incident neutrons was accomplished with a Beryllium window monitor placed in the path of the incident beam. When a specified number of incident neutrons reached the Be monitor, the sample stage moved the sample to a new location. Additional information related to the neutron beam monitor is presented in Section 4.4.9.

The diffracted beam analyzer consisted of 32 neutron-sensitive wires. The angular spacing between adjacent wires was 0.08°, hence the total angular span of the DB analyzer was ±1.24° from the desired Bragg peak position. The center wire was positioned exactly at the specified angular position where a Bragg peak was expected.

The wires of the analyzer were connected to a signal counter and a processing unit. When a diffracted neutron collided with a detector wire, the neutron's angular position was recorded and counted.
An example of the data recorded by the DB analyzer wires for an expected peak at -41.241° is presented in Table 8.

These results are graphically presented in Figure 48. The plot of raw neutron count data was subsequently fitted with a Gaussian curve. This fitting was carried out automatically with a MS Excel macro available to ANDI researchers [63].

The Gaussian fitting incorporated a linear least squares algorithm (Newton-Raphson). The fitting procedure returned three parameters that characterized the peak:

1. Integrated intensity: The integrated intensity was related to the peak amplitude, A and peak width, σ, via Equation 24:

$$\text{Integrated Intensity} = \sqrt{2\pi}\sigma A\frac{10000}{Mon} \tag{24}$$

Where:

'10000' was an arbitrarily chosen monitor value.

The integrated intensity was normalized by the MON value, thus enabling comparison of peaks collected using different diffractometer parameters and settings.

Table 8: Example of neutron count data.

Analyzer wire angular position [°]	**Count of incident neutrons**
-42.543	17
-42.465	14
-42.386	15
-42.304	15
-42.222	22
-42.134	20
-42.052	15
-41.966	36
-41.883	39
-41.809	58
-41.712	93
-41.63	152
-41.541	170
-41.457	215
-41.37	261
-41.276	241
-41.199	204
-41.11	92
-41.022	50
-40.942	29
-40.853	17
-40.773	9
-40.686	17
-40.598	24
-40.516	19
-40.426	12
-40.344	23
-40.255	14
-40.176	13
-40.092	16
-40.006	12
-39.929	11

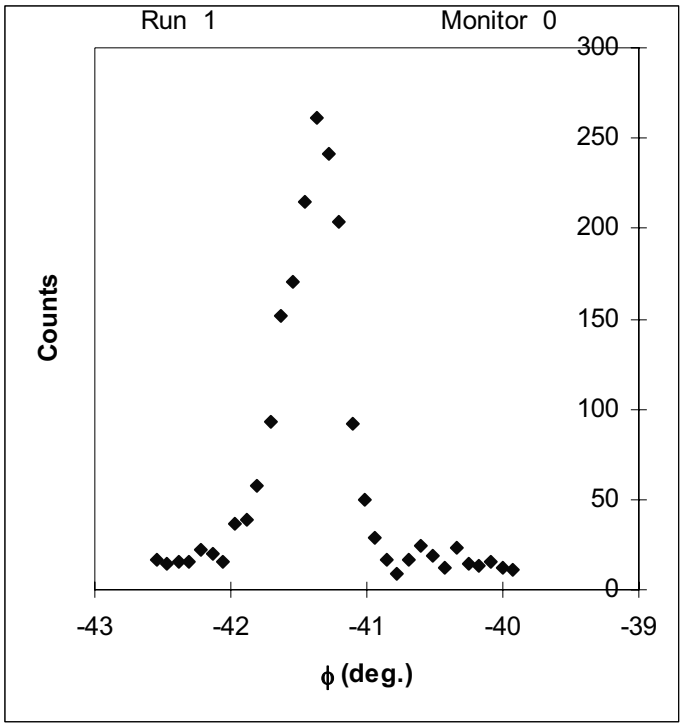

Figure 48: Raw neutron count data.

2. Peak position: The peak position was based on the centre of the Gaussian fitting curve. This value was used for subsequent calculation of residual strains.

3. Peak width: The peak width was calculated as the full-width at half-maximum (FWHM). The FWHM was calculated via Equation 25, as follows:

$$\text{FWHM} = 2\sqrt{2\ln(2)}\sigma \tag{25}$$

The macro application also calculated the error for estimation of each parameter along with parameters describing the background and the quality of the fit (i.e., χ^2 statistic). A summary of the parameters evaluated for each peak is presented in Table 9 [64]. The raw data and a discretized (i.e., low-resolution in Φ) curve indicating the Gaussian fit are shown in Figure 49. For peak position determination, the software used a "smooth" continuous Gaussian fit curve.

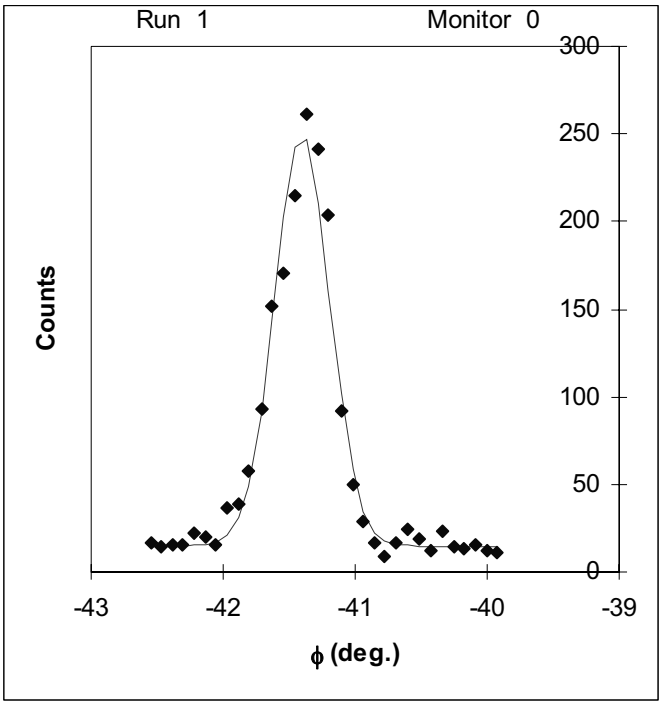

Figure 49: Gaussian fitting of raw data.

Table 9: Summary of Gaussian fitting output parameters.

Parameter	Description
Integrated Intensity	The integrated area under the diffraction peak according to the fit of the data.
Uncertainty in Integrated Intensity	The uncertainty in the integrated intensity based on the quality of the fit.
Peak Position	The central position of the diffraction peak according to the fit of the data.
Uncertainty in Peak Position	The uncertainty in the peak position.
Peak Width (FWHM)	The width of the diffraction peak according to the fit of the data expressed as the full-width at half-maximum.
Uncertainty in FWHM	The uncertainty in the FWHM.
Flat Background	Elevation of the horizontal background. The parameter was normalized in the same manner as the integrated intensity.
Uncertainty in Flat Background	The uncertainty in the background.
χ^2	Quality of the fit parameter

Before proceeding with analysis of any ND experimental data, the statistics in Table 9 pertaining to each peak were examined. If the statistics pertaining to the peak were not satisfactory, the measurement at that specific location in the sample was either repeated (beam time permitting) and a longer beam monitor value was used to ensure sufficient neutron count at the detector. If repeat experiments were not possible, then the raw peak data were rejected and the data point was excluded from further analysis. In this process, the following criteria (Table 10) were used to determine the validity of a peak:

Table 10: Peak rejection criteria.

Parameter	Criterion
Neutron Count	Should be above 100.
Integrated Intensity	Should be above 1.0 (higher values are desirable).
Peak Height : Background Ratio	Should be more than 10.

The uncertainty associated with each Bragg peak measurement was also examined. The statistical uncertainty as indicated by error bars (representing one standard deviation) associated with Bragg-peak estimation is presented in Figure 50.

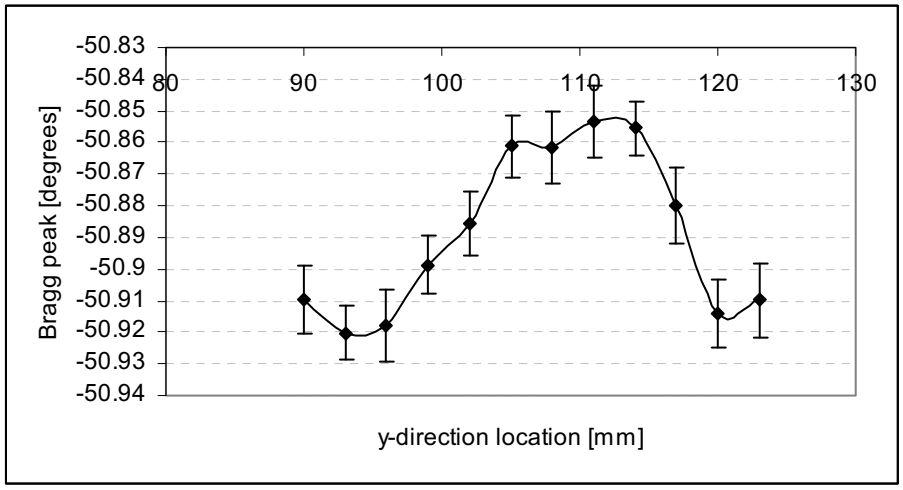

Figure 50: Strain profile with error bars indicating one standard deviation.

The uncertainty in Bragg peak measurement was related to several sources of error associated with the neutron diffraction technique of strain measurement and subsequent statistical treatment of diffracted beam counter data. These sources of error included neutron counting statistics (i.e., efficiency of neutron counters) and departure from Gaussian peak shape. They do not incorporate additional uncertainties that may arise from systematic errors in the data collection process such as uncertainties in the condition of

the stress-free reference material, geometric aberrations (e.g., divergence) of the neutron beam, large-grain misalignment, texture gradients, elastic constants or other unknown intergranular and phase-interaction strains.

4.4.9 Selection of Neutron Beam Monitor Values

In order to obtain statistically significant diffraction peaks and their positions, the incident beam monitor value had to be adjusted to allow sufficient number of diffracted neutrons to enter the DB analyzer. However, long MON values would result in unnecessary counting and inefficient beam time use.
The initial 'MON' value was estimated based on several trial-and-error ND experiments. To determine the optimal monitor value, the neutron beam sampling volume was located at an arbitrary location in the sample and the number of diffracted neutrons was counted. For the AZ91D alloy, the experiments revealed that a base monitor of 100,000 counts (i.e., MON = 100,000) was sufficient.

In the case of the AE42 alloy, due to the much larger grain size, the peak statistics at 100,000 base monitor were poor. As a result, the count monitor was increased to 150,000. Further, PSI-angle oscillation (± 8°) was used to enhance the counting statistics.

Prior to setting the monitor, it was noted that different crystallographic reflections had a different neutron reflectivity. This reflectivity was quantified by the Q-scattering value, as obtained from "POWDER" program. This program was available to the ANDI user community. The relative reflectivity of the $(10\bar{1}0)$: (0001): $(10\bar{1}1)$: $(10\bar{1}2)$ was 1/5:1/5:1:1/3, respectively. Therefore, when writing the DSCAN program (Section 4.4.10) monitor integer multipliers (5, 5, 1 and 3) were entered to ensure efficient and statistically correct diffraction analysis for all crystallographic reflections.

4.4.10 DSCAN Program

Acquisition of diffraction data along the linescans was made by a computer connected to the diffracted beam analyzer. The computer also controlled the spectrometer sample stage servo motor drives. The control of the drives was achieved via a "DSCAN" program. DSCAN parameters specified for every linescan are given in Table 11.

A typical screen-shot of the DSCAN interface is shown in Figure 51. Once the DSCAN command program was developed, the scan sequence was initiated and continued automatically. When strain

mapping for a given casting was complete, the casting was removed from the sample stage and deposited into a safe storage area, to allow dissipation of any residual radiation. Upon clearing with AECL's radiation surveyor, the casting was brought back to Ryerson University and sectioned for metallographic analysis.

Table 11: DSCAN program parameters.

Parameter	Description
Run #	Tracks the scan number
2TM	Monochromator angle specifying the incident beam wavelength
PSI	Half-angle of diffraction peak of interest
PHI	Angle of diffraction peak of interest
No.STEPS	Number of steps of increment DELTA for travel in the desired direction
DRIVE	Name of servo motor to be driven – XPOS, YPOS, ZPOS
DELANG	Step size for drive travel in the desired direction
NPTS	Number of points / increments to be made in the specified DRIVE direction
MON	Integer multiplier of the base monitor
X-AXIS	X-position origin
Y-AXIS	Y-position origin
Z-AXIS	Z-position origin

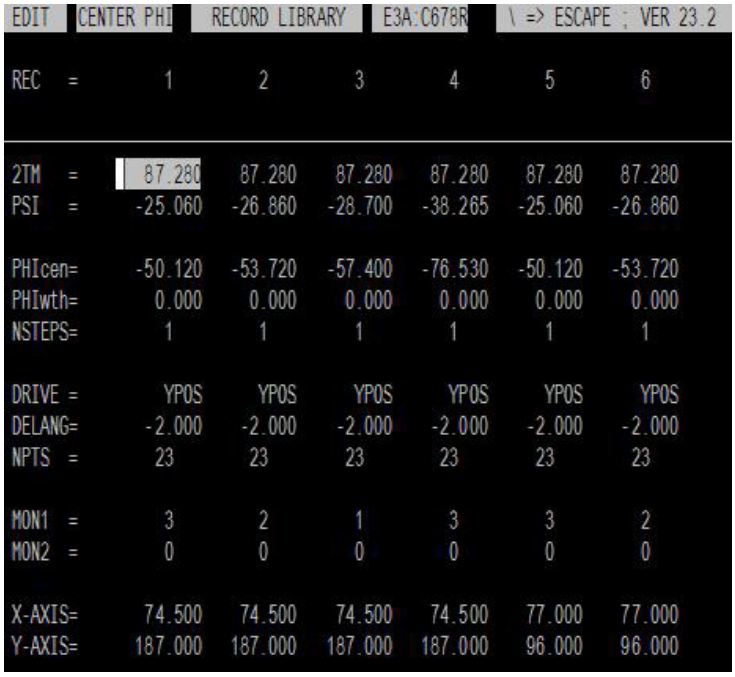

Figure 51: DSCAN screenshot.

4.5 Microscopy

Representative samples from castings analyzed by ND were prepared for optical and scanning electron microscopy. The location of the samples with respect to the casting geometry is presented in Figure 52 - Figure 54. The location of samples was deliberately chosen to enable observation of the following features of the casting microstructure (Table 12).

Throughout this thesis, labels such as "AZ91D / 250 / S1", "AE42 / 340 / S6", etc., indicating the source of micrographs are used. These labels indicate the alloy type, mold temperature and sample location in the casting.

Table 12: Samples for microstructure analysis.

Sample	Feature of interest
#1	General microstructure of cross section of the horizontal bar at the bar's midsection (2^{nd} thermocouple).
#2	Microstructure of casting skin at the bar's midsection.
#3	General microstructure of cross section of the bar near the bar's critical region (1^{st} thermocouple).
#4	Microstructure of the casting surface at the critical region.
#5	Microstructure of the casting surface at the critical region.
#6	Microstructure of the casting interior at the critical region.
#7	Microstructure of the casting interior at the critical region.
#8	Microstructure in the downsprue.

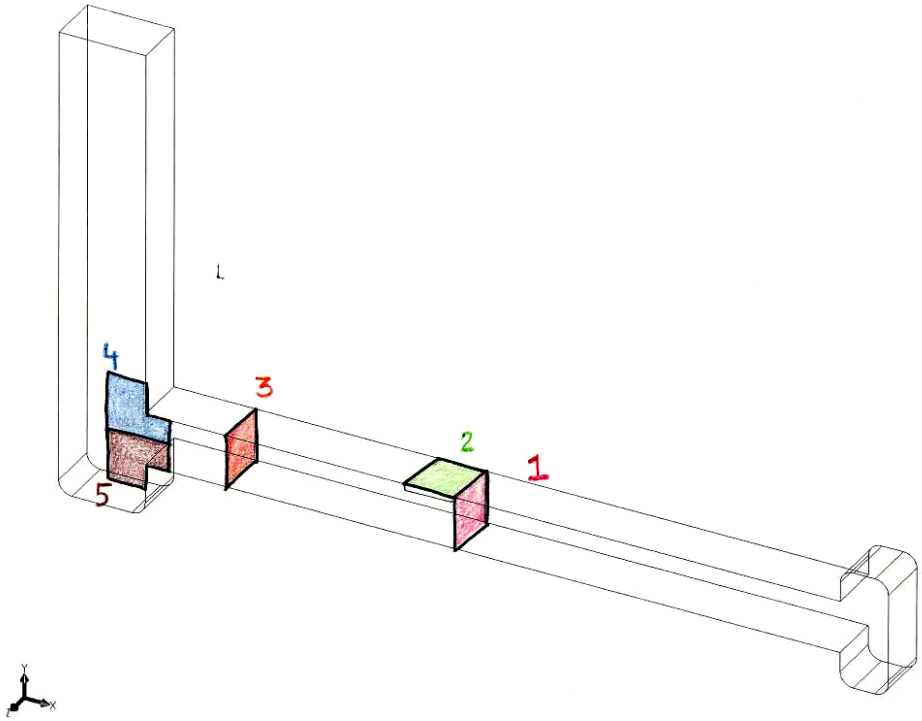

Figure 52: Locations of metallography samples #1 - #5.

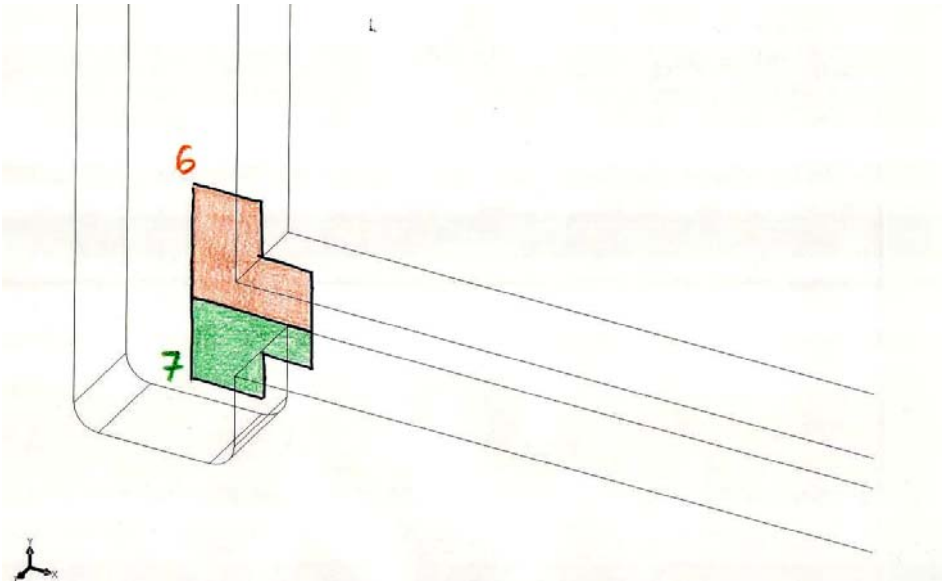

Figure 53: Locations of metallography samples #6 and #7.

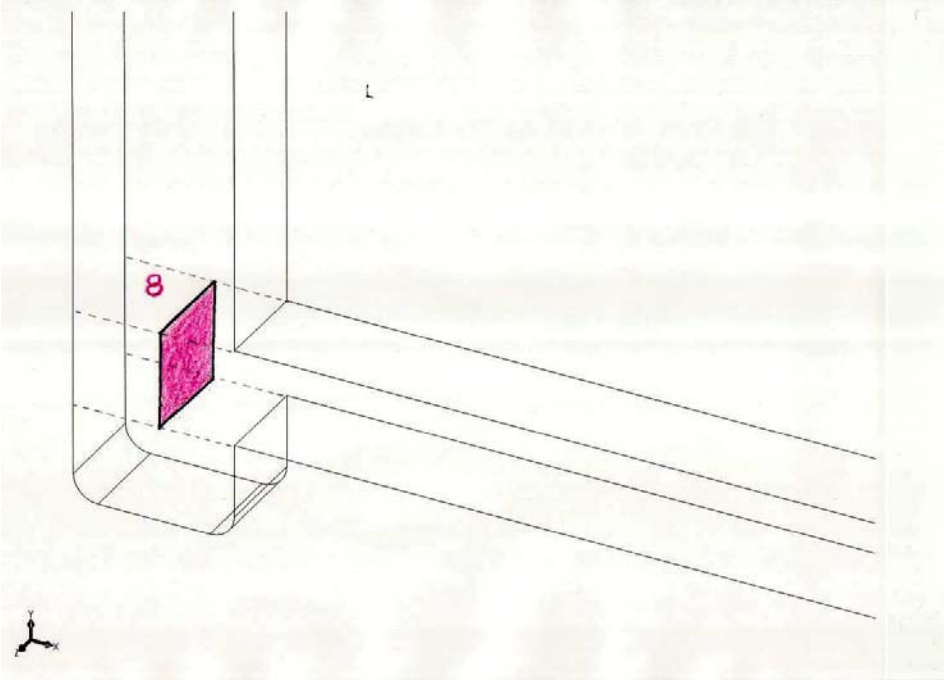

Figure 54: Location of metallography sample #8.

Individual metallographic specimens were mounted in a clear plastic Lucite mount using a Buehler SimpliMet 2000 automatic mounting press. The Lucite medium was allowed to cure at 170 °C for 12 minutes and was cooled with a stream of cold water for 5 minutes. The mounted specimens were then placed into a specimen holder of a LECO AP-60 automatic polisher. The following polishing procedure (Table 13) was followed for both alloys:

Table 13: Polishing procedure for microscopic examination of as-cast samples.

Paper grit / Cloth	**Wheel speed [RPM]**	**Load (per sample) [LBS]**	**Time [min]**
180	150	5	Until plane
320	150	5	3
600	150	5	3
Lecloth + 5 μm alumina	150	5	4
Lecloth + 1 μm diamond paste	150	5	4
Chemomet + 0.5 μm colloidal silica	Manual polish	-	15 sec

In order to determine the alloy grain size, the microscopic specimens were etched with an etchant suitable for polarized light optical microscopy. The AZ91D and AE42 alloys required different etchants to reveal their grain structure:

- AZ91D alloy: The etchant consisted of 50 mL distilled water, 150 mL anhydrous ethyl alcohol and 1 mL acetic acid. The solution was prepared fresh. A sample was immersed in the solution for two minutes and agitated during etching. The sample was removed, rinsed with methanol and dried with a blast of hot air. Blasting with hot air was critical for proper development of the etchant and subsequent observation of the alloy grain structure.
- AE42 alloy: The etching procedure consisted of immersing the alloy sample in the etchant used for AZ91D alloy for two minutes. Then, the sample was placed into a second solution consisting of 90 mL distilled water and 10 mL hydrofluoric acid. Subsequently, the sample was rinsed with warm water and dried with a blast of hot air.

Selected specimens were analyzed using JEOL JSM-6380LV scanning electron microscope at the Dept. of Mechanical and Industrial Engineering at Ryerson University. The SEM operating conditions (e.g., voltage, detector type, working distance, etc.) are indicated in each SEM micrograph.
In order to enhance the contrast of constitutive phases present in each alloy and to avoid damage due to chemical etching of alloy specimen surfaces, differential interference contrast (DIC) microscopy was carried out using Zeiss AxioVert optical microscope. Further, dark field (DF) and bright field (BF) microscopy was also carried out to observe the general microstructure of individual alloys at 50x, 200x and 500x magnifications.

A Canon Digital Rebel XT eight megapixel camera was used to capture the micrographs. This camera was not a part of the Zeiss imaging system. As a result, the micrographs do not contain embedded scale markers. However, the magnification is included for every micrograph.

Observation of the casting surface was also performed with a Leitz Wild M8 stereo microscope. Magnifications of 6x, 25x and 50x were used to observe the samples.

4.6 MAGMASOFT® Simulations

Computer modeling in MAGMASOFT® was carried out to assist with understanding of casting mold filling, solidification and defect formation. In order to perform the simulations, fundamental information

about the experiments were submitted to Mr. M. Proske and Ms. D. Gaddam of Magma Foundry Technologies Inc. (MFT). Three dimensional drawings of the casting and the mold were created in SolidWorks® software. Alloy compositions obtained from spark emission spectrometer were also submitted. The raw temperature data from embedded casting thermocouples along with temperature data collected from the three in-mold thermocouples were provided to MFT. Three sets of thermocouple data (from three repeat casting trials) were provided for each casting condition.

Upon consultation with MFT staff, the scope of the simulations was determined and desired outputs identified. For the four casting conditions indicated in Table 14, the following results were sought:

1. HTC as a function of temperature.
2. Casting filling temperature.
3. Filling velocity.
4. Solidification temperature profile.
5. Hot spot location.
6. Casting stress.
7. Casting displacement.

Table 14: Casting conditions simulated in MAGMASOFT®.

Simulation	Alloy	Pouring temperature [°C]	Mold temperature [°C]
1	AZ91D	720	210
2	AZ91D	720	250
3	AE42	765	340
4	AE42	765	390

In order to enable the computation of the governing equations, suitable boundary (BC) and initial conditions (IC) were specified. The following conditions were relevant for the simulations used in this project.

1. Temperature:
    a. Metal: equal to the alloy pouring temperature.
    b. Mold: equal to the permanent mold initial temperature.

2. Velocity:
    a. The initial velocity was approximated using local 1-D velocity field for the inlet region.
    b. No-slip condition at mold wall.
3. Pressure:
    a. The static pressure for the inlet was set at the atmospheric pressure level.

The boundary conditions applicable to the system incorporated the development of an air-gap during casting solidification. The effective values of thermal conductivity were calculated during the simulation process using instantaneous fractions of solids. Further, the development of the alloy specific heat was approximated using linear model joining discrete (experimental) data measurements performed at room temperature up to the solidus temperature. Further, MAGMASOFT® was used to carry out thermal analysis using virtual thermocouples. Four virtual thermocouples were defined (Figure 55) in the simulation and cooling curves were generated for these locations. The virtual thermocouples were located 10 mm (half-way) through the thickness of the casting. The location of the thermocouples was selected as follows:

#1 – "*Middle of sprue*": centre of the sprue in the critical region.

#2 – "*Hot tear*": casting critical region; 7 mm from the right edge of the sprue and 7 mm below the upper edge of the horizontal bar.

#3 – "*Skin at midsection*": casting skin at the horizontal bar's mid-section (3 mm below the surface of the top edge, 127 mm right of the sprue's right edge).

#4 – "*Center at midsection*": casting centre at the horizontal bar's mid-section (10 mm below the surface of the top edge, 127 mm right of the sprue's right edge).

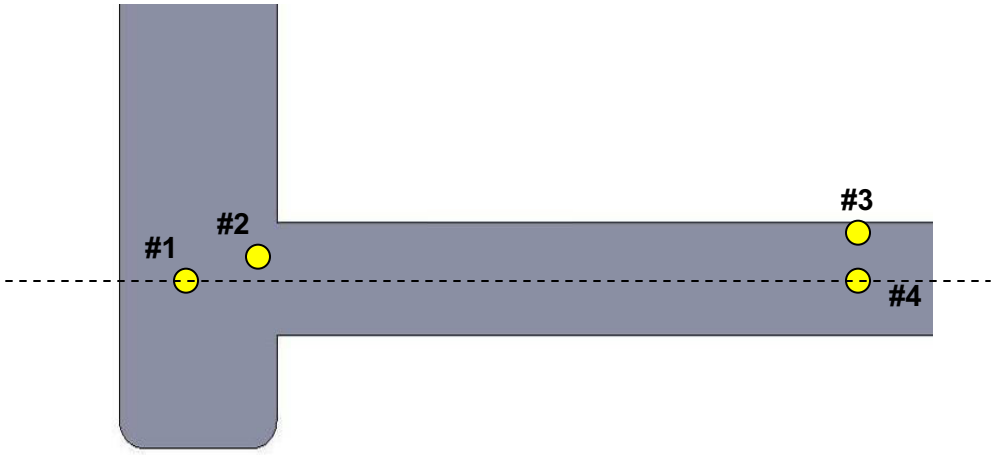

Figure 55: Locations of virtual thermocouples.

4.7 Fraction of Solids Model

Fraction of solids, f_s, evolution may be calculated from raw temperature data using several mathematical formulations. In this research, a model developed by Tacke *et al.* [65] was used for calculating the instantaneous fraction of solid during solidification. It was expected that, due to the relatively high cooling rates experienced by the casting, the concentration of solute at the solid-liquid interface was not constant. As a result, solute was rejected into the liquid and the local solidus and liquidus temperatures changed during alloy solidification. The validity of the model, given by Equation 26 was empirically tested and excellent correlation was demonstrated [12].

$$f_s = \frac{T_L - T + \frac{2}{\pi}(T_S - T_L)\left\{1 - \cos\left[\frac{\pi(T - T_L)}{2T_S - T_L}\right]\right\}}{(T_L - T_S)\left[1 - \frac{2}{\pi}\right]} \tag{26}$$

Where:

T_L = non-equilibrium liquidus temperature

T_S = non-equilibrium solidus temperature

T = instantaneous alloy temperature

4.8 Mechanical Testing

The 260 mm long horizontal bars were sectioned axially into two equal parts. Each part was machined according to ASTM B-577M standard for tensile specimens. A minimum of two castings (i.e., four tensile samples) were obtained for each test condition in order to ensure repeatability of mechanical testing.

Tensile tests were carried out at room temperature using UNITED STM-50KN desk-top tensile testing machine. Selected castings were also sectioned and coupons for Vickers microhardness were prepared. These samples were prepared according to metallography polishing techniques described in Section 4.5. A Buehler MICROMET5130 microhardness tester with a pyramidal diamond tip was used to measure Vickers microhardness.

Chapter 5 – Experimental Results and Discussion

This chapter presents the results of experiments carried out in this research. Each result is discussed and related to the onset of hot tearing. Specifically, the evolution and observation of hot tears on the macro-scale (Section 5.1), casting microstructure (Section 5.2), thermal analysis (Section 5.3) and neutron diffraction (Section 5.4) are presented. A comprehensive discussion of the interactive effects between the fundamental parameters is presented in Section 5.5. [†]

5.1 General Observation of the Castings

Castings ejected from the steel mold were allowed to naturally cool to room temperature and visually inspected. Castings which did not meet required criteria (e.g., complete fill or adequate pouring cup size) were rejected and excluded from further analysis. The following text focuses on the AZ91D and AE42 castings produced at the onset of hot tearing and subjected to ND. [‡]

It was observed that the onset of hot tearing in the AZ91D castings made at 720 °C pouring temperature was between 210 °C and 250 °C mold temperature. In the case of the AE42 alloy cast at 765 °C pouring temperature, the onset of hot tearing was between 340 °C and 390 °C mold temperature. The term "low mold temperature casting" refers to a casting made at a mold temperature of 210 °C (AZ91D) or 340 °C (AE42). These two castings had visible surface hot tears. The term "high mold temperature casting" refers to a casting made at a mold temperature of 250 °C (AZ91D) or 390 °C (AE42). These two castings were free of visible surface hot tears.

AZ91D Castings

As Figure 56 shows, the AZ91D casting made at 210 °C mold temperature had a hairline crack in the vicinity of the 90° junction of the horizontal bar and the downsprue. This crack was present on the front side of the casting, but did not extend to the back side. Further, a hairline hot tear was observed propagating from the 90° corner towards the center of the downsprue. Increasing the mold temperature from 210 °C to 250 °C eliminated formation of visible surface hot tears at the 90° corners, as can be observed by comparing Figure 56 to Figure 57.

[†] *Much of the data presented in this chapter has been published in peer-reviewed journals, as indicated in footnotes.*

[‡] *Parts of sections 5.1.1 – 5.1.3 have been published in*: Bichler, L., Lee, K., Elsayed, A. and Ravindran, C., "Effect of mold and pouring temperature on the hot tearing of AZ91 magnesium alloy", International Journal of Metalcasting, Vol. 1., No. 2, 2008, pp. 43 – 56; Bichler, L., D'Elia, F. and Ravindran, C., "Reduction of hot tears in AZ91 magnesium alloy: Effect of cooling rate", AFS Transactions, Vol. 117, 2008, Paper 08-109.

The casting made at 210 °C mold temperature shows a significant surface discoloration in the downsprue. The discoloration extended from the pouring cup towards the critical region and was likely related to the formation of magnesium-based oxides during mold filling. These oxides began to form when the molten alloy entered the casting cavity and was no longer protected by the CO_2 cover gas. As the molten metal filled the cavity, it was exposed to ambient air for ~ 5 seconds, which was sufficient to initiate an oxidation reaction at the advancing metal front. This hypothesis and the kinetics of oxide formation in AZ91D alloy in ambient atmosphere were studied in a separate set of simple experiments. A small amount of AZ91D was melted in a steel crucible. When unprotected with CO_2 covergas, melt oxidation in the crucible initiated with the formation of a thin gray film on the molten metal surface. Subsequently, a relatively thick (~ 1cm) gray crust of MgO developed. The MgO crust prevented direct contact between molten magnesium and the ambient atmosphere, thus decreasing the rate of oxidation. However, with sufficient time (~ 25 seconds), the MgO cracked, disintegrated and formed a fine white powder, which was highly combustible. Also, the crust disintegration exposed a fresh liquid metal surface to the ambient atmosphere, thereby renewing the crust and continuously feeding the oxidation process. Based on these experiments, the discoloration of the casting surface in Figure 56 was likely associated with the first stage of oxidation, i.e., thin film formation. This hypothesis was verified when thin film oxides were observed in the casting interior and resulted in the formation of folds, as discussed in detail in Section 5.2.4. Unlike in the case of the downsprue, the horizontal bar's surface appeared free of oxides. Thus, the film oxides were successfully retained in the bottom trap of the downsprue, as intended.

The back side of the horizontal bar contained a surface defect resembling frozen metal flow lines. These flow lines formed as the advancing liquid melt contacted the relatively cooler mold and began to solidify. The flow lines indicate several problems associated with filling of the horizontal bar:

1. Multiple metal streams were present during filling of the horizontal bar. These streams began to solidify upon contact with the relatively cool mold. Consequently, temperature gradients between the streams developed and prevented their proper fusion, resulting in flowlines.
2. High melt turbulence developed in the area of the critical region. This was observed by the non-uniform and random shape of the flowlines.
3. Melt turbulence likely entrapped air in the casting leading to the formation of surface blisters.

Thus, the critical region of the casting was inherently rich in defects. In the 210 °C mold temperature casting, the region with flowlines and other defects (e.g., blisters) extended approximately 5 cm downstream along the horizontal bar. Increasing the mold temperature from 210 °C to 250 °C

significantly decreased the downstream length of the defect-rich area to ~ 1 cm. As will be discussed in Appendix A1.3.3, these observations are in general agreement and support the casting filling pattern predicted by MAGMASOFT® (development of highly-turbulent and reversing metal flow in the casting's critical region).

For both AZ91D castings, the bottom part of the downsprue, i.e., the trap, shows a small amount of flashing. This flashing was the result of insufficient clamping force between the steel mold and the mating closing plate allowing liquid metal to penetrate a small gap (< 1mm) between these mold parts. The flashing formed during the initial stage of mold filling, when the liquid metal viscosity was low. Typically, such flashing is undesirable as it deteriorates the surface finish of a casting and must be removed in post-casting operations. However, the flashing observed in the experiments did not interfere with the solidification pattern of the casting and did not impact the hot tearing tendency of the casting. Thus, presence of flashing on the casting was neglected.

It was further observed that the downsprue portion of the casting contained markings from the ejector pins. These marks were made by some of the ejector pins protruding out of the mold or, conversely, being recessed into the mold. Movement of the ejector pins was caused by a 0.0035" clearance between the ejector pin and the pin-hole. When the mold was closed, utmost care was taken to align the ejector pins flush with the cavity wall. However, during mold filling, the molten metal pushed the pins into the steel mold, which subsequently created a small protrusion on the casting surface. These surface protrusions were up to 2 mm high. Similarly as in the case of the flash around the edges of the casting, these protrusions did not alter the casting solidification profile or the stress distribution in the casting. Consequently, these marks were neglected in subsequent analysis.

AE42 Castings

Casting experiments performed with the AE42 alloy revealed the alloy's very high tendency to hot tearing. All castings made at 720 °C and 740 °C pouring temperatures exhibited severe hot tears. The onset of hot tearing was reached only when the pouring temperature increased to 765 °C and the associated cooling rate sufficiently decreased. For mold temperatures less than 300 °C, hot tears forming at the 90° junction corner extended several centimeters into the downsprue. At a 340 °C mold temperature, a hairline crack formed at the upper edge of the horizontal bar, as shown in Figure 58a. This hairline crack was visible only on the front side of the casting. When the mold temperature was increased to 390 °C, surface hot tears were eliminated, as observed in Figure 59.

(a) Front *(b) Back*

Figure 56: Critical region of AZ91D casting made at 210 °C mold temperature.

(a) Front *(b) Back*

Figure 57: Critical region of AZ91D casting made at 250 °C mold temperature.

Similarly, as in the case of the AZ91D alloy castings, the downsprue of the AE42 casting made at the low mold temperature (i.e., 340 °C) shows a surface discoloration. This discoloration was most apparent above the critical region of the downsprue, where highly turbulent metal flow developed, thus exposing large surface area of liquid magnesium to ambient atmosphere and promoting melt oxidation. However, in the case of the AE42 castings, which contain rare-earth elements (which prevent Mg oxidation as a result of RE preferential oxidization), the overall extent of surface discoloration was lower than in the AZ91D alloy castings. Thus, the amount of film oxides entrapped in the casting was lower in the AE42 alloy than in the AZ91D alloy, as later verified with microscopic examination.

The AE42 castings show distinct flow lines in the horizontal bar, near the critical region. In particular, the back side of the AE42 casting made at 390 °C mold temperature shows a clear trace of the metal filling pattern. The observed “wave” suggests that the horizontal bar did not fill uniformly from the bottom edge up. Instead, the flow lines indicate that a broken and turbulent metal flow front advanced axially from the entrance of the horizontal bar towards the anchor of the casting. Such a filling pattern is typically undesirable as it potentially promotes entrapment of air and oxides in the casting interior. Further, turbulent filling establishes significant temperature gradients in the casting, leading to thermal strain gradients or solutal inhomogeneity. Observation of the flowlines on the casting surface was in agreement with numerical simulations of the AE42 casting filling process (Appendix A1.3.3).

(a) Front *(b) Back*

Figure 58: Critical region of AE42 casting made at 340 °C mold temperature.

(a) Front *(b) Back*

Figure 59: Critical region of AE42 casting made at 390 °C mold temperature.

5.1.1 Visual Inspection of Specimens for Microscopy

Sectioning of individual castings at eight locations, as indicated in Figure 52 to Figure 54, enabled observation of the casting microstructure at locations of interest. Observing the samples with macro optics and a low magnification microscope revealed general information about casting macro porosity, hot tear propagation and casting fill defects (e.g., folds) in the casting interior. Figure 60 to Figure 63 show macro-images of the specimens used for microscopic analysis (Section 5.2). Since each sample was extracted from the casting with a view to observing specific features of interest (Table 12), the features of interest for specific samples (e.g., Sample #1 for the two mold temperatures and two alloys) are described hereunder.

Sample #1

Sample #1 reveals the cross section of the horizontal bar, half-way along the axial length of the horizontal bar. The specimens from Figure 60 - Figure 63 revealed that shrinkage porosity formed in the centre of the horizontal bar's cross section. In ingot casting, this porosity is referred to as "centerline shrinkage porosity". Presence of centerline shrinkage porosity suggests that the skin regions solidified rapidly due to their contact with the relatively cool mold. During its solidification, the skin consumed liquid metal from the bar's centre in order to feed its shrinkage. Consequently, the centre region was depleted of liquid and shrinkage porosity readily nucleated at late stages of solidification. As the mold temperature increased for either alloy, the extent of centerline porosity in the horizontal bar decreased. This suggests that with an increase in mold temperature, the axial feeding of the horizontal bar improved. However, since centerline porosity was observed even in the high mold temperature castings of both alloys, it appears that elevating the mold temperature did not allow ideal feeding of the entire horizontal bar. Thus, presence of extensive porosity in Samples #1 suggests that the formation of shrinkage porosity in the critical region of the casting (discussed later) was not the result of isolated feeding problems in the critical region. Instead, inadequate feeding of the entire horizontal bar occurred.

Sample #2

Sample #2, which was extracted from the top edge surface of the horizontal bar near the bar's axial midsection, indicates that only minimal porosity formed in the skin regions. Minimal levels of porosity were expected, since the skin regions solidified rapidly (due to contact with cool mold) with sufficient liquid metal feed from the centerline regions. Thus, comparison of Sample #1 and #2 supports the hypothesis that the horizontal bar solidified from the metal mold interface towards the centre of the horizontal bar and hoop solidification direction was present.

Sample #3

Sample #3 shows the cross section of the horizontal bar, similar to Sample #1, but in the critical region of the casting where hot tears were observed. Comparison of Samples #1 and Samples #3 from the same casting suggests that the amount of centerline shrinkage porosity remained similar for the two locations.

Inspection of Samples #3, especially in the case of AZ91D castings revealed large sub-surface cavities near the top edge of the horizontal bar. These cavities coincided with surface blisters observed in Figure 56. Formation of the blisters was possibly related to melt turbulence resulting in air entrapment in casting interior. The blisters were not observed in Samples #1, thus suggesting that melt turbulence decreased with downstream filling of the horizontal bar.

The size of the blisters appeared to decrease with increasing mold temperature. Such observation could be related to improved fluidity of the molten metal at higher mold temperatures. Further, supported by slower casting solidification, the alloy remained amenable to deformation and the blisters with entrapped air possibly collapsed. However, for both alloys, the cooling rates in the region with blisters remained too high to allow complete fusion of the cavity walls. This phenomenon was similar to incomplete fusion of multiple metal streams, which resulted in the formation of folds in the casting interior, as will be discussed in Section 5.2.4.

Samples #4 and #6

In the case of Samples #4 and #6 from the AZ91D castings, a mold temperature increase from 210 °C to 250 °C eliminated blisters and folds from the critical region. Thus, on the macro scale, soundness of the critical region improved.

A detailed discussion of hot tear evolution in these samples will be presented in Section 5.2.2, where these samples were examined with several high power microscopes. With respect to the current macro analysis of the samples, it was noted that hot tears formed at the 90° corner and propagated towards the downsprue interior. The extent of hot tears in Samples #4 and #6 was similar, suggesting that hot tears progressed similarly on the horizontal bar's surface (Sample #4) as well as in its interior (Sample #6).

Samples #5 and #7

Samples #5 and #7 were extracted from the bottom edge of the horizontal bar's critical region. For both alloys, hot tears nucleating in this region were eliminated with an increase of the mold temperature. This region was not expected to exhibit significant hot tearing, since the bottom portion of the downsprue, i.e., the bottom trap, was not restricted in contraction. The free contraction of the trap possibly enabled relaxation of evolving stresses near the bottom 90° corner during solidification. However, presence of hot tears in this region suggests that sufficient relaxation of stresses did not occur, or that hot tears likely formed either: 1) at a very late stage of solidification, or 2) after completion of solidification of the bottom trap. If the hot tears nucleated above the solidus temperature, i.e., case 1, then the cause of hot tear nucleation could be related to insufficient feeding of the bottom 90° corner region. However, if the hot tears formed after solidification of the trap was complete, i.e., case 2, then these hot tears would be induced by the thermal contraction of the horizontal bar.

It was also observed that Samples #5 or #7 of any castings did not exhibit any indications of subsurface blistering or folds caused by melt turbulence. Such observation suggests that the melt temperature during the trap's filling was significantly higher than the melt temperature during filling of the upper edge of the horizontal bar, several seconds later. Due to elevated melt temperature during filling of the bottom edge, the metal streams were able to properly fuse and avoid blister formation.

Sample #8

Inspection of Sample #8 from all castings revealed the presence of extensive centerline shrinkage porosity. A porosity band formed half-way through the thickness of the casting and was aligned in the *y*-direction. In the case of the AZ91D casting at 250 °C mold temperature, a set of two narrower bands formed, instead of a single band as observed in the other castings.

The presence of the extensive centerline porosity in Sample #8 suggests that the horizontal bar's entrance region (near the 90° junction) experienced severely limited feeding during late stages of solidification. It is likely that similarly as in the solidification of the horizontal bar, rapid hoop solidification of the downsprue promoted formation of centerline porosity in the downsprue. Thus, liquid metal was drawn by the solidifying skin of the downsprue and insufficient liquid feeding did not heal the porosity. Increasing the mold temperature improved the feeding of the downsprue and decreased the extent of centerline porosity in Sample #8.

Section Summary

The macro examination of the microscopy specimens suggests that hot tear nucleation was likely related to casting feeding. Hot tears were observed to propagate from the 90° corners, suggesting that the stress concentration imposed by the 90° corner was relevant for hot tear nucleation. Upon nucleation, hot tears propagated towards the sprue interior towards areas of high shrinkage porosity.

Upon solidification of the critical region, thermal contraction of the horizontal bar possibly promoted further opening of the nucleated hot tears. Also, thermal contraction possibly caused formation of hairline hot tears near the bottom edge 90 ° corner (in the vicinity of the bottom trap of the downsprue). For both alloys, increasing the mold temperature decreased the extent of shrinkage porosity, hot tearing and additional casting defects, such as blisters, folds and surface oxides.

5.1.2 AZ91D Hot Tearing Susceptibility Index

The HSI values calculated via Equation 23 for AZ91D castings at various mold and pouring temperatures reveal that HSI values above 60 (unitless) represent castings with severe hot tears inducing separation of the horizontal bar from the downsprue in the critical region.

It was expected that an increase of pouring temperature would decrease the hot tearing susceptibility, regardless of the mold temperature. This trend was observed only for mold temperatures above ~220 °C. For mold temperatures less than ~220 °C, the hot tearing tendency appeared to increase with increasing pouring temperature. This trend suggests that the initial thermal shock at the metal-mold interface and the formation of a solid skin possibly played an important role on the nucleation of hot tears in the critical region. For example, at 720 °C pouring temperature and low mold temperatures (< 220 °C), the thermal shock possibly induced a deformation (strain) shock in the skin region. The ensuing non-uniform material deformation likely promoted microcrack formation. Further, temperature gradients developing along the horizontal bar would result in its inhomogeneous axial contraction. Consequently, at high pouring and low mold temperatures, the degree of strain inhomogeneity was high, leading to a high susceptibility for hot tear formation [66].

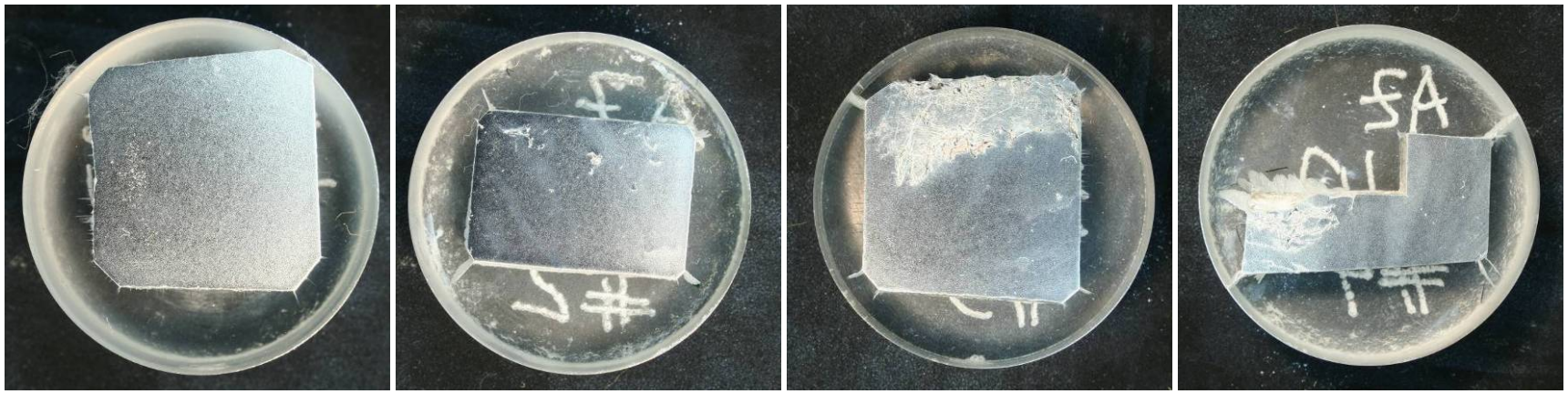

(a) Sample #1 *(b) Sample #2* *(c) Sample #3* *(d) Sample #4*

(e) Sample #5 *(f) Sample #6* *(g) Sample #7* *(h) Sample #8*

Figure 60: AZ91D metallographic samples (macro images), 210 °C mold temperature.

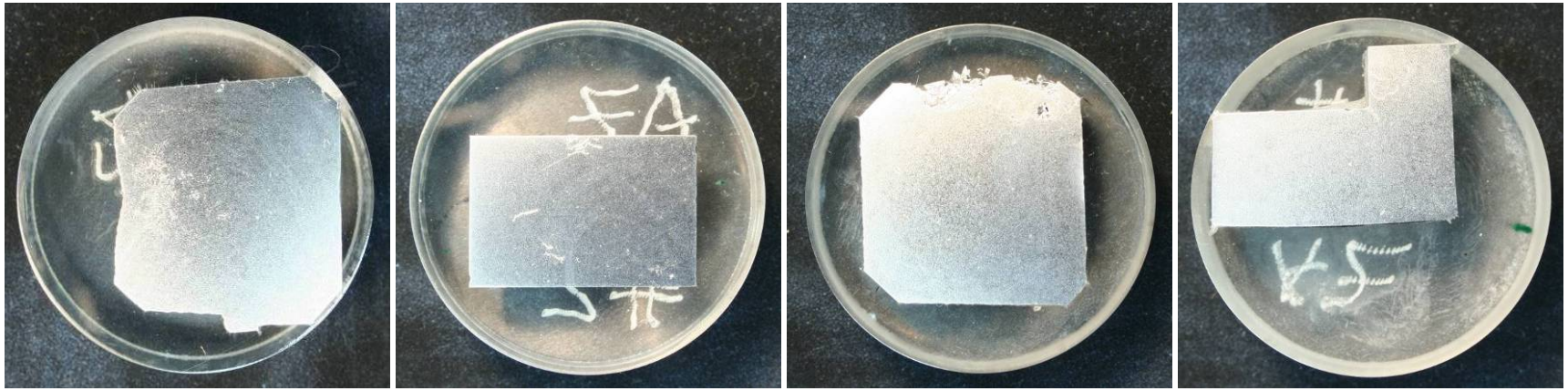

(a) Sample #1 *(b) Sample #2* *(c) Sample #3* *(d) Sample #4*

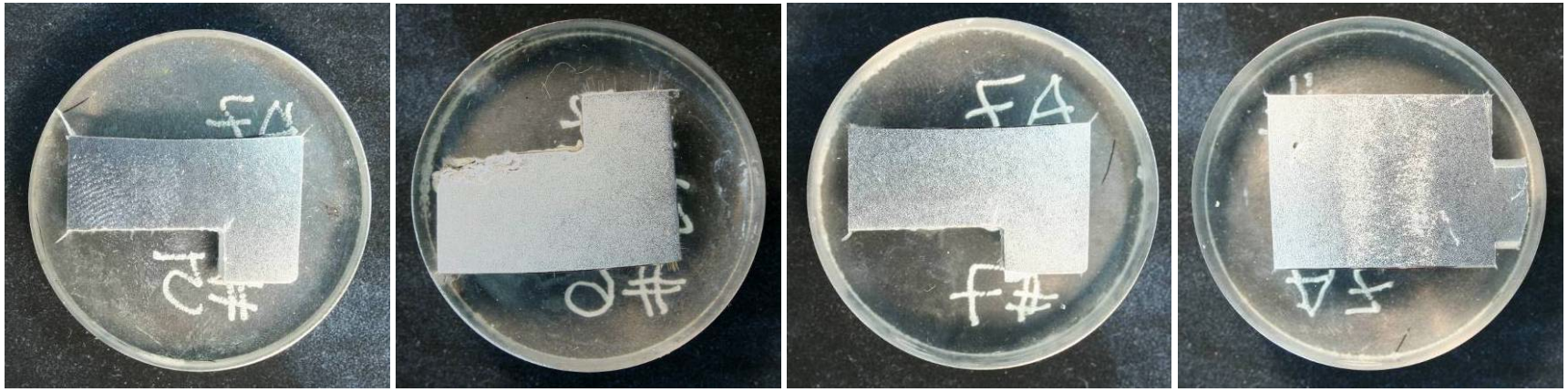

(e) Sample #5 *(f) Sample #6* *(g) Sample #7* *(h) Sample #8*

Figure 61: AZ91D metallographic samples (macro images), 250 °C mold temperature.

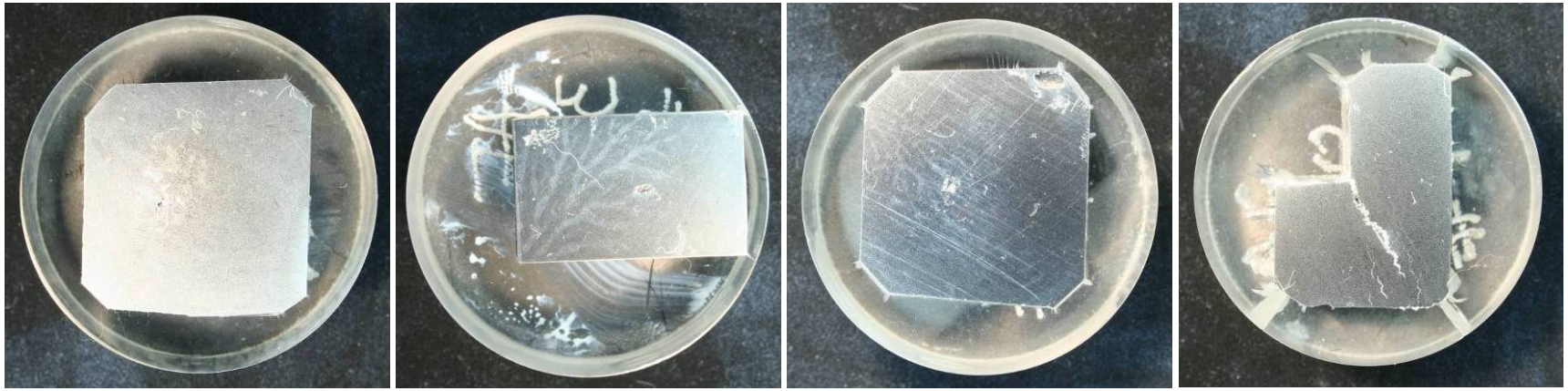

(a) Sample #1 *(b) Sample #2* *(c) Sample #3* *(d) Sample #4*

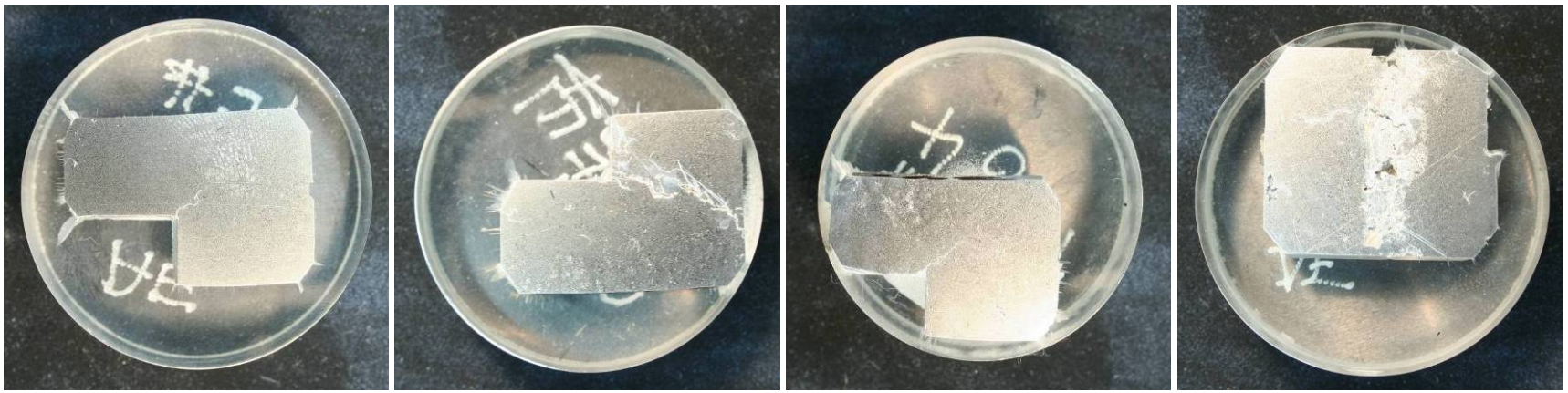

(e) Sample #5 *(f) Sample #6* *(g) Sample #7* *(h) Sample #8*

Figure 62: AE42 metallographic samples (macro images), 340 °C mold temperature.

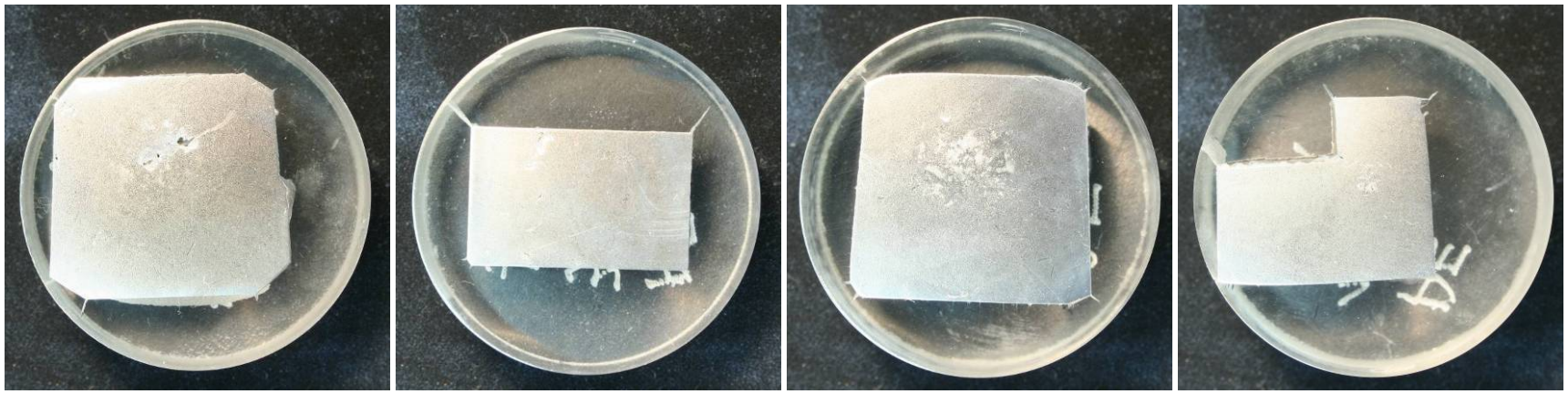

(a) Sample #1 *(b) Sample #2* *(c) Sample #3* *(d) Sample #4*

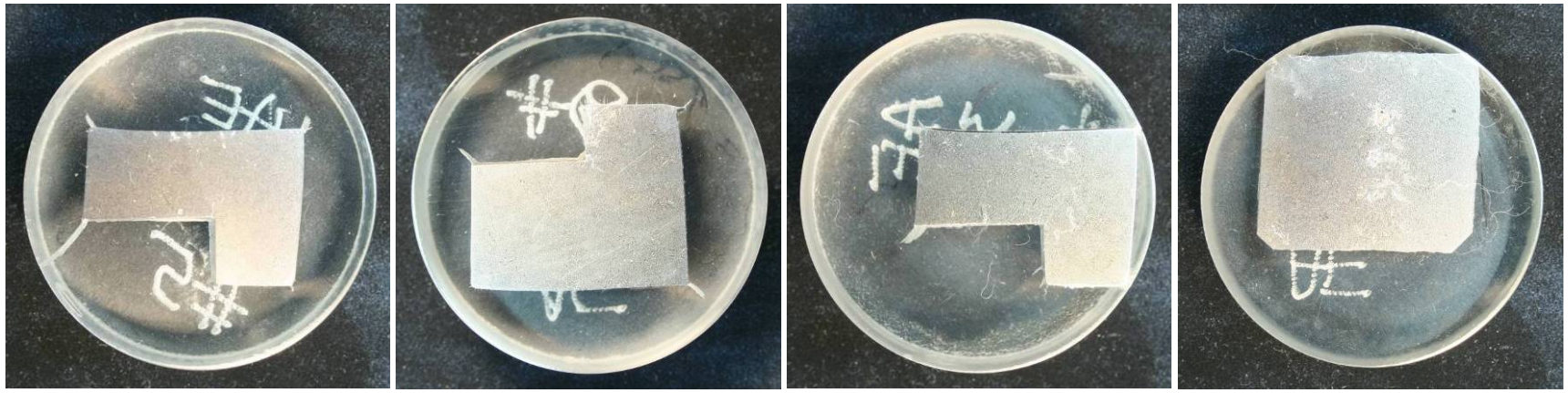

(e) Sample #5 *(f) Sample #6* *(g) Sample #7* *(h) Sample #8*

Figure 63: AE42 metallographic samples (macro images), 390 °C mold temperature.

5.1.3 Mechanical Testing

Mechanical testing of the tensile specimens machined from the horizontal bars of AZ91D castings was carried out at room temperature to observe the effect of the mold temperature on the as-cast yield strength of the alloys. These castings were made at 700 °C pouring temperature.

It was expected that with increasing mold temperature, the yield strength would decrease due to an increase in grain size. However, as observed in Figure 64, the yield strength initially increased for mold temperatures from 140 °C to 220 °C, followed by a gradual decrease thereafter.

The parabolic strength dependency was likely related to the alloy microstructure. For low mold temperatures, the casting solidified rapidly and only a small amount of the hard and brittle Mg-$Mg_{17}Al_{12}$ eutectic formed at the grain boundaries. Consequently, strengthening by this phase was minimal and the resultant alloy was relatively weak. With an increase in mold temperature, precipitation strengthening by the β-$Mg_{17}Al_{12}$ phase occurred with a concomitant increase in yield strength. With additional increase of the mold temperature beyond 220 °C, the decreasing cooling rates enabled coalescence of the β-phase in the interdendritic regions. Also, the alloy's grain size began to increase. Thus, the load-bearing surface area per unit volume decreased, resulting in a decrease of the yield strength of the alloy [67].

Vickers microhardness (HV) was determined for Samples #3. Measurements were obtained at the skin and center regions of the horizontal bar and are presented in Figure 65.

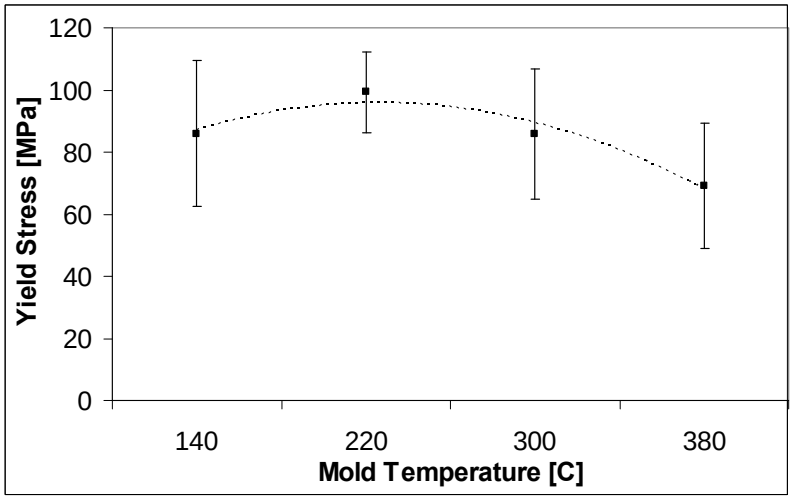

Figure 64: Effect of mold temperature on as-cast AZ91D yield stress. 700 °C pouring temperature.

The micro hardness followed a similar parabolic trend with varying mold temperature as the yield strength. However, the microhardness peak was noted at ~ 300°C, instead of 220 °C (for yield strength). Also, it was observed that the skin regions exhibited higher hardness than the bar's center regions. This result may be related to the finer grain size observed in the bar's skin regions (Section 5.2.1). Due to faster solidification rate at the metal-mold interface, the skin regions likely experienced grain-boundary strengthening and retained high hardness and strength. However, at the same time, the relatively high strength would decrease the skin region's ductility. Thus, the development of strain gradients in the critical region, in conjunction with the limited ductility of the skin, resulted in relatively easy crack nucleation in the casting skin [67].

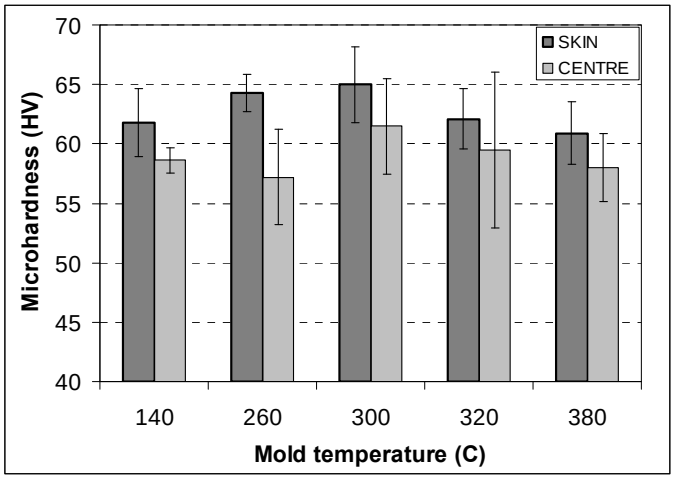

Figure 65: Effect of mold temperature on as-cast AZ91D microhardness. 700 °C pouring temperature.

5.2 Microscopic Analysis

The samples described in Section 4.5 were polished and prepared for various microscopic analyses to characterize features of interest.

- Light Optical Microscopy (LOM) with i) Bright Field (BF), ii) Dark Field (DF) and iii) Differential Interference Contrast (DIC) polarized light (PL) modes. Micrographs at magnifications 50x, 200x and 500x were used to observe the general microstructure of the alloys.
- Stereo Microscopy (SM) was used to image the samples at magnifications 6x, 20x and 50x. In particular, SM was used while determining the grain-size of the alloys.
- Scanning Electron Microscopy (SEM) images at magnifications 1000x and 2000x with Back-Scattered Electron (BSE) detector in place were obtained to observe the hot tear nucleation sites,

segregation phenomena, morphology of the interdendritic regions and the structure of folds and interdendritic cavities.

Each of these microscopic techniques revealed unique features of the alloy's microstructure related to the alloy's susceptibility to hot tearing. These observations are presented in the following sections.

The LOM and SM micrographs were obtained with a high resolution dSLR camera. Since the camera was not controlled by the microscope software, a length scale could not be embedded in the micrographs. However, the magnification level is provided with each micrograph caption.

5.2.1 Grain Size

The grain size in AZ91D and AE42 Samples #3 was determined. Sample #3 was selected due to its proximity to the region with hot tears.

In order to accurately measure the grain diameter, extensive specimen preparation, as outlined in Section 4.5 was carried out. In principle, an etchant film was created on the specimen, i.e., the substrate, where the film's structure was governed by the specimen's grain structure. As Figure 66 shows, the etchant film developed ridges and cracks, which varied with the alignment (orientation) for each substrate grain. As a result, the etchant film produced grain contrast. Micrographs illustrating the general grain structure of the castings are presented in Figure 67 to Figure 70.

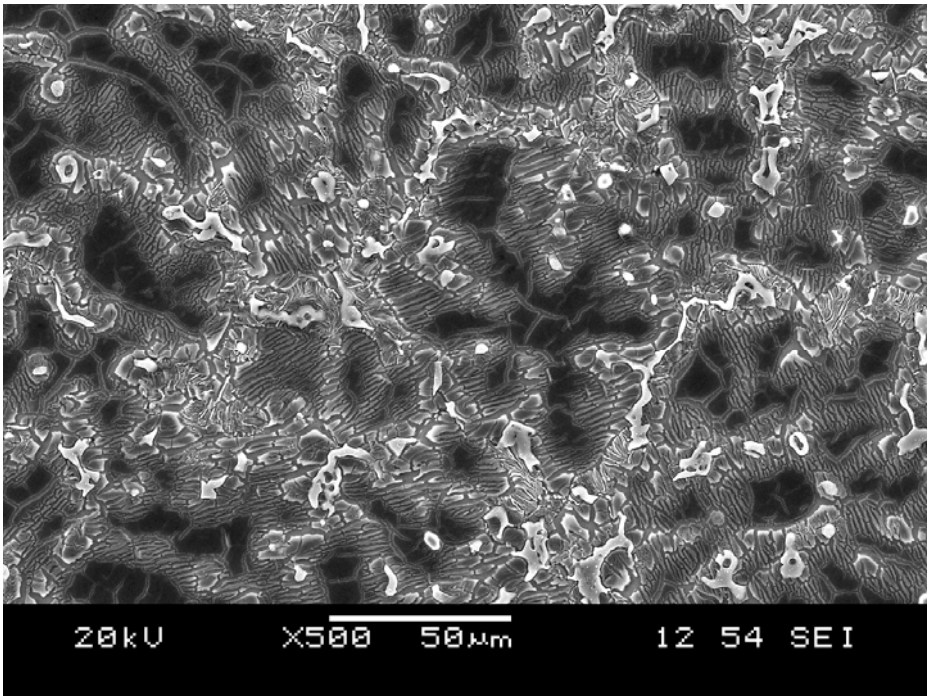

Figure 66: Etchant film used to reveal alloy grains.

As Figure 67 - Figure 70 show, a significant difference in grain size was observed at the horizontal bar's centre and its edge (i.e., near the metal-mold interface). OmniMet® image analysis software was used to quantify the grain diameter and its distribution for these two regions and the results are presented in Figure 71.

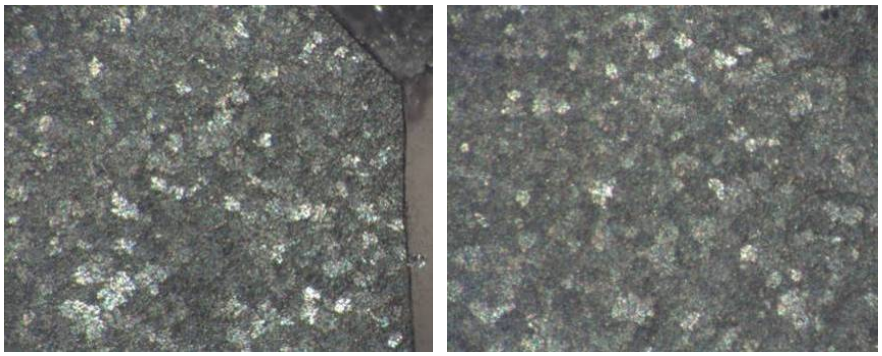

(a) Edge (b) Center

Figure 67: Grain structure of AZ91D alloy at 210 °C mold temperature (SM, 25x).

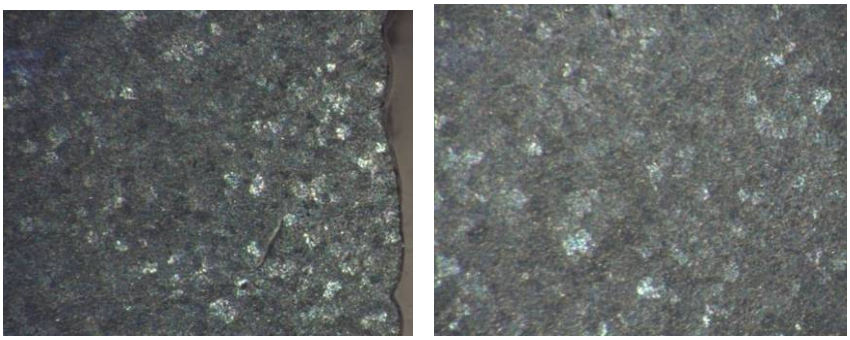

(a) Edge (b) Center

Figure 68: Grain structure of AZ91D alloy at 250 °C mold temperature (SM, 25x).

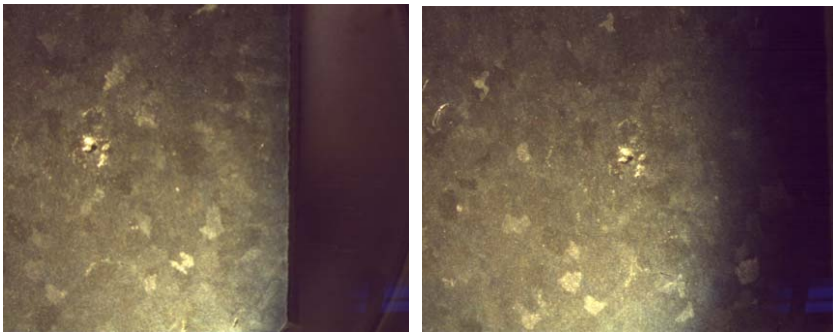

(a) Edge (b) Center

Figure 69: Grain structure of AE42 alloy at 340 °C mold temperature (SM, 6x).

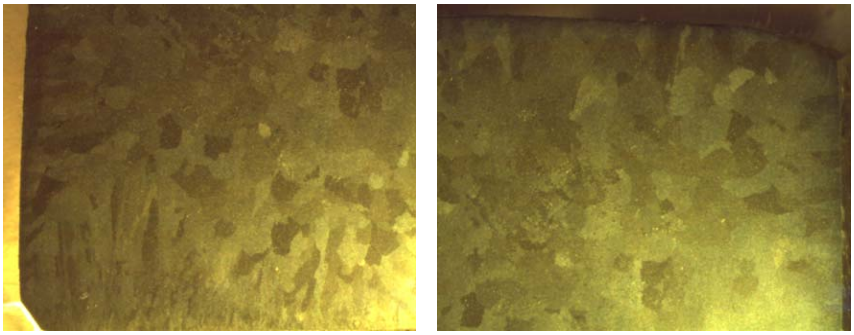

(a) Edge (b) Center

Figure 70: Grain structure of AE42 alloy at 390 °C mold temperature (SM, 6x).

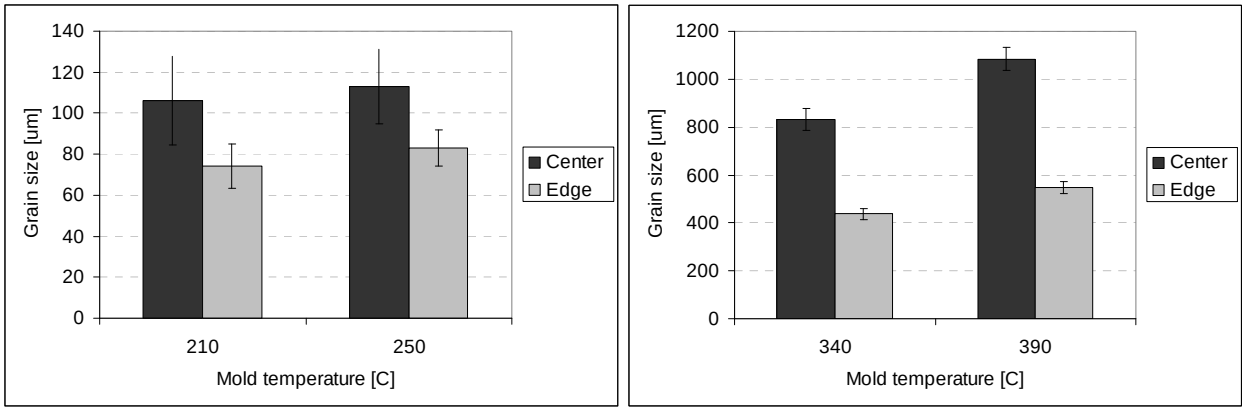

(a) AZ91D alloy. *(b) AE42 alloy.*

Figure 71: Average grain diameter.

Observing the effect of mold temperature on the grain size, Figure 71a shows that increasing the mold temperature from 210 °C to 250 °C increased the AZ91D's grain size by 6.6 % and 12.5% for the center and edge regions, respectively. In the case of the AE42 casting, Figure 71b, increasing the mold temperature from 340 °C to 390 °C resulted in a more significant grain diameter increase of 30.4% and 25.1% at the center and skin regions, respectively.

Figure 71 confirms that the grain size over the casting cross section was not homogeneous. For both alloys, the casting centre showed a significantly larger grain diameter, in comparison to the casting edge. The grain size at the centre was greater than the skin by 43.2%, 36.1%, 90.3% and 98.1% for the AZ91D / 210, AZ91D / 250, AE42 / 340 and AE42 / 390 casting conditions, respectively. This grain size variation was likely the result of cooling rate variation over the horizontal bar's cross section. At the metal-mold interface, rapid grain nucleation caused restricted α-Mg grain growth, leading to a fine grain size.
In contrast, the horizontal bar's centre regions were the last area to solidify, thus enabling extended grain growth leading to relatively coarse grain structure.

The micrographs for the AZ91D castings (Figure 67 and Figure 68) suggest that grains were equiaxed without any preferred grain growth direction. The only exception were a few grains in the skin region, where grains elongated in the direction of the maximum temperature gradient. In the case of the AE42 alloy, equiaxed grains were also observed in the center regions of the horizontal bars. However, for the 390 °C mold temperature casting, the relatively slow cooling rate of the horizontal bar enabled the skin region grains to elongate in the direction of heat flow (i.e., towards the centre of the horizontal bar), resulting in the formation of columnar grains.

This inhomogeneous grain structure suggests a limitation in the current approach of eliminating hot tears in AE42 castings. Increasing the mold temperature to 390 °C has effectively prevented hot tearing, but it also: 1) resulted in a very large grain size (~ 400 – 1100 μm) and, 2) reduced grain size homogeneity due to the formation of columnar grains at the mold walls. Such phenomena would possibly result in a non-isotropic material. Thus, in the as-cast state, these AE42 castings may not have had industrially attractive properties.

Section Summary

The grain size analysis revealed that the AZ91D castings at the onset of hot tearing had grain size between 80 – 120 μm. For the AE42 alloy, the grain size was 400 – 1100 μm. These observations suggest that the AZ91D alloy was possibly stronger in the semi-solid state due to grain-boundary strengthening. Thus, the AZ91D was capable of bearing greater load during solidification and hot tearing occurred at lower mold temperatures (210 °C – 250 °C) than in the case of the AE42 alloy. In the AE42 alloy, the non-homogeneous casting grain structure likely promoted formation of intergranular strain gradients, contributing to a higher susceptibility to hot tearing. Further, due to the requirement for relatively high mold temperatures in order to avoid hot tearing, the AE42 casting grain size was very large and inhomogeneous, thus making the casting less industrially attractive.

5.2.2 Hot tear Nucleation and Propagation

The following section presents the results of micro- and macroscopic analyses aimed at characterizing the nucleation and propagation of hot tears in the AZ91D and AE42 castings.

5.2.2.1 AZ91D Casting at 210 °C Mold Temperature

Visual inspection of the casting after ejection from the mold revealed hairline hot tears in the vicinity of the 90° junction between the horizontal bar and the downsprue. Upon sectioning, the casting showed additional hot tears in the interior, as illustrated in Figure 60. Further, a crack was observed ~ 1.2 cm to the left of the 90° junction, as seen in Figure 37d. This crack was likely related to subsurface blisters, which weakened the material and enabled crack formation during thermal contraction of the horizontal bar upon cooling to room temperature.

Microscopic observation of Sample #7, which had a clearly visible hot tear (3.5 mm long) revealed that the hot tear propagated through a region of extensive sub-surface interdendritic porosity, as shown in Figure 72.

Detailed observation of the hot tear path and surrounding pores in Figure 73 revealed facets (crack segments) oriented at nearly 90° angle to each other. The axes of these facets were aligned with the *x*- and *y*-axes of the casting. Thus, it appears the *x*-direction contraction of the horizontal bar or the *y*-direction contraction of the downsprue contributed to porosity opening and hot tear propagation in the critical region. Therefore, the observed plastic damage (i.e., porosity and hot tears) was caused by the axial contractions of these casting components in addition to limited feeding of the critical region. Had there been sufficient feeding, these shrinkage pores would be filled with interdendritic liquid and healed. Also, sufficient liquid feeding would reduce the extent of axial tension of the horizontal bar and the downsprue, thereby avoiding hot tearing. These predictions were confirmed during the analysis of AZ91D casting made at 250 °C mold temperature (Section 5.2.2.2).

The overall direction of hot tear propagation was also examined. Hot tears appeared to nucleate in the casting skin near the 90° corner. The sharp corner imposed a stress concentration in a material region with limited ductility and developing stress was sufficient to initiate a hot tear. Then, the tear propagated towards the sprue interior via interdendritic channels with shrinkage pores. The interdendritic regions were the last area of the microstructure to solidify, thus contained traces of low melting temperature eutectics on the grain boundaries. These eutectics, along with already present shrinkage pores, possibly assisted hot tear propagation. The composite image in Figure 72 shows, that the length of the main (continuous) hot tear was relatively short in comparison to the total area affected by the severe porosity. Thus, it appears that development of the hot tear was one manifestation of a general material damage in the critical region of the casting. In summary, it appears that the formation of a hot tear was influenced by two factors:

1) Stress concentration was necessary to amplify the evolving thermal and mechanical stresses to exceed the semi-solid strength of the material and initiate a hot tear.
2) Hot tears propagated via interdendritic regions towards damaged casting areas, e.g., regions with high interdendritic porosity.

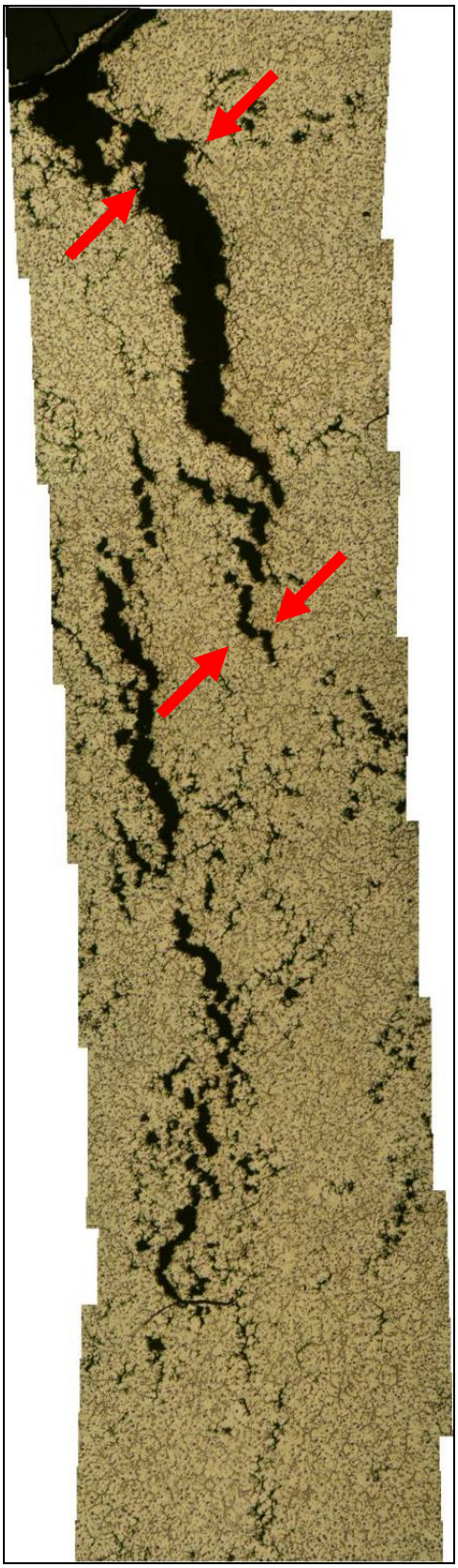

Figure 72: Hot tear in AZ91D / 210 / S7 (BF, composite image).

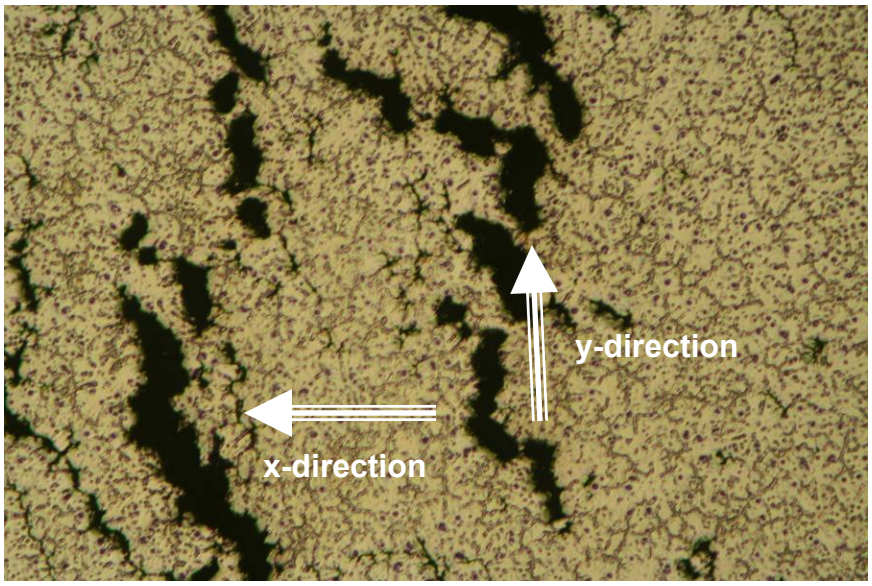

Figure 73: Interdendritic shrinkage porosity in AZ91D / 210 / S1 (BF, 200x).

5.2.2.2 AZ91D Casting at 250 °C Mold Temperature

Visual examination of the AZ91D casting produced at 250 °C mold temperature did not reveal the presence of surface hot tears. However, microscopic analysis of samples from the critical region's interior revealed a hairline hot tear just below the surface of the casting, as shown in Figure 74a. The root of the hot tear was exactly at the 90° corner (region of maximum stress concentration). This hot tear was not continuous, as shown in Figure 74b, and several solid bridges (connecting either side of the crack) were observed along its length. The total length of the hot tear was 1.8 mm. Figure 74b also suggests that shrinkage porosity was not present in the vicinity of the hot tear, as was observed in the AZ91D / 210 casting.

The area just above the hot tear contained a fold defect, resembling collapsed cavities formed by melt turbulence. Formation of folds will be discussed later in Section 5.2.4.

Microscopic examination of Sample #7 (showing the microstructure half-way through the casting thickness) revealed the presence of a 0.4 mm long hot tear near the top edge of the horizontal bar. This hot tear was visible only at 200x magnification, as shown in Figure 75. The hot tear propagated through the interdendritic regions and the tip of the hot tear terminated near isolated voids of shrinkage porosity. This porosity did not show any preferential growth direction; however, some of the pores were interconnected. This observation suggests that in the critical region half-way through the casting thickness, where the cooling rate was relatively low, the material remained in the semi-solid state longer, thus experiencing limited feeding (similar to centerline porosity). As a result, shrinkage porosity formed.

However, these shrinkage cavities were uni-directional, suggesting that the contractions of the horizontal bar (*x*-direction) or the downsprue (*y*-direction) were not sufficient to elongate microcracks in these directions (as was the case in the AZ91D / 210 casting), form hot tears, or drive a microcrack towards the region of high porosity. Therefore, it appears that by increasing the mold temperature, casting feeding improved and the amount of thermal strain in the critical region decreased. With lower thermal strain and thermal strain rate, interdendritic liquid feeding compensated for the axial contraction of the horizontal bar and the downsprue, thereby preventing nucleation of hot tears.

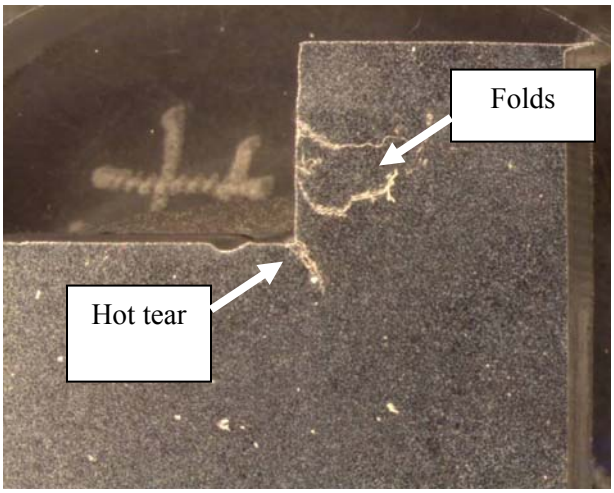

(a) Critical region of the casting with a hot tear and folds (SM, 6x).

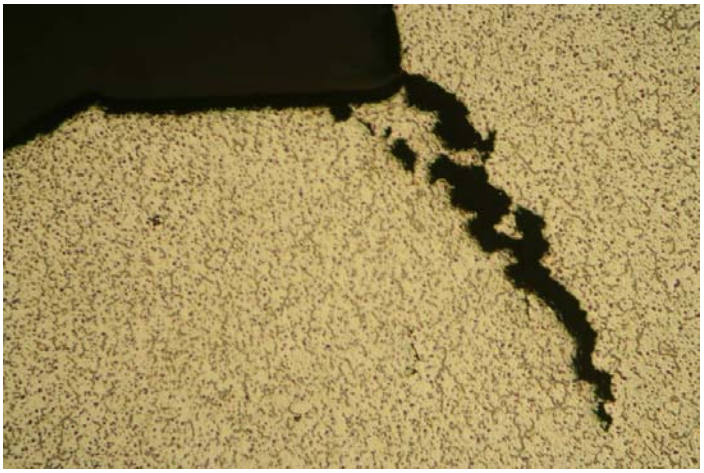

(b) Detail of a hot tear (BF, 50x).

Figure 74: Hot tear in AZ91D / 250 / S4.

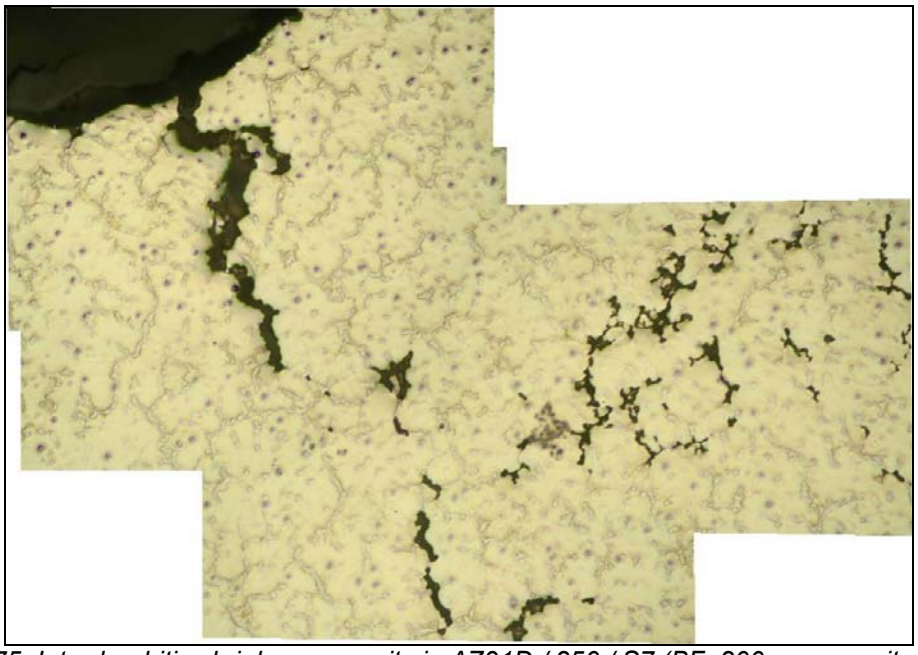

Figure 75: Interdendritic shrinkage porosity in AZ91D / 250 / S7 (BF, 200x, composite image).

Inspection of metallographic Sample #5 revealed that a hairline crack also formed at the bottom edge of the horizontal bar, as shown in Figure 76. Again, this crack was visible only under a microscope. The region surrounding the hot tear did not exhibit interdendritic shrinkage porosity. Absence of shrinkage porosity suggests that crack formation was not necessarily the result of poor interdendritic feeding. Consequently, it is likely that this crack developed due to the *x*-direction thermal contraction of the horizontal bar at very high fractions of solid. This crack nucleation mechanism is supported by Figure 76b, which shows that the root of the hot tear propagated perpendicular to the axial contraction of the horizontal bar.

(a) Bottom corner (SM, 6x). *(b) Bottom corner (BF, 50x).*

Figure 76: Hairline hot tear in AZ91D / 250 / S5.

Inspection of the remaining samples from the critical region of the casting revealed isolated clusters of interconnected shrinkage porosity, as shown in Figure 77. The presence of these relatively small porosity clusters suggests that at the elevated mold temperature (250 °C) casting feeding sufficiently improved to compensate the casting's volumetric contraction (thereby preventing formation of large hot tears); however, in some regions, interdendritic feeding remained difficult and isolated shrinkage pores formed. These results reveal that formation of shrinkage porosity was possibly the first step in the process of hot tear formation.

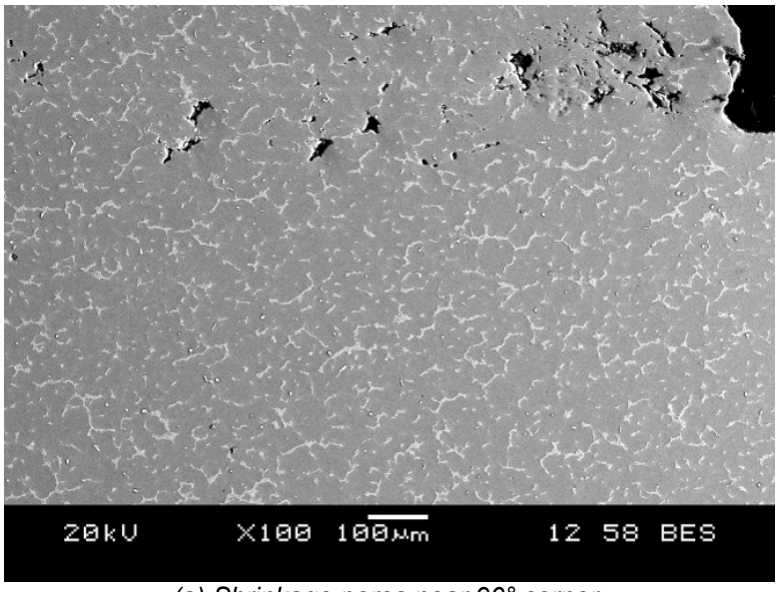

(a) Shrinkage pores near 90° corner.

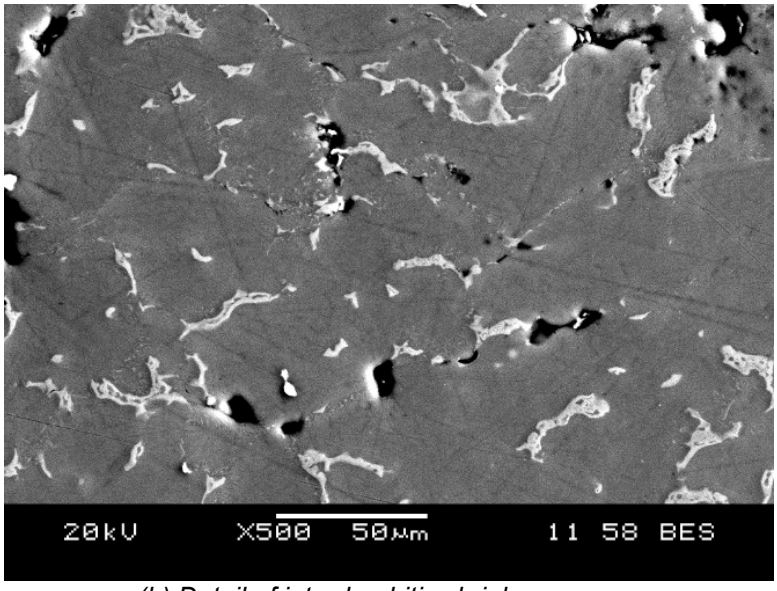

(b) Detail of interdendritic shrinkage pores.
Figure 77: Sub-surface porosity in AZ91D / 250 / S6.

5.2.2.3 AE42 Casting at 340 °C Mold Temperature

Analysis of the metallographic samples from an AE42 casting produced at 340 °C mold temperature revealed that the hot tear observed on the casting surface (e.g., Figure 39d) extended well into the casting interior. This hot tear was 10.33 mm long and propagated at nearly 45° angle to the top edge of the horizontal bar, as shown in Figure 78a. Also, the figure shows that numerous microcracks formed in parallel with the main hot tear. All of these hot tears appeared to have a symmetric fracture surface on either side of the crack, as observed in detail in Figure 78b.

Figure 79 and Figure 80 show additional hot tears observed in the remaining metallographic specimens from the casting. None of the hot tears in the 340 °C mold temperature casting were seen to be associated with formation of interdendritic shrinkage porosity, as was the case for the AZ91D castings. The AE42 hot tears appeared to propagate along dendrite and grain boundaries.

Figure 80 also indicates that the hot tear consisted of perpendicular segments. These segments were aligned with the direction of the axial contractions of the horizontal bar and the downsprue. Thus, it appears that these contractions assisted in propagating the hot tear. Further, the general hot tear propagation direction coincided with the direction of the maximum stress gradient at the 90° corner. Thus, it appears that propagation of hot tears in the AE42 alloy was related to the tendency to release stress or strain in the material. In other terms, a significant stress level developed at the 90° corner. To relieve this stress, a crack nucleated.

As indicated above, interdendritic shrinkage porosity was absent from the vicinity of the hot tear. Therefore, the hot tears formed either at very late stages of solidification or in an already solidified material. Support of this hypothesis was given by observing the hot tears in Sample #6, in Figure 79b. The figure shows that a band of cavities formed at the crack tip. The cavities did not branch into random directions and did not extend uni-directionally through the interdendritic regions (as typical shrinkage porosity). Instead, it appears that the cavities formed as a result of tensile strain (not shear strain) induced by thermal contraction of the horizontal bar or the downsprue.

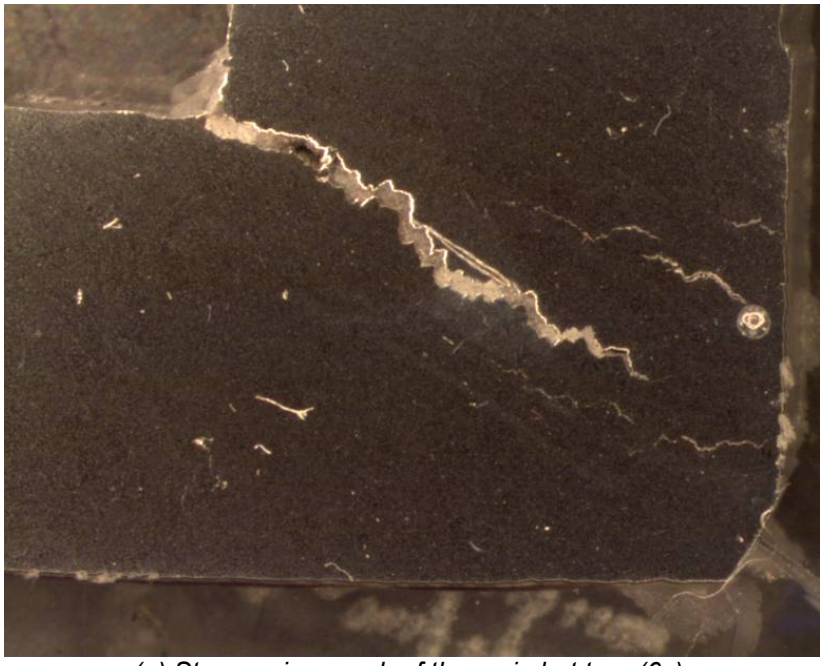

(a) Stereo micrograph of the main hot tear (6x).

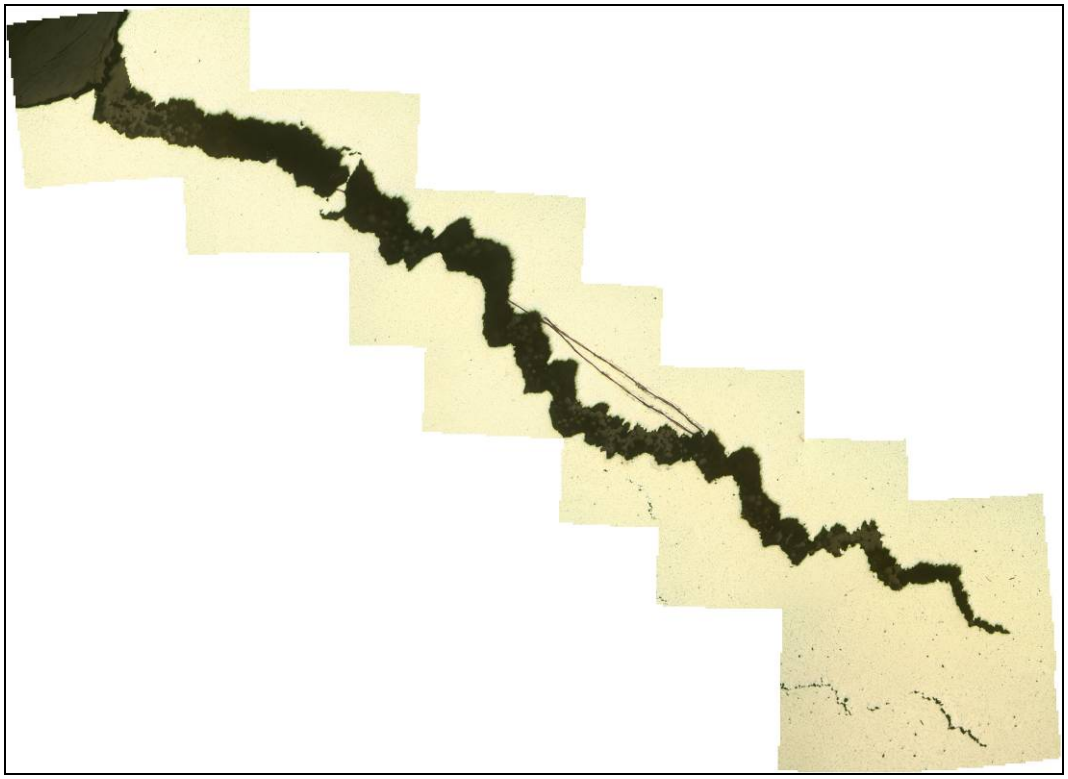

(b) Detail of the hot tear in (a).

Figure 78: Primary hot tear in AE42 / 340 / S4 (composite image).

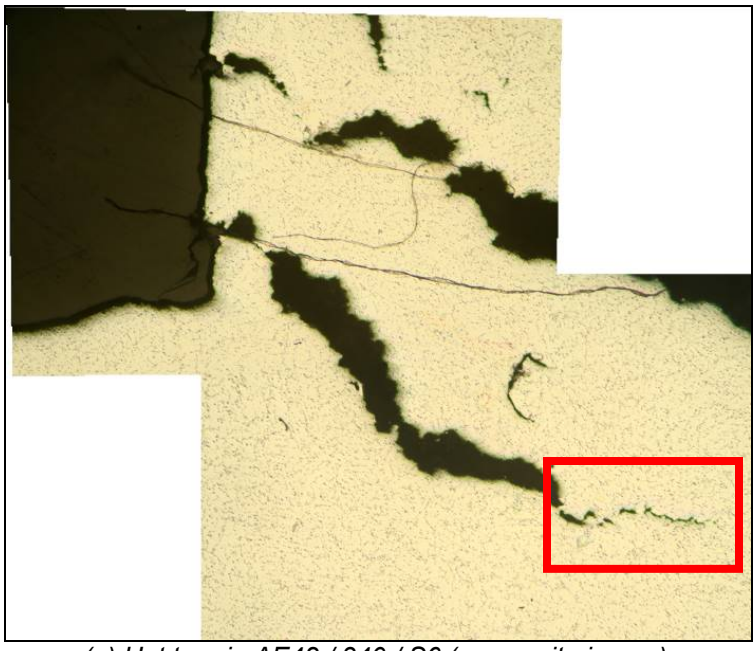

(a) Hot tear in AE42 / 340 / S6 (composite image).

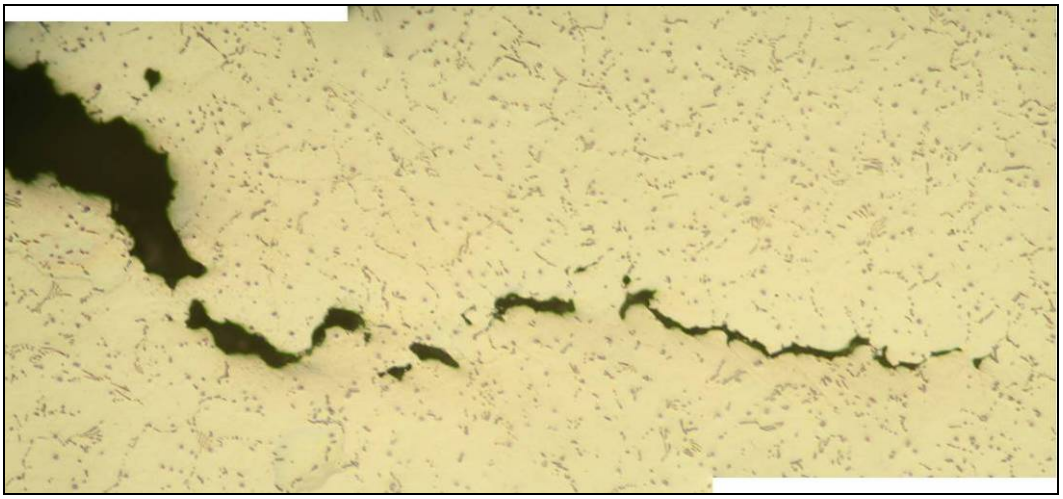

(b) Hot tear tip from AE42 / 340 / S6 (composite image, 200x).
Figure 79: Hot tear propagation in AE42 / 340 / S6 (composite image).

The cracks in Figure 80 were observed to propagate along the grain boundaries as well as the interdendritic regions. This trend became evident, in particular, as the mold temperature increased to 390 °C, as discussed in the following section.

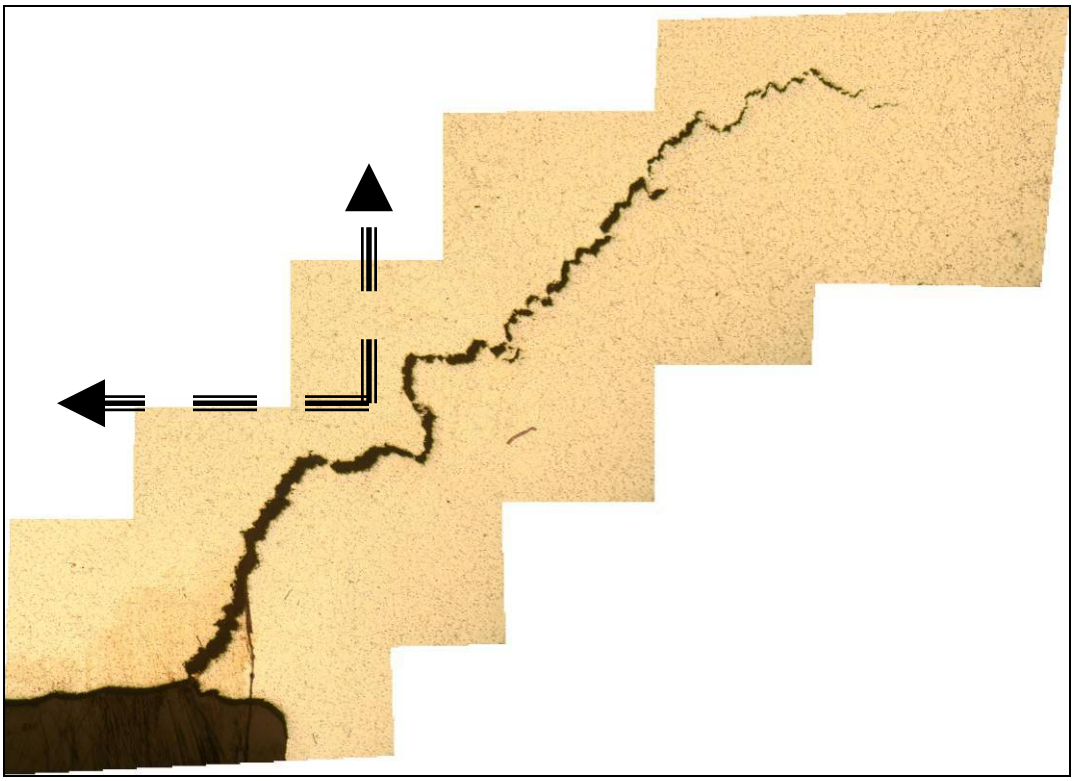

Figure 80: Hot tear in AE42 / 340 / S7 (composite image).

5.2.2.4 AE42 Casting at 390 °C Mold Temperature

A casting produced at 390 °C mold temperature did not show visible hot tears on the casting surface. Metallographic analysis revealed presence of hairline hot tears in the casting interior (Figure 81). Some of these hot tears extended to the casting surface; however, the crack root was not detectable with the naked eye.

Microscopic hot tears were observed on the bottom edge of the horizontal bar. These hot tears appeared to propagate almost exclusively along the grain boundaries, as seen in Figure 81b. Further, these hot tears propagated without the assistance of shrinkage porosity.

Analysis of Sample #7 (Figure 82) revealed the same general crack propagation path. The hot tear initiated as a hairline crack at the 90° corner. A few dendrite branches were visible on the crack edges. However, the crack path followed a grain boundary (visible by the orientation of dendrites within individual grains) as indicated with arrows.

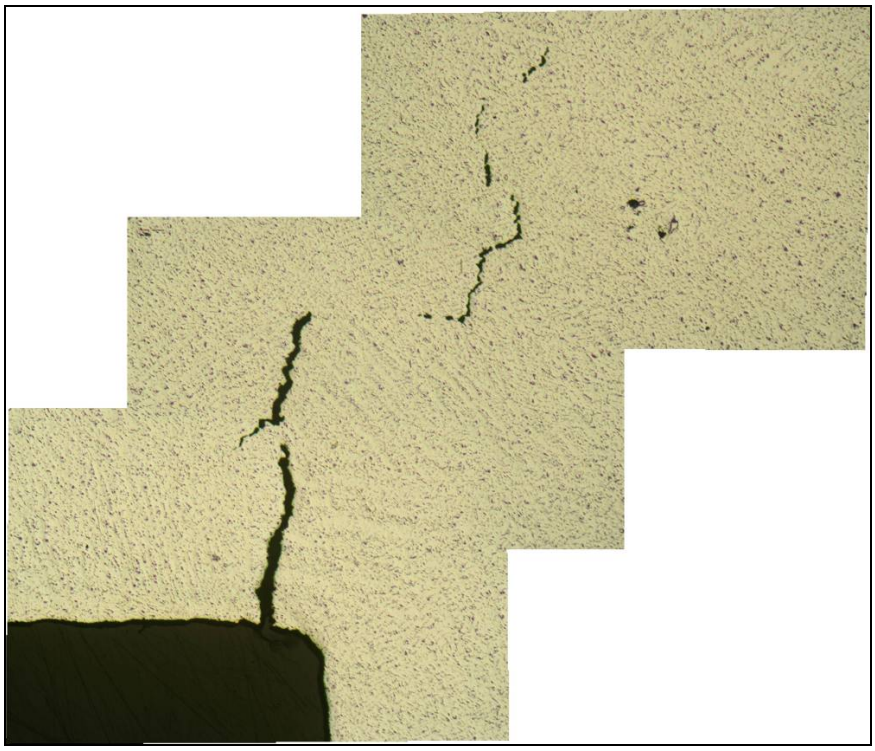

(a) Crack propagation (composite image).

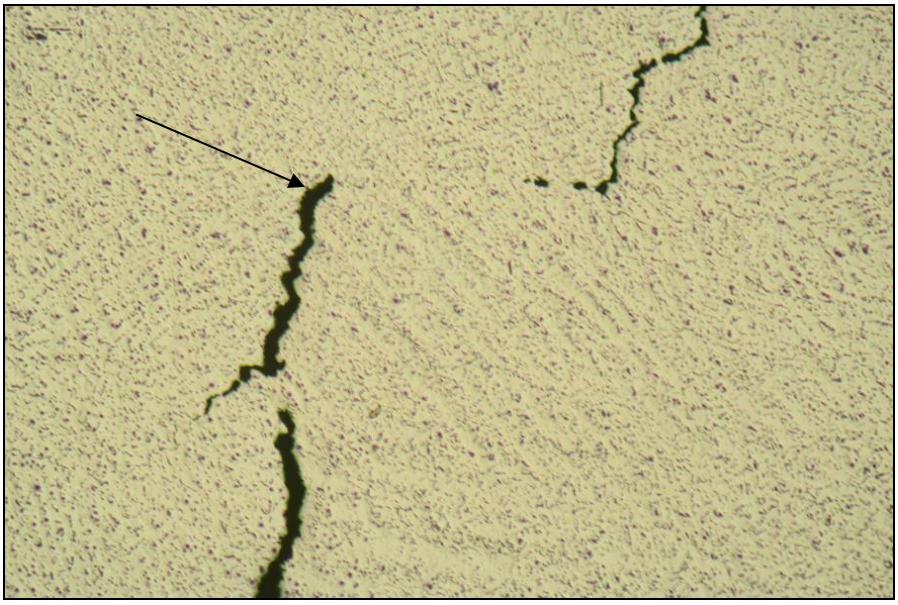

(b) Grain boundary cracking (BF, 100x).
Figure 81: Hairline hot tear in AE42 / 390 / S5.

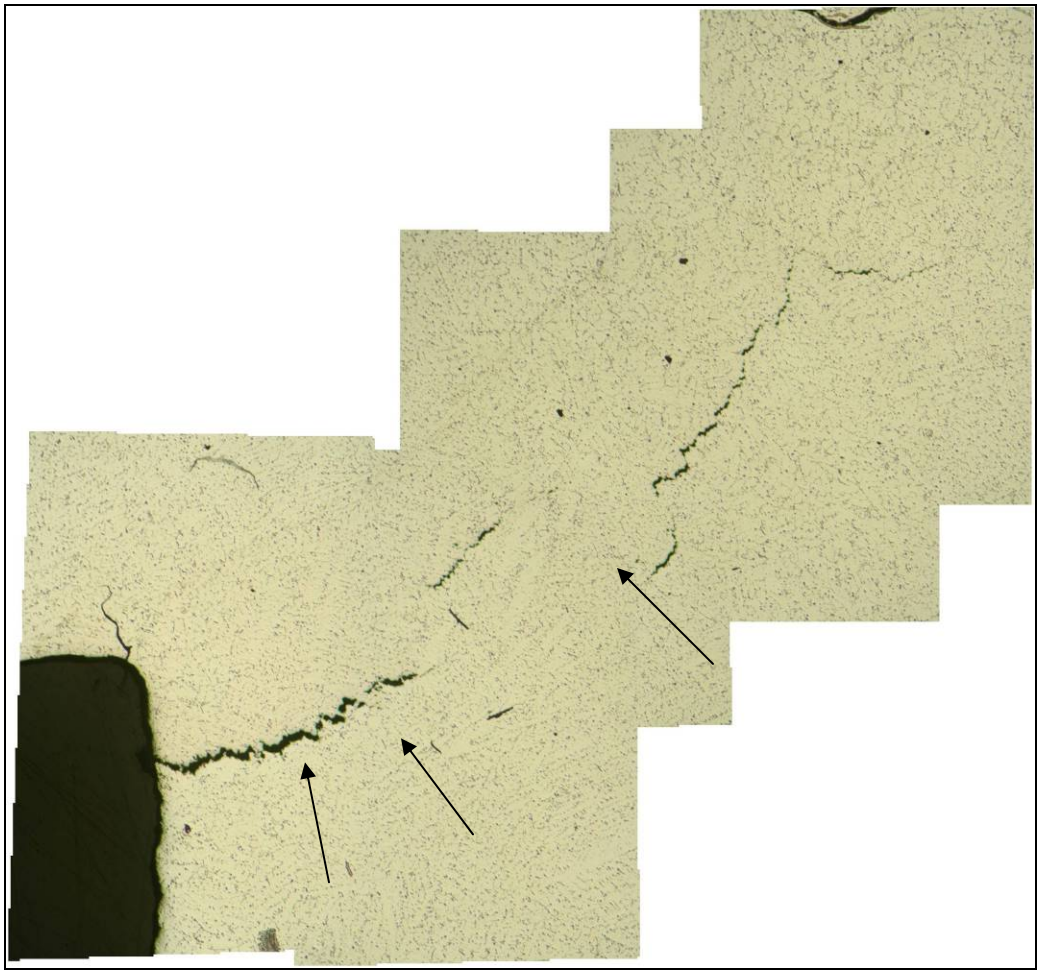

Figure 82: Hot tear in AE42 / 390 / S7 (composite image).

High magnification observation of hot tears with an SEM revealed the presence of needle-like (acicular) Al_xRE_y rare-earth intermetallic phase connecting crack boundaries near the crack tip, as shown in Figure 83a – c. Some of the needles fractured, indicating that these needles were very well bonded to the α-Mg dendrites, but were not able to sustain the same level of stress or strain. This observation partially accounts for the occurrence of grain boundary cracking observed in the AE42 alloy castings. With the presence of Al_xRE_y needles pinning dendrites, the interdendritic bond strength improved and locally disabled hot tear propagation. As a result, crack propagation became easier along the grain boundaries.

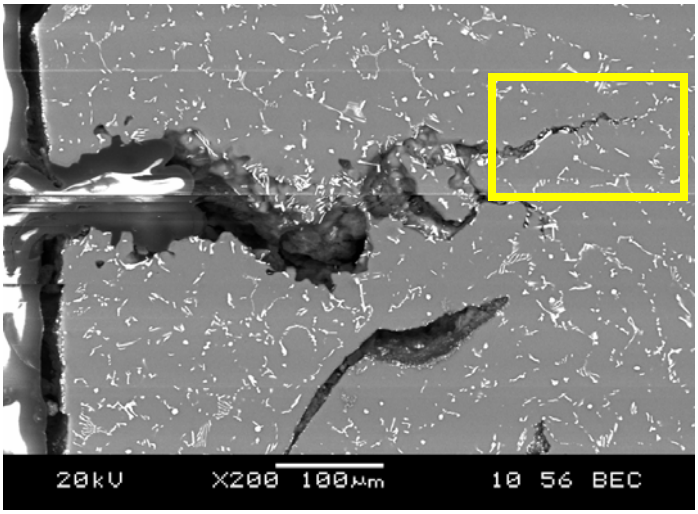

(a) Tip of a hot tear.

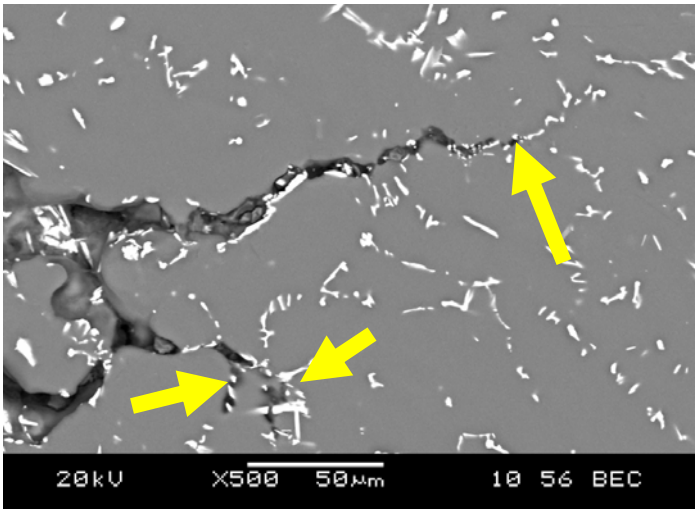

(b) Al_xRE_y needles pinning fracture boundaries.

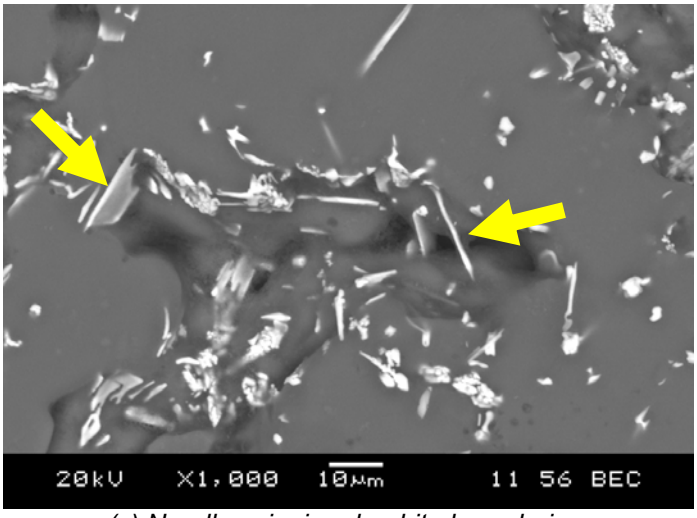

(c) Needles pinning dendrite boundaries.
Figure 83: Hot tear in AE42 / 390 / S6.

Section Summary

The microscopic analysis of the hot tears in the two alloys provided the following key observations:

1. In the AZ91D alloy, hot tears initiated at the 90° corner due to a high stress level (i.e., stress concentration). Subsequently, hot tears propagated through regions with high shrinkage porosity towards the casting interior. When the mold temperature increased from 210 °C to 250 °C, interdendritic liquid feeding improved and reduced the extent of shrinkage porosity, thereby reducing the alloy's hot tearing tendency.
2. In the case of the AE42 alloy, hot tears also nucleated at the 90° corners of the critical region. Hot tear propagation was driven predominantly by axial contractions of the horizontal bar and the downsprue, exhibited as piece-wise crack propagation in orthogonal directions. Shrinkage porosity was not readily observed in the vicinity of the hot tear. Further, the Al_xRE_y intermetallics in the AE42 alloy were seen to pin dendrites, resulting in hot tear propagation along the grain boundaries, in the general direction of the maximum stress gradient.

5.2.3 Alloy Microstructure

The general microstructure of the four castings was inspected at various locations (as illustrated in Figure 52 - Figure 54) using a light optical microscope with DIC module and magnifications of up to 500x. Subsequently, SEM was used to observe the morphology of the second phases at high magnifications (up to 4000x). Also, X-ray chemical analysis was carried out with SEM-EDX to estimate the chemical composition of alloy constituents.

5.2.3.1 LOM - General Microstructure

AZ91D Castings

Micrographs in Appendix 2 (Figure A2. 1 - Figure A2. 4) show the general microstructure of the two AZ91D castings. Micrographs at 500x magnification were obtained to observe the interdendritic regions.

As Figure 84 shows, the microstructure of the AZ91D alloy consisted of primary α-Mg dendrites and β-$Mg_{17}Al_{12}$ intermetallic compound located in the interdendritic regions. Further, cuboids of manganese-aluminum (Mn-Al) intermetallic compound were seen randomly dispersed throughout the microstructure. In addition, in some of the micrographs, particles of diamond polishing compound were seen embedded in the soft magnesium matrix.

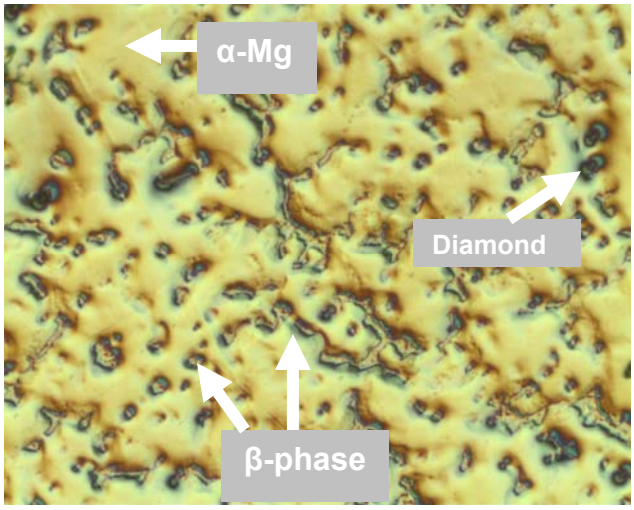

Figure 84: General microstructure of AZ91D alloy (DIC, 200x).

Observing the microstructure of Sample #1 and #2, it was noted that the slower cooling rate at the horizontal bar's center (Sample #1) possibly enabled agglomeration of the β-phase particles. Non-equilibrium solidification of the casting resulted in solute rejection ahead of the solid-liquid interface, leading to a local decrease of the solidus temperature in the interdendritic liquid and liquid agglomeration. In contrast, the casting skin (Sample #2) experienced higher cooling rate and faster α-Mg grain nucleation, resulting in smaller and dispersed β-phase regions in comparison to Sample #1. These observations are in agreement with the fine grain size (Figure 71) and increased microhardness (Figure 65) measured in the skin regions.

It was also observed that the casting samples extracted from the critical region (Samples #4 – 7) contained marginally larger amount of β-$Mg_{17}Al_{12}$ intermetallic phase than Samples #1 or #2, which were located in the horizontal bar's midsection. This observation indicates that the cooling rate varied along the horizontal bar. In the midsection, the bar solidified rapidly due to fast hoop solidification, but in the critical region, the relatively hot downsprue allowed accumulation of the β-phase. Enhanced growth of β-phase in the critical region would possibly influence an alloy's hot tearing tendency in two ways. First, formation of $Mg_{17}Al_{12}$ phase would decrease the alloy's ductility, thus increasing the hot tearing tendency. Secondly, the increased amount of the low melting temperature eutectic would enable enhanced interdendritic feeding at high fractions of solid, thus decreasing the hot tearing tendency.

Micrographs of Sample #8 reveal a reduction in the amount of β-phase in the downsprue (in comparison to Samples #4 - #7), as illustrated in Figure 85. As discussed in Section 5.1.1, Sample #8 exhibited a

significant amount of centerline shrinkage porosity, which indicates the absence of liquid and β-phase at the end of solidification. Thus, these micrographs confirm that the horizontal bar or the downsprue drew eutectic liquid from the critical casting region. The lack of feeding during the bar's contraction resulted in the development of significant negative pressures imposed on the dendritic skeleton in the critical region, leading to the formation of shrinkage porosity and susceptibility for material damage.

Optical microscopy also suggests that increasing the mold temperature from 210 °C to 250 °C resulted in a marginal enlargement of the β-phase regions. A detailed quantitative analysis of the effect of mold temperature on the size of the β-phase regions is presented in Section 5.2.3.2. Figure 86 indicates that in a casting made at 250 °C mold temperature, the cooling rates were low enough to enable solid-state precipitation of lamellar-$Mg_{17}Al_{12}$ intermetallic compound at the grain boundaries. This precipitation was observed only in Sample #6 (sample with hot tears). Thus, formation of this precipitate may suggest that the cooling rate associated with the onset of poor interdendritic liquid feeding (and hot tearing) was similar to that associated with the solid state precipitation of lamellar β-phase.

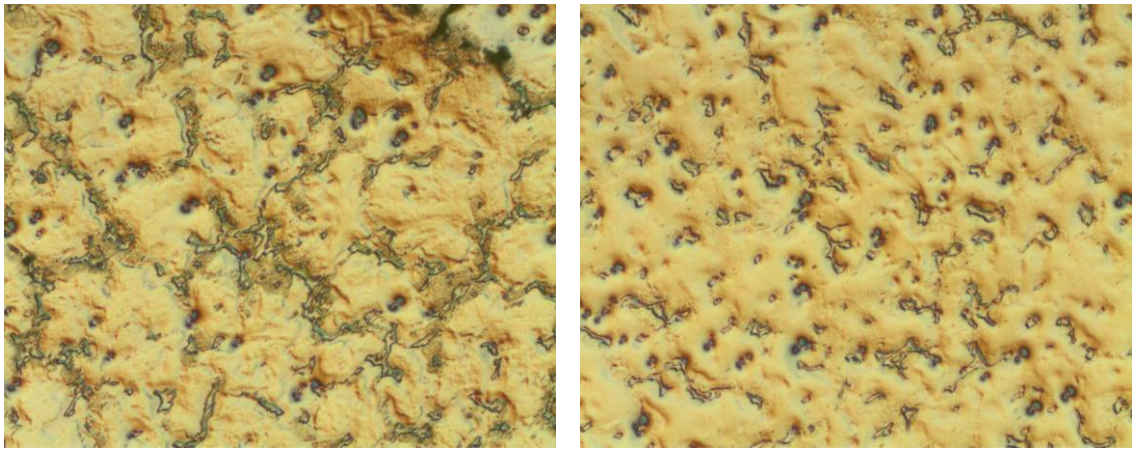

(a) Sample #6. *(b) Sample #8.*

Figure 85: General microstructure of AZ91D / 250 casting in the critical region (BF, 200x).

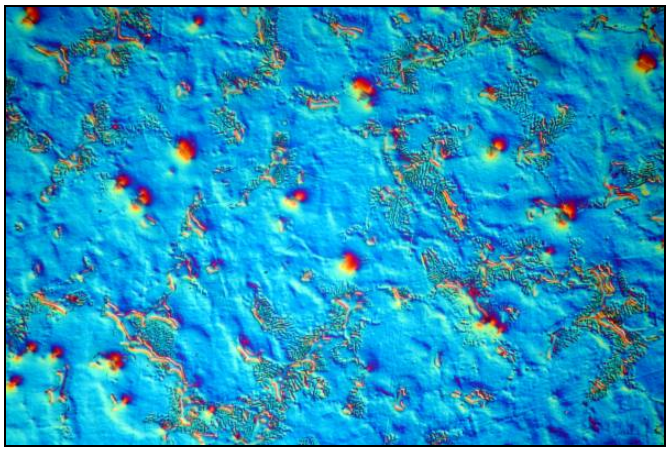

Figure 86: Precipitation of lamellar β-phase on dendrite boundaries in AZ91D / 250 / S6 (DIC, 500x).

AE42 Castings

Micrographs in Appendix 2 (Figure A2. 5 - Figure A2. 8) show the as-cast microstructure of the AE42 castings made at 340 °C and 390 °C mold temperatures at magnifications of 200x and 500x. It was observed that the AE42 alloy microstructure consisted of primary magnesium dendrites, with Al_xRE_y intermetallics in the interdendritic regions. Also, Al-Mn cuboids were observed in the matrix.

Inspection of the micrographs from different locations across the casting suggests that the alloy microstructure was, in general, uniform. This observation indicates that the horizontal bar at locations of Samples #1 - #8 solidified at approximately the same rate. Had significant thermal gradients developed, i.e., axial gradients along the horizontal bar, a possible change in the primary or secondary phase morphology would be observed.

Observing the alloy microstructure in Figure 87, it appears that increasing the mold temperature from 340 °C to 390 °C enabled formation of developed dendrite branches. This result was not expected, since formation of well developed dendrite arms is related to the development of solute gradients in the liquid phase during solidification. Solute gradients readily develop in conditions of rapid alloy cooling, when the solubility of rare earth elements (e.g., Ce, Nd and La) in α-Mg is limited.

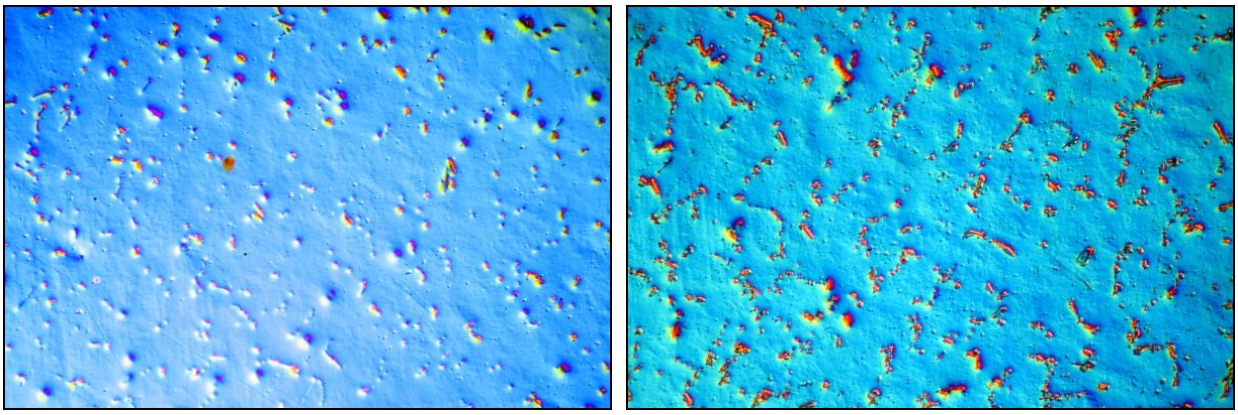

(a) 340 °C mold temperature. *(b) 390 °C mold temperature.*
Figure 87: AE42 microstructure, Sample #4 (DIC, 500x).

Figure 87 also suggests that as the mold temperature increased from 340 °C to 390 °C and the time available for α-Mg and second phase growth was extended, the morphology of the Al_xRE_y particles began to change and several types of the rare-earth intermetallic compounds were observed. The dominant morphologies of the Al_xRE_y phase were needles and particles. A detailed discussion on the stoichiometry and morphology of the Al_xRE_y phases is the focus the following section.

5.2.3.2 Morphology of Second Phases

SEM analysis was carried out to characterize the morphology of the interdendritic regions in the AZ91D and AE42 alloy castings. This effort was undertaken in recognition of the impact of the interdendritic region morphology on the feedability of the castings at late stages of solidification. The results are presented in Appendix 3 (Figure A3. 1 - Figure A3. 2 for AZ91D alloy and Figure A3. 3 - Figure A3. 4 for AE42 alloy). A detailed analysis of the interdendritic regions and intermetallic compounds was performed with SEM-EDX to estimate their composition. The maximum solubilities of the primary alloying elements for the AZ91D and AE42 alloys are provided in Table 15 [61]. The equilibrium binary phase diagrams for the AZ91D alloy (Mg-Al) and AE42 alloy (Mg-Ce) are presented in Figure 88 [68].

Table 15: Solubility limits for primary alloying elements in AZ91D and AE42 alloys.

Element	Solubility limit for binary magnesium alloy [%]	System
Aluminum	12.7	Eutectic
Cerium	0.8	Eutectic
Manganese	2.2	Peritectic
Neodymium	0.6	Eutectic
Zinc	6.2	Eutectic

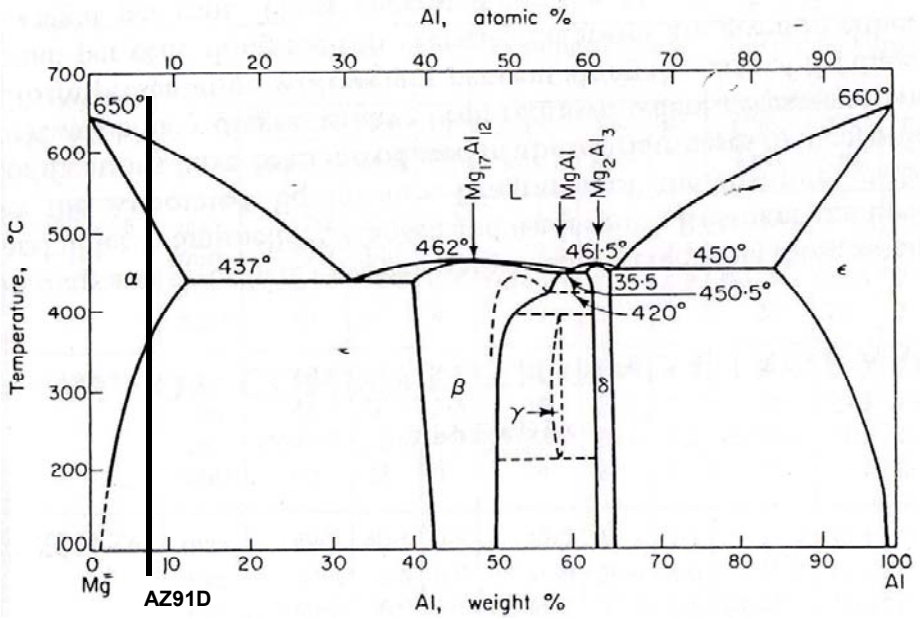

(a) Mg-Al binary phase diagram.

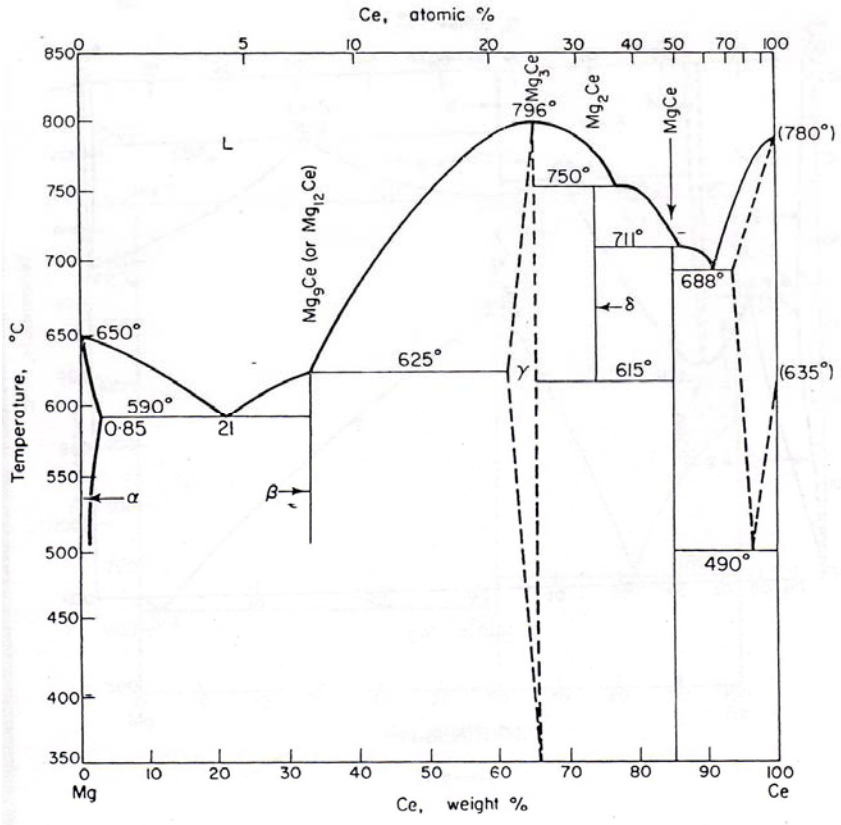

(b) Mg-Ce binary phase diagram.

Figure 88: Mg-Al and Mg-Ce binary phase diagrams [68].

AZ91D Alloy

The results of elemental X-ray mapping of the β-phase regions are presented in Figure 89. The map shows that the interdendritic region contained aluminum and magnesium. Further, aluminum was also present in solid solution of the α-Mg dendrites. In the case of zinc, no preferential segregation was observed, as zinc remained in solution throughout the alloy.

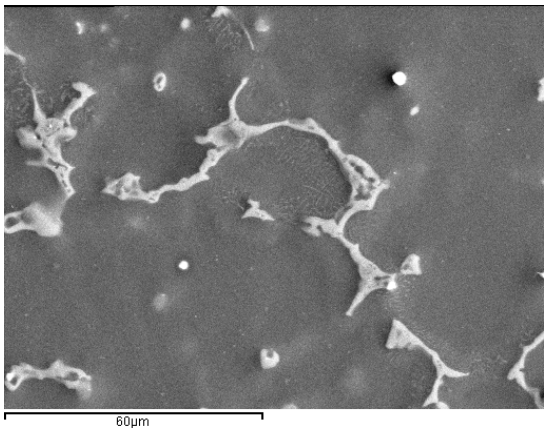

(a) Area for X-ray mapping.

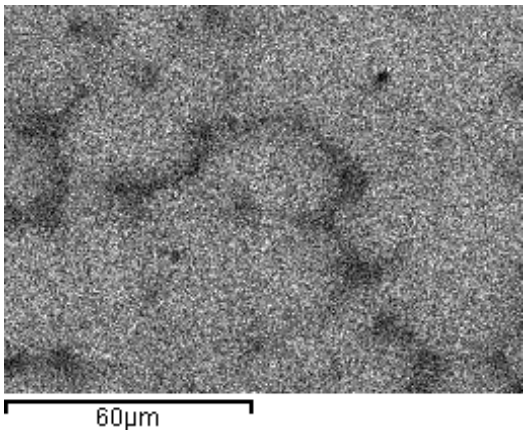

(b) Magnesium

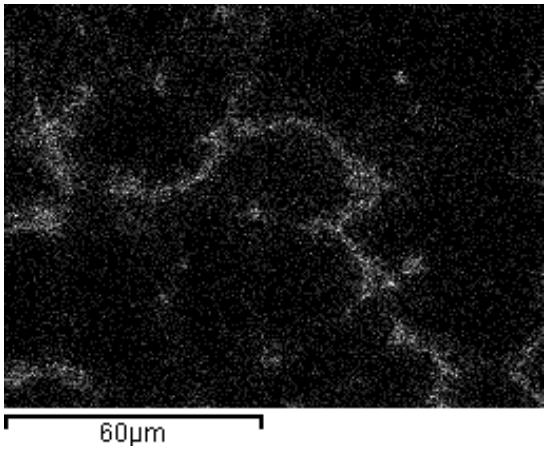

(c) Aluminum

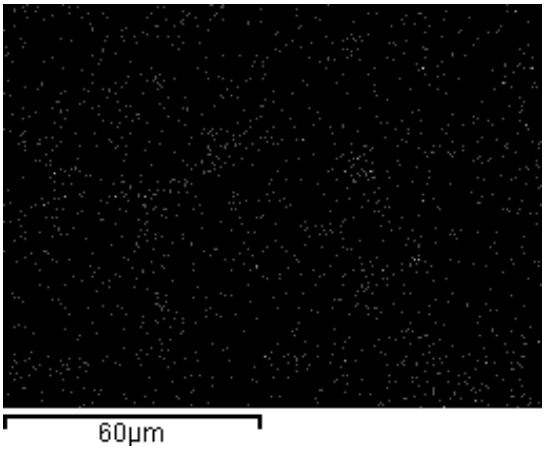

(d) Zinc

Figure 89: X-ray map of β-phase intermetallic in AZ91D / 250 / S1.

Figure 90 shows a detailed view of the β-phase regions in the AZ91D castings at the two mold temperatures. Mold temperature increase from 210 °C to 250 °C resulted in only a marginal increase in the size of the β-phase. A more notable effect was observed when the mold temperature was varied through a wide range of temperatures, as illustrated in Figure 91. "Percent area" represents the area fraction of the β-phase regions per image frame, while the "Diameter" represents the average ferret (diameter) of the β-phase region. As Figure 91 shows, the total percent area of the β-phase remained nearly constant for mold temperatures between 140 – 390 °C, thus confirming the chemical stability of

the alloy within this mold temperature range (i.e., fading of elements did not occur). However, the effect of the mold temperature on the β-phase morphology was evident. When the mold temperatures exceeded 340 °C, the average β-phase diameter rapidly increased from 23 μm to 37 μm. This significant increase is illustrated in Figure 92. Thus, with increasing mold temperature, coalescence of the eutectic liquid and formation of coarse β-phase particles became possible and contributed to a decreasing tendency for hot tearing [66].

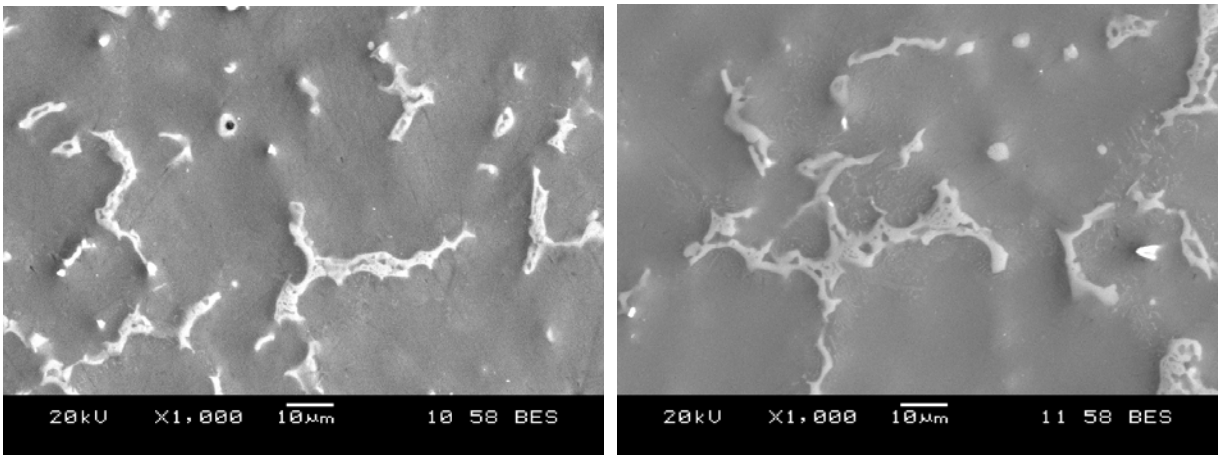

(a) 210 °C mold temperature. *(b) 250 °C mold temperature.*

Figure 90: Morphology of β-phase regions in AZ91D casting Samples #3.

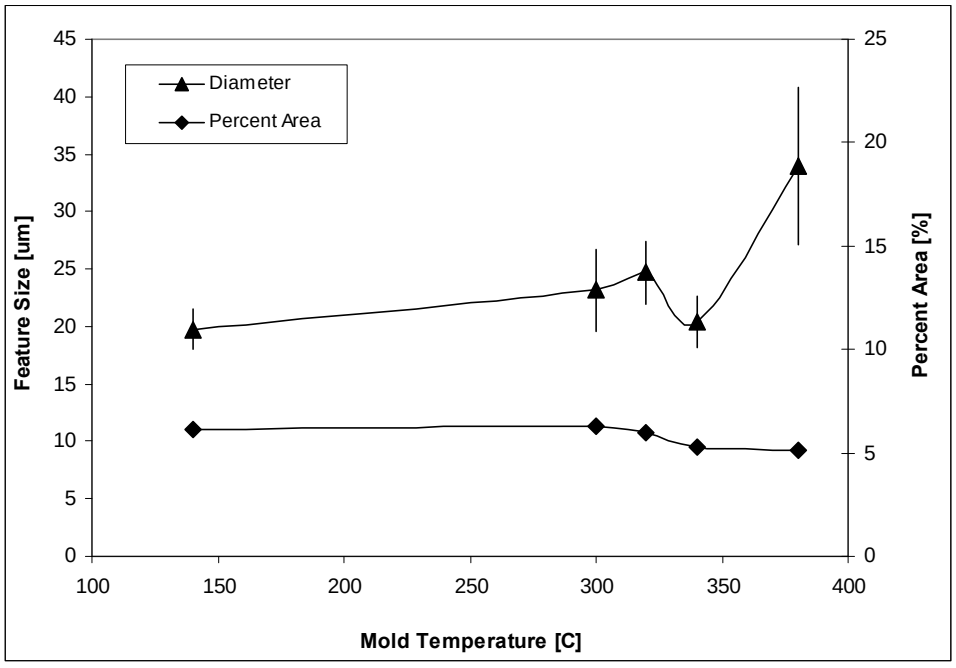

Figure 91: Effect of mold temperature on the size of β-phase regions.

The morphology of the primary magnesium dendrites was also affected by the alloy's cooling rate. At high cooling rates (low mold temperatures), the development of finely branched dendrites was necessary to re-establish chemical equilibrium at the solid-liquid interface. Conversely, at high mold temperatures, solute homogeneity did not necessitate rapid dendrite branching. As a result, the 380 °C mold temperature casting contained nearly equiaxed grains with a very few dendrite arms, as seen from Figure 92.

Examination of the morphology of the eutectic phases revealed the development of a divorced eutectic structure, where each eutectic constituent appeared as a massive phase, instead of the characteristic finely divided (lamellar) mixture. Further, it was observed that as the mold temperature increased from 140 °C to 380 °C, the typical partially divorced eutectic structure, which forms at high cooling rates, gradually transformed into a fully divorced eutectic structure. Figure 93 and Figure 94 show this transformation in detail. In a fully divorced eutectic, the two eutectic phases are completely separate in the microstructure. Each interdendritic region consists of a single β-$Mg_{17}Al_{12}$ particle surrounded by eutectic α-Mg, which has grown from the primary dendrites. A partially divorced eutectic morphology is characterized by 'islands' of eutectic α-Mg within the β-$Mg_{17}Al_{12}$ phase [18]. The interdendritic region in the 210 °C mold temperature casting contained particles of eutectic α-Mg (~ 0.5 – 2 μm in diameter). These particles may have acted as stress risers, thus providing possible nucleation sites for shrinkage porosity or a hot tear. Also, the fully divorced eutectic structure is favorable for eutectic liquid flow at high fractions of solid [69].

As discussed above, increasing the mold temperature from 210 °C to 250 °C reduced the size of the α-Mg particles in the β-phase regions. In some casting areas, the α-Mg particles were completely eliminated from the interdendritic regions. In such cases, solid state precipitation of lamellar β-$Mg_{17}Al_{12}$ phase from the grain boundaries in to the α-Mg dendrites occurred, as observed in Figure 94. The mechanism of lamellar β-$Mg_{17}Al_{12}$ phase formation involved a reaction between the supersaturated β-phase and the α-Mg dendrites. Diffusion of Al and Mg across the dendrite boundary resulted in consumption of the α-Mg particles in the interdendritic regions and subsequent solid-state precipitation of lamellar β-$Mg_{17}Al_{12}$ phase. This phase transformation was likely related to the slow cooling rate at 250 °C mold temperature, which enabled diffusion of elements across the interdendritic boundary regions.

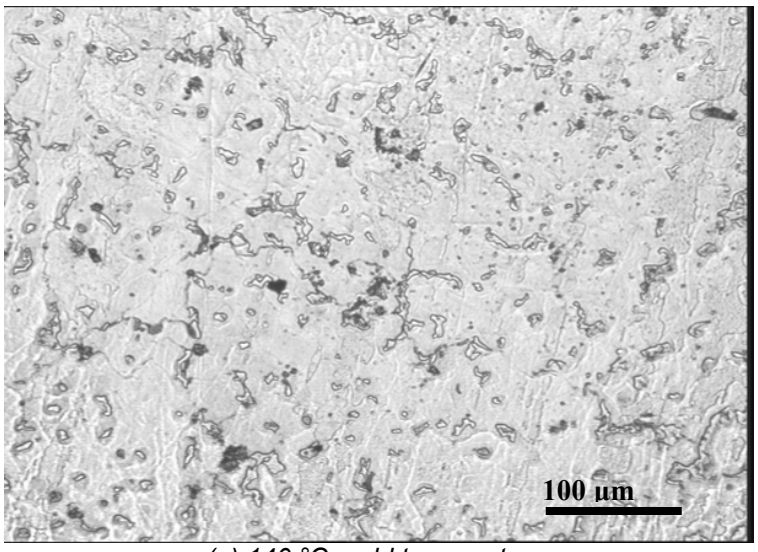

(a) 140 °C mold temperature.

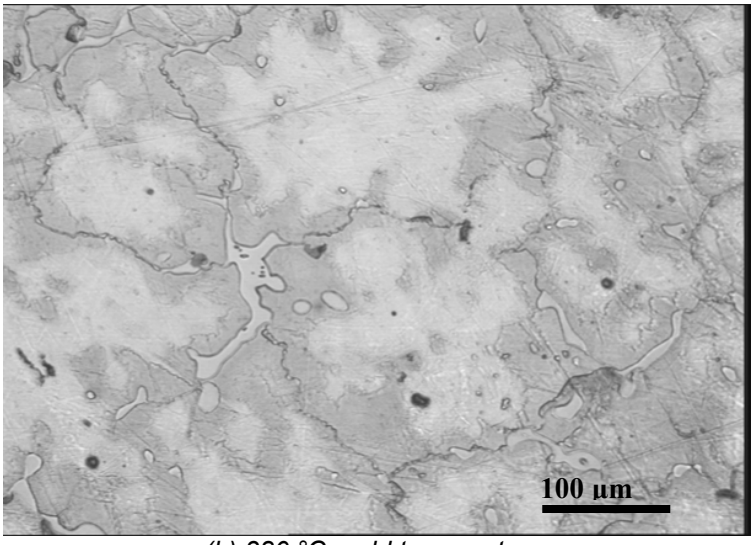

(b) 380 °C mold temperature.

Figure 92: Morphology of β-phase regions at 140 °C and 390 °C mold temperatures in AZ91D alloy (LOM).

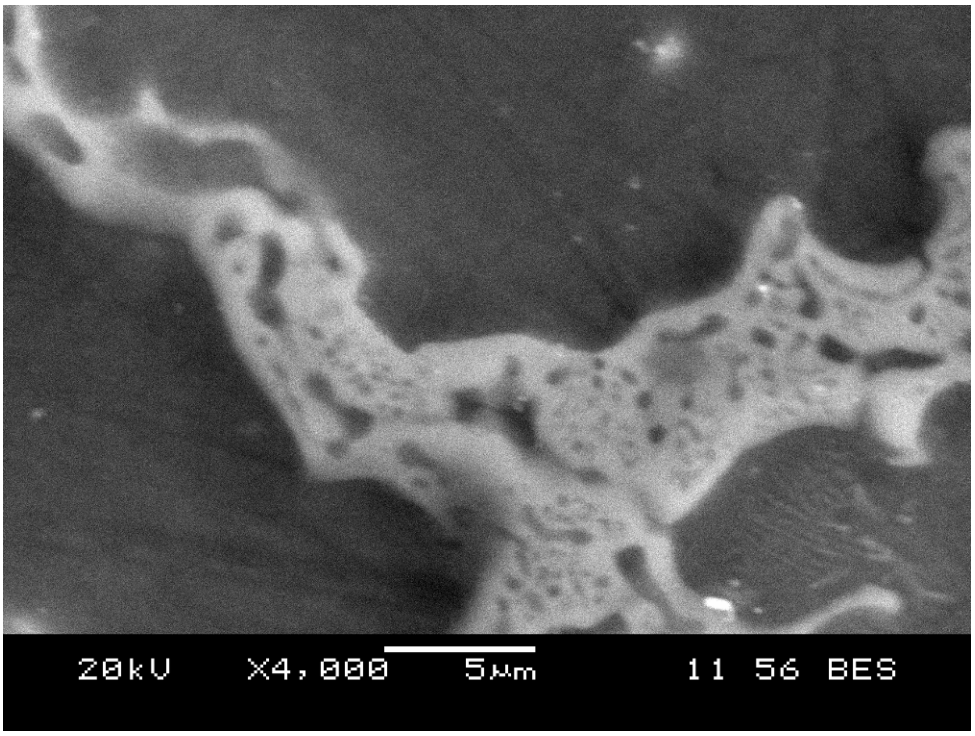

Figure 93: Structure of β-phase particle in AZ91D / 210 / S6.

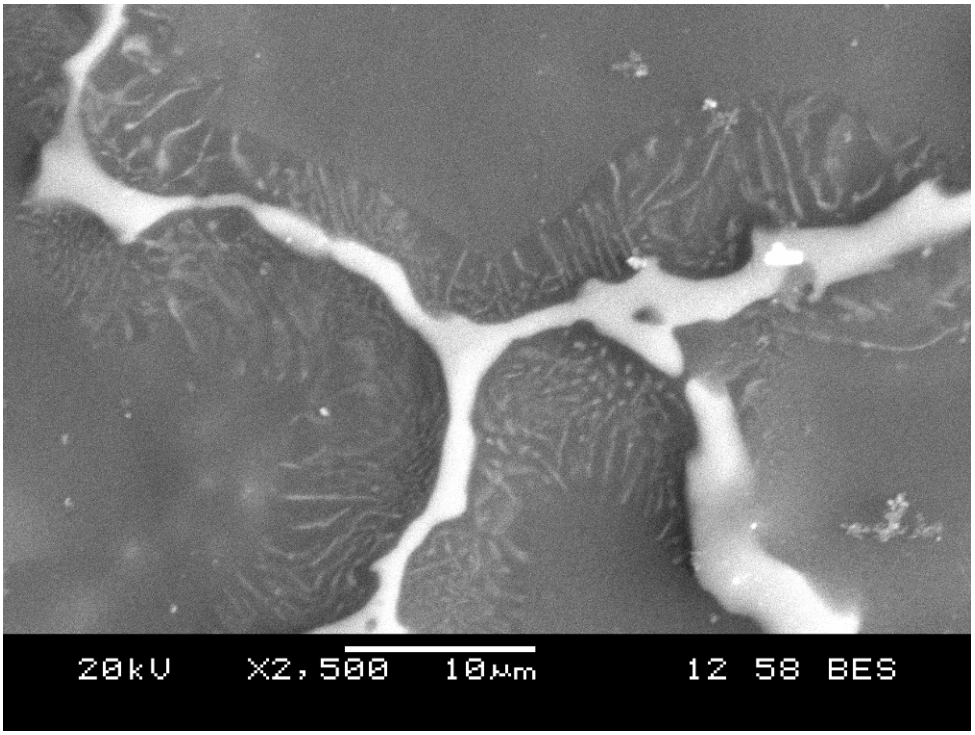

Figure 94: Structure of β-phase particle and precipitation of lamellar $Mg_{17}Al_{12}$ in AZ91D / 250 / S1.

AE42 Alloy

Micrographs showing detailed microstructure of the two AE42 castings at various casting locations are presented in Appendix 3. It was observed that the dominant morphology of the second phases in the AE42 alloy consisted of needle-like (acicular) and particulate precipitates. Performing X-ray mapping on these phases confirmed that both phases were Al_xRE_y intermetallics. The rare earths present were cerium, lanthanum, neodymium and praseodymium, which are the constituents of the mischmetal added to the AE42 alloy. It was also observed that cuboid Al-Mn precipitates (~ 2 μm diameter) formed.

Comparison of micrographs for Samples #1 and #8 (Figure 95) suggests that the longer solidification time in the downsprue possibly enabled fragmentation of the acicular Al_xRE_y precipitates. In the case of Sample #1, the precipitates were ~ 15 – 18 μm long. In the case of the sprue region (Sample #8), the size was between ~ 12 – 15 μm. Fragmentation of the acicular Al_xRE_y phase could be indicative of its metastability at high temperatures and low cooling rates.

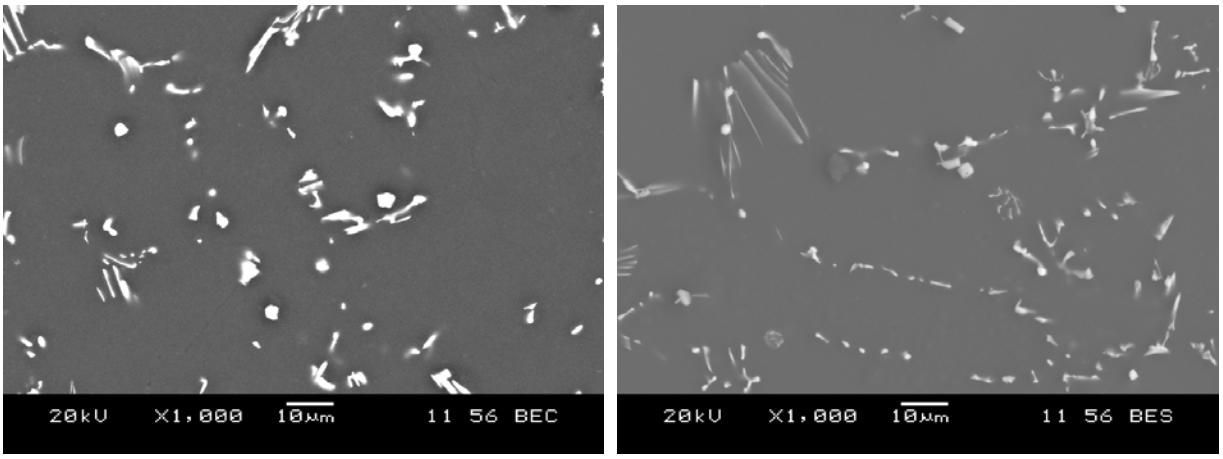

(a) Sample #1. *(b) Sample #8.*

Figure 95: Morphology of Al_xRE_y precipitates in AE42 alloy at 390 °C mold temperature.

It was also noted that increasing the mold temperature influenced the size and agglomeration of the particulate Al_xRE_y phase. The average size increased from ~ 4 – 6 μm to ~ 7 – 10 μm with mold temperature increase from 340 °C to 390 °C. Growth of these particles may suggest that with slower cooling, the rare earths in the supersaturated α-Mg matrix may have segregated towards the RE-rich interdendritic boundaries and subsequently precipitated in the form of Al_xRE_y particulates. To verify this hypothesis, a semi-quantitative chemical analysis (X-ray mapping) of the Al_xRE_y phases was carried out with SEM-EDX (Figure 96). This analysis was intended to observe possible local variation of solute in the alloy matrix.

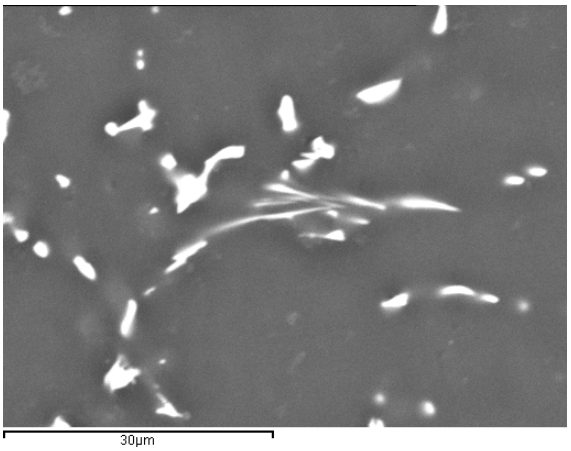

(a) Area for X-ray mapping

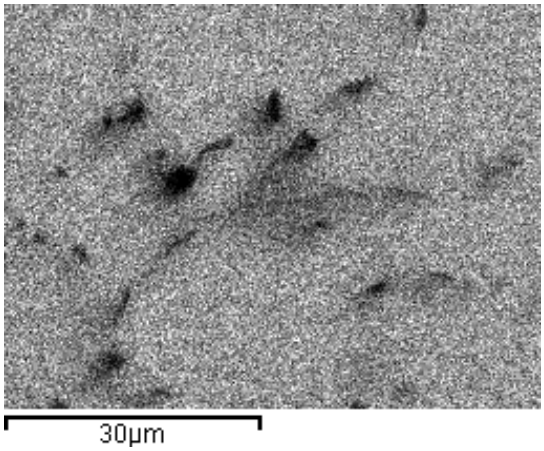

(b) Magnesium

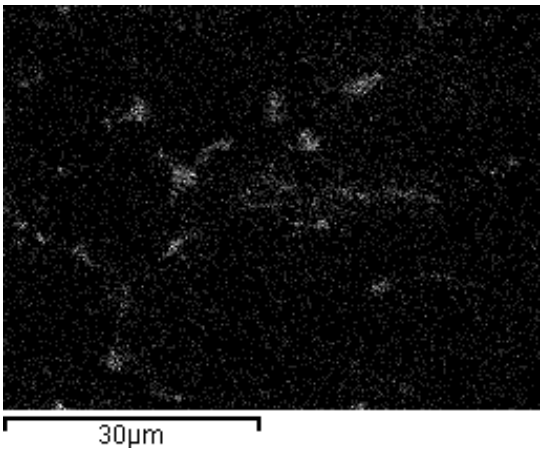

(c) Aluminum

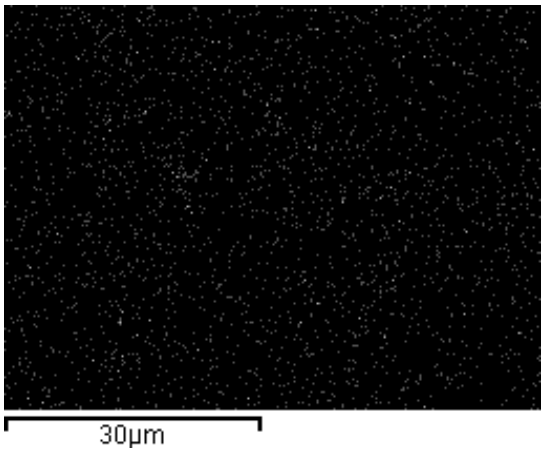

(d) Manganese

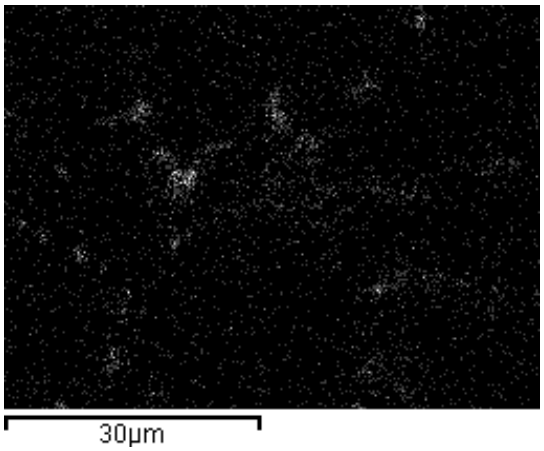

(e) Cerium

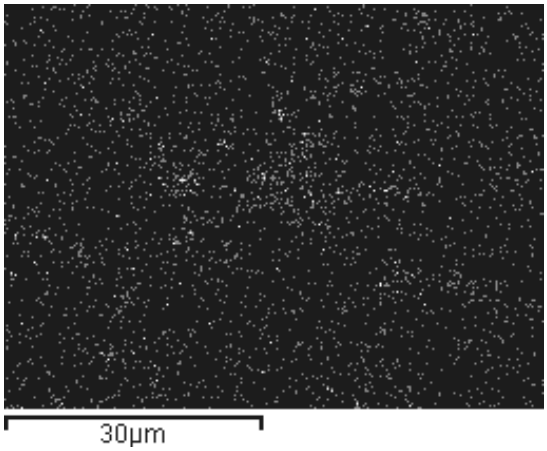

(f) Lanthanum

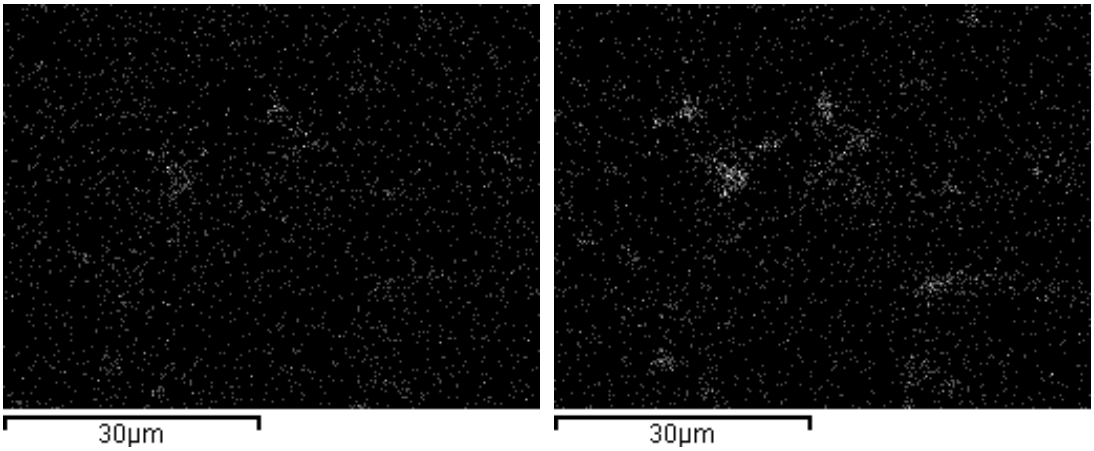

(g) Praseodymium *(g) Neodymium*

Figure 96: X-ray map of Al_xRE_y intermetallic phase in AE42 alloy cast at 390 °C mold temperature.

The X-ray maps in Figure 96 confirmed the presence of aluminum and RE's in the intermetallics. However, the SEM-EDX instrument resolution did not allow observation of solute segregation or presence of solute gradients within the grains. Thus, the exact stoichiometry of the Al_xRE_y phase had to be estimated using published data.

In the case of the AE42 alloy, formation of the rare-earth second phase intermetallics follows complex solidification paths. The stoichiometry and morphology of the Al_xRE_y intermetallics depends on the local chemical composition of the alloy [70]. Two dominant morphologies of Al_xRE_y phase may be observed: acicular (needle-like) $Al_{11}RE_3$ and particle-like Al_2RE [71, 72]. It has been reported that Nd partitions into the Al_2RE phase, while La segregates preferentially into the $Al_{11}RE_3$ phase. Thus, the occurrence of $Al_{11}RE_3$ vs. Al_2RE in the alloy depends on the local La:Nd ratio. La:Nd ratio below 0.7 promotes formation of Al_2RE phase, whereas higher La:Nd ratios promote formation of $Al_{11}RE_3$ phase [73]. It has been also reported that the $Al_{11}RE_3$ phase is unstable and decomposes to Al_2RE phase at elevated temperatures. During this decomposition, Al atoms are released and subsequently react with Mg atoms to form $Mg_{17}Al_{12}$ phase. Formation of this phase results in a significant loss of the alloy's creep resistance [72].

In order to validate the expected stoichiometries of the acicular and particulate Al_xRE_y phases, SEM-EDX point analysis was carried out. This chemical analysis was semi-quantitative and the absolute values reported in the following text may not be used as valid (absolute) chemical analysis results (for such quantitative analysis, elemental standards for the AE-type alloy would have to be incorporated to the SEM-EDX system). Also, the probe size (i.e., sampling volume) for the SEM-EDX system made accurate chemical analysis difficult. The probe size used was ~ 40 µm wide, while the particles of interest were

< 10 μm in width, thus making their chemical analysis difficult. To obtain accurate chemical analysis of the precipitates, Electron Probe Micro Analysis (EPMA) with resolution of ~ 1 μm would be required. Nevertheless, considering the limitations of the SEM-EDX approach, a spectral point analysis was carried out. Three spectra as indicated in Figure 97 were acquired.

The SEM-EDX suggests that the matrix in the vicinity of the RE precipitates remained nearly pure magnesium. The lamellar and particulate phases were analyzed and the elemental analyses suggest, that Spectrum #2 had a La:Nd ratio of 1.98, while Spectrum #4 had a La:Nd ratio of 0.11. Thus, these results agree with published data, and the acicular particles observed in the current castings were likely $Al_{11}RE_3$, while the particulates were Al_2RE. This analysis also agrees with the X-ray maps presented in Figure 96, where elevated Nd count was recorded near the Al_2RE particles.

The morphology of the Al_xRE_y precipitates possibly had a significant effect on the alloy strength and ensuing hot tearing tendency. As Figure 98 shows, $Al_{11}RE_3$ needles formed between adjacent dendrites and likely pinned these dendrites, thereby limiting their relative motion. When the interdendritic strain during solidification exceeded the acicular $Al_{11}RE_3$'s ductility (e.g., due to porosity formation) the needles fractured (Figure 98c). As the mold temperature increased to 390 °C, the $Al_{11}RE_3$ phase appeared to transform to particulate Al_2RE phase. This phase may have originated from accelerated segregation of Nd in the alloy or from the thermal degradation (fragmentation) of the $Al_{11}RE_3$ phase. With the appearance of the Al_2RE phase, the dendrite boundaries were pinned to a lesser extent and the alloy made at 390 °C mold temperature became relatively more ductile and less susceptible to hot tearing.

In the regions with localized chemical inhomogeneity, clusters with unique Al_xRE_y morphology were observed (Figure 99). Due to slow cooling at 390 °C mold temperature, liquid enriched in rare-earths was pushed towards the dendrite boundaries. As a result, the local Ce content may have reached the eutectic level of 4.3 wt % [61] and lamellar Al_xRE_y phase formed. However, the elevated Ce levels could not be verified with SEM-EDX due to the instrument's large sampling (probe) spot size.

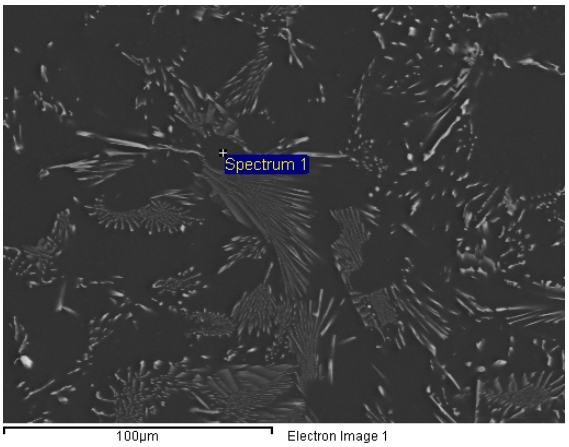

Element	Weight%
Spec 1	
Mg K	100.58
S K	0.01
Cl K	-0.20
La L	-0.11
Pr L	-0.23
Nd L	-0.05
Totals	100.00

(a)

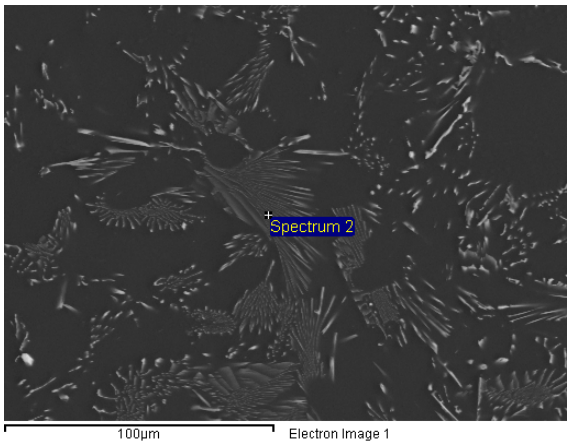

Element	Weight%
Spec 2	
Mg K	88.90
Al K	4.76
S K	0.01
Cl K	-0.07
La L	1.85
Ce L	3.25
Pr L	0.39
Nd L	0.93
Totals	100.00

(b)

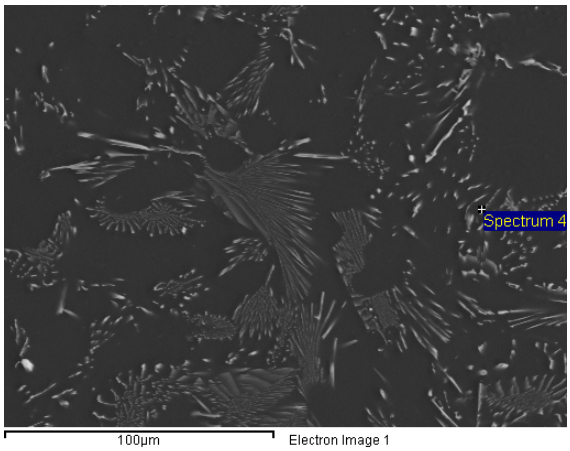

Element	Weight%
Spec 4	
Mg K	95.29
Al K	2.93
S K	0.10
Cl K	-0.13
La L	0.06
Ce L	1.07
Pr L	0.11
Nd L	0.57
Totals	100.00

(c)

Figure 97: SEM-EDX spectra of Al_xRE_y particles.

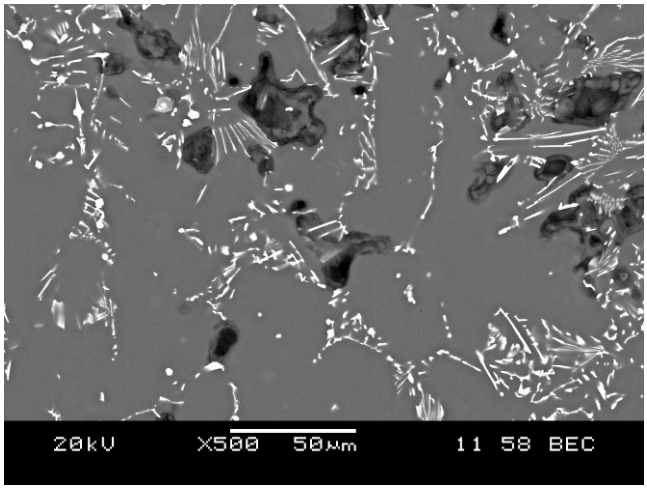

(a)

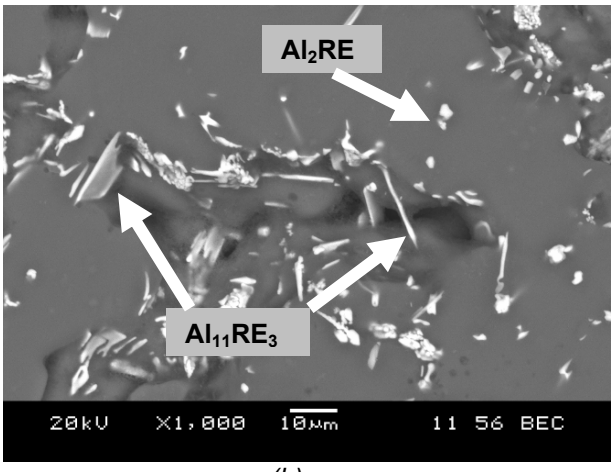

(b)

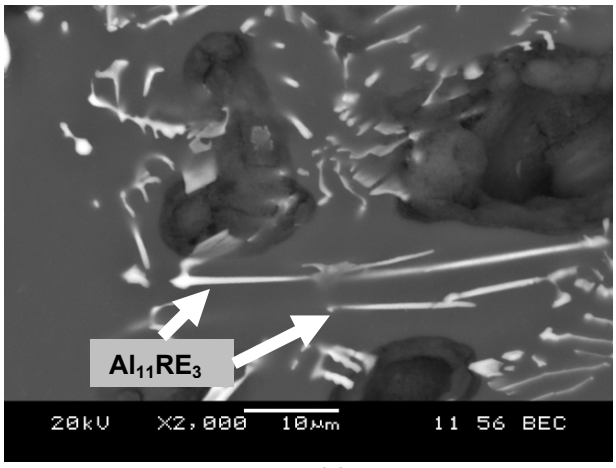

(c)

Figure 98: Needles of Al_xRE_y intermetallics pinning grain boundaries in AE42 / 340 / S3.

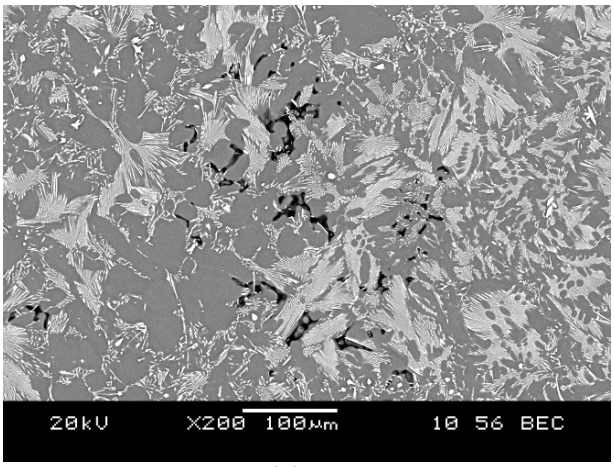

(a)

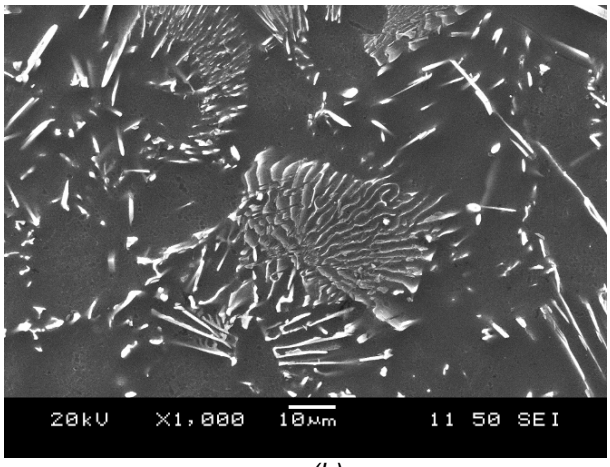

(b)

Figure 99: Lamellae of Al_xRE_y intermetallics in AE42 / 390 / S3.

5.2.4 Formation of Fold Defects

Microscopic examination of specimens in Figure 60 - Figure 63 revealed presence of sub-surface voids connected into complex networks. Analysis of the voids suggested that these defects were the result of improper fusion of merging metal fronts. Thus, these defects were classified as folds. The mechanism of fold formation was seen to be alloy specific.

AZ91D Alloy

Microscopic analysis of the casting specimens in the vicinity of the 90° junction (Samples #4 - #7) revealed regions with sub-surface folds, as visible in Figure 60d and Figure 60f. Figure 100 shows a representative SEM image of heavily folded region. As can be observed, the size of the folded region was significantly greater than that of shrinkage or gas porosities. Thus, folds were observed to form in addition to traditional casting defects.

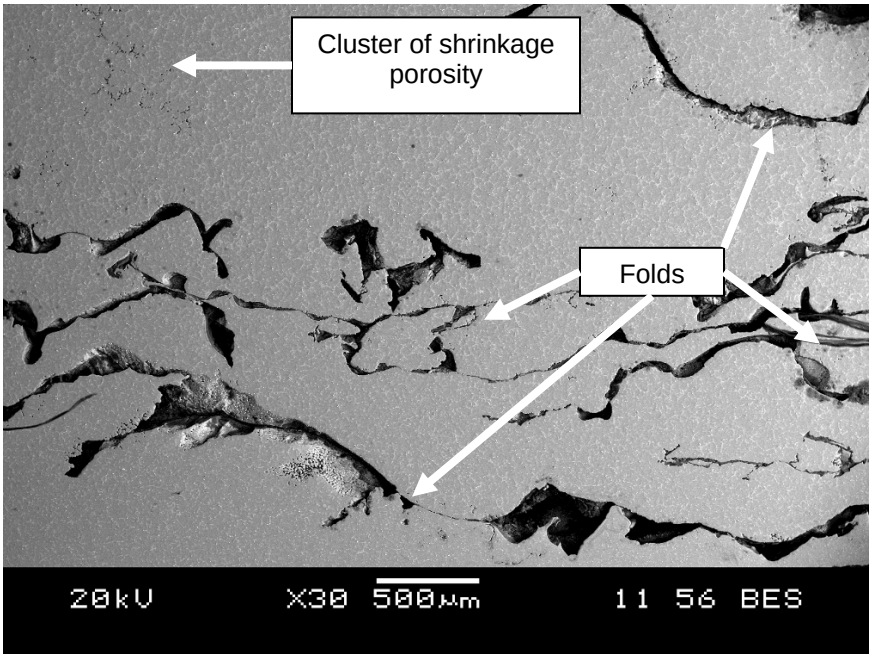

Figure 100: Subsurface folds in AZ91D / 210 / S6.

Additional examples of folds in AZ91D castings are presented in Figure 101.

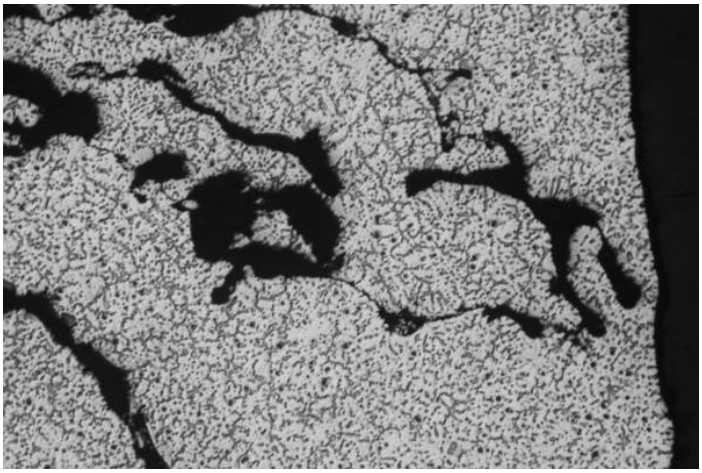

(a) Subsurface fold in AZ91D / 210 / S3 (BF, 50x).

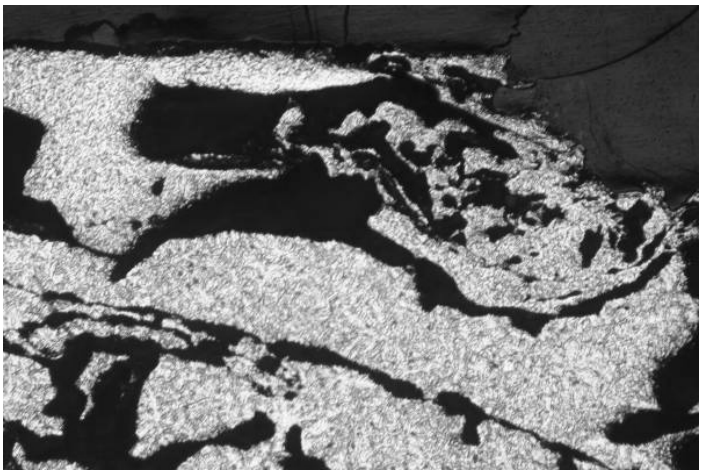

(b) Surface fold in AZ91D / 210 / S6 (BF, 50x).

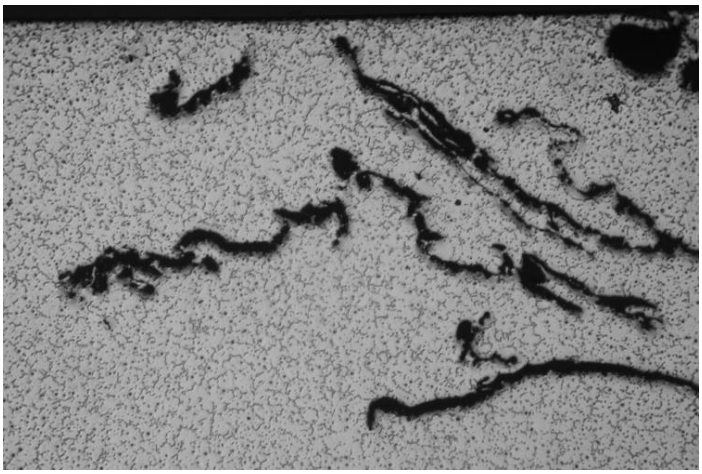

(c) Subsurface fold in AZ91D / 250 / S2 (BF, 50x)
Figure 101: Folds in AZ91D castings.

Typically, formation of folds is attributed to the development of: 1) temperature gradients; or, 2) velocity gradients in the melt during mold filling. In addition, bulk melt turbulence during mold filling promotes chilling of the metal fronts and additional development of temperature and velocity gradients.

Folds resulting from significant temperature gradients (i.e., inhomogeneous cooling) have discernible microstructure variation on either side of the fold. This mismatch of microstructure prevents proper fusion of the fold surfaces upon contact. As Figure 101 illustrates, the microstructure across the fold regions in the AZ91D castings was relatively uniform, suggesting that folds in these castings did not evolve due to significant thermal gradients.

In the AZ91D castings, the location of the folds coincided with the location of the (turbulent) flow lines observed on the casting surface, as discussed in Section 5.1. Thus, these folds likely formed due to melt turbulence and velocity gradients. This prediction is in agreement with the results of MAGMASOFT® analysis (Appendix A1.3), which predicted the development of high-velocity multiple metal streams in the critical region during mold filling.

Melt turbulence and fragmentation of the metal front into multiple metal streams increased the melt surface area exposed to the ambient air in the mold. Since the metal front in the mold was not protected with the CO_2 covergas, magnesium oxide formed and created a physical barrier between the merging metal streams, thereby hindering their proper fusion. SEM-EDX mapping was carried out on the fold region, as shown in Figure 102 to identify the chemical constituents of the oxide barrier. The figure shows that the fold region contained high levels of oxygen (with a small amount of Mg). Aluminum was retained in the $Mg_{17}Al_{12}$ intermetallic located in the interdendritic regions. Manganese formed as small cuboid crystals of Al-Mn intermetallics. Zinc, which is present at 1 wt% in the AZ91D alloy, was distributed throughout the microstructure in solid solution with magnesium. Therefore, it is likely that the oxide present in the fold region was MgO.

Additional examination of the fold region revealed that the Al-Mn cuboids segregated near the fold region, as shown in Figure 103. Small (white) particles were seen to agglomerate on dendrite walls, suggesting that these particles were rejected during solidification and pushed by the growing α-Mg dendrites. These precipitates were frequently observed on either side of a fold, as illustrated in Figure 104. Formation of these precipitates, however, was not seen as a necessary condition for fold formation.

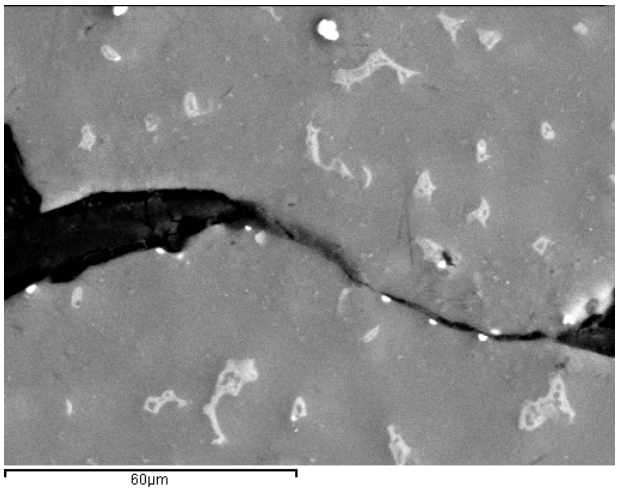

(a) Electron image.

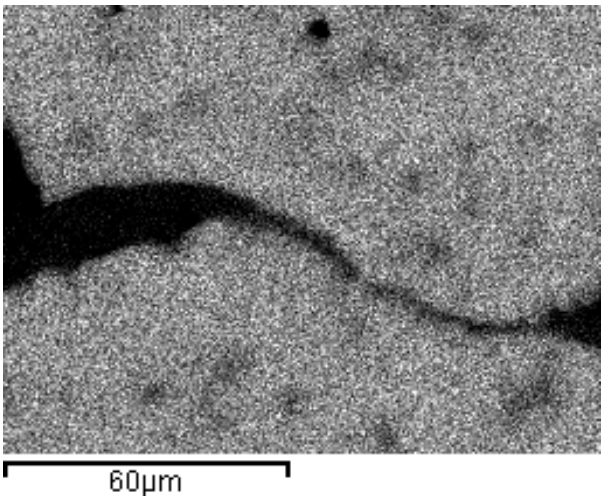

(b) Magnesium

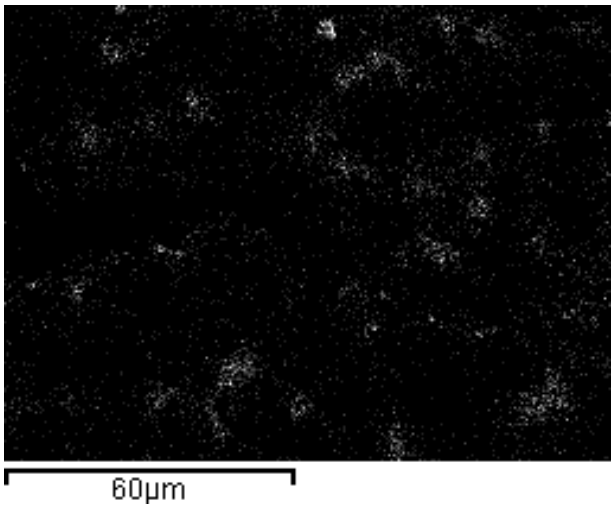

(c) Aluminum

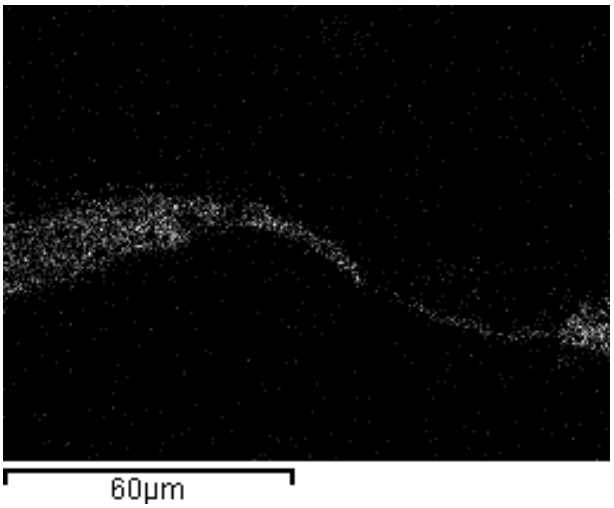

(d) Oxygen

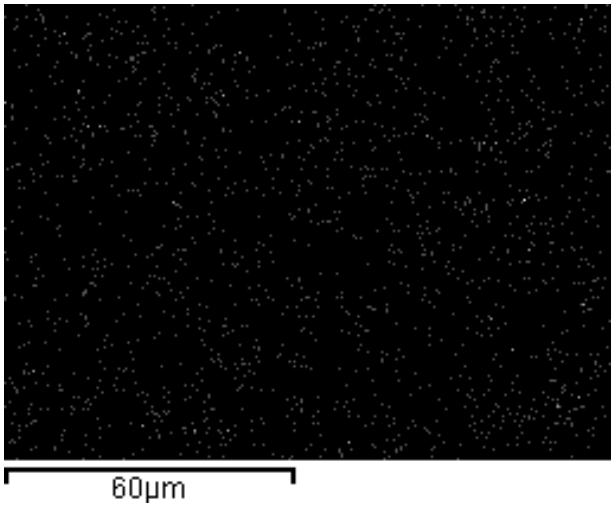

(e) Zinc

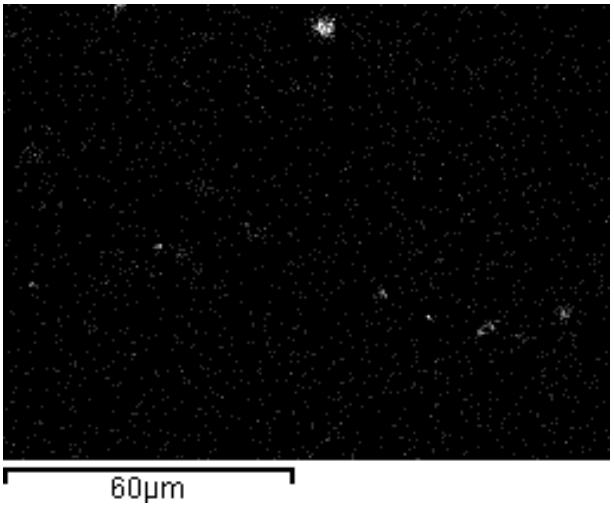

(f) Manganese

Figure 102: X-ray map of a fold in AZ91D / 210 / S6.

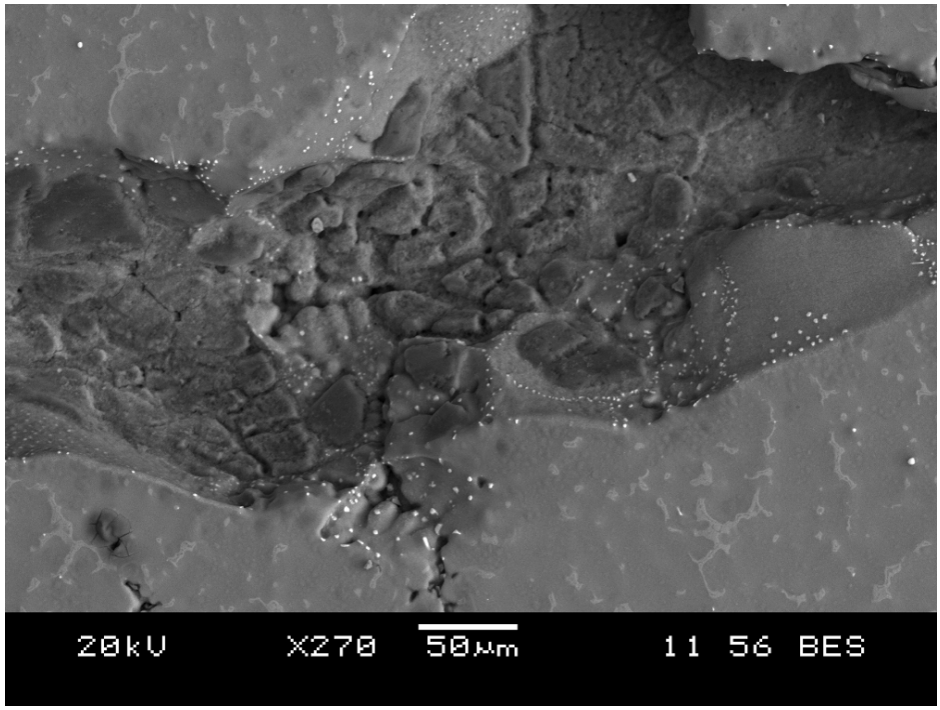

Figure 103: Void cavity near fold region with Al-Mn particles.

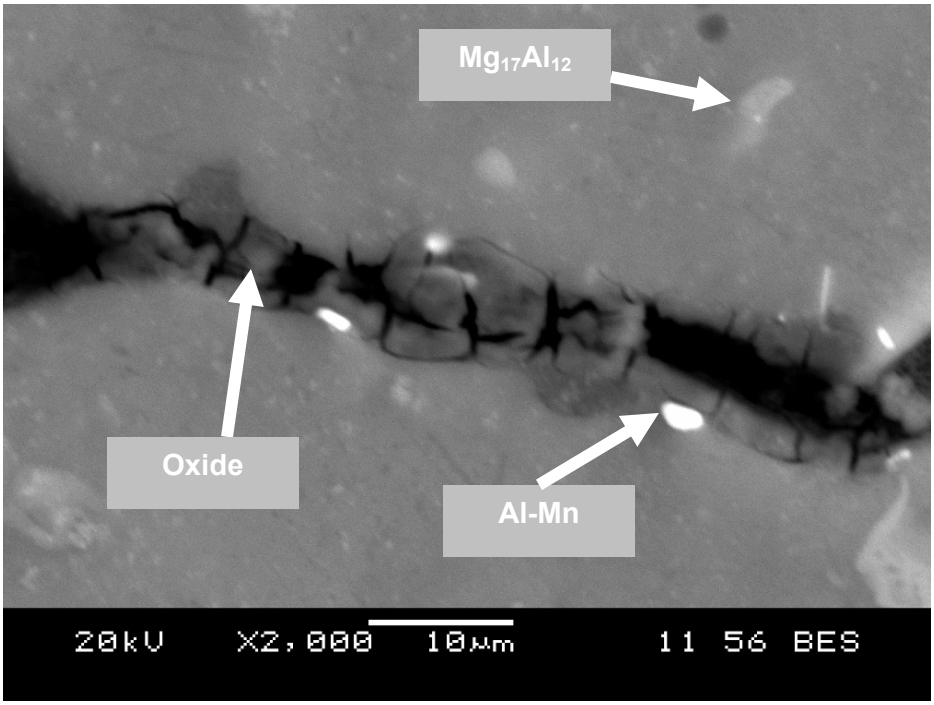

Figure 104: Oxide film and Al-Mn particulates in AZ91D / 210 / S6.

The MgO also formed on the walls of internal cavities, as observed in Figure 105 .

.

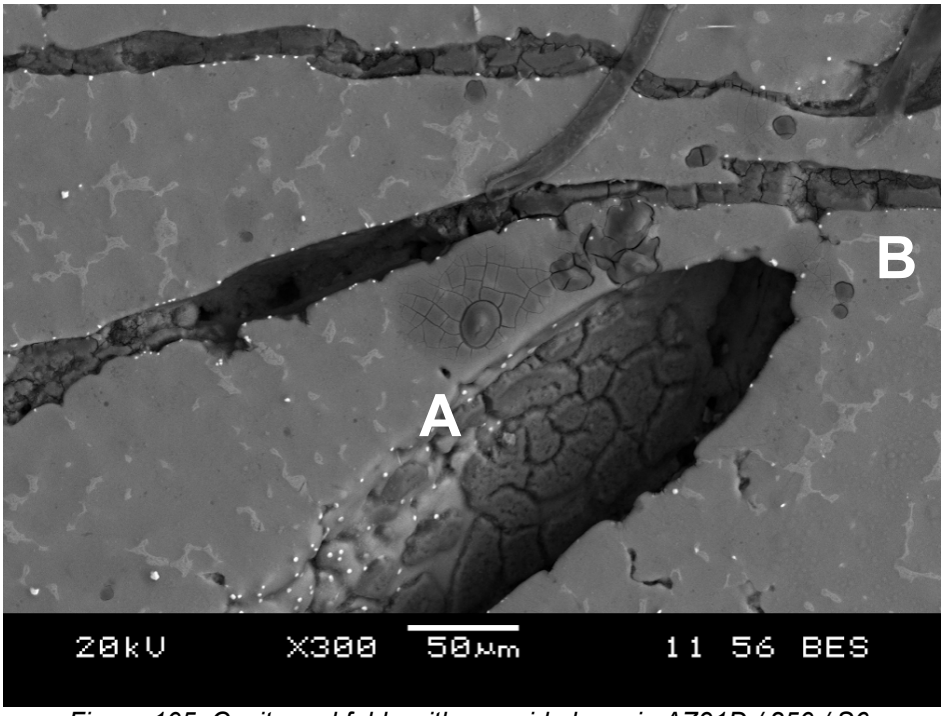

Figure 105: Cavity and folds with an oxide layer in AZ91D / 250 / S6.

The oxide layers forming on cavity walls were seen to be highly fragmented and typically less than 10 µm thick (Figure 106a), while oxides entrapped between two metal fronts were thicker (Figure 106b). Thick oxide formation between two metal fronts could be related to the possibility of oxide growth from each of the merging metal front surfaces.

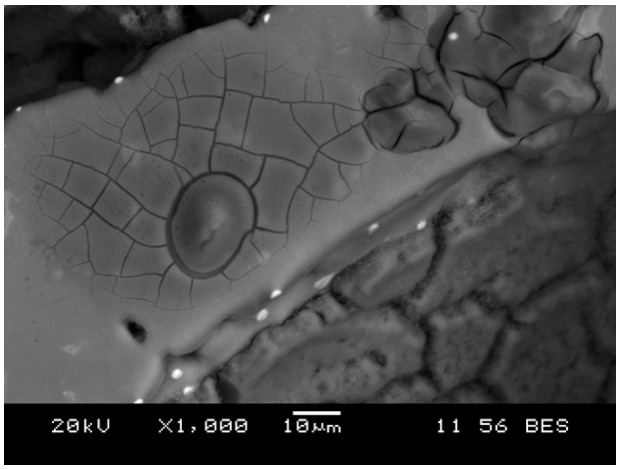

(a) Detail of region "A" from Figure 105.

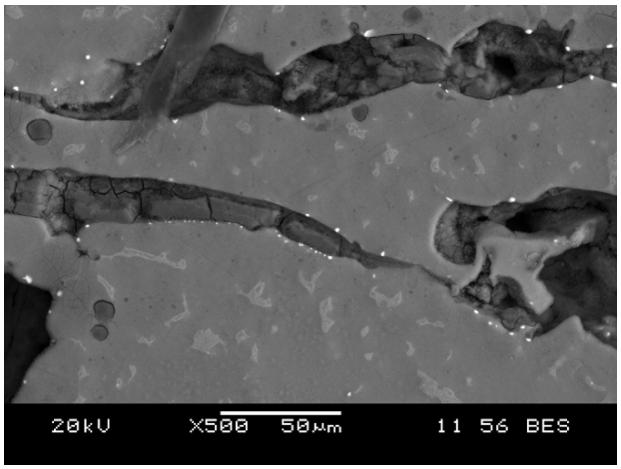

(b) Detail of region "B" from Figure 105.

Figure 106: Details of oxides in Figure 105.

Therefore, it appears that the formation of folds in the AZ91D alloy resulted from turbulent metal flow, breaking the metal front into multiple metal streams. Due to the exposure of the multiple metal streams to oxygen-rich ambient atmosphere in the mold, the metal streams began to oxidize, leading to the formation of ~ 10 μm thick oxide layer. This layer acted as a physical barrier between the metal streams and prevented their proper fusion, thus creating a fold. It was also noted, that despite the formation of the oxide layer, which is highly exothermic reaction, the microstructure on either side of the fold was relatively uniform. Thus, significant temperature gradients did not develop across the fold.

AE42 Alloy

Examination of the metallographic samples from AE42 castings made at 340 °C and 390 °C mold temperatures also revealed sub-surface cavities. Similarly, as in the AZ91D castings, these cavities did not appear to be shrinkage pores or entrapped gas, as illustrated in Figure 107. Further, these cavities were located in the vicinity of turbulent flow lines observed on the casting surface in the critical region.

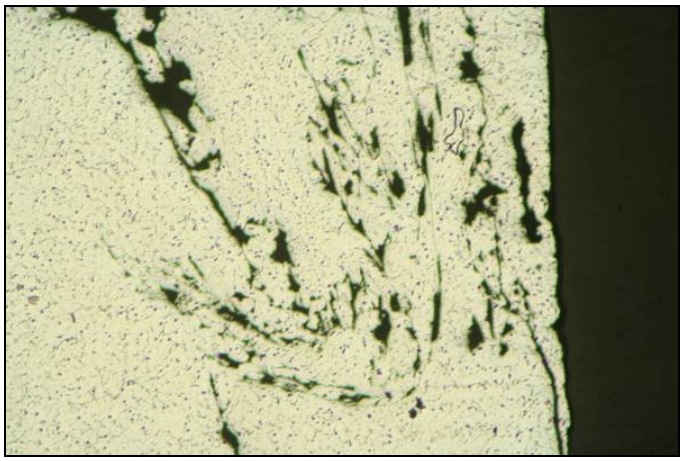

Figure 107: Sub-surface folds in AE42 / 390 / S6 (BF, 50x).

In the case of the AZ91D alloy, a layer of MgO oxide formed at the advancing metal front and prevented proper fusion of merging metal streams during casting filling. In the case of the AE42 castings, examination of the fold cavities did not reveal a significant amount of entrapped oxides. Such an observation is supported by the known increased oxidation resistance of the AE42 alloy. Instead, segregated RE-rich intermetallic compounds were observed in the folds. As example, Figure 108 - Figure 110 show the fold defect and segregated intermetallics in detail. The figures suggest that the layer of intermetallics was at the leading edge of the advancing metal front and did not allow proper fusion of joining metal fronts, thereby creating a gap between merging metal streams.

The layer of intermetallics was typically continuous. However, as Figure 109 shows, in regions of high cavity curvature, the layer of intermetallics fragmented. It is likely that the layer of intermetallics was harder (with a lower ductility) than the magnesium matrix and was not able to sustain the same extent of deformation as the matrix during thermal contraction of the casting. As a result, the layer of intermetallics fragmented.

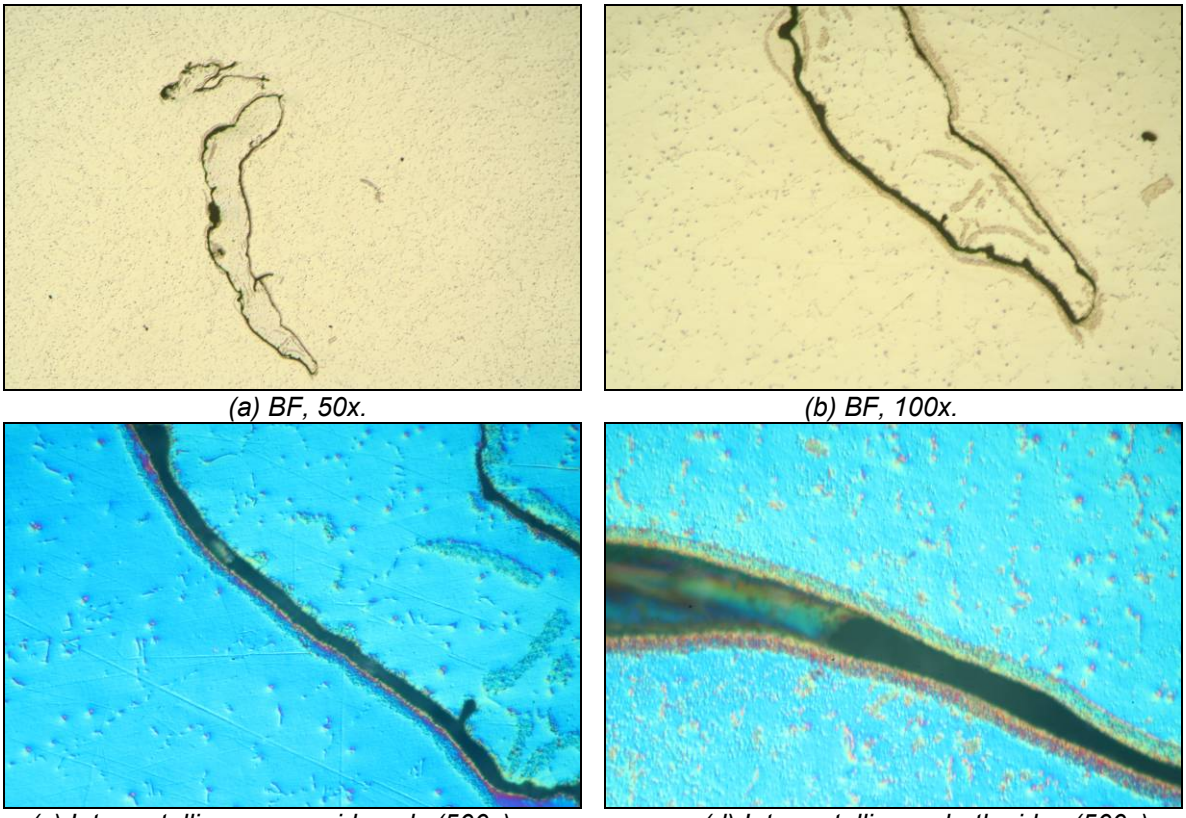

(a) BF, 50x. *(b) BF, 100x.*

(c) Intermetallics on one side only (500x). *(d) Intermetallics on both sides (500x).*

Figure 108: Fold in AE42 / 340 / S3 with segregated intermetallic compounds.

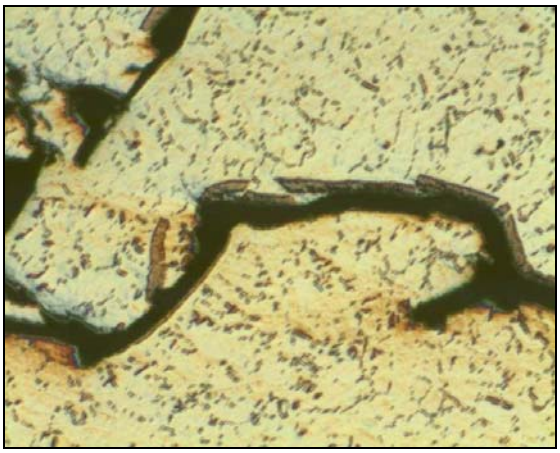

Figure 109: Fragmentation of intermetallic compound in AE42 / 390 / S6 (DIC, 200x).

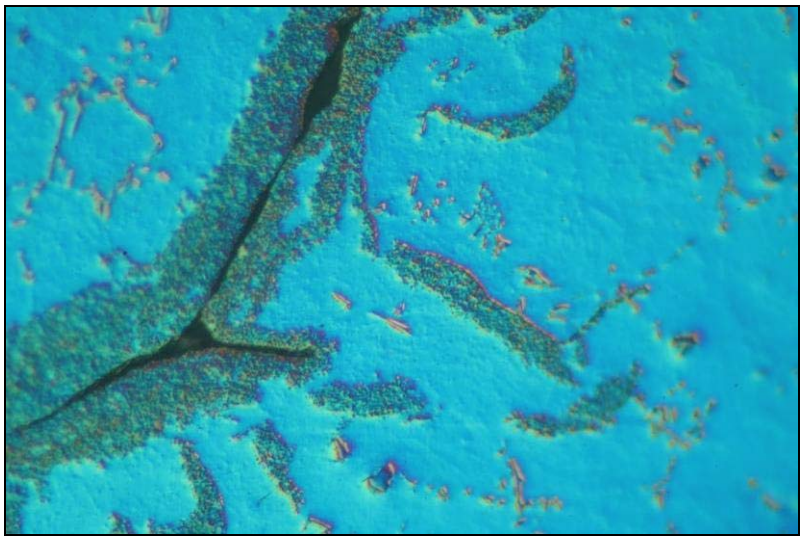

Figure 110: Improper fusion of metal fronts in the fold region (DIC, 500x).

SEM imaging of the fold region revealed that the layer of intermetallics consisted of very fine particles (< 4 μm) decorating the fold boundaries, as shown in Figure 111a. In addition, flakes of an unknown phase (possibly an oxide) were observed in some parts of the fold cavity (Figure 111b). The flakes did not form a continuous layer.

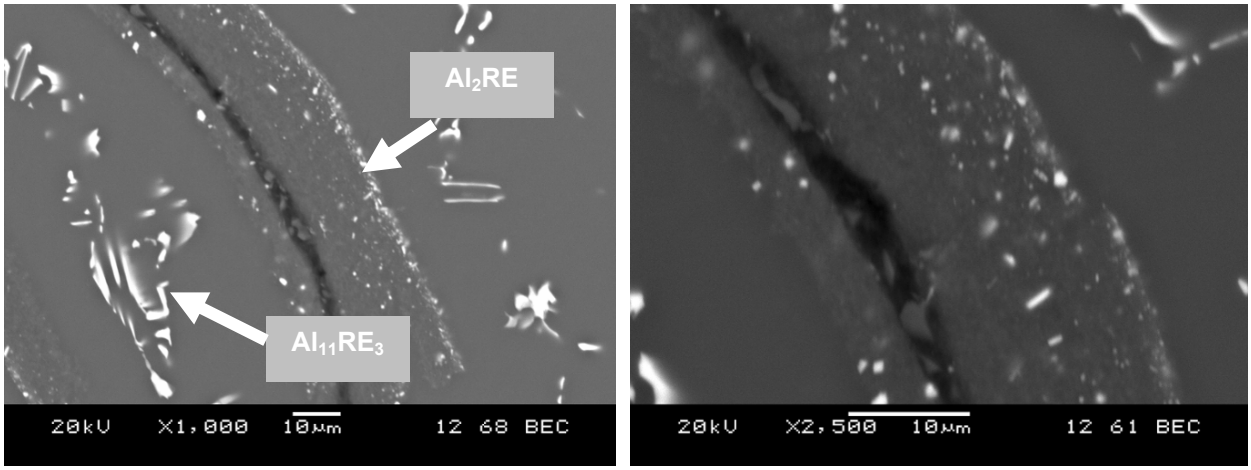

(a) Al_xRE_y intermetallic compounds. *(b) Oxide flakes in fold region.*

Figure 111: Fold region intermetallics and oxide flakes (SEM).

SEM-EDX analysis was carried out to obtain the chemical composition of the phases in the fold region. A linescan across the fold as well as X-ray map of the fold region are presented in Figure 112 and Figure 113.

The X-ray results suggest that the small particles of the intermetallic layer were enriched in Neodymium (~60 counts), Aluminum (~ 150 counts), while Lanthanum remained relatively low (~ 35 counts). As a result, it is likely that these fine particles at the fold boundary were Al_2RE. This analysis is consistent with the results presented in Section 5.2.3.2. The X-ray maps of Figure 112 and Figure 113 also indicate that the flakes trapped between the merging fronts contained elevated level of oxygen, thus suggesting possible presence of MgO.

Therefore, chemical analysis of the fold regions suggests that melt turbulence resulted in chilling and fragmentation of the metal front into multiple metal streams and promoted segregation of Al_2RE precipitates. These precipitates were significantly smaller (< 4 μm) than the matrix dendrite cells (~ 400 μm) and it is likely that the precipitates were pushed by the growing dendrites during solidification.

The resulting layer of Al_2RE intermetallics hindered proper fusion of the merging metal streams, resulting in the formation of a fold. Occasionally, the layer of the Al_2RE precipitates fragmented along the fold boundaries indicating that it was unable to sustain casting contraction or solidification stresses to the same extent as the α-Mg matrix.

In addition, it was observed that the fold cavity contained traces of oxygen-rich MgO flakes, which formed during exposure of the metal stream to air. The amount of entrapped oxides, however, was not as significant as in the case of the AZ91D alloy castings.

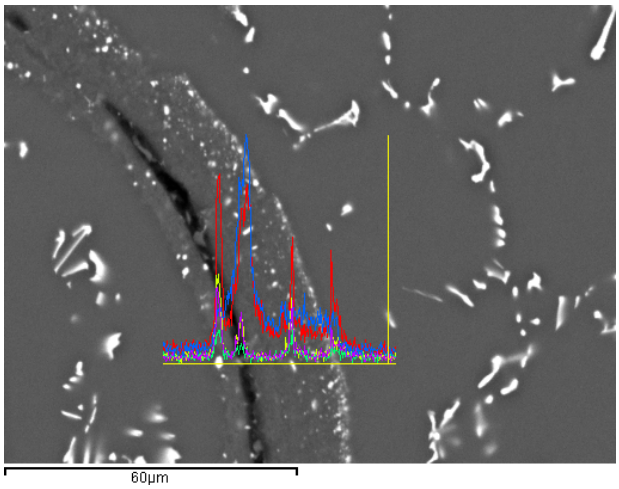

(a) Location of linescan.

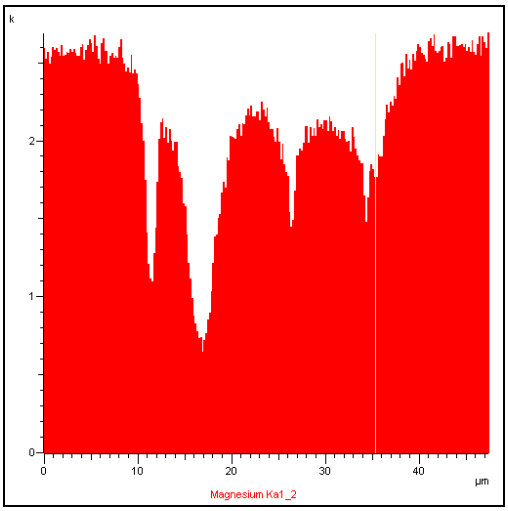

(b) Magnesium

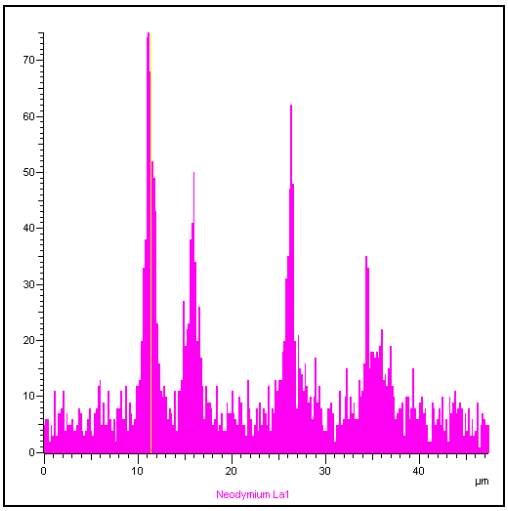

(c) Neodymium

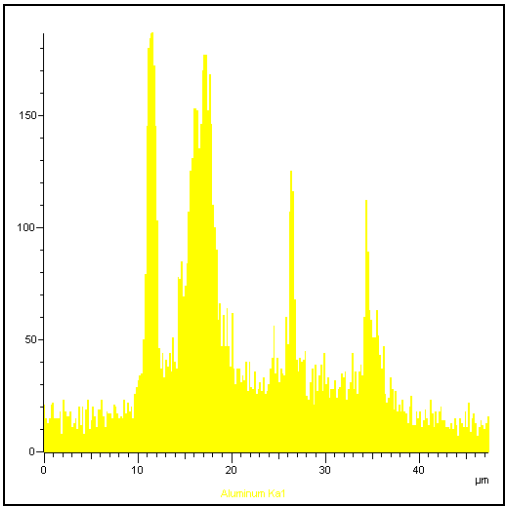

(d) Aluminum

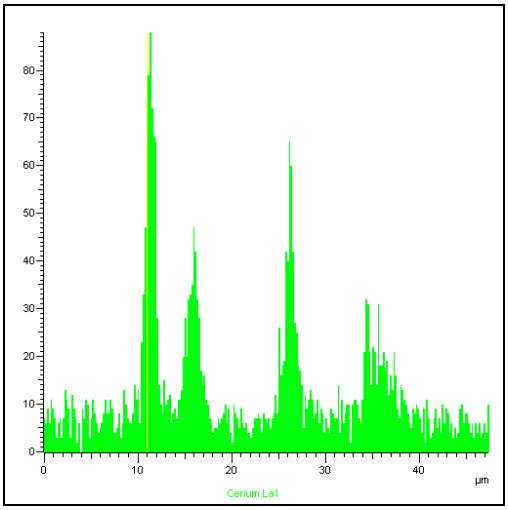

(e) Cerium

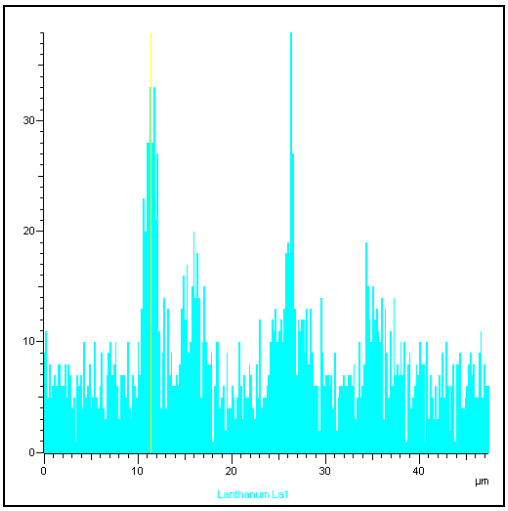

(f) Lanthanum

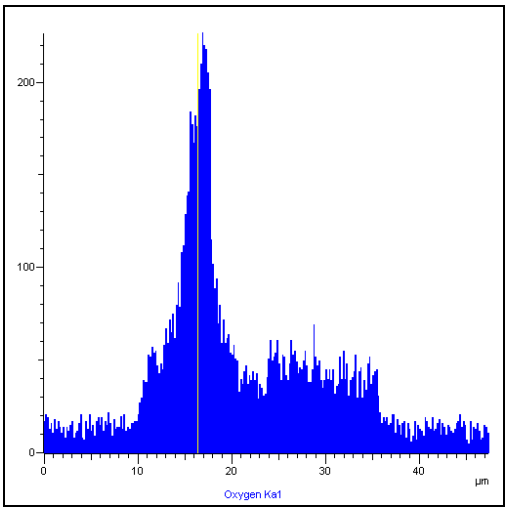

(g) Oxygen

Figure 112: Linescan (K-line) X-ray spectra.

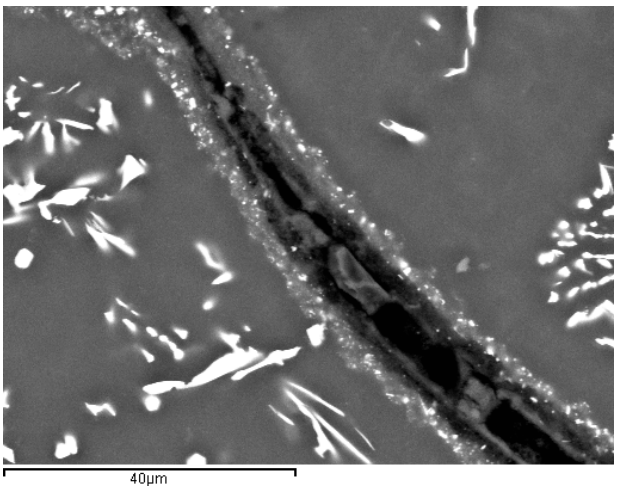

(a) Area for X-ray mapping.

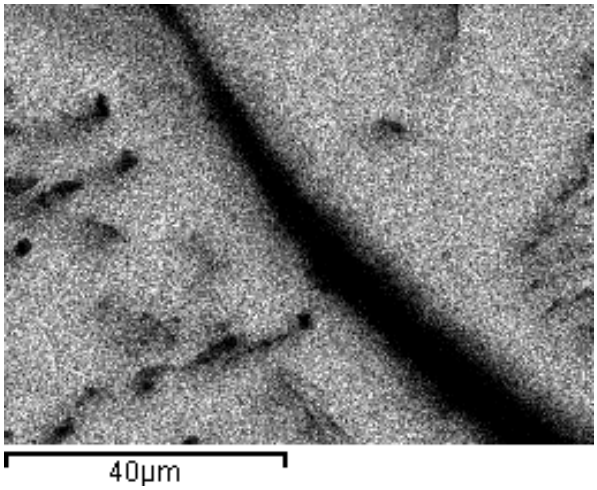

(b) Magnesium

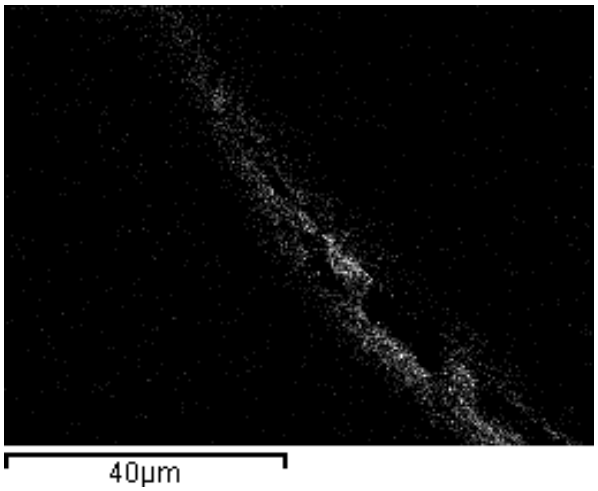

(c) Oxygen

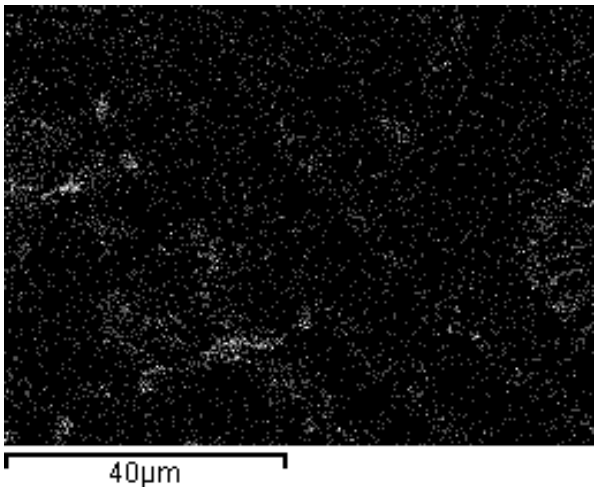

(d) Cerium

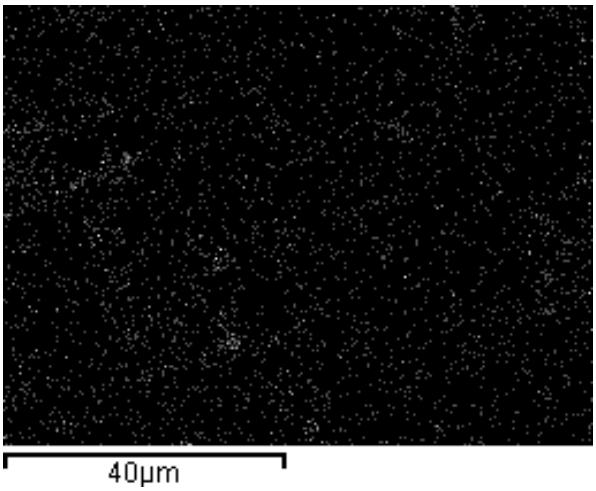

(e) Praseodymium

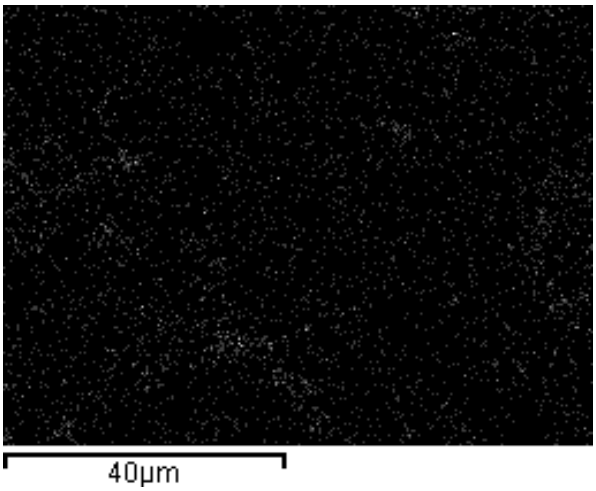

(f) Lanthanum

Figure 113: X-ray map of a fold in AE42 / 340 / S3.

Section Summary

Folds were present in the critical region of both alloy castings in areas of high melt turbulence. The presence of folds in this region would significantly deteriorate the casting homogeneity and soundness.

Unique features associated with fold formation were observed for the two alloys. In the case of the AZ91D alloy, a layer of MgO created a barrier, approximately 10 μm in width, which prevented proper fusion of merging metal streams. In the case of the AE42 alloy, segregation of Al_2RE fine precipitates (< 4 μm) at the metal front created a layer of local microstructural inhomogeneity. The layer of Al_2RE subsequently prevented fusion of merging metal streams, resulting in a fold.

5.2.5 Casting Porosity

Casting shrinkage porosity was seen to play an important role for the propagation of hot tears in AZ91D castings. As a result, a detailed quantitative shrinkage porosity analysis was carried out and is presented in the following text.

In the case of the AE42 alloy, hot tears were seen to propagate along the grain boundaries, rather than via interconnected shrinkage pores. Shrinkage porosity formed only as localized clusters in casting regions last to solidify (e.g., near the downsprue) and this porosity was not likely the primary factor contributing to the onset of hot tearing in the AE42 castings. In order to prevent hot tearing of the AE42 alloy castings, the mold temperature had to be relatively high. As a result of the slow cooling, the mechanical strength of the alloy was likely low. In order to bring the strength back to acceptable levels, the castings would have to be processed (e.g., by heat treatment). Such processing, however, distorts shrinkage porosity. Thus, since post-casting processing was not investigated in this research, quantitative porosity evaluation in the AE42 castings was not carried out. However, qualitative assessment of the porosity in the AE42 castings is included in this section.

AZ91D Alloy

Figure 114 presents the results of porosity measurements by optical image analysis software. These measurements were made on Sample #3 (located in the critical region) of castings produced at 700 °C pouring temperature and various mold temperatures. The results suggest that the porosity levels for all casting trials remained below 3.0 %, which is typical with PMC castings.

Figure 114 suggests a clear dependence of casting porosity on the mold temperature. The dependence was confirmed by performing ANOVA statistical analysis at the 95% confidence level. The critical test statistic was $F_{crit} = 2.7$, while the statistic based on measurements was $F = 27.7$. Thus, the mold temperature had a statistically significant effect on the casting porosity. Similarly, ANOVA analysis was performed on porosity measurements in castings produced at various pouring temperatures (680 and 700 °C). At the 95% confidence level, the pouring temperature did not have a statistically significant effect on the casting porosity. For example, for 220 °C mold temperatures, the critical test statistic was $F_{crit} = 3.1$, while the test statistic based on experimental measurements was $F = 1.1$. Same conclusions were obtained for remaining mold temperatures.

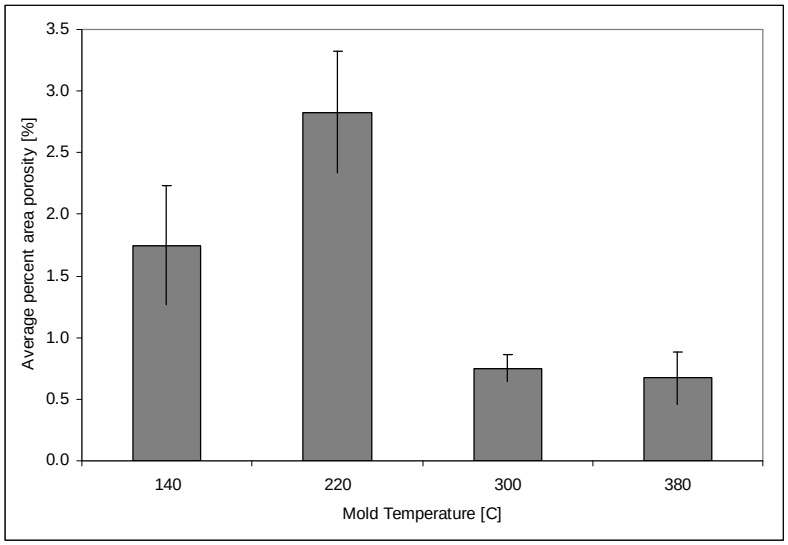

Figure 114: Effect of mold temperature on AZ91D casting porosity.

As Figure 114 shows, the shrinkage porosity level increased for mold temperatures from 140 – 220 °C, reaching a maximum of 2.7% at 220 °C mold temperature. Subsequently, shrinkage porosity decreased for higher mold temperatures. This trend correlated with the microscopic observations of the β-phase morphology and expected feedability of the casting. Upon increasing the mold temperature from 140 °C to 220 °C, the casting porosity increased as the solidification time increased and the alloy remained in the mushy state for a longer period of time. This trend is well documented and related to dendrite coherency and subsequent difficulty of bulk metal feeding [74]. With further increase of the mold temperature above 220 °C, the β-phase regions started to coalesce and grow, as discussed in Section 5.2.3.2. This growth enabled improved interdendritic feeding of the casting at late stages of solidification, resulting in decreased shrinkage porosity.

Shrinkage porosity was observed to nucleate between individual dendrites (Figure 115a), as well as between secondary dendrite arms of a single dendrite (Figure 115b). These regions were the last areas of the casting to solidify. Due to inadequate feeding by liquid melt, the shrinkage pores forming in the casting induced a negative pressure of 101.325 kPa on the solid dendritic structure. This load may have contributed to the initiation of plastic damage of the solid crystal matrix. The amount of shrinkage porosity was particularly high in Sample #8, where centerline shrinkage porosity bands formed in the downsprue, as illustrated in Figure 116.

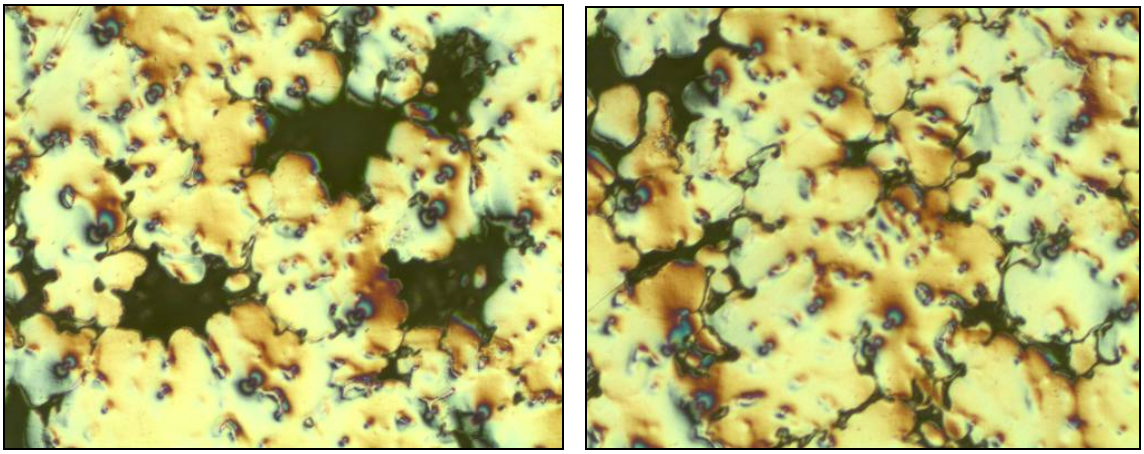

(a) *(b)*

Figure 115: Interdendritic shrinkage pores in AZ91D / 210 / S1 (DIC, 200x).

(a) Bands of centerline porosity (SM,6x).

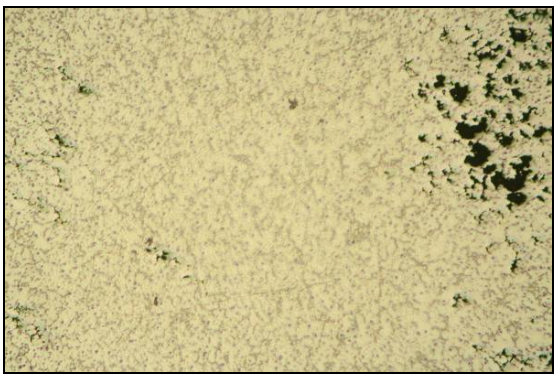

(b) Edge of porosity band (BF, 50x).

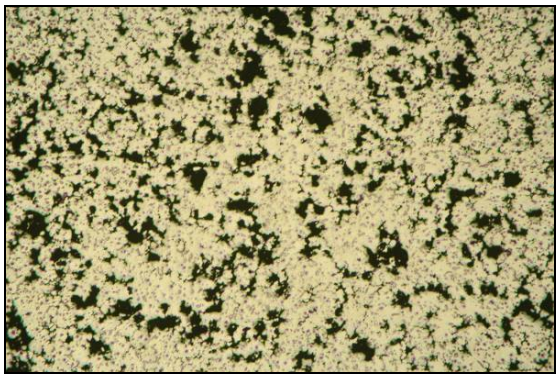

(c) Interior of shrinkage porosity band (BF, 50x).

Figure 116: Centerline porosity in AZ91D / 250 / S8.

An SEM detail of the shrinkage porosity is presented in Figure 117. The SEM micrographs suggest that the shrinkage pores formed as a result of dendrite arm separation (due to thermal contraction), as observed in Figure 117b. It was also noted that the exposed dendrites did not show traces of the eutectic β-phase, thus confirming that the centerline porosity formed due to severely limited feeding of the critical region.

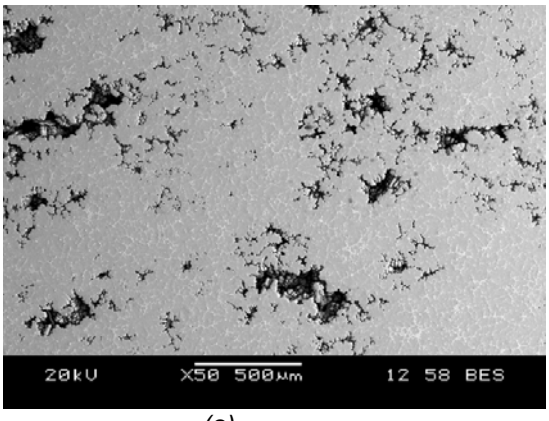

(a)

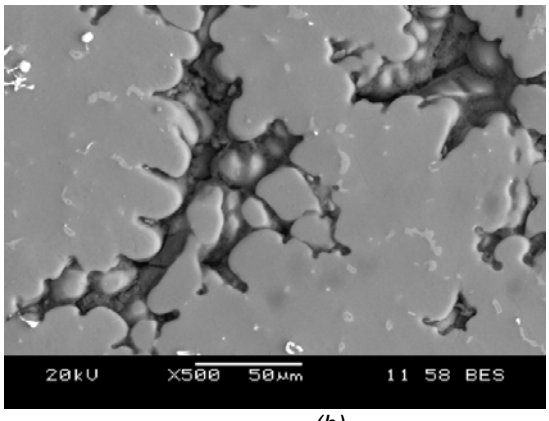

(b)

Figure 117: Shrinkage pores within porosity bands in AZ91D / 210 / S8.

Clearly, the absence of interdendritic liquid was seen to contribute to the formation of shrinkage pores. Conversely, SEM observations also revealed that in some instances, when interdendritic feeding was still possible, the eutectic liquid was able to terminate propagation of shrinkage pores, as indicated with arrows in Figure 118. This suggests that mobility and feeding of the eutectic liquid were critical for the growth of shrinkage pores (and hot tears) in the AZ91D castings.

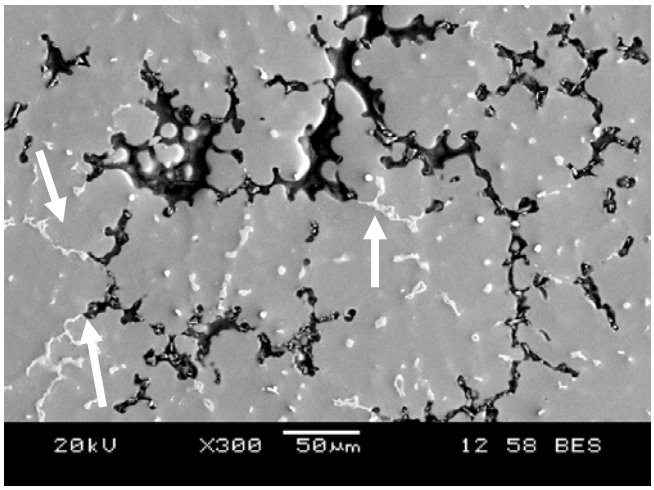

Figure 118: Interconnected shrinkage pores in AZ91D / 250 / S1.

AE42 Alloy

Shrinkage porosity in the AE42 castings produced at 340 °C and 390 °C mold temperatures was observed as localized clusters in casting regions expected to suffer from poor feeding. For example, Figure 119a shows a cluster of shrinkage porosity in the downsprue region adjacent to the centerline porosity band.

As Figure 119b indicates, individual pores extended only over a few dendrites and did not show any preferential growth direction. The pores within the cluster remained isolated, rather than forming a continuous network. Such observation suggests that the liquid phase in the AE42 alloy did not have long-range continuity and was present only as isolated pockets. This could be possibly the result of rapid α-Mg nucleation during AE42's solidification. Absence of continuous liquid along the dendritic boundaries would make feeding at high fractions of solid difficult, resulting in a very high susceptibility of the AE42 alloy to hot tearing.

As the mold temperature increased from 340 °C to 390 °C, the casting cooling rate decreased and extended the period when liquid phase was present. It appears that the extended solidification resulted in

partial agglomeration of shrinkage pores into interconnected clusters as seen in Figure 120. Thus, with increasing mold temperature, the continuity of the interdendritic liquid increased and interdendritic feeding improved.

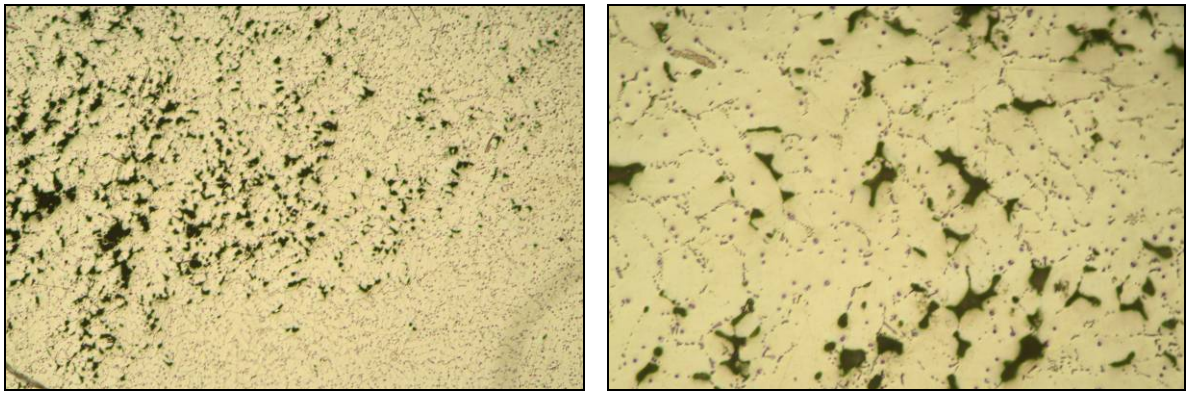

(a) BF, 50x. *(b) BF, 200x*

Figure 119: Shrinkage porosity cluster in AE42 / 340 / S8.

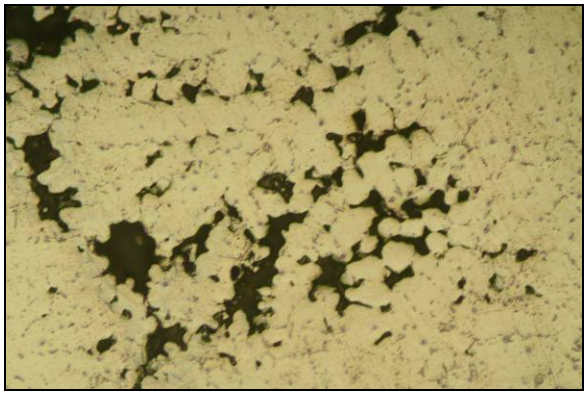

Figure 120: Interconnected shrinkage pores in AE42 / 390 / S1 (BF, 100x).

Section Summary

The results suggest that formation of interdendritic shrinkage porosity was related to the mobility of interdendritic liquid in the castings. In the AZ91D alloy, shrinkage pores formed extensive networks suggesting long-range continuity of interdendritic liquid. Increasing the mold temperature improved continuity of the liquid film. In the case of the AE42 alloy, the shrinkage pores were isolated, indicating absence of a continuous liquid film on the grain boundaries at late stages of solidification. Only when the mold temperature increased, the shrinkage porosity formed connected clusters.

5.3 Thermal Analysis

Thermal analysis was carried out following methodologies presented in the classical text "Solidification Characteristics of Aluminum Alloys, Vol. 3: Dendrite Coherency" [74]. This text describes the characterization and analysis techniques for solidification and microstructure evaluation of commercial aluminum alloys. In this text, aluminum alloys with solidification, microstructure and strength properties similar to the two magnesium alloys used in this research were considered. The concepts developed for these aluminum alloys were extended to the current magnesium alloys. This approach was necessary due to the absence of thermal analysis data for the AZ91D and AE42 alloys. Thus, it is recognized that the coherency and rigidity points estimated in this section for the AZ91D and AE42 alloys carry a degree of uncertainty. However, the relative trends and comparisons are expected to remain valid.

5.3.1 Solidification Characteristics of AZ91D and AE42 Alloys

Solidification of AZ91D and AE42 magnesium alloys is similar to solidification of hypoeutectic aluminum alloys as outlined in Reference 74. The key solidification events may be summarized as follows:

At the start of solidification, small and equiaxed crystals develop throughout the melt and remain separate from one another. As the crystals take shape of dendrites, the dendrites impinge upon one another and a continuous solid network forms throughout the material; this event is called the "coherency point".
At coherency, the dendrite growth velocity can be estimated using the average linear growth velocity of dendrite tips (calculated by dividing the average grain radius by the time period from the instance of grain nucleation to the coherency point).

Prior to onset of dendrite coherency, mass feeding of the casting by liquid takes place. During mass feeding, bulk casting deformation may occur and is exhibited, for example, by a drop of the riser head. After coherency, feeding must proceed interdendritically. With progressing solidification and as dendrites ripen, interdendritic feeding becomes increasingly difficult. The practical limit for gravity interdendritic feeding is the "rigidity point", when the liquid phase ceases to be continuous and forms isolated pockets between dendrites. The rigidity point depends on the alloy system, grain size, degree of structure modification, cooling rate, etc. Feeding beyond the rigidity point may be only accomplished if external stress is applied to induce capillary flow between dendrites (e.g., HPDC).

A summary of the solidification events and their relationship to feeding is presented in Table 16 [74]. The solidus and liquidus temperatures for the AZ91D and AE42 alloys are presented Table A1. 2.

Table 16: Solidification and feeding events in Aluminum alloys.

Solidification Event	Feeding Characteristics
Before coherency point	Complete mass feeding of a slurry of melt and solid particles is possible
↓	↓
At coherency point	Mass flow becomes restricted
↓	↓
Between coherency and rigidity points	Gravity feeding by interdendritic flow is still possible
↓	↓
After rigidity point	Further interdendritic flow is restricted and must be supported by pressure
↓	↓
Well beyond rigidity point	Feeding is possible only with sufficient pressure to collapse the dendritic network

These concepts were used to investigate the solidification and feeding behavior of the AZ91D and AE42 alloys. Temperature data obtained from virtual thermocouples from MAGMASOFT® were used for this investigation. Using the virtual thermocouple data enabled assessment of solidification history in the critical region of the castings where hot tears formed (data label: "Hot tear"). The locations of the four virtual thermocouples (#1 – Middle of sprue, #2 – Hot tear, #3 – Skin at bar midsection and #4 – Center at bar midsection) were indicated in Figure 55. The maximum temperature difference (for the entire simulation) between the virtual thermocouple at the center of bar midsection (TC #4) and experimental temperature data was ~ 10 °C. The validity of using the virtual thermocouples for temperature analysis is discussed in Appendix 1.3.1.

The cooling curves, cooling rates and fraction of solid development for the four locations are presented in Appendix 4 (Figure A4. 1 - Figure A4. 4). On these cooling curves, several temperatures of interest were identified, as illustrated in Figure 121. Subsequently, the cooling curves were used to calculate the local solidification time (LST), corresponding to the time interval between the non-equilibrium liquidus and solidus temperatures. The results are presented in Table 17.[†]

[†] *Much of the following text has been published in:* Bichler, L., Ravindran, C. and Sediako, D., "Onset of Hot Tearing in AE42 Magnesium Alloy", Canadian Metallurgical Quarterly (Accepted: November, 2008); Bichler, L., Ravindran, C. and Sediako, D., "Stress and Strain Evolution at the Onset of Hot Tearing in AZ91D Magnesium Alloy", Metallurgical and Materials Transactions A, (Submitted: January 2009).

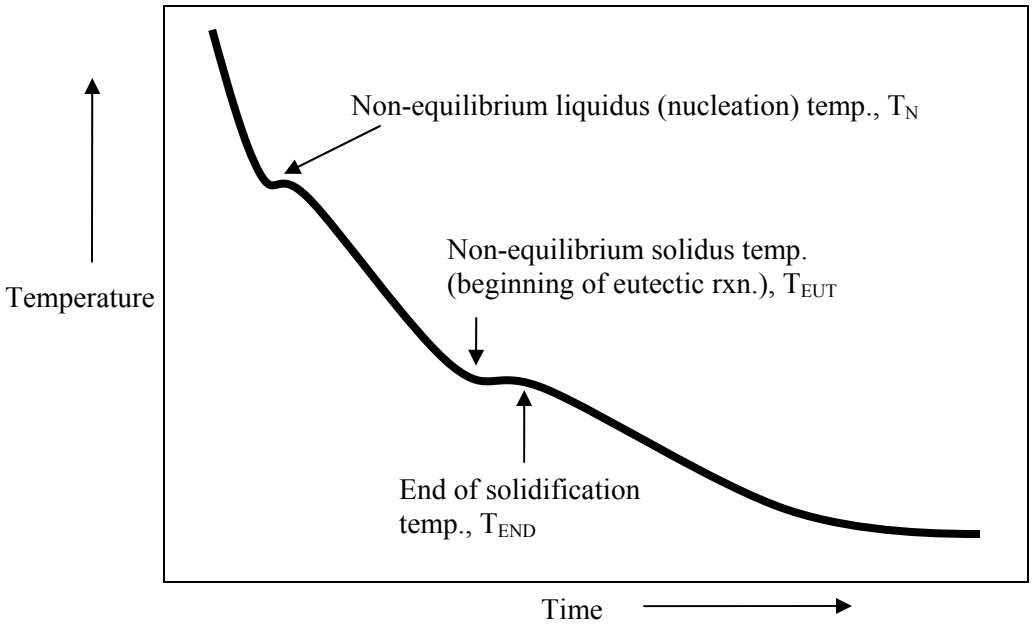

Figure 121: Non-equilibrium liquidus, solidus and eutectic temperatures used in thermal analysis.

Table 17: Local solidification time in hot tear region.

Alloy	Mold temperature [°C]	LST [s]
AZ91D	210	21.9
	250	24.7
AE42	340	18.5
	390	22.9

Table 17 shows that increasing the mold temperature increased the LST by 2.8 s and 4.4 s, for the AZ91D and AE42 alloys, respectively. With increased LST, the alloys remained in the semi-solid state longer, thus enabling enhanced liquid feeding of the critical casting region.

Casting microstructure analysis in the critical region (Section 5.2.3.2) revealed that by increasing the mold temperature and LST, the size of the interdendritic regions increased and eutectic phase was present. Table 18 supports this observation and suggests that slower casting solidification at 250 °C and 390 °C mold temperatures extended the duration of the eutectic reaction by 44% and 26% for the AZ91D and the AE42 alloys, respectively. As a result, the greater amount of eutectics forming near the end of solidification improved long range feeding of the casting.

Table 18: Duration of eutectic reaction in hot tear region.

Alloy	Mold temperature [°C]	Duration of eutectic reaction [s]
AZ91D	210	7.4
	250	10.8
AE42	340	5.1
	390	6.9

In order to determine the intervals (in terms of time, temperature or fraction of solids) between the coherency, rigidity and end-of-solidification points, the fractions of solid corresponding to these events had to be estimated. At the time of writing this thesis, limited literature was available on these solidification points for the AZ91D or AE42 alloys. As a result, data for aluminum alloys with similar microstructure and solidification characteristics provided in Reference 74 were used in estimating the aforesaid critical fractions of solid. The alloys used for this analysis, along with their coherency and rigidity points are presented in Table 19 and Table 20. Figure 122 shows the microstructure of these four aluminum alloys [74].

Table 19: Dendrite coherency and rigidity fractions of solid for Al alloys similar to AZ91D.

Aluminum alloy	$f_{s\text{-coherency}}$ [%]	$f_{s\text{-rigidity}}$ [%]	Freezing range [°C]
201	26	62	78
518	22	70	86
Average	**24**	**66**	**82**

Table 20: Dendrite coherency and rigidity fractions of solid for Al alloys similar to AE42.

Aluminum alloy	$f_{s\text{-coherency}}$ [%]	$f_{s\text{-rigidity}}$ [%]	Freezing range [°C]
713	24	79	45
357	29	72	55
Average	**26**	**75**	**50**

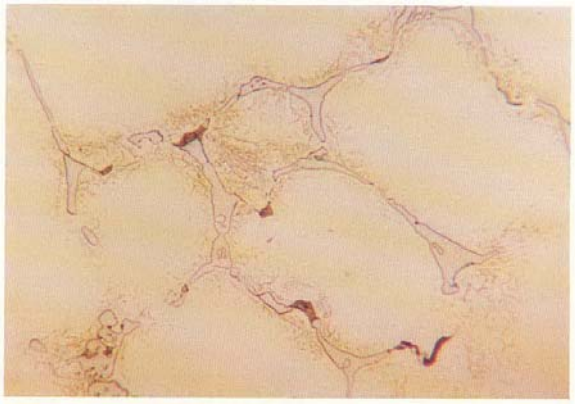

(a) 201 Alloy (550x)

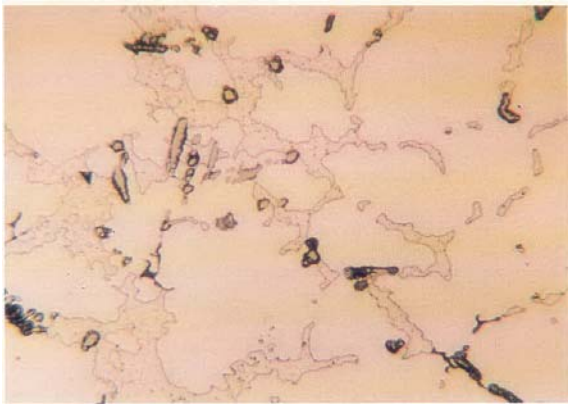

(b) 518 Alloy (550x)

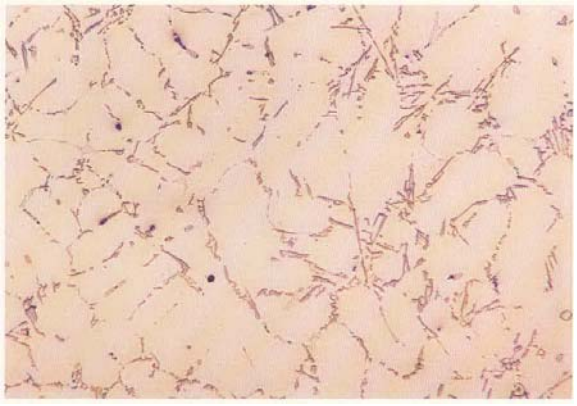

(c) 357 Alloy (550x)

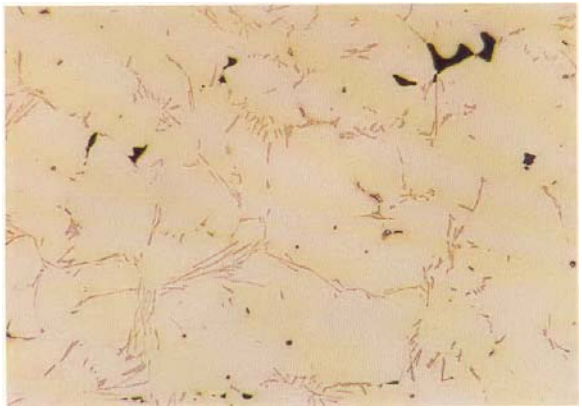

(d) 713 Alloy (550x)

Figure 122: Microsctructures of 201, 518, 357 and 713 aluminum alloys.

The $f_{s\text{-}coherency}$ estimate in Table 19 was compared to a study on the solidification and microstructure of AZ91 alloy [75]. Real-time torque measurements revealed that the dendrite coherency point in the AZ91 alloy was between 14 – 28%. Thus, the value of 24% estimated from the data of aluminum alloys appears reasonable, irrespective of the difference in the freezing ranges of Al and Mg alloys. However, it is recognized that the estimate of the coherency and rigidity points based on data for aluminum alloys may not be totally accurate, since not all alloy parameters (e.g., freezing range, microstructure, second phases, etc.) were identical for the aluminum and magnesium alloys.

Using the average values from Table 19 and Table 20, the solidification characteristics for the AZ91D and AE42 alloys were estimated from the fraction of solids curves. The results are summarized in Table 21 and Table 22.

Table 21: Thermal analysis data.

Alloy / Mold temperature [°C]	Start		Coherency		Rigidity	Eutectic		End	
	T_N [°C]	t_N [s]	T_C [°C]	t_C [s]	T_R [°C]	T_{EUT} [°C]	f_{EUT} [%]	T_{END} [°C]	t_{END} [s]
AZ91D / 210	598.0	0.0	580.5	4.9	548.8	428.0	99.9	398.0	34.0
AZ91D / 250	601.0	1.6	581.0	7.2	544.0	428.0	99.2	409.0	40.6
AE42 / 340	625.3	2.1	624.7	3.4	615.9	609.6	89.2	574.9	21.0
AE42 / 390	625.4	3.7	624.8	5.4	615.8	611.0	86.3	582.1	26.6

Table 22: Differences of temperature and fraction solid at temperatures of interest.

Alloy / Mold temperature [°C]	T_N-T_C [°C]	T_C-T_R [°C]	f_R-f_C [%]	T_R-T_{END} [°C]	1-f_R [%]	$t_C - t_N$ [s]
AZ91D / 210	17.5	31.7	40.0	150.8	34.1	4.9
AZ91D / 250	20.0	37.0	40.6	135.0	34.2	5.7
AE42 / 340	0.6	8.8	46.8	41.1	28.9	1.2
AE42 / 390	0.6	8.9	47.4	33.8	28.5	1.7

The relevant observations ensuing from these solidification parameters are discussed individually:

$T_N - T_C$:

This parameter indicates the temperature drop between the nucleation and the coherency temperature. The greater this temperature range, the longer the alloy flows freely. Further, within this interval, bulk feeding is possible and no stresses develop in the casting. As a result, hot tear nucleation is unlikely.
It was observed that the AZ91D alloy had a significantly wider $T_N - T_C$ temperature range than the AE42 alloy. This result supports the experimentally observed poor castability of the AE42 alloy in comparison to the AZ91D alloy. As observed, the AE42 alloy reached dendrite coherency nearly immediately after filling of the mold, which made subsequent interdendritic feeding the dominant feeding mechanism in the AE42 casting.

It was further observed that in the case of the AZ91D alloy, increasing the mold temperature increased the $T_N - T_C$ interval to further extend bulk feeding. Comparable increase of the $T_N - T_C$ interval was not observed in the AE42 casting. With improved bulk feeding at elevated mold temperature, volumetric shrinkage contraction in the AZ91D alloy was relieved by incoming liquid metal feed and the net stresses on the developing dendritic structure decreased.

As the nucleation temperature for the AZ91D alloy remained near its equilibrium value (~ 598 °C) (for both mold temperatures), the increase in the $T_N - T_C$ range with increased mold temperature suggests that increasing the mold temperature delayed the onset of dendrite coherency.

$t_C - t_N$:

This time interval represents the duration of mass feeding. Higher value of $t_C - t_N$ is desirable, as it indicates extended feeding of the casting by a low viscosity melt.

The AZ91D alloy had nearly five times longer $t_C - t_N$ interval than the AE42 alloy. Again, this result supports the observed superior castability of the AZ91D alloy over that of the AE42 alloy. Due to the extended $t_C - t_N$ interval, the AZ91D alloy filled larger portion of the casting before dendrite coherency occurred. With improved bulk feeding, solidification stresses developed later and possibly remained lower in magnitude upon subsequent casting solidification.

The $t_C - t_N$ parameter was used to estimate the dendrite growth velocity for each alloy. Observing the average grain size for the four casting conditions (Figure 71), the average growth velocity was calculated. The results in Table 23 indicate that the short freezing range of the AE42 alloy in conjunction with relatively high cooling rates induced very high dendritic growth (branching) velocities. As a result, the alloy had a high susceptibility for hot tearing.

Table 23: Average dendrite growth velocity.

Alloy / Mold temperature [°C]	**Growth velocity [µm/s]**
AZ91D / 210	10
AZ91D / 250	9
AE42 / 340	346
AE42 / 390	319

$T_C - T_R$:

This parameter represents the temperature range between coherency and rigidity points when interdendritic liquid flow was the primary feeding mechanism. Long T_C-T_R range suggests that interdendritic liquid was mobile and compensated solidification shrinkage, closed shrinkage pores or healed incipient hot tears. Within this interval, solidification stresses begin to develop, but the tendency for hot tearing remains low.

In the case of the AZ91D alloy, the T_C - T_R temperature range was approximately four times longer than in the case of the AE42 alloy. Thus, as a result of the relatively slow dendrite growth velocity, the interdendritic channels in the AZ91D alloy remained open and interdendritic feeding of the AZ91D casting was easier than in the case of the AE42 alloy casting, where rapid grain growth and dendrite branching made interdendritic feeding of the casting difficult.

It was also observed that increasing the mold temperature extended the AZ91D's $T_C - T_R$ range by 5.3 °C, or nearly 20% of this critical freezing range. The enhanced feeding would decrease the tendency to develop solidification shrinkage porosity. Since formation of shrinkage porosity induces pressure on dendrites, reduction of shrinkage porosity would decrease the stresses imposed on the solidifying dendritic network. In the case of the AE42 alloy, this period remained unchanged with an increase of the mold temperature, suggesting that interdendritic feeding possibly did not significantly influence the onset of hot tearing in the AE42 alloy.

$f_R - f_c$:

This range of solid fraction indicates the relative difficulty of interdendritic flow after dendrite coherency occurred and may be indicative of the bulk alloy rheology (viscosity) during solidification. The longer this range, the longer the period when a viscous semi-solid slurry is present during solidification.
A material with a short $f_R - f_C$ range (e.g., pure metals have zero range) are easier to cast than alloys with long $f_R - f_C$ range, in which case interdendritic feeding must be accomplished through increasingly tortuous interdendritic paths.

It was observed that the AZ91D alloy had ~15% shorter $f_R - f_C$ range than the AE42 alloy. This is in agreement with the $T_N - T_C$ and $T_C - T_R$ indicators: the AE42 alloy became coherent quickly after cooling below the nucleation temperature and dendritic structure remained coherent for a long period of time. Thus, it is likely that the bulk viscosity of the AE42 alloy during mold filling was higher than that of the AZ91D alloy, which is consistent with the observed difficulty in producing AE42 alloy castings.

For both alloys, increasing the mold temperature increased the $f_R - f_C$ range, suggesting that the alloys remained semi-solid for a longer period of time due to the slower cooling of the bulk material. For castings made at 250 °C and 390 °C mold temperatures, respectively, liquid was present as a continuous film on the grain boundaries for a longer period of time. Consequently, increasing the mold temperature decreased the tendency for interdendritic shrinkage porosity and hot tearing due to improved interdendritic feeding.

$T_R - T_{END}$:

This range represents a critical temperature range of solidification when interdendritic feeding is minimal and the material shrinks without adequate compensation by liquid feed. During this period, relatively high solidification stresses develop and the tendency for shrinkage porosity and hot tearing is high. This range is also indicative of the ability of the material to sustain thermal (solidification) stress prior to complete solidification.

Observing the results in Table 22, the (absolute) value of this critical range was 3.8x higher for the AZ91D alloy than for the AE42 alloy. Thus, initially, it might be expected that the hot tearing tendency of the AZ91D alloy should be higher than that of the AE42 alloy, which is contrary to experimental trials. To explain this observation, the strength of the material in this range was considered. The enhanced strength of the AZ91D alloy could possibly be related to the higher aluminum content. However, a more prominent strengthening factor would be the grain size effect. As discussed in Section 5.2.1, the grain size of the AZ91D alloy was nearly an order of magnitude smaller than that of the AE42 alloy. Thus, using a simplified form of the Hall-Petch relationship (Equation 27) it is evident that the grain size of the material has a significant influence on the material's yield stress

$$\sigma = \sigma_o + kd^{-1/2} \tag{27}$$

Where:

σ = yield stress σ_o = stress to activate dislocation motion

k = constant d = grain diameter

Considering the average grain diameter from Figure 71 and assuming constant k and σ_o for both alloys, then the calculated $\sigma_{AZ91D} : \sigma_{AE42}$ ratio was 3.0, while the $(T_R - T_{END})_{AZ91D} : (T_R - T_{END})_{AE42}$ ratio was 3.8. Therefore, it appears that the grain size significantly contributed to the strengthening of the semi-solid

material. Thus, this result of thermal analysis suggests that despite the AZ91D's longer critical interval with minimal feeding, the alloy was stronger and less prone to hot tearing due to its fine grain size.

The possible influence of the $T_R - T_{END}$ feeding on formation of shrinkage porosity was also considered. In the AZ91D alloy, extensive shrinkage porosity in the vicinity of hot tear nucleation site (e.g., Figure 72) was observed. In the case of the AE42 alloy, the $T_R - T_{END}$ range was relatively short and the tendency for porosity nucleation was low, which agrees with microscopic observations of the critical casting region.

$1\text{-}f_R$:

This parameter is indicative of the amount of thermal contraction occurring after dendrite rigidity occurs. Within this range, the bulk material contracts without adequate liquid feeding, resulting in the evolution of thermal stress in the solid dendritic structure. A short $1\text{-}f_R$ range indicates that only a relatively small amount of solidification contraction remains after rigidity. Thus, a short $1\text{-}f_R$ range is desirable.

The values of $1\text{-}f_R$ for the two alloys were similar. Increasing the mold temperature did not appear to significantly influence this parameter.

5.3.2 Estimation of Alloy Mechanical Response in the Semi-Solid State

The fraction of solid curves were used to estimate the mechanical response of the semi-solid AZ91D and AE42 alloys. Estimation of the alloy's strength and ductility using thermal analysis data has been extensively studied in steels and extended to other alloys [76, 77, 78] via the concepts of zero ductility temperature (ZDT) and zero strength temperature (ZST).

The zero ductility temperature is obtained from high-temperature tensile tests and corresponds to the temperature when an alloy fails in a "brittle" manner, i.e., with zero ductility. Typically, this event corresponds to the occurrence of liquid phase on the grain boundaries.

The zero strength temperature corresponds to temperature during a series of high temperature tensile tests when a test sample is no longer able to sustain any applied load and fails. This event does not necessarily coincide with the ZDT, since a well developed dendritic network (capable of bearing load) exists even if liquid phase is present between dendrite arms.

Due to the lack of available literature on the mechanical behavior of magnesium alloys in the semi-solid state, the ZST and ZDT were estimated to occur at $f_s = 0.75$ and $f_s = 0.99$ respectively, based on published data for aluminum alloys [76]. The fraction of solids development curves for the castings are presented in Figure 123 and Figure 124.The times of ZST and ZDT obtained from these curves are presented in Table 24.

Table 24: Thermal analysis data used for determining critical residence time interval.

Alloy / Mold temperature [°C]	**$t_{0.75}$ [s]**	**$t_{0.99}$ [s]**	**Δt [s]**	**Thermal strain rate [%/s]**
AZ91 / 210	9.4	16.2	6.8	0.6
AZ91 / 250	12.5	20.2	7.6	0.5
AE42 / 340	13.2	17.3	4.1	1.1
AE42 / 390	17.7	23.0	5.2	0.8

The data suggest that the time interval between ZST and ZDT, i.e., the residence time ($t_{ZST\text{-}ZDT}$), increased with increasing mold temperature. Thus, the period near the end of solidification when feeding was critical was extended.

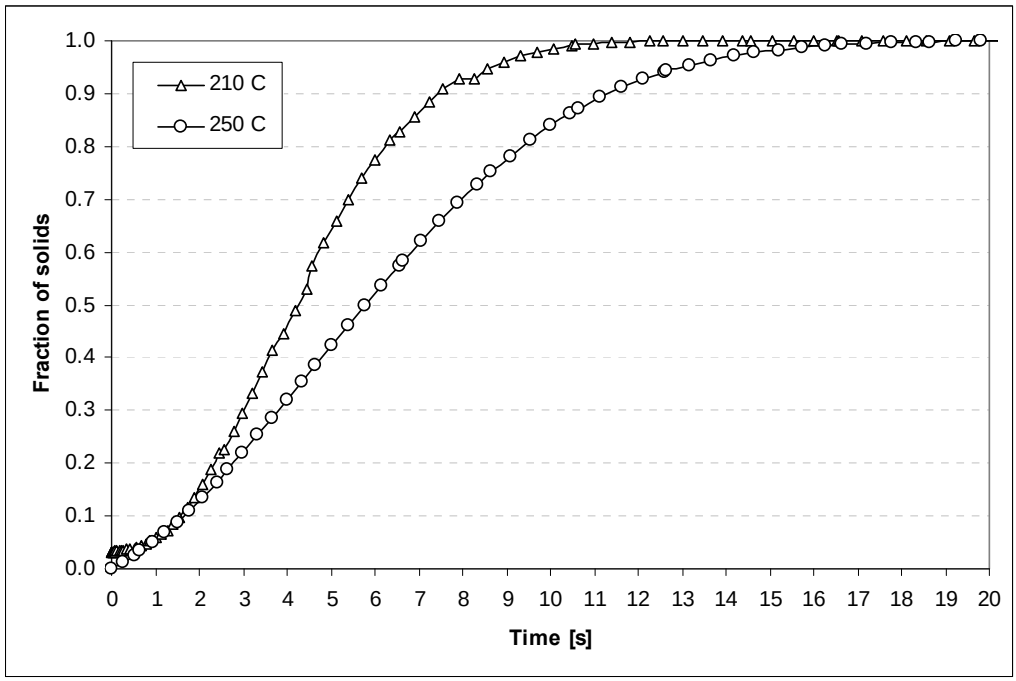

Figure 123: Fraction of solids development in the critical region of AZ91D casting.

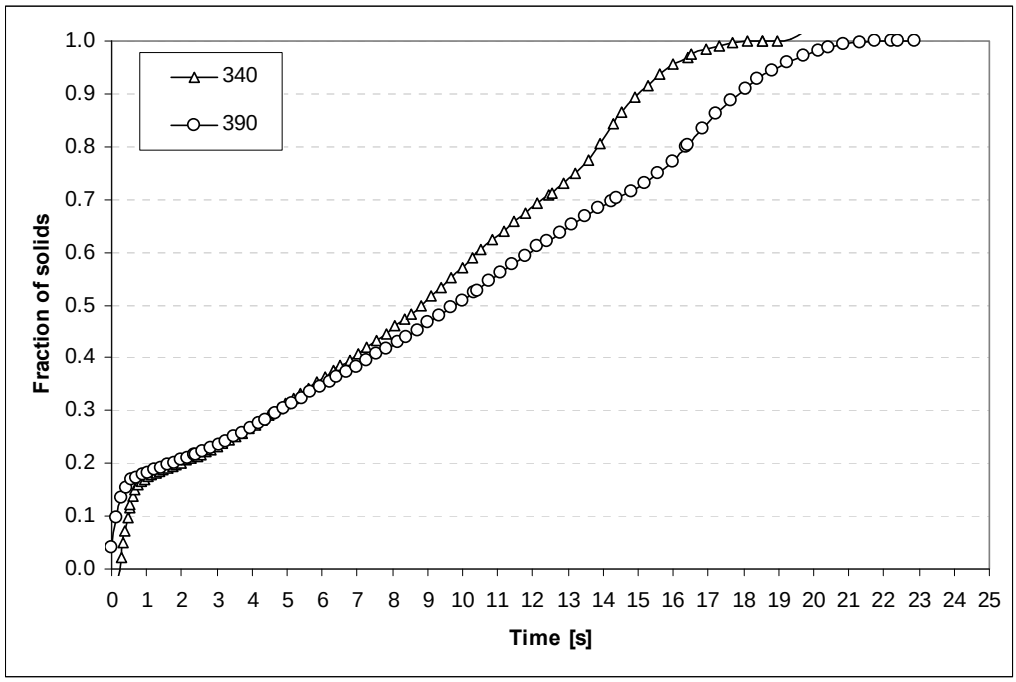

Figure 124: Fraction of solids development in the critical region of AE42 casting.

Analysis of the f_s curves for the AZ91D alloy (Figure 123) suggests that the residence time between ZST and ZDT was 6.8 seconds for a casting with a hot tear and 7.6 seconds for a casting without a hot tear. Within this time interval, both castings had to accommodate approximately 2% volumetric contraction associated with this temperature interval (total alloy shrinkage due to phase change was ~ 8%). The casting without a hot tear had nearly 12% longer time to accommodate this contraction, suggesting that thermal stresses and strains evolved slower.

In case of steel castings, the residence time was successfully related to the critical fracture stress of the material at the solidus temperature [76,79]. This critical stress was seen to be a function of the square-root of the residence time. Thus, it may be approximated that a casting without a hot tear was able to accommodate additional 28% increase in stress prior to yielding and developing a hot tear. Thus, in summary, a casting made at 250 °C mold temperature did not exhibit hot tearing due to its lower thermal stress and stress evolution rate [80].

In the case of the AE42 alloy, increasing the mold temperature also increased the vulnerable time interval. The time when the alloy remained amenable to deformation increased by ~27%.

Considering that each alloy had to accommodate ~ 2% of the total solidification shrinkage between the ZST and ZDT interval, the thermal strain rate during the vulnerable time period was estimated

(i.e., amount of solidification shrinkage divided by time interval to accommodate the shrinkage) and is also presented in Table 24. It was observed that the strain rate was significantly lower in the AZ91D alloy castings than in the AE42 castings. Increasing the mold temperature decreased the thermal strain by 17% and 27% for the AZ91D and AE42 alloys, respectively. With a lower solidification strain rate, the casting could be fed interdendritically by incoming liquid metal feed from the downsprue to avoid nucleation of hot tears. The lower solidification shrinkage strain rate during the vulnerable period was possibly an additional factor contributing to the lower hot tearing susceptibility of the AZ91D in comparison to the AE42 alloy.

Section Summary

The results of thermal analysis indicate that the AZ91D and AE42 alloys exhibit distinct behavior with respect to fraction of solids development. The AZ91D alloy remained liquid for a relatively long period of time, thus bulk feeding of the casting could take place. In contrast, the AE42 alloy became coherent quickly after filling of the critical region and subsequent feeding had to be accomplished interdendritically.

The AZ91D alloy had a significantly longer temperature interval between the coherency and rigidity points than the AE42 alloy. Thus, interdendritic feeding could proceed and solidification shrinkage could be compensated by incoming liquid feed from the downsprue. In the case of the AE42 alloy, rapid grain growth and branching of dendrites made interdendritic feeding of the casting difficult, thereby making it susceptible to hot tearing.

Both alloys had a comparable temperature interval after dendrite rigidity was attained and before complete solidification. However, due to grain boundary strengthening, the AZ91D alloy was able to sustain greater load than the AE42 alloy prior to fracture. As a result, the onset of hot tearing in the AZ91D alloy occurred at much lower mold temperatures (and higher cooling rates) than in the AE42 alloy.

Analysis of the vulnerable time intervals for the two alloys revealed, that castings made at higher mold temperatures were able to accommodate greater load due to slower thermal strain development. With slower strain evolution, interdendritic liquid feeding was able to compensate volumetric casting shrinkage, thereby alleviating solidification stresses developing in the castings.

5.4 Neutron Diffraction

Neutron diffraction was used to carry out elastic residual strain mapping in castings with distinct levels of hot tearing. During the initial stage of neutron diffraction studies, experiments were performed to determine if residual strains were retained in castings after ejection from the permanent mold. This analysis was performed for AZ91D samples made at four mold temperatures. The neutron diffraction results of these initial experiments are presented in Section 5.4.1.

With successful completion of the initial trials, strain mapping was carried out in the two AZ91D and two AE42 castings of interest. In the case of AZ91D alloy castings, strain was measured in three orthogonal directions, thus enabling subsequent use of Hooke's law to calculate the (residual) principal stresses in the castings. In the case of the AE42 castings, only a limited number of scans was performed, due to restrictions on the neutron beam time. In addition, the AE42 alloy exhibited very large grain size at the onset of hot tearing, which further complicated counting of diffracted neutrons. Also, the large grain size likely deteriorated the as-cast mechanical properties, thereby making the alloy industrially less attractive. As a result, detailed ND analysis of the AE42 alloy castings was not undertaken and attention was focused on the AZ91D castings. The results of all strain measurements are presented in Section 5.4.2 - Section 5.4.4.

Texture analysis was also performed on the AZ91D castings in order to determine whether the material retained crystallographic isotropy during high temperature deformation at the onset of hot tearing. The results are discussed in Section 5.4.5.

Upon verifying material isotropy, Hooke's law was used to calculate the residual stresses in the AZ91D castings. The stress distributions for the top edge and the downsprue scans are presented in Section 5.4.6.[†]

The strain measurements presented in this section were performed at room temperature. The effect of linear thermal expansion between the solidus temperature (when hot tears nucleated) and the room temperature is discussed in Section 5.5.

[†] *Much of this work presented in this section has been published in*: Bichler, L., Ravindran, C. and Sediako, D., "Onset of Hot Tearing in AE42 Magnesium Alloy", Canadian Metallurgical Quarterly (Accepted: November, 2008); Bichler, L., Ravindran, C. and Sediako, D., "Stress and Strain Evolution at the Onset of Hot Tearing in AZ91D Magnesium Alloy", Metallurgical and Materials Transactions A (Submitted: January 2009); Bichler, L., Ravindran, C. and Sediako, D., "Neutron Diffraction Measurement of Strain Required for the Onset of Hot Tearing in AZ91D Magnesium Alloy", Trans. Indian Institute of Metals, Vol. 61, No. 3, 2008, pp. 1 – 8.

5.4.1 Retention of Residual Strains

Four samples presented in Figure 45 were used to perform initial study on the retention of residual strains in the castings upon ejection from the permanent mold. The residual strain in these samples was expected to be lower than that in un-cut (complete) castings, since sectioning of the samples likely relieved some of the residual strains. However, if definite trends of residual strain dependency on the mold temperature could be observed in these four samples, then un-cut castings would likely exhibit fully retained elastic residual strains and enable meaningful residual strain analysis at the onset of hot tearing.

The four initial AZ91D castings were produced in a separate set of experiments than castings used in the later phase of the research. The four castings were made at 700 °C pouring temperature and mold temperatures of 220, 320, 340 and 380 °C. For all samples, ε_x was measured along the specimen centerline. For selected specimens, ε_x was also measured along the top and bottom edges. The ε_x profiles for the four samples are presented in Appendix A5.1 (Figure A5. 1 - Figure A5. 4) for crystallographic reflections $(10\bar{1}0)$, (0001), $(10\bar{1}1)$ and $(10\bar{1}2)$.

Due to the preliminary nature of these experiments, strain development in these samples is briefly discussed in the following text. A detailed discussion on the evolution of elastic residual strains and stresses in complete castings, which was the focus of this research, is presented in Section 5.4.2 – 5.4.4.

Observing the severity of hot tears in the samples (Figure 45) it appears that the onset of hot tearing occurred between 320 °C and 340 °C mold temperatures for these 700 °C pouring temperature castings. It was noted, that contrary to expectations, the length of the hot tears marginally increased with mold temperature increase from 320 °C to 340 °C. As all four specimens were used only to verify strain retention in casting after ejection from the mold, no extensive repeat trials were performed to clarify the hot tear length anomaly.

Observing Figure A5. 1 - Figure A5. 4, unique trends of residual strain development were observed for each of the crystallographic reflections investigated:

Prismatic $(10\bar{1}0)$ reflection:

The results in Appendix 5.1 indicate that tensile strain developed for the $(10\bar{1}0)$ planes for all castings with hot tears. Only in the case of the 380 °C mold temperature sample, $(10\bar{1}0)$ tension decreased and mixed tensile and compressive residual strains were observed. For this reflection, there was no distinct

feature (in strain magnitude) at the location of the hot tear. As a result, it does not appear that deformation of $(10\bar{1}0)$ planes was directly involved during the onset of hot tearing in these specimens.

Basal (0001) reflection:

A severe hot tear formed in the 220 °C mold temperature sample (Figure 45a). The basal reflection linescan in Figure 125a suggests that a relatively high tensile residual strain (~0.3%) developed along the centerline of the critical region. Macroscopic examination of the casting specimen revealed that the center portion of the horizontal bar remained connected to the downsprue via a solid bridge, while the top and bottom edges fractured near the 90° corners. Thus, the residual strain along the top and bottom edges was relieved, whereas the solid bridge retained tension, as supported by the ND measurements.

Increasing the mold temperature towards the onset of hot tearing (320 °C and 340 °C) resulted in a decrease of the severity of hot tears on the top and bottom edges of the horizontal bar (i.e., the size of the solid bridge between the horizontal bar and the downsprue increased). As a result, the measured strain profiles began to exhibit more complex patterns along the centerline, since strain could be transmitted through the solid bridge. The ε_x profiles for these two castings also demonstrate that even hairline hot tears on the top and bottom edges of the horizontal bar affected the relaxation of elastic residual strains in the critical region. As the mold temperature increased to 380 °C, compressive residual strains began to evolve in the horizontal bar ($x > 0$ mm) as observed in Figure 125b, thus preventing nucleation or propagation of hot tears. A more detailed discussion of the relationship between hot tearing and strain (compressive or tensile) is presented in Section 5.4.2.1 – 5.4.2.4.

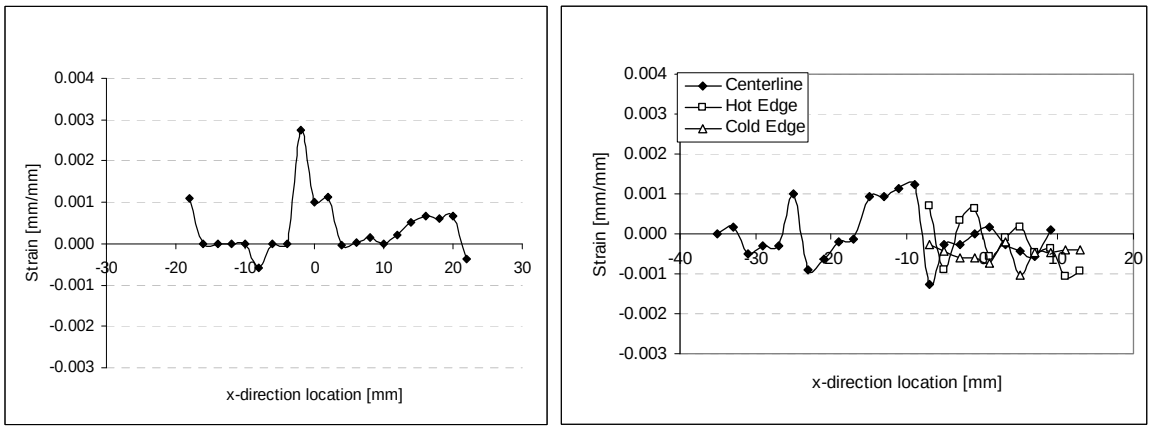

(a) 220 °C mold temperature. *(b) 380 °C mold temperature.*

Figure 125: Residual strain for AZ91D castings (preliminary trials) for (0001) reflection.

Pyramidal ($10\bar{1}1$) reflection:

The pyramidal ($10\bar{1}1$) planes, like the basal planes, suggest that hot tearing was related to the evolution of tensile strain. For a casting at 220 °C mold temperature, tension was recorded in the critical region. As the mold temperature approached the onset of hot tearing between 320 °C and 340 °C, mixed strains were established. Increasing the mold temperature to 380 °C resulted in the development of compressive strain along the centerline, top and bottom edges.

Pyramidal ($10\bar{1}2$) reflection:

The trends observed for the secondary pyramidal ($10\bar{1}2$) reflection, were similar to those of the primary pyramidal plane ($10\bar{1}1$) discussed above. Increasing the mold temperature from 220 °C resulted in the reduction of tensile strain in the critical region, reaching a compressive state at 380 °C mold temperature.

In addition, a unique relationship between the pyramidal ($10\bar{1}2$) and the prismatic ($10\bar{1}0$) planes was observed. Development of tension for the ($10\bar{1}0$) prismatic planes resulted in compression for the ($10\bar{1}2$) secondary pyramidal plane. Such deformation is consistent with the assumption of elastic deformation of the hexagonal close packed (HCP) Mg crystal. Specifically, tension along the a_1, a_2 or a_3-axes promotes c-axis contraction. However, for a perfectly elastic response, tension for ($10\bar{1}0$) should result in ($10\bar{1}1$) and (0001) compression, which was not always followed. Therefore, the crystal deformation was not perfectly elastic and some energy was dissipated in plastic deformation of the ($10\bar{1}1$) and (0001) planes.

Section Summary

The four AZ91D samples unequivocally demonstrated that residual strain was retained in castings after ejection from the mold. Further, ND measurements revealed unique ε_x values along the specimen centerline. Thus, these preliminary experiments demonstrated that neutron diffraction was capable of quantifying casting deformation at the onset of hot tearing and providing previously unavailable data.

Specifically, castings with hot tears contained tensile strain in the vicinity of the 90° corner. As the mold temperature increased and the severity of hot tears decreased, the tensile strain became compressive. This trend indicates that tensile strain was required to nucleate, open and propagate hot tears.
It was further noted that formation of hairline hot tears (e.g., on the top and bottom edges of the horizontal bar) locally relieved elastic residual strain in the material. Also, the material between the hot tears, i.e., a

solid bridge, retained residual strains and enabled transmittal of strains between the horizontal bar and the downsprue. As a result, the centerline regions developed complex strain profiles.

These trends are investigated and discussed in greater detail in the following sections, where the strain mapping results for complete castings are presented.

5.4.2 Residual Strain in x-Direction

Residual strain in the *x*-direction was seen to play a significant role on the evolution of hot tears in the critical regions of both alloy castings. Evolution of ε_x was the result of the axial contraction of the horizontal bar between the anchor and the downsprue.

This strain was measured for all castings along several linescans, as illustrated in Figure 41. A discussion of ε_x trends for individual casting conditions is presented in the following text.

5.4.2.1 AZ91D Casting at 210 °C Mold Temperature

The residual strain profiles for the AZ91D casting made at 210 °C mold temperature are presented in Appendix A5.2 (Figure A5. 5 - linescans in the horizontal bar, and Figure A5. 6 - downsprue cross-scan). Average strain for the entire length of the linescan and associated strain variance data are presented in Figure 126.

The ND measurements indicate that significant tensile residual strain developed for the $(10\bar{1}0)$ and (0001) reflections. In the case of the $(10\bar{1}1)$ and $(10\bar{1}2)$ reflections, mixed strain values were observed. In particular, these later two reflections show a significant strain discontinuity in the critical region ($-10 < x < 10$ mm), as illustrated in Figure 127.

For all three horizontal linescans (i.e., top edge, centerline and bottom edge), tensile strain was observed in the downsprue ($x < 0$ mm) for $(10\bar{1}1)$ and $(10\bar{1}2)$ reflections. Subsequently, the tensile ε_x decreased near the 90° corner. The relaxation of ε_x at this location was likely the result of plastic damage, associated with porosity formation or hot tearing. As observed in Figure 72, abundant shrinkage porosity nucleated in this region and enabled dissipation of elastic strain.

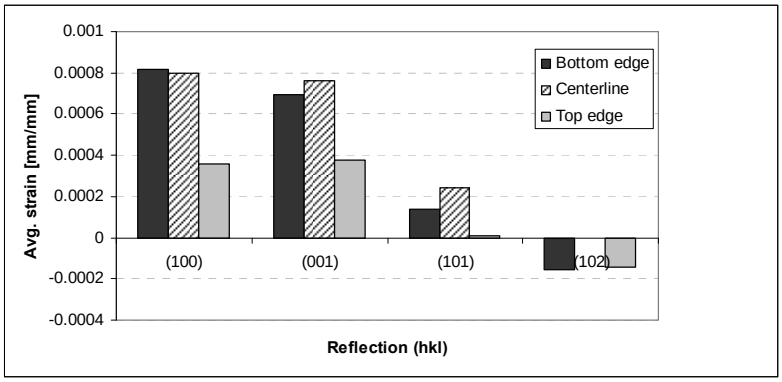

(a) Average strain.

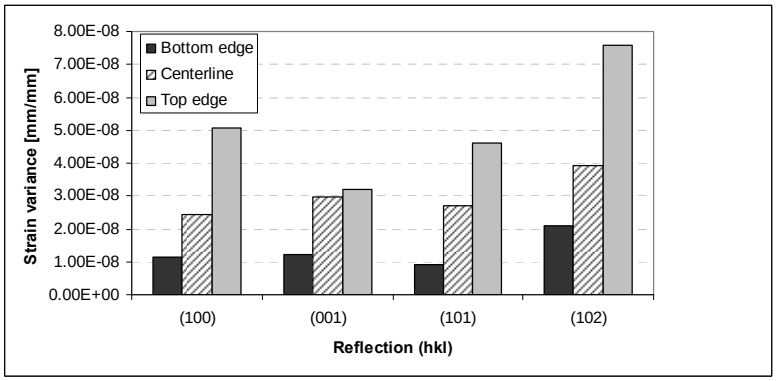

(b) Strain variance.

Figure 126: Average strain and strain variance for AZ91D casting at 210 °C mold temperature.

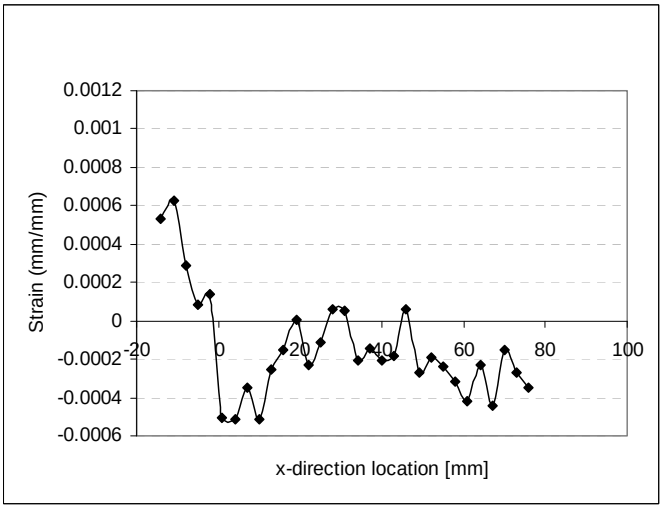

Figure 127: ε_x profile for top edge linescan for AZ91D casting at 210 °C mold temperature. Reflection: $(10\bar{1}2)$.

The average strain values for the three linescans in Figure 126 provide information about the general deformation of the horizontal bar. The figure indicates that the bottom edge of the horizontal bar was in relative tension with respect to the top edge of the horizontal bar. This result was related to the expected filling sequence of the horizontal bar: the bar filled from the bottom edge upwards, with the top edge being the last area to fill, as indicated by MAGMASOFT® (Appendix A1.3.2).

Upon filling of the horizontal bar, the alloy in contact with the relatively cool mold at the bottom edge started to solidify and formed a thin skin. As the bottom edge skin cooled, it began to contract. As it contracted, it compressed adjacent centerline regions of the casting. In order to maintain force equilibrium, the centerline regions resisted the compression of the bottom edge and thereby induced tensile strain in the bottom edge. This process repeated again for the solidifying centerline region and the top edge. As a result, the bottom edge developed relatively highest tensile strain. In contrast, the top edge of the horizontal bar was the last area to solidify and was allowed to deform the longest, thus locally relieving some of the developing strains.

The strain variance data (Figure 126b) suggest that the top edge of the horizontal bar solidified with high strain variation (i.e., strain gradients), in comparison to the centerline or bottom edge. This result is also in agreement with the mold filling characteristics predicted by MAGMASOFT®. A turbulent wave-like metal flow was predicted to form at the top edge, while a relatively uniform flow was predicted for the bottom edge of the horizontal bar. The inhomogeneous mold filling, cooling and subsequent evolution of thermal strain gradients during solidification likely promoted formation of weak spots along the horizontal bar's top edge.

As hoop solidification initiated and progressed from the mold walls inward (i.e., toward the horizontal bar's center) the center regions became depleted in liquid. This resulted in the evolution of centerline shrinkage porosity as discussed in Section 5.2.5. Shrinkage porosity contributed to the development of elevated tensile strain along the centerline in comparison to the surrounding top and bottom edges. As Figure 126a shows, for the (0001), $(10\bar{1}1)$ and $(10\bar{1}2)$ reflections the average tensile residual strain in the centerline region exceeded that of the skin regions. The presence of a relatively high tensile strain along the centerline lowered the amount of additional strain necessary to attain a critical fracture strain required for hot tear nucleation or propagation. Thus, the centerline regions were relatively highly susceptible to material failure.

Observing the ε_x profiles for the bottom edge in Figure 128, it was noted that only a minor discontinuity in strain values (i.e., strain gradients) was observed near the bottom edge 90° corner.

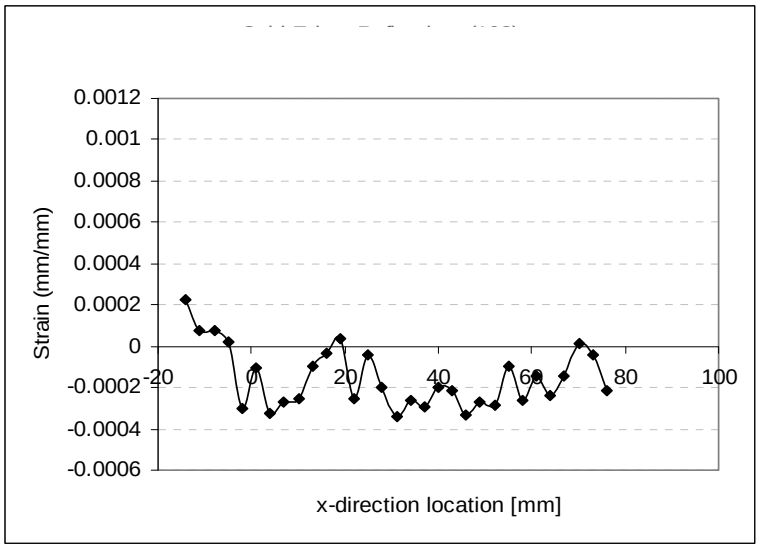

Figure 128: ε_x profile for bottom edge linescan for AZ91D casting at 210 °C mold temperature. Reflection $(10\bar{1}2)$.

In contrast, the top edge (Figure 127) showed a significant relief of strain at the 90° corner ($x \sim 0$ mm). The good strain homogeneity along the bottom edge suggests that the unrestrained contraction of the bottom trap of the downsprue possibly reduced the effect of the strain concentration at the bottom 90° corner. In contrast, the strains near the top edge 90° corner were intensified by the axial contraction of the downsprue. The mechanism associated with the strain intensification near the top edge 90° corner was likely as follows:

It was observed that a strain discontinuity (at $x \sim 0$ mm) along the top edge consisted of a region with low (or compressive) strain surrounded by relatively tensile strain (e.g., Figure 127). Under ideal (i.e., unrestrained) conditions, the horizontal bar would contract in the positive x-direction (towards the anchor) and the downsprue in the positive y-direction. These ideal contractions would act at 90° relative to each other. However, the downsprue and the horizontal bar were connected in the critical region and mutually influenced each others contraction. The significant x-direction contraction at the 90° corner offset the downsprue's contraction vector from being perfectly vertical, as schematically illustrated in Figure 129. Consequently, the downsprue's strain vector had a $-x$ direction component. As a result, the ε_x strains on either side of the 90° corner became tensile, but acted in opposite directions. Thus, tensile ε_x

strains on either side of the 90° corner pulled the material in the critical region apart, promoting opening of shrinkage pores and enabling the nucleation and propagation of hot tears.

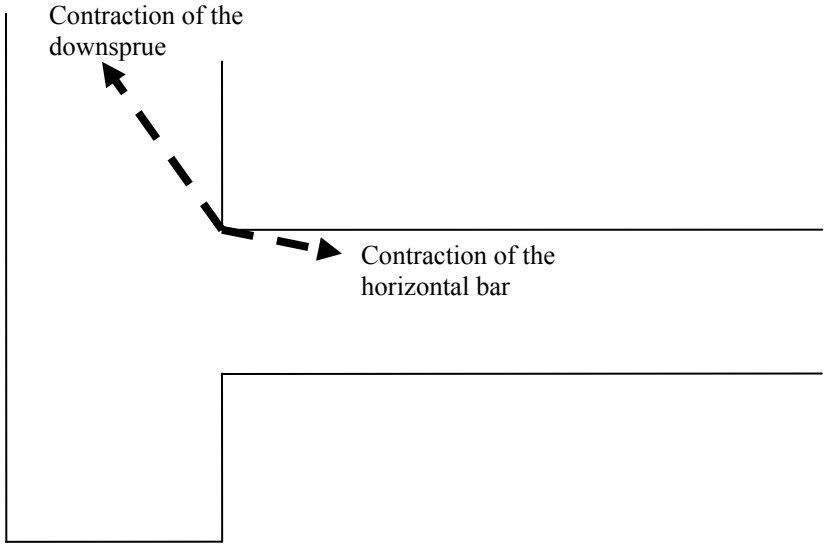

Figure 129: Schematic of thermal strains.

The strain intensification at the top edge 90° corner was examined in detail using data from the downsprue cross-scan. The ε_x profile in Figure A5. 6 confirmed that significant tension evolved in the sprue. The increased tension in the downsprue between $-20 < y < 0$ mm indicates that the axial contraction of the horizontal bar influenced material deformation well into the downsprue and *vice versa*. However, it was observed that the effect of *x*-direction contraction of the horizontal bar was not symmetrical across the $-20 < y < 0$ mm region. As can be observed in Figure 130, the tensile peak of the strain profile shifted towards the top edge corner. This shift was accentuated by the free contraction of the bottom trap of the downsprue (resulting in relaxation of strain near the bottom edge 90° corner). Thus, it follows that the top edge 90° corner was more likely to induce hot tears than the bottom edge 90° corner. This prediction is supported by visual observations of the hot tear lengths at these two corners.

Analysis of the average strain values for individual crystallographic reflections revealed additional information about the deformation of the HCP crystal. It can be shown, that a tension for (0001) planes (*c*-axis extension) should result in $(10\bar{1}0)$ compression and $(10\bar{1}1)$ and $(10\bar{1}2)$ tension. Observing the results in Figure 126, tension for the (0001) basal planes did not result in compression of $(10\bar{1}0)$ or $(10\bar{1}1)$ planes, suggesting that plastic crystal deformation possibly occurred. As porosity formation and

hot tearing are associated with plastic material deformation, it is thus possible that formation of these defects may have dissipated some of the strain energy of the HCP crystals.

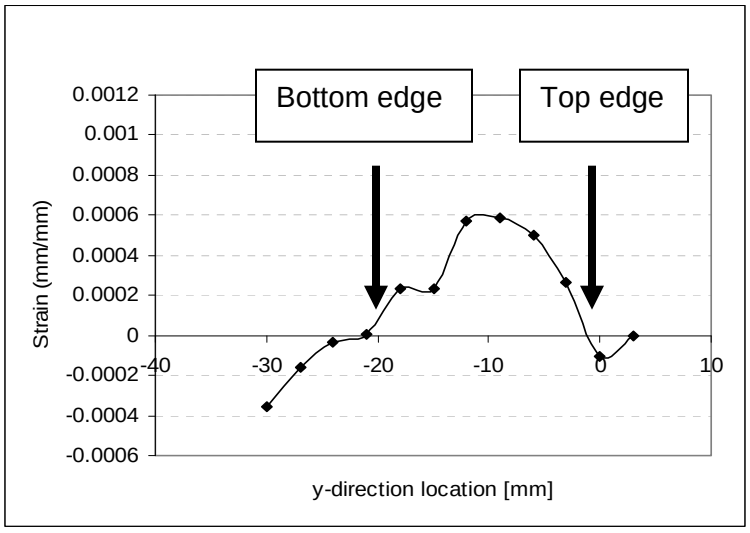

Figure 130: ε_x profile for $(10\bar{1}1)$ sprue cross-scan in AZ91D casting at 210 °C mold temperature.

Further, the data in Figure 126a also suggest that the prismatic $(10\bar{1}0)$ and basal (0001) planes were able to sustain higher tensile strains than the pyramidal planes. Two phenomena were considered in order to explain this behavior: 1) formation of β-$Mg_{17}Al_{12}$ incoherent precipitates on the basal planes, and 2) variation of stiffness of different crystallographic slip systems:

1. The β-$Mg_{17}Al_{12}$ incoherent precipitates forming on the (0001) planes assist in pinning grain boundaries [61, 68]. Therefore, this phase would be effective in hindering dislocation motion along the basal planes and enhancing their relative strength.
2. Gharghouri *et al.* [81] carried out *in-situ* determination of the elastic constants using neutron diffraction for Mg-7.7wt%Al alloy (the AZ91D alloy used in the current research was Mg-8.6wt%Al). The reported Young's modulus values for the $(10\bar{1}0)$, (0001) and $(10\bar{1}1)$ reflections were 38 GPa, 44 GPa and 60 GPa, respectively. The planes $(10\bar{1}0)$ and (0001) are evidently less stiff than $(10\bar{1}1)$. Thus, in order to explain the high strength of the $(10\bar{1}0)$ and (0001) planes, it appears that the presence of the β-$Mg_{17}Al_{12}$ precipitates significantly contributed to resisting dislocation motion along these planes.

5.4.2.2 AZ91D Casting at 250 °C Mold Temperature

The ε_x residual strain profiles for AZ91D casting made at 250 °C mold temperature are presented in Appendix A5.2 (Figure A5. 7 - Figure A5. 8). It may be observed that several data points are missing along the linescans. This was the result of experimental difficulties in obtaining sufficient count of diffracted neutrons in order to enable Gaussian fitting and statistically significant peak analysis. The plots of average strain and strain variance are provided in Figure 131.

Analysis of the results revealed that increasing the mold temperature from 210 °C to 250 °C resulted in only a marginal decrease of the average ε_x residual strain, but in a significant decrease of the strain variance (especially along the top edge). This observation indicates that both castings (210 °C and 250 °C) had to contract by approximately the same amount during cooling to room temperature; thus, their bulk (total) average strain was similar. However, increasing the mold temperature homogenized the temperature and strain distribution (i.e., strain gradients), resulting in the reduction of ε_x strain gradients along the horizontal bar.

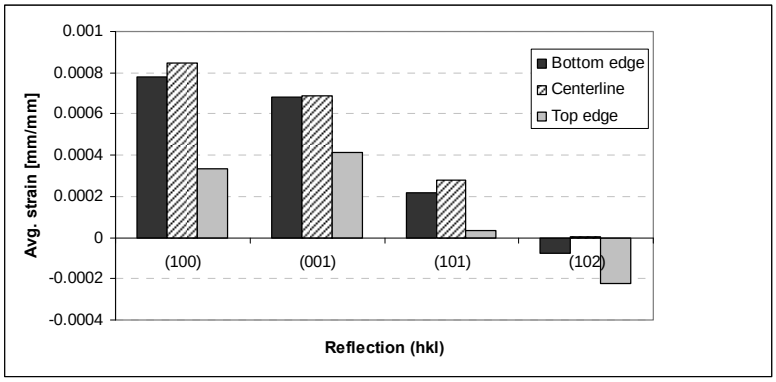

(a) Average strain.

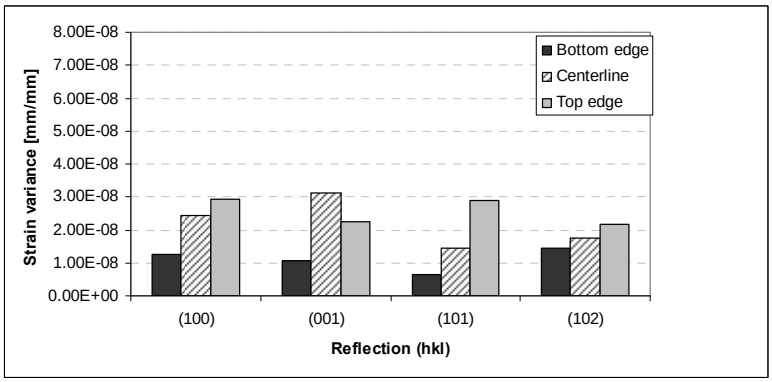

(b) Strain variance.

Figure 131: Average strain and strain variance for AZ91D casting at 250 °C mold temperature.

The decrease of strain gradients was particularly evident for the $(10\bar{1}1)$ and $(10\bar{1}2)$ reflections, as illustrated in Figure 132.

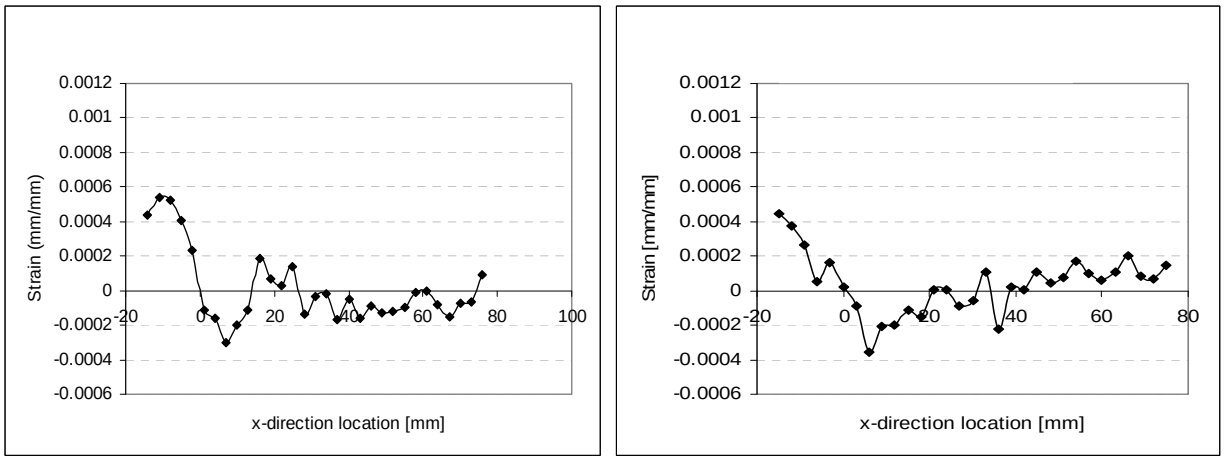

(a) 210 °C mold temperature. *(b) 250 °C mold temperature.*

Figure 132: ε_x profile for $(10\bar{1}1)$ top edge linescan in AZ91D castings.

In the case of a casting with a hot tear, the ε_x strain in the sprue region was 0.000514 mm/mm (tensile). Residual strains were relieved in the area of the hot tear, as indicated by a drop in the strain profile in Figure 132a. The ε_x in the horizontal bar to right of the 90° junction was tensile 0.000182 mm/mm (locations: 15 – 20mm). In the case of a casting without a hot tear, the ε_x strain in the downsprue was also tensile 0.000441 mm/mm. However, contrary to the cracked casting, the region to the right of the 90° junction possessed compressive ε_x strain of 0.000113 mm/mm. The strains in the 250 °C mold temperature casting became tensile only far away from the 90° junction.

This difference in the ε_x strain profile at the top edge 90° corner was related to the feeding of the casting. At high mold temperatures, interdendritic liquid feeding was possible for a longer period of time. Thus, the axial contraction of the horizontal bar was compensated by incoming liquid metal feed from the downsprue and the developing strains were continuously alleviated. However, for the low mold temperature casting, the horizontal bar solidified and contracted without adequate compensation by liquid metal and tensile strains developed. Increasing the mold temperature decreased the strain gradients and made the casting deformation more homogeneous. As can be observed from Table 25, by increasing the mold temperature, the strain variance (averaged for all reflections) decreased by 23, 50 and 105 % for the bottom edge, centerline and top edge linescans, respectively. With an increase in the mold temperature, axial feeding of the horizontal bar improved (large β-phase interdendritic regions) and formation of hot spots decreased (Appendix A1.3.5). These factors, along with directional solidification, likely decreased

formation of local stress concentrations along the horizontal bar and decreased the susceptibility of the casting to initiate hot tears.

Table 25: Percent decrease in strain variance with mold temperature increase from 210 °C to 250 °C.

Reflection	Bottom edge	Centerline	Top edge
$(10\bar{1}0)$	-7.0	0.9	74.3
(0001)	17.4	-5.6	42.5
$(10\bar{1}1)$	40.1	86.8	58.9
$(10\bar{1}2)$	44.6	121.7	246.1
Average [%]	**23**	**50**	**105**

Similarly, as observed for the 210 °C mold temperature casting, the ε_x strain for different crystallographic reflections exhibited non-elastic behavior. Tension for the $(10\bar{1}0)$ planes did not result in *c*-axis contraction, which would be manifested by (0001), $(10\bar{1}1)$ and $(10\bar{1}2)$ compression.

Further, it was observed that the $(10\bar{1}0)$ and (0001) reflections did not exhibit a significant decrease in residual strain with the onset of hot tearing. This could be again related to the formation of β-$Mg_{17}Al_{12}$ precipitates on the basal planes, as discussed in Section 5.4.2.1. These precipitates may have effectively prevented dislocation motion and strengthened the basal planes, thus making them less responsive to deformation. The $(10\bar{1}1)$ and $(10\bar{1}2)$ planes appeared to be more sensitive to deformation. Considering that there are twelve of the $(10\bar{1}1)$ and twelve of the $(10\bar{1}2)$ planes in a single HCP crystal, while there are only six $(10\bar{1}0)$ and two (0001) planes, it is likely that slip along the $(10\bar{1}1)$ and $(10\bar{1}2)$ planes readily occurred. Slip along these planes was further made possible by the high temperature of the material, which possibly allowed the HCP crystal to reorient such that the $(10\bar{1}1)$ and $(10\bar{1}2)$ planes were aligned favorably for slip [82].

Observing the results of ε_x measurement along the downsprue cross-scan (Figure A5. 8), the peak of the strain profile shifted towards the top edge, indicating that axial contraction of the downsprue contributed to strain intensification at the top edge 90° corner. Similar mechanism for ε_x intensification near the top edge corner (discussed in Section 5.4.2.1) likely applied.

The neutron diffraction cross-scan results were also qualitatively compared to the simulation results for deformation obtained from MAGMASOFT® (Appendix A1.3.8). MAGMASOFT® suggested that in the case of a 210 °C mold temperature casting, high strain developed at the 90° corners of the horizontal bar and a lower strain in the bar's midsection. For a casting at 250 °C mold temperature, MAGMASOFT® predicted a more complex deformation pattern in the critical region. ND measurements, however, did not validate these predictions. In general, as the mold temperature increased the magnitude of ε_x strain decreased. Further, the general ND profile was similar for the two mold temperatures (high tension in the downsprue, followed by a relaxation near the 90° corner). Thus, the experimental strain measurements did not support the predictions made by MAGMASOFT®.

5.4.2.3 AE42 Casting at 340 °C Mold Temperature

The results of residual ε_x strain measurement along the three linescans in the horizontal bar of the AE42 casting made at 340 °C mold temperature are presented in Appendix A5.2 (Figure A5. 9). The results of the downsprue cross scan are presented in Figure A5. 10 and average strain values (averaged over the entire linescan length) are provided in Figure 133.

Unlike in the case of the AZ91D castings, evolution of significant tensile or compressive strains along the horizontal bar (i.e., in the x-direction) was not observed, as Figure 134a illustrates. In particular, the strain in the critical region did not show elevated tension or relaxation at the 90° corners, as was observed in the AZ91D castings (e.g., Figure 132). The lack of axial strain trend could be explained with the assistance of the results of MAGMASOFT® simulations. It was predicted that the AE42 alloy castings solidified rapidly in the hoop direction along the entire length. Thus, x-direction solidification rate (velocity) along the bar was not dominant. The limited effect of axial ε_x strains were further confirmed by analyzing the sprue cross-scan results in Figure 134b. There was only minimal increase of ε_x in the critical region between $-20 < y < 0$ mm. Thus, possibly due to the fast solidification of the AE42 alloy, complex residual strain profiles did not have sufficient time to develop.

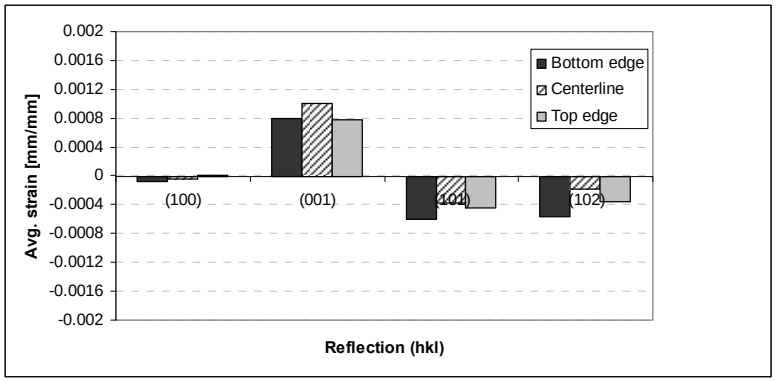

(a) Average strain.

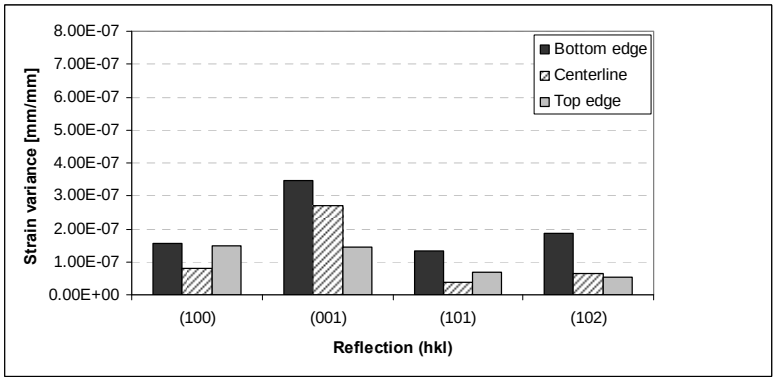

(b) Strain variance.

Figure 133: Average strain and strain variance for AE42 casting at 340 °C mold temperature.

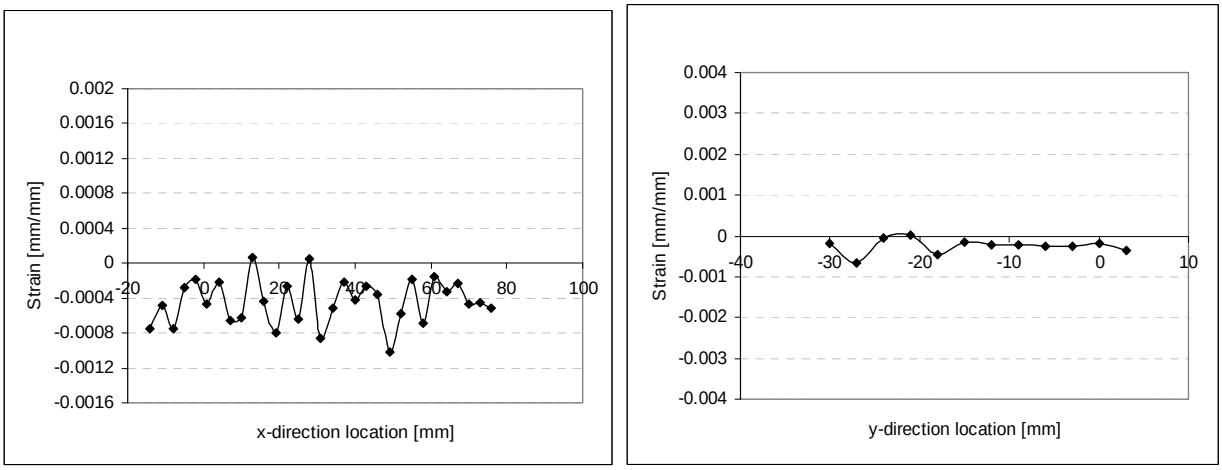

(a) Top edge scan. *(b) Sprue cross-scan.*

Figure 134: ε_x profile for $(10\bar{1}1)$ reflection for AE42 casting at 340 °C mold temperature.

The average strain values for (0001) plane in Figure 133 indicate that the bottom and top edges had lower tension than the centerline region. This could be related to the formation of hot tears at the edges.

Hot tears may have alleviated the residual strain along the horizontal bar. Evidently, even a hairline crack was sufficient to relax the ε_x strain, suggesting that the material was brittle.

Observing the average strain values in Figure 133a, reflections $(10\bar{1}0)$, $(10\bar{1}1)$ and $(10\bar{1}2)$ evolved compressive residual strain, while basal (0001) planes carried significant tensile strain. Thus, since deformation along $(10\bar{1}0)$, $(10\bar{1}1)$ and $(10\bar{1}2)$ planes was compressive, plastic deformation of the HCP crystal occurred, similarly as in the case of AZ91D castings.

The strain variance results in Figure 133b suggest that the bottom edge of the casting had elevated strain non-uniformity in comparison to the centerline or top edge. Evolution of the strain gradients along the bottom edge was possibly related to the rapid solidification of the alloy upon contact with the mold (i.e., presence of a thermal shock). Melt temperature variation during mold filling of the bottom edge in conjunction with the short freezing range of the alloy resulted in inhomogeneous fraction of solids and strain gradient evolution. Comparing the magnitude of the ε_x strain variance in Figure 133b to that of the AZ91D alloy (e.g., Figure 126b or Figure 131b), it is apparent that the AE42 alloy solidified more uniformly. That is, due to the rapid hoop solidification of the AE42 casting, axial ε_x strain profiles did not have sufficient time to develop.

5.4.2.4 AE42 Casting at 390 °C Mold Temperature

Residual strain profiles for the three linescans along the horizontal bar of the AE42 casting made at 390 °C mold temperature are presented in Appendix A5.2 in Figure A5. 11. The sprue cross-scan results are presented in Figure A5. 12 and the strain averages and variance for the linescans are presented in Figure 135.

Comparison of Figure 133a and Figure 135a reveals that increasing the mold temperature marginally decreased the ε_x tension in the horizontal bar of the 390 °C mold temperature casting. This trend was expected, as slower casting solidification enabled interdendritic liquid feeding to accommodate solidification shrinkage, resulting in a decrease of residual strain.

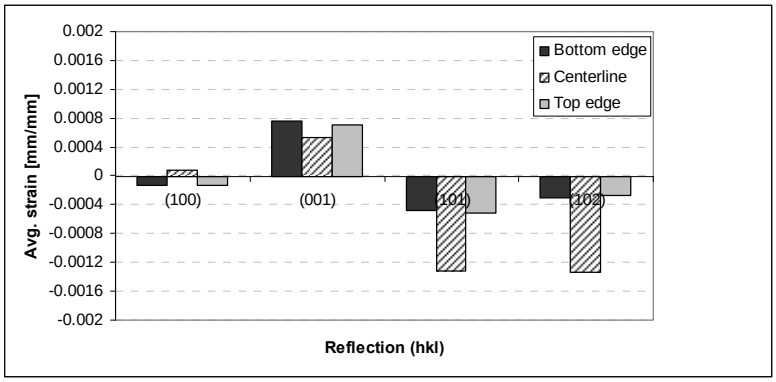

(a) Average strain.

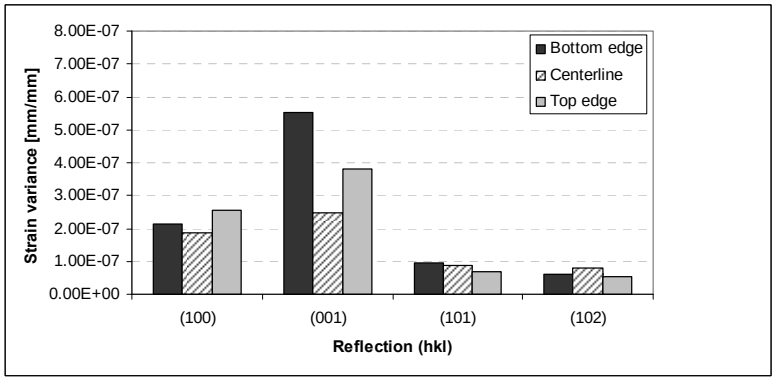

(b) Strain variance.

Figure 135: Average strain and strain variance for AE42 casting at 390 °C mold temperature.

Relating the average strain at the casting edges (top and bottom) to that of the centerline, it is evident from Figure 135a that the casting edges were in tension with respect to the centerline region. This trend differs from that observed in the 340 °C mold temperature casting. It appears that increasing the mold temperature slowed down the hoop solidification rate and extended the mushy state for the centerline region. As the edges solidified, they began to contract (in the hoop direction) and compress the material in the centerline region, which was still semi-solid. Thus, with slower cooling, a more complex solidification strain pattern was allowed to develop.

Figure 135b suggests that with slower casting solidification, the material was allowed to develop localized axial strain gradients, which resulted in increased axial strain variance in comparison to the 340 °C casting. MAGMASOFT® simulations suggested that the solidification time of the centerline regions increased by 16 seconds (Appendix A1.3.4) with an increase in mold temperature. Thus, this significant extension of the solidification time likely enabled development of complex strain patterns along the horizontal bar. Therefore, the ND measurements qualitatively support the results of MAGMASOFT® simulation.

Comparing Figure 133 to Figure 135 it appears that the (0001) tension decreased when the mold temperature increased. Specifically, considering the average strain for the entire horizontal bar's cross section (i.e., including bottom edge, centerline and top edge), increasing the mold temperature decreased the average strain from 8.56×10^{-7} mm/mm to 6.66×10^{-7} mm/mm, a 28.5% decrease. Thus, increasing the mold temperature decreased tension along the horizontal bar.

Similarly, as in the case of a casting made at 340 °C mold temperature, the cross-scan in the downsprue did not indicate a significant variation in the critical region (i.e., between $-20 < y < 0$ mm). Thus, in general, the effect of the horizontal bar's axial contraction did not extend deep into the downsprue.

5.4.3 Residual Strain in y-Direction

Residual strain measurement in the *y*-direction was carried out for the two AZ91D castings. Strain was measured along the vertical cross-scan. This scan provided information about the downsprue's axial deformation. Also, ε_y was measured along the top edge of the horizontal bar, which later enabled computation of residual stress along this linescan. The ε_y measurement was accomplished by re-orienting the casting on the diffractometer specimen table.

The results of ε_y strain measurement along the top edge are presented in Appendix A5.3 (Figure A5. 13 and Figure A5. 15 for the 210 °C and 250 °C mold temperature casings, respectively). The cross-scan results are presented in Figure A5. 14 and Figure A5. 16. A summary of average strain and strain variance (for entire linescan) along the top edge and the cross-scan are presented in Figure 136 and Figure 137, respectively.

Figure 138 shows that unlike in the case of ε_x along the top edge, the ε_y did not develop a significant discontinuity in the critical region of the horizontal bar. There appeared to be a relative tension in the downsprue ($-15 < x < 0$ mm); however, a dip in the ε_y profile in the critical region (as noted, for example in Figure 132a) was not observed and the ε_y remained negative (i.e., compressive) along the entire linescan. Compressive strain suggests that the horizontal bar was free to contract in the *y*-direction. Further, compression in the ε_y was enhanced by the axial contraction of the downsprue, which had a tendency to press the top edge of the horizontal bar against the mold.

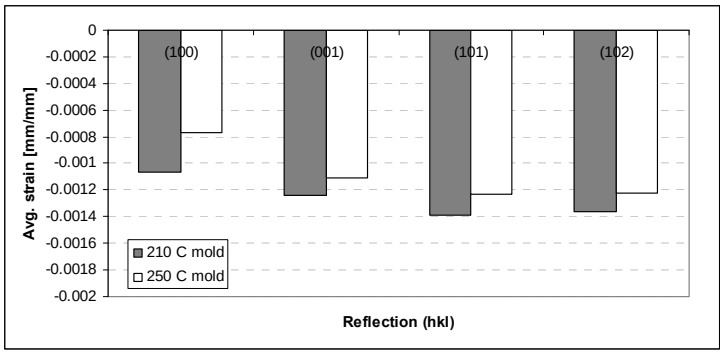

(a) Average strain.

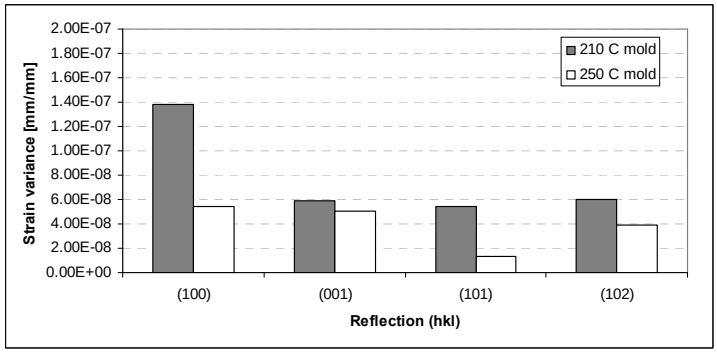

(b) Strain variance.

Figure 136: Average ε_y strain and variance for entire top edge of AZ91D castings.

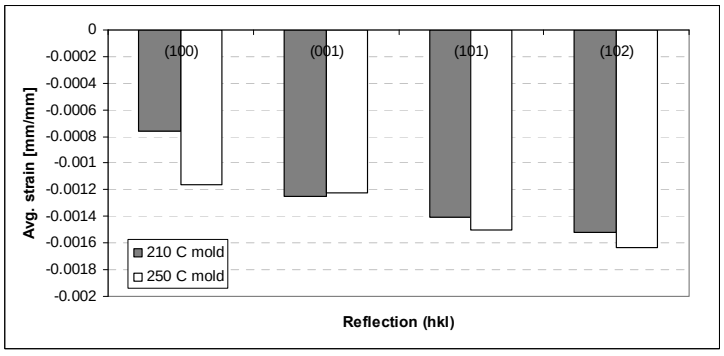

(a) Average strain.

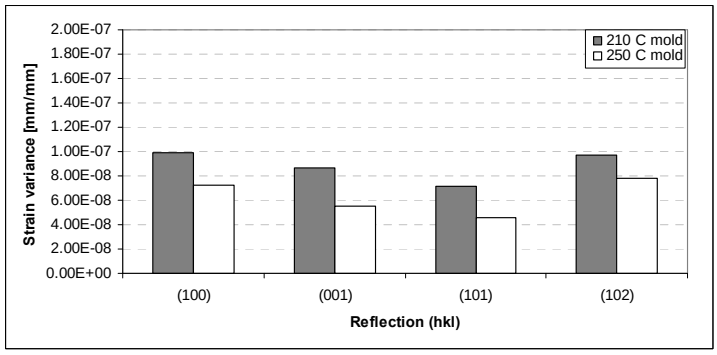

(b) Strain variance.

Figure 137: Average ε_y strain and variance for entire cross-scan of AZ91D castings.

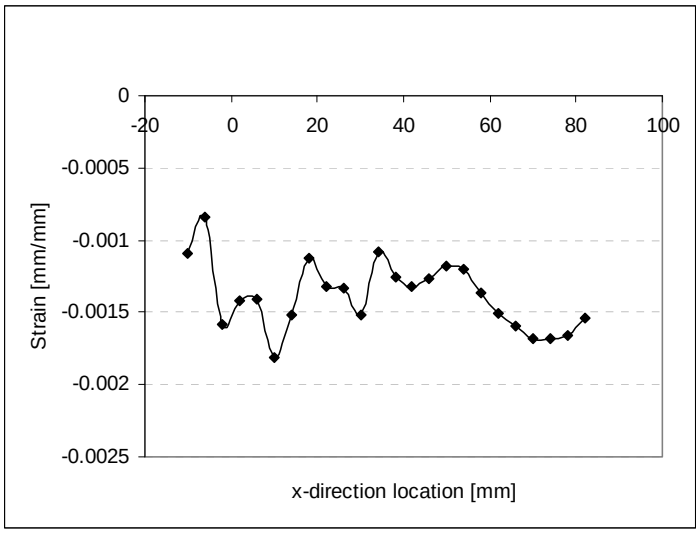

Figure 138: ε_y profile for $(10\bar{1}1)$ top edge linescan in AZ91D casting at 210 °C mold temperature.

The results of ε_y strain measurements were compared to the deformation predicted by MAGMASOFT® in Figure A1. 42 (in Appendix A1.3.8). It was observed that MAGMASOFT® predicted formation of horizontal iso-strain bands along the bar. The width of the bands remained relatively uniform along the bar (except near the 90° corners). Since the top edge linescan had a relatively small variance, it was possibly located within one of the iso-strain bands.

Relating the neutron diffraction ε_y measurements to the MAGMASOFT® displacement results for the 250 °C mold temperature simulation (Figure A1. 43b) confirms that the horizontal bar was expected to develop compressive strain along the top edge. With increasing mold temperature, the axial contraction of the downsprue decreased, along with its tendency to press the horizontal bar vertically upwards against the mold wall, and the ε_y decreased (Figure 136). Hence, the simulation results are in qualitative agreement with the results of neutron diffraction.

Analysis of the cross-scan measurements in Figure 139a revealed that the top edge 90° corner imposed a restriction on the *y*-direction contraction of the downsprue, leading to ε_y strain intensification near $y \sim 0$ mm. For sprue locations within the junction ($-20 < y < 0$ mm), relative tension developed in the material due to the downsprue's restricted displacement. The bottom trap of the downsprue ($y < -20$ mm) was able to contract without restriction, as it was free from geometrical restraints of the mold. Also, the upper portion of the downsprue ($y > 0$ mm) was also able to contract (to a limited extent), since feeding of molten metal from the pouring cup was capable of compensating the downsprue's solidification shrinkage and thermal contraction. Thus, relative *y*-direction tension developed between the

two 90° corners, as seen in Figure 139. Intensification of tensile strain near the top edge was also observed and made the top edge 90° corner more susceptible to hot tearing.

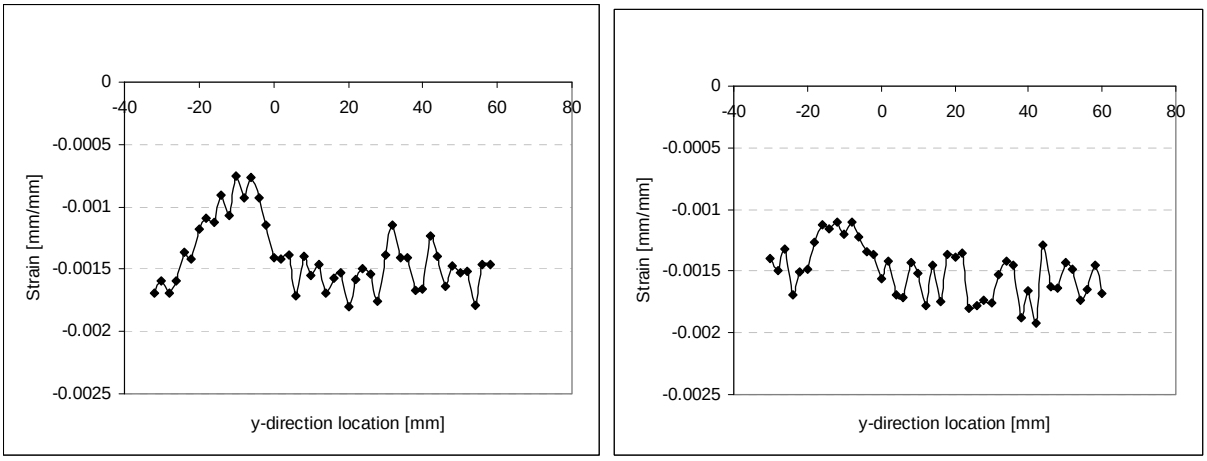

(a) 210 °C mold temperature. *(b) 250 °C mold temperature.*

Figure 139: ε_y profile for $(10\bar{1}1)$ sprue cross-scan for AZ91D casting at 210 °C mold temperature.

With increasing mold temperature, the relative tension between $-20 < y < 0$ mm decreased, as observed in Figure 139b. Also, the ε_y strain gradients along the top edge decreased, as noted in Figure 136b.

The cross-scan ε_y data in Figure A5. 14 also indicate that reflections $(10\bar{1}1)$ and $(10\bar{1}2)$ were more sensitive to material deformation, as these reflection exhibited moderate strain intensification near the top edge 90° corner. This result agrees with observations in Section 5.4.2, where ε_x for $(10\bar{1}1)$ and $(10\bar{1}2)$ reflections also exhibited greater tensile strain in the same region. Thus, it is possible that deformation due to the orthogonal contractions of the horizontal bar and the downsprue was accommodated by slip on the $(10\bar{1}1)$ and $(10\bar{1}2)$ planes relatively easily.

5.4.4 Residual Strain in z-Direction

The residual strain in *z*-direction was measured along the top edge and the downsprue cross-scan of the two AZ91D castings. The ε_z measurements were performed to enable calculation of residual stresses in the critical region of the AZ91D castings.

The results for the linescans are presented in Appendix A5.4 (Figure A5. 17 - Figure A5. 20). The average strain and its variance are presented in Figure 140 and Figure 141 for the top edge and cross-scans, respectively.

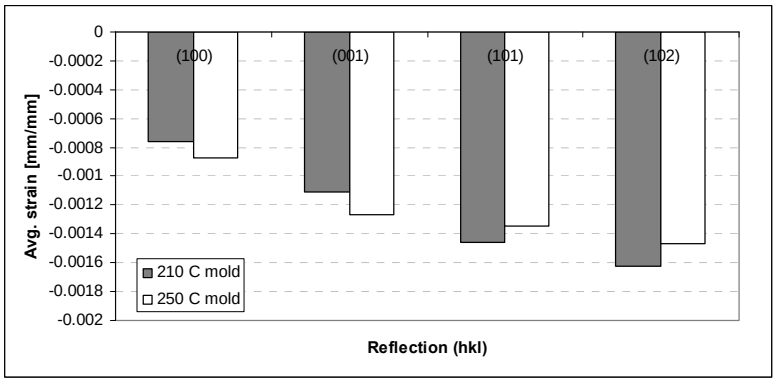

(a) Average strain.

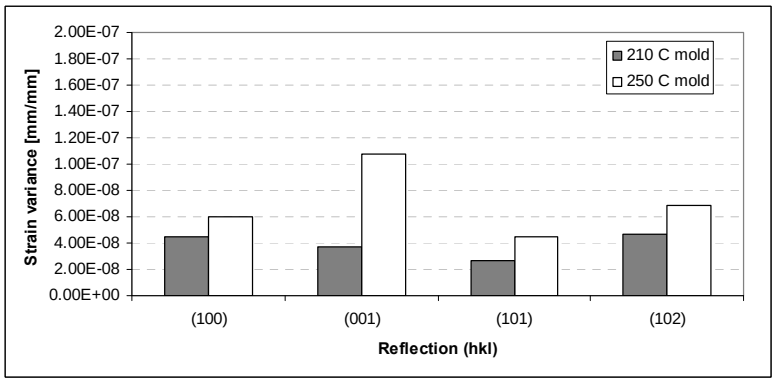

(b) Strain variance.

Figure 140: Average strain and strain variance along the top edge of AZ91D castings.

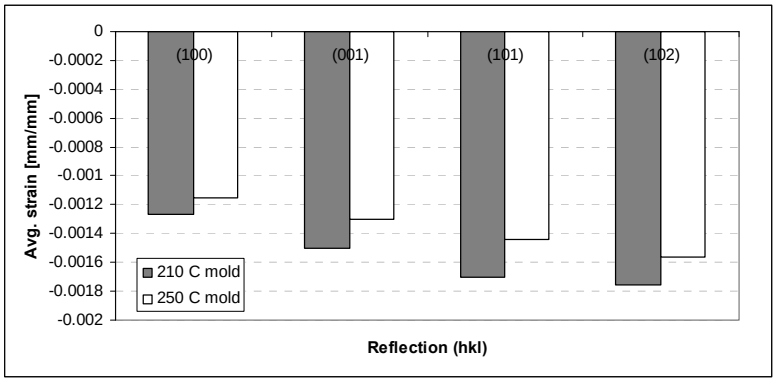

(a) Average strain.

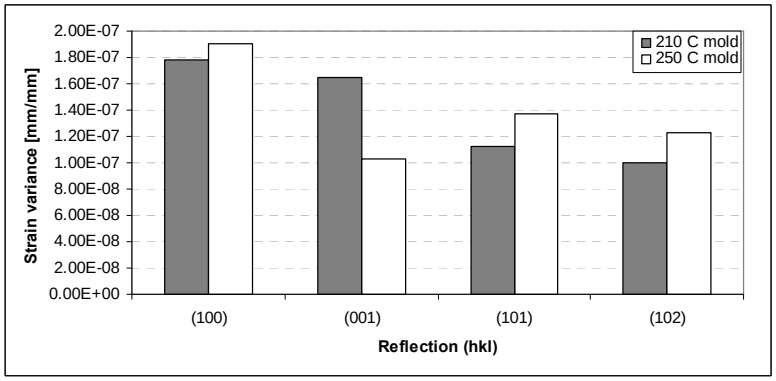

(b) Strain variance.

Figure 141: Average strain and strain variance along the cross-scan of AZ91D castings.

As Figure 140a and Figure 141a indicate, the ε_z strain remained compressive for all reflections. The compressive state indicates that the horizontal bar and the downsprue were free to contract in the *z*-direction upon solidification. The free contraction was expected, since there were no geometrical restrictions imposed by the mold on the casting. Thus, the ε_z strain likely did not contribute to the nucleation or propagation of hot tears in the critical region of the casting.

Observing the top edge ε_z profiles in Figure 142, no clear discontinuity was observed near the 90° corner, (i.e., near $x \sim 0$ mm) for either mold temperature casting. Only a minor relative increase of tension was noted in the downsprue of the 210 °C mold temperature casting. Since the horizontal bar solidified from the mold-wall inwards, complex strain gradients in the *z*-direction did not develop and the overall strain was relatively uniform.

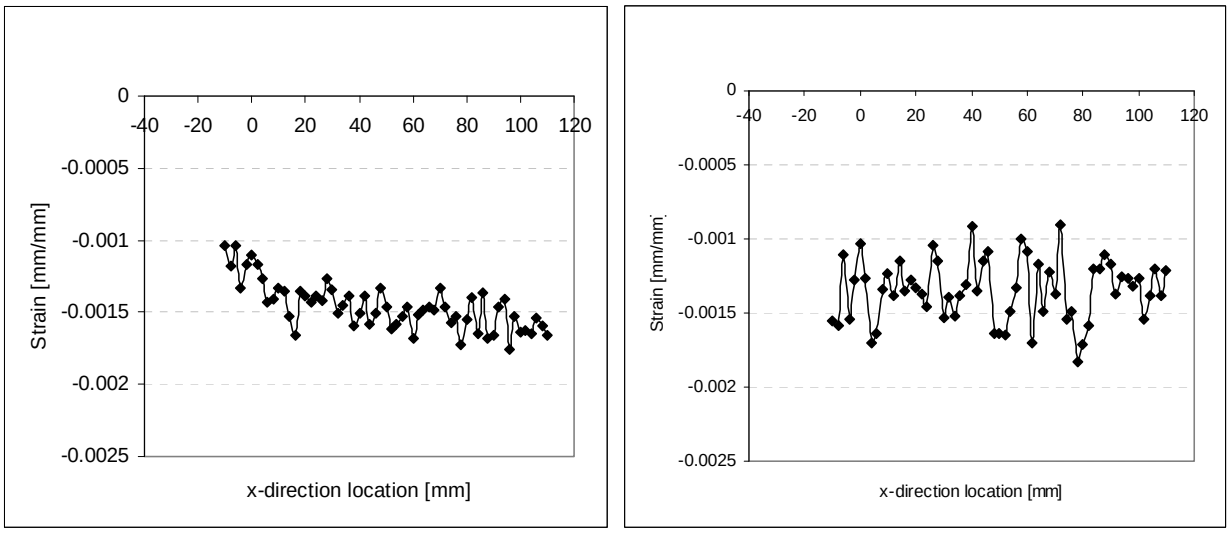

(a) 210 °C mold temperature. *(b) 250 °C mold temperature.*

Figure 142: ε_z profile for $(10\bar{1}1)$ top edge linescan for AZ91D castings.

As the mold temperature increased from 210 °C to 250 °C, the *z*-strain variance increased, as noted by comparing Figure 140b with Figure 141b. This increase may have been related to the longer solidification time of the material. Due to longer solidification, high-temperature (creep) deformation on the unrestrained casting (in *z*-direction) may have distorted the casting and increased the residual strain variance. This casting distortion, however, likely did not affect the hot tearing tendency of the material, since ε_z always remained compressive.

The predicted deformation from MAGMASOFT® was related to the strain measurements with neutron diffraction. A horizontal bar at 210 °C mold temperature (Figure A1. 42c) was predicted to develop several iso-strain bands of approximately equal width. In the vicinity of the critical region, the iso-bands merged and become non-uniform, suggesting a more complex deformation state. As the mold temperature increased to 250°C, MAGMASOFT® predicted disappearance of the iso-strain bands and the development of complex ε_z strain patterns in the critical region. As a result, strain variance along the horizontal bar was predicted to increase with an increase of mold temperature. This prediction is supported by ND measurements. Thus, qualitatively, MAGMASOFT® predictions may be correct; however, the numerical values of the simulated deformations could not be validated.

Observing the results for the cross-scan measurements in Figure 143, intensification of tensile strain towards the top edge 90° corner was observed for both mold temperatures. The strain in the downsprue trap regions remained more compressive than at adjacent locations. Therefore, the ND strain

measurements reveal that all three strains (ε_x, ε_y and ε_z) experienced tensile intensification at the top edge 90° corner (i.e., at $y \sim 0$ mm). As a result, development of tensile stress at this corner was plausible.

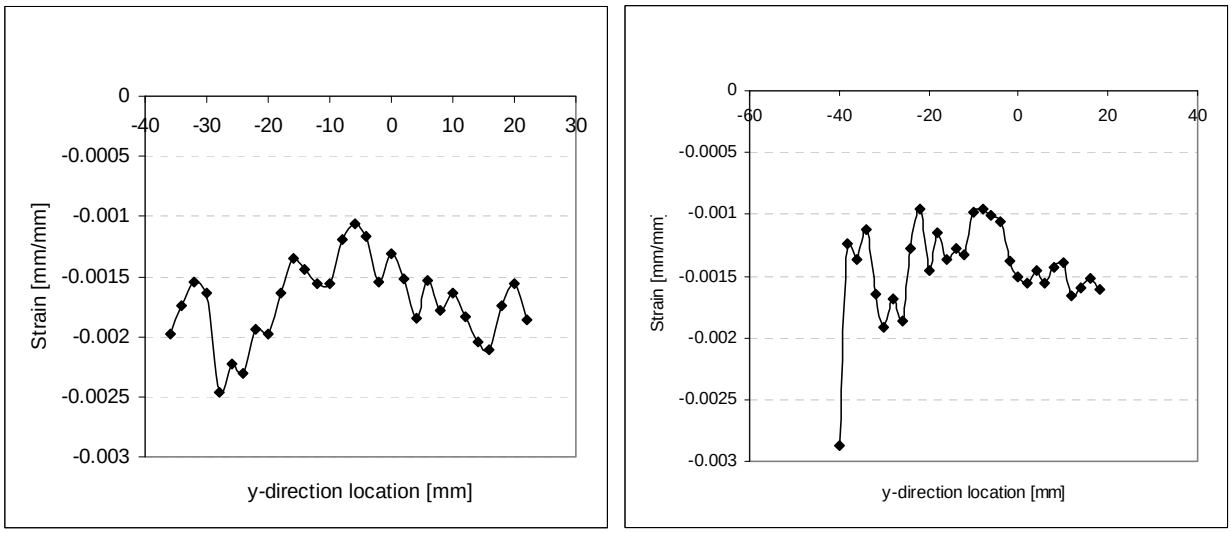

(a) 210 °C mold temperature. *(b) 250 °C mold temperature.*

Figure 143: ε_z profile for $(10\bar{1}1)$ sprue cross-scan for AZ91D castings.

5.4.5 Texture Analysis

Texture analysis was performed on AZ91D casting specimens presented in Section 5.4.1. The texture specimens were extracted from the critical regions of the castings. Texture analysis was performed for eleven crystallographic reflections, as described in Section 4.4.7. The results are presented in Appendix A5.5, including pole figures for a stress-free sample.

Analysis of all pole figures revealed that texture did not develop for any of the AZ91D samples cast in the temperature range of 220 °C – 380 °C. None of the pole figures indicated preferential orientation of the HCP crystal. As a result, the pole figures show that the as-cast AZ91D samples were isotropic and the HCP crystals were randomly oriented in the material. This conclusion was relevant for subsequent computation of residual stresses. The residual stress was determined from residual strain using Hooke's law (Equation 22). In this equation, the Young's modulus, E, and Poisson's ratio, υ, were used to relate strain in three orthogonal directions (ε_x, ε_y and ε_z) to appropriate principal stresses. Ideally, the elastic constants should be determined for individual reflections via *in-situ* tensile test under the neutron beam. As such experiments were not performed as a part of this research, the results of texture analysis enable the use of bulk AZ91D's elastic constants (e.g., available from the literature) in Hooke's law.

5.4.6 Residual Stress in AZ91D Castings

The ε_x, ε_y and ε_z residual strains measured in AZ91D castings along the top edge and the cross-scan were used in Equation 22 to calculate the principal stresses σ_x, σ_y and σ_z. The elastic constants E and υ were obtained from Reference 61. Subsequently, the principal stresses were used to evaluate the vonMises stress criterion (σ_m) using Equation 28. The results for the horizontal bar top edge and downsprue critical region are presented in Figure 145 - Figure 152.

$$\sigma_m = \frac{\sqrt{2}}{2}\left[\left(\sigma_x - \sigma_y\right)^2 + \left(\sigma_y - \sigma_z\right)^2 + \left(\sigma_x - \sigma_z\right)^2\right] \tag{28}$$

In the case of the ε_x strain measurements in the 210 °C mold temperature casting, several ND data points were not obtained due to the difficulty in generating statistically significant Gaussian fit of the raw neutron count data. As a result, during stress calculation at the location where ε_x was not available, average ε_x calculated from neighboring locations was used. Further, due to time restrictions on the neutron beam time, ε_x was not measured along the entire length of the downsprue cross-scan (the measurements were stopped for $y > 5$ mm). As a result, residual stress values for $y > 5$ mm are only approximate values consisting of ε_y and ε_z contributions.

Residual Stress Along Top Edge

The strain measurements along the top edge of the horizontal bar (Figure 145 - Figure 148) for both mold temperatures suggest that ε_x was generally tensile or mixed, while ε_y and ε_z were compressive. The residual stresses calculated from these strains were expected to follow similar trends. Due to the compressive contributions of y and z-direction strains, the residual stresses in all three directions were compressive, except at locations where relatively high tension in ε_x exceeded the compressive contributions of ε_y and ε_z. Since ε_x and σ_x were tensile in a casting with a hot tear, ND measurements confirm that these components were the main contributors to the initiation and propagation of hot tears in the critical region.

In the case of the $(10\bar{1}0)$ and (0001) reflections, tensile σ_x stress in the critical region reached 8.3 MPa and 12.1 MPa, as observed in Figure 145c and d. The corresponding ε_x strain was 0.06 and 0.05%, respectively. Thus, the ND results suggest that once the elastic residual stress reached ~ 8 – 12 MPa at a location of a stress concentration, plastic deformation of the HCP crystal initiated, resulting in the formation of shrinkage porosity or hot tears.

As the mold temperature increased from 210 °C to 250 °C, the tensile ε_x strain in the critical region decreased in magnitude. Consequently, the magnitude of σ_x decreased as well. The decrease of ε_x and σ_x was related to enhanced interdendritic feeding, as discussed in Section 5.4.1. With increased mold temperature, the coherency and rigidity points were delayed to later stages of solidification [74], resulting in improved interdendritic feeding and lower thermal stresses. Consequently, mechanical stresses due to interference between casting contraction and mold contraction did not reach levels required for hot tear nucleation.

As the mold temperature increased to 250 °C, tensile or mixed ε_x developed along the horizontal bar. However, the σ_x remained compressive along the entire linescan due to the significant compressive ε_y and ε_z strains developing at the high mold temperatures. Thus, the ND results demonstrate that in order to nucleate hot tears, both tensile stress and strain must be present. This condition was satisfied in the 210 °C mold temperature casting near the 90° top edge corner.

Residual Stress Along the Cross-scan

The results in Figure 149 - Figure 152 reveal the development of ε_x tension in the critical region ($-20 < y < 0$ mm). Similarly, as in the case of the top edge scan along the horizontal bar, the downsprue ε_x was tensile relative to ε_y and ε_z as well. As a result, the calculated stress in the critical region followed a similar trend as in the horizontal bar. In regions where the magnitude of ε_x was sufficiently tensile to exceed the contributions of compressive ε_y and ε_z, the resulting σ_x was tensile, otherwise all three stresses remained compressive.

The stress along the cross-scan reached a significantly higher level than at the 90° corner. A maximum tensile σ_x stress of 31 MPa ((0001) reflection) and 45 MPa ($(10\bar{1}0)$ reflection) was measured near the centerline. For the $(10\bar{1}0)$ reflection, tensile σ_y stress of 9 MPa also developed. The locations of tensile σ_x and σ_y stresses ($y \sim -10$ mm) coincided with the location of maximum HTI predicted by MAGMASOFT®. Thus, the tensile stresses support the prediction of massive shrinkage porosity development. This porosity was directly observed in downsprue Samples #8.

As the mold temperature increased, the residual stresses decreased. For the $(10\bar{1}0)$ and (0001) reflections, the σ_x decreased to 17 MPa and 4 MPa, respectively. The stresses for reflections $(10\bar{1}1)$ and $(10\bar{1}2)$ remained compressive along the entire linescan.

These results provide valuable insight into the possible mechanism of hot tear initiation and propagation. At the 210 °C mold temperature, the *x*-direction contraction of the horizontal bar induced tensile σ_x stress in the critical region. Also, due to the axial contraction of the downsprue, tensile σ_y stress developed in the downsprue in the critical region. As a result, a critical stress necessary to nucleate hot tears was reached. Specifically, a tensile stress of ~ 8 – 12 MPa developed. With progressing solidification and due to the opposing directions of the stress vectors, the hot tear was driven via the weakest regions (i.e., areas with shrinkage porosity) towards the downsprue interior, where tensile stress of ~ 31 – 45 MPa developed (Figure 144a). As the mold temperature increased to 250 °C mold temperature (Figure 144b), the stress at the top edge 90° corner became compressive of 5 MPa and tensile stress at the bar centerline decreased to 17 MPa.

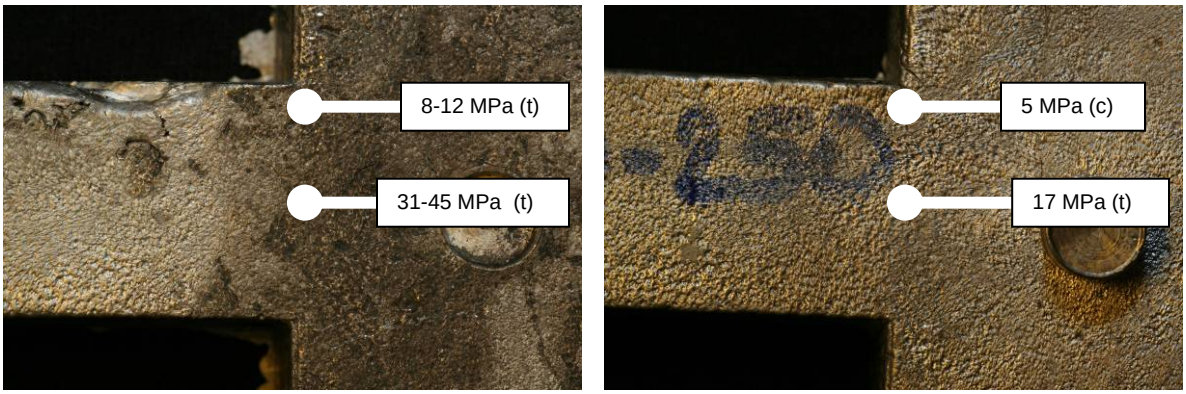

(a) 210 °C mold temperature. *(b) 250 °C mold temperature.*

Figure 144: Stress magnitude in AZ91D castings (t = tensile, c = compressive).

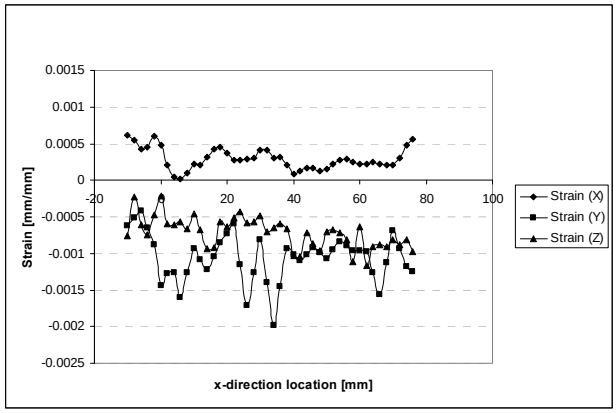

(a) $(10\bar{1}0)$ *residual strain profile.*

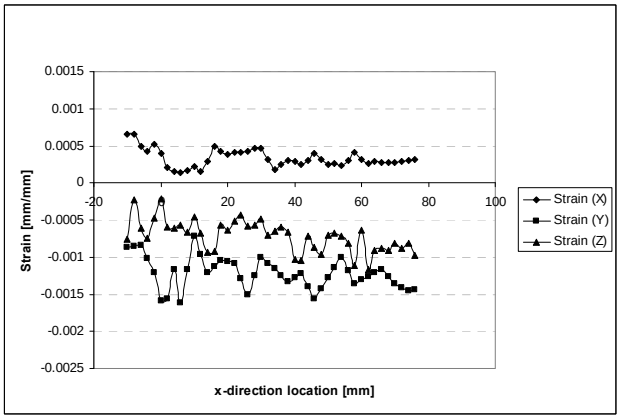

(b) (0001) *residual strain profile.*

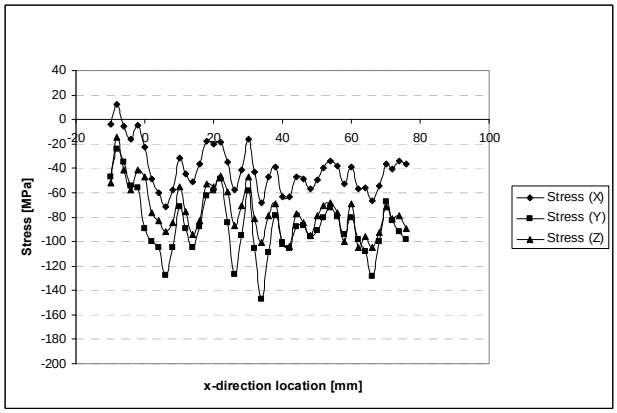

(c) $(10\bar{1}0)$ *residual stress profile.*

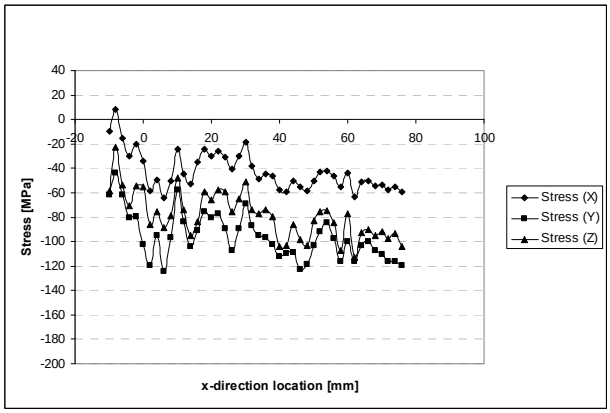

(d) (0001) *residual stress profile.*

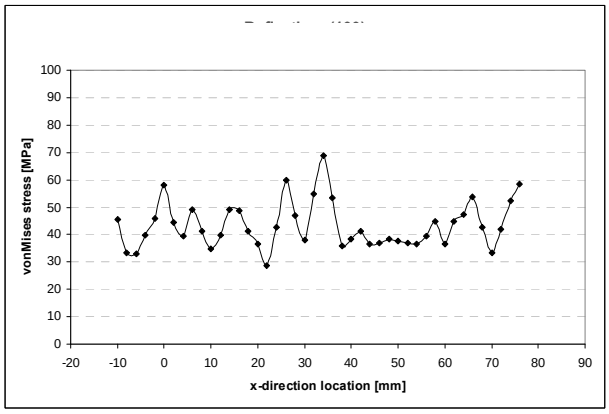

(e) $(10\bar{1}0)$ *vonMises stress profile.*

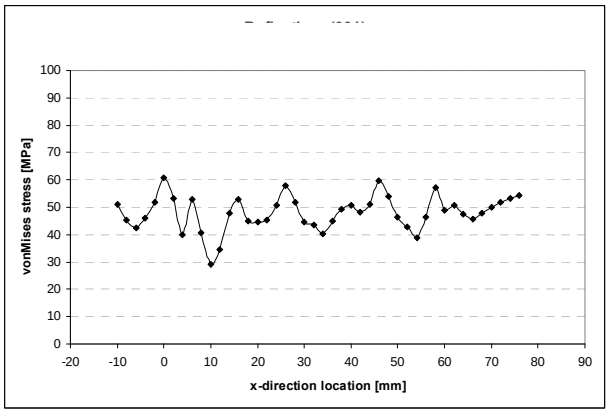

(f) (0001) *vonMises stress profile.*

Figure 145: ND strain, stress and vonMises profiles along the horizontal bar for AZ91D casting at 210 °C mold temperature; Reflections $(10\bar{1}0)$ *and* (0001).

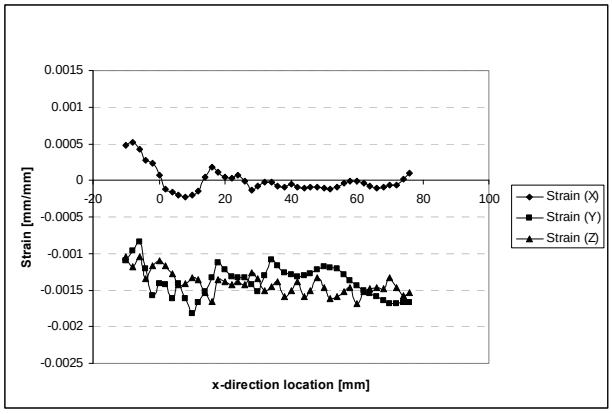

(a) $(10\bar{1}1)$ *residual strain profile.*

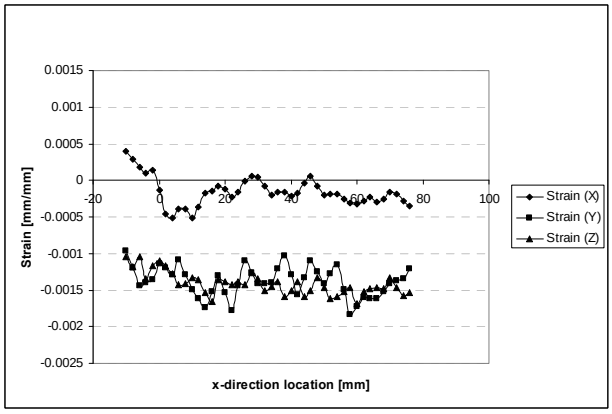

(b) $(10\bar{1}2)$ *residual strain profile.*

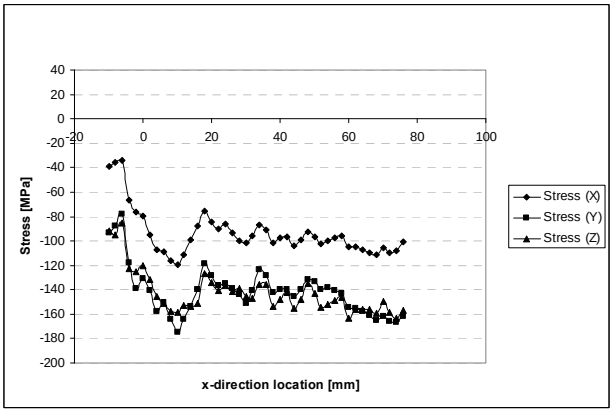

(c) $(10\bar{1}1)$ *residual stress profile.*

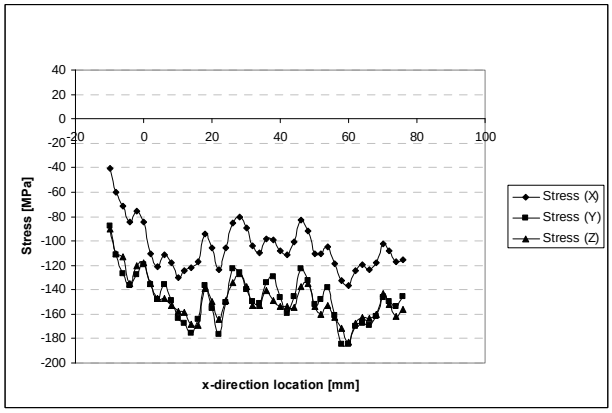

(d) $(10\bar{1}2)$ *residual stress profile.*

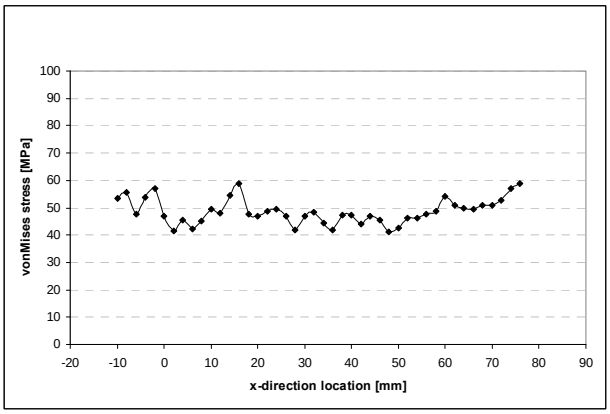

(e) $(10\bar{1}1)$ *vonMises stress profile.*

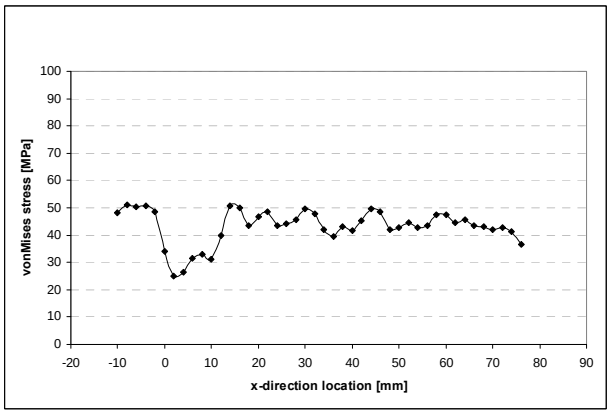

(f) $(10\bar{1}2)$ *vonMises stress profile.*

Figure 146: ND strain, stress and vonMises profiles along the horizontal bar for AZ91D casting at 210 °C mold temperature; Reflections $(10\bar{1}1)$ *and* $(10\bar{1}2)$.

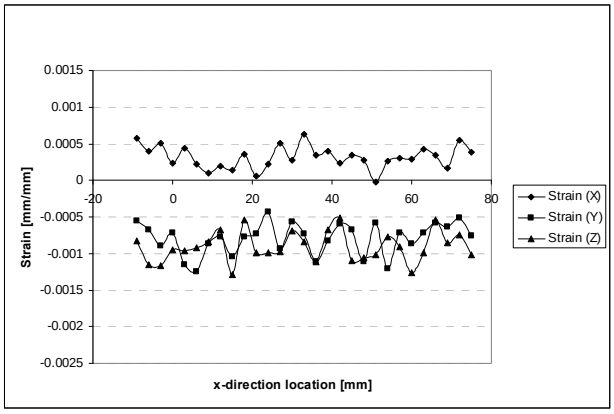

(a) $(10\bar{1}0)$ *residual strain profile.*

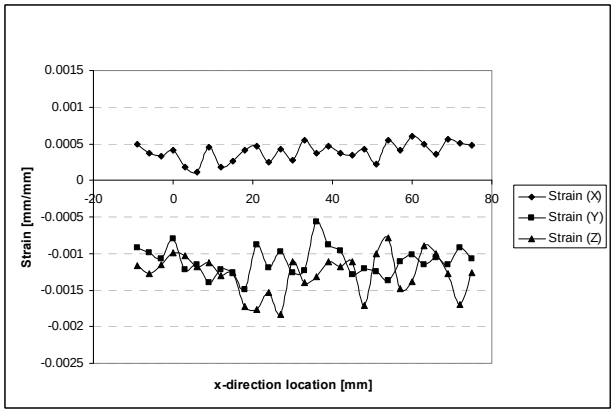

(b) (0001) *residual strain profile.*

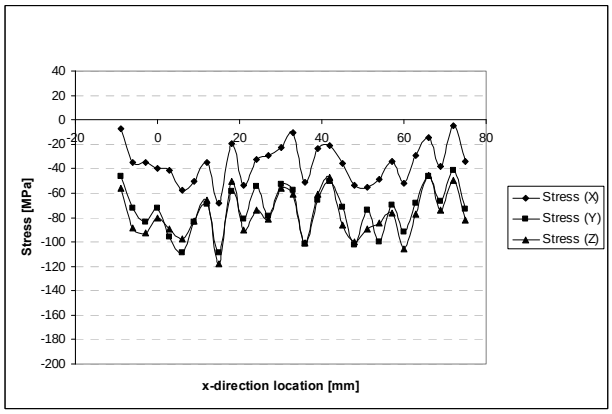

(c) $(10\bar{1}0)$ *residual stress profile.*

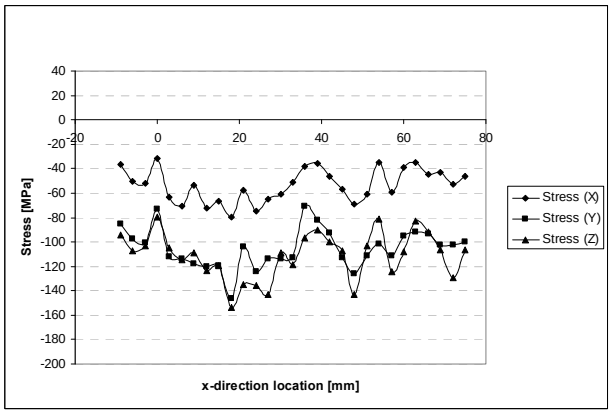

(d) (0001) *residual stress profile.*

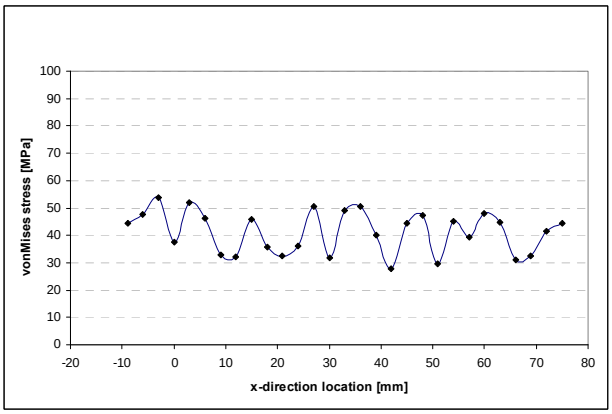

(e) $(10\bar{1}0)$ *vonMises stress profile.*

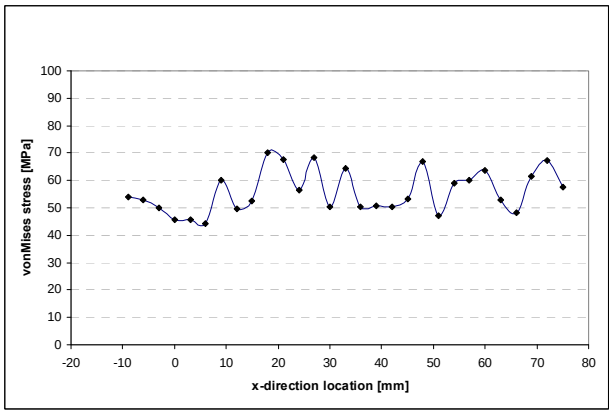

(f) (0001) *vonMises stress profile.*

Figure 147: ND strain, stress and vonMises profiles along the horizontal bar for AZ91D casting at 250 °C mold temperature; Reflections $(10\bar{1}0)$ *and* (0001).

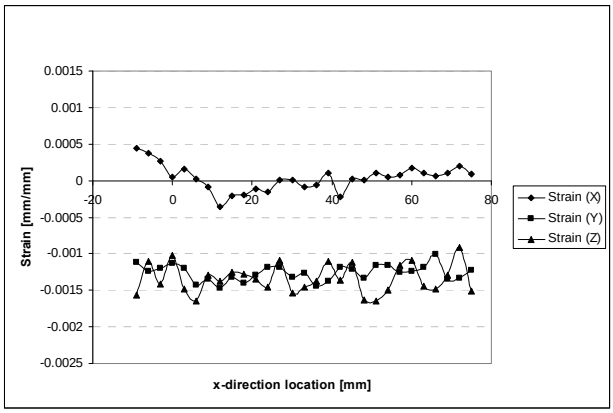

(a) $(10\bar{1}1)$ *residual strain profile.*

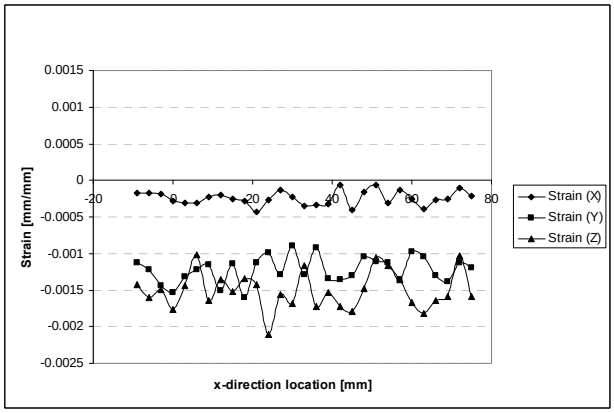

(b) $(10\bar{1}2)$ *residual strain profile.*

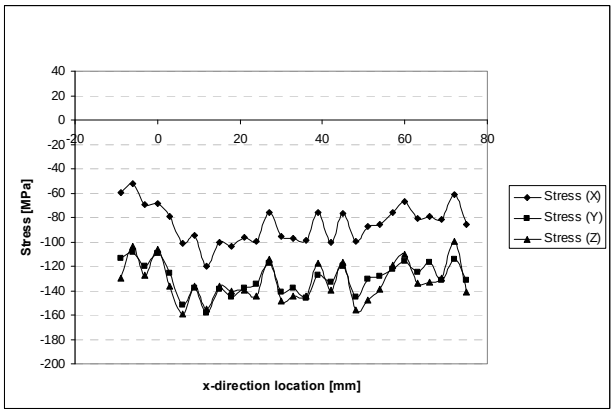

(c) $(10\bar{1}1)$ *residual stress profile.*

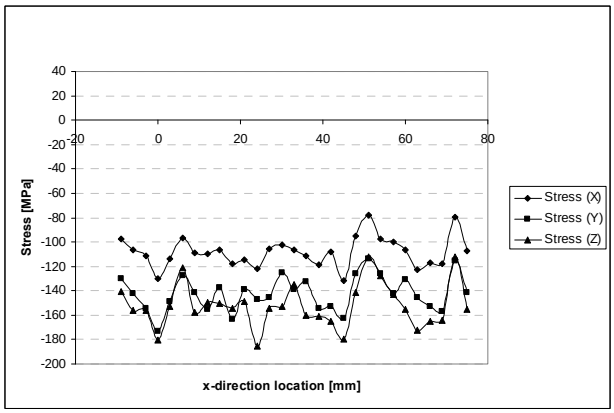

(d) $(10\bar{1}2)$ *residual stress profile.*

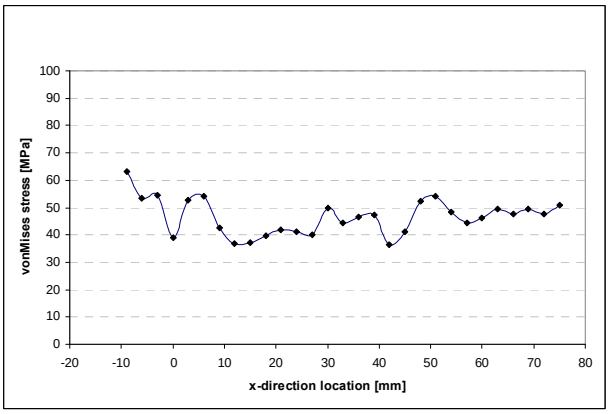

(e) $(10\bar{1}1)$ *vonMises stress profile.*

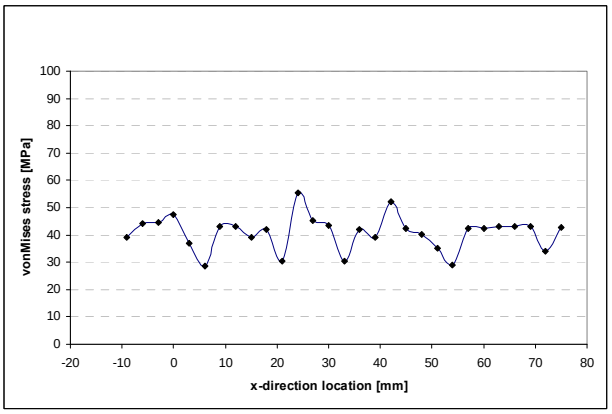

(f) $(10\bar{1}2)$ *vonMises stress profile.*

Figure 148: ND strain, stress and vonMises profiles along the horizontal bar for AZ91D casting at 250 °C mold temperature; Reflections $(10\bar{1}1)$ *and* $(10\bar{1}2)$.

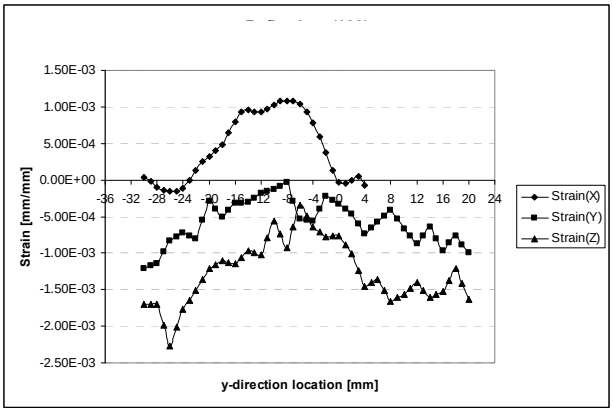

(a) $(10\bar{1}0)$ *residual strain profile.*

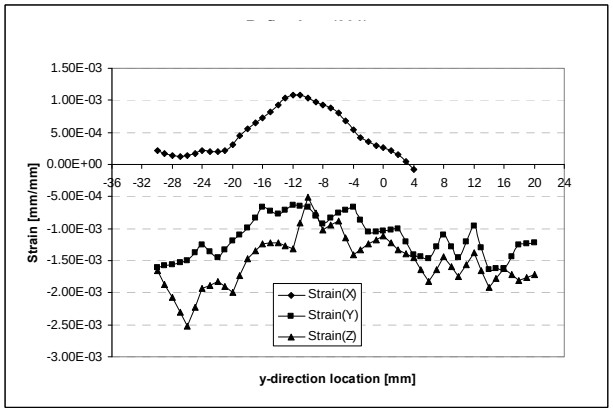

(b) (0001) *residual strain profile.*

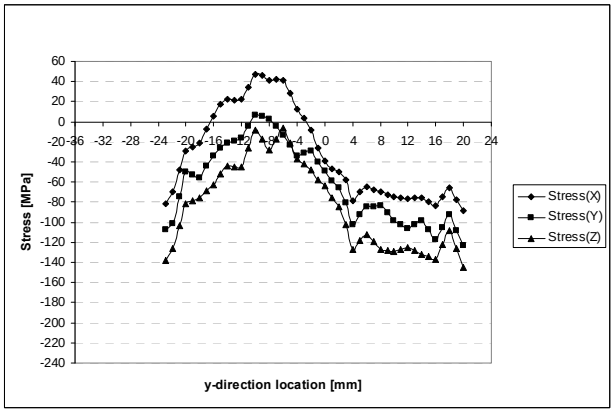

(c) $(10\bar{1}0)$ *residual stress profile.*

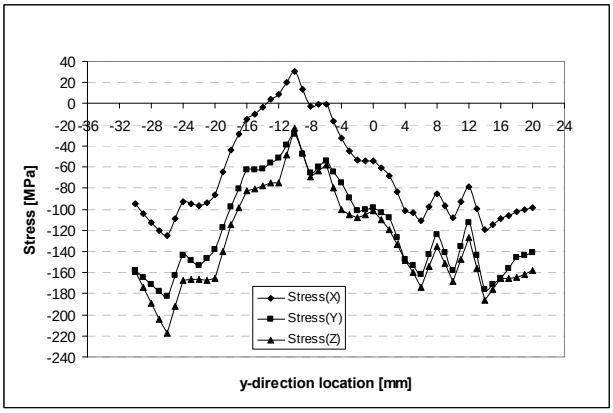

(d) (0001) *residual stress profile.*

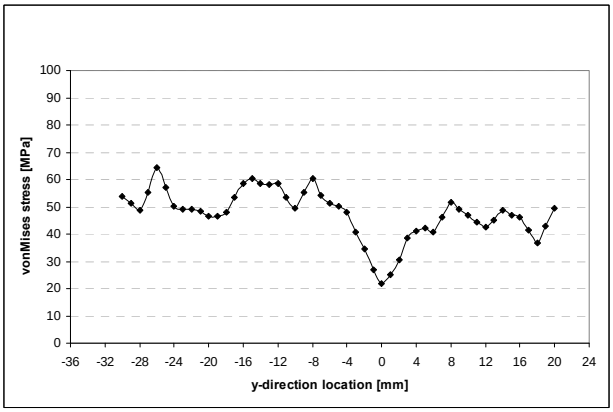

(e) $(10\bar{1}0)$ *vonMises stress profile.*

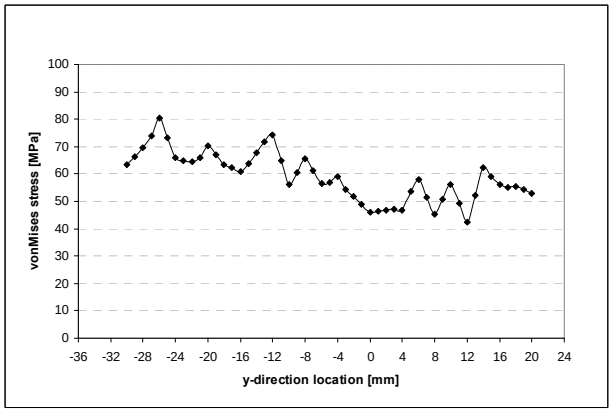

(f) (0001) *vonMises stress profile.*

Figure 149: ND strain, stress and vonMises profiles along the cross-scan for AZ91D casting at 210 °C mold temperature; Reflections $(10\bar{1}0)$ *and* (0001).

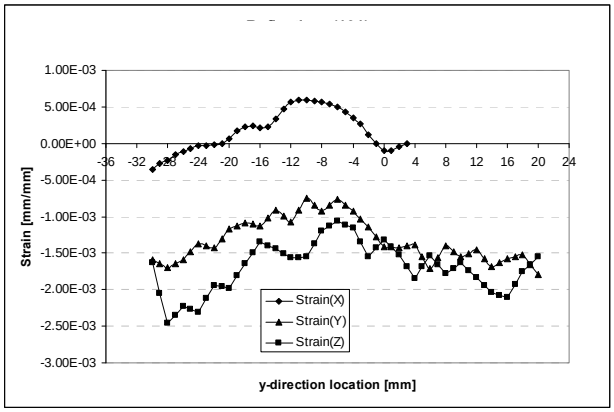

(a) $(10\bar{1}1)$ *residual strain profile.*

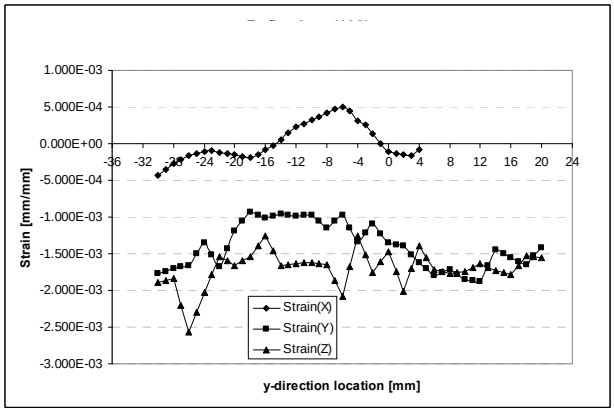

(b) $(10\bar{1}2)$ *residual strain profile.*

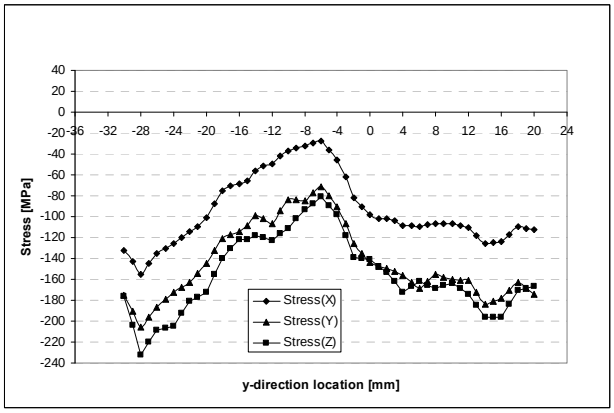

(c) $(10\bar{1}1)$ *residual stress profile.*

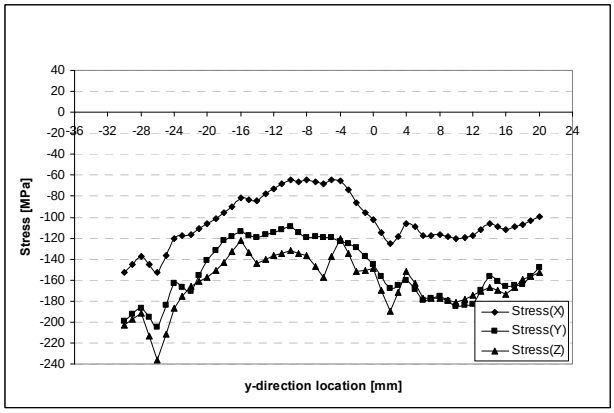

(d) $(10\bar{1}2)$ *residual stress profile.*

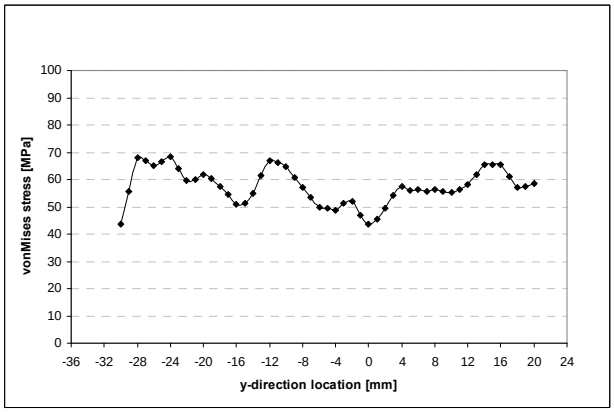

(e) $(10\bar{1}1)$ *vonMises stress profile.*

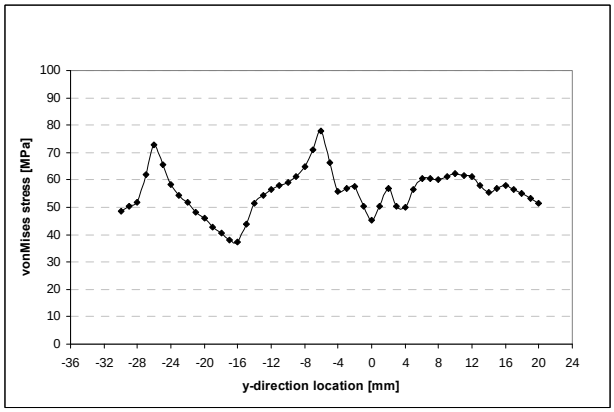

(f) $(10\bar{1}2)$ *vonMises stress profile.*

Figure 150: ND strain, stress and vonMises profiles along the cross-scan for AZ91D casting at 210 °C mold temperature; Reflections $(10\bar{1}1)$ *and* $(10\bar{1}2)$.

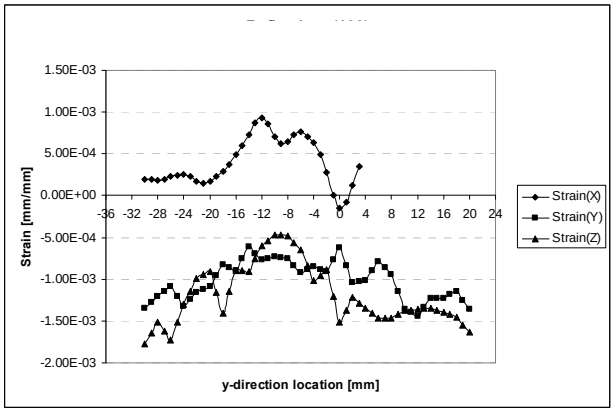

(a) $(10\bar{1}0)$ *residual strain profile.*

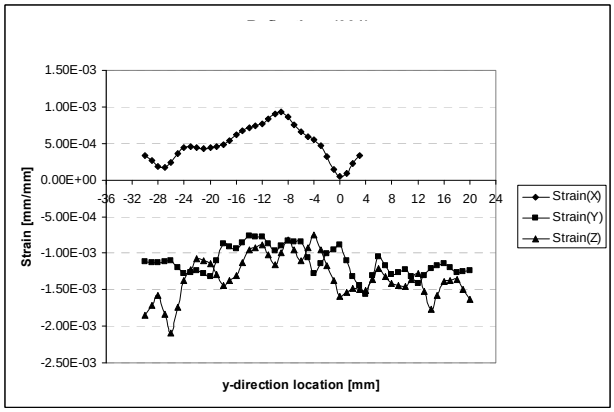

(b) (0001) *residual strain profile.*

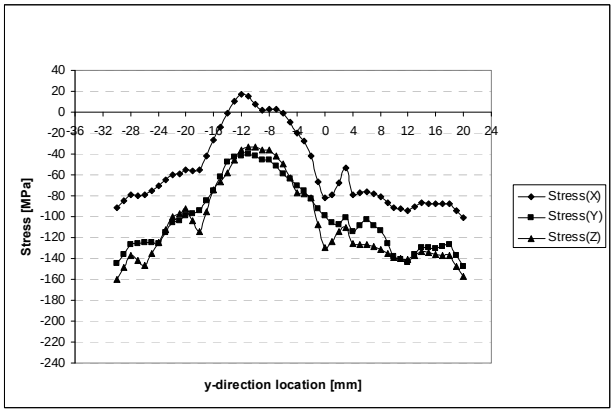

(c) $(10\bar{1}0)$ *residual stress profile.*

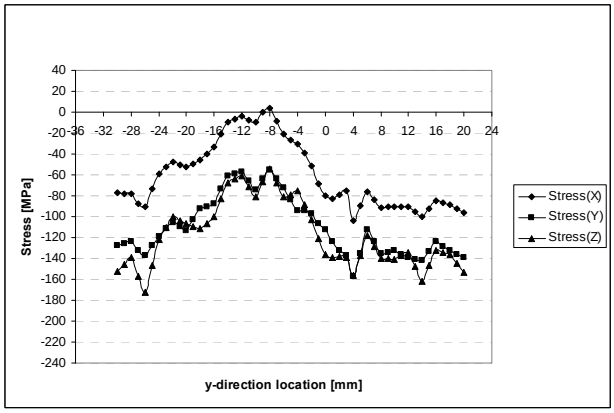

(d) (0001) *residual stress profile.*

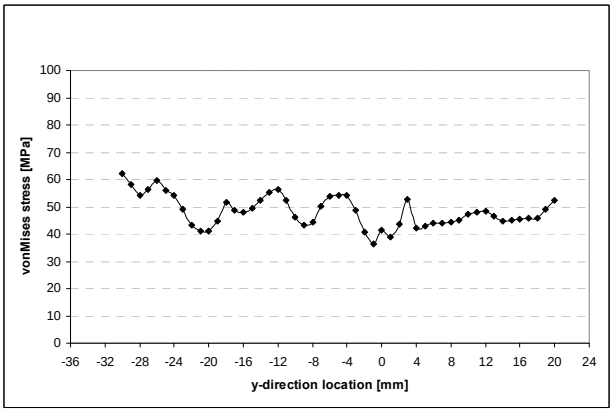

(e) $(10\bar{1}0)$ *vonMises stress profile.*

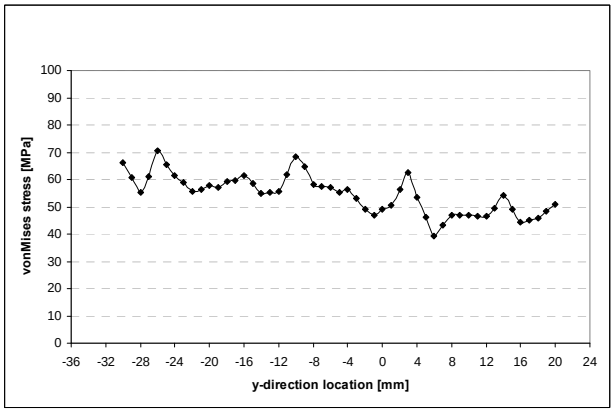

(f) (0001) *vonMises stress profile.*

Figure 151: ND strain, stress and vonMises profiles along the cross-scan for AZ91D casting at 250 °C mold temperature; Reflections $(10\bar{1}0)$ *and* (0001).

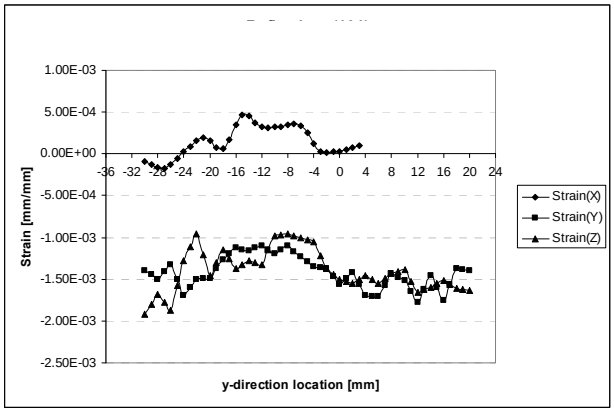

(a) $(10\bar{1}1)$ *residual strain profile.*

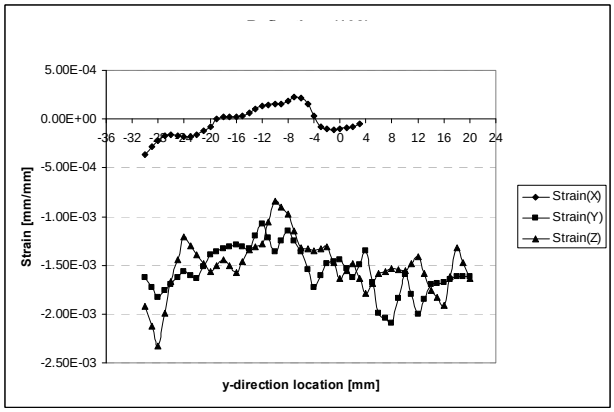

(b) $(10\bar{1}2)$ *residual strain profile.*

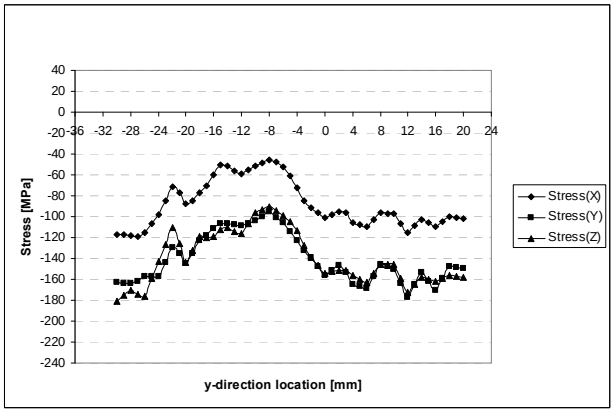

(c) $(10\bar{1}1)$ *residual stress profile.*

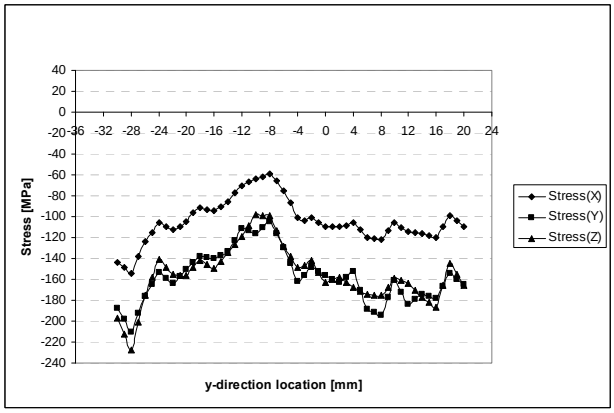

(d) $(10\bar{1}2)$ *residual stress profile.*

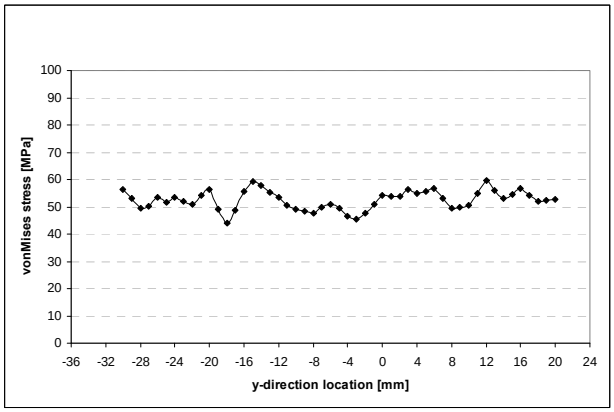

(e) $(10\bar{1}1)$ *vonMises stress profile.*

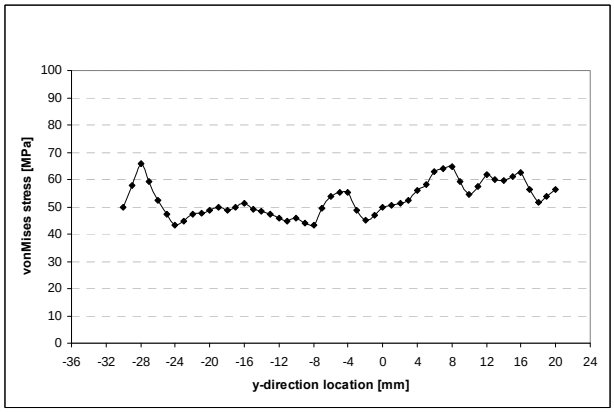

(f) $(10\bar{1}2)$ *vonMises stress profile.*

Figure 152: ND strain, stress and vonMises profiles along the cross-scan for AZ91D casting at 250 °C mold temperature; Reflections $(10\bar{1}1)$ *and* $(10\bar{1}2)$.

Examination of the vonMises critical stress values in Figure 145 - Figure 152 revealed that this criterion is likely not suitable for predicting material failure at the solidus temperature. The difficulty of using this criterion was related to:

1. Majority of principal stresses were compressive and prevented material failure. As experiments demonstrated, tensile stress was required to initiate opening of shrinkage pores, nucleation and propagation of hot tears.
2. The vonMises critical stress exceeded the expected yield stress of the material for all casting conditions, despite a decrease in the vonMises stress with increasing mold temperature.
3. The vonMises criterion is traditionally used to predict failure of ductile materials. AZ91D or AE42 alloys at room temperature are considered ductile, with elongation to fracture exceeding 5%. However, the ε_x strain values in the critical region indicate that an elastic strain of ~0.05% was sufficient to initiate material failure. Thus, the alloys at the solidus temperature no longer exhibit ductile behavior, but fail in a brittle-like manner. Therefore, the vonMises criterion is not suitable for such conditions.

Therefore, instead of using traditional criterion functions (e.g., vonMises, Tresca) to predict material failure at the onset of hot tearing, a new approach based on the maximum allowable strain should be developed. A strain-based criterion may be preferred, since the constitutive relationships between stress and strain in the semi-solid region are not well established.

5.5 Interactive Effects

The results and discussion of the fundamental parameters (e.g., alloy microstructure, hot tear nucleation and stress/strain) were presented in Sections 5.1 – 5.4. The current section attempts to expand the discussion by focusing on the interactive effects between the fundamental parameters. Specifically, the thesis objectives outlined in Chapter 1 are addressed as follows: Section 5.5.1 discusses the effect of PMC process parameters on the onset of hot tearing. Section 5.5.2 relates the effect of PMC process parameters to the formation of casting defects. The interactions between the fundamental parameters influencing hot tearing (i.e., microstructure, solidification, strain and stress) are discussed in Section 5.5.3.

5.5.1 Effect of PMC Process Parameters on Hot Tearing

Performing extensive casting trials with the AZ91D and AE42 magnesium alloys revealed that variation of the mold temperature had the most profound influence on the alloy's hot tearing tendency [83].
In order to slow down casting solidification and prevent hot tearing, increasing the mold temperature was seen to be more effective than increasing the alloy pouring temperature. This trend was expected, since the heat content, calculated using Equation 29, for the H-13 steel mold and the magnesium alloy show significantly different level of sensitivity to an incremental temperature change.

$$q = mc_p \Delta T \tag{29}$$

Where:

q = heat content c_p = specific heat
m = mass ΔT = temperature change

For example, considering 1 cm^3 of the AZ91D alloy, a 20 °C temperature change increases the alloy's heat content by ~730 J, while the same temperature increase of 1 cm^3 of the mold (H-13 steel) adds ~1250 J to the system. Thus, with a greater heat content increase per unit of temperature, the mold temperature had a more significant impact on the casting cooling rate and fillability than the pouring temperature.

For the current casting geometry, all hot tears formed at the 90° corner of the junction between the downsprue and the horizontal bar. These hot tears emanated from the 90° corner towards the downsprue interior. For the AZ91D alloy cast at 720 °C pouring temperature, the onset of hot tearing occurred between 210 °C and 250 °C mold temperature. For the AE42 alloy at 765 °C pouring temperature, the onset of hot tearing occurred between 340 °C and 390 °C mold temperature.

It is recognized that the absolute values of the pouring and mold temperatures associated with the onset of hot tearing in each alloy may not be applicable for other casting geometries. For example, increasing the length of the horizontal bar would decrease the onset mold temperature, since a larger surface area would accelerate the horizontal bar's solidification and contraction rates and cause hot tearing to occur at a lower mold temperature. Increasing the cross-section of the downsprue would likely decrease the onset mold temperature, since a greater amount of liquid metal would be available for feeding of the critical region at the end of solidification of the horizontal bar. In addition, changing the angle between the horizontal bar and the downsprue would also influence the hot tearing tendency at the junction. It is expected that when the angle between the axes of the downsprue and the horizontal bar exceeds 90°, the hot tearing tendency in the critical region would decrease, since the extent of the horizontal bar's restricted deformation would decrease. In contrast, when the angle between the downsprue and the horizontal bar decreases below 90°, the hot tearing tendency would be expected to increase, as a stronger stress concentration would develop at the junction.

The presence of the pouring cup on the top of the downsprue was also seen to influence formation of hot tears in the critical region of the casting. Experiments demonstrated that more severe hot tears formed near the top edge 90° corner than at the bottom edge 90° corner. Intensification of the tensile stress at the 90° top edge was the result of the restricted axial contraction of the downsprue between the top edge 90° corner and the pouring cup. In contrast, the bottom trap's contraction was unrestrained in the *y*- and *z*-directions, thus enabling relaxation of residual stresses upon solidification.

Due to the above factors, the mold and pouring temperatures associated with the onset of hot tearing could vary for different casting geometries. Thus, the alloy cooling rate was proposed as a more descriptive parameter. The average alloy cooling rates at the top edge 90° corner (where hot tears readily formed) were obtained from MAGMASOFT® simulation and are summarized in Table 26. The reported cooling rates were associated with the liquidus and solidus temperatures.

As Table 26 indicates, the cooling rates for the AZ91D alloy were significantly higher than for the AE42 alloy. This is in agreement with the significantly lower mold and pouring temperatures associated with the onset of hot tearing in the AZ91D alloy.

Table 26: Cooling rates in the critical casting region.

Alloy / Mold temperature [°C]	Cooling rate [°C/s]
AZ91D / 210	15.1
AZ91D / 250	10.2
AE42 / 340	8.3
AE42 / 390	7.7

The range of the cooling rates at the onset of hot tearing was greater for the AZ91D alloy than for the AE42 alloy. The wider cooling rate range suggests that the AZ91D alloy is a more robust casting alloy and is less sensitive to process temperature fluctuations than the AE42 alloy. The AE42 alloy required significantly lower cooling rates (~55%) than the AZ91D alloy to enable adequate interdendritic liquid feeding.

One of the key factors impeding interdendritic feeding in the AE42 alloy was the presence of the Al_xRE_y intermetallic compounds in the interdendritic regions [80]. During solidification of the AE42 alloy, numerous RE-rich intermetallics form, segregate towards the interdendritic region and possibly hinder interdendritic feeding. These are $Al_{11}RE_3$, Al_2RE, $Mg_{12}RE$, $Al_{10}RE_2Mn_7$ and $MgCe_2$ [84]. Anyanwu *et al*. [71] suggested that when the RE/Al ratio exceeds 1.4, the Al is consumed by $Al_{11}RE_3$ and other Al_xRE_y phases, thus preventing formation of $Mg_{17}Al_{12}$ phase. Further, Hu *et al*. [85] suggested that the melting point of the Al_2RE phase is well above the liquidus point of the α-Mg phase and it may agglomerate in the interdendritic regions during α-Mg growth. In addition, Bakke *et al*. [70] suggested that the Al_xRE_y intermetallics agglomerating at the phase boundaries deteriorate AE42 alloy's ductility. In the current research, segregation of Al_xRE_y intermetallics in the interdendritic regions was observed (e.g., Figure 83a). The acicular $Al_{11}RE_3$ phase spanned across the interdendritic regions, while particulate Al_2RE decorated the dendrite boundaries. Consequently, the presence of ~6% volume fraction of Al_xRE_y intermetallics (determined via image analysis) and the reduction of Al in the interdendritic liquid likely impeded interdendritic feeding and deteriorated the alloy's ductility.

Further, the rapid onset of dendrite coherency and dendrite branching (Section 5.3.1) fragmented the interdendritic liquid, thus making long range interdendritic feeding of the AE42 castings difficult. The cumulative deleterious impact of the above factors was overcome only when the solidification rate of the casting remained relatively low.

Microscopic examination of the horizontal bar's cross section of both alloys revealed a significant variation in the grain morphology. For example, in the AZ91D casting, a skin layer (~150μm thick) with fine grains formed at the metal-mold interface, suggesting that the region experienced accelerated grain nucleation (due to rapid solidification induced by the relatively cool steel mold) than the horizontal bar centerline region. During subsequent thermal contraction of the horizontal bar, the skin region was able to sustain relatively higher stresses (due to grain boundary strengthening) than the centerline regions. However, as a result of the higher strength, the ductility of the skin region was likely limited. As a result, the skin was not able to accommodate the same level of casting deformation as the centerline region and significant strain gradients developed across the casting cross-section. These strain gradients contributed to the nucleation of microcracks in the skin. The cracks subsequently enlarged during thermal contraction of the horizontal bar. In order to alieve the grain non-uniformity, the mold temperature had to be increased from 210 °C to 250 °C . Thus, in the case of the AZ91D castings, increasing the mold temperature reduced intergranular strain gradients and improved bulk strain homogeneity, as verified with ND. In the case of the AE42 alloy castings, the very low cooling rates necessary to achieve sufficient interdendritic flow and prevent hot tearing resulted in the formation of elongated (columnar) grains in the skin regions, as observed in Figure 70b. Thus, the optimal cooling rate condition was exceeded. However, formation of columnar grains in the skin region was not seen to directly nucleate hot tears in the skin of the AE42 castings.

5.5.2 Effect of PMC Process Parameters on the Formation of Casting Defects

As discussed in the previous section, manipulation of the mold temperature significantly influenced the alloy's susceptibility to hot tearing. In addition, variation of the mold temperature influenced formation of additional casting defects such as surface oxides, folds and frozen metal flow lines on the casting surfaces.

Oxidation of magnesium alloys is known to be one of the key technological impediments to their wider application in the automotive industry [59]. In this research, melt oxidation was suppressed with carbon dioxide covergas. With adequate protection, oxide formation was stabilized and controlled. However, upon pouring the molten metal into the permanent mold, the metal stream became exposed to the ambient atmosphere in the mold cavity and began to oxidize. In the case of the AZ91D castings, oxidation was manifested as discoloration of the casting surface in the area of the downsprue. Oxidation in the downsprue occurred since this region remained relatively hot for the longest period of time. Also, the metal flow in this casting region was highly turbulent as predicted with MAGMASOFT® simulations

(e.g., Figures in Appendix A1.3.3) thus exposing a large surface area to molten metal to the ambient air. Further, the molten metal front separated into multiple streams, thereby increasing the possibility of melt oxidation and subsequent oxide film entrapment in the casting interior.

Metallographic and SEM/EDX analyses confirmed presence of oxide films in the downsprue and the critical region (e.g., Figure 104). These oxides were observed to be responsible for the formation of fold defects in the AZ91D alloy, as they created a physical barrier between merging metal fronts. Further, the critical region adjacent to the downsprue experienced a reversing metal flow (at the end of the horizontal bar's filling), which promoted additional entrainment of oxides in the casting. The resulting folds possibly increased localized strain and solute non-uniformity and deteriorated the bulk casting quality.

Formation of folds in the AE42 alloy castings was not directly related to melt oxidation. Due to the presence of rare-earth elements, oxide formation was suppressed and delayed [86]. Thus, the extent of downsprue surface oxidation or the entrainment of oxides in the casting interior was relatively low. However, segregation of Al_2RE intermetallics at the advancing metal front was seen to promote fold formation. Due to the relatively fast solidification of the AE42 alloy (i.e., non-equilibrium solidification), the solubility of alloying elements in the magnesium matrix decreased, thereby promoting solute segregation to the leading edge of the advancing metal front. Further, due to the short freezing range of the alloy, solidification possibly occurred at multiple locations of the metal front, resulting in globular solidification pattern. The resulting solutal inhomogeneity resulted in preferential precipitation of Al_2RE phase, creating a microstructural discontinuity between two merging metal fronts. As a result, fusion of the metal fronts was impeded and a fold formed (e.g., Figure 110). For both casting alloys, fold formation was not seen to be directly related with the nucleation of hot tears.

5.5.3 Fundamental Mechanisms Influencing Hot Tearing in Magnesium Alloys

This research was carried out in order to advance the understanding of the fundamental concepts influencing initiation and propagation of hot tears in AZ91D and AE42 magnesium alloys. The classical factors (i.e., microstructure, solidification and stress/strain) were studied and related to the onset of hot tearing.

Analysis of the results presented in Chapter 5 revealed that all three factors were interrelated and can not be isolated or studied independently in an effort to predict hot tearing. Thus, an overview of the interactive effects between these three parameters is presented in the following text.

5.5.3.1 Effect of Alloy Microstructure

Microscopic examination of the alloys revealed that the morphology of the primary grains and the interdendritic channels, along with the morphology of the second phases, significantly influenced an alloy's susceptibility to hot tearing. In addition, the local solidification conditions and the development of a stress concentration in the critical region contributed to hot tearing.

1. The liquid permeability (i.e., interdendritic feeding) of the semi-solid alloy was governed by the morphology of the interdendritic regions [87]. The morphology of the interdendritic regions was related to the alloy's solidification rate: at high cooling rates (and non-equilibrium solidification), solute was rejected into the liquid ahead of the solid-liquid interface and promoted formation of well-branched dendrites. Formation of well branched dendrites created small and dispersed interdendritic liquid regions. As a result, liquid phase was not continuous and interdendritic feeding was difficult. Inadequate interdendritic feeding was manifested as solidification shrinkage porosity. When the mold temperature increased, primary Mg phase branching decreased, enabling formation of relatively large interdendritic regions and long-range interdendritic feeding of the casting. Thus, at high mold temperature, the bulk volumetric shrinkage of the horizontal bar could be compensated by liquid metal feed from the downsprue, thereby reducing the mechanical load on the crystal matrix.
2. Formation of intermetallics in the interdendritic regions (e.g., partially divorced eutectic structure in the AZ91D alloy or $Al_{11}RE_3$ needles in the AE42 alloy) likely obstructed interdendritic liquid flow [80]. Precipitation of these intermetallics was stimulated by rapid alloy solidification causing solute segregation at the solid-liquid interface.
3. In the case of the AE42 alloy, it was observed that the acicular $Al_{11}RE_3$ phase possibly deteriorated into particulate Al_2RE phase. With this transformation, the strength of the interdendritic boundaries decreased, thus enabling relative motion (i.e., sliding) of individual dendrites during high temperature deformation. As a result of the alloy's enhanced ductility, the tendency to hot tearing possibly decreased.
4. Microscopic examination revealed that the skin of the horizontal bar consisted of fine grains and contained only minimal shrinkage porosity. In contrast, the horizontal bar centerline regions exhibited larger grains and centerline shrinkage porosity. Centerline shrinkage porosity suggests that solidification progressed in the hoop direction from the mold wall towards the horizontal bar's centre. As the skin solidified, liquid was drawn from the centerline to feed the skin's contraction, resulting in centerline porosity.

5. Hot tears typically formed at the top edge 90° corner of the horizontal bar. The 90° corner imposed a stress concentration and enabled development of a critical stress necessary for nucleation of hot tears. Microstructural observation revealed that once a hot tear nucleated, it propagated from the 90° corner via the interdendritic regions towards the downsprue interior. In the case of the AZ91D alloy, the interdendritic regions were enriched with the low melting temperature $Mg_{17}Al_{12}$ phase, which weakened the interdendritic regions and enabled hot tear propagation at high fractions of solid. In the case of the AE42 alloy, hot tears were seen to propagate along the interdendritic as well as the grain boundary regions. Needles of $Al_{11}RE_3$ phase were seen to locally pin neighboring dendrites (e.g., Figure 98) and enhance the interdendritic bond strength. As a result, AE42's hot tears were forced to propagate along the relatively weaker grain boundaries (e.g., Figure 81b).
6. Microscopic analysis also revealed that hot tears propagated discontinuously along perpendicular segments, coinciding with the orthogonal axes of the downsprue and the horizontal bar (e.g., Figure 80). Piece-wise crack propagation along the orthogonal segments indicates that the axial contractions of downsprue and the horizontal bar were the driving force for hot tear propagation. As the mold temperature increased, the extent of discontinuous and piece-wise hot tear propagation decreased. This observation was supported by ND measurements, which suggested a decrease in stress levels in the *x*- and *y*-directions with an increase in mold temperature. For example, at 210 °C mold temperature (Figure 149c), both *x*- and *y*-direction stresses reached tensile state (near the centerline), while in the case of the 250 °C mold temperature casting (Figure 151c), only the *x*-direction stress remained tensile.
7. Observation of the hot tears revealed symmetric features on the hot tear fracture surfaces, confirming that tensile forces were responsible for the opening of hot tears. This observation is in agreement with ND stress measurements, which identified tensile stress as a necessary condition for the nucleation of hot tears.
8. Variation of the solidification rate in the AZ91D alloy had a significant impact on the structure of the β-phase regions [67]. As the mold temperature increased, the β-phase transformed from a partially divorced eutectic into a fully divorced eutectic structure. This transformation potentially eliminated particles acting as stress risers and reduced the tendency of the bulk alloy to nucleate hot tears. In the case of the AE42 alloy, the microstructure along the horizontal bar remained uniform (ND measurements confirm a relatively uniform strain levels along the horizontal bar).

5.5.3.2 Effect of Cooling Rate

The alloy cooling rate was varied by manipulating the mold temperature. The interactions between the alloy cooling rate, microstructure and stress/strain parameters based on the results of thermal analysis are discussed in the following text.

1. Increasing the mold temperature decreased the cooling rate and extended the interval of interdendritic feeding (Table 22), delayed the onset of dendrite coherency and decreased the rate of dendrite branching (Table 23). These factors assisted in retaining the interdendritic feeding paths open during solidification in order to enable compensation of casting solidification shrinkage.
2. High cooling rates in the short freezing range AE42 alloy resulted in high dendrite growth velocities (Table 23). Rapid branching of the primary dendrites disrupted the continuity of the interdendritic liquid. As a result, isolated liquid pockets developed and long range feeding of the AE42 casting was difficult. In contrast, long freezing range AZ91D alloy enabled the liquid phase to retain continuity as a liquid film on the grain and dendrite boundaries, thereby enabling long-range feeding of the casting. These trends were confirmed by examining the shrinkage porosity morphology and distribution in respective castings. In the AE42 alloy, shrinkage pores were small, independent and dispersed throughout the microstructure. When the mold temperature increased, the shrinkage pores formed connected clusters (e.g., Figure 120). In the case of the AZ91D alloy, interdendritic shrinkage pores formed continuous networks spanning several dendrites. These porosity observations indirectly reveal that the continuity of the interdendritic liquid was significantly more extensive in the AZ91D alloy than in the AE42 alloy.
3. In the case of the AZ91D alloy, increasing the mold temperature extended the duration of the eutectic reaction (Table 18), thus allowing formation of eutectic phases in the interdendritic regions. The eutectics assisted liquid feeding at late stages of solidification.
4. In the case of the AZ91D alloy, the cooling rate of the horizontal bar was not uniform. Radial and axial thermal gradients developed, as predicted with MAGMASOFT® simulations (Appendix A1.3.4). Rapid cooling at the metal-mold interface caused evolution of fine grains in the skin regions and induced centerline shrinkage porosity in the horizontal bar center (e.g., Figure 116). As a result of the thermal gradients, strain gradients developed during subsequent solidification. ND measurements confirmed development of complex strain profiles at the top edge and the casting centerline with variation of the cooling rate (e.g., Figure A5. 5k vs. Figure A5. 5l).
5. In the case of the AE42 alloy, the horizontal bar solidified rapidly along its entire length [80]. As a result, complex strain patterns did not have sufficient time to develop in the *x*-direction, as

determined from ND measurements. This result also agrees with the observed uniform alloy microstructure along the length of the horizontal bar (Section 5.2.3.1).

5.5.3.3 Effect of Stress and Strain

The following discussion presents the interactive phenomena between stress / strain measured with ND and the casting microstructure and solidification kinetics.

1. Development of tensile stress was required for the nucleation of hot tears in AZ91D castings. Tensile stress was required to separate dendrites and form interdendritic cavities, or expand shrinkage pores into hot tears. ND measurements along the top edge linescan show that stress of ~8 - 12 MPa was sufficient to initiate a crack at the top edge 90° corner (e.g., Figure 145c). Further, tensile stress was recorded during a cross-scan of the sprue in the critical region of the casting (e.g., Figure 149c) and reached a level of ~ 31 – 45 MPa. These tensile stresses caused dendrites to separate and nucleate interdendritic porosity. Presence of shrinkage porosity made hot tear propagation during cooling easier, since the negative pressure imposed on the solid crystal network by the shrinkage pores increased the effective stress levels in the solid crystals (i.e., pre-loaded the solid network). As a result, the additional stress (e.g., mechanical load due to restrained casting contraction within the mold) required to initiate hot tears decreased.
2. In the case of the AZ91D alloy, the horizontal bar filled from the bottom edge towards the top edge. Further, the horizontal bar solidified in the radial direction from the mold wall inwards. As a result, inhomogeneous temperature along the horizontal bar induced strain gradients along the horizontal bar as well as through its cross-section. The residual strain profiles obtained with ND support this solidification path. Further, this solidification path and deformation evolution were also predicted in MAGMASOFT® simulations.
3. With increasing mold temperature, the tensile residual stresses decreased and a net compressive residual stress state was achieved in the critical region (due to compressive contributions of *y*- and *z*-direction contractions). This general trend was observed in the AZ91D castings, as well as in the AZ91D castings examined during the preliminary stage of this research.
4. Measurement of residual strain in several crystallographic directions revealed that the deformation of the HCP crystal was not perfectly elastic [88]. Crystallographic planes $(10\bar{1}1)$ and $(10\bar{1}2)$ were seen to be more sensitive to high temperature deformation. This sensitivity was possibly related to their re-orientation for non-basal slip at elevated mold temperatures [82].

5. The axial contraction of the bar and the downsprue was seen to be responsible for the development of significant tensile stresses in the critical region (Section 5.4.2.1). This observation supports the results of other researchers [33, 36] who varied alloy's hot tearing severity by adjusting the axial length of a casting bar (thereby influencing the extent of axial contraction in their casting experiments).
6. Increasing the mold temperature increased the free contraction (and strain variance) in the *z*-direction. However, for all casting trials, the *z*-direction strain remained compressive, thus the increase in *z*-direction strain variance likely did not significantly impact nucleation of hot tears.
7. The residual strain and stress profiles measured with ND were not symmetrical about the centerline axis of the horizontal bar in the critical region (e.g., Figure 130). An intensification of tension was observed towards the top edge 90° corner of the horizontal bar. This intensification was the result of the restricted contraction of the downsprue above the top edge 90° corner. In contrast, the downsprue trap near the bottom edge 90° corner of the casting possibly experienced stress relaxation due to its unrestrained contraction. This prediction was consistent with visual observation of the hot tear severity at these two 90° corners.

One of the objectives of this research was to determine the magnitude of stress in the AZ91D alloy required to trigger a hot tear. In summary, the results suggest that for a casting with a hot tear a tensile residual stress of 45 MPa (reflection $(10\bar{1}0)$) developed in the downsprue, as observed in Figure 149. The region affected by the tension was 13 mm wide. For (0001) reflection, 31 MPa tensile stress developed and acted over 5 mm wide region. In a casting without a hot tear, tensile stress was observed only for reflection $(10\bar{1}0)$ and reached a magnitude of 17 MPa. The width of the region where tensile stresses developed was 4 mm. These results suggest that the critical stress associated with the onset of hot tearing was between 17 – 30 MPa.

At the time of writing this thesis, reliable literature on the yield strength of AZ91D alloy near the solidus temperature was not available. The only study on the elevated temperature tensile strength of AZ91-type alloy was recently published by Cizek *et al*. [89].These researchers conducted high temperature tensile tests with custom made (non-ASTM) tensile specimens. The tensile strength and elongation as a function of temperature are presented in Figure 153. Micrographs in Figure 154 show the microstructure and material damage of tensile specimens tested at 460 °C temperature (~30 °C above the solidus temperature).

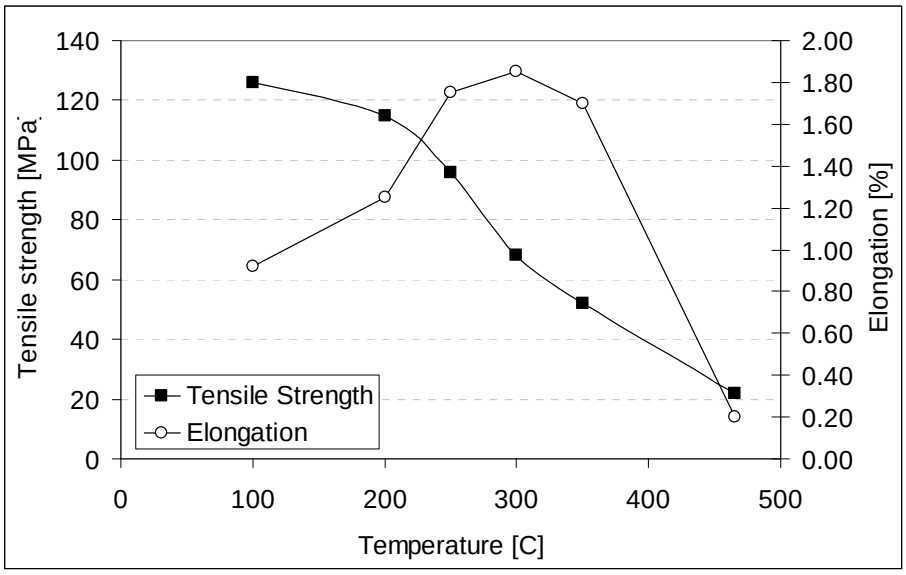

Figure 153: Tensile strength and elongation of AZ91 alloy at elevated temperatures [89].

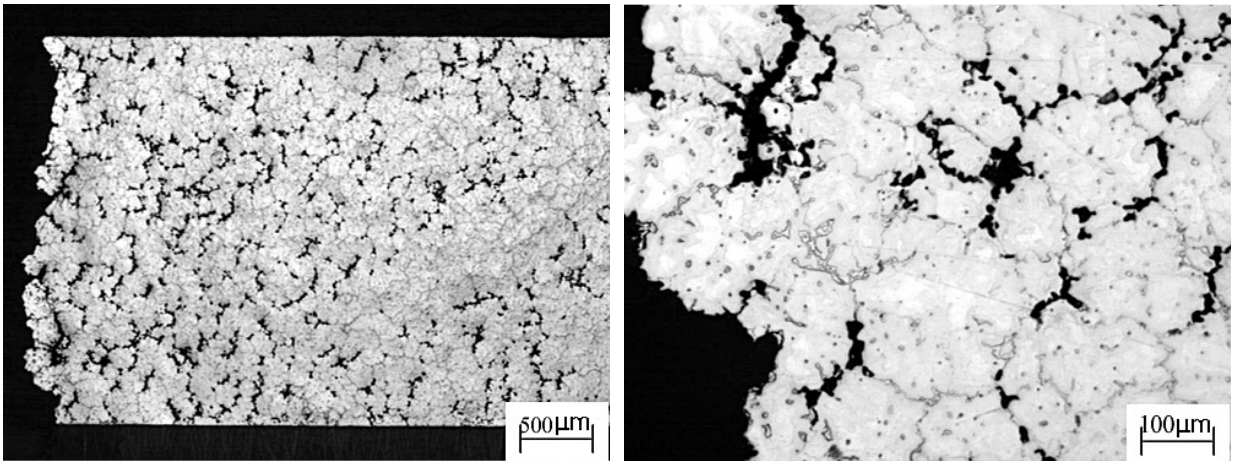

(a) *(b)*

Figure 154: Micrographs of fracture surfaces of uniaxially tested AZ91 alloy at 460 °C [89].

The tensile strength of the AZ91 alloy at the solidus temperature according to Cizek *et al*. was 25.5 MPa. This value is also in general agreement with the stress measurements performed with ND in this research. For a casting with a hot tear, the residual stress in the critical region exceeded the reported tensile strength by 5.5 MPa for (0001) reflection. In the case of a casting without hot tears, the tensile stress remained 8.5 MPa below the reported tensile strength of the alloy. These results lend a significant degree of credibility to the approach of using ND for characterizing the stress levels in the AZ91D casting at the onset of hot tearing. It was suggested [90] that the elastic stresses, which continuously develop in the casting during solidification remain locked-in the crystal matrix upon solidification. It is recognized that a

portion of the residual stresses are relieved with casting ejection from the permanent mold. However, the same amount of relaxation would be expected in a casting with and without a hot tear. Thus, the narrow deviation of the residual stresses from the expected high temperature tensile strength (25.5 MPa) suggests that the elastic stresses measured with ND provide valuable information about the stress levels in a casting at the onset of hot tearing.

Observation of micrographs in Figure 154a indicates that numerous internal cavities formed near the fracture surface of Cizek *et al.*'s tensile specimen. The cavities formed in a direction perpendicular to the tensile axis. As reported by Cizek *et al.*, material damage occurred predominantly in the interdendritic regions and voids propagated around individual dendrites. These results of Cizek *et al*. are consistent with the observations made in the current research, where the interdendritic cracks were seen to propagate in piece-wise segments perpendicular to the tensile axes of the horizontal bar and the downsprue (e.g., Figure 73). Thus, Cizek *et al.*'s results support the claim that tensile stress was required for the nucleation of a hot tear and subsequent material failure.

The results of Cizek *et al*. further demonstrate that tensile load applied to a semi-solid material creates interdendritic cavities similar (in shape) to shrinkage porosity. These cavities result from the mechanical separation of dendrites. In contrast, classical shrinkage porosity cavities result from the absence of interdendritic liquid during solidification. Thus, micrographs presented in Section 5.2.2 were examined and shrinkage pores along with the tip of a hot tear were inspected. The micrograph in Figure 155a shows that a casting with a hot tear contained traces of eutectic phase along the hot tear edge, as indicated with arrows. Thus, this cavity possibly formed due to mechanical separation of dendrites. In contrast, cavities in a casting without a hot tear (Figure 155b) did not contain any trace of eutectic liquid present on the cavity walls and the cavities were the result of solidification shrinkage.

The residual strains reported in this dissertation did not incorporate the effect of linear thermal expansion / shrinkage associated with casting's cooling from the solidus temperature to the room temperature. Thus, the strain in the casting at the solidus temperature (T_s) may differ from that measured at room temperature (T_{RT}) using neutron diffraction. However, the inaccuracy introduced by the linear thermal contraction of the horizontal bar between $T_S \rightarrow T_{RT}$ was within the experimental error. The following discussion provides additional details.

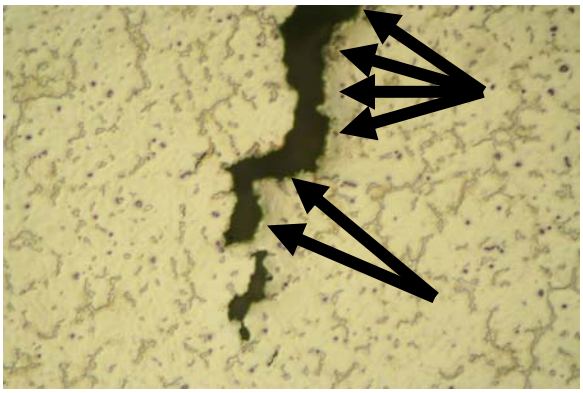

(a) Tip of a hot tear in AZ91D / 210 °C mold temperature, Sample #4 (BF, 200x).

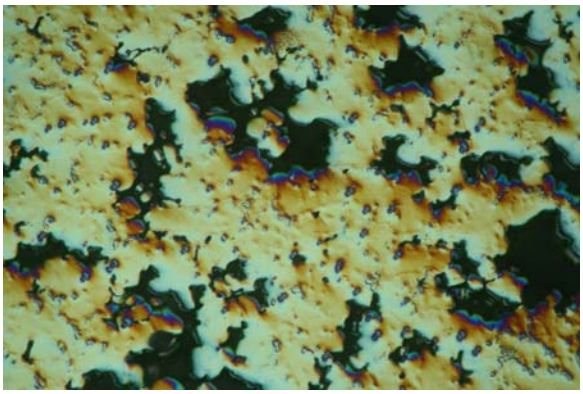

(b) Porosity cluster in AZ91D / 250 °C mold temperature, Sample #8 (DIC, 200x).
Figure 155: Hot tear tip and shrinkage porosity.

During the horizontal bar's cooling from the solidus temperature to the room temperature, the horizontal bar contracted. This contraction altered the lattice strain in the critical region of the casting. The development of lattice strain (tensile or compressive) during casting solidification and cooling was divided into three stages:

I. Cooling of the casting from the liquidus to the solidus temperature. During this stage, volumetric shrinkage of the casting associated with a phase change gradually induced tensile *x*-direction strains in the critical casting region. In the 210 °C mold temperature casting, the combined mechanical and thermal strain at the end of Stage I reached a level sufficient to trigger hot tearing.

II. Below the solidus temperature, the solid horizontal bar continuously contracted within a rigid mold. As a result, additional tension in the critical region of the casting developed (mechanical load) and further increased the lattice spacing (beyond that present at the solidus temperature). Stage II contraction continued until casting ejection from the mold.

III. After five minutes of pouring the liquid alloy into the permanent mold, the mold was opened and the casting ejected within approximately 2 minutes. Upon ejection, the horizontal bar

contracted freely, since any geometrical constraints no longer restricted the bar's contraction. Thus, the lattice strain decreased. The free contraction proceeded from the end of Stage II until cooling of the casting to the room temperature. The lattice strains present at the end of Stage III were the elastic residual lattice strains measured with neutron diffraction.

Thus, it is evident that the strain at the onset of hot tearing and the strain at room temperature were possibly not identical. As a result, the magnitude of strain increase during Stage II tension and strain decrease during Stage III contraction were examined.

Estimation of Stage II and Stage III strains was accomplished with the use of cooling curves obtained from embedded thermocouples in the casting. As Figure 156 shows, for the 210 °C mold temperature casting, the temperature at the end of solidification was ~432 °C. When the casting was ejected from the mold (after seven minutes of initiating the pour) the temperature in the critical region decreased to ~230 °C.

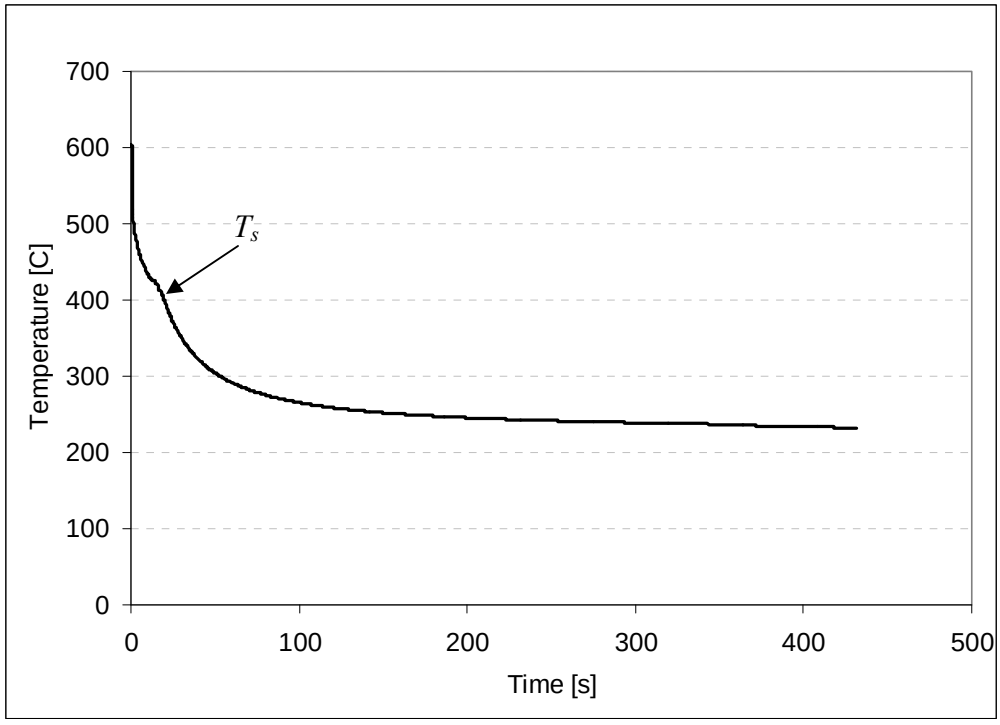

Figure 156: Casting solidification history in the critical region. AZ91D casting at 210 °C mold temperature.

The incremental displacement, Δl, which developed in the horizontal bar due to temperature variation, was calculated using Equation 30:

$$\Delta l = \alpha(\Delta T)L \tag{30}$$

Where:

α = coefficient of linear thermal expansion (CTE)

ΔT = temperature difference

L = characteristic length of the bar

The values of temperature-dependent CTE were obtained from Reference 61. The results indicate that the horizontal bar length change for Stage II from 432 °C to 230 °C was 6.04 x 10^{-3} m (tensile). For Stage III from 230 °C to 23 °C the length change was 5.58 x 10^{-3} m (compressive). Thus, the net displacement due to contraction of the horizontal bar between the solidus temperature (when hot tearing occurred) and the room temperature at which residual strains were measured was 4.60 x 10^{-4} m. Considering the entire horizontal bar, the above net displacement corresponded to a tensile *x*-direction strain of 1.18 x 10^{-4}. This value of net strain could be used as a correction factor for all *x*-direction residual strain measurements reported in this dissertation. However, it is recognized that during horizontal bar's contraction within Stage II, the alloy temperatures exceed the homologous temperature (50% of solidus temperature) and creep induced phenomena, such as grain boundary sliding, possibly took place [91]. Grain boundary sliding would decrease the strain evolved during Stage II. Further, the time interval when creep effects possibly influenced the strain distribution in the casting was relatively short (~ 6 minutes). Quantification of creep-induced strain relaxation was beyond the scope of this research.

Assuming elastic response of the AZ91D alloy between the solidus and room temperatures, and adjusting Young's modulus for temperature variation within this range, the net tensile strain of 1.18 x 10^{-4} corresponded to a 4.40 MPa net tensile stress. Thus, the maximum tensile stress values measured with ND in the downsprue were possibly over-estimated by up to 4.40 MPa. As a result, the stress at the onset of hot tearing in the 210 °C mold temperature AZ91D casting may have been 40.6 MPa for reflection $(10\bar{1}0)$ and 26.6 MPa for (0001) reflection. Both of these stress values exceed the tensile strength of the alloy as reported by Cizek *et al*., and remain consistent with earlier discussion of results, which excluded the influence of linear thermal expansion / contraction on the magnitude of residual strains.

In addition to evaluating the thermal expansion and contraction of the casting, the thermal expansion of the permanent mold was also considered. Figure 157 shows the temperature profile recorded by the in-mold thermocouple near the critical region. This thermocouple was placed 2 mm below the surface of the horizontal bar cavity. The figure suggests that the mold temperature in the immediate vicinity of the

thermocouple increased from 210 °C to 261 °C when the molten metal was poured into the mold cavity. Thereafter, the mold temperature decreased and approached a constant temperature of ~ 227 °C. Performing similar thermal strain analysis as with the horizontal bar above, the net (local) thermal strain experienced by the mold temperature variation was 1.7×10^{-4}, which is an order of magnitude smaller than residual strains measured with ND. Further, this thermal strain represents local value at the thermocouple only. The bulk of the steel mold experienced a lower temperature fluctuation, thereby resulting in a lower thermal strain magnitude. In addition, the mounting of the mold was not rigid and the mold was able to expand in the *x*-direction. Thus, the mold temperature variation and associated thermal strain imposed by the mold on the casting was not likely significant.

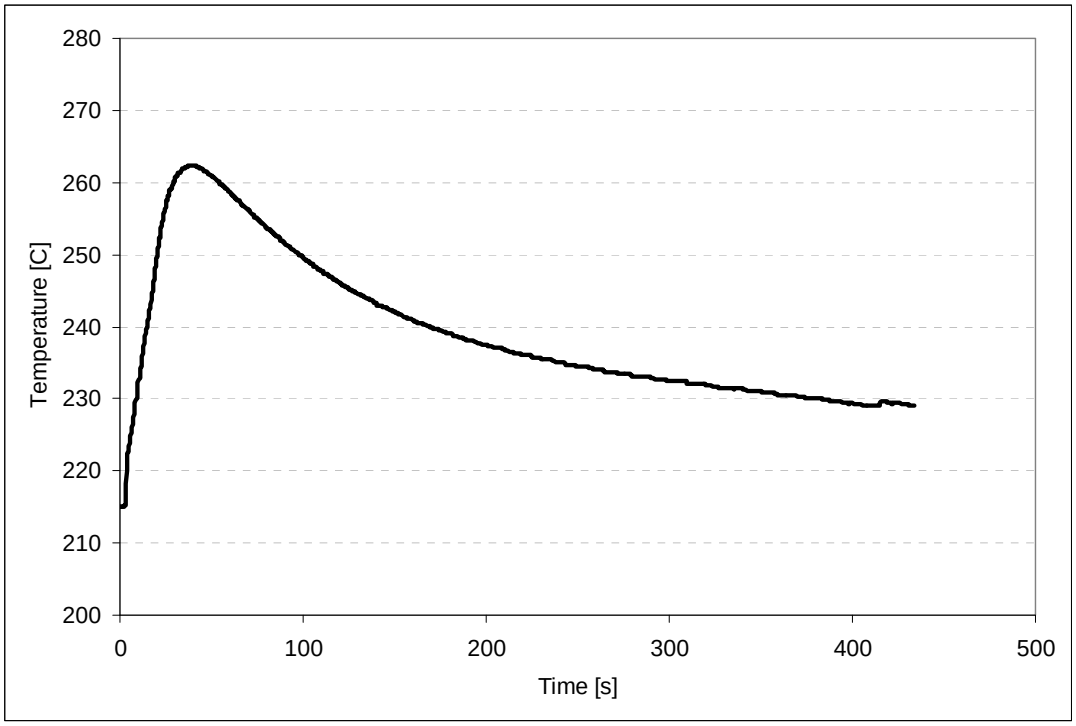

Figure 157: Temperature history of in-mold thermocouple near the critical region.

Chapter 6 – Conclusions

The results of this study indicate that the hot tearing susceptibility of permanent mold cast AZ91D and AE42 magnesium alloys can be manipulated by suitably adjusting the mold temperature. For an AZ91D alloy poured at 720 °C, the onset of hot tearing occurred between 210 °C and 250 °C mold temperatures. For an AE42 alloy poured at 765 °C, the onset of hot tearing occurred between 340 °C and 390 °C mold temperatures.

The fundamental mechanisms associated with the onset of hot tearing in the two magnesium alloys were identified as follows:

AZ91D Alloy

Hot tears nucleated in the skin region, where the ductility of the semi-solid material was limited. Nucleation of microcracks occurred at a stress concentration (90° corners of the junction of the horizontal bar and the downsprue). At the top edge corner, a tensile stress of 8 – 12 MPa developed. Subsequent thermal contraction of the casting and evolution of shrinkage porosity further increased the tensile stress in the critical region of the material to ~31 – 45 MPa. The tensile stresses exceeded the yield strength of the semisolid alloy and shrinkage porosity was followed by nucleation and propagation of a hot tear. The axial contractions of the horizontal bar and the downsprue provided energy to propagate the hot tear.

As the mold temperature increased, the size of the interdendritic feeding paths increased and long range interdendritic feeding of the casting improved. Thus, feeding compensated the casting's volumetric contraction. As a result, the magnitude of tensile stresses in the critical region decreased to ~ 17 MPa. This tensile stress, acting near the 90° corner, nucleated isolated pockets of interdendritic shrinkage porosity; however, the stress was not sufficient to nucleate or propagate hot tears.

Development of tensile ε_x strain along the horizontal bar was observed for both AZ91D castings. The ε_y and ε_z strains remained compressive. In the 210 °C mold temperature casting, the tensile ε_x strain at the 90° corner reached ~ 0.0005 – 0.0006 mm/mm. Upon increasing the mold temperature, the tensile ε_x strain in this region marginally decreased to ~ 0.0004 – 0.0005 mm/mm. Thus, ε_x strain due to the shrinkage and contraction of the horizontal bar remained a dominant factor in potential damage initiation in the critical casting region. With the increase of the mold temperature, however, the ε_y and ε_z strains became more compressive. The increased compression in the latter two directions resulted in the lowering of the net principal stresses in the critical region, as discussed above.

AE42 Alloy

Castability of the AE42 alloy was seen to be impeded by the presence of rare earth elements. The presence of acicular $Al_{11}RE_3$ intermetallic compound pinning the grain boundary increased the alloy's susceptibility to hot tearing by decreasing the alloy's ductility. Hot tears nucleated at the 90° corners of the casting and propagated in the direction of the maximum stress gradient. The $Al_{11}RE_3$ phase strengthened interdendritic bonds, diverting hot tear propagation to the grain boundaries. The presence of the $Al_{11}RE_3$ phase was further seen to hinder interdendritic feeding of the casting at high fractions of solid. When hot tears formed, the tensile strain at the 90° corner reached 0.0009 mm/mm.

As the mold temperature increased, a fraction of the acicular $Al_{11}RE_3$ phase was observed to transform into particulate Al_2RE. Consequently, the permeability of the interdendritic regions improved. As a result, the tensile residual strain decreased to 0.0007 mm/mm. In the AE42 alloy, shrinkage porosity was not observed to play a fundamental role on hot tearing. Instead, the rate of solidification shrinkage and thermal contraction appeared to influence formation of hot tears and grain boundary cracking.

Additional conclusions of the research were as follows:

1. Grain size analysis revealed that the AZ91D casting at the onset of hot tearing had a grain size between 80 – 120 μm. In the case of the AE42 alloy, the grain size was 400 – 1100 μm. Further, it was observed that the casting skin regions had finer grains, possibly columnar, while the bar's center had large equiaxed grains. These observations suggest that the semi-solid AZ91D alloy was possibly stronger (due to grain-boundary strengthening) than the AE42 alloy. Thus, the AZ91D alloy was capable of bearing greater load at the onset of hot tearing than the AE42 alloy.
2. In the case of the AZ91D alloy, the mold temperature of 250 °C possibly induced a critical casting cooling rate (~ 10 °C/s) when healing of incipient hot tears became possible and interdendritic liquid remained mobile in the interdendritic channels. Transformation of the $Mg_{17}Al_{12}$ intermetallic from partially to a fully divorced structure also likely enhanced interdendritic liquid flow and possible healing of shrinkage pores and hot tears.
3. Formation of interdendritic shrinkage porosity was related to the mobility of interdendritic liquid during solidification. Microstructural analysis of the AZ91D alloy revealed formation of interconnected shrinkage porosity networks, suggesting long-range continuity of the interdendritic liquid. In the case of the AE42 alloy, the shrinkage pores were isolated, indicating absence of a continuous film on the grain boundaries. For both alloys, increasing the mold temperature increased the volume and long-range continuity of the interdendritic liquid.

4. Formation of centerline shrinkage porosity was related to inhomogeneous casting contraction. MAGMASOFT® simulations confirmed development of a significant hoop solidification rate. As a result, at low mold temperatures, inadequate axial feeding of the horizontal bar promoted formation of centerline shrinkage porosity.
5. Formation of fold defects in the AZ91D alloy was related to the entrapment of MgO in the casting interior. This oxide formed a physical barrier between merging metal streams, thus preventing their proper fusion. In the AE42 alloy, segregation of Al_2RE intermetallics at the leading-edge of the advancing metal front created a microstructural incompatibility across the fold and prevented proper fusion of merging metal streams.
6. In the AZ91D alloy, crystallographic texture did not develop in castings produced at mold temperatures between 220 °C – 380 °C.
7. Lack of accurate knowledge of the governing mechanisms during high-temperature deformation of the AZ91D or AE42 alloys (e.g., porosity evolution or microstructure contribution to material failure) were seen to influence the validity of numerical simulations of casting stress and deformation.
8. Calculation of the vulnerable interval between ZST and ZDT revealed unique behavior of magnesium alloys at the end of solidification. Typically, short duration of this critical interval is desired. However, in the AZ91D and AE42 alloys, an increase of the mold temperature (to eliminate hot tears) corresponded to an increase of the ZST – ZDT interval. Thus, in the case of magnesium alloys, the rate of casting shrinkage within this interval is possibly more critical than the absolute duration of the interval.
9. The vonMises criterion was demonstrated to be unsuitable for prediction of alloy failure at the onset of hot tearing. Thus, instead of using traditional criterion functions based on principal stresses (e.g., vonMises, Tresca) to predict material failure at the onset of hot tearing, a new approach based on the maximum allowable strain should be developed. A strain criterion may be preferred, since the constitutive relationships between stress and strain in the semi-solid region are not well established for magnesium alloys.

Chapter 7 – Recommendations for Future Work

This research provided the foundation for continuation of research into the hot tearing behavior of magnesium alloys. As this research was focused only on the fundamental aspects of hot tear nucleation, several additional factors should be investigated in order to gather additional information about the onset of hot tearing. For example:

1. Perform *in-situ* ND strain measurements to determine dynamic strain evolution in a casting during solidification.
2. Perform ND strain mapping on a casting while in the mold, in order to determine the degree of stress relaxation due to casting removal from the mold.
3. Implement real-time X-ray tomography to observe evolution of hot tears during alloy solidification.
4. Investigate the impact of casting geometry (e.g., geometry of stress concentrations) on an alloy's tendency for hot tearing.
5. Test the predictive capability of classical hot tearing criterion functions to validate the current results.
6. Perform transmission electron microscopy to identify and study the role of intermetallic inclusions on liquid feeding at late stages of solidification.
7. Develop new methods to carry out high temperature mechanical testing of alloys in the semi-solid state.
8. Develop new models or criterion functions to be implemented in numerical simulation software to predict the onset of hot tearing.
9. Investigate the effect of microstructure modifying techniques (e.g., grain refinement) on manipulating an alloy's tendency for hot tearing.
10. Perform hot tearing studies with additional magnesium or aluminum alloys in order to study the impact of specific alloy characteristics on the hot tearing tendency.

References

1. Eskin, D. G., Suyitno, Katgerman, L., "Mechanical properties in the semi-solid state and hot tearing of aluminum alloys", Progress in Materials Science, Vol. 49**,** 2004, pp. 629 – 711.

2. Hort, N., Dieringa, H. and Kainer, K. U., "Hot tearing of magnesium alloys", Transactions of the Indian Institute of Metals, Vol. 58, No. 4, 2005, pp. 703 – 708.

3. Wang, Y., Sun, B., Wang, Q, Zhu, Y. and Ding, W., "An understanding of the hot tearing mechanism in AZ91 magnesium alloy", Materials Letters, Vol. 53, 2002, pp. 35-39.

4. Sigworth, G.K., "Hot tearing of metals", AFS Transactions, Vol. 104, 1996, pp. 1053 – 1062.

5. Rappaz, M., Drezet, J. M. and Gremaud, M., "A new hot-tearing criterion", Metallurgical and Materials Transactions, Vol. 30A(2), 1999, pp. 449 – 455.

6. Gruzleski, J. E., Microstructure development during metalcasting, American Foundry Society, Inc., Des Plaines, IL, 2000, p. 109.

7. Chojecki, A., Telejko, I. and Bogacz, T., "Influence of chemical composition on the hot tearing formation of cast steel", Theoretical and Applied Fracture Mechanics, Vol. 27, 1997, pp. 99 – 105.

8. Borland, J.C., "Generalized theory of super-solidus cracking in welds and castings", British Welding Journal, Vol. 7, 1960, pp. 508 – 512.

9. Clyne, T. W. and Davies, G. J., "A comparison of experimental results and theoretical predictions relating to dependence of solidification cracking on composition", The Metals Society, 1979, pp. 275 – 278.

10. Campbell, J., Castings, Butterworth-Heinemann, 1991, pp. 173 – 174.

11. Forest, B. and Bercovici, S., "Solidification technology in the foundry and casthouse", The Metals Society, 1983, pp. 607 – 612.

12. Prokhorov, N. N. and Bochai, M. P., Svarochnoe Proizvodstvo, Vol. 2, 1958, pp. 1 – 2.

13. Metz, S. A. and Flemings, M. C., "A fundamental study of hot tearing", AFS Transactions, Vol. 78, 1970, pp. 453 – 460.

14. Novikov, I. I., Goryachelomkost tsvetnykh metallov i splavov (Hot shortness of non-ferrous metals and alloys), Nauka, Moscow, USSR, 1966.

15. Belov, N. A., Aksenov, A. A. and Eskin, D. G., Iron in aluminum alloys: impurity and alloying element, London: Taylor and Francis, 2002.

16. Qingchun, L., Songyan, Z. and Chi, L., "Study of material properties of Al-Cu alloys in semi-solid state during solidification", in Proceedings of the 7th International Conference on Strength of Metals and Alloys, Montreal, Canada, Pergamon Press, Vol. 2, 1985, pp. 1651 – 1656.

17. Instone, S., St.John, D. and Grandfield, J., “New apparatus for characterizing tensile strength development and hot cracking in the mushy zone“, International Journal of Cast Metals, Vol. 12, 2000, pp. 441 – 456.
18. Dahle, A. K., Lee, Y. C., Nave, M. D., Schaffer, P. L. and StJohn, D. H., “Development of the as-cast microstructure in magnesium-aluminum alloys”, Journal of Light Metals, Vol. 1, No. 1, 2001, pp. 61 – 72.
19. Singer, A.R.E. and Cottrell, S.A., “Properties of the Al-Si alloys at temperatures in the region of the solidus”, Journal of Institute of Metals, Vol. 73, 1946, pp. 33 – 54.
20. Pumphrey, W.I. and Jennings, P.H., “A consideration of the nature of brittleness above the solidus in castings and welds in aluminum alloys”, Journal of Institute of Metals, Vol. 75, 1948, pp. 235 – 256.
21. Mukai, T., Yamanoi, M., Watanabe, H. and Higashi, K., “Ductility enhancement in AZ31 magnesium alloy by controlling its grain structure”, Scripta Materialia, Vol. 45, 2001, pp. 89 – 94.
22. Monroe, C. and Beckermann, C., “Development of a hot tear indicator for steel castings”, Materials Science and Engineering A, Vol. 413, 2005, pp. 30 – 36.
23. Novikov, I. I. and Novik F. S., “Mechanism of plastic deformation of alloys in the range of melting temperatures“, Doklady Akademie Nauk SSSR, Ser. Fiz., Vol. 7, 1963, pp. 1153 – 1155.
24. Prokhorov, N. N., Russian Casting Production, Vol. 2, 1962, pp. 172 – 175.
25. Pellini, W. S.,”Strain theory of hot tearing”, Foundry, Vol. 80, 1952, pp. 125 – 199.
26. Williams, J. A., Singer, A. R. E., “Deformation, strength and fracture above the solidus temperature”, Journal of Institute of Metals, Vol. 96, 1968, pp. 5 – 12.
27. Patterson, K., Giesserei, Vol. 40, No. 12, 1953, pp. 597 – 605.
28. Fredriksson, H., Haddad-Sabzevar, M., Hansson, K. and Kron, J., “Theory of hot crack formation”, Materials Science and Technology, Vol. 21, No. 5, 2005, pp. 521 – 529.
29. Suyitno, Eskin, D.G. and Katgerman, L., “Structure observations related to hot tearing of Al-Cu billets produced by direct-chill casting”, Materials Science and Engineering A, Vol. 420, 2006, pp. 1 – 7.
30. Sun, Z., “A study of solidification crack susceptibility using the solidification cycle hot-tension test”, Materials Science and Engineering A, Vol 154, 1992, pp. 85 – 92.
31. Cao, G. and Kou, S., “Hot cracking of binary Mg-Al alloy castings”, Materials Science and Engineering A, Vol. 417, 2006, pp. 230 – 238.
32. Wang, Y.., Wang, Q., Wu, G., Zhu, Y. and Ding, W., “Hot-tearing susceptibility of Mg-9Al-xZn alloy”, Materials Letters, Vol. 57, 2002, pp. 929 – 934.
33. Cao, G. and Kou, S., “Hot cracking susceptibility of ternary Mg-Al-Ca alloys”, Advanced Materials Research, Vols. 15-17, 2007, pp. 501 – 506.

34. Tang, B., Li, S.-S., Wang, X.-S. and Rong Wu, D.-B.Z, "An investigation on hot-crack mechanism of Ca addition into AZ91D alloy", Journal of Materials Science, Vol. 40, 2005, pp. 2931 – 2936.
35. Weichao, Z., Shuangshou, L., Bin, T., Daben, Z. and Xutao, G., "Effect of rare earths on hot cracking resistant property of Mg-Al alloys", Journal of Rare Earths, Vol. 24, 2006, pp. 346 – 351.
36. Pekguleryuz, M. O. and Vermette, P., "A study on hot-tear resistance of magnesium diecasting alloys", AFS Transactions, Vol. 115, 2006, pp. 1 – 8.
37. Datta, G.I. and Karunakar, D.B., "A study on the hot tearing in Al-1%Sn cast alloys", Proceedings of the Institute of Mechanical Engineers, Vol. 220-B7, 2006, pp. 1131 – 1139.
38. Singer, A.R.E. and Jennings, P.H., "Hot shortness of the Aluminum-Silicon alloys of commercial quality", Journal of Institute of Metals, Vol. 73, 1947, pp. 197 – 212.
39. Warrington, D. and McCartney, D.G., "Determination of strain during hot tearing by image correlation", Cast Metals, Vol. 2, No. 3, 1989, pp. 134 – 143.
40. Novikov, I.I. and Grushko, O.E., "Hot cracking susceptibility of Al-Cu-Li and Al-Cu-Li-Mn alloys", Material Science Technology, Vol. 11, 1995, pp. 926 – 932.
41. Davidson, C., Viano, D., Lu, L. and StJohn, D., "Observation of crack initiation during hot tearing", International Journal of Cast Metals, Vol. 19, No. 1, 2006, pp. 59 – 65.
42. Farup, I., Drezet, J.-M. And Rappaz, M., "In-situ observation of hot-tearing formation in succinonitile-acetone", Acta Materialia, Vol. 49, 2001, pp. 1261 – 1269.
43. Dickhaus, C.G., Ohm, L. and Engler, S., "Mechanical properties of solidifying shells of aluminum alloys", AFS Transactions, Vol. 101, 1993, pp. 677-684.
44. Healey, A., Transactions of the Institute of Rubber Industries, Vol. 44, 1926, p. 334.
45. Lahaie, D.J. and Bouchard, M., "Physical modeling of the deformation mechanism of semisolid bodies and a mechanical criterion for hot tearing", Metallurgical and Materials Transactions B, Vol. 32B, 2001, pp. 697 – 705.
46. Zhao, L., Baoyin Wang, N., Sahajwalla, V. and Pehlke, R.D., "The rheological properties and hot tearing behaviour of Al-Cu alloy", International Journal of Cast Metals Research, Vol. 13, No. 3, 2000, pp. 167 – 174.
47. Magnin, B., Maenner, L., Katgerman, L. and Engler, S., "Ductility and rheology of Al-4.5%Cu alloy from room temperature to coherency temperature", Materials Science Forum, Vol. 1209, 1996, pp. 217 – 222.
48. Suyitno, Kool, W.H. and Katgerman, L., "Micro-mechanical model of hot tearing at triple junctions in DC casting", Materials Science Forum, Vols. 396 – 402, 2002, pp. 179 – 184.

49. Niyama, E., in: "Japan-US joint seminar on solidification of metals and alloys", Tokyo, Japan Society for Promotion of Science, 1977, pp. 271 – 282.
50. Feurer, U., "Matematisches Modell der Warmribneigung von binaren Aluminiumlegierungen", Geisserei-forschung, Vol. 28, 1970, pp. 75 – 80.
51. Schneider, M. C. and Andersen, S., "The simulation to analyze macrosegregation, hot tears, heat treatment in steel castings", Modern Casting, Vol. 90, No. 5, 2000, pp. 39 – 43.
52. Squires, G. L., Introduction to the theory of thermal neutron scattering, Dover Publications Inc., Mineola, New York, 1978, pp. 2 – 10.
53. Mura, T., Micromechanics of defects in solids, Martinus Nijhoff Publishers, The Hague, Netherlands, 1982, p. 1 (accessed online via: books.google.ca, January 2007).
54. Fitzpatrick, M. E. and Lodini, A., Analysis of residual stress by diffraction using neutron and synchrotron radiation, Taylor and Francis, London, 2003, pp. 47 – 48.
55. Egner-Walter, A. and Olive, S., "Using stress simulation to tackle distortion and cracking in castings", MAGMA GmbH, Aachen, Germany, 2008, pp. 1 – 13.
56. Gharghouri, M., The 9th Summer School on Neutron Scattering, Canadian Neutron Beam Centre, Chalk River Laboratories, June 5 – 8, 2006, pp. 1 – 30.
57. Cullity, B.D., Elements of X-ray Diffraction, Addison-Wesley Publishing Co., 1956, p. 433.
58. Machinery's handbook, 5th Ed., New York, Industrial Press, The Machinery Publishing Company, Ltd., 1920, p. 798.
59. Fruehling, J. W. and Hanawalt, J. D., "Protective atmospheres for melting magnesium alloys", AFS Transactions, Vol. 77, 1969, pp. 159 – 164.
60. Rogge, R. B., Holden, T. M. and Root, J. H., "Standard diffractometer set-up procedure for applied neutron diffraction for industry experiments", Atomic Energy of Canada Ltd. (AECL), RC-1652 / ANDI, 1996, pp. 1 – 16.
61. Avedesian, M. and Baker, H., Magnesium and magnesium alloys, ASM International, Materials Park, OH, 1999 .
62. Root, J., "POLCON Software", ANDIware CD-Rom, 2008.
63. Rogge, R., "Fitting algorithm and uncertainty determination", ANDIware CD-Rom, 2008, p. 1.
64. Gharghouri, M., "Gaussian fitting program output", ANDIware CD-Rom, 2008, pp. 1 – 3.
65. Tacke, K., Grill, A., Miyazawa, K. and Schwerdtfeger, K., "Macrosegregation in strand cast steel: computation of concentration profiles with a diffusion model", Arch. Eisenhuttenwes, Vol. 52, No. 1, 1981, pp. 15 – 20.

66. Bichler, L., Lee, K., Elsayed, A. and Ravindran, C., "Effect of mold and pouring temperature on the hot tearing of AZ91 magnesium alloy", International Journal of Metalcasting, Vol. 1., No. 2, 2008, pp. 43 – 56.
67. Bichler, L., D'Elia, F. and Ravindran, C., "Reduction of hot tears in AZ91 magnesium alloy: effect of cooling rate", AFS Transactions, Vol. 117, 2008, Paper 08-109.
68. Emley, E.F., Principles of Magnesium Technology, Pergamon Press, London, UK, 1966.
69. Nave, M.D., Dahle, A. K. and StJohn, D.H., "Eutectic growth morphologies in Magnesium-Aluminum alloys", Magnesium Technology 2000, TMS, 2000, pp. 233 – 242.
70. Bakke, P. and Westengen, H., "Die casting for high performance – Focus on alloy development", Advanced Engineering Materials, Vol. 5, No. 12, 2003, pp. 879 – 885.
71. Anyanwu, I. F., Gokan, Y., Suzuki, A., Kamado, S., Kojima, Y., Takeda, S. and Ishida, T., "Effect of substituting cerium-rich mischmetal with lanthanum on high temperature properties of die-cast Mg-Zn-Al-Ca-RE alloys", Materials Science and Engineering A, 2004, pp. 93 – 99.
72. Zhu, S. M., Gibson, M. A., Nie, J. F., Easton, M. A. and Abbott, T. B., "Microstructural analysis of the creep resistance of die-cast Mg-4Al-2RE alloy", Scripta Materialia, Vol. 58, 2008, pp. 477 – 480.
73. Powell, B. R., Rezhets, V., Balogh, M. P. and Waldo, R. A., "Microstructure and creep behavior in AE42 magnesium die-casting alloy", JOM, 2002, pp. 34 – 38.
74. Arnberg, L., Backerud, L. and Chai, G., in Solidification characteristics of aluminum alloys, Vol. 3: Dendrite coherency, AFS, Des Plaines, IL., 1996, pp. 28 – 59.
75. Barber, L. P., "Characterization of the solidification behavior and resultant microstructures of magnesium-aluminum alloys", MASc. thesis, McMaster University, 2004, pp. 1 – 108.
76. Sediako, D., Sediako, O. and Lin, K. J., "Some aspects of thermal analysis and technology upgrading in steel continuous casting", Canadian Metallurgical Quarterly, Vol. 38, No. 5, 1999, pp. 377 – 386.
77. Seol, D. J., Wok, Y. M., Oh, K. H., Shin, Y.C. and Yim, C. H., "Mechanical behavior of carbon steels in the temperature range of mushy zone", ISIJ International,Vol. 40, No. 4, 2000, pp. 356 – 363.
78. Won, Y. M., Kim, K. H., Yeo, T. J. and Oh, K. H., "Effect of cooling rate on ZST, LIT and ZDT of carbon steels near melting point", ISIJ International, Vol. 38, No. 10, 1998, pp. 1093 – 1099.
79. Wolf, M., Hiebler, H., Zirngast, J. and Bernhard, C.,"Inner crack formation in continuous casting: stress or strain criterion?", Proc. 77th Steelmaking Conference, Chicago, 1994, pp. 405 – 416.
80. Bichler, L., Ravindran, C. and Sediako, D., "Onset of hot tearing in AE42 magnesium alloy", Canadian Metallurgical Quarterly (Accepted: November, 2008).
81. Gharghouri, M., Weatherly, G., Embury, J. and Root, J., "Study of the mechanical properties of Mg-7.7at.% Al by in-situ neutron diffraction", Philosophical Magazine,Vol. 79, 1997, pp. 1671 – 1695.

82. Barnett, M. R.,"Twinning and the ductility of magnesium alloys: Part I: "Tension" twins", Materials Science and Engineering A, Vol. 464, 2007, pp. 1 – 7.
83. Bichler, L., Ravindran, C. and Sediako, D.,"Neutron diffraction measurement of strain required for the onset of hot tearing in AZ91D magnesium alloy", Transactions of the Indian Institute of Metals, Vol. 61, No. 3, 2008, pp. 1 – 8.
84. Yang, M., Pan, F., Zhang, J. and Zhang, J., Mat. Sci. Forum, Magnesium: Science, Technology and Applications, Vol. 488-489, 2005, pp. 923 – 926.
85. Hu, H., Yu, A., Li, N. and Allison, J. E., Materials and Manufacturing Processes, Vol. 18, No. 5, 2003, pp. 687 – 717.
86. Ravi Kumar, N. V., Blandin, J. J., Suery, M. and Grosjean, E., "Effect of alloying elements on the ignition resistance of magnesium alloys", Scripta Materialia, Vol. 49, 2003, pp. 225 – 230.
87. Bichler, L., Lee, K., Elsayed, A. and Ravindran, C., "Effect of mold temperature and pouring temperature on hot tearing of AZ91D magnesium alloy", Materials Science and Technology, ASM/TMS Conference, Detroit, MI, September 16 - 18, 2007.
88. Bichler, L., Ravindran, C. and Sediako, D., "Stress and strain evolution at the onset of hot tearing in AZ91D magnesium alloy", Metallurgical and Materials Transactions A (Submitted: January 2009).
89. Cizek, L., Greger, M., Dobrzanski, L. A., Juricka, I., Kocich, R., Pawlica, L. and Tanski, T., "Mechanical properties of magnesium alloy AZ91 at elevated temperatures", Journal of Achievements in Materials and Manufacturing Engineering, Vol. 18, No. 1 – 2, 2006, pp. 203 – 206.
90. Private communication with Dr. D. Sediako, September 2008.
91. Dieter, G., Mechanical Metallurgy, 2nd Ed., McGraw-Hill, 1976, p. 487.
92. Flender, E. and Hartmann, G., "Modeling and simulation in high pressure die casting", MAGMA GmbH, Aachen, Germany, 2008, pp. 1 – 18.
93. Hartmann, G. and Sturm, J. C.,"Optimized development of die casting and die casting processes" MAGMA GmbH, Aachen, Germany, 2008, pp. 1 – 14.
94. Hattel, J., Fundamentals of numerical modelling of casting processes, Polyteknisk-Forlag, 2005, pp. 327 – 351.
95. MAGMASOFT® 4.4 Manual, MAGMA GmbH, Aachen, Germany, 2002.
96. Murphy, J.D., "Turbulence modelling", in Cheremisinoff, N. P. (ed.), Encyclopedia of Fluid Mechanics - Complex Flow Phenomena and Modelling, Vol. 6, Gulf Publ. Co, Houston, 1987, pp. 1131 – 1151.
97. Hartmann, G. and Egner-Walter, A. in: "Fertigungsoptimierung dunnwandiger Gussteile aus Leichtmetall", Vortrag auf dem Internationale Deutschen Druckgasstag, Dusseldorf, 2005, pp. 1 – 13.

98. Egner-Walter, A. and Hartmann, G., “Closing the gap between CAE supported design and manufacturing simulation”, MAGMA GmbH, Aachen, Germany, 2008, pp. 1 – 18.
99. Sturm, J., Hepp, E. and Egner-Walter, A.,“Integration of casting simulation into crash simulation”, MAGMA GmbH, Aachen, Germany, 2008, pp. 1 – 6.
100. Sediako, D., MacDonald, W. and Hibbins, S., “Mould thermal analysis in direct-chill casting of magnesium alloys”, Magnesium Technology 2008, TMS, 2008, pp. 215 – 219.
101. Barone, M. R. and Caulk, D. A., “Analysis of liquid metal flow in die casting”, International Journal of Engineering Science, Vol. 38, 2000, pp. 1279 – 1302.

Appendix 1 - MAGMASOFT® Numerical Simulation of the Casting Process

A1.1 Software Overview

Commercial programs for simulation of casting processes have been on the market for nearly 20 years. Performance and credibility of software simulations has expanded and improved over this period. For example, the majority of steel castings and high-volume part casting processes have been extensively optimized with the help of numerical simulations [92]. As a result, casting process simulations have gained wide acceptance and have become an important tool of quality assurance programs [93].

Currently, MAGMASOFT® is the state-of-the-art numerical simulation and modeling software for casting processes. MAGMASOFT® is a computational fluid dynamics software with several modules developed specifically for the metalcasting industry. It is the most frequently used software in the foundry and casting industries. As a result, MAGMASOFT® was used to carry out computer simulations in this research.

Literature describing the fundamental theories used in MAGMASOFT® modeling was obtained privately from Magma Foundry Technologies, Inc. (MFT). It is beyond the scope of this dissertation to describe, in detail, the simulation methodologies and mathematical algorithms involved in MAGMASOFT®. In addition, this information is a trade secret of MFT and is not publicly available. As a result, the current section provides an introduction and an overview of the software and the physical and mathematical models implemented in MAGMASOFT®. Much of the information provided in this chapter has been obtained in confidence from MFT in the form of software manuals. Also, Reference 94 – "Fundamentals of Numerical Modelling of Casting Processes" by J. Hattel has been used extensively in this section. This reference was written by one of the developers of MAGMASOFT® and thus describes, in extensive detail, the mathematical models used in the software.

For the purposes of this research, MAGMASOFT® was used as an engineering tool. Thus, extensive numerical modeling and optimization were *not* intended. As a result, only the fundamental details pertinent to the simulations are described herein. The reader is encouraged to consult Reference 94 for detailed information regarding mathematical formulations and simulation methodologies, if necessary.

In order to run a casting simulation, the following steps need to be carried out [92]:

1. **3D modeling**

   The first step in a simulation is to create a three-dimensional model of the casting, mold and other relevant casting process features (e.g., runners, vents, flow gates, etc.).

2. **Meshing**

   The complete 3D model is meshed. The mesh is generated automatically in MAGMASOFT® and results in elements with finite volume. Subsequently, the mesh may be manually refined in critical casting areas. However, the mesh must be constructed such that there are at least three elements side-by-side through a wall thickness. The completion of the 3D model and the enmeshment are known as 'pre-processing'.

3. **Predefinition of the process parameters**

   The required process parameters, such as the melt and mold temperatures and the chronological sequence of the casting process (e.g., ejection of the casting from the mold) must be specified. Further, boundary and initial conditions must be defined.

4. **Execution (solving) of the simulation**

5. **Evaluation of the results**

   'Post-processor' prepares the simulation results (e.g., tables, images, videos, etc.).

Outline of the simulation solution methodology performed by MAGMASOFT® follows. This information was obtained from References 94 and 95.

The governing equations of the simulation are solved using a numerical method called the "Cartesian cut-cell technique". In this method, the domain of calculations is subdivided into a non-uniform, multi-material mesh of Cartesian elements, as illustrated in Figure A1. 1 [95]. The figure also shows the real geometry of the casting that cuts the Cartesian mesh in an arbitrary way. In this manner, the real boundary of the casting marks two sides of the mesh: i) the mold side and, ii) the casting side (the elements of the melt have dots in their centers).

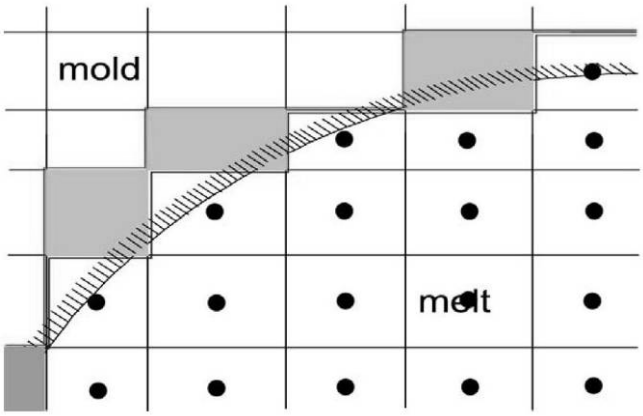

Figure A1. 1: Example of a Cartesian mesh [95].

The mesh elements through which the real boundary passes are called “cut-cells” and are formed by the mold and the melt material. MAGMASOFT® solver uses a unique approach to deal with cut-cells. The division of the cell is modeled using volume and surface correction factors called “porosities”. Two kinds of porosities are defined in MAGMASOFT®:

1. Volume porosity – defined as the ratio of the melt volume inside an element to the entire geometrical volume of the Cartesian element.

2. Surface porosity – defined as the ratio of the surface of an element available for the melt to the total surface area of the Cartesian element.

The surface and volume porosities are introduced into the transport equations. Surface porosities are used while calculating fluxes of mass, momentum and energy. Volume porosity factors are used to calculate volume integrals involved in the governing equations.

MAGMASOFT® further includes two important models for the simulation of solidifying metal flow during mold filling [92]:

Viscosity Model

The solver implements a variable viscosity model, where the temperature-dependent melt viscosity for each mesh element is calculated from the fraction solid of the element and the viscosity value at the liquidus temperature. Above the liquidus temperature, the viscosity variation is neglected and assumed constant.

Wall Friction Model

The friction force acting upon the liquid melt at the mold wall is one of the major opposing forces to the advancing liquid metal. The friction force is proportional to the melt surface area in contact with the mold wall and is calculated using the surface porosities. The resulting friction force is introduced into the momentum differential equations.

A1.2 Mathematical and Physical Models of Simulation

Detailed description of the MAGMASOFT® simulation software is beyond the scope of this thesis. Further, the computational algorithms involved in the simulations are proprietary trade secret of MFT.

The objective of performing casting simulations was to assist in the understanding of mold filling, temperature distribution, stress evolution and casting deformation during casting solidification. These quantities were derived from the solution of the three dimensional Navier-Stokes differential equations of momentum, energy and continuity. Stress and deformation of the casting were calculated in the MAGMA*stress*® module, which used the computed 3D temperature field as a boundary condition to determine thermal stresses.

Derivation of the general Navier-Stokes equations implemented in MAGMASOFT® is presented in Reference 94. As MAGMASOFT® modeling was not a primary focus of this research, detailed derivations and software development analysis are not presented. However, a summary of the key mathematical models is presented in the following text:

Momentum Equation (Mold Filling)

Momentum differential equation describes the momentum of a fluid through an infinitesimal finite volume. The equation considers the change of momentum in and out of the control volume via convection, which originates from the bulk motion of the fluid. Also, surface and body forces acting on the control volume are included in the equation. For the current project, mold filling under gravity conditions was simulated. Therefore, the surface forces consider atmospheric pressure.

For simulation of molten metal flow, the momentum equation was modified to account for melt turbulence. Turbulence of a flow significantly influences momentum, heat and mass transfer, chemical reactions and transport of species. Attributes intrinsic to the turbulent phenomena are: three-dimensionality, time dependence, anisotropy and non-linearity [96]. To model the velocity field during mold filling, MAGMASOFT® approximates flow turbulence via the time averaged Reynolds's equation using the k-ε method. In this method, the turbulence eddies may be considered as lumps of fluid, which collide and exchange momentum. Detailed analysis of turbulent phenomena in casting simulations is beyond the scope of this thesis. Additional details may be obtained from Reference 94.

The three dimensional momentum equation was solved in coupled mode with the heat conduction equation in order to consider the heat loss of the melt during mold filling and subsequent density and viscosity change of the advancing melt. The algorithm associated with this numerical solution is a trade secret of MFT.

Energy Equation (Alloy Solidification)

The total energy of a system consists of its internal and kinetic energy. In PMC of alloys, the kinetic energy contribution to the total energy is much smaller than the internal energy. However, for example, in the case of HPDC simulations, the molten metal acquires high velocities and its kinetic energy can not be neglected [94]. In principle, the energy equation states, that the rate of accumulation of internal and kinetic energy is equal to the net rate of inflow of internal and kinetic energy by convection, plus the net rate of heat addition by conduction and radiation, minus the net rate of work done by the system on surroundings plus the strength of the internal heat sources/sinks.

In the case of PMC simulations, simplifying conditions may be invoked during solution of the energy equation: i) work done against gravity is negligible, and ii) rate of work done against static pressure is negligible.

The thermal energy equation was used to obtain the three dimensional temperature distribution in the casting during filling. Also, the local solidification time, cooling rate and temperature gradients were obtained. The calculation domain included the casting as well as the steel mold. Further, the values of the effective transport parameters (e.g., thermal conductivity, viscosity, etc.) were varied according to the fraction of solids development in the melt. As a result, the level of contact between the casting and the surrounding mold (given by the relative expansions / contractions of these two simulation domains) was considered by the model. However, a specific value indicating the level of contact between the casting and the mold was not assigned.

Continuity Equation

The mass conservation principle states that the change of mass within a control volume over an incremental time is equal to the mass entering less the mass leaving the control volume. The main parameter governed by the continuity equation is the alloy density, ρ.

A1.2.1 Models for Calculation of Solidification Stresses

The major impediment to modeling residual stresses in casting simulations is the absence of experimentally validated laws describing material behavior at high temperatures. The phenomena occurring at high temperatures, such as creep and the formation of an air gap at the casting-mold interface (causing a reduction of contact between mold wall and the casting) are not known with the desired accuracy [97].

Thus far, the most accurate residual stress predictions were achieved with iron castings. The good correlation between simulated and experimental castings was related to the extensive knowledge of microstructure development in irons, since the microstructure governs the mechanical response of the alloys.

In the case of aluminum and magnesium alloys, only limited success was achieved in predicting residual stresses. Successful modeling of casting stress evolution in light alloys is hindered by the formation of micro- and macro defects (e.g., porosity), which have a strong influence on the resultant casting mechanical response. These defects impact the strength of the alloy more than the microstructure alone. As a result, since the formation of these casting defects can not be accurately predicted yet, the overall accuracy of the stress simulations remains questionable [98].

The calculation of residual stresses is typically carried out in a decoupled two-stage process. Stress calculations are carried out in a separate module called MAGMA*stress*®, where the 3D temperature field determined from MAGMASOFT® solidification simulation is taken as an external boundary condition to calculate thermo-plastic response of the casting. Stress development is modeled in relation to restraints imposed by the mold, as well as temperature inhomogeneities in the casting [99].

MAGMA*stress*® calculations consider the following phenomena [94]:

1. Solidification
2. Thermomechanical response of the casting
3. Shrinkage-dependent interfacial heat transfer
4. Mold distortion
5. Temperature and time-dependent plasticity

The stress calculation also considers the dimensional restriction imposed on the casting by the surrounding mold. The combined effects are modeled in MAGMASOFT® via non-linear, temperature dependent elasto-plastic approach with isotropic hardening in the alloy [98]. It is suggested the reader consults pages 343 – 483 of Reference 94 for detailed explanation of the above concepts and relevant theories of stress modeling during alloy solidification.

A1.2.2 MAGMAdatabase®

The validity of any casting simulation largely depends on the accuracy of material properties for the entire simulation temperature range. For this purpose, MAGMASOFT® implements a proprietary database

developed by MFT, which contains information about popular commercial alloys used in HPDC, PMC and sand casting processes. The MAGMA*database*® is accumulated from data from various reputable sources that are based on the best available scientific methods and knowledge.

For simulation experiments, the MAGMA*database*® was used as a source of material and property data. Specifically, the following were used:

1. Density: Expressed as a function of temperature.
2. Specific heat capacity: Expressed as a function of temperature.
3. Fraction of solid development: Expressed as a function of temperature.
4. Latent heat of the alloy: The quantity of heat being absorbed or evolved during a phase transformation.
5. Solidification morphology: Parameter describing the shape of the primary phase to solidify (used for the calculation of feeding effects). The parameter is influenced by the alloy chemistry and the dynamic solidification conditions (cooling rate) during the simulation.
6. Feeding efficiency: Percentage of solidified melt within a control volume up to which feeding of liquid melt is possible.
7. Rheology model: MAGMASOFT® assumes Newtonian rheological model for semi-solid alloys.
8. Exact material composition.
9. Standard material properties: Expressed as a function of temperature (e.g., Yield stress, ductility).
10. Interfacial Heat Transfer Coefficient: Defined as the proportionality coefficient between the heat flux and the temperature difference driving the flow of heat, expressed by Equation 31. The heat transfer coefficient values were obtained from empirical tests performed under laboratory conditions at MAGMA Geissereitechnologie GmbH, in Aachen, Germany. For the purposes of this thesis, HTC values available in the 'AZ91-HPDC' module were used.

$$HTC = \frac{\Delta Q}{A \Delta T \Delta t} \tag{31}$$

Where:

ΔQ = heat input

A = heat transfer surface area

ΔT = temperature difference between solid surface and surrounding fluid

Δt = time period

The data in the MAGMA*database*® were compared to thermo-physical data obtained from the literature. For the AZ91D alloy, the values of latent heat, specific heat, thermal conductivity, viscosity, density and ultimate tensile strength as a function of temperature (from room temperature up to the solidus temperature) were provided to MFT. In the case of the AE42 alloy, only limited data were available in the literature, thus the proprietary MAGMA*database*® was used instead.

A1.3 Results of MAGMASOFT® Computer Simulations

Numerical modeling of the casting process was carried out in MAGMASOFT® software. Specifically, modeling of the heat transfer coefficient (Section A1.3.1), casting filling temperature (Section A1.3.2), casting filling velocity (Section A1.3.3), casting solidification temperature (Section A1.3.4), hot spot formation (Section A1.3.5), hot tear evolution (Section A1.3.6), maximum principal stress (Section A1.3.7) and casting deformation (Section A1.3.8) was carried out. A summary of the simulation results is presented in Section A1.3.9, while detailed simulation results are presented in Section A1.3.10.

All simulations were performed at Magma Foundry Technologies, Schaumburg, IL, USA, by Mr. M. Proske and Ms. D. Gaddam. Experimental data collected during casting trials at the Centre for Near-net-shape Processing of Materials were used to perform the simulations. The final results were obtained from MFT in the form of videos (e.g., mold filling and temperature evolution), images (e.g., casting displacement) or MS Excel spreadsheets (e.g., cooling curves for virtual thermocouples).

A1.3.1 Estimation of the Heat Transfer Coefficient

In order to carry out any of the numerical simulations, the boundary conditions imposed on the computer model had to be specified. One of the unknown boundary conditions was the interfacial heat transfer coefficient between the molten metal and the steel mold.

To manually estimate the HTC as a function of temperature, Mr. Proske and Ms. Gaddam made use of MFT's proprietary HTC database. The heat transfer coefficients in the database were obtained from Mg HPDC experiments carried out by MFT's industrial partners. HTC values generated in similar casting conditions (e.g., mold material, mold coating, alloys) were considered for this research.

To simplify the HTC estimation process, the casting solidification was divided into three stages with distinct HTC values:

1. Liquid metal filling of the casting cavity: During this stage, the contact between the molten metal and the steel mold was nearly 'perfect', resulting in high HTC values.
2. Formation of an air-gap: In this stage, the solidifying casting contracted and pulled away from the mold wall. The developing air-gap increased the resistance to heat transfer from the molten metal to the mold. Thus, the HTC values decreased.
3. Solid casting contraction: Cooling of a casting to room temperature promotes further contraction of the casting, resulting in the formation of a definite air gap with nearly constant HTC value.

Due to the manual approach to optimize the HTC, additional simplifying assumptions were made. As it was not feasible to manually assign a unique HTC value to every surface of the casting, Mr. Proske proposed an approach based on his extensive experience in software modeling of high pressure die casting processes:

1. As the horizontal bar of the casting cooled and contracted within the steel mold, selected casting surfaces were pressed against the mold wall. These surfaces retained high HTC values.
2. Casting surfaces free to contract in all directions were assigned temperature-dependent HTC values.

The surfaces with high contact pressure and constant high HTC are shown in Figure A1. 2. For these surfaces, the HTC (obtained from MFT HTC database) was set to 2700 W/m^2K.

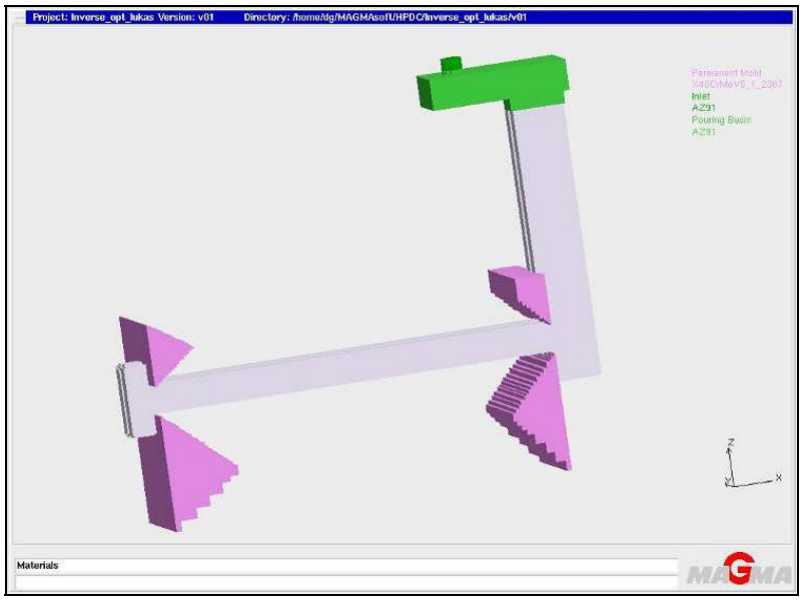

Figure A1. 2: Casting surfaces with constant HTC.

With these assumptions in effect, a manual inverse method to estimate the HTCs was performed. In order to assess the validity of the results, a simulated cooling curve (from a virtual thermocouple defined at the same location as an experimental thermocouple) was compared to an experimental cooling curve. The temperature dependent HTC values were manually adjusted such that the difference between the simulated and experimental cooling curves decreased. A parameter (considering the difference between the two cooling curves) was optimized using the least squares technique (the sum of the squares was minimized). In this process, the first 300 seconds of the simulation were considered.

Throughout the optimization process, a perfect match (i.e., zero temperature difference) between the experimental and simulated cooling curves was not achieved. However, the best match between the two cooling curves was obtained when the HTC followed a profile as shown in Figure A1. 3. This HTC profile yielded the minimum difference between the simulated and experimental cooling curves. Table A1. 1 presents the average and maximum temperature differences between these cooling curves for all time-steps (i.e., entire simulation) for both casting locations (i.e., near the sprue and at the horizontal bar midsection). As can be observed, the average temperature difference was ~ 10 °C and ~ 6 °C for the AZ91D and AE42 alloy castings. The value of the lower HTC boundary (500 W/m^2K) is possibly indicative of a high level of contact between the casting and the surrounding steel mold. Experiments performed during DC casting of magnesium alloys suggest that the HTC in casting regions with a significant air-gap typically range between 130 – 180 W/m^2K [100]. Thus, the HTC profile in Figure A1. 3 possibly over-estimates the rate of cooling of the casting at the end of solidification and during cooling to the room temperature.

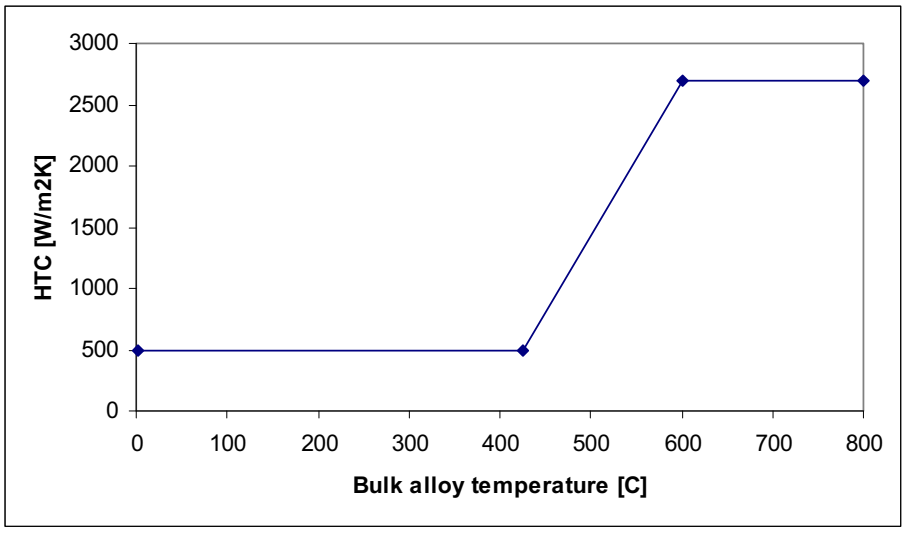

Figure A1. 3: HTC vs. Alloy temperature determined by MAGMASOFT(R).

Table A1. 1: Temperature difference between experimental and simulated cooling curves.

Alloy / Mold temperature [°C]	Average temperature difference [°C]	Maximum temperature difference [°C]
AZ91D / 210	10.6	23.1
AZ91D / 250	10.2	24.3
AE42 / 340	6.4	12.6
AE42 / 390	6.1	14.7

A lower temperature difference could be possibly achieved with autonomous optimization tools, additional thermocouple data or a greater computing capacity of the simulation computer. However, due to the manual approach to optimize the HTC curve, the average temperature difference achieved with HTC profile as illustrated in Figure A1. 3 was deemed acceptable. Thus, subsequent modeling with this HTC profile was expected to provide reasonable information about the casting solidification and filling processes.

A1.3.2 Casting Filling Temperature

Casting filling temperature simulations provided information about the molten metal temperature as the metal filled the casting cavity. Detailed results of the simulations are presented in Appendix A1.3.10.1. The images were extracted from a video showing the filling path of the alloy from entry into the pouring cup, until the completion of filling of the entire mold cavity. The images were captured in 0.5 second intervals in order to capture the development and progression of the metal front during filling.

Figure A1. 4 shows that the molten metal entered the downsprue in free fall until reaching the bottom trap of the downsprue. During this period, the AZ91D alloy cooled from the 720 °C pouring temperature by 115 °C and 47 °C for the 210 °C and 250 °C mold temperatures, respectively. For the AE42 alloy, the decreases in temperature from the 765 °C pouring temperature were 120 °C and 82 °C for the 340 °C and 390 °C mold temperatures, respectively. Considering the liquidus temperatures of the two alloys (Table A1. 2 or phase diagrams in Figure 88), it is thus likely that at low mold temperature the molten metal entering the horizontal bar possibly consisted of liquid with nucleating small droplets of semi-solid material.

Figure A1. 4 also suggests that after the molten metal filled the bottom trap of the downsprue, the metal front splashed upwards and entered the horizontal bar, impinging on the upper edge / surface of the

horizontal bar in the critical region. The metal stream continued along the upper surface for ~ 2.5 cm down the horizontal bar, until it came into contact with the bottom edge of the horizontal bar. This flow path likely created a pocket of air in the critical region of the casting.

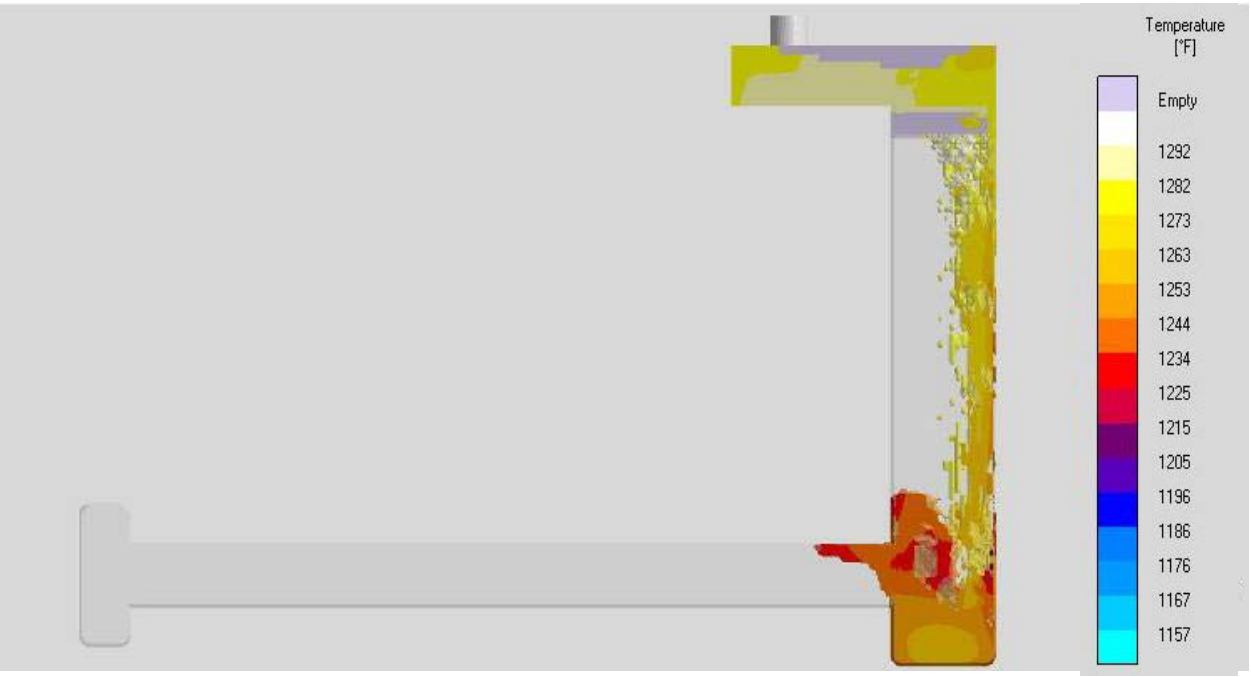

Figure A1. 4: Simulated metal temperature for AZ91D casting at 250 °C mold temperature.

Table A1. 2: Freezing range of AZ91D and AE42 alloys [61].

	AZ91D alloy	**AE42 alloy**
Liquidus temperature [°C]	598	625
Solidus temperature [°C]	425	590
Freezing range [°C]	173	35

As filling of the horizontal bar continued, molten metal traveled downstream towards the anchor restraint. After filling the end restraint, a molten metal front emerged from the end restraint cavity and formed a small wave, as indicated in Figure A1. 5. This wave traveled upstream towards the sprue.

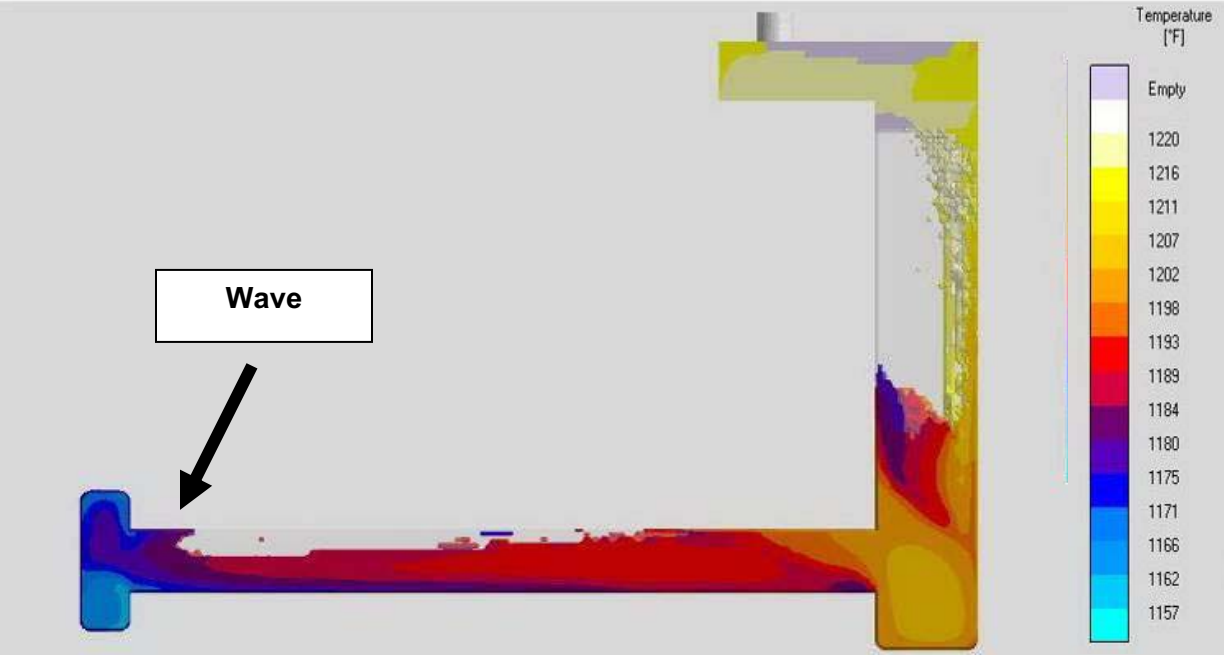

Figure A1. 5: Formation of a wave in the horizontal bar (AE42 casting at 340 °C mold temperature).

Formation of the air pocket in the critical region and the wave in the horizontal bar contributed to metal flow turbulence and temperature gradient evolution along the top edge of the horizontal bar. Further, the wave likely contributed to the development of velocity gradients in the critical region. As discussed in Section 5.2.4, microscopic analysis of the casting interior revealed folds in this region of the casting. Macroscopic observation of the casting surfaces (Section 5.1) revealed the presence of frozen metal flow lines on the walls of the horizontal bar. These flow lines (e.g., Figure 59b) followed similar direction as the metal velocity vectors at the end of horizontal bar filling predicted by MAGMASOFT®. Therefore, the location of the observed folds was in general agreement with the location of high melt turbulence predicted by MAGMASOFT® simulations.

The temperature of the casting in the critical region at the instance of complete filling of the horizontal bar (e.g., time = 3.0 - 3.5s) was examined and is presented in Table A1. 3. It was observed that the critical region of castings without hot tears remained well above the liquidus temperature, while castings with hot tears cooled to a temperature only a few degrees above the liquidus temperature of each alloy. Thus, the critical region began to solidify immediately after filling of the horizontal bar. Subsequent feeding of the horizontal bar was impeded by developing dendrites in this region and the hot tearing tendency of the alloys at this location was high.

Table A1. 3: Melt temperature at the entrance to the horizontal bar.

	AZ91D		AE42	
	210 °C mold temperature	**250 °C mold temperature**	**340 °C mold temperature**	**390 °C mold temperature**
Melt temperature [°C]	601	667	630	662

A1.3.3 Casting Filling Velocity

MAGMASOFT® simulations provided information about the three dimensional velocity field during mold filling. The results are presented in Appendix A1.3.10.2. These figures were extracted from a video paused at the same time-steps as the casting temperatures during mold filling.

The results were analyzed and the magnitude of metal front velocity at three instances of interest during mold filling was observed. Specifically, bulk metal velocity was recorded for the metal front at the:

1. entrance to the horizontal bar at the beginning of the filling of the horizontal bar (flow direction: towards the end restraint),
2. wave tip forming after filling the anchor (flow direction: towards the downsprue) and,
3. critical region at the end of filling of the horizontal bar at the end of horizontal bar filling.

These velocities are summarized in Table A1. 4.

Table A1. 4: Ranges of metal front velocities during mold filling..

Alloy / Mold temperature [°C]	**Metal front velocity [cm/s]**		
	Entrance	**Wave**	**Critical region**
AZ91D / 210	50 – 90	140	0 – 50
AZ91D / 250	30 – 50	50	0 – 35
AE42 / 340	80 – 120	100	40 – 80
AE42 / 390	50 – 85	100	40 – 80

The results in Table A1. 4 suggest that the molten metal entered the critical region of the horizontal bar relatively fast. The Reynolds number calculated using the entrance velocities (30 – 120 cm/s) was

between 6000 – 24000, based on kinematic viscosity of 10^{-6} m^2/s [101] and characteristic hydraulic diameter of 20 mm (i.e., assuming square cross-section of the horizontal bar). Thus, the metal flow at the entrance was in the turbulent regime. As filling continued, the temperature decreased and melt viscosity increased, causing slowing down of the metal front.

Once the end restraint filled, a wave formed at the anchor and advanced back towards the sprue. Flow direction and development of the wave is illustrated in the figures of Appendix A1.3.10.2. The wave velocity was relatively high, since the volume of the empty mold cavity continuously decreased while the mass flow rate into the mold (via downsprue) remained constant. Thus, the fast propagating wave promoted development of velocity gradients along the top edge of the horizontal bar and in the critical region, as seen in Figure A1. 6. Further, the turbulence created by the advancing wave (observed in simulation videos illustrating the metal flow path) possibly also contributed to the entrapment of surface oxides near the top edge of the horizontal bar. This entrapment was verified with microscopic analysis of folds. The cumulative effect of these factors would likely deteriorate the casting soundness in the critical region and increase the tendency for hot tear formation along the top edge of the horizontal bar.

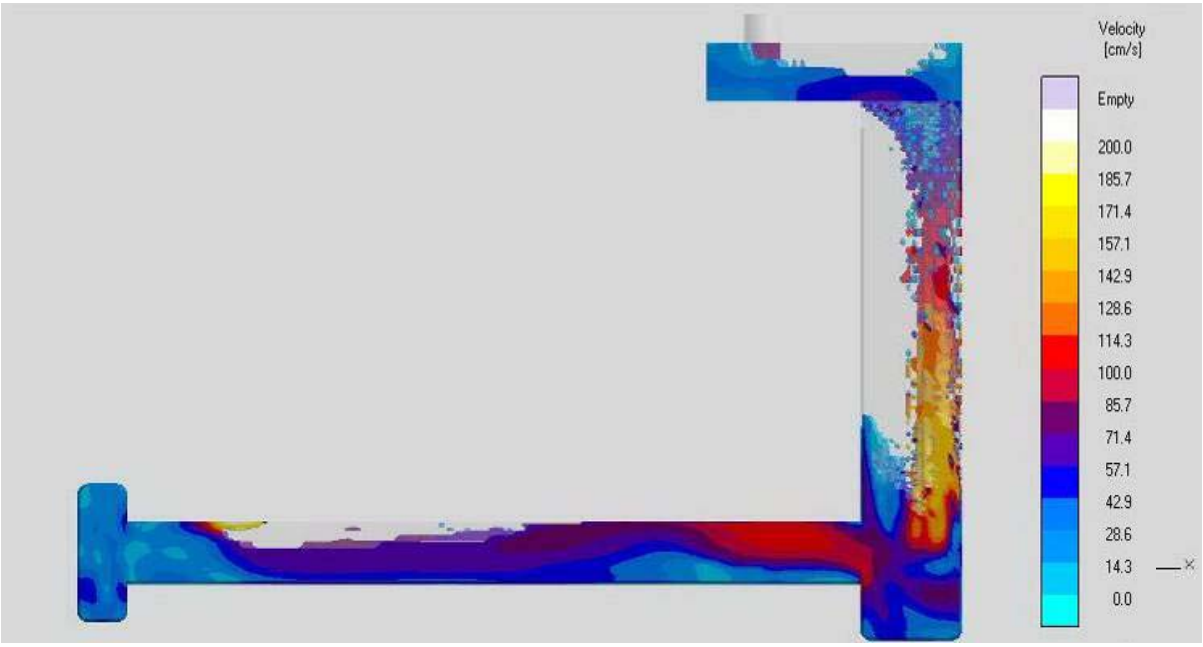

Figure A1. 6: Metal filling velocity at 3.0s for AZ91D casting at 210 °C mold temperature.

In addition to the formation of velocity gradients along the horizontal bar during its filling, localized gradients over the bar cross section developed as well. For example, as observed in the critical region of Figure A1. 7, the metal in the middle of the horizontal bar was nearly stationary (light blue), while the

metal at the top and bottom edges of the horizontal bar was still moving. This simulation result further supports the hypothesis of fold development due to velocity gradients in the critical region.

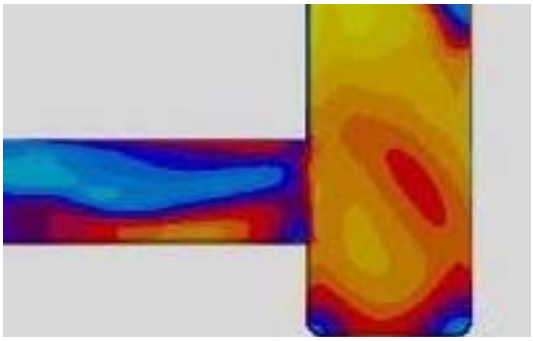

Figure A1. 7: Detail of critical region from Figure A1. 31f.

Simulation videos showing real-time direction of metal flow during mold filling further suggest that a circular flow pattern was established in the critical region, as indicated in Figure A1. 8. Molten metal entering the horizontal bar cavity in the critical region impinged on the upper edge of the horizontal bar (after ~1.5s of simulation) and was moving at relatively high velocities (~80 – 180 cm/s) to the left, while the metal at the bottom of the horizontal bar was nearly stationary. This velocity inhomogeneity and flow path direction possibly contributed to the entrapment of mold gases or oxides in the casting. The associated non-uniform melt cooling possibly created a bulk metal feed with solid agglomerates, as suggested in Appendix A1.2. Such bulk feed is undesirable as it promotes evolution of localized strain gradients during subsequent casting solidification and contraction.

Analysis of the velocity results revealed one of the limitations associated with numerical modeling of the metal velocity. In order to carry out the simulations in MAGMASOFT®, a parameter specifying the duration of mold filling was required. Thus, prior to proceeding with computer simulations, casting experiments were carried out to time the duration of mold filling. The experiments revealed that the mold filled between 4.7 – 5.0 seconds. There was no observable difference in the pouring time for the two alloys or the mold temperatures investigated. Thus, the same value of "total pouring time" was used for all the simulations.

From the velocity data presented in Table A1. 4, it appears that the molten metal traveled faster in cooler molds than in hotter molds. This trend is counter intuitive, since a colder mold would increase the rate of solidification, with concomitant increase in melt viscosity. However, in order to satisfy the "total fill

time" criterion for the simulation, the metal velocity had to be increased for colder molds. This result is questionable and it is recognized that the velocity simulations carry a degree of uncertainty.

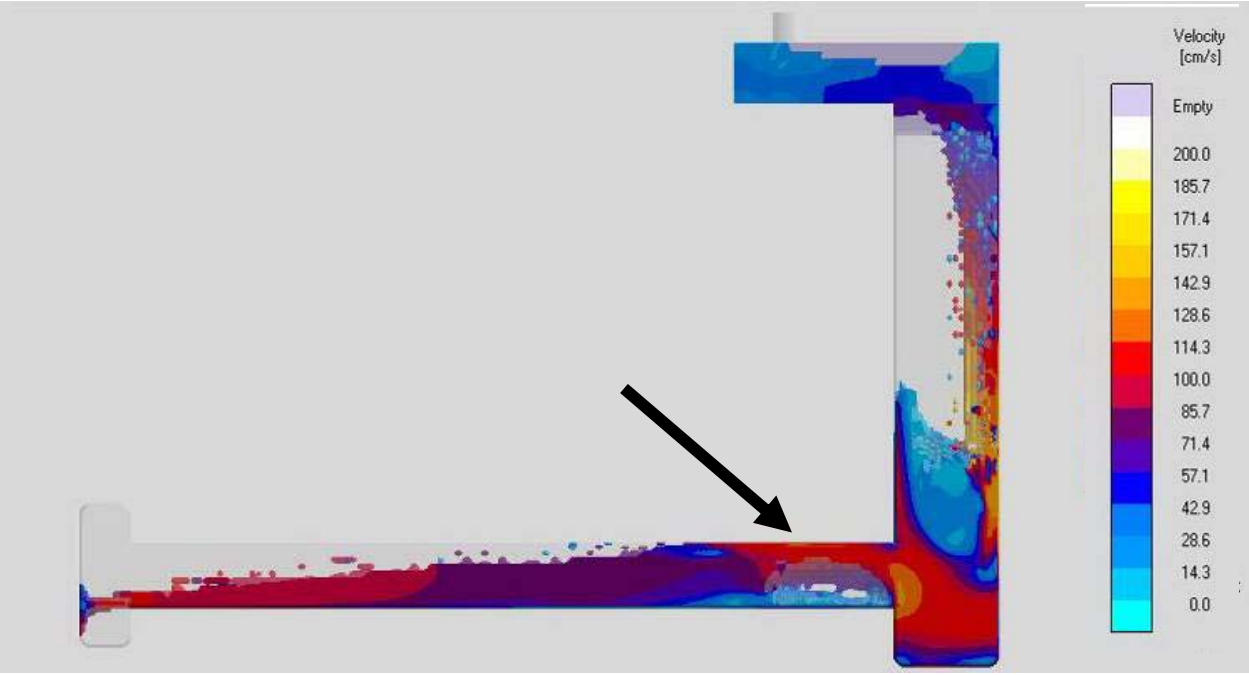

Figure A1. 8: Metal front velocity distribution in the critical region in AE42 casting at 390 °C mold temperature.

A1.3.4 Casting Solidification Temperature

The casting solidification temperature was calculated from the instance of complete filling of the mold until the casting cooled below the solidus temperature. The results were obtained in the form of a video, from which screenshots were extracted at desired time intervals and are presented in Appendix A1.3.10.3. Also, additional screen shots were obtained from the video to examine moments of interest during casting solidification. In these figures, the color scale indicates the temperature of the casting, while no-color indicates that a particular casting region already solidified.

Simulation results confirm that casting solidification began at the anchor, continued through the horizontal bar towards the downsprue and finally progressed to the pouring cup placed on top of the mold. This general solidification pattern was observed for all casting conditions and for both alloys.

The results revealed that in the case of the 210 °C mold temperature casting, the horizontal bar solidified in ~ 32 seconds (e.g., Figure A1. 9), while in the case of the 250 °C mold temperature casting, the same

level of solidification was achieved in ~36 seconds. Similarly, in the case of the AE42 castings, the horizontal bar solidified in ~ 20 seconds for the 340 °C mold temperature, while it solidified in ~ 36 seconds at 390 °C mold temperature. These results clearly demonstrate the impact of increasing the mold temperature on extending the solidification time of the horizontal bar.

The freezing ranges of the AZ91D and AE42 alloys were presented in Table A1. 2. In the case of the AZ91D alloy (with ~ 170 °C long freezing range), the extended time of solidification primarily affected fraction of solids development and associated interdendritic feeding. In the case of the AE42 alloy (freezing range of ~ 35 °C), the horizontal bar's solidification time increased by nearly 80% with an increase of the mold temperature. Such a significant increase would considerably reduce the solidification shrinkage rate and also the casting thermal contraction rate, thereby decreasing the overall rate of thermal stress evolution in the casting during solidification.

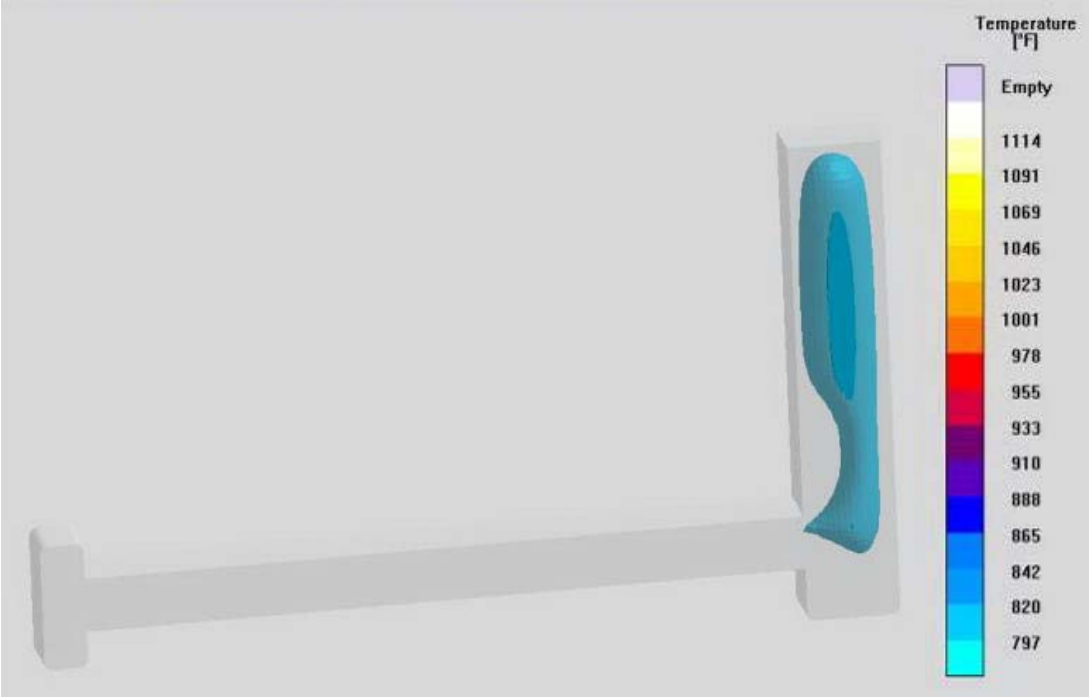

Figure A1. 9: End of solidification of the horizontal bar at 32s. Simulation for AZ91D casting at 250 °C mold temperature.

Detailed analysis of the solidification temperature along the horizontal bar revealed that solidification of the horizontal bar progressed in two directions: 1) axial solidification (from the anchor towards the sprue), and 2) hoop solidification (from the mold walls towards the center of the horizontal bar). With respect to the casting quality, directional solidification (where the axial solidification exceeds the hoop

solidification) is desirable. However, it was observed that for both alloys at the lower mold temperatures (though more prominent in the AZ91D alloy), the relatively fast hoop solidification prevented directional solidification. Further, the hoop solidification rate was not uniform along the horizontal bar, resulting in creation of liquid pockets along the horizontal bar, as indicated in Figure A1. 10a. Formation of isolated pockets of liquid metal is detrimental to casting soundness, as adequate feeding of such regions is not possible, resulting either in external shape change (e.g., implosion of casting surface) or in the formation of interior shrinkage porosity. In addition, formation of liquid pockets promotes solute segregation in these regions, resulting in a localized depression of the solidus temperature and strain gradient development in the surrounding material.

The inhomogeneous casting contraction caused by the liquid pockets likely contributed to the formation of hot tears in the critical region of the casting. Due to pocket formation near the anchor, the contraction of the pocket pulled the bar's midsection towards the anchor. This displacement in turn pulled the material in the horizontal bar's critical region towards the anchor and intensified the contact stresses at the 90° corners of the critical region. Subsequently, axial contraction of the downsprue acted in an orthogonal direction to the contraction of the horizontal bar, thereby again intensifying the effect of the stress concentration at the 90° corner.

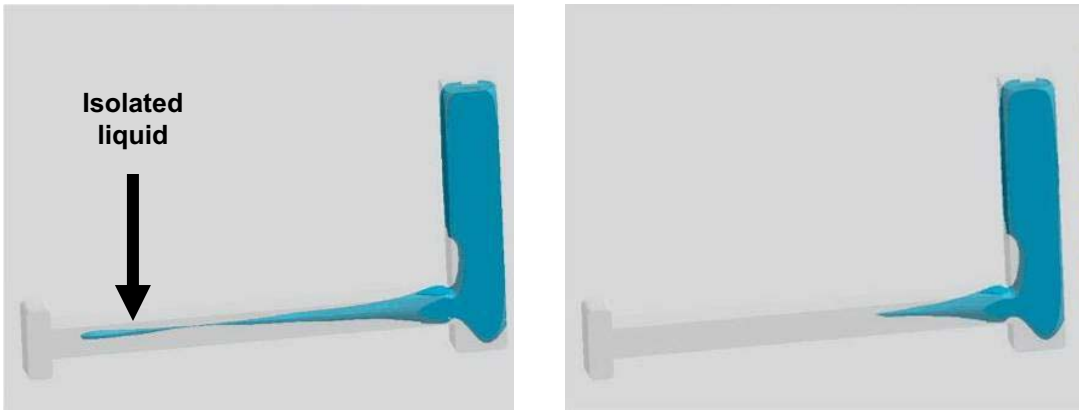

(a) Time = 26.0 seconds. *(b) Time = 26.7 seconds.*

Figure A1. 10: Centerline solidification of AZ91D casting at 210 °C mold temperature.

It was observed that increasing the mold temperature was effective to re-establish directional solidification in the horizontal bar, such that solidification progressed from the anchor towards the downsprue. Also, increasing the mold temperature reduced the size of the liquid pockets (hot spots) thus likely alleviating and decreasing the stress levels at the 90° corner in the critical region.

Analysis of the results further revealed that downsprue solidification also contributed to inhomogeneous and hindered feeding of the critical region of the horizontal bar. As can be observed in Figure A1. 11, the molten metal in the downsprue began to solidify at the vertical surface near the 90° corner, and solidification progressed towards the centre of the sprue. The accelerated solidification of the downsprue near the 90° corner was related to the localized high heat transfer coefficient on the vertical surface, caused by high level of contact between the mold and the casting.

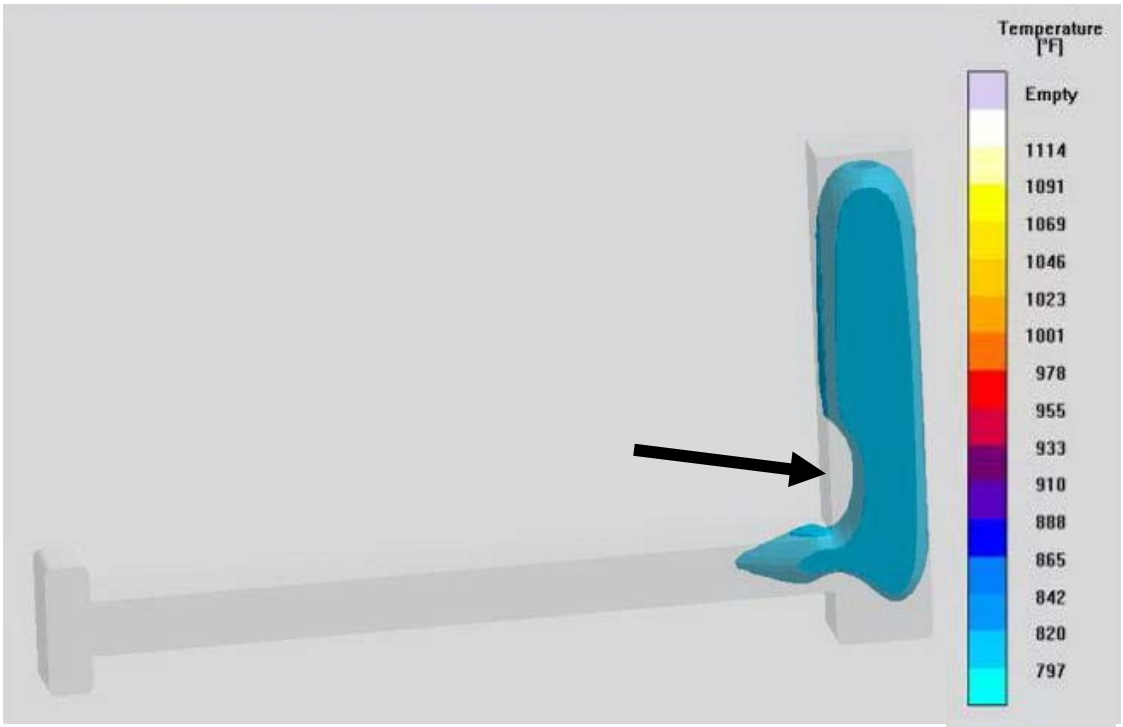

Figure A1. 11: Axial (hoop) solidification of the downsprue above the critical region for AZ91D casting at 210 °C mold temperature.

The decreasing cross section of the downsprue (where liquid melt could pass) prior to complete filling of the horizontal bar likely made feeding of the horizontal bar difficult. In effect, solidification of the downsprue caused choking of the liquid metal flow into the horizontal bar. This choking effect was reduced with an increase of the mold temperature, since the downsprue's hoop solidification slowed down. For example, Figure A1. 12 illustrates casting temperatures at 20s after casting solidification initiated, suggesting that increasing the mold temperature delayed the sprue choking effect (in the case of the AE42 castings, choking was delayed by at least 12 seconds).

The solidification temperature simulation results further show that the bar centerline was the last region to solidify (e.g., Figure A1. 13). As a result, adequate feeding along the centerline would be necessary to

avoid centerline shrinkage porosity. However, at low mold temperatures, fast hoop solidification and the formation of liquid pockets made centerline feeding difficult. Thus, shrinkage porosity developed.

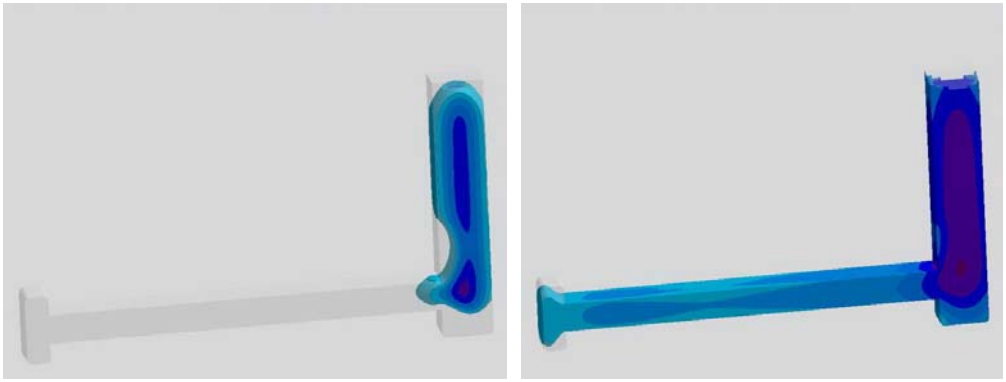

(a) 340 °C mold temperature. *(b) 390 °C mold temperature.*

Figure A1. 12: Extent of solidification in AE42 castings after 20 seconds.

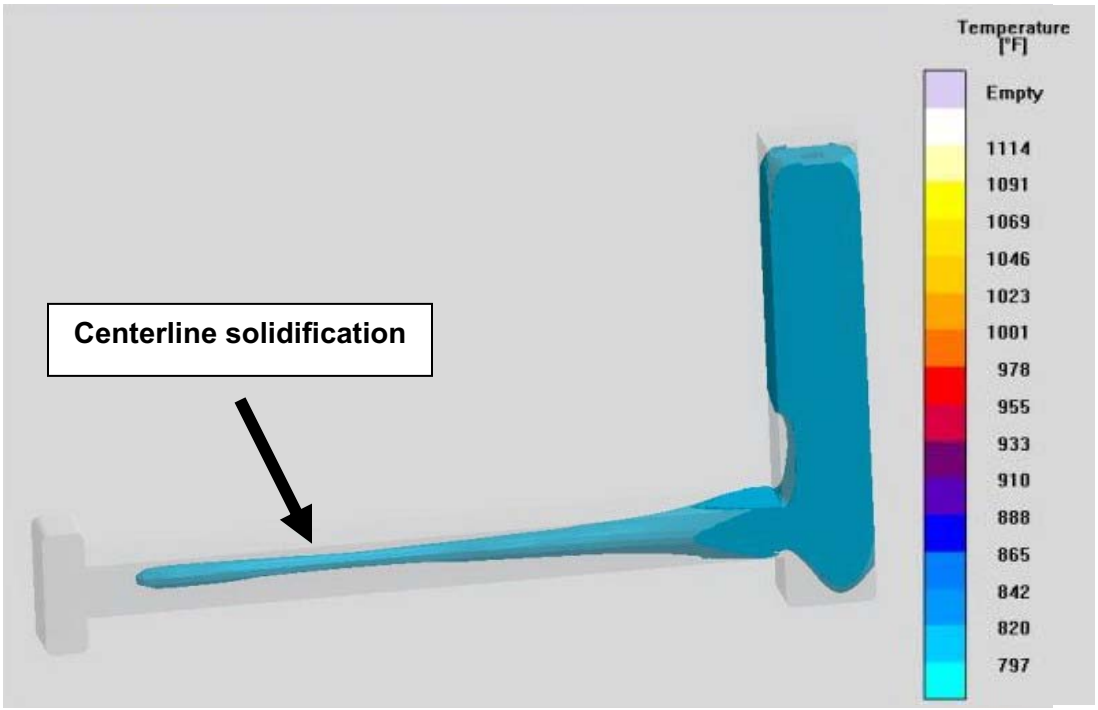

Figure A1. 13: Centerline solidification in AE42 alloy at 390 °C mold temperature.

For both alloys, increasing the mold temperature slowed down the hoop solidification and established directional solidification of the horizontal bar. Further, slower solidification rates in the downsprue delayed the onset of choking of liquid in the downsprue. These factors have cumulatively reduced the tendency for hot tearing in the critical region of the castings made at elevated mold temperatures.

A1.3.5 Hot Spot Formation

The evolution of hot spots in a casting results in the formation of isolated liquid metal pockets surrounded by solid material. During hot spot's solidification, its shrinkage can not be compensated by incoming liquid feed, which makes the hot spot region highly prone to nucleate shrinkage porosity.

As Figure A1. 14 and Figure A1. 15 indicate, hot spots formed in all castings. Typically, one hot spot formed in the horizontal bar and two in the downsprue. It is likely that all hot spots had an effect on the formation of hot tears in the critical region of the casting. The orientation of the principal axes of the hot spots in the horizontal bar and the downsprue were orthogonal. Thus, solidification shrinkage of these hot spots would induce orthogonal thermal strain at the 90° corner of the critical region.

Increase of the mold temperature improved the casting's temperature homogeneity. The size of the hot spots decreased, as seen by comparing Figure A1. 14a and Figure A1. 14b, or Figure A1. 15a and Figure A1. 15b. Thus, increasing the mold temperature likely improved thermal strain homogeneity, thereby decreasing an alloy's tendency to hot tearing.

As Figure A1. 14 and Figure A1. 15 indicate, two hot spots typically formed in the downsprue of the casting, separated by a solid bridge. Formation of the solid bridge between the hot spots was related to the high contact stress and ensuing high HTC between the solidifying casting and the mold above the 90º corner. The lower of the two hot spots, in particular, would impact the hot tearing tendency in the critical region. First, the hot spot was isolated from liquid metal feed, thus enabling formation of porosity, as confirmed by observation of metallography Samples #8. Secondly, the hot spot possibly enabled local solute segregation at the dendrite boundaries, leading to the depression of local solidus temperature and resulting in the accumulation of eutectic phases and microstructural inhomogeneity, as was observed for the AE42 casting at 390 °C mold temperature trial (Figure 99).

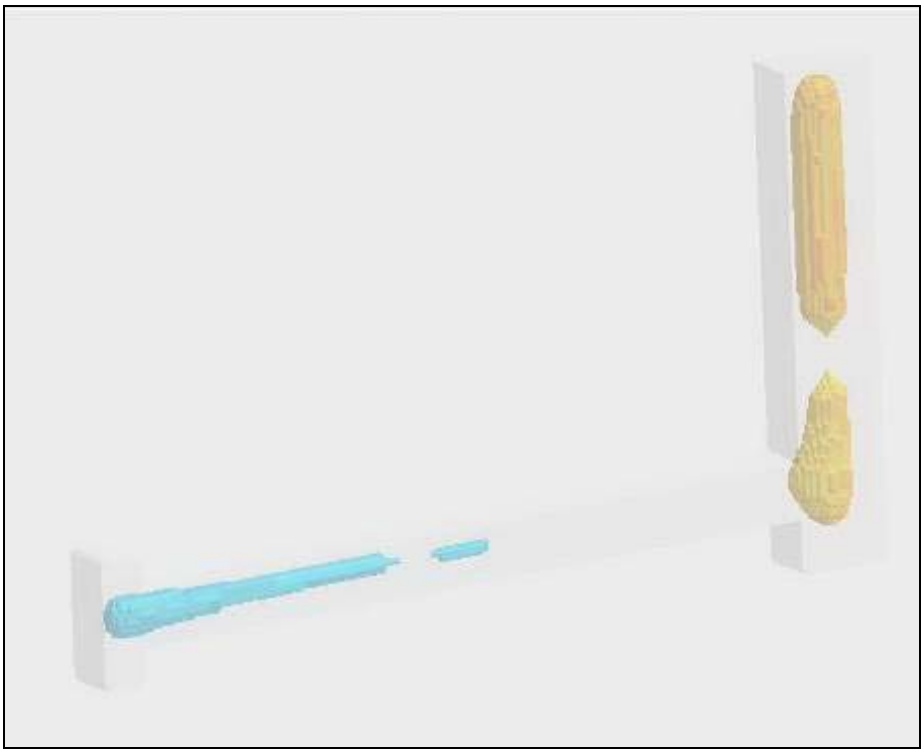

(a) 210 °C mold temperature.

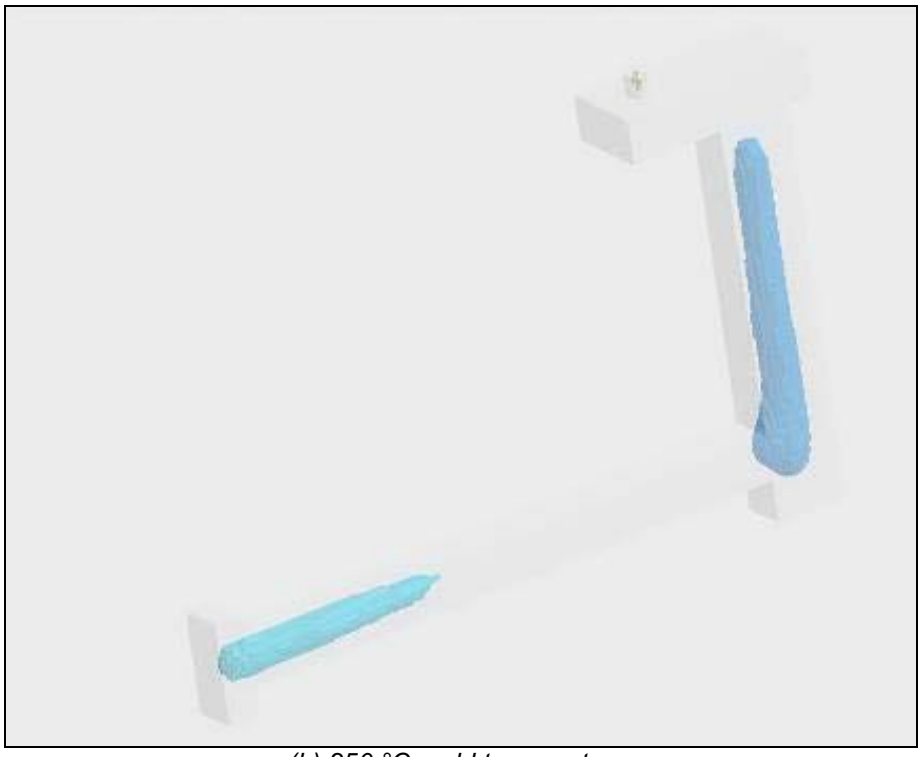

(b) 250 °C mold temperature.

Figure A1. 14: Hot spots in AZ91D castings.

(a) 340 °C mold temperature.

(b) 390 °C mold temperature.

Figure A1. 15: Hot spots in AE42 castings.

A1.3.6 Prediction of Hot Tear Evolution

Prediction of hot tears in any simulation software is currently the subject of extensive research. As was discussed in the literature review (Section 2.3.2.6), at the time of writing this dissertation, no reliable hot tearing criterion was available to predict the severity, location or shape of hot tears in non-ferrous shape castings.

Hot tear prediction in MAGMASOFT® was carried out using a new (prototype) version of the MAGMA*stress*® module. The simulation was carried out under supervision of Mr. Proske of MFT.

Due to the prototype nature of the new MAGMA*stress*® module, the information contained herein is of confidential nature. These results represent the current highest level of sophistication that MAGMASOFT® is capable of in predicting the onset of hot tearing. The mathematical formulation of the hot tearing criterion is proprietary information of MFT. However, private discussion with Mr. Proske yielded the following information:

The MAGMASOFT® model for hot tear formation uses the vonMises criterion. Thus, it combines the three principal stresses into an equivalent stress. An elastic trial stress is calculated by the simulation. If this trial stress exceeds the yield stress, the elastic trial stress is reduced to the level of the vonMises stress and a plastic stress is introduced to stabilize the model. In effect, this approach prevents the vonMises stress from diverging from the yield stress, which frequently occurs in modeling of non-linear solidification phenomena.

The simulation of hot tear evolution also considers the level of contact between the casting and the mold, thus reflecting a change in the local stress distribution due to the formation of an air gap or high contact pressures.

The result of the simulations was a non-dimensional index called the “Hot Tear Index (HTI)”. A value of zero suggests no tendency for hot tearing, while increasing HTI indicates increasing tendency to material’s plastic damage and hot tearing. Thus, the index can identify casting areas prone to plastic damage during alloy solidification. The (absolute) numerical value of the HTI does not represent a physical quantity.

The results of the HTI calculations are presented in Appendix A1.3.10.4. The figures were extracted from a video at specific times of interest. In addition, for each casting condition, the instance when HTI reached a maximum value in the critical region of the casting was examined.

The results indicate that shortly after casting solidification initiated near the anchor of the horizontal bar, small levels of plastic deformation occurred near the 90° corners of the anchor (e.g., Figure A1. 16). This damage, however, was significantly less in magnitude than the damage experienced at the 90° corners of the horizontal bar near the downsprue at later stages of solidification. Once the anchor solidified and axial solidification of the bar progressed, the plastic damage transferred through the horizontal bar towards the critical region. As the 90° corners (on either side of the horizontal bar) opposed the axial contraction of the horizontal bar, plastic damage accumulated in the critical region. The magnitude of HTI in the critical region was nearly an order of magnitude higher than at any other location recorded elsewhere on the casting. Thus, the simulation results were correct in identifying casting area most susceptible to hot tearing.

Figure A1. 16: Plastic damage near anchor of AZ91D horizontal bar at 210 °C mold temperature after 14s.

Depending on the alloy and mold temperature, the location of maximum HTI was seen to shift towards the sprue or towards the horizontal bar. The exact location could be related to the net displacement of the critical region, governed by the contractions of the horizontal bar and the downsprue. In the low mold temperature trials, the horizontal bar solidified rapidly in the hoop direction without proper compensation for the bar's axial contraction. As a result, plastic deformation readily occurred closer to the horizontal bar. Only when the mold temperature increased, feeding of the horizontal bar improved and the development of plastic damage was delayed. Thus, the HTI reached a maximum value in an area closer to the downsprue.

Comparison of actual hot tears observed on the casting surface and the maximum HTI locations confirms a reasonable agreement. For example, as Figure 78 illustrates, the hot tear in AE42 alloys propagated from the 90° corner towards the center of the sprue, as predicted by MAGMASOFT®. Thus, the effect of alloy type and mold temperature was subjected to detailed analysis and the following events were considered:

- Onset of HTI near anchor: Time (in 'sec') during casting solidification when plastic damage started to occur in the horizontal bar near the anchor (at the 90° corners).
- Maximum value of HTI near anchor: Maximum value of HTI near the anchor.
- Onset of HTI at 90° junction: Time (in 'sec') during casting solidification when plastic damage initiated in the critical region where hot tears were experimentally observed (at the 90° junction of the horizontal bar and the downsprue).
- Maximum HTI of edge: The highest observed HTI value near the top edge of the horizontal bar in the critical region of the casting.
- Maximum HTI of interior: The highest observed HTI value in the casting interior (downsprue or horizontal bar) in the critical region of the casting.
- Time to reach max. HTI: Time elapsed during casting solidification until the maximum HTI value was reached in the critical region of the casting.

The results of the analysis are presented in Table A1. 5.

Table A1. 5: HTI analysis.

Alloy / Mold temperature [°C]	Anchor		Critical region			Time to reach max. HTI [s]
	Onset of HTI [s]	Maximum value of HTI	Onset of HTI [s]	Maximum HTI of edge	Maximum value of HTI	
AZ91D / 210	14	0.0092	20	0.0334	0.050	32
AZ91D / 250	18	0.0035	26	0.0248	0.049	36
AE42 / 340	10	0.0090	12	0.0110	0.068	30
AE42 / 390	18	0.0029	24	0.0050	0.049	36

The results in Table A1. 5 suggest that plastic damage (i.e., maximum HTI value) took longer to evolve in the AZ91D alloy at the anchor and at the critical region of the casting, than it did for the AE42 alloy castings (i.e., stresses evolved quickly during AE42's solidification). Further, in the case of the AE42 alloy, the time between the onset of plastic damage at the anchor and the critical region was only 2 seconds and 6 seconds for the 340 °C and 390 °C mold temperatures, respectively. These intervals for the AZ91D alloy were 6 seconds and 8 seconds for the 210 °C and 250 °C mold temperature trials, respectively. Therefore, the simulations suggest that the rapid solidification of the AE42 alloy caused rapid development and transmittal of plastic damage across the horizontal bar.

The data in Table A1. 5 indicate a decrease of the maximum HTI with increasing mold temperatures, as expected. The data in Table A1. 5 also document that the highest hot tearing tendency evolved in the casting interior and not in the casting skin of the horizontal bar. The interior was the last region to solidify and due to poor feeding, plastic damage likely occurred. Thus, this result supports the microscopic observations in Section 5.2.2, where hot tears were seen to nucleate at the 90° corner and propagate towards the location of highest shrinkage porosity, i.e., the sprue center. This prediction is also consistent with ND stress measurements (Section 5.4) and theories suggesting that solidification stresses accumulate in the last liquid to solidify.

The instance of the maximum HTI value in the critical region (as indicated in Table A1. 5) was related to the casting solidification temperature, obtained in Appendix A1.3.2, and repeated in Figure A1. 17. In the case of Figure A1. 17c, the AE42 alloy at 340 °C mold temperature solidified rapidly, with temperature data below the scale bar. However, the remaining images show that the instance of maximum HTI value was associated with the end of solidification of the horizontal bar. In particular, it was associated with the disappearance of liquid in the critical region.

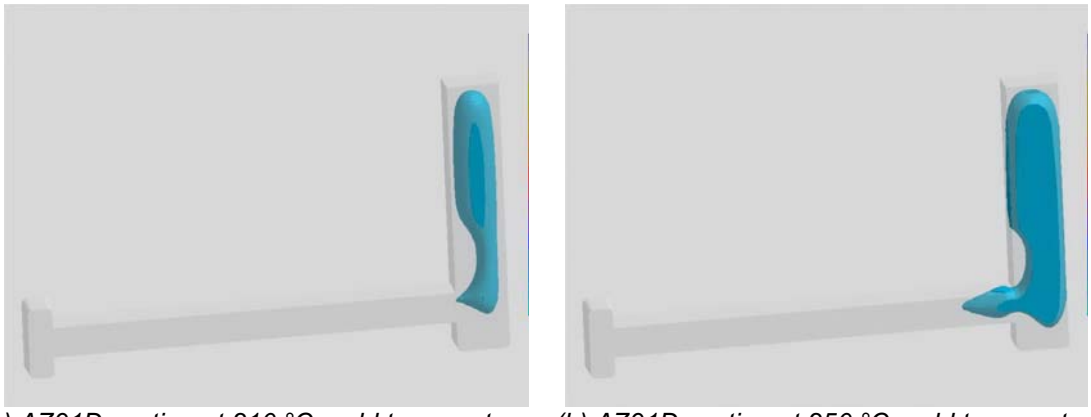

(a) AZ91D casting at 210 °C mold temperature. *(b) AZ91D casting at 250 °C mold temperature.*

(c) AE42 casting at 340 °C mold temperature. *(d) AE42 casting at 340 °C mold temperature.*

Figure A1. 17: Casting solidification temperature at instance of maximum HTI.

As data in Appendix A1.3.10.1 indicate, the melt temperature of the AZ91D alloy at the instance of maximum HTI was ~ 450 °C, which is ~22 °C above the alloy's non-equilibrium solidus temperature of ~ 428 °C. This observation is in agreement with the work of Pellini [25], who suggested that hot tears nucleate ~15 °C above the solidus temperature at high fractions of solid (the melt temperature of 450 °C corresponded to 99.75% fraction of solid for the AZ91D alloy). Therefore, the HTI results suggest that hot tears in the long freezing range AZ91D alloy propagated just above the solidus temperature, in regions of high shrinkage porosity and elevated stress.

In the case of the AE42 alloy, the alloy temperature in the critical region when maximum HTI was reached was also ~ 450 °C. The validity of this result, however, warrants close examination. The solidus temperature for the AE42 alloy is 590 °C and the AE42 alloy is expected to be completely solid at 450 °C. This anomalous result may be explained by considering the following cases:

1. The material property data in the MAGMA*database*® for the AE42 alloy are incomplete or inaccurate, as literature with thermo-physical properties for this alloy is limited. As a result, the AE42's property data were approximated with those of AZ91D. Therefore, the HTI calculated for the AE42 alloy is an approximation of the true value, at best.
2. If the thermo-physical values used in MAGMASOFT® are valid and hot tearing in the AE42 alloy in fact occurred at ~ 450 °C, then this result would suggest that there are different mechanisms responsible for hot tearing in the AE42 and AZ91D alloys. In the case of the AZ91D alloy, shrinkage porosity and insufficient feeding may be responsible for hindered compensation of casting shrinkage. However, in the case of the AE42 alloy, the alloy solidified rapidly and hot tears were caused by mechanical stresses, resulting from incompatibility between the thermal contraction of the casting and the rigid mold. Therefore, in the case of the AE42 alloy, insufficient feeding of the casting was possibly not the primary cause of hot tearing. This hypothesis was supported by the limited shrinkage porosity observed in the AE42 alloy castings.
3. Due to the high fraction of solids developed in the AE42 alloy (Section 5.3), severe solute rejection occurred at the solid-liquid interface. As a result, the non-equilibrium solidus temperature may have locally decreased. However, solute rejection alone would not be sufficient to account for ~ 140 °C suppression of the solidus temperature.

Accurate explanation of these phenomena should be the subject of future research.

A1.3.7 Maximum Principal Stress

The maximum principal stress was calculated in the MAGMA*stress*® module, based on the 3D temperature field obtained from MAGMASOFT® temperature simulation and the MAGMA*database*® thermo-physical material property data for the AZ91D and AE42 alloys. Figure A1. 18 - Figure A1. 19 show the calculated stress levels in the casting at simulation time of 60 seconds. This instance was selected for analysis of the maximum principal stresses (and displacements, Appendix A1.3.8) with due consideration to the fact that mold filling occurred within the first 5 seconds of the simulation, followed by casting solidification for ~ 50 seconds.

The results clearly indicate that the segment of the horizontal bar between the anchor and the downsprue was in tension. It was observed that the stress distributions along the horizontal bars made at lower mold temperatures (i.e. 210 °C for the AZ91D alloy and 340 °C for the AE42 alloy) were similar in profile, but differed in magnitude. In these castings, accelerated hoop solidification of the horizontal bar induced significant stress concentrations at the 90° ends of the horizontal bar. These stress concentrations created dominant stress points.

Castings produced at higher mold temperatures remained in the semi-solid state for a longer period of time, which allowed partial feeding of the horizontal bar and alleviation of stresses and associated solidification shrinkage. Thus, a complex stress profile developed along the horizontal bar. The critical regions of the 250 °C and 390 °C mold temperature castings had non-symmetrical stress profiles. Specifically, the stress gradients at the 90° corners seemed to re-orient towards the downsprue, suggesting that the horizontal bar's contraction was no longer the dominant contributor to material deformation.

The stress level in the critical region was examined and is provided in Table A1. 6. The room temperature yield stress and ultimate tensile strength [61] are provided in the table for comparison with the computed stress values.

Table A1. 6: Stress level in castings of interest.

Alloy / Mold temperature [°C]	**Stress at anchor [MPa]**	**Stress at 90° corner [MPa]**	**Room temperature yield stress [MPa]**	**Room temperature UTS [MPa]**
AZ91D / 210	85	78	97	165
AZ91D / 250	147	107		
AE42 / 340	62	55	145	230
AE42 / 390	281	381		

The results presented in Table A1. 6 indicate that the stress level in the critical region increased with increasing mold temperature, which contradicts expectations. Higher mold temperatures were expected to extend feeding of the casting thereby allowing reduction of solidification stresses in the critical region. As observed in experiments and verified with ND (Section 5.4), the stress levels in the critical region indeed decreased. Thus, these MAGMASOFT® stress calculations bear uncertainty.

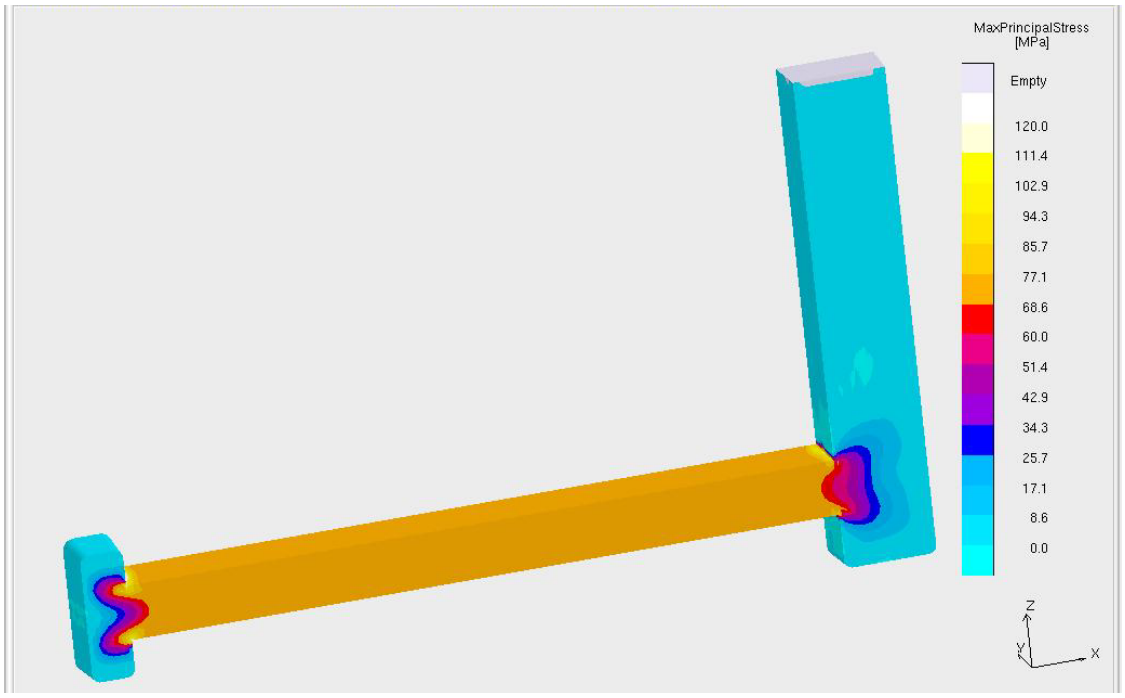

a) 210 °C mold temperature.

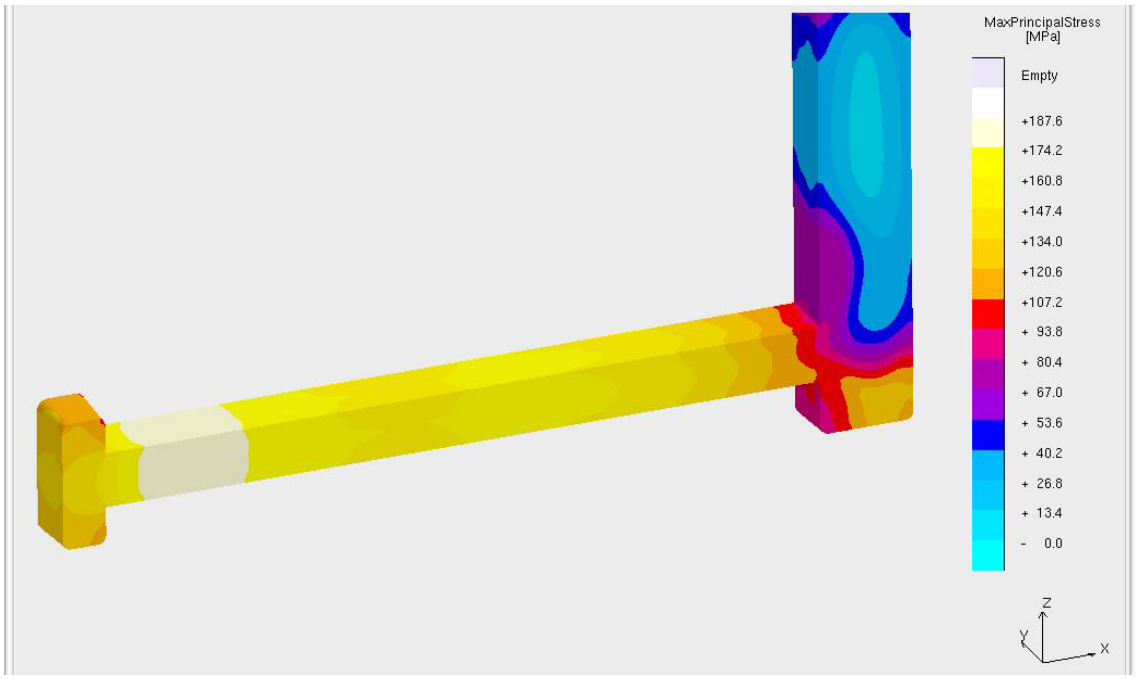

b) 250 °C mold temperature.

Figure A1. 18: Maximum principal stress in AZ91D castings.

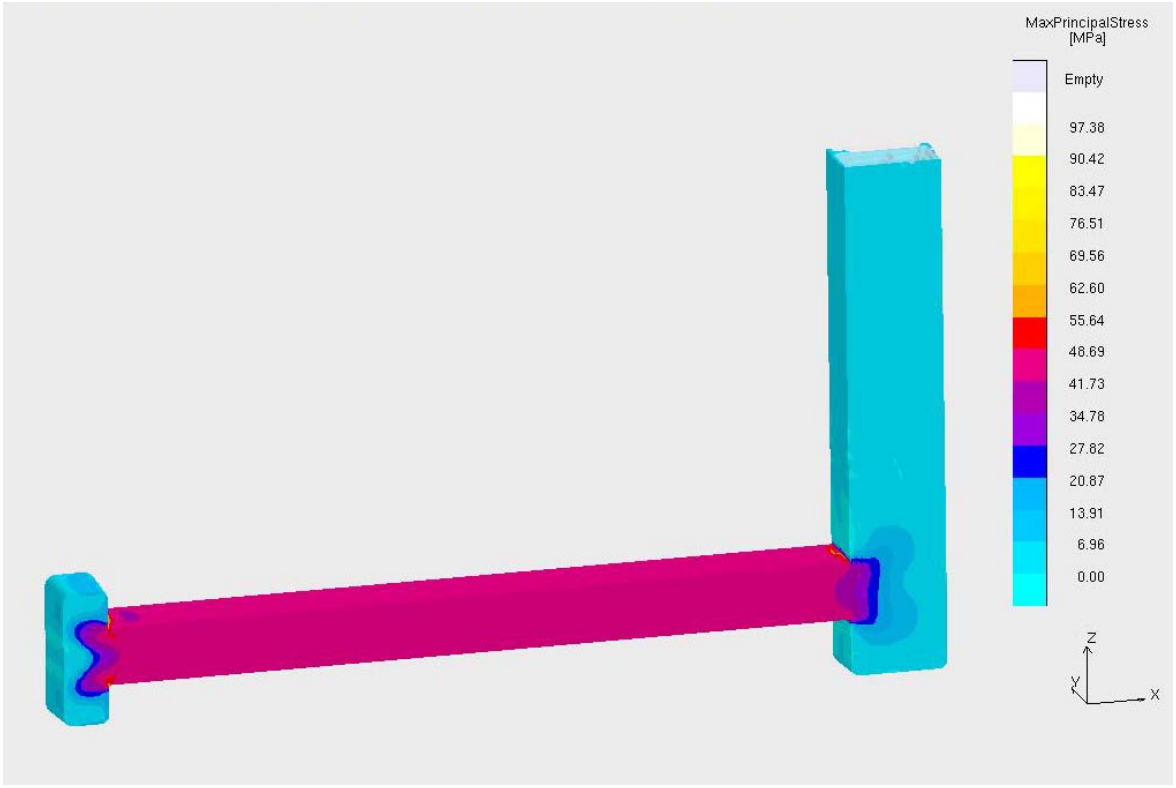

a) 340 °C mold temperature.

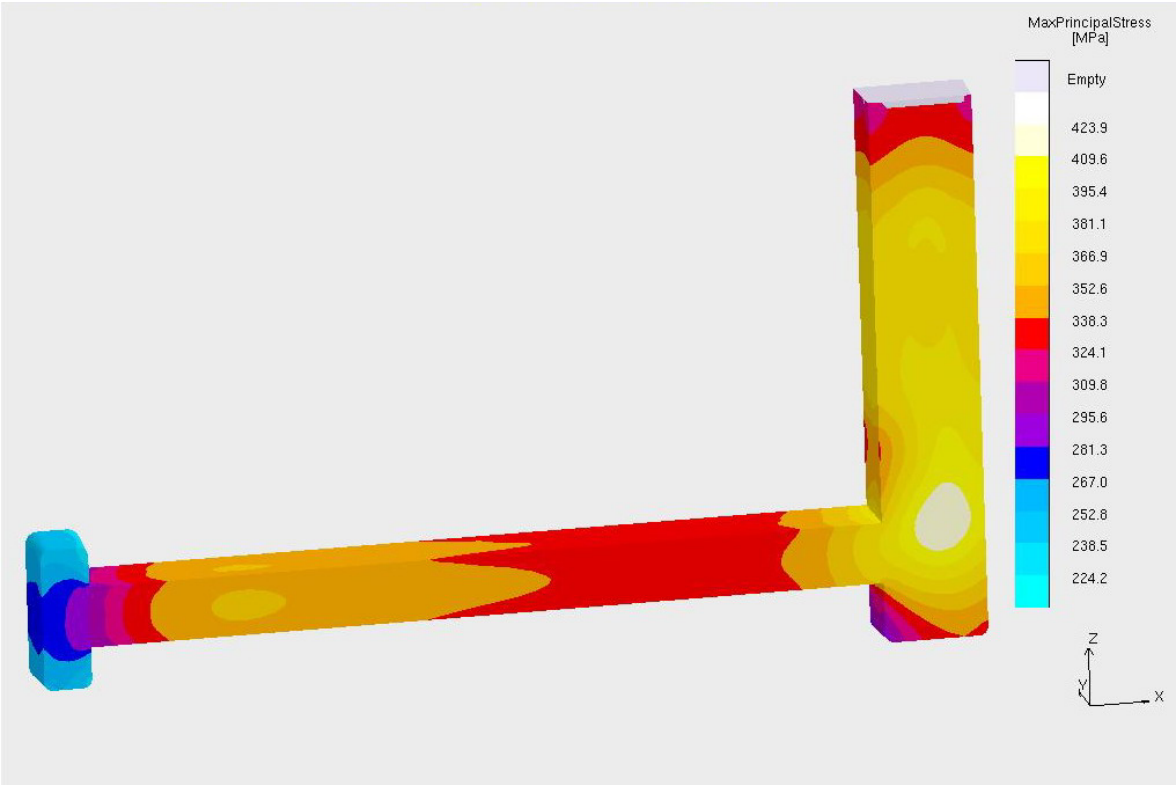

b) 390 °C mold temperature.

Figure A1. 19: Maximum principal stress in AE42 castings.

The results of the stress calculation were also compared to the estimated yield strength of the alloy at elevated temperatures, as shown in Figure A1. 20. The elevated temperature yield stress values in the figures were obtained from MFT [95] and were the same as used for HTI calculations. It can be observed that all computed stress values exceeded the expected yield stress of the material, suggesting that plastic damage occurred in all castings. For example, the stress levels determined for the AE42 alloy cast at 390 °C mold reached ~ 380 MPa in the critical region. This stress value is ~150 MPa above the room temperature UTS value for this alloy. Clearly, the calculations of the stress magnitude in the casting are questionable.

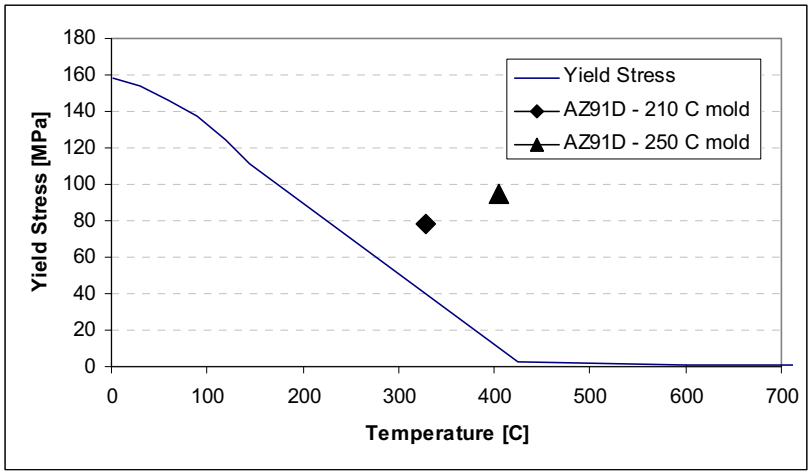

(a) AZ91D castings.

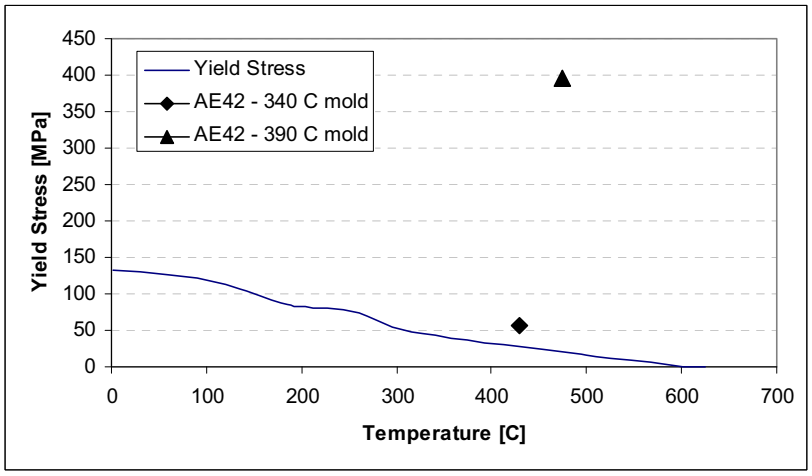

(b) AE42 castings.

Figure A1. 20: Stress condition in the critical region.

Analysis of the stress distribution at the anchor location indicates that increasing the mold temperature increased the stress levels. Further, the anchor stress levels also exceeded the elevated temperature yield stress estimated from literature. Thus, according to MAGMASOFT®, hot tears should have formed at the

anchor as well. This prediction contradicts experimental observations, since all hot tears of all castings formed only in the critical region.

The profile (distribution) of the stresses in the critical casting region was also examined. Arrows in Figure A1. 21 indicate the approximate direction of the maximum stress gradient in the critical region. Comparison of the hot tear propagation direction (e.g., Figure 60g and Figure 62g) to the direction of maximum stress gradient shows reasonable agreement. For the higher mold temperatures of both alloys, i.e., 250 °C and 390 °C, respectively, the stress profile in the critical region changed and suggests that the contribution of the downsprue to the net stress state was important. Thus, it appears that the calculated stress profiles possibly show a realistic stress distribution in the critical region. However, the magnitude of the calculated stresses was questionable.

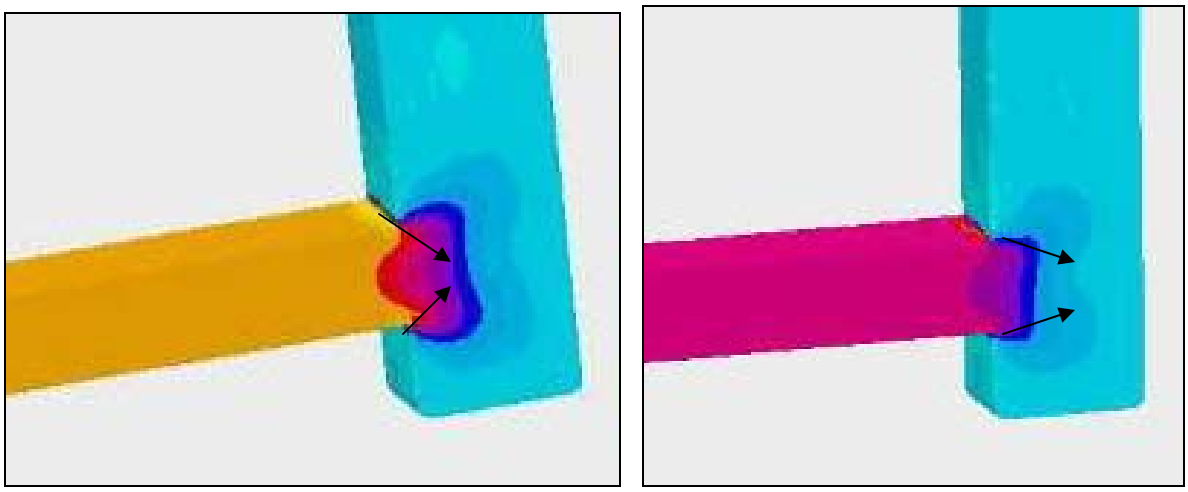

(a) AZ91D alloy, 210 °C mold temperature. *(b) AE42 alloy, 340 °C mold temperature.*

Figure A1. 21: Detailed stress profile in the critical casting region.

It is of interest to note that stress modeling in MAGMASOFT® has been experimentally validated for steel castings, where hot tearing was accurately predicted. Success of these simulations was ascribed to knowledge of the material's high temperature response. In the case of magnesium alloys, the effect of microstructure and shrinkage porosity on material failure and response remains unknown, thereby making stress calculations difficult.

The uncertainty in the validity of the stress calculations clearly demonstrates one of the fundamental limitations in modeling solidification stresses. Due to the limited knowledge of the governing mechanisms during high-temperature deformation of the AZ91D and AE42 alloys, absence of accurate thermo-physical data (in particular near the solidus temperature) and the inability to account for alloy

specific properties (e.g., formation of Al_xRE_y precipitates in the AE42 alloy), the modeling of stresses at the onset of hot tearing in magnesium alloy castings was not successful. These limitations were also identified by other researchers [51], who attempted similar simulations with aluminum alloys.

A1.3.8 Casting Displacement

MAGMASOFT® was used to estimate the casting displacement during solidification. This modeling encompassed solidification shrinkage as well as the thermal contraction of the casting within the steel mold. The thermal expansion and contraction of the H-13 steel mold were considered in the simulations as well. The results of the displacement calculations are presented in Appendix A1.3.10.5. For each casting condition, the displacement in the *x, y*, and *z*-directions is presented. The figures show the original casting shape (transparent grey) along with a color-coded trace indicating the incremental displacement range. For clarity, arrows indicating the bulk deformation of the key casting components (anchor, critical region and downsprue) were added to the figures. As explained in the previous section, the displacement values presented in the figures correspond to a simulation time of 60 seconds. Thus, the results relate to the bulk casting displacement just after completion of casting solidification.

In general, the dominant casting displacement was that of the horizontal bar along the *x*-direction, for all casting conditions and both alloys. The driving force for this displacement was the axial contraction of the horizontal bar. Adjusting the mold temperature had a significant impact on the magnitude of the *x*-direction displacement. Similarly, displacement in the *y*-direction, driven by the axial contraction of the downsprue, was also influenced by the variation of the mold temperature. However, displacement in the *z*-direction did not appear to be affected by the mold temperature. These general deformation trends are schematically summarized in Figure A1. 22.

The figures in Appendix A1.3.10.5 were used to quantify the deformation of the critical region. Specifically, the relative displacements, as indicated in Figure A1. 23, were determined and the results are presented in Table A1. 7. The following nomenclature indicates the direction of displacement in the critical region:

x-direction: away = displacement away from the sprue

y-direction: up = horizontal bar displaces (bows) up

z-direction: compression = cross section of the horizontal bar shrinks

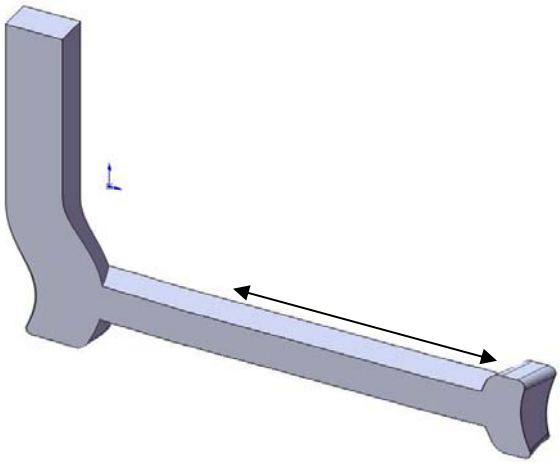

(a) x-direction displacement.

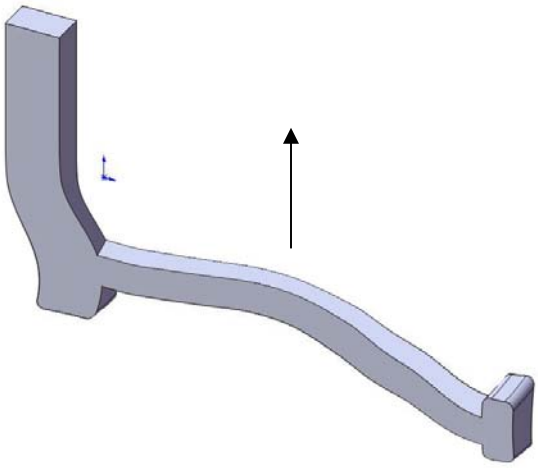

(b) y-direction displacement.

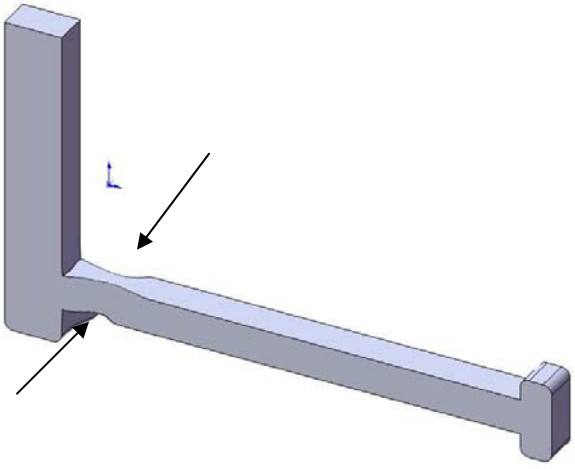

(c) z-direction displacement.

Figure A1. 22: Schematic illustration of casting displacements.

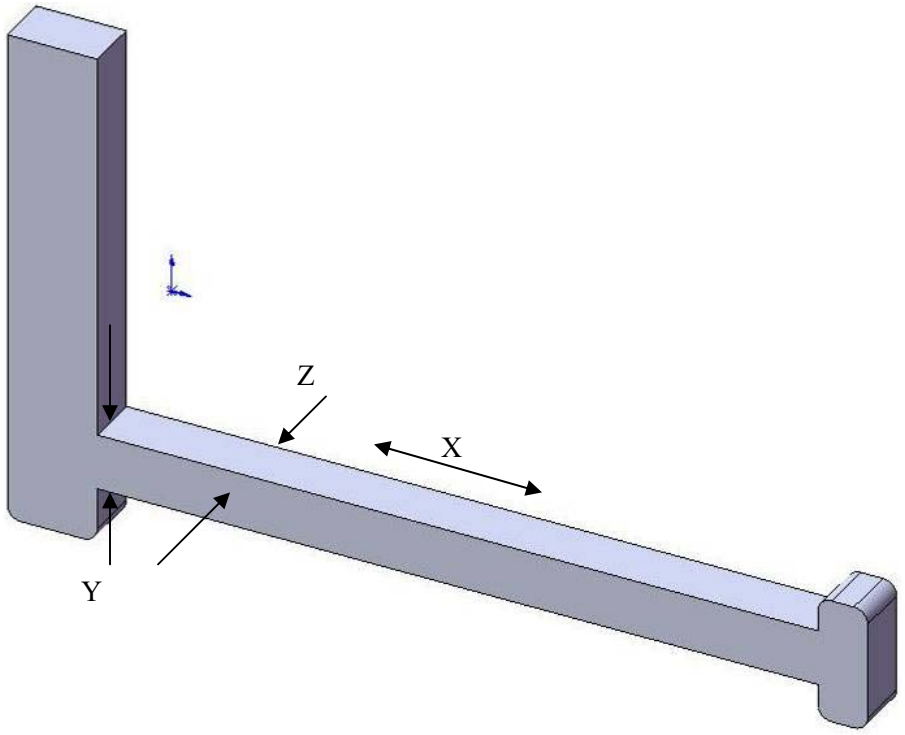

Figure A1. 23: Schematic illustration of investigated contractions in the critical region.

In the case of the *z*-direction deformation, it was noted that all of the surfaces of the casting were displaced inwards. Thus, the values presented in Table A1. 7 represent the 'net' deformation compression.

Table A1. 7: Net displacement (in 'mm') of the horizontal bar in the critical region.

Deformation direction	**AZ91D – 210 °C mold temperature**	**AZ91D – 250 °C mold temperature**	**AE42 – 340 °C mold temperature**	**AE42 – 390 °C mold temperature**
X	0.21 (away)	0.02 (away)	0.11 (away)	0.07 (away)
Y	0.01 (up)	0.002 (up)	0.06 (up)	0.02 (down)
Z	0.21 (comp.)	0.02 (comp.)	0.25 (comp.)	0.16 (comp.)

Considering that these displacements were obtained at a cross section of 20 mm wide x 20 mm thick and 20 mm away from the downsprue, a characteristic (gage) length of 20 mm was used to normalize the displacements. However, the resulting strain (Table A1. 8) can not be directly compared to the elastic residual strain obtained via neutron diffraction in Section 5.4.

Table A1. 8: Strain (in '%') of the horizontal bar in the critical region.

Strain direction	AZ91D – 210 °C mold temperature	AZ91D – 250 °C mold temperature	AE42 – 340 °C mold temperature	AE42 – 390 °C mold temperature
X	+1.05	+0.10	+0.55	+0.35
Y	+0.04	+0.01	+0.31	-0.09
Z	-1.05	-0.08	-1.29	-0.82

Observing data in Table A1. 8, several general trends were identified. First, the *x*-direction tensile strain in the hot tear region significantly decreased with increasing mold temperature for the AZ91D alloy. Secondly, it was observed that the AE42 alloy was less sensitive to mold temperature increase than the AZ91D alloy, since the decrease of strain was less pronounced.

It was observed that the *x*-direction deformation was the primary factor contributing to the displacement of the critical region (a relatively high tensile *x*-direction strain developed). In contrast, the *z*-direction strain was compressive for all casting conditions, indicating that solidification contraction in the *z*-direction was not restricted and likely did not play a role on hot tearing.

In the case of the *y*-direction strain, positive values were observed for both AZ91D and the AE42 / 340°C simulations. In these cases, MAGMASOFT® suggested that the horizontal bar was pressed upwards against the top edge of the mold cavity. This displacement was driven by the axial contraction of the downsprue, which occurred after the horizontal bar solidified. With increasing mold temperature, the rate of sprue contraction decreased due to enhanced feeding of molten metal from the pouring cup, hence the net *y*-direction strain decreased as well.

It was further observed that the *x*-direction contraction of the horizontal bar confirmed the expected tendency of the bar to press against the mold wall and induce high contact stresses on the vertical surfaces near the critical region. Thus, the assumption made during developing simulation parameters, that high HTC values should be used on the vertical surfaces, appears reasonable.

The *y*- and *z*- strains in the critical region suggest that the material experienced "necking", as illustrated in Figure A1. 24. The severity of necking decreased with increasing mold temperature. This necking indicates that:

1. Feeding of the horizontal bar at low mold temperatures was choked.
2. The critical region experienced elevated stress levels due to decreasing cross sectional area and increasing true stress.
3. The critical region had a relatively high localized tendency for severe deformation, thus having non-uniform strain distribution.

All of these factors would contribute to elevated tendency for hot tear nucleation in the critical region.

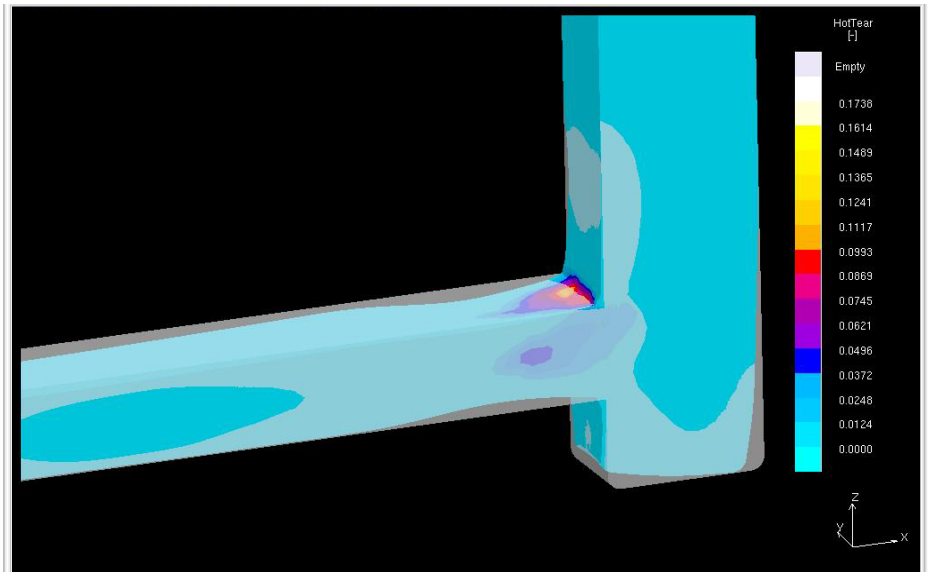

Figure A1. 24: Necking of the horizontal bar in the critical casting region.

The displacement results further indicate that significant strain gradients developed in the critical region of the casting. For example, in the case of the AZ91D casting at 210 °C mold temperature, Figure A1. 25 suggests that deformation in the horizontal bar at x = 20 mm was -0.17 mm, while it was –0.02 mm at the 90° corner. Normalizing these deformations by the characteristic length of 20 mm, the corresponding strain values between these locations were 0.89% and 0.13%, respectively, resulting in a strain gradient of 0.038%/mm. In the case of the AZ91D casting at 250 °C mold temperature, the deformations at the same location were -0.02 mm and -0.0009 mm, respectively (Figure A1. 25) and the strain gradient was 0.00064%/mm. Thus, increasing the mold temperature significantly affected the deformation homogeneity and the magnitude of strain gradients in the critical region. By improving strain homogeneity via higher mold temperature, the tendency for hot tearing decreased.

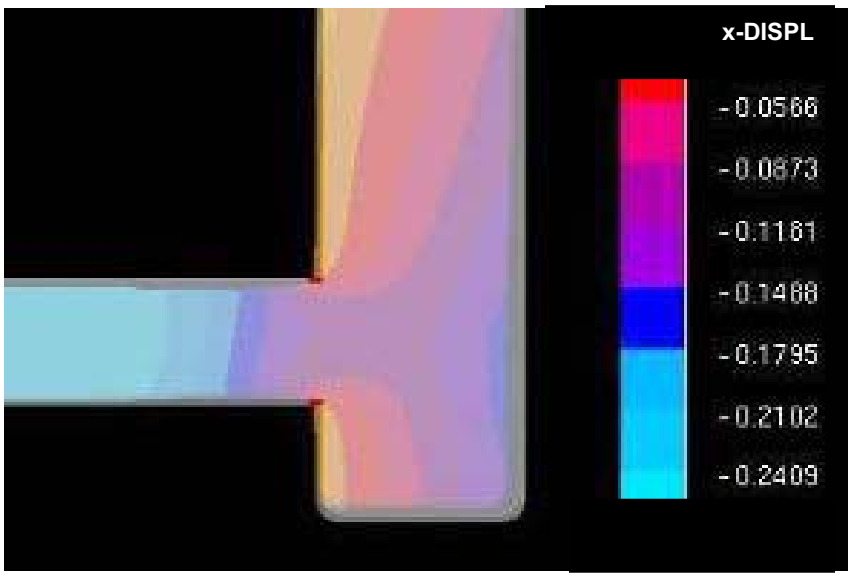

(a) AZ91D alloy, 210 °C mold temperature.

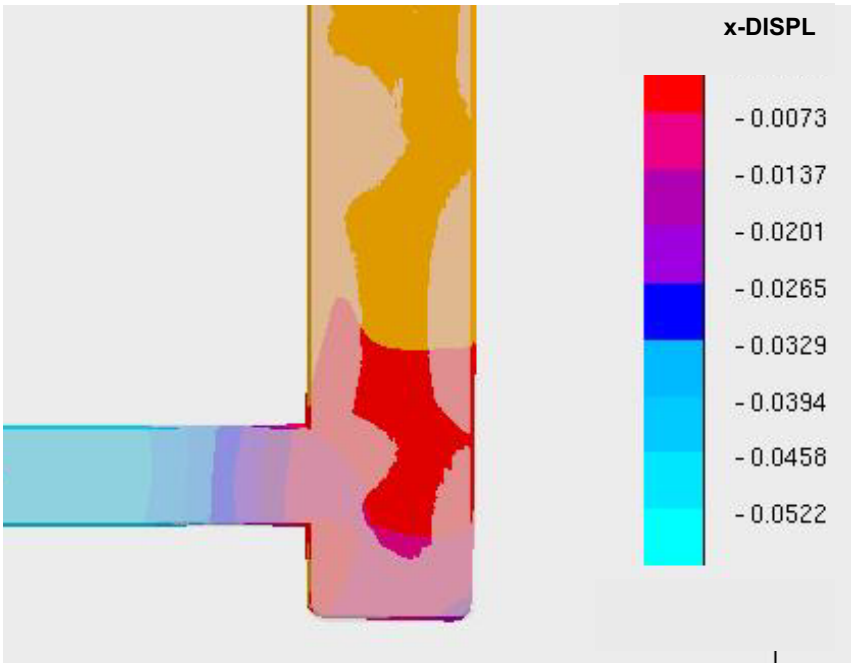

(b) AZ91D alloy, 250 °C mold temperature.

Figure A1. 25: Detail of deformation in the critical region.

A1.3.9 Summary of MAGMASOFT® Simulation Results

Performing casting simulation in MAGMASOFT® software provided information about the solidification and mold filling phenomena in casting of AZ91D and AE42 alloys. The simulations were based on replication of experimental cooling conditions by the computer model. The average difference in temperatures between the experimental thermocouple data and simulated virtual cooling curves was ~10°C. However, as MAGMASOFT® modeling of casting solidification was not one of the principal objectives of this research, the accuracy of some of the simulation results did not achieve desired levels and additional future research is necessary for a meaningful computational modeling and analysis of the solidification process.

Visual inspection of the casting surface defects suggested that the mold filling pattern predicted by MAGMASOFT® (e.g., melt turbulence and reversing wave-front) was reasonable. Thus, the predictions of the casting temperatures and the metal filling / velocity profile appeared to be in general agreement with experimental observations. However, calculation of stresses and deformation via MAGMA*stress*® module yielded questionable results. The quantitative results of the stress and deformation behavior at the onset of hot tearing conflicted with visual casting observations and experimental stress/strain measurements by ND. One of the contributing factors to the inaccuracy of the results was due to the simulation's inability to account for the change in the alloy microstructure and interdendritic feeding with increasing mold temperature. Also, precipitation of intermetallic phases (e.g., $Al_{11}RE_3$ in AE42 alloy) was not considered in the simulations, as well as the development solidification defects (e.g., interdendritic shrinkage porosity and solute segregation). Lastly, the knowledge of accurate thermophysical data for the AZ91D and AE42 alloys was limited, thus making accurate prediction of high temperature mechanical response of the material difficult.

MAGMASOFT® succeeded in qualitatively predicting various attributes of the casting process:

1. Hot Tearing Index (HTI) reached a maximum at a casting location coincident with extensive shrinkage porosity. However, neither the path of hot tear propagation, nor the severity of hot tearing could be identified using the HTI criterion.
2. Numerical modeling revealed that solidification of the horizontal bars manufactured at low mold temperatures resulted in rapid hoop solidification, preventing the establishment of axial solidification. As a result, evolution of hot-spots was possible, leading to localized suppression of the solidus temperature in the hot spot region and subsequent porosity formation. As the mold temperature increased, the size of the hot spots decreased, suggesting that casting solidification became more uniform, interdendritic feeding improved and casting soundness improved.

3. Considering the qualitative results in Appendix A1.3.8, increasing the mold temperature decreased the deformation gradients in the casting. Further, MAGMA*stress*® qualitatively predicted a deformation discontinuity in the critical region of the casting, both of which were in agreement with ND measurements.
4. MAGMASOFT® predicted the magnitude of the displacement in the *x*-direction to significantly exceed the magnitude of displacements in the *y*- or *z*-directions. This prediction was consistent with ND results (e.g., Figure 145a).
5. The MAGMA*stress*® results further suggested that the axial contraction of the downsprue pressed the top edge of the horizontal bar against the mold surface, thus contributing to the development of compressive stress along the top edge. The qualitative aspect of this result is in agreement with the ND strain measurements along the top edge.
6. Simulation of metal flow in the casting cavity revealed formation of multiple metal streams in the critical casting region. Formation of multiple metal streams likely exposed a large surface area of molten metal to the ambient atmosphere in the mold cavity and enabled the metal's oxidation. Formation of oxide inclusions in this region was confirmed by microscopic analysis (e.g., Figure 104).
7. MAGMASOFT® revealed that the hoop solidification of the downsprue (just above the critical region) at low mold temperatures choked liquid metal flow into the horizontal bar. This prediction was in agreement with the experimentally observed extensive porosity in metallographic Samples #8 (Section 5.2.5). The extent of choking decreased with increasing mold temperature, since elevated mold temperatures slowed down the hoop solidification rate of the downsprue.

A1.3.10 Detailed Graphical Results of MAGMASOFT® Simulations

A1.3.10.1 Casting Filling Temperature

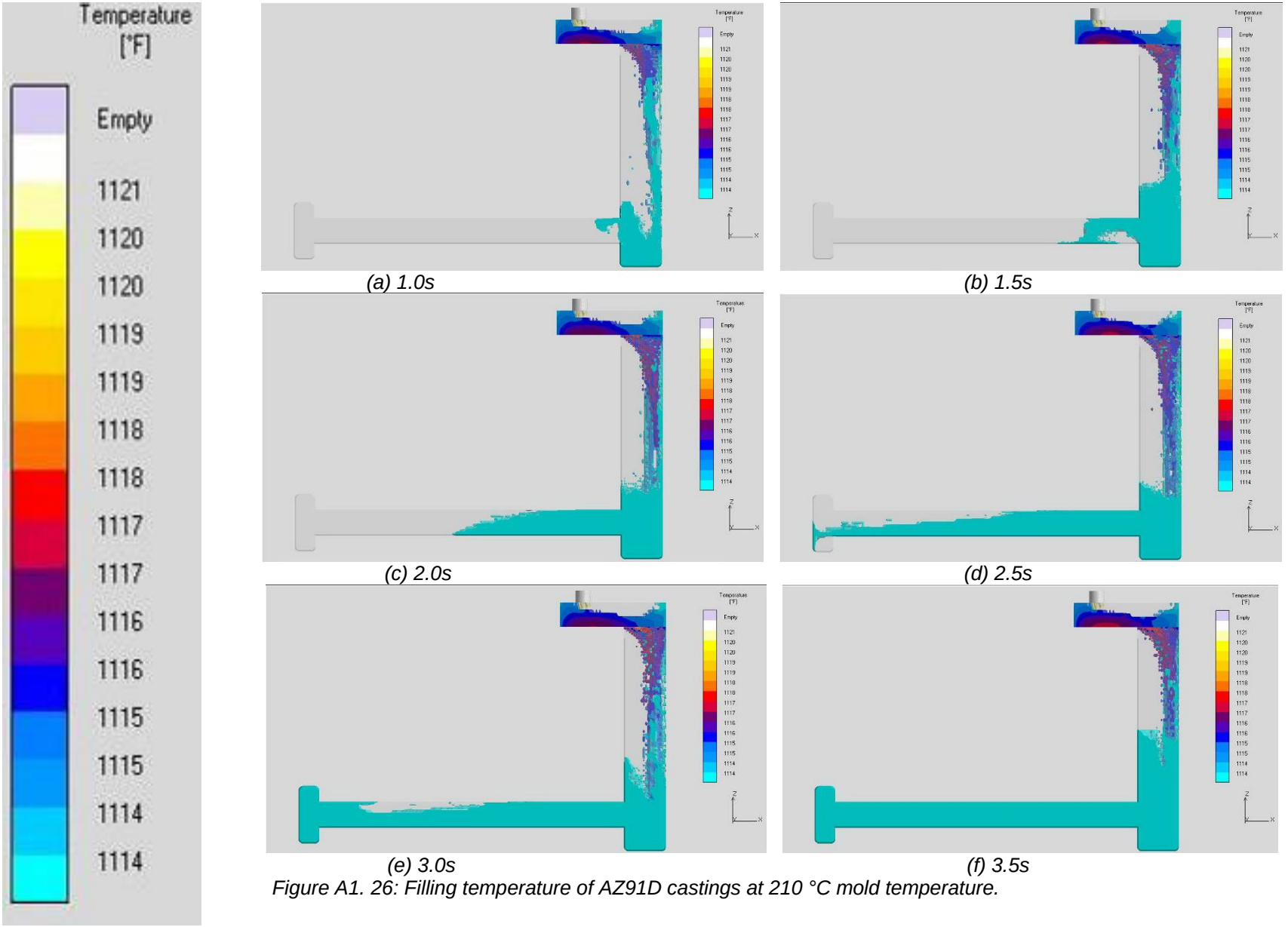

(a) 1.0s (b) 1.5s

(c) 2.0s (d) 2.5s

(e) 3.0s (f) 3.5s

Figure A1. 26: Filling temperature of AZ91D castings at 210 °C mold temperature.

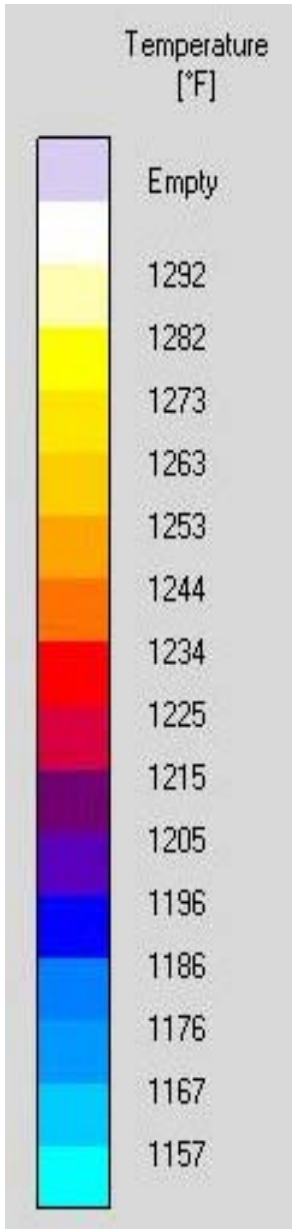

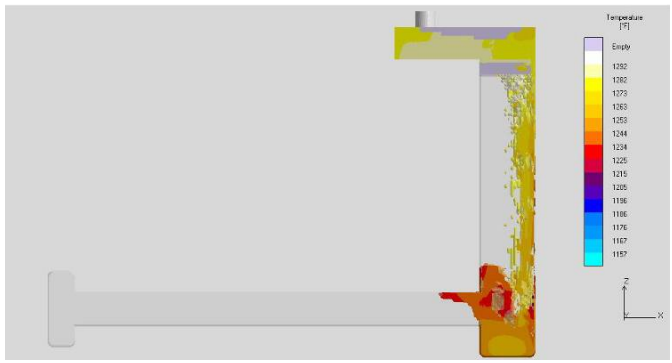

(a) 1.0s

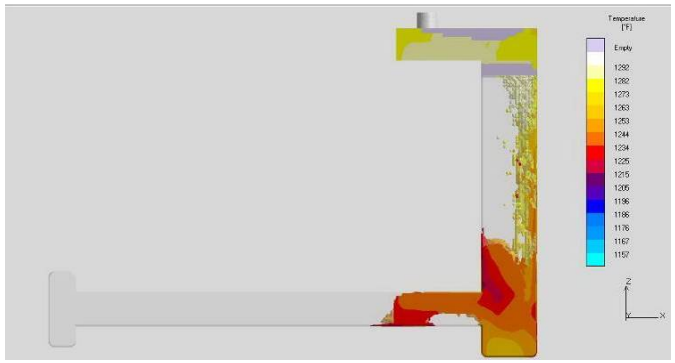

(b) 1.5s

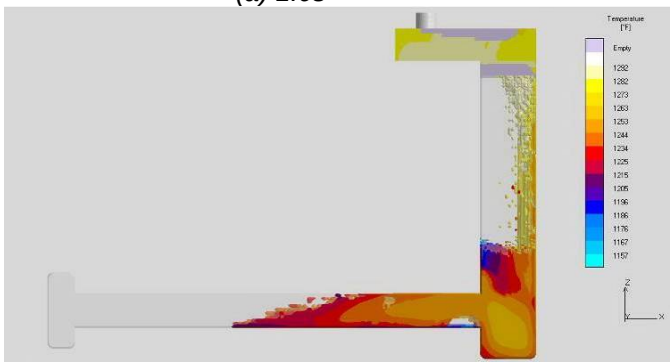

(c) 2.0s

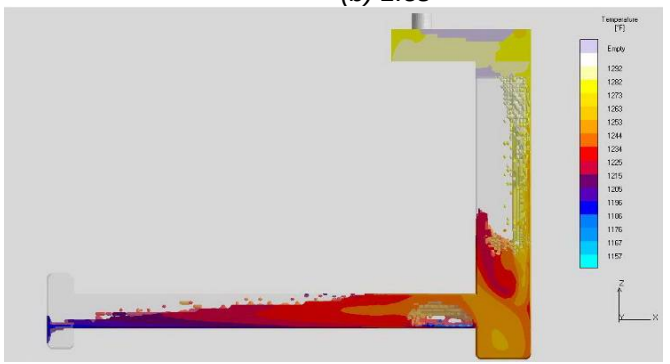

(d) 2.5s

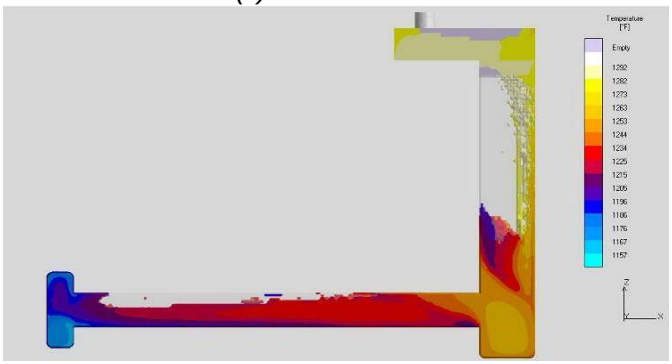

(e) 3.0s

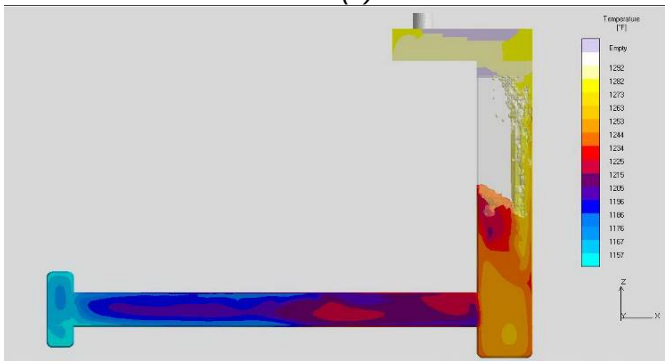

(f) 3.5s

Figure A1. 27: Filling temperature of AZ91D casting at 250 °C mold temperature.

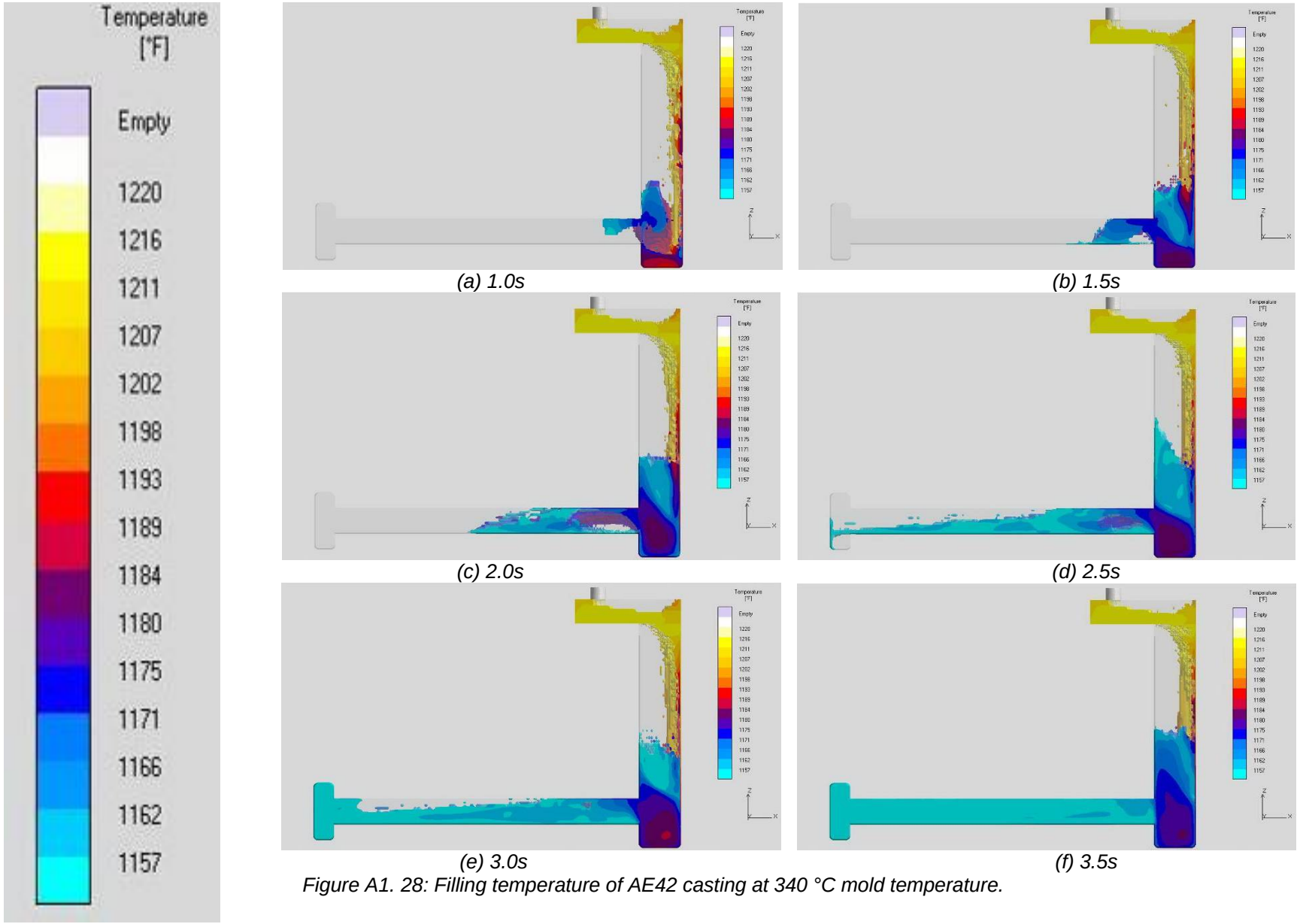

(a) 1.0s (b) 1.5s

(c) 2.0s (d) 2.5s

(e) 3.0s (f) 3.5s

Figure A1. 28: Filling temperature of AE42 casting at 340 °C mold temperature.

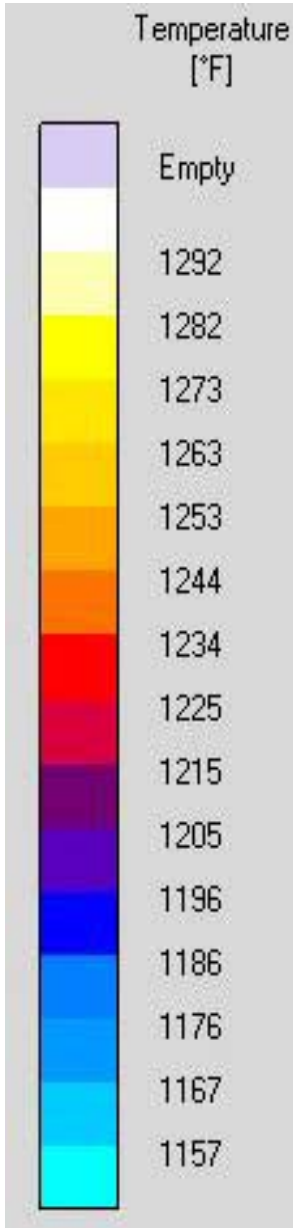

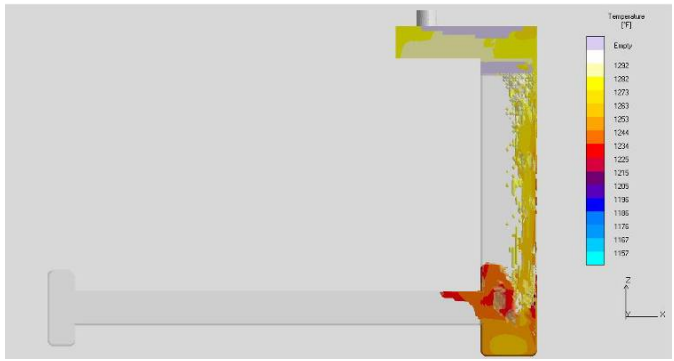

(a) 1.0s

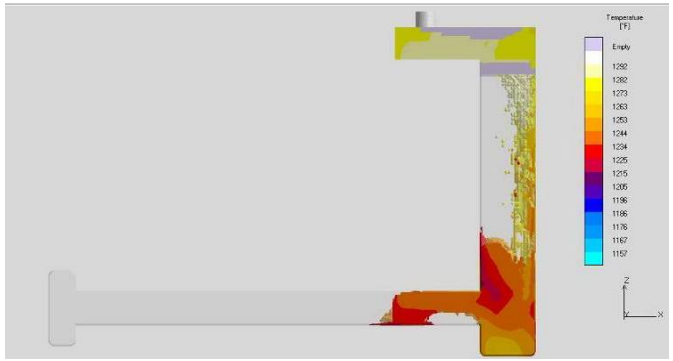

(b) 1.5s

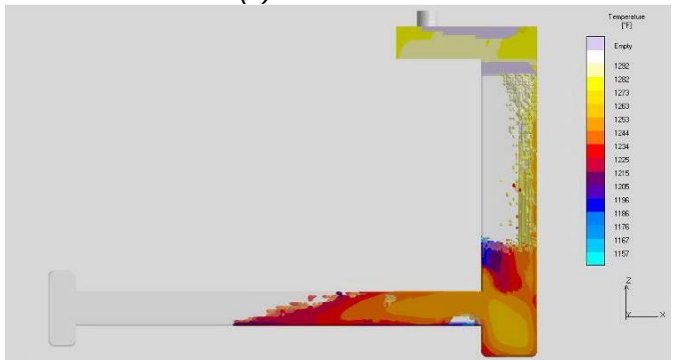

(c) 2.0s

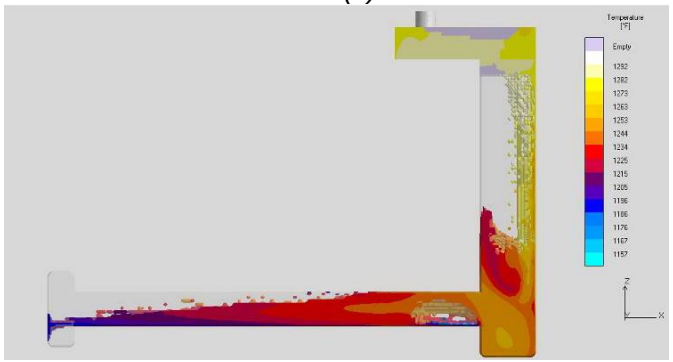

(d) 2.5s

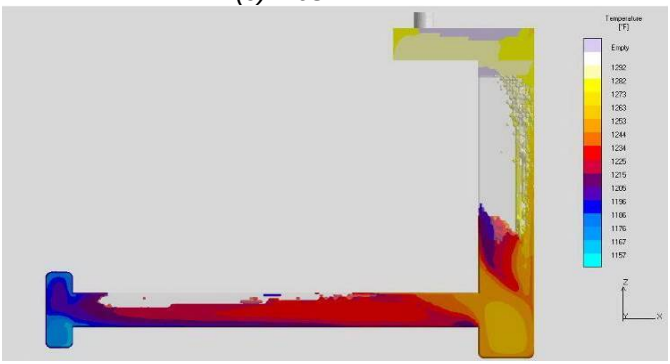

(e) 3.0s

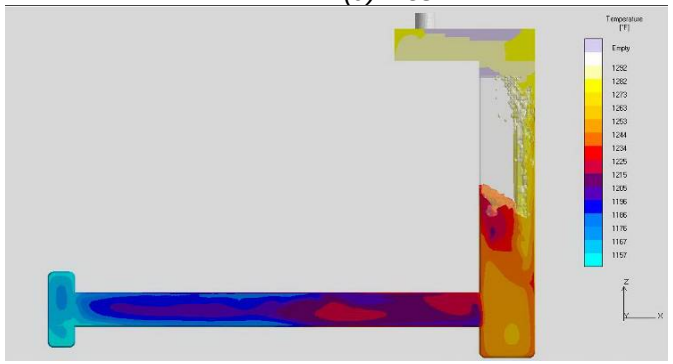

(f) 3.5s

Figure A1. 29: Filling temperature of AE42 casting at 390 °C mold temperature.

A1.3.10.2 Casting Filling Velocity

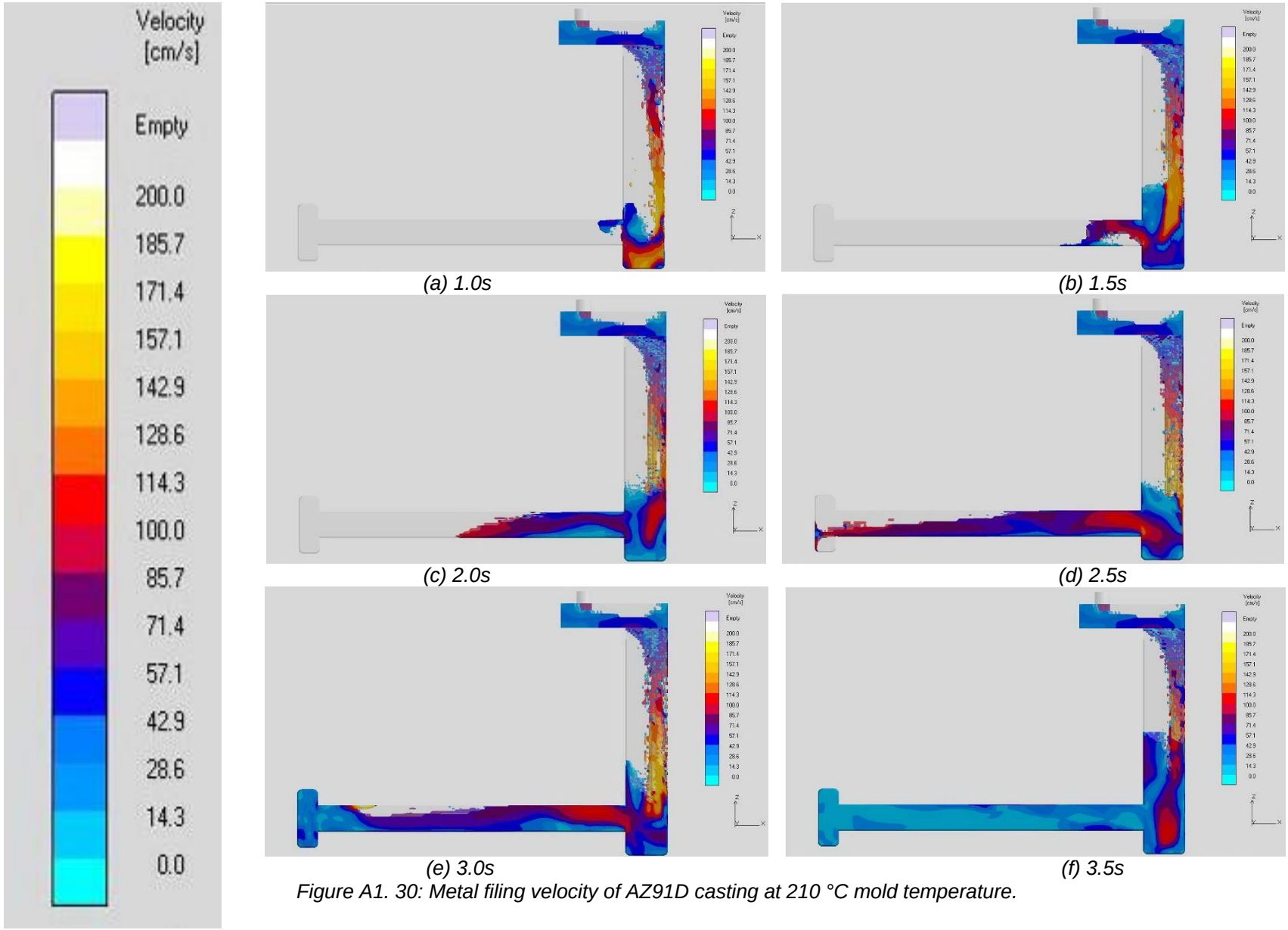

(a) 1.0s (b) 1.5s

(c) 2.0s (d) 2.5s

(e) 3.0s (f) 3.5s

Figure A1. 30: Metal filing velocity of AZ91D casting at 210 °C mold temperature.

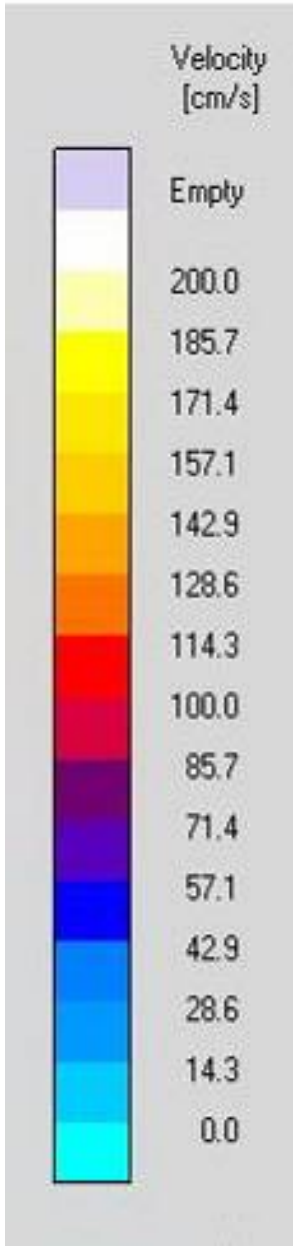

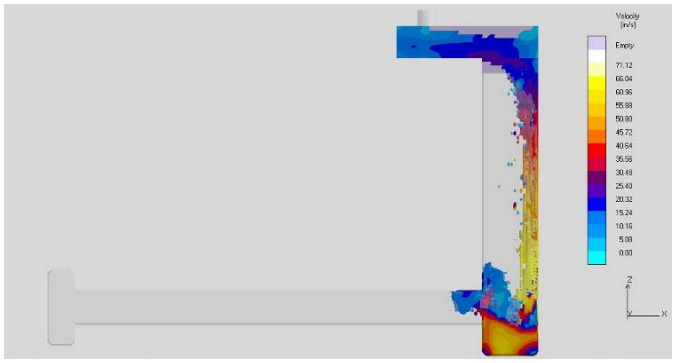

(a) 1.0s

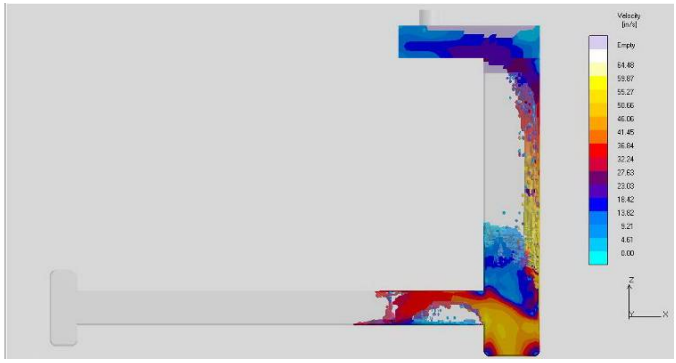

(b) 1.5s

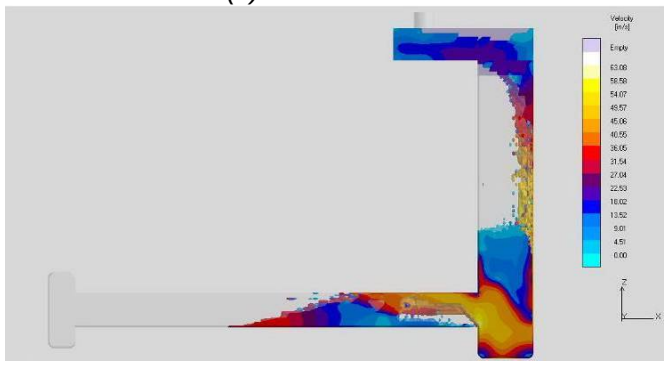

(c) 2.0s

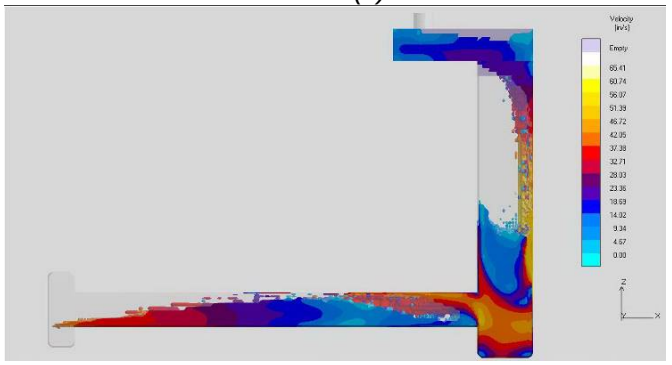

(d) 2.5s

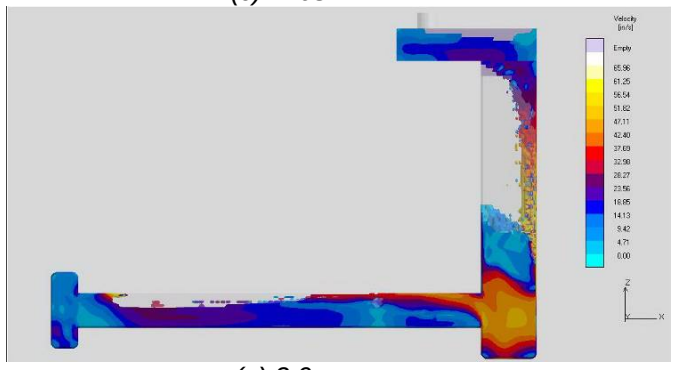

(e) 3.0s

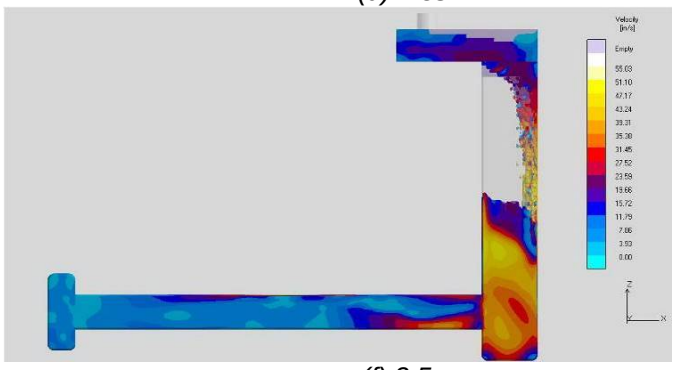

(f) 3.5s

Figure A1. 31: Metal filing velocity of AZ91D casting at 250 °C mold temperature.

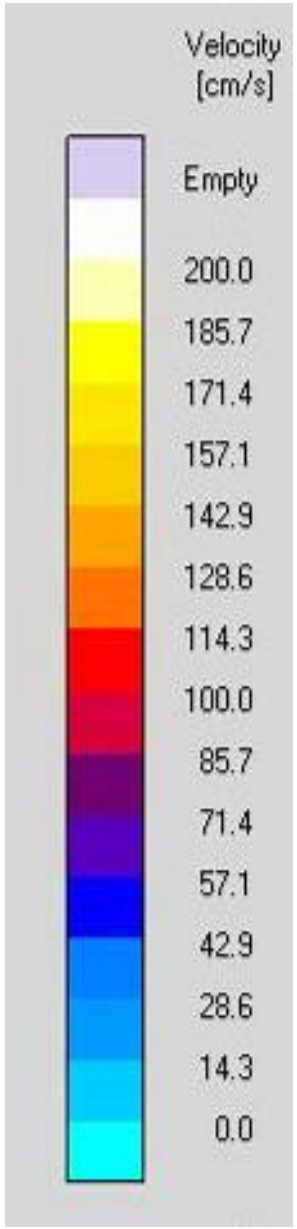

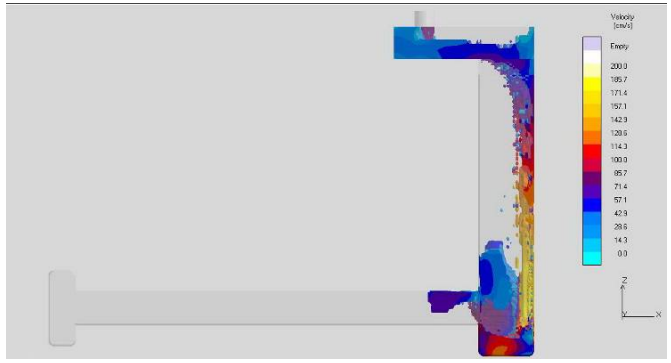

(a) 1.0s

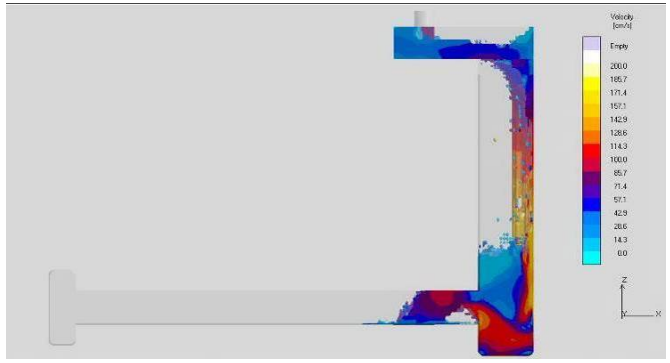

(b) 1.5s

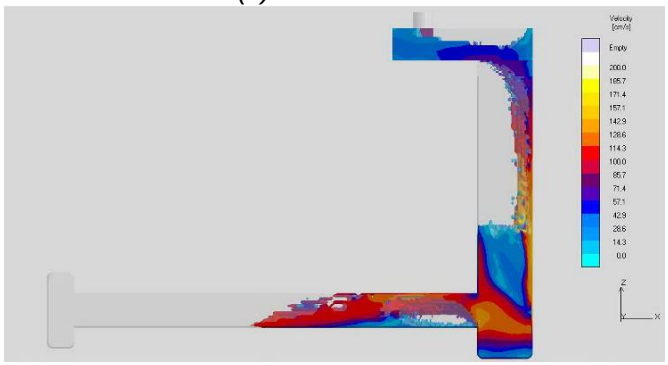

(c) 2.0s

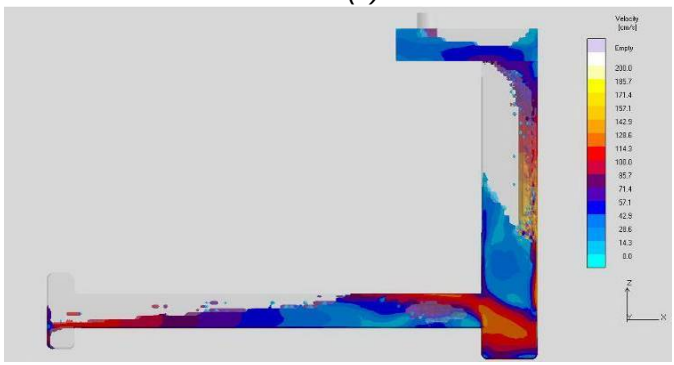

(d) 2.5s

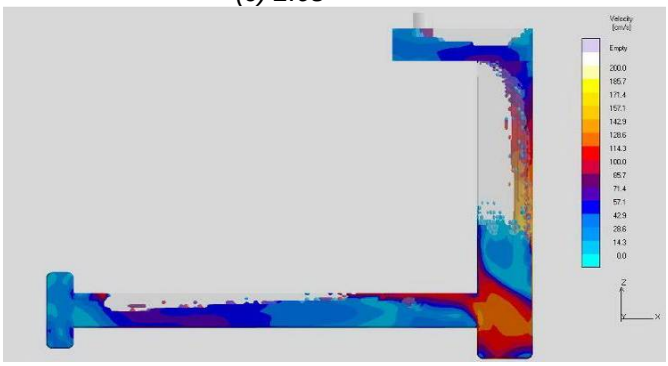

(e) 3.0s

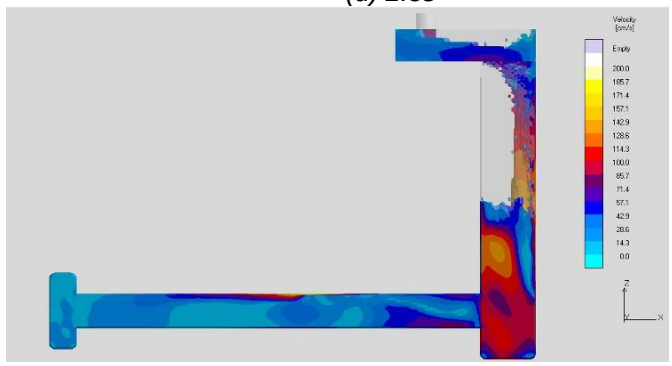

(f) 3.5s

Figure A1. 32: Metal filing velocity of AE42 casting at 340 °C mold temperature.

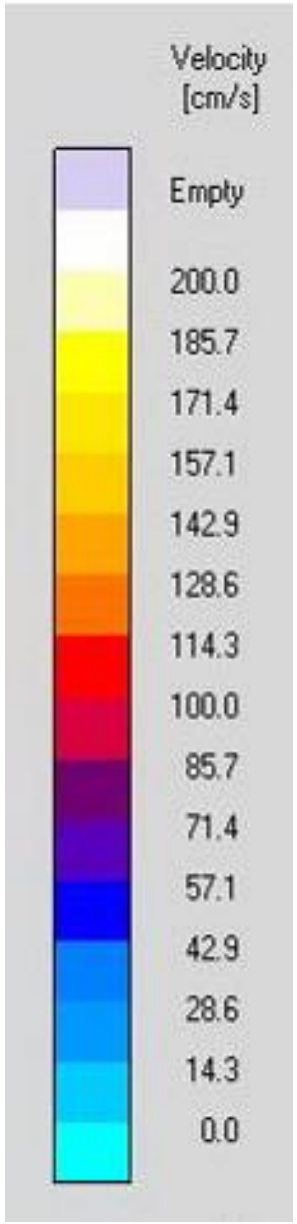

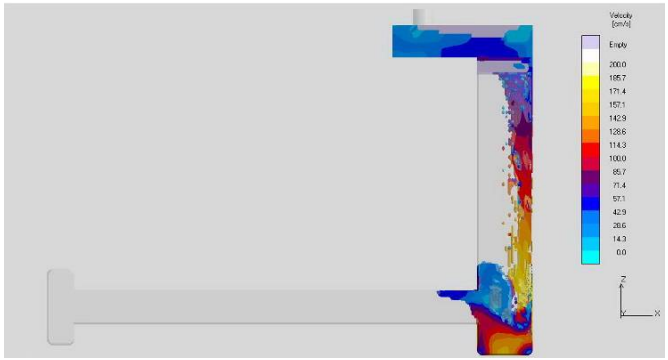

(a) 1.0s

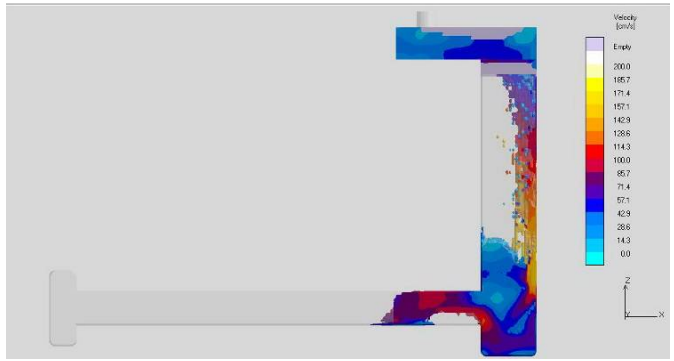

(b) 1.5s

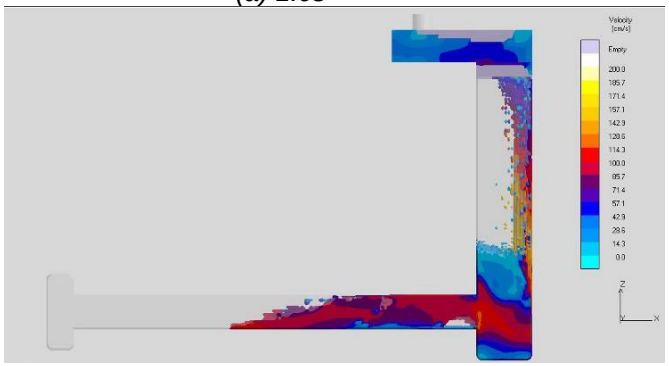

(c) 2.0s

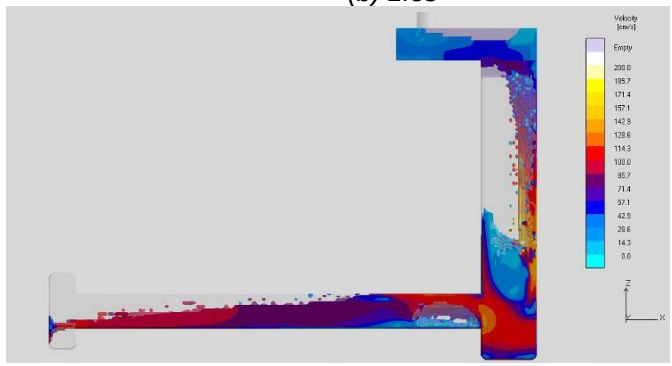

(d) 2.5s

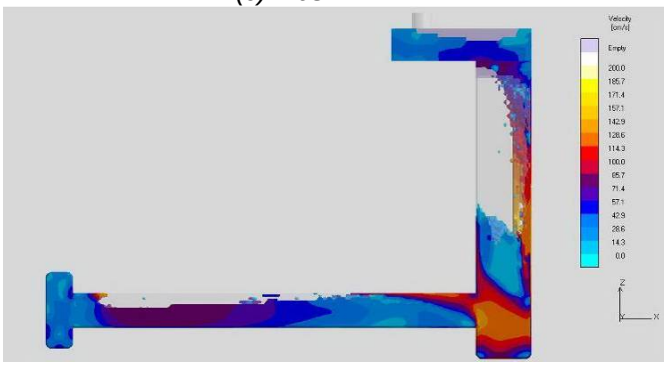

(e) 3.0s

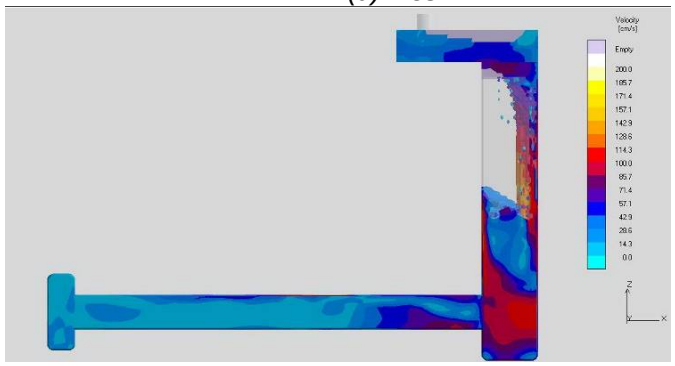

(f) 3.5s

Figure A1. 33: Metal filing velocity of AE42 casting at 390 °C mold temperature.

A1.3.10.3 Casting Solidification Temperature

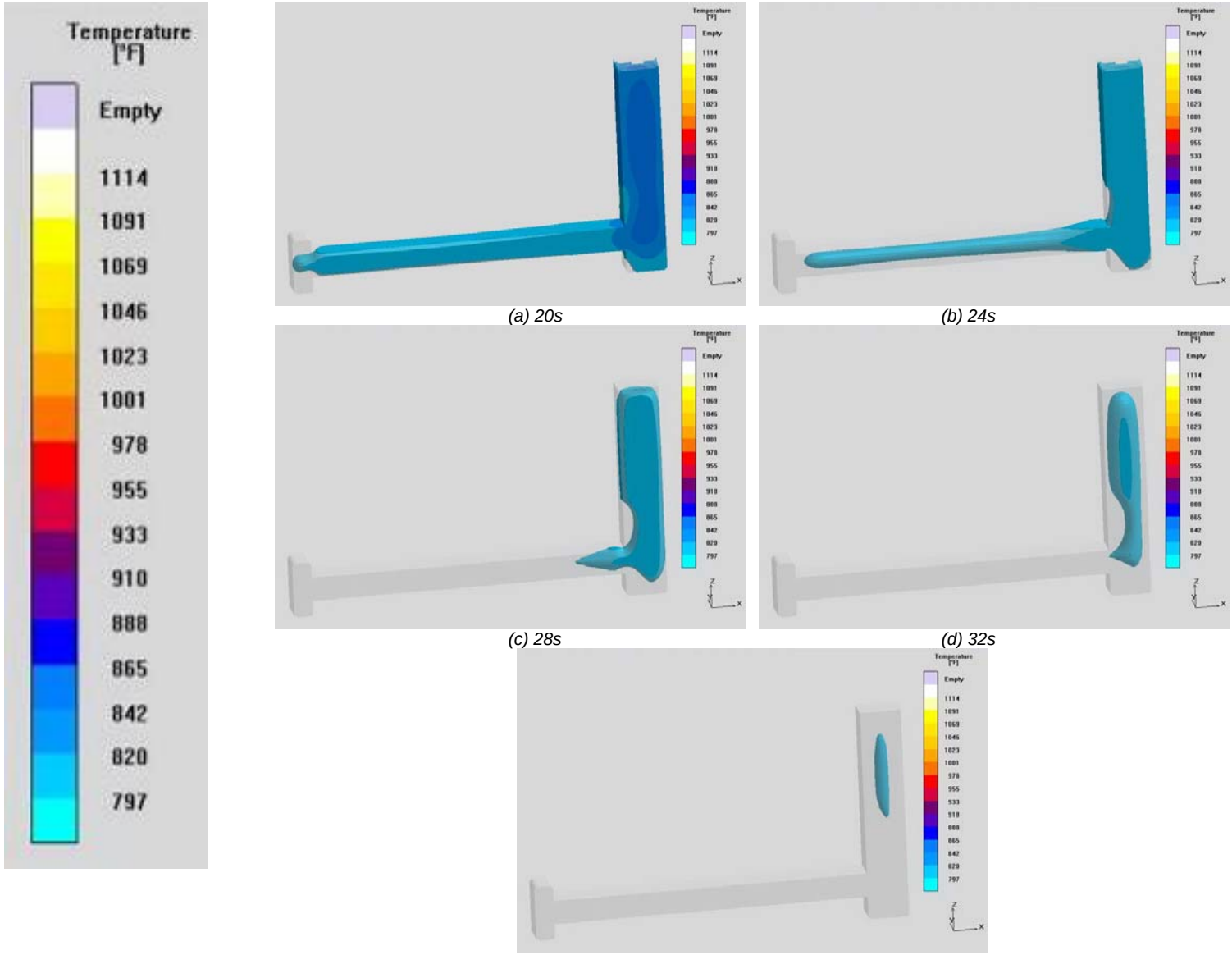

(a) 20s *(b) 24s*

(c) 28s *(d) 32s*

(e) 36s

Figure A1. 34: Solidification temperature of AZ91D casting at 210 °C mold temperature.

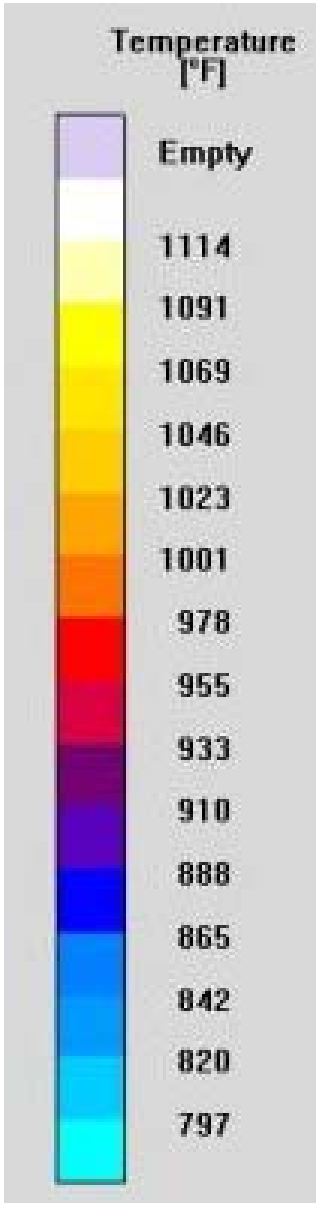

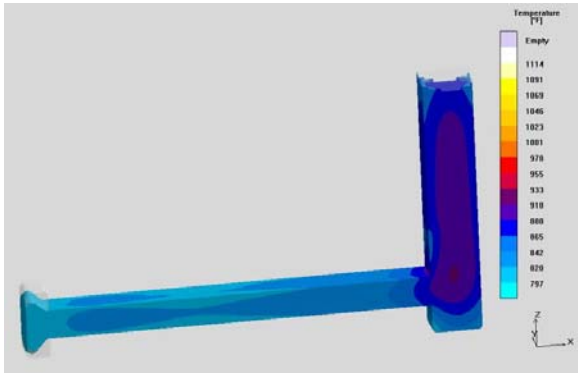

(a) 20s

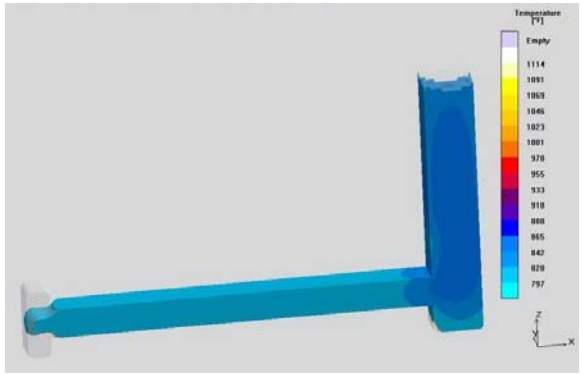

(b) 24s

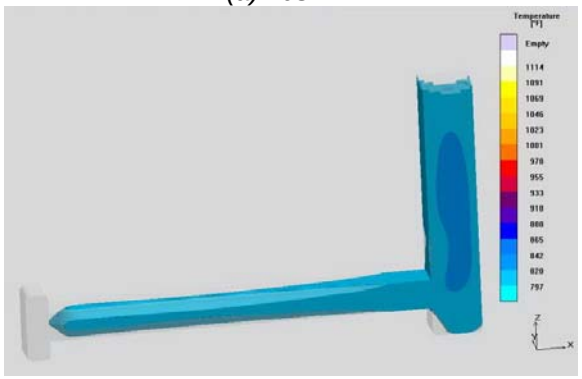

(c) 28s

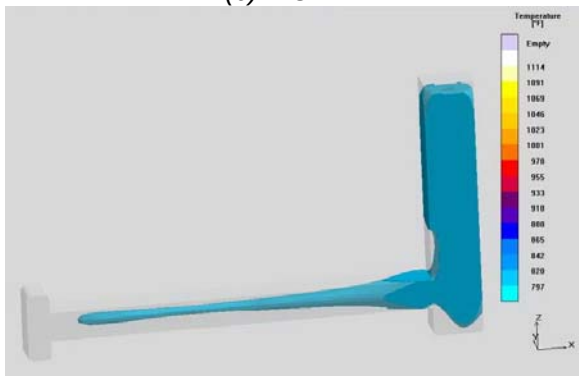

(d) 32s

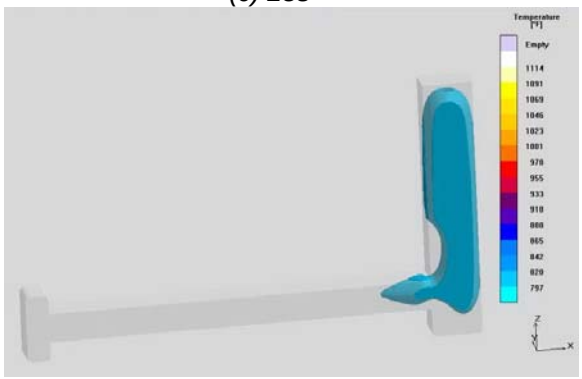

(e) 36s

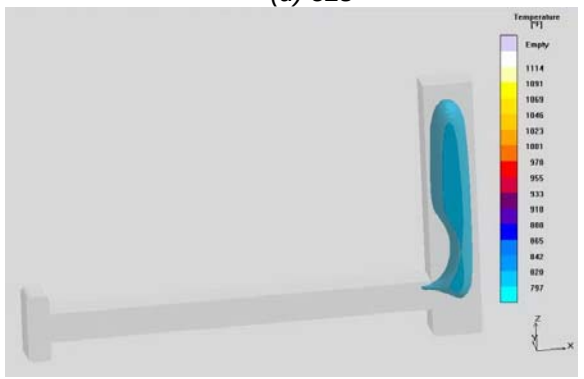

(f) 40s

Figure A1. 35: Solidification temperature of AZ91D casting at 250 °C mold temperature.

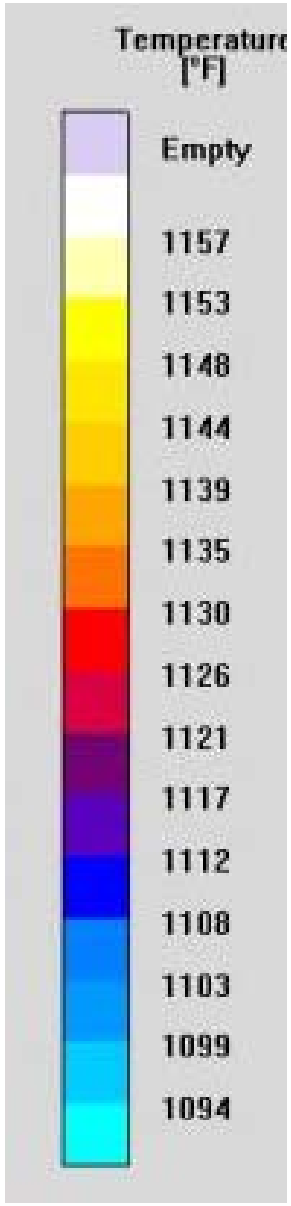

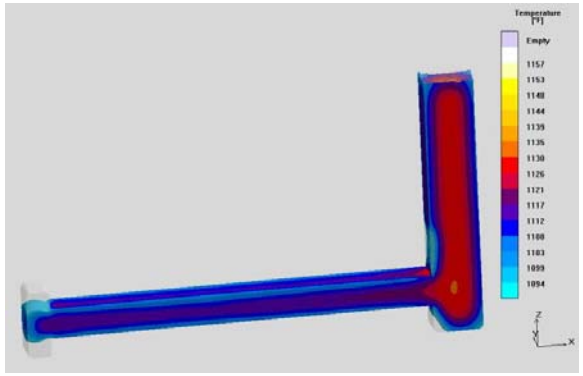

(a) 12s

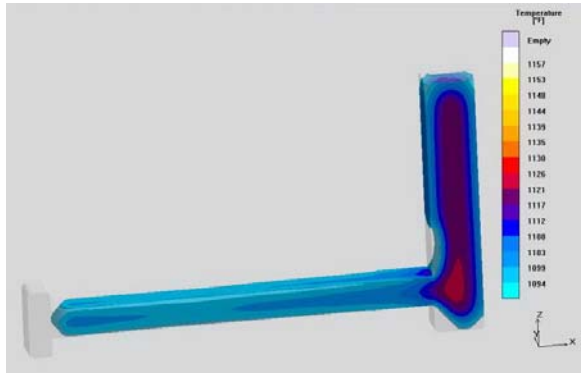

(b) 16s

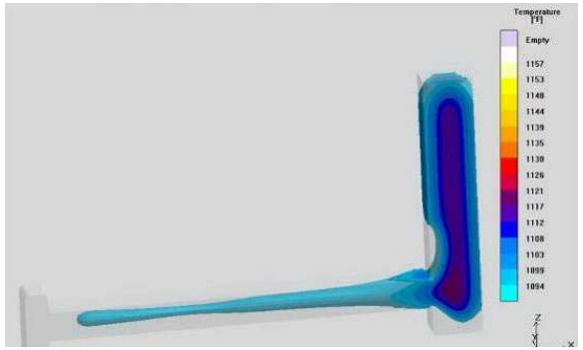

(c) 18 s

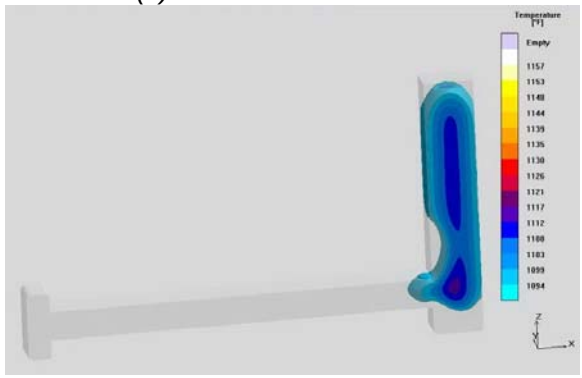

(d) 20s

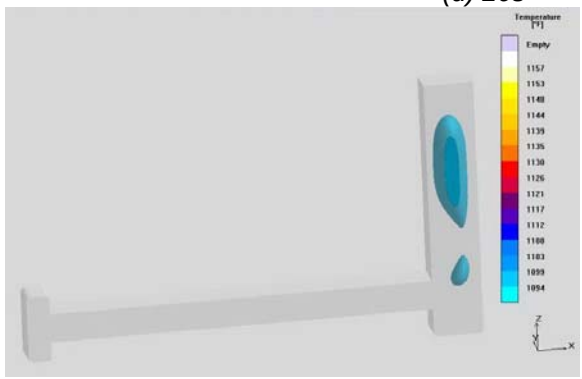

(d) 24s

Figure A1. 36: Solidification temperature of AE42 casting at 340 °C mold temperature.

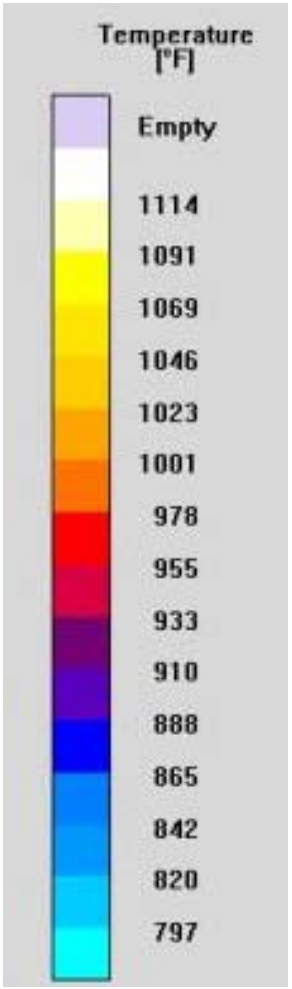

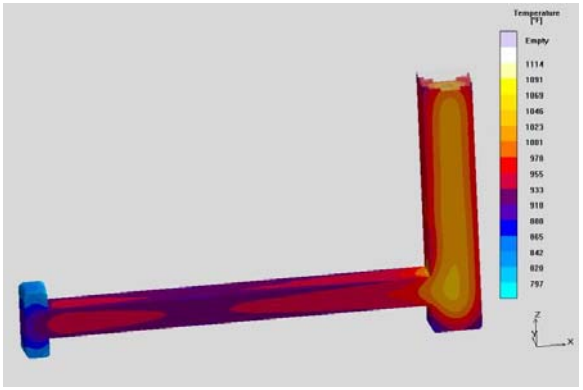

(a) 12 s

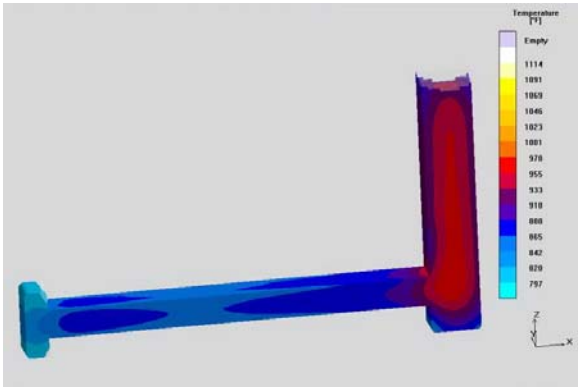

(b) 16s

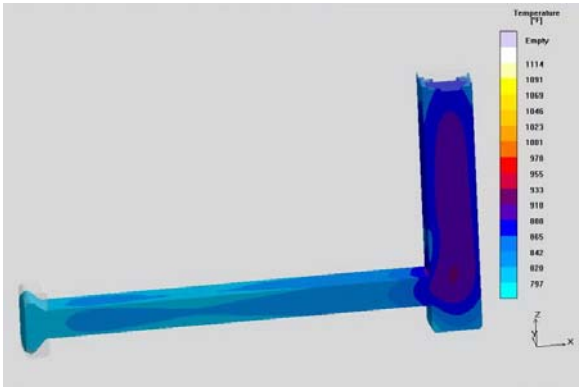

(c) 20 s

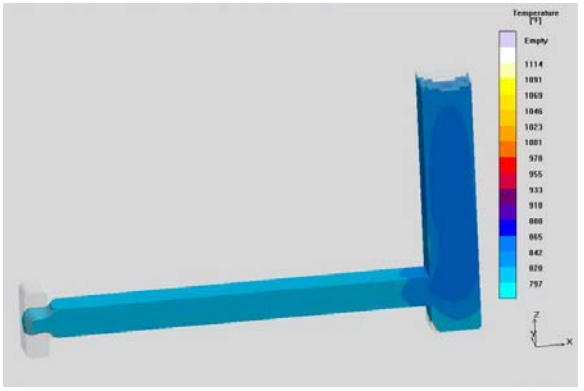

(d) 24 s

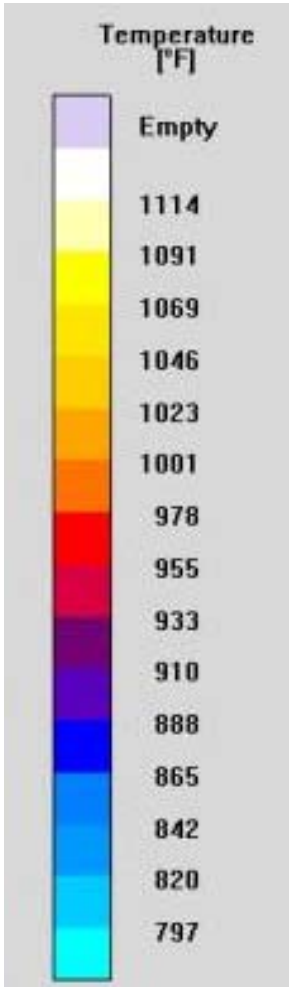

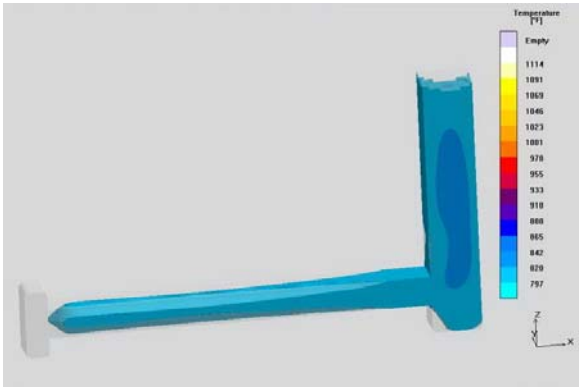

(e) 28 s

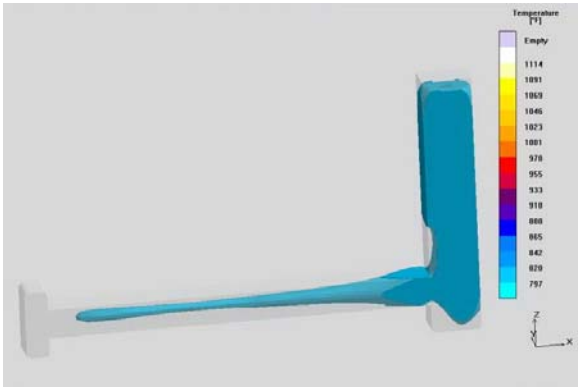

(f) 32 s

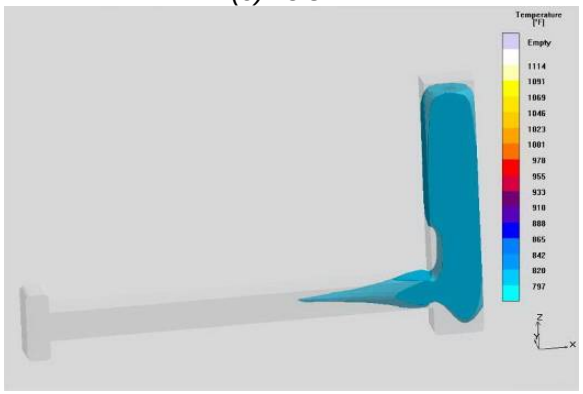

(g) 33 s

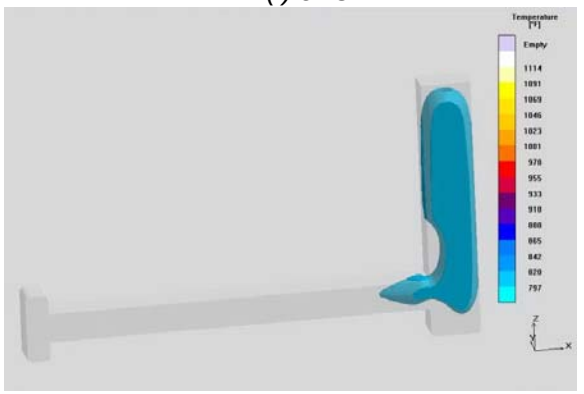

(h) 36 s

Figure A1. 37: Solidification temperature of AE42 casting at 390 °C mold temperature.

A1.3.10.4 Prediction of Hot Tear Evolution

(a) 14 s

(b) 18 s

(c) 20 s

(d) 24 s

(e) 26 s

(f) 28 s

(g) 32 s

Figure A1. 38: HTI in AZ91D casting at 210 °C mold temperature.

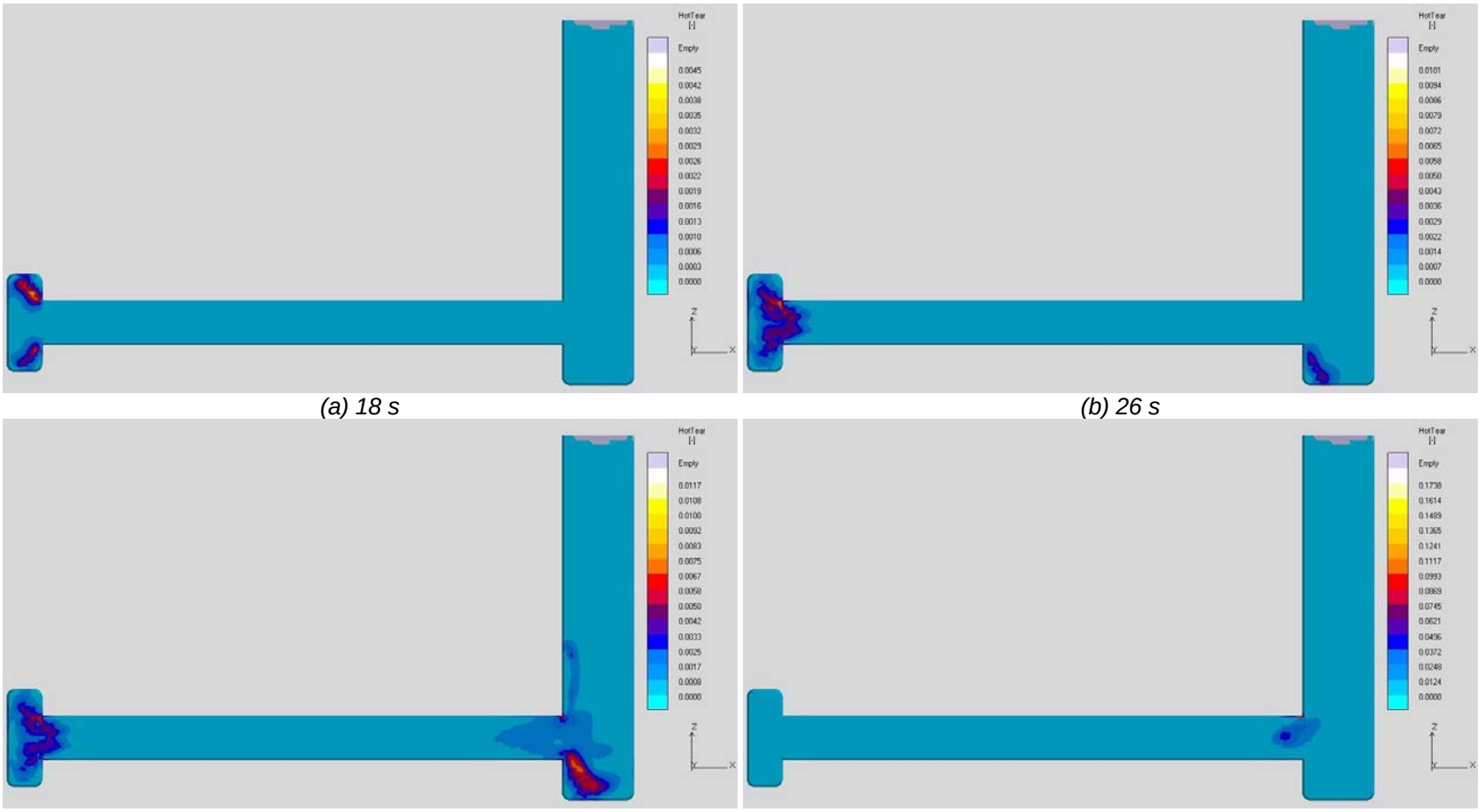

(a) 18 s *(b) 26 s*

(c) 30 s *(d) 36 s*

Figure A1. 39: HTI in AZ91D casting at 250 °C mold temperature.

(a) 10 s

(b) 12 s

(c) 14 s

(d) 18 s

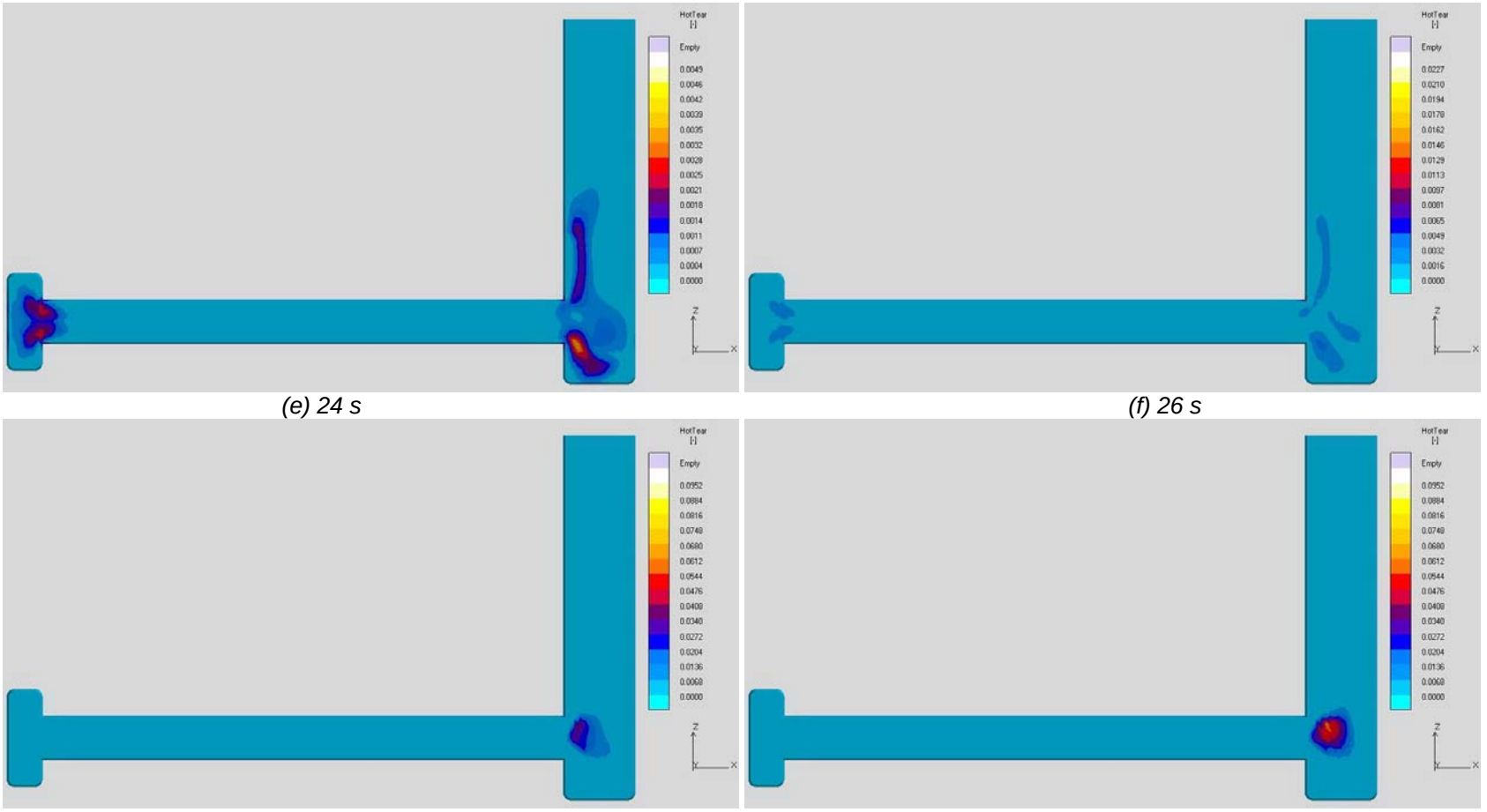

(e) 24 s *(f) 26 s*

(g) 28 s *(h) 32 s*

Figure A1. 40: HTI in AE42 casting at 340 °C mold temperature.

(a) 18 s

(b) 24 s

(c) 28 s

(d) 32 s

(e) 36 s

Figure A1. 41: HTI in AE42 casting at 390 °C mold temperature

A1.3.10.5 Casting Displacement

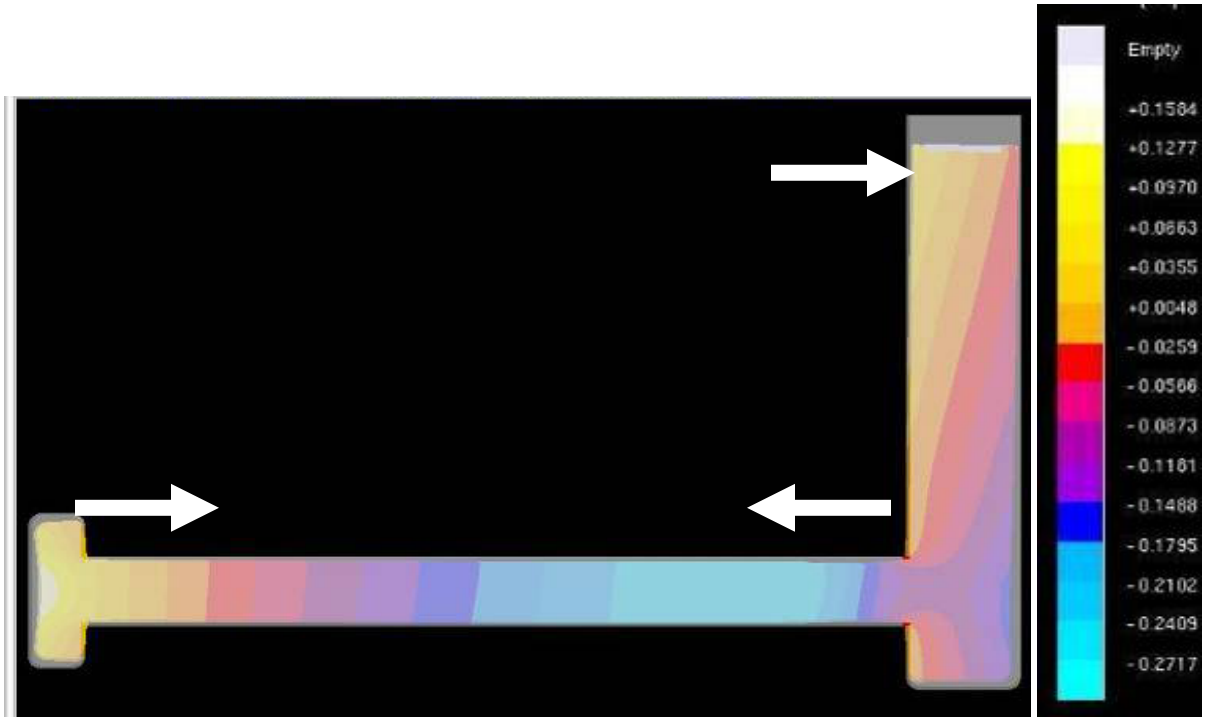

(a) Displacement in x-direction (mm).

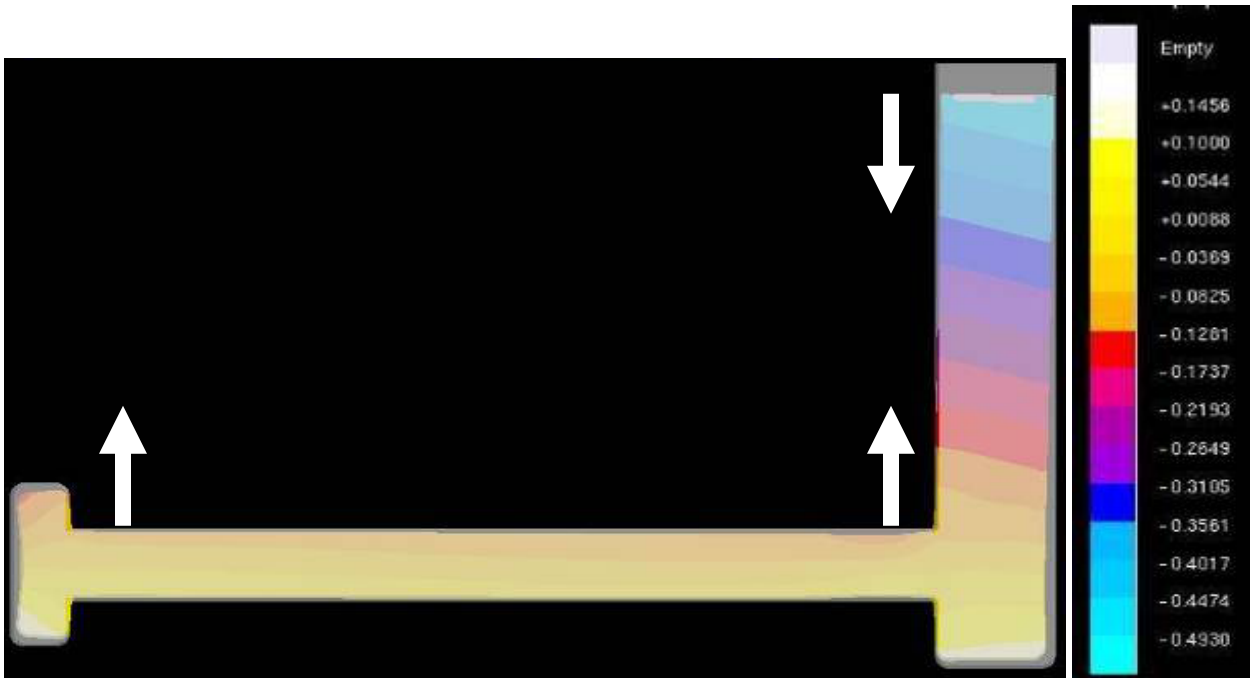

(b) Displacement in y-direction (mm).

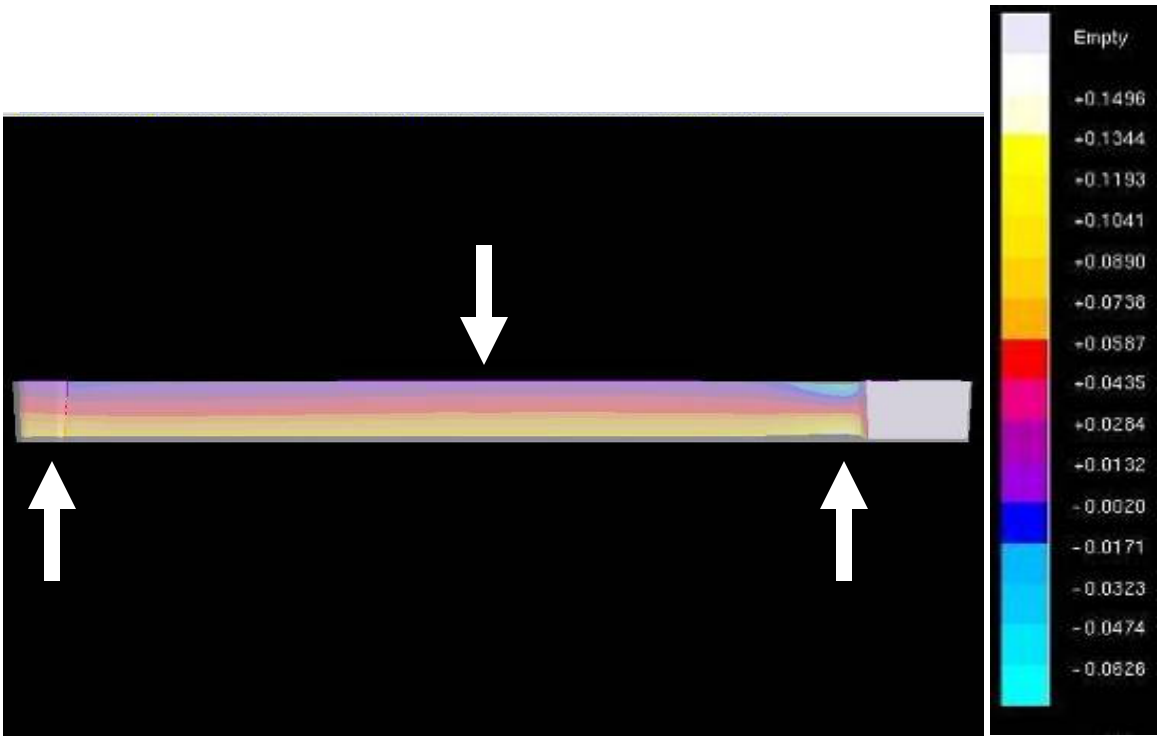

(c) Displacement in z-direction (mm).

Figure A1. 42: Displacement of AZ91D casting at 210 °C mold temperature.

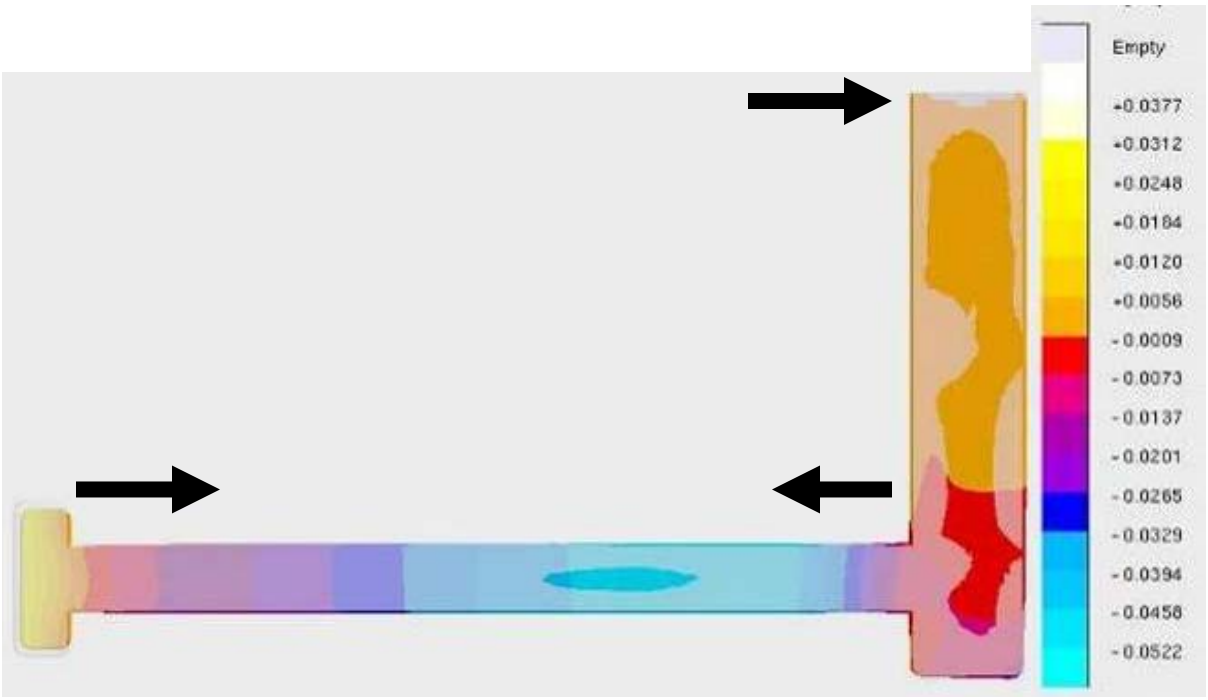

(a) Displacement in x-direction (mm).

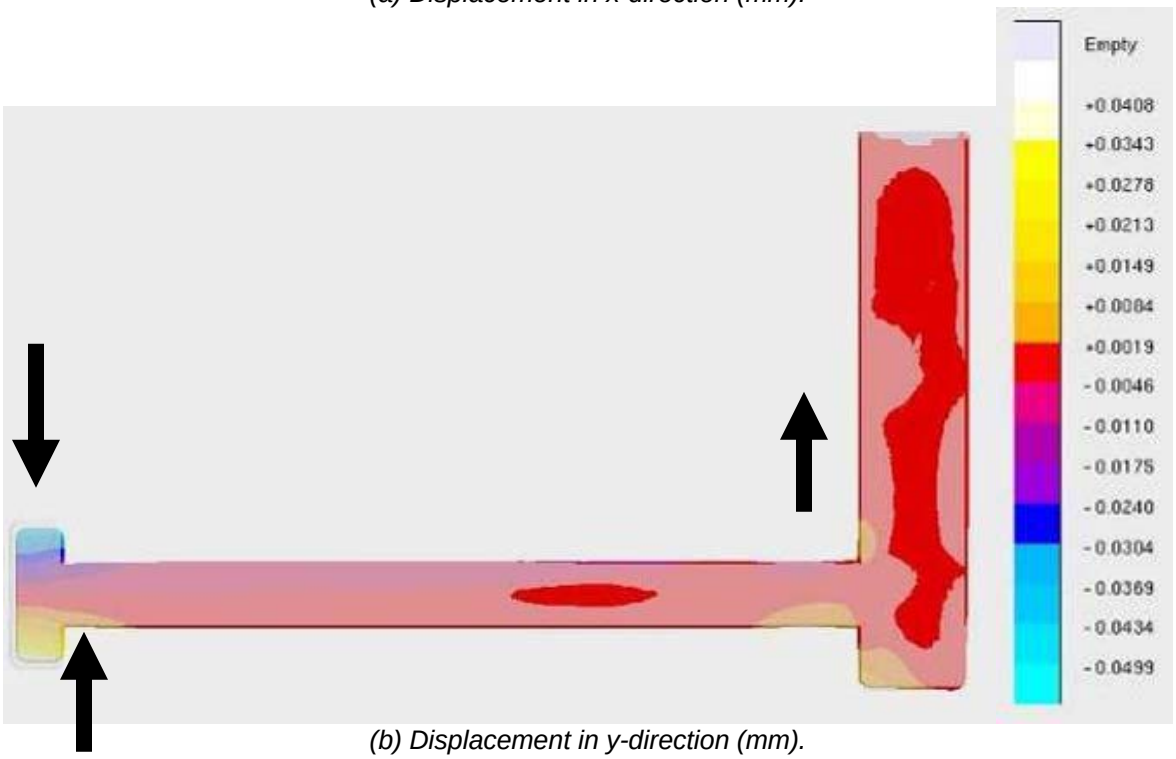

(b) Displacement in y-direction (mm).

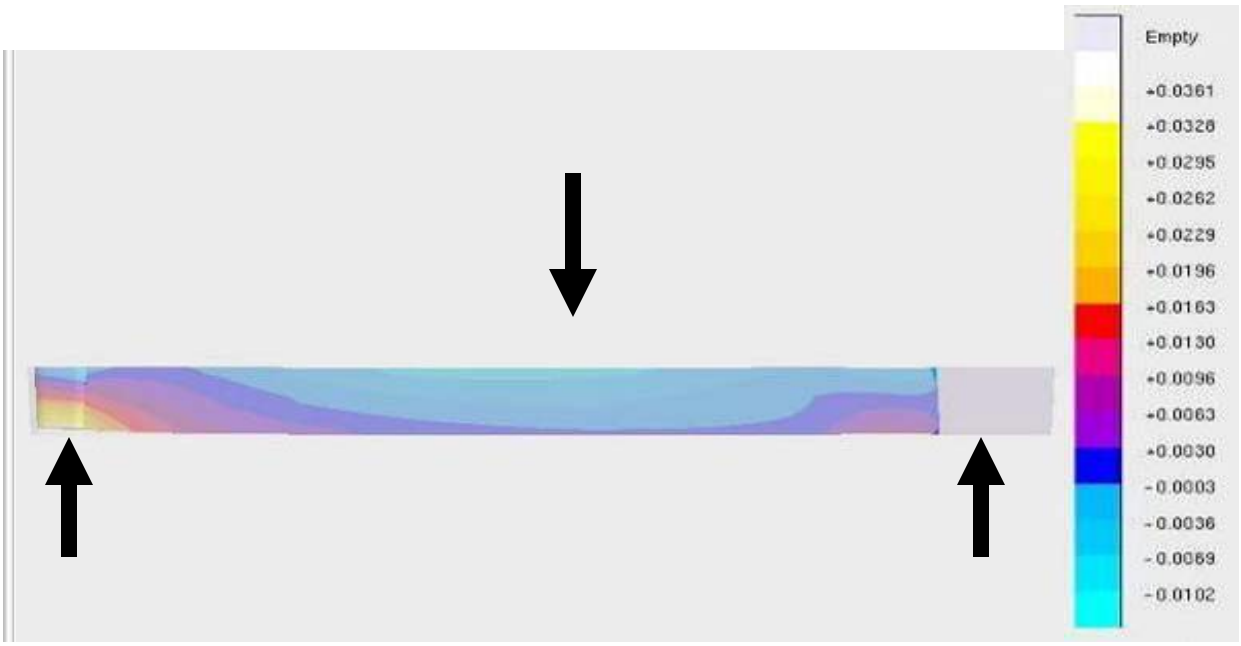

(c) Displacement in z-direction (mm).

Figure A1. 43: Displacement of AZ91D casting at 250 °C mold temperature.

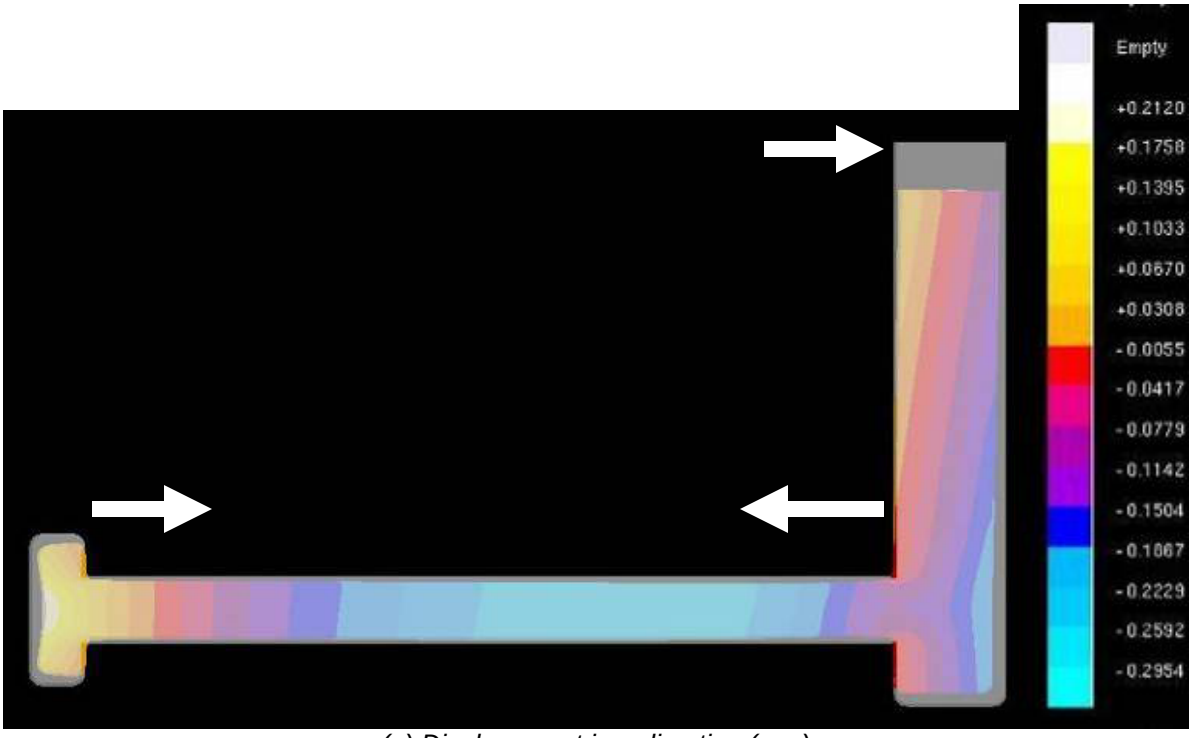

(a) Displacement in x-direction (mm).

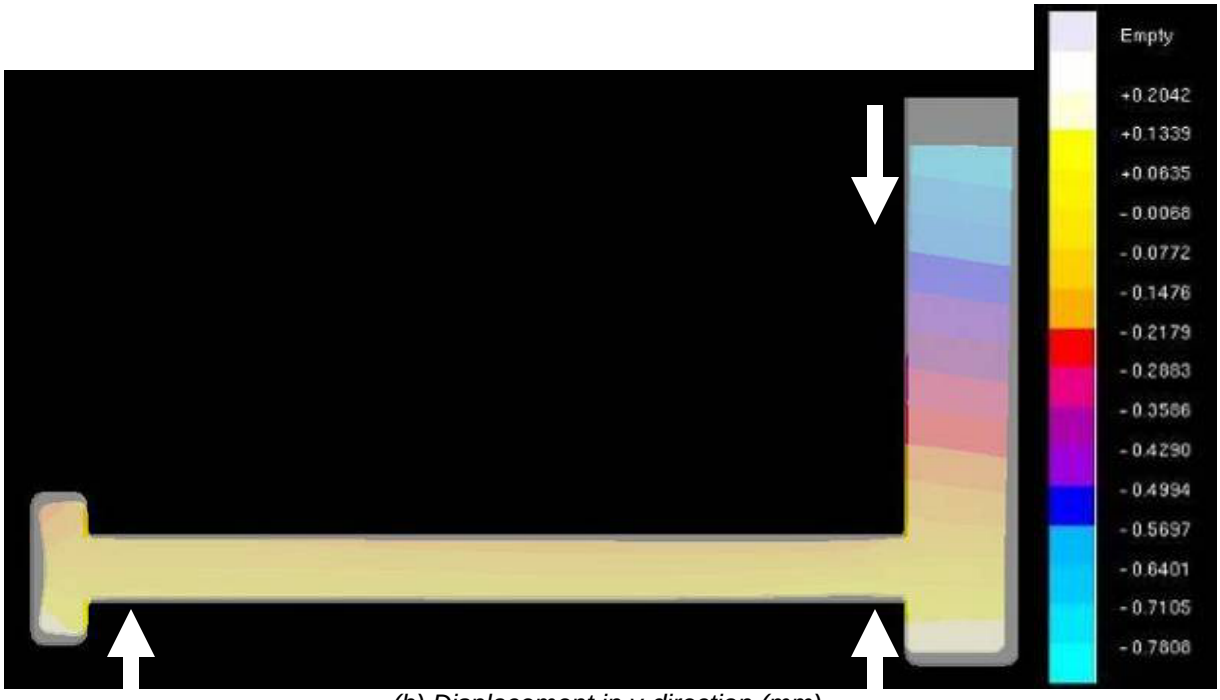

(b) Displacement in y-direction (mm).

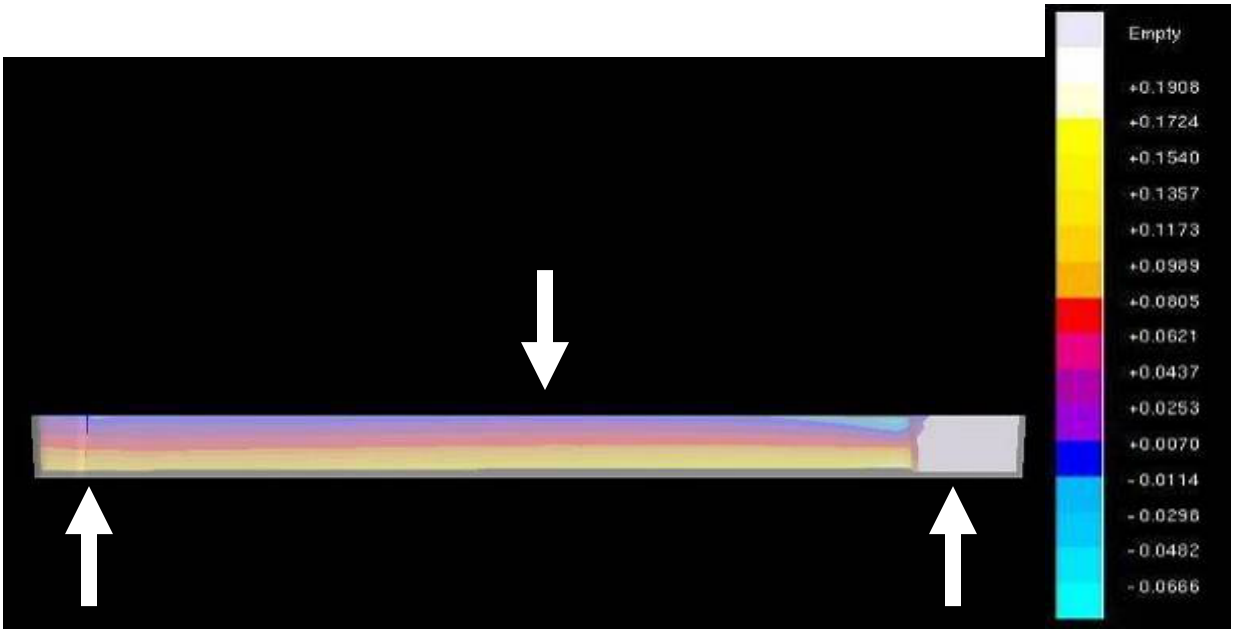

(c) Displacement in z-direction (mm).

Figure A1. 44: Displacement of AE42 casting at 340 °C mold temperature.

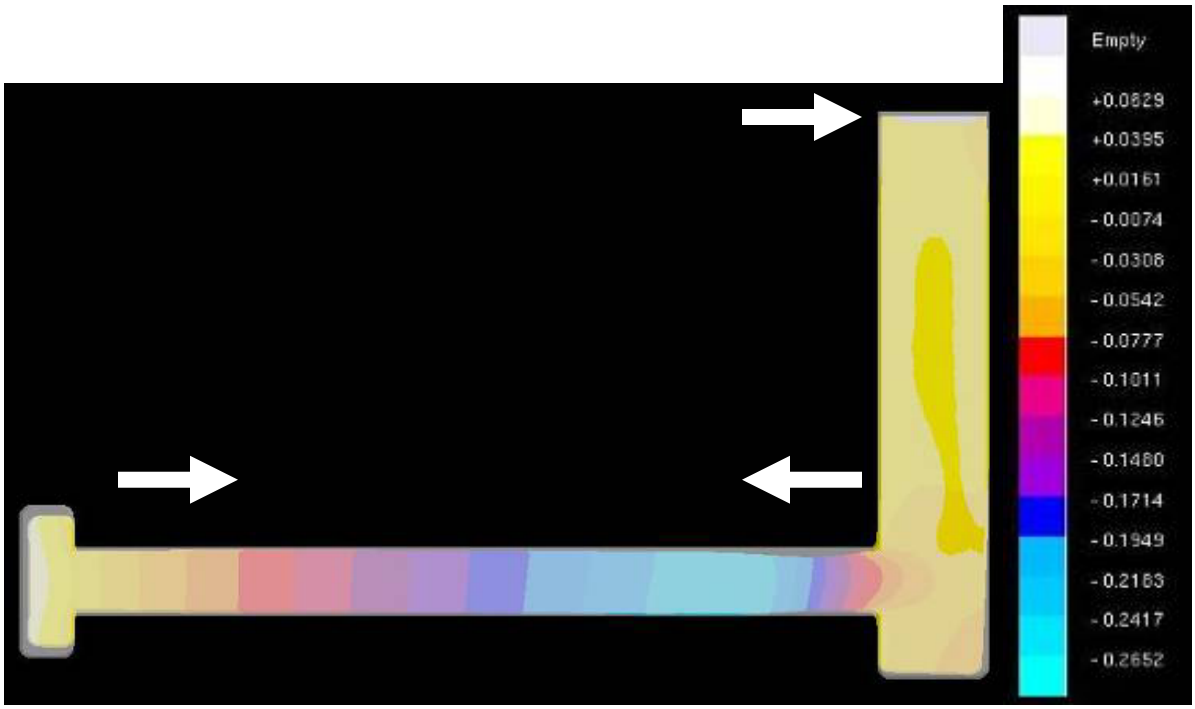

(a) Displacement in x-direction (mm).

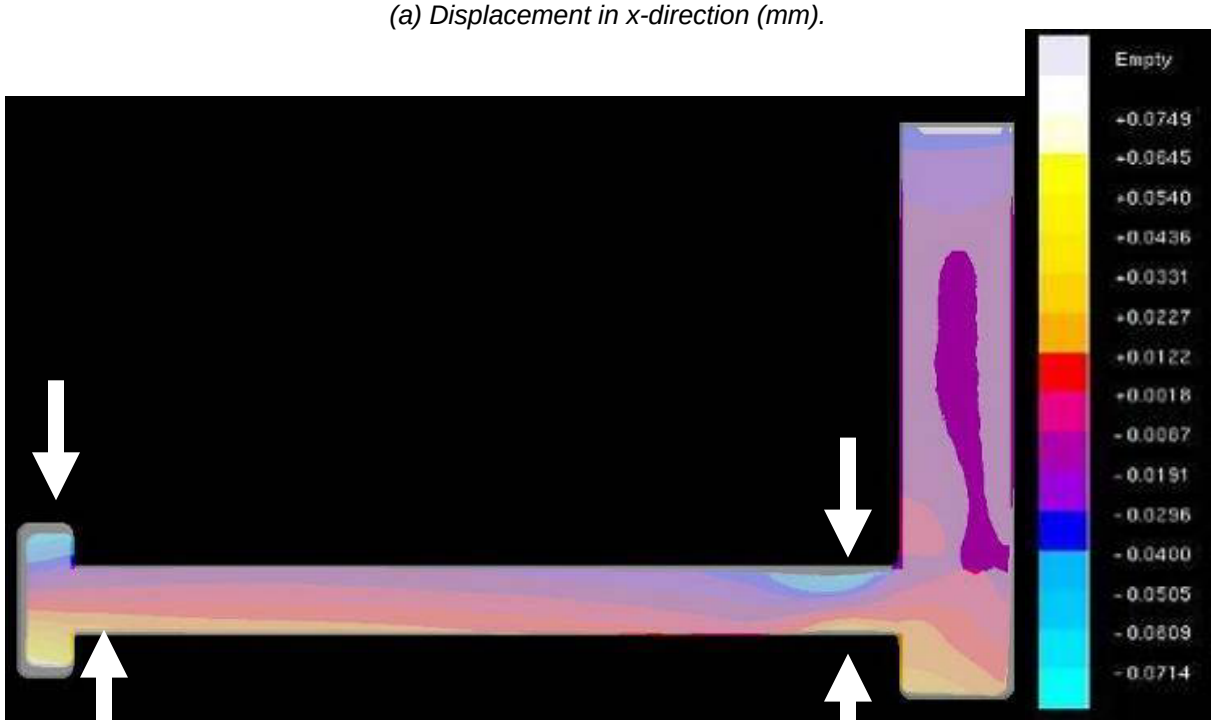

(b) Displacement in y-direction (mm)

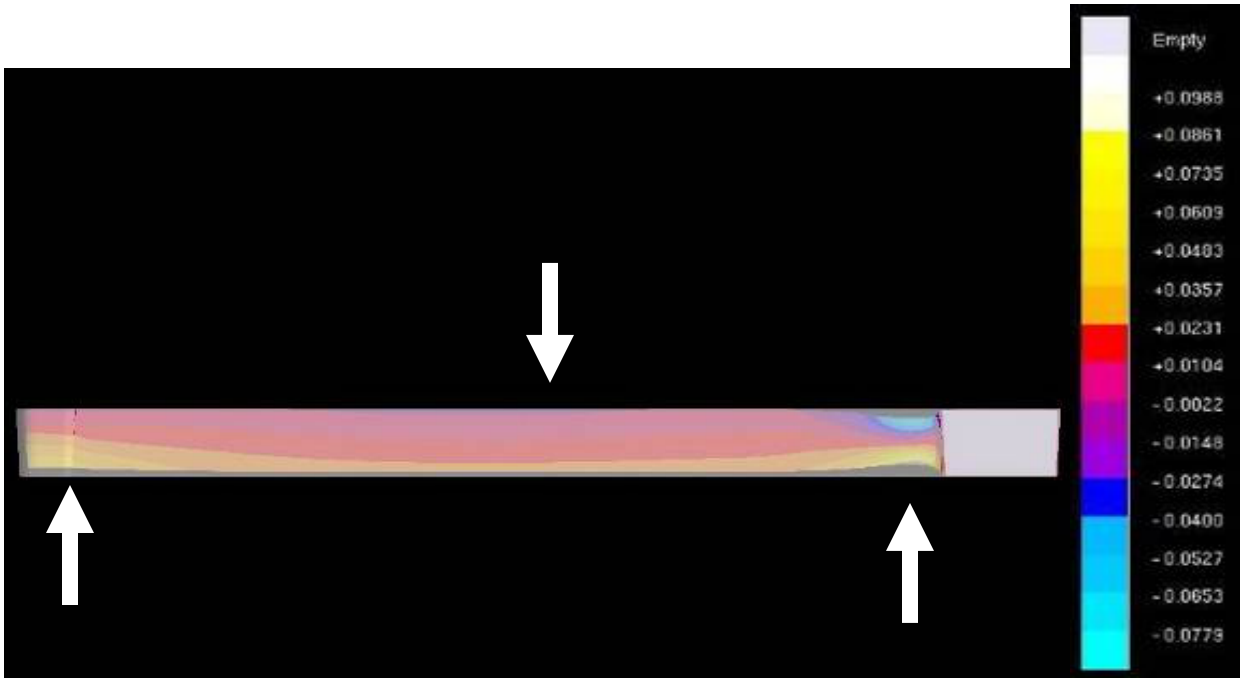

(c) Displacement in z-direction (mm).

Figure A1. 45: Displacement of AE42 casting at 390 °C mold temperature.

Appendix 2 – General Alloy Microstructure

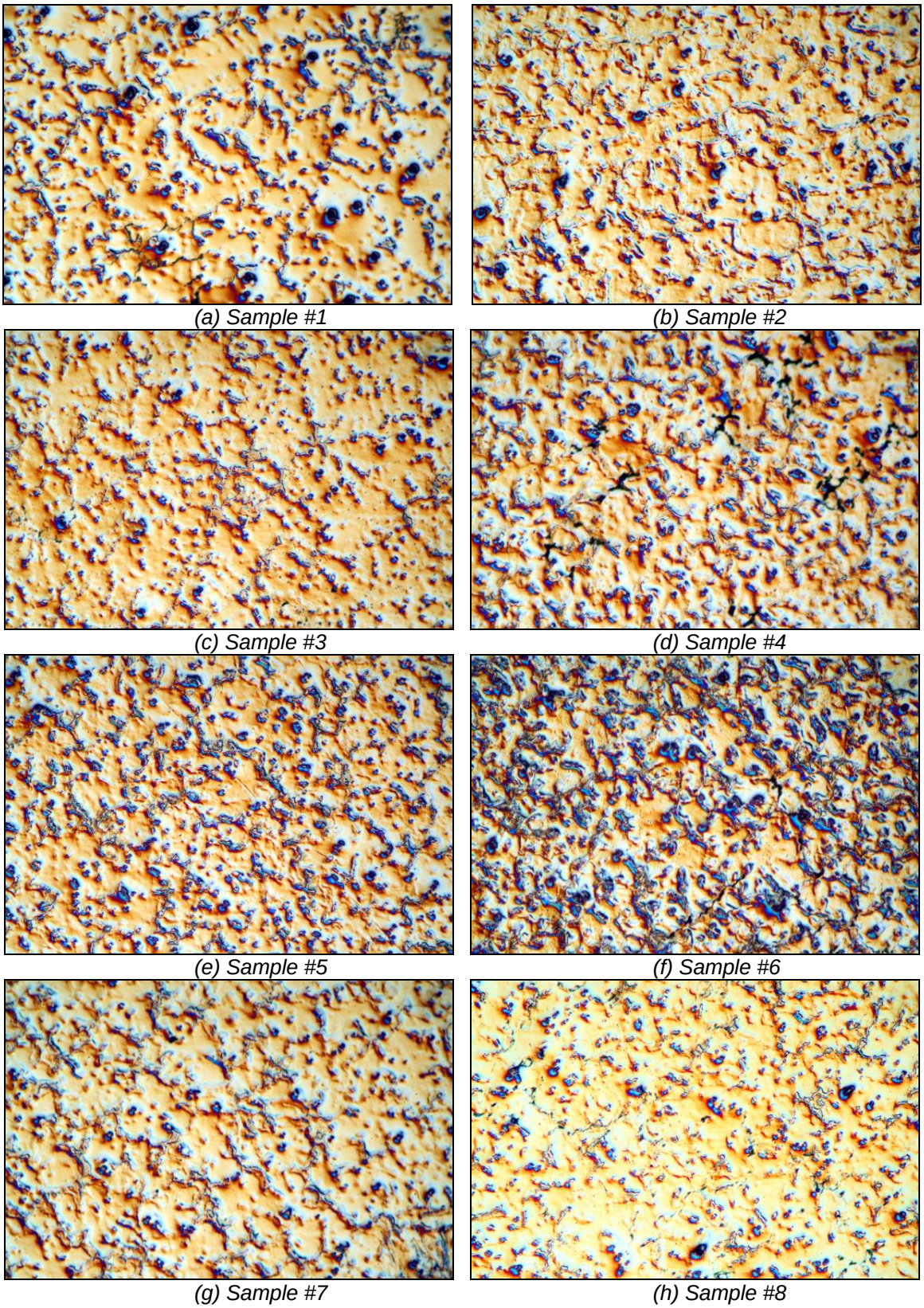

(a) Sample #1 *(b) Sample #2*

(c) Sample #3 *(d) Sample #4*

(e) Sample #5 *(f) Sample #6*

(g) Sample #7 *(h) Sample #8*

Figure A2. 1: AZ91D general microstructure, 210 °C mold temperature (as-cast, DIC, 200x).

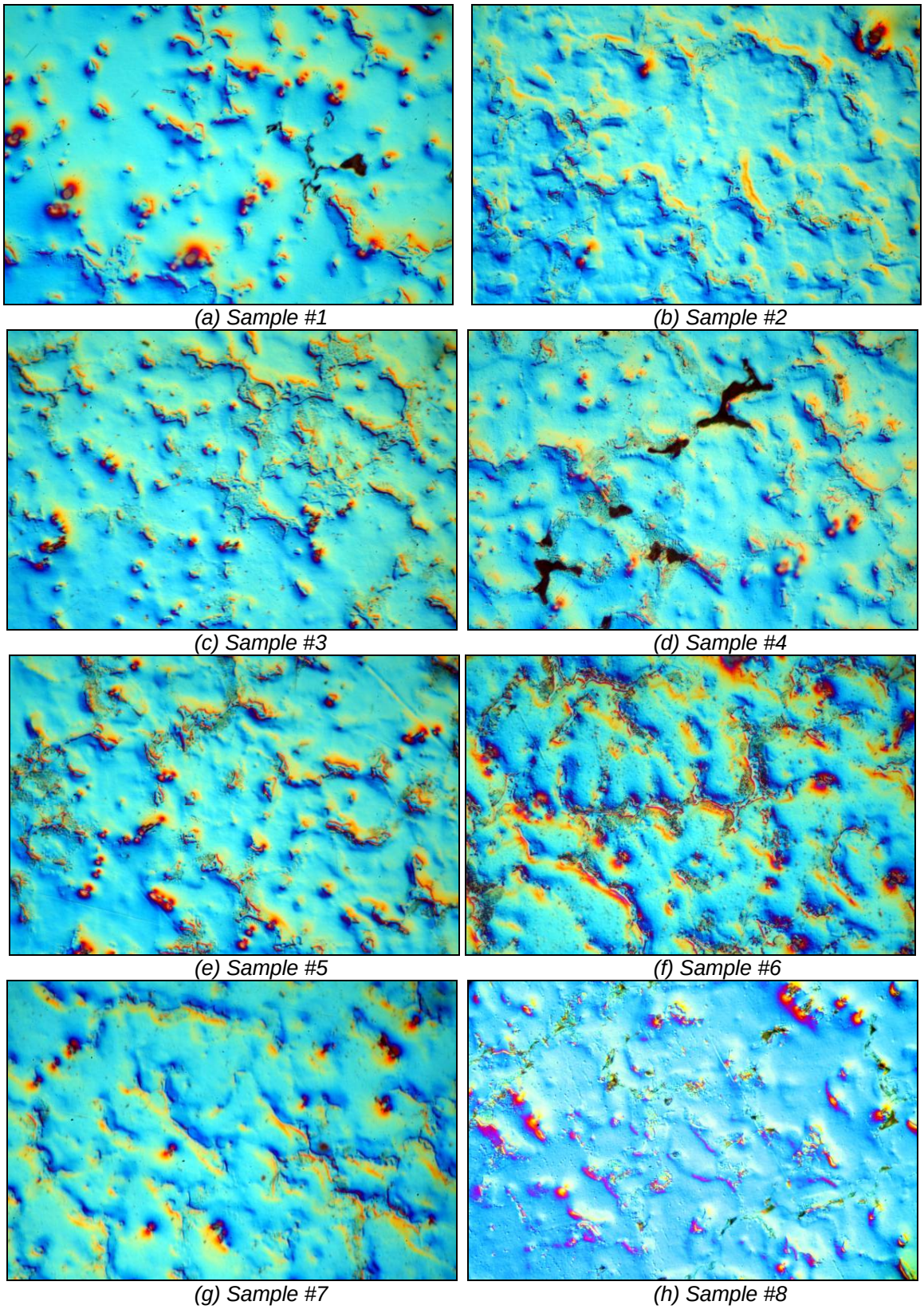

(a) Sample #1 *(b) Sample #2*

(c) Sample #3 *(d) Sample #4*

(e) Sample #5 *(f) Sample #6*

(g) Sample #7 *(h) Sample #8*

Figure A2. 2: AZ91D general microstructure, 210 °C mold temperature (as-cast, DIC, 500x).

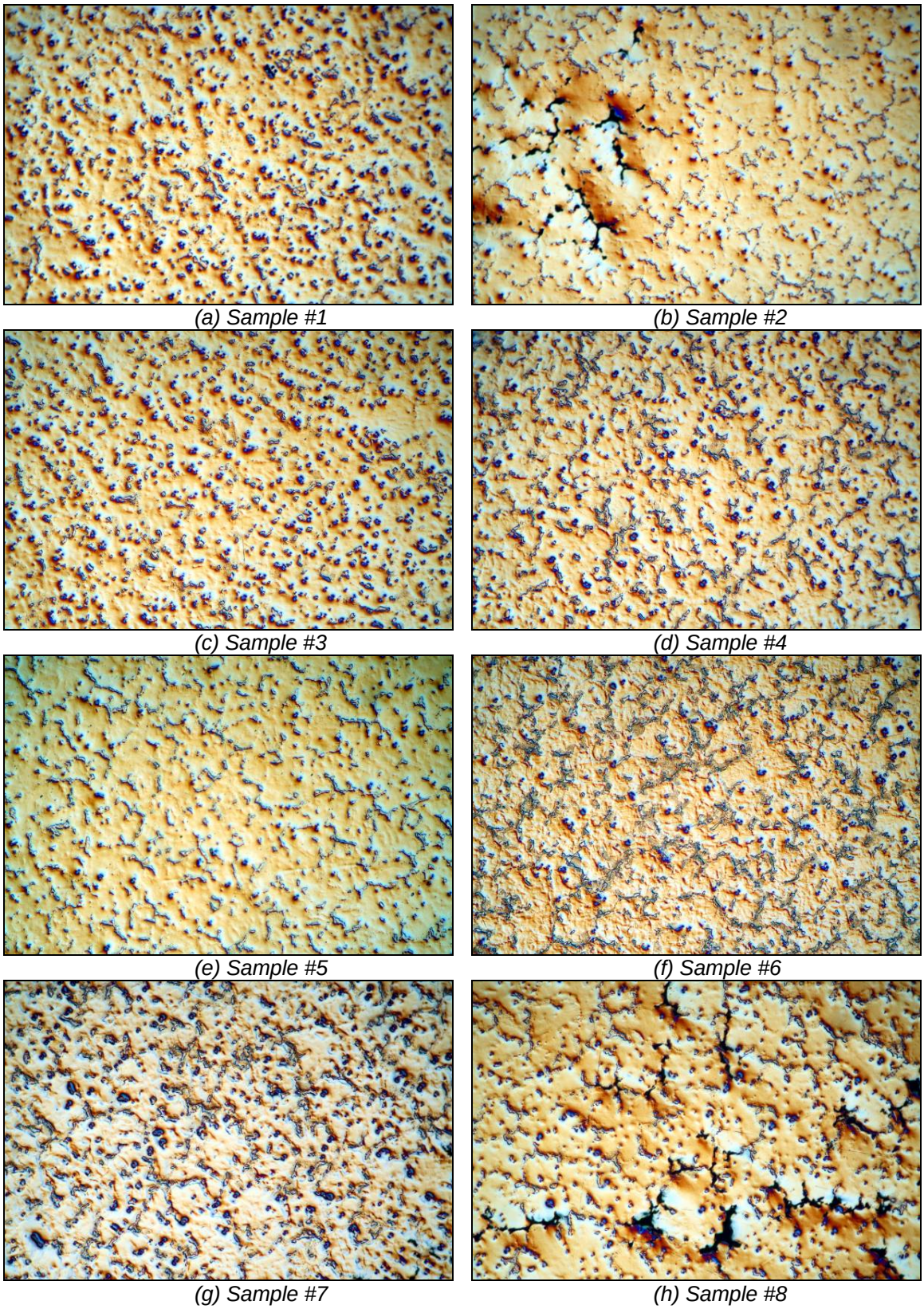

(a) Sample #1 *(b) Sample #2*

(c) Sample #3 *(d) Sample #4*

(e) Sample #5 *(f) Sample #6*

(g) Sample #7 *(h) Sample #8*

Figure A2. 3: AZ91D general microstructure, 250 °C mold temperature (as-cast, DIC, 200x).

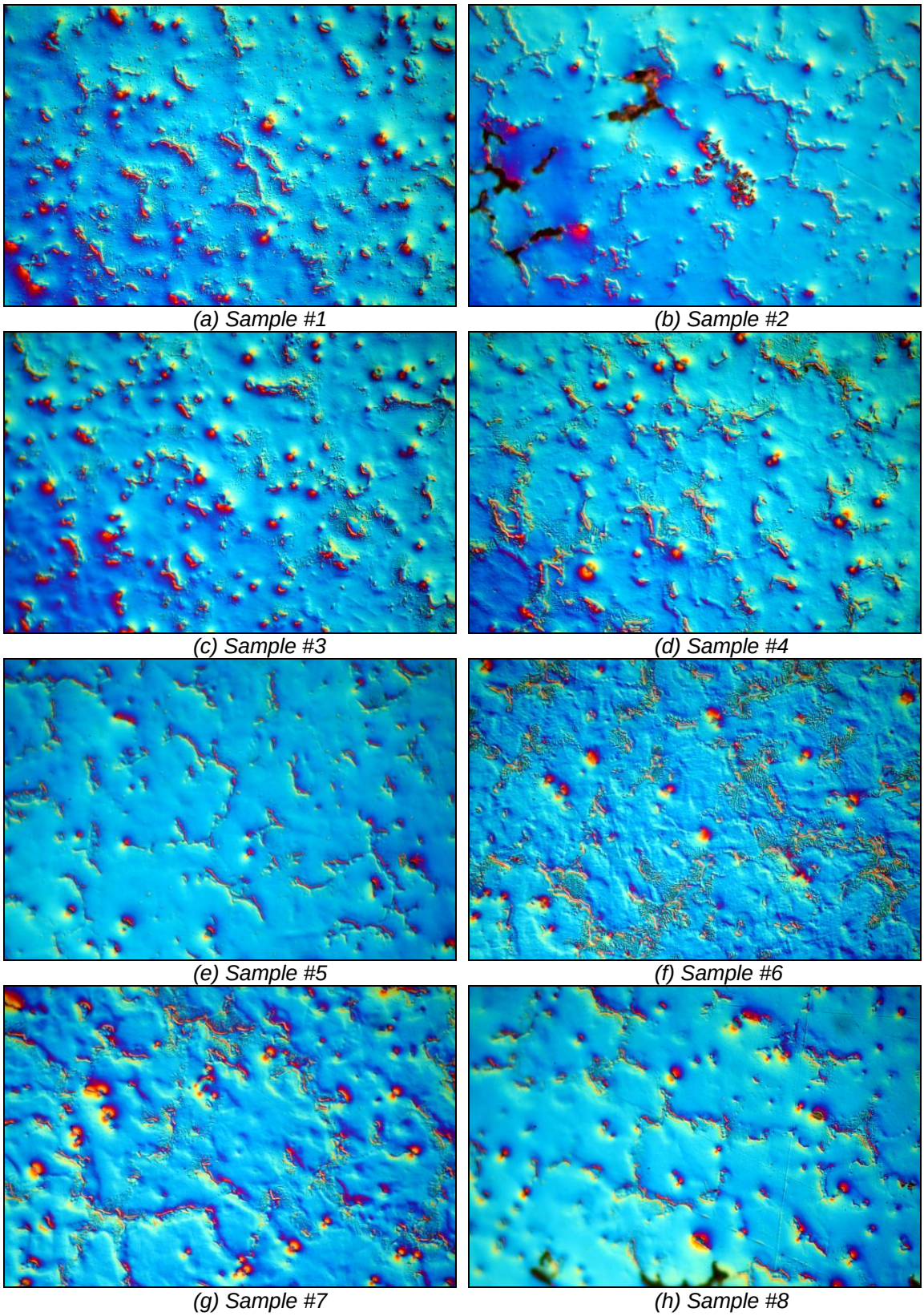

(a) Sample #1 *(b) Sample #2*

(c) Sample #3 *(d) Sample #4*

(e) Sample #5 *(f) Sample #6*

(g) Sample #7 *(h) Sample #8*

Figure A2. 4: AZ91D general microstructure, 250 °C mold temperature (as-cast, DIC, 500x).

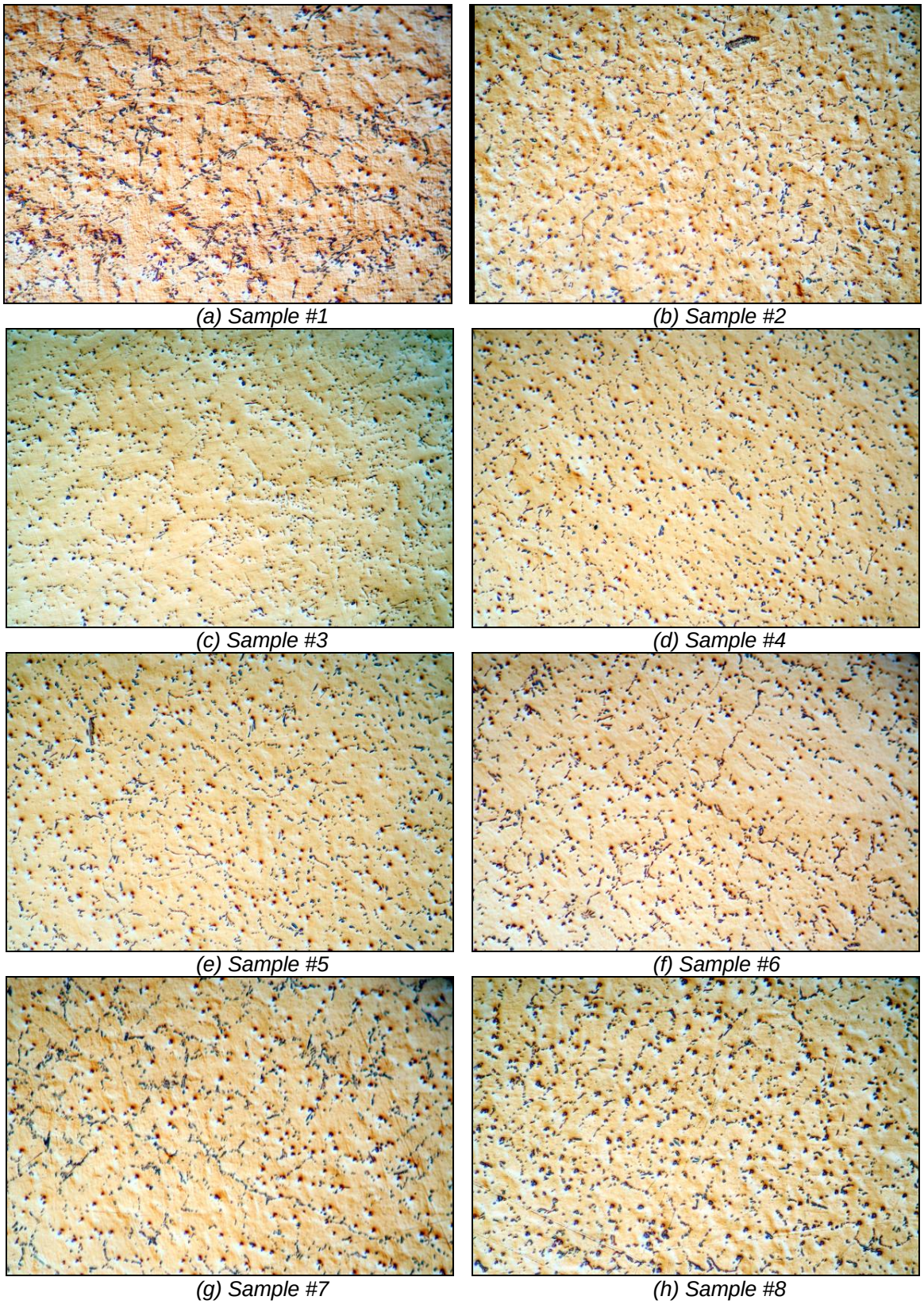

(a) Sample #1 *(b) Sample #2*

(c) Sample #3 *(d) Sample #4*

(e) Sample #5 *(f) Sample #6*

(g) Sample #7 *(h) Sample #8*

Figure A2. 5: AE42 general microstructure, 340 °C mold temperature (as-cast, DIC, 200x).

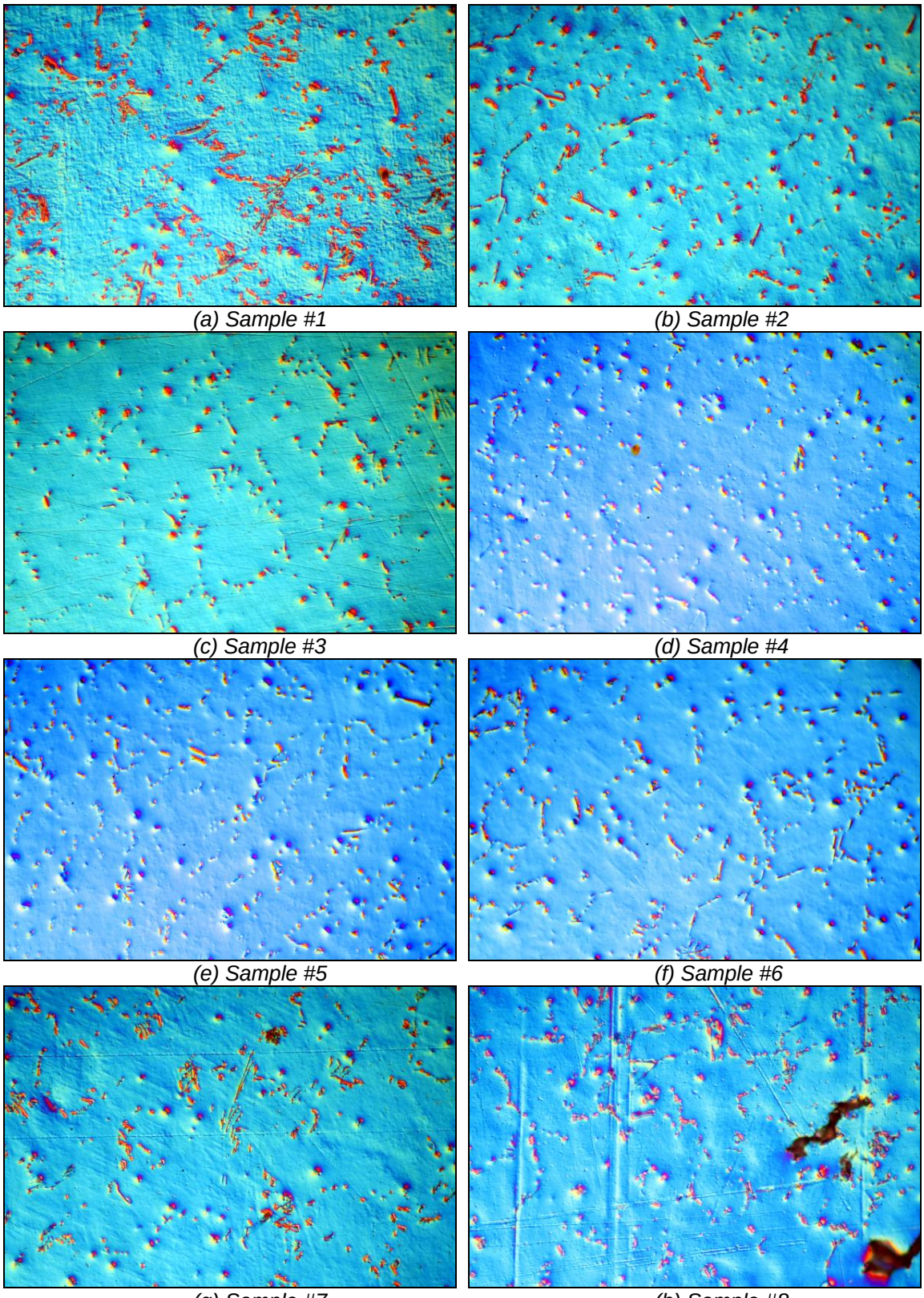

(a) Sample #1 *(b) Sample #2*

(c) Sample #3 *(d) Sample #4*

(e) Sample #5 *(f) Sample #6*

(g) Sample #7 *(h) Sample #8*

Figure A2. 6: AE42 general microstructure, 340 °C mold temperature (as-cast, DIC, 500x).

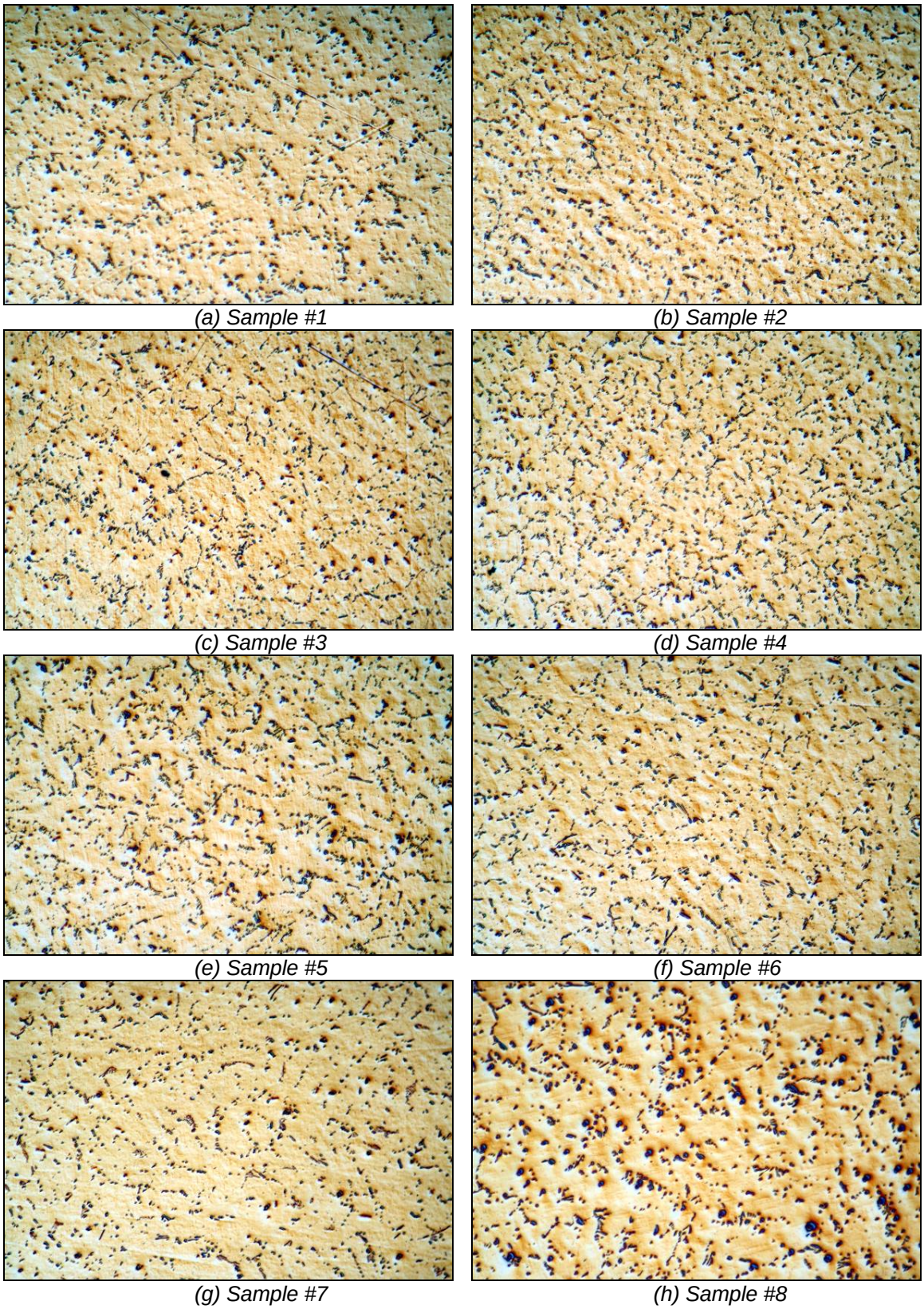

(a) Sample #1 *(b) Sample #2*

(c) Sample #3 *(d) Sample #4*

(e) Sample #5 *(f) Sample #6*

(g) Sample #7 *(h) Sample #8*

Figure A2. 7: AE42 general microstructure, 390 °C mold temperature (as-cast, DIC, 200x).

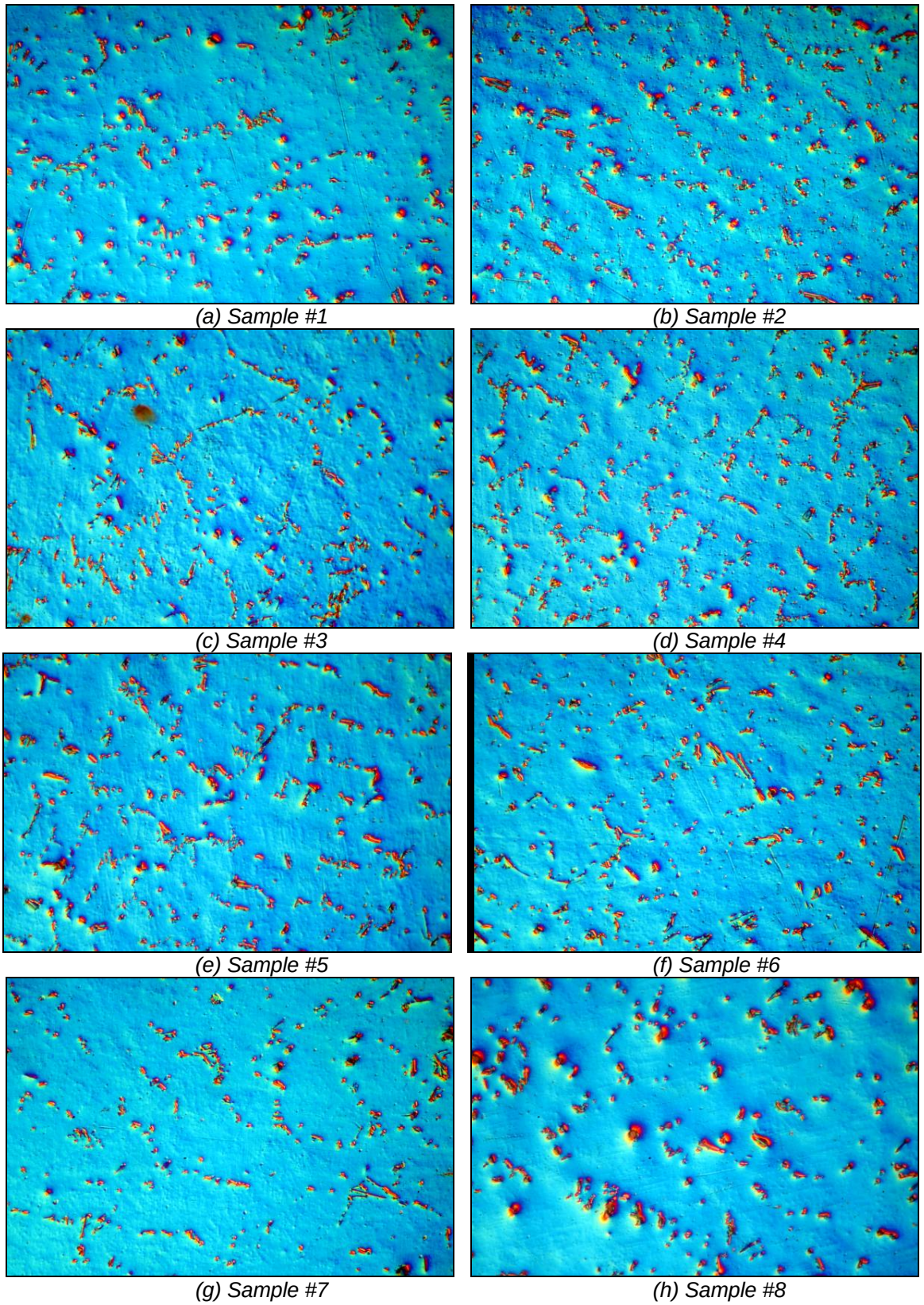

(a) Sample #1 *(b) Sample #2*

(c) Sample #3 *(d) Sample #4*

(e) Sample #5 *(f) Sample #6*

(g) Sample #7 *(h) Sample #8*

Figure A2. 8: AE42 general microstructure, 390 °C mold temperature (as-cast, DIC, 500x).

Appendix 3 – Micrographs of Second Phases

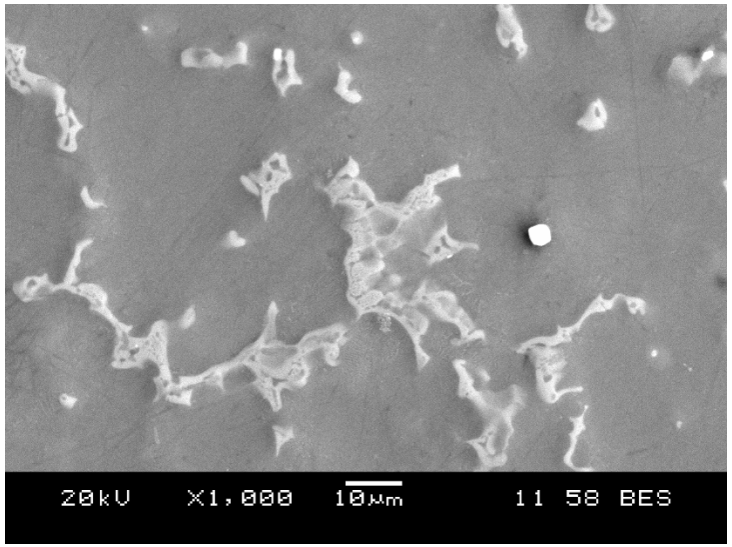

(a) Sample #1 (1000x)

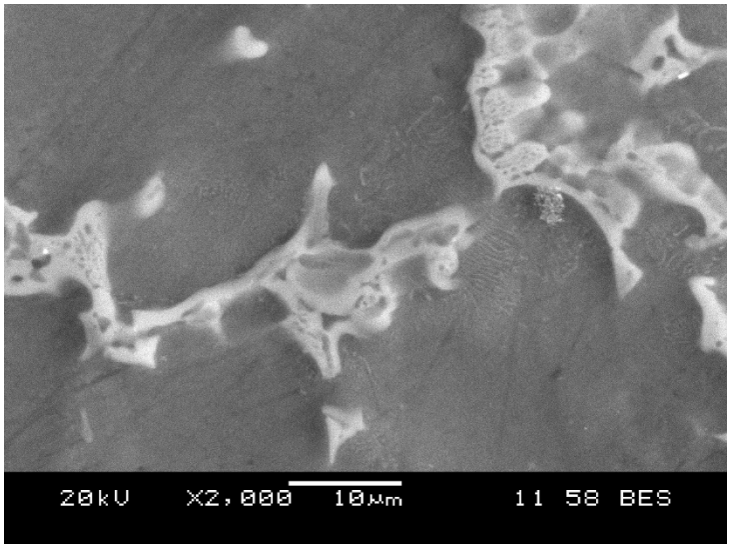

(b) Sample #1 (2000x)

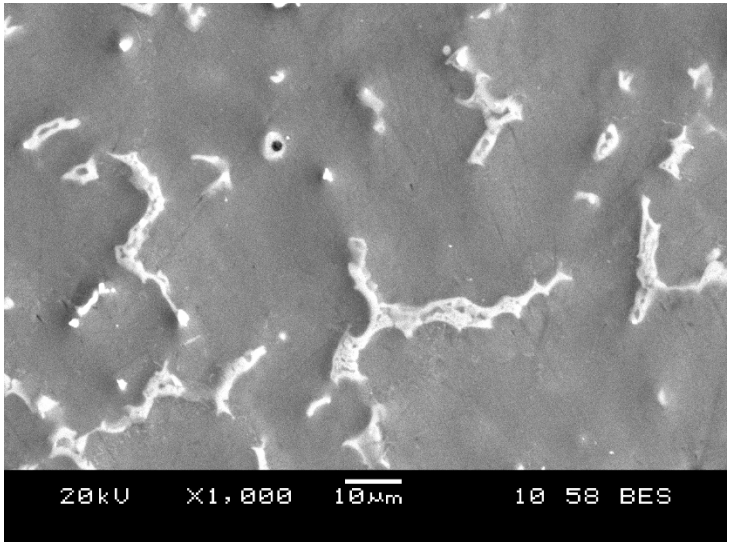

(c) Sample #3 (1000x)

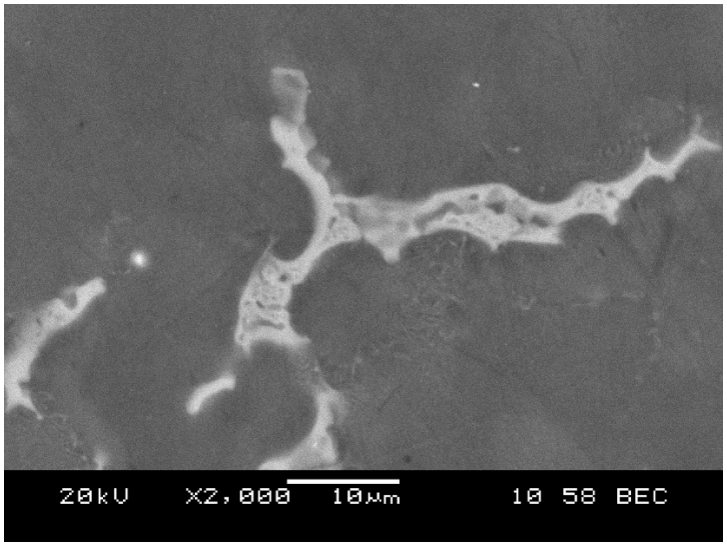

(d) Sample #3 (2000x)

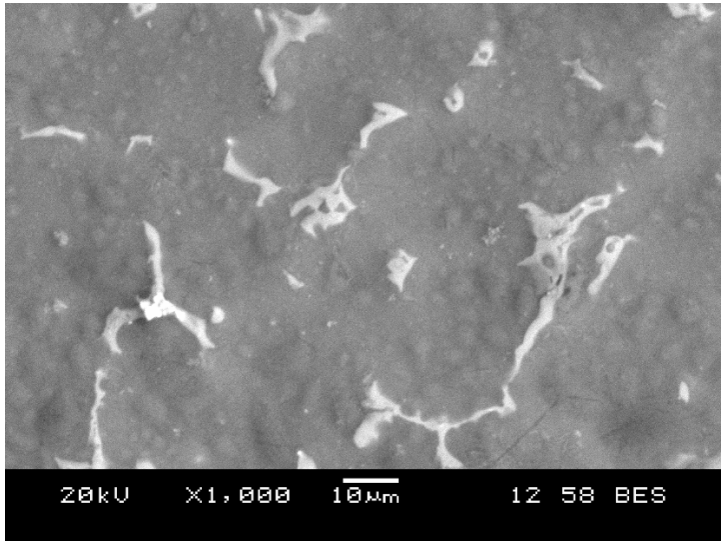

(e) Sample #6 (1000x)

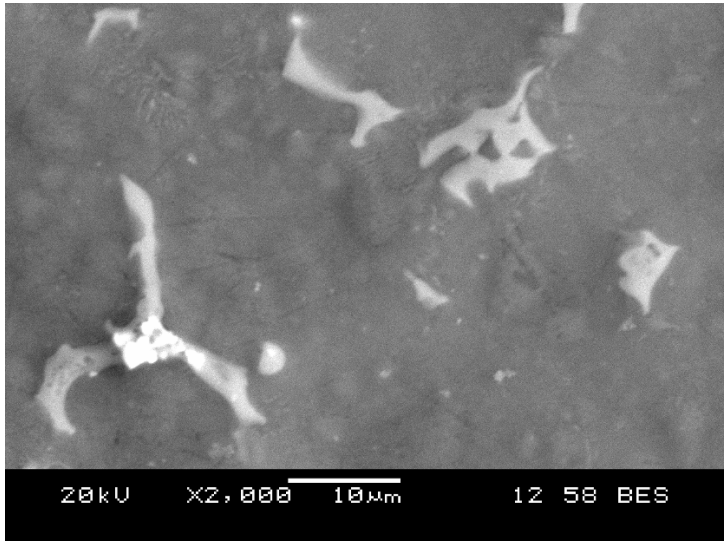

(f) Sample #6 (2000x)

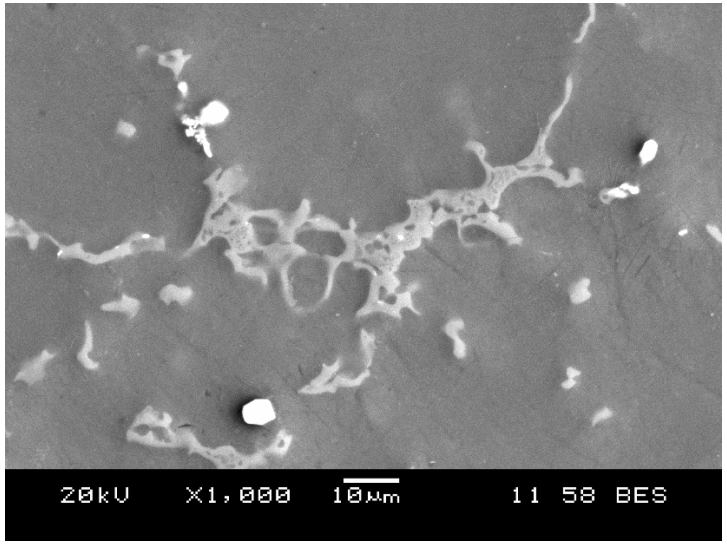

(g) Sample #8 (1000x)

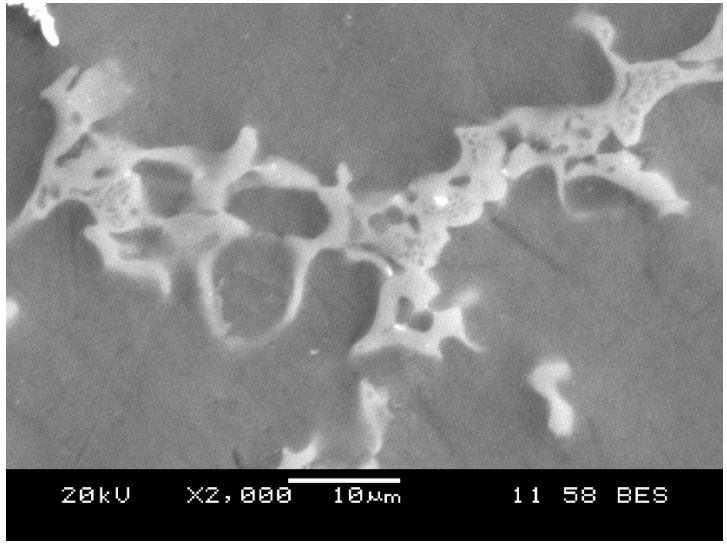

(h) Sample #8 (2000x)

Figure A3. 1: Morphology of second phase in AZ91D casting made at 210 °C mold temperature.

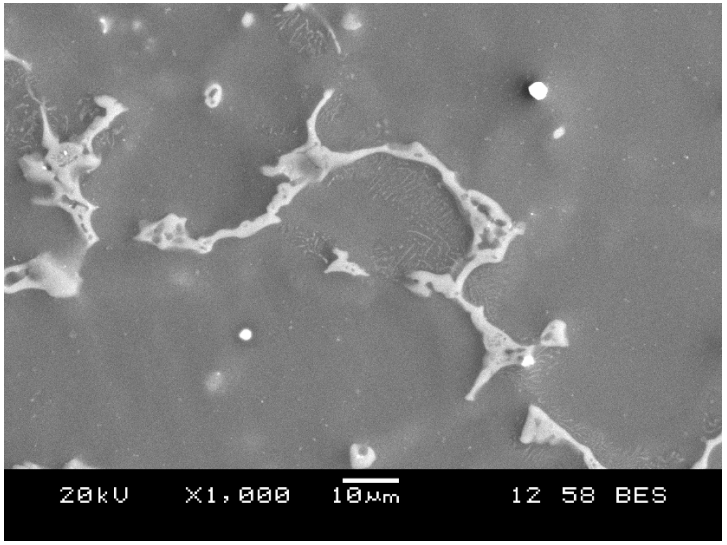

(a) Sample #1 (1000x)

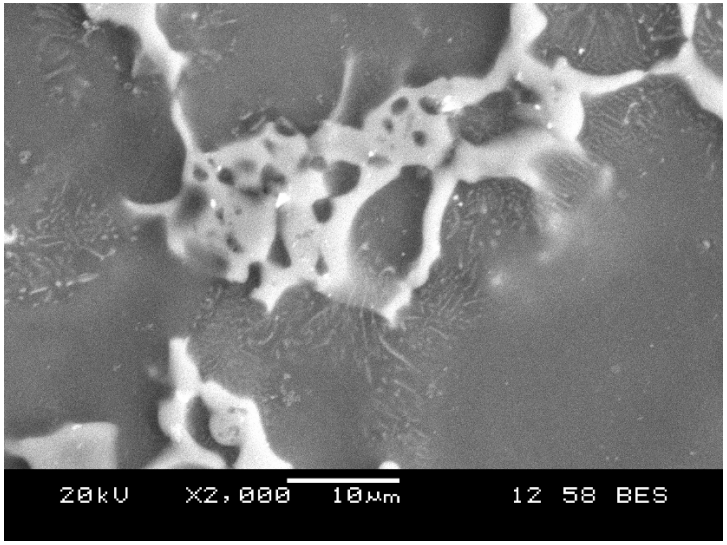

(b) Sample #1 (2000x)

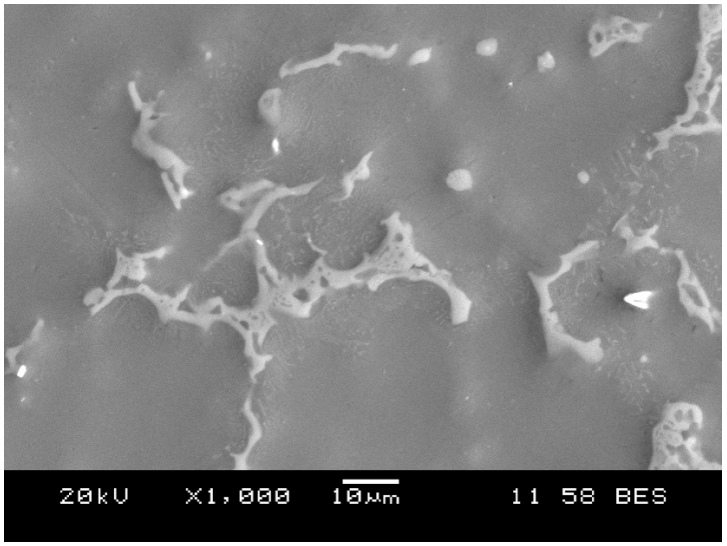

(c) Sample #3 (1000x)

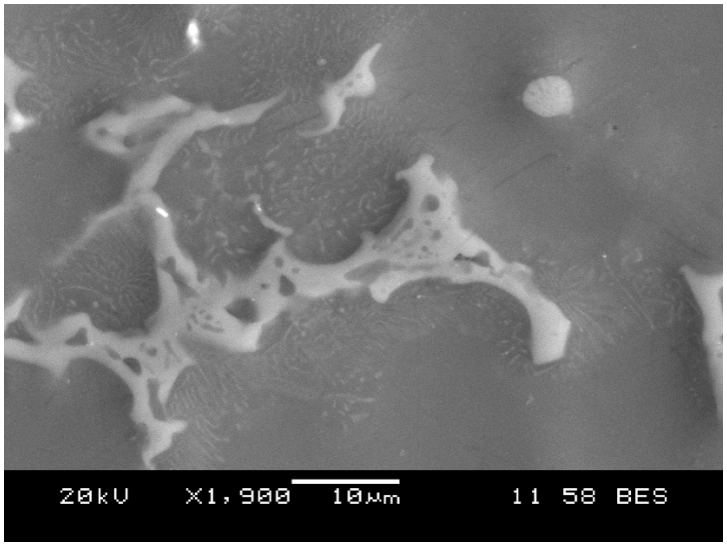

(d) Sample #3 (2000x)

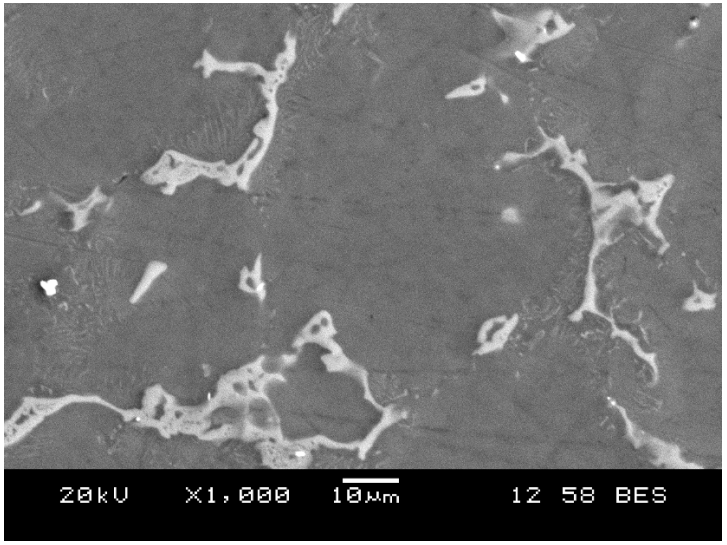

(e) Sample #6 (1000x)

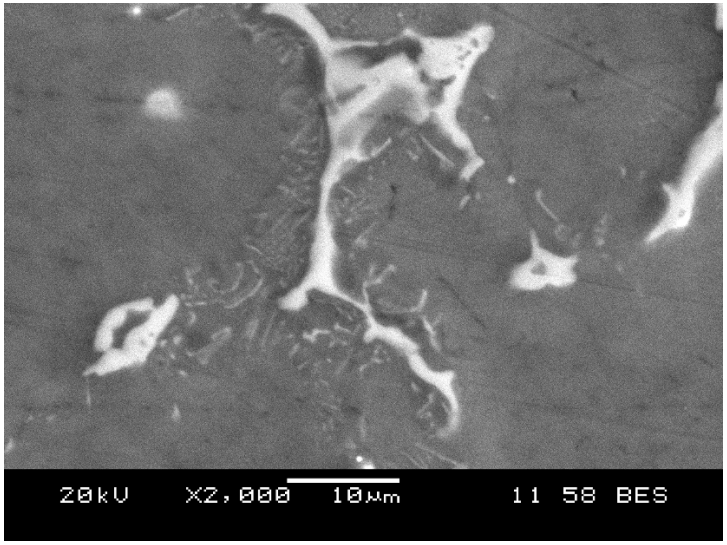

(f) Sample #6 (2000x)

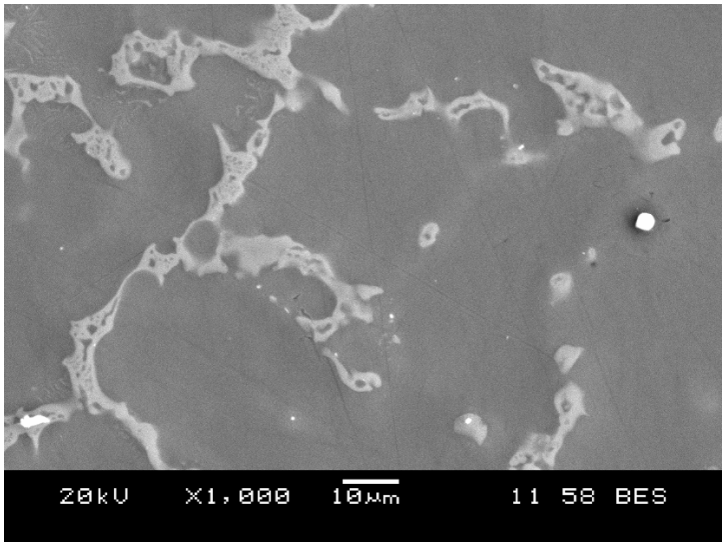

(g) Sample #8 (1000x)

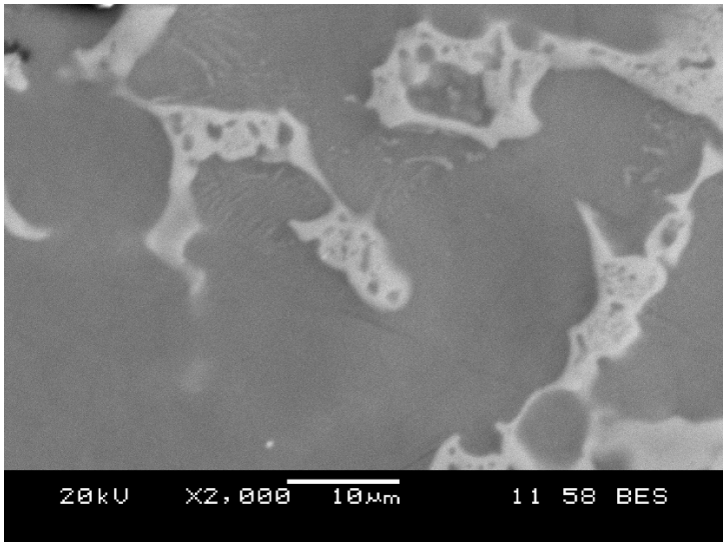

(h) Sample #8 (2000x)

Figure A3. 2: Morphology of second phase in AZ91D casting made at 250 °C mold temperature.

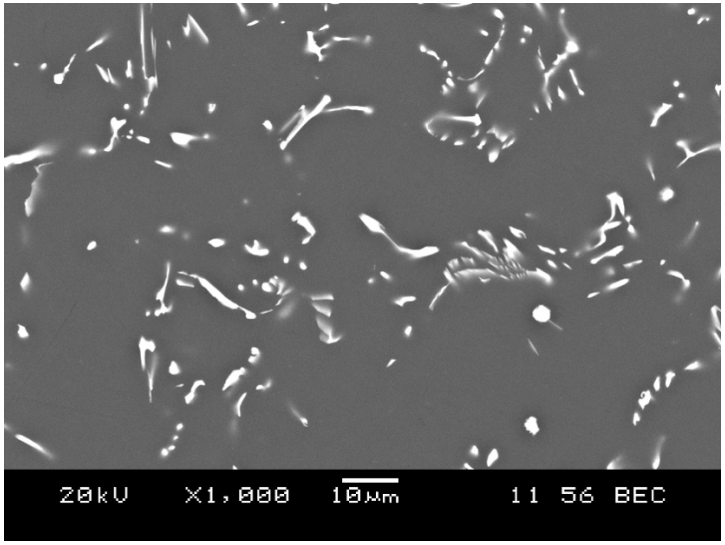

(a) Sample #1 (1000x)

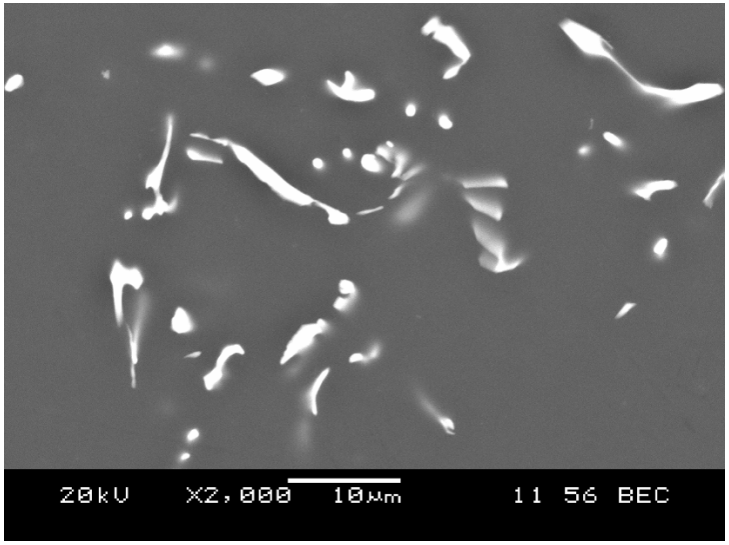

(b) Sample #1 (2000x)

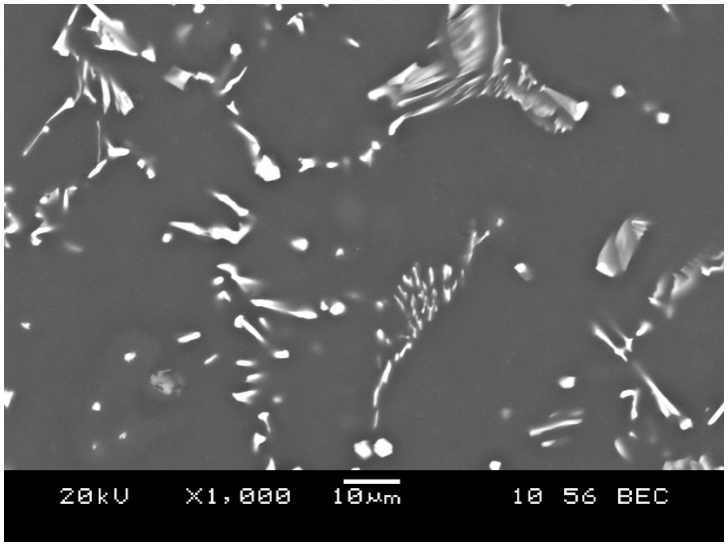

(c) Sample #3 (1000x)

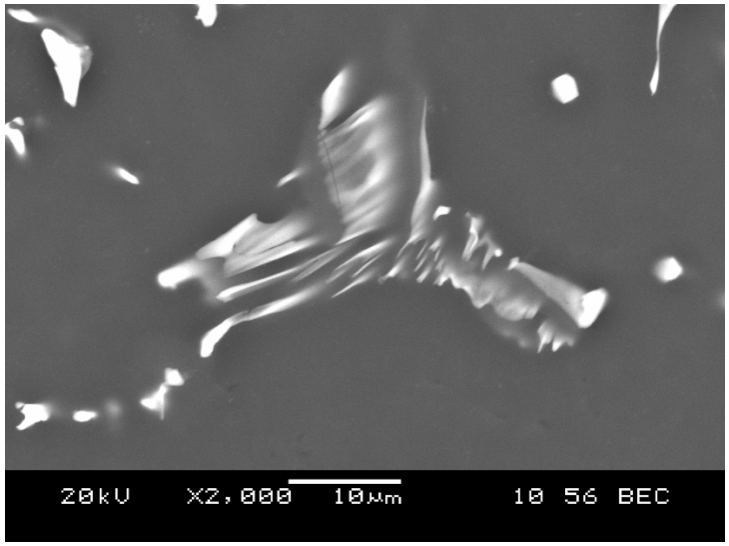

(d) Sample #3 (2000x)

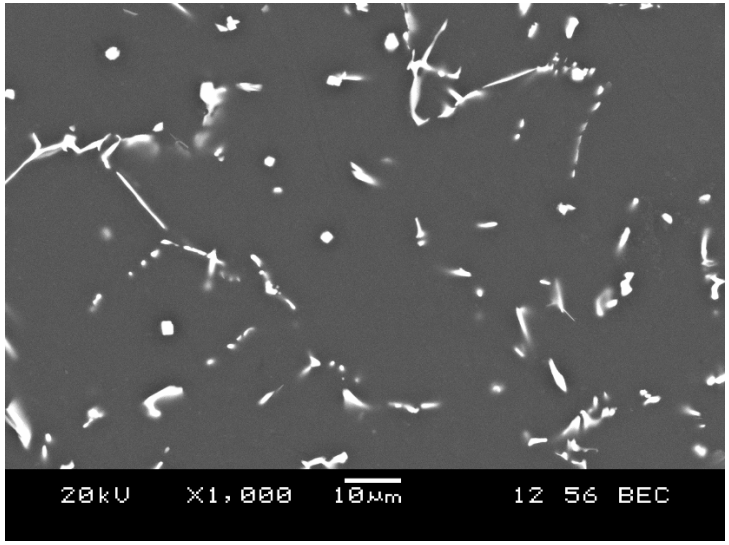

(e) Sample #6 (1000x)

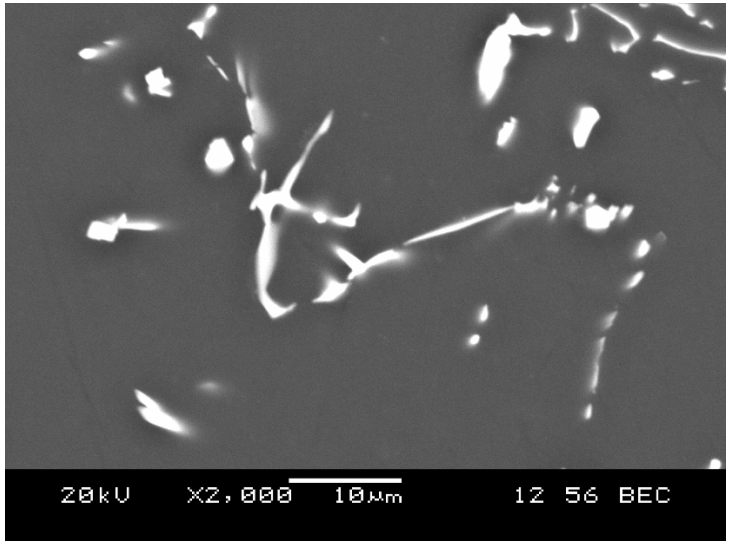

(f) Sample #6 (2000x)

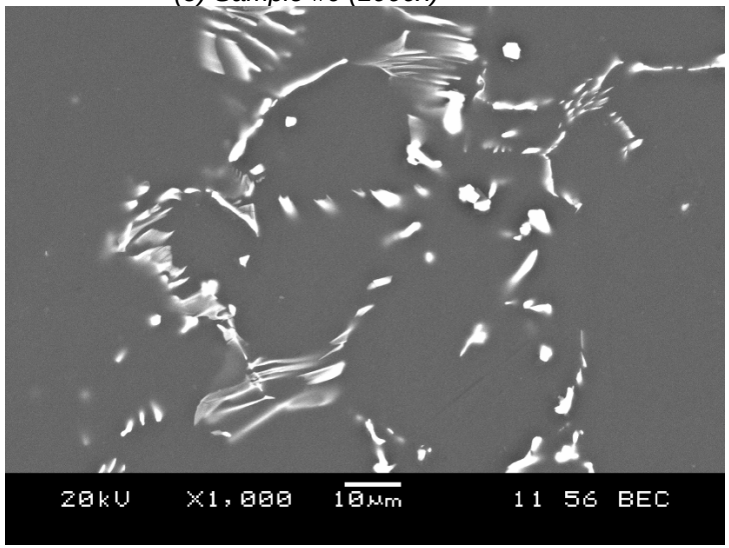

(g) Sample #8 (1000x)

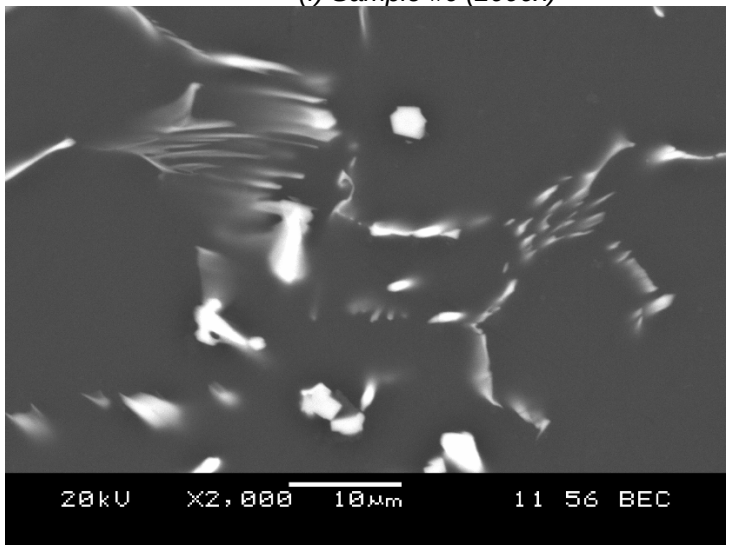

(h) Sample #8 (2000x)

Figure A3. 3: Morphology of second phase in AE42 casting made at 340 °C mold temperature.

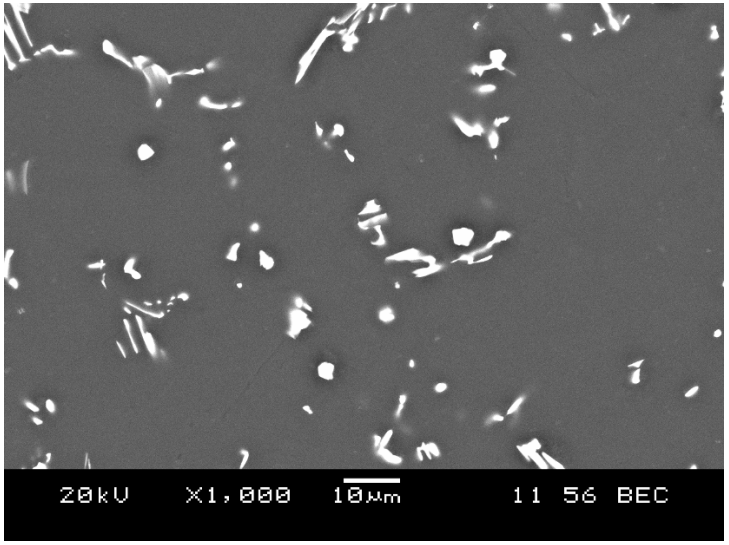

(a) Sample #1 (1000x)

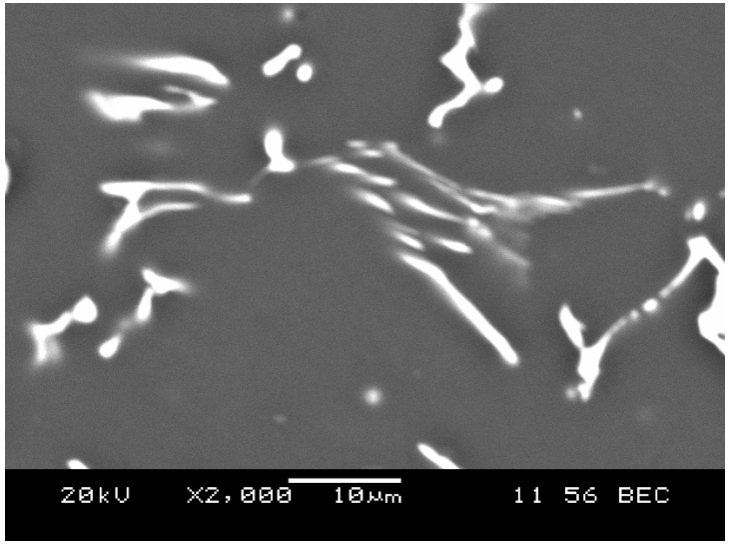

(b) Sample #1 (2000x)

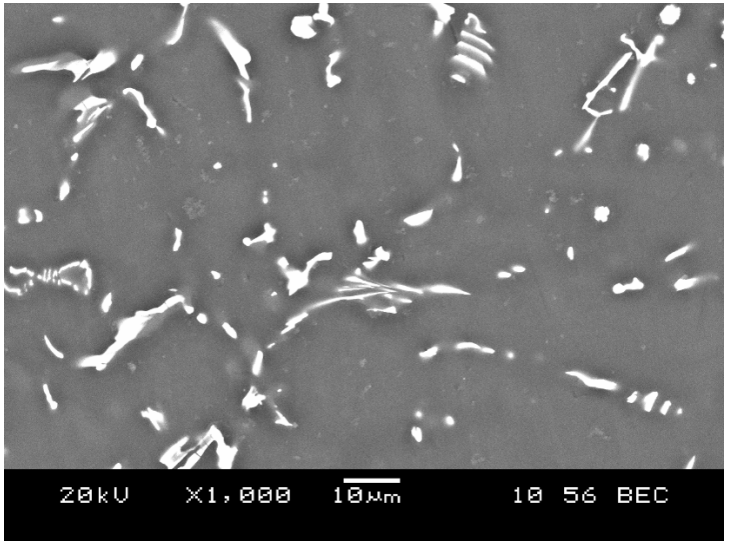

(c) Sample #3 (1000x)

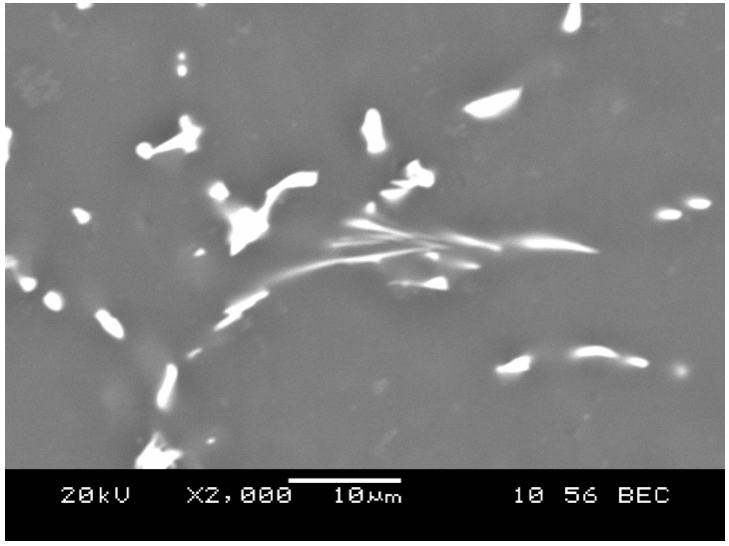

(d) Sample #3 (2000x)

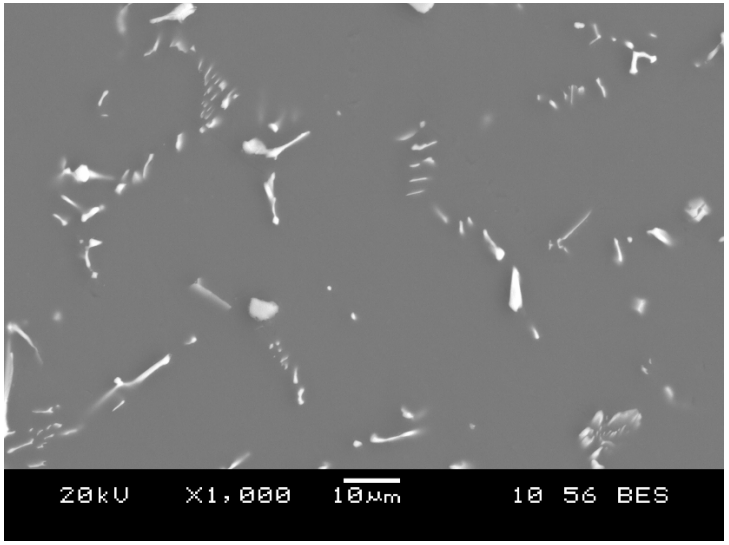

(e) Sample #6 (1000x)

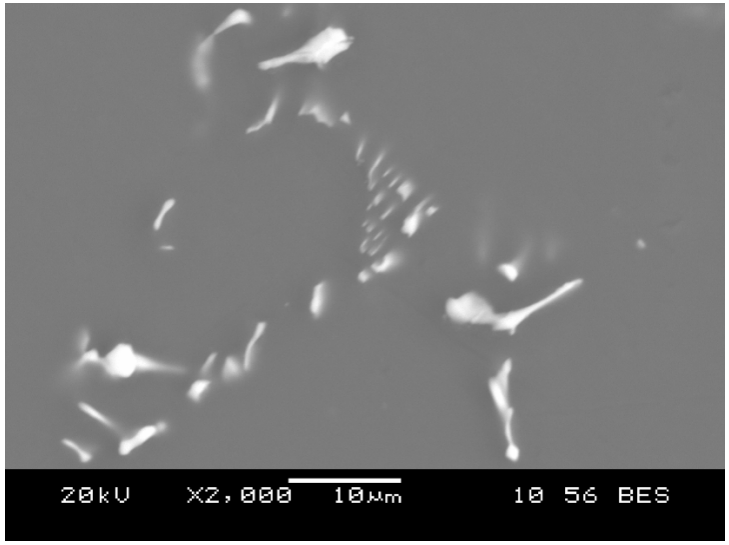

(f) Sample #6 (2000x)

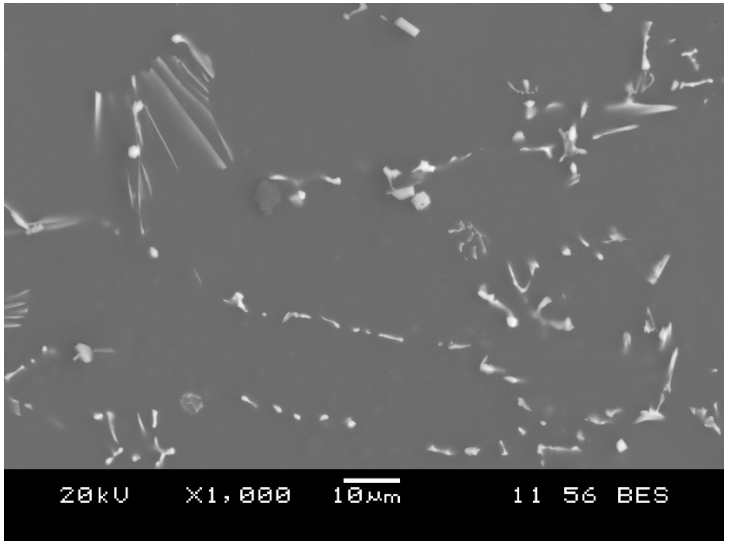

(g) Sample #8 (1000x)

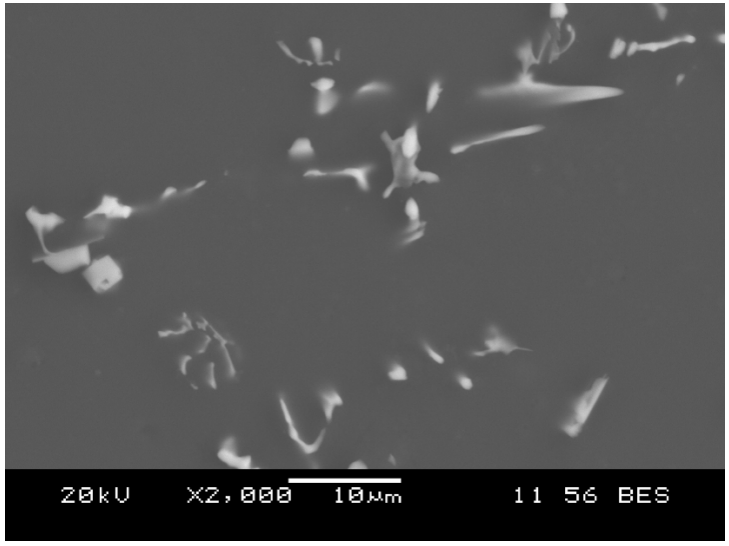

(h) sample #8 (2000x)

Figure A3. 4: Morphology of second phase in AE42 casting made at 390 °C mold temperature.

Appendix 4 – Thermal Analysis

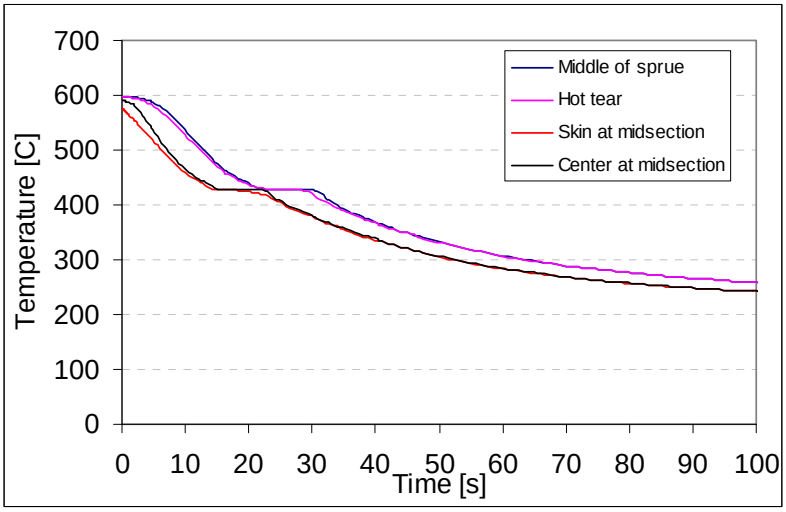

(a) Cooling curves.

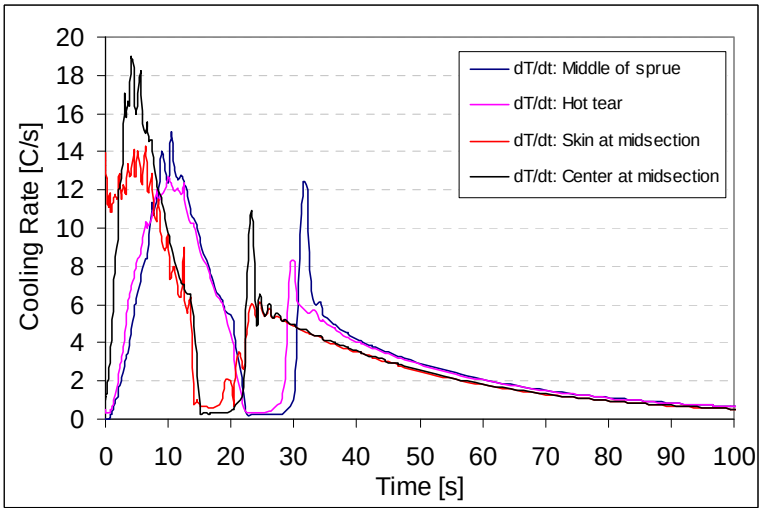

(b) Cooling rates.

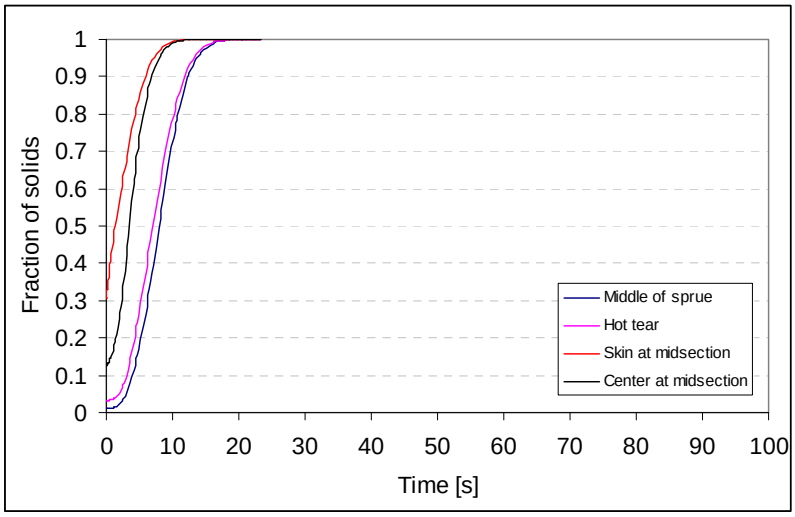

(c) Fraction of solids development.

Figure A4. 1: Solidification history data for AZ91D casting at 210 °C mold temperature.

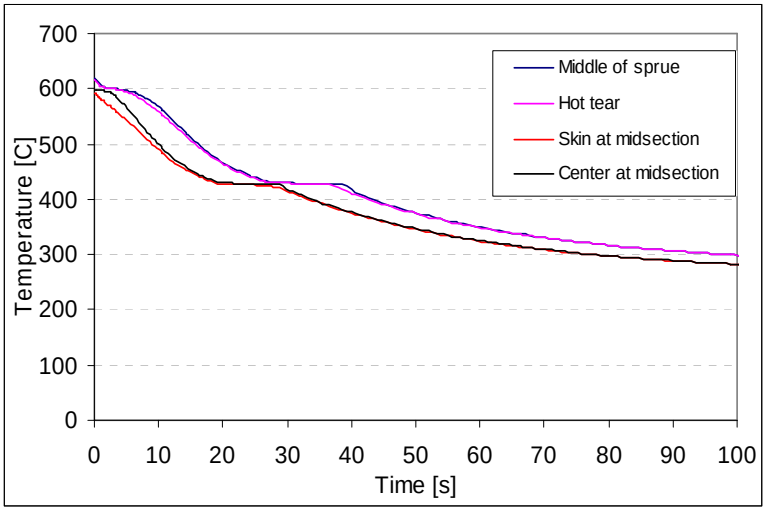

(a) Cooling curves.

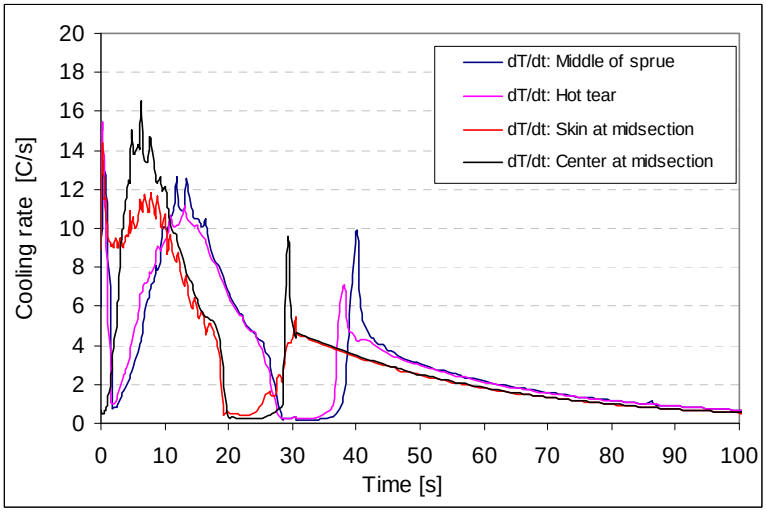

(b) Cooling rates.

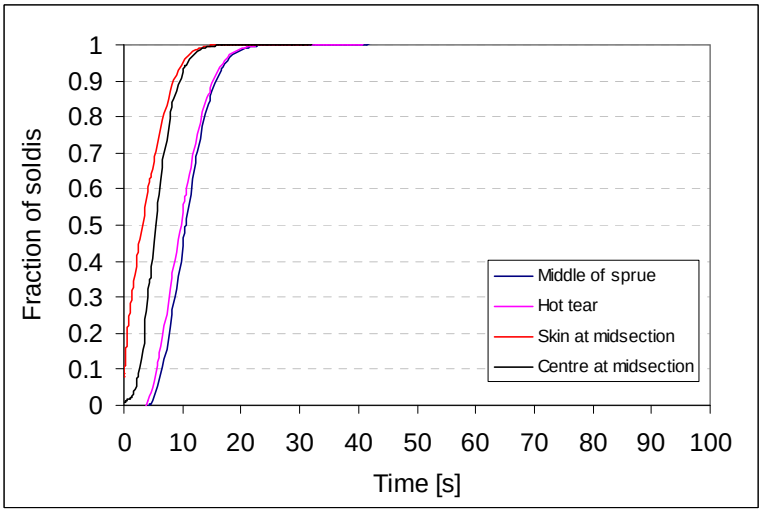

(c) Fraction of solids development.

Figure A4. 2: Solidification history data for AZ91D casting at 250 °C mold temperature.

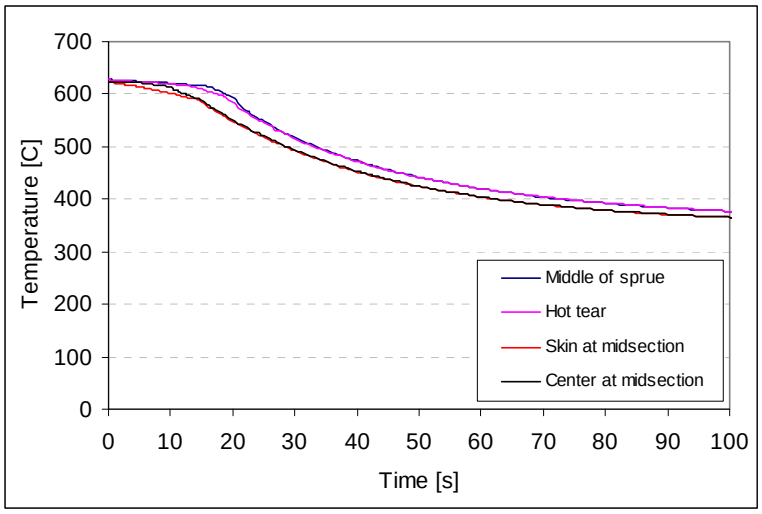

(a) Cooling curves.

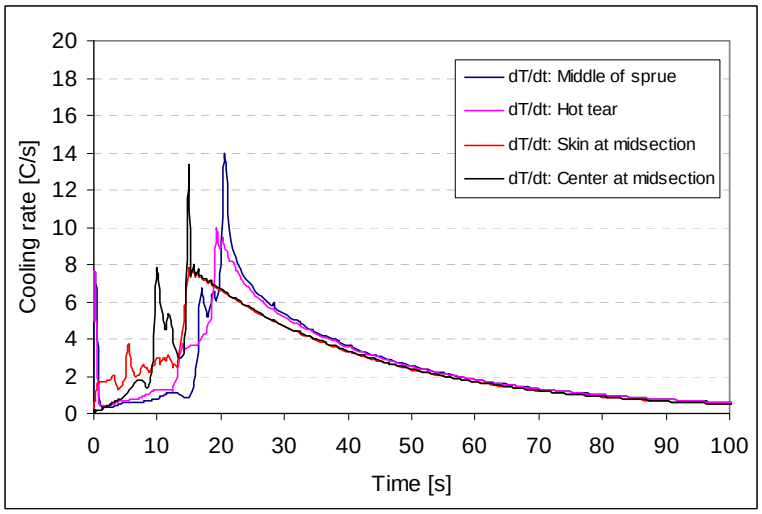

(b) Cooling rates.

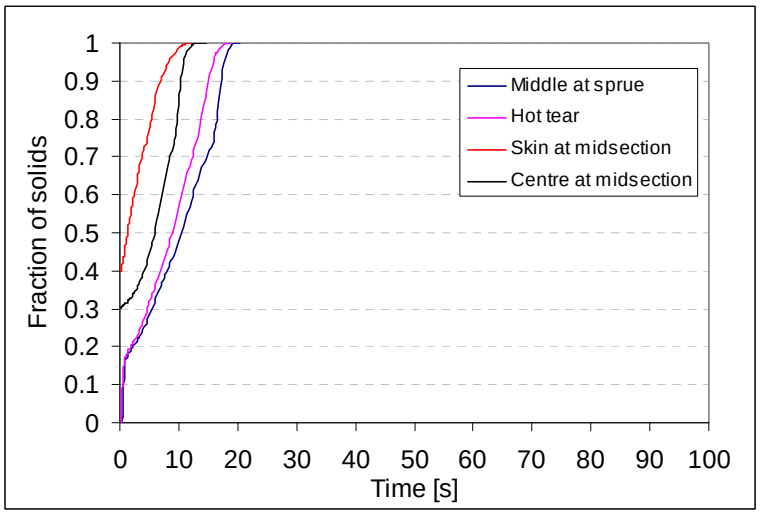

(c) Fraction of solids development.

Figure A4. 3: Solidification history data for AE42 casting at 340 °C mold temperature.

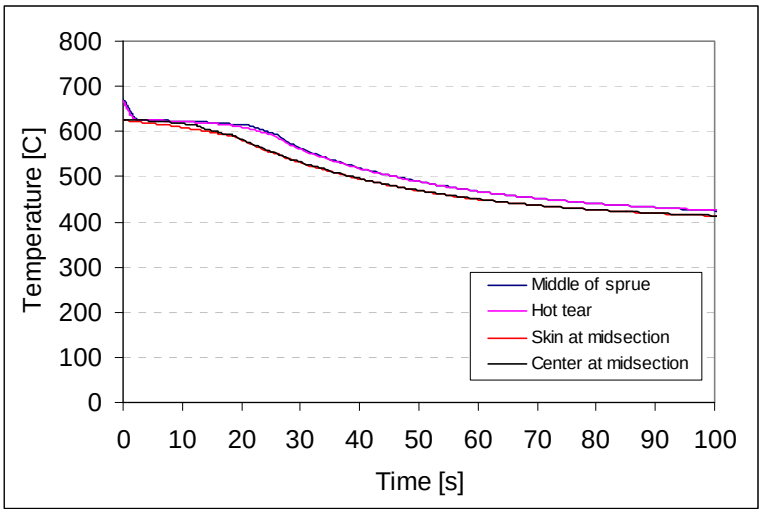

(a) Cooling curves.

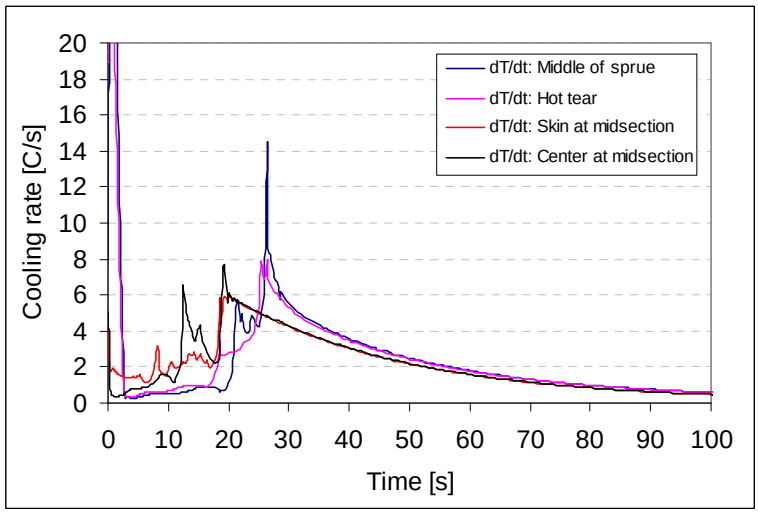

(b) Cooling rates.

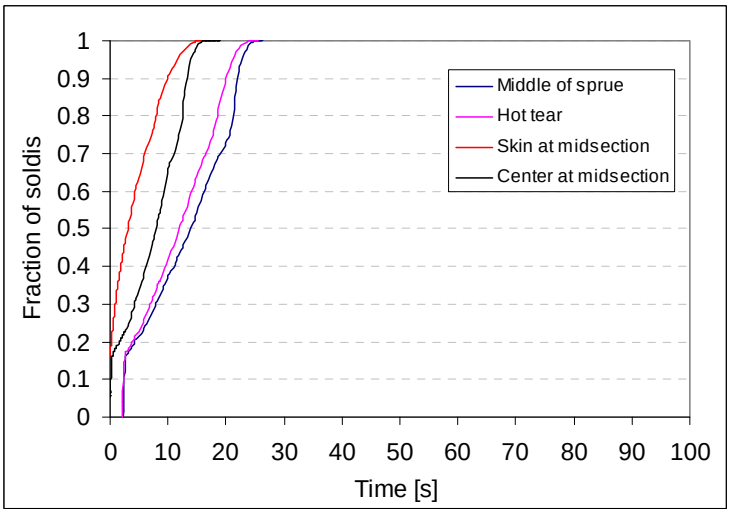

(c) Fraction of solids development.

Figure A4. 4: Solidification history data for AE42 casting at 390 °C mold temperature.

Appendix 5 – Neutron Diffraction

A5.1 Retention of Residual Strain

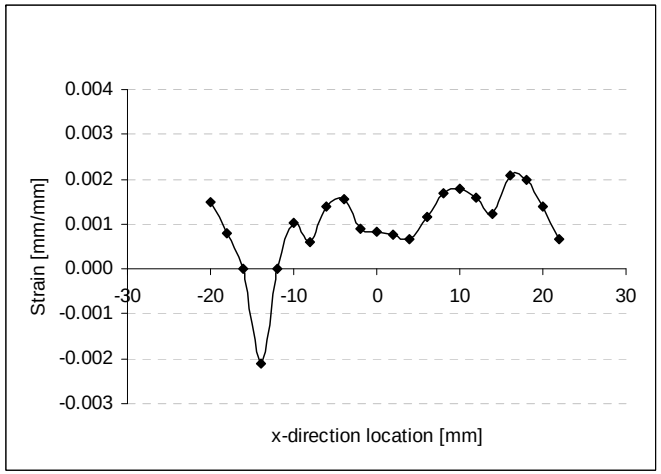

(a) Reflection: $(10\bar{1}0)$

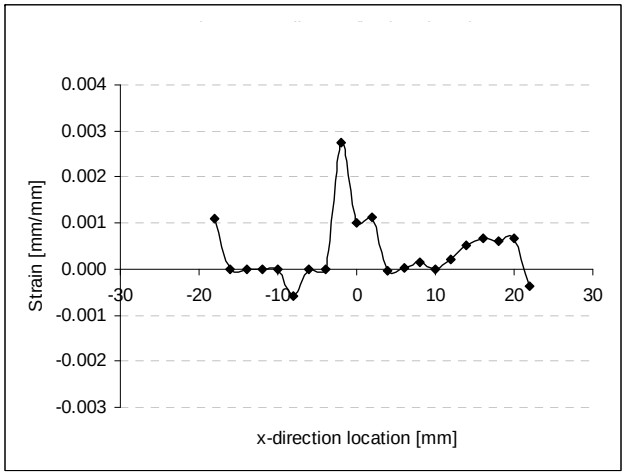

(b) Reflection: (0001)

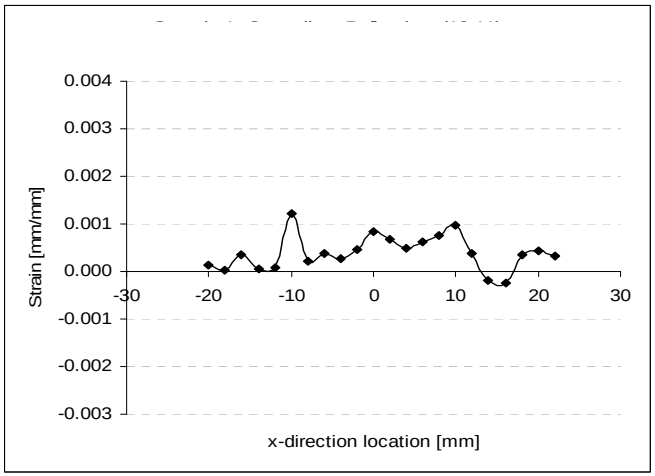

(c) Reflection: $(10\bar{1}1)$

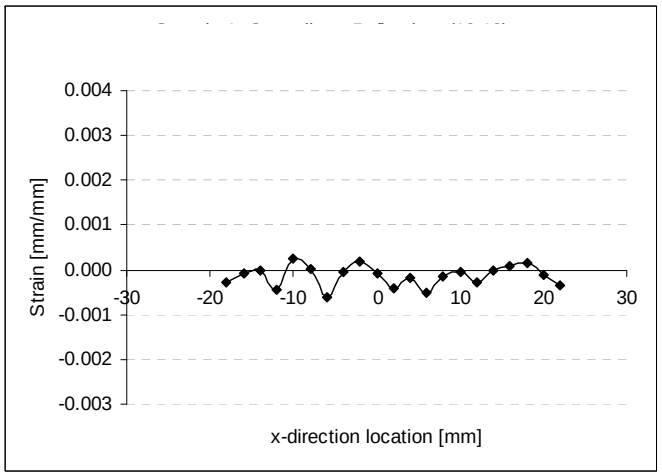

(d) Reflection: $(10\bar{1}2)$

Figure A5. 1: ε_x strain for AZ91D specimen (220 °C mold temperature).

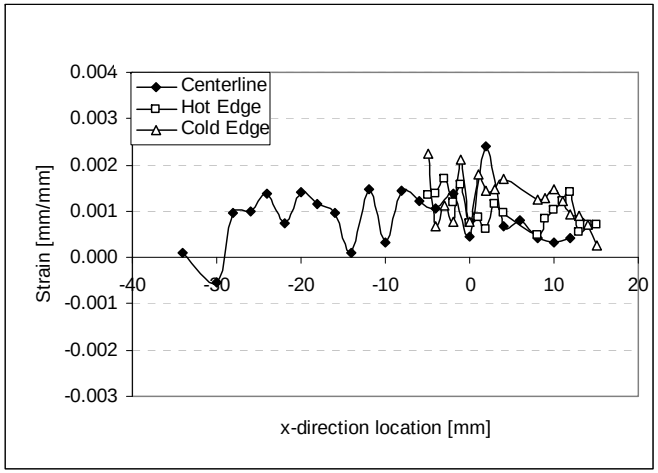

(a) Reflection: $(10\bar{1}0)$

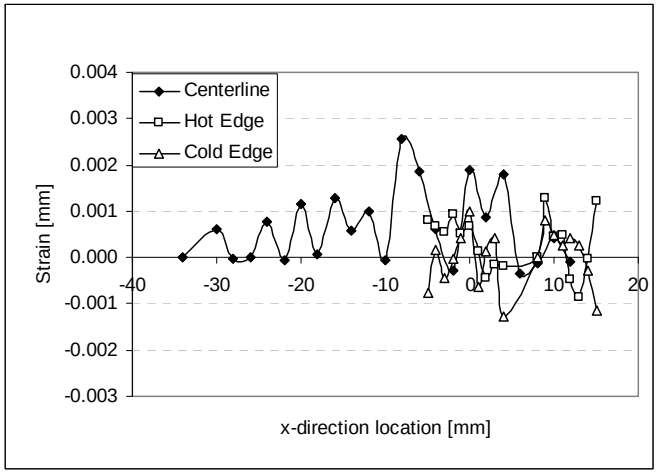

(b) Reflection: (0001)

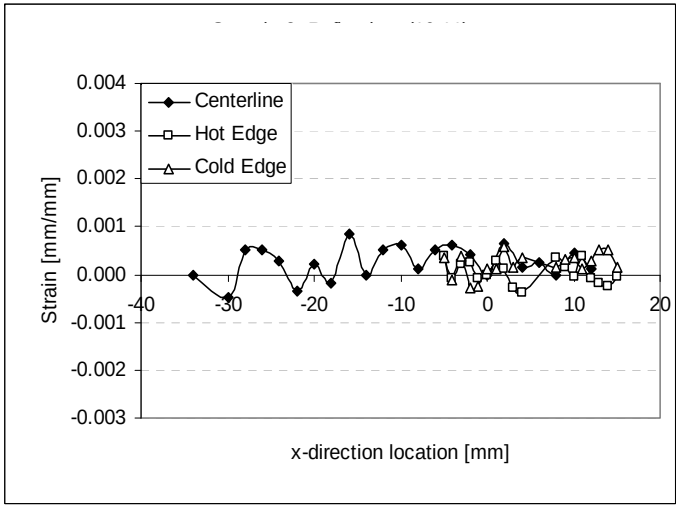

(c) Reflection: $(10\bar{1}1)$

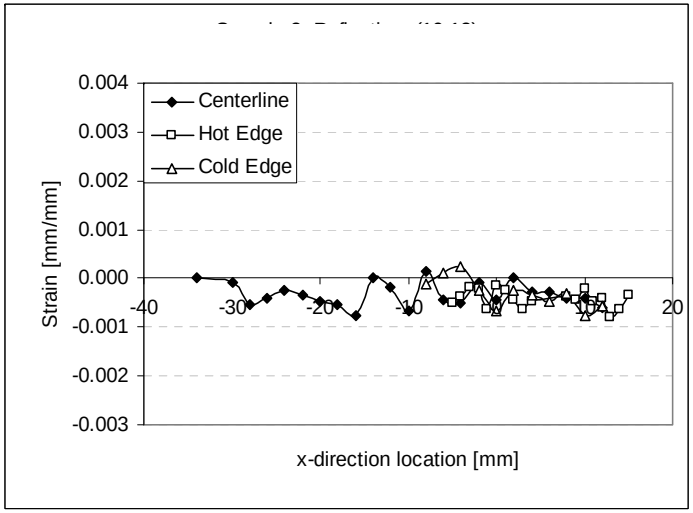

(d) Reflection: $(10\bar{1}2)$

Figure A5. 2: ε_x strain for AZ91D specimen (320 °C mold temperature).

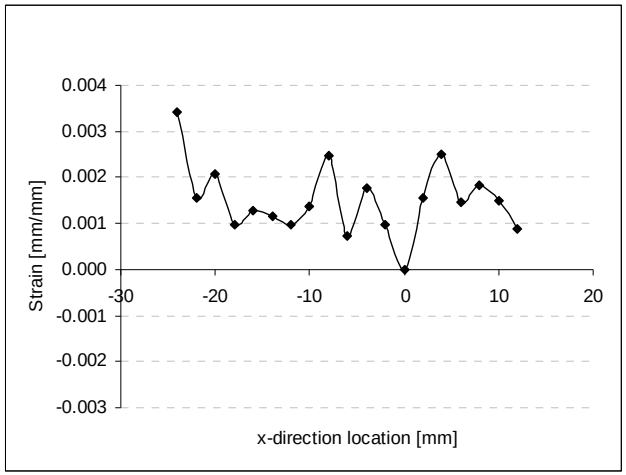

(a) Reflection: $(10\bar{1}0)$

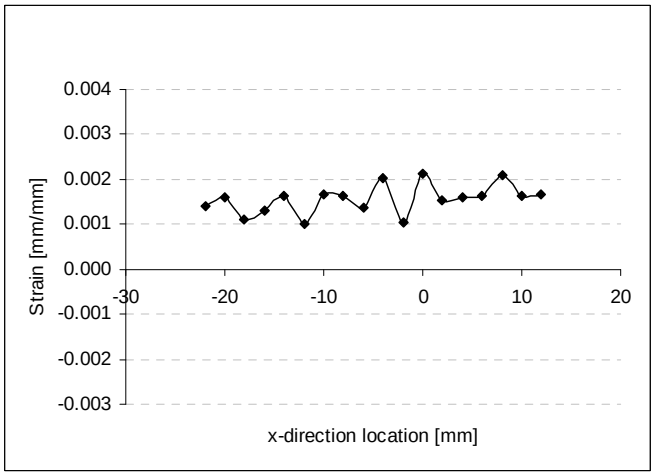

(b) Reflection: (0001)

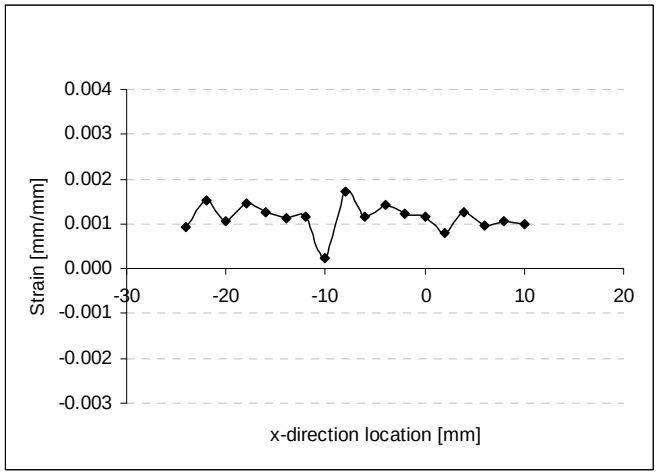

(c) Reflection: $(10\bar{1}1)$

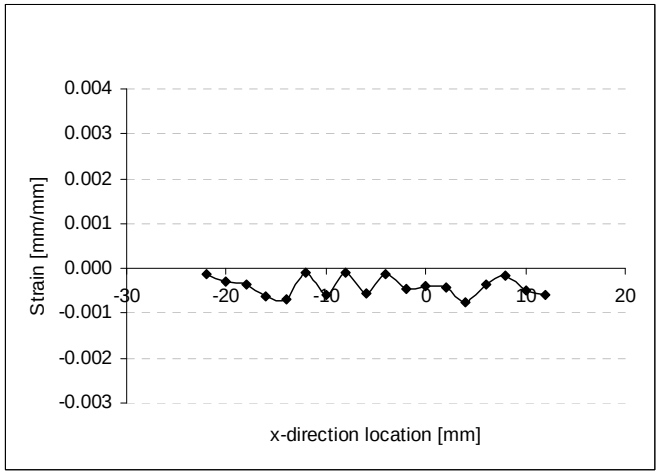

(d) Reflection: $(10\bar{1}2)$

Figure A5. 3: ε_x strain for AZ91D specimen (340 °C mold temperature).

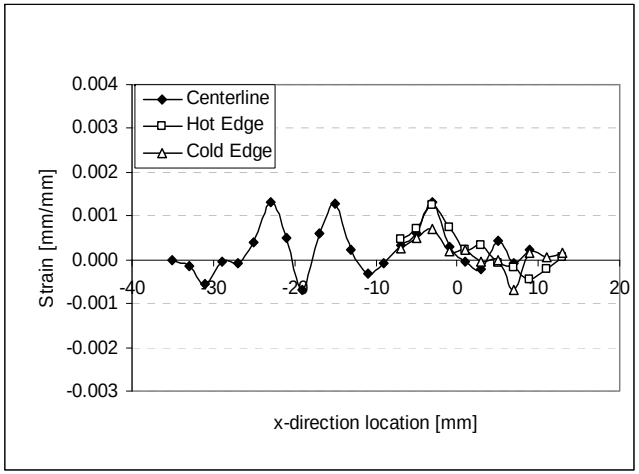

(a) Reflection: $(10\bar{1}0)$

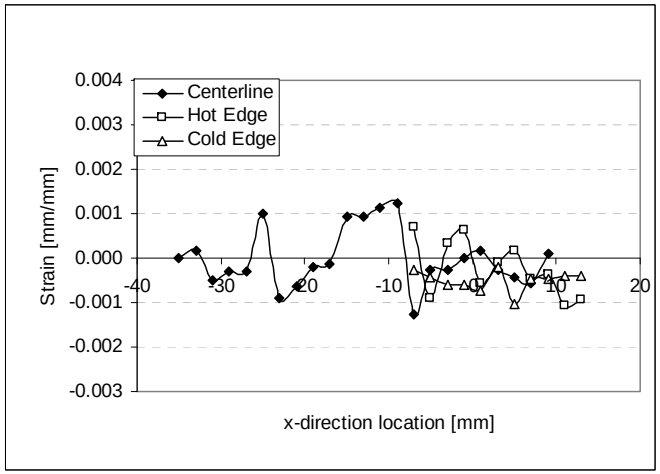

(b) Reflection: (0001)

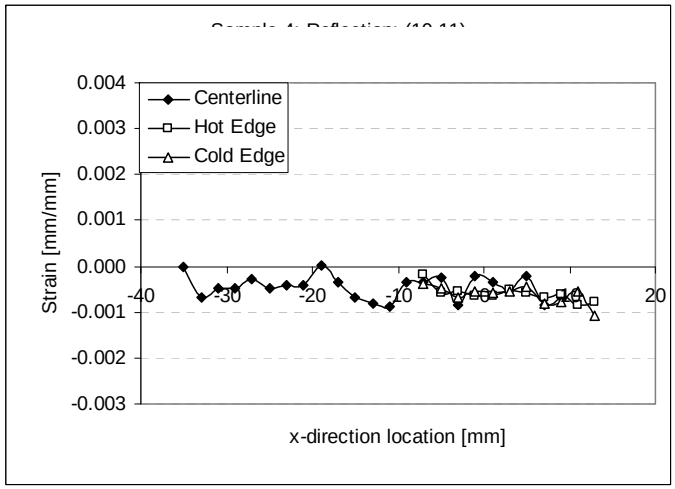

(c) Reflection: $(10\bar{1}1)$

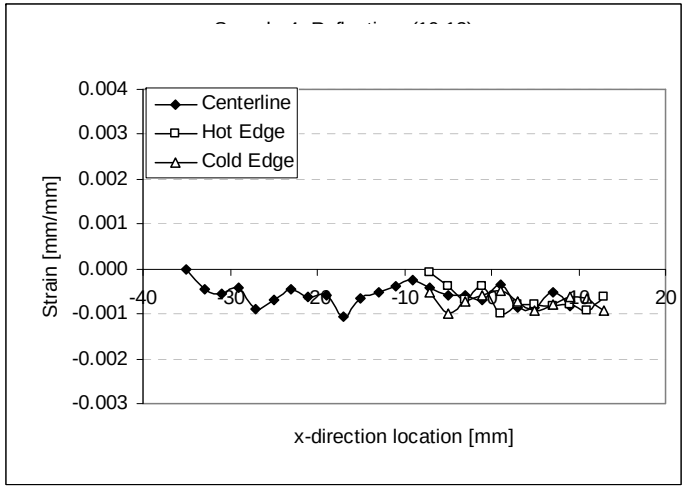

(d) Reflection: $(10\bar{1}2)$

Figure A5. 4: ε_x strain for AZ91D specimen (380 °C mold temperature).

A5.2 Residual Strain in x-Direction

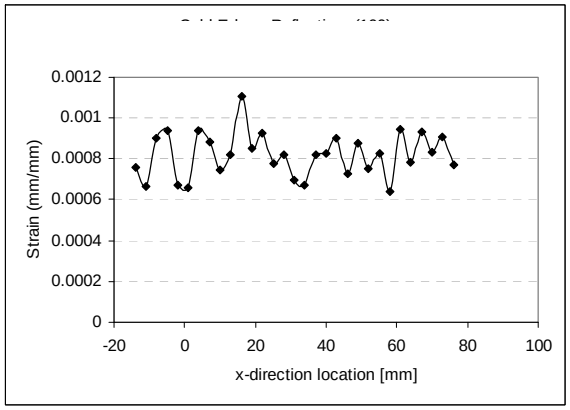

(a) Bottom edge; Reflection: $(10\bar{1}0)$

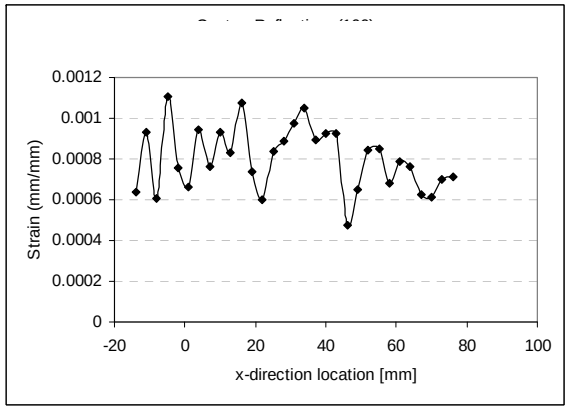

(b) Centerline; Reflection: $(10\bar{1}0)$

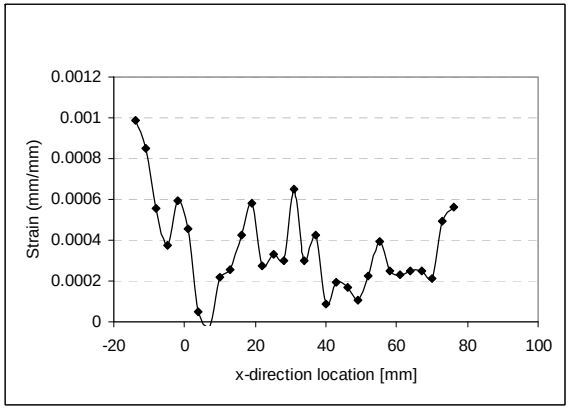

(c) Top edge; Reflection: $(10\bar{1}0)$

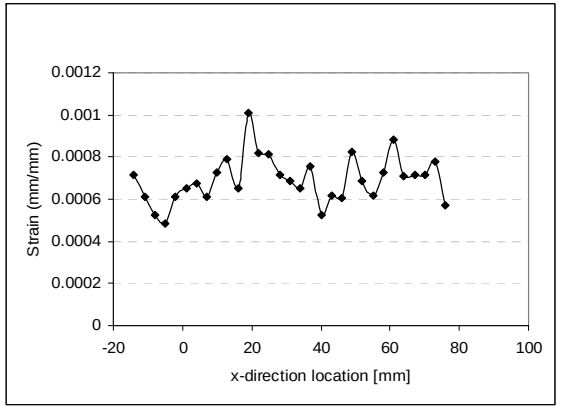

(d) Bottom edge; Reflection: (0001)

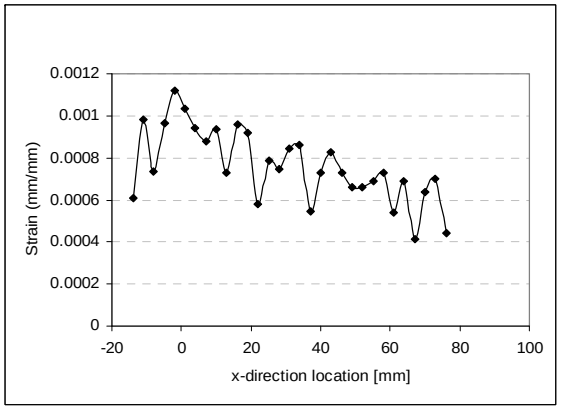

(e) Centerline; Reflection: (0001)

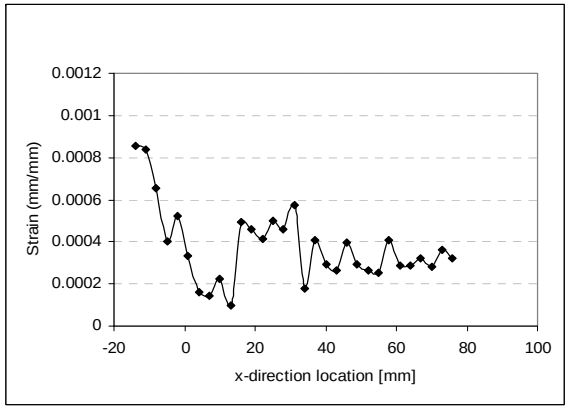

(f) Top edge; Reflection: (0001)

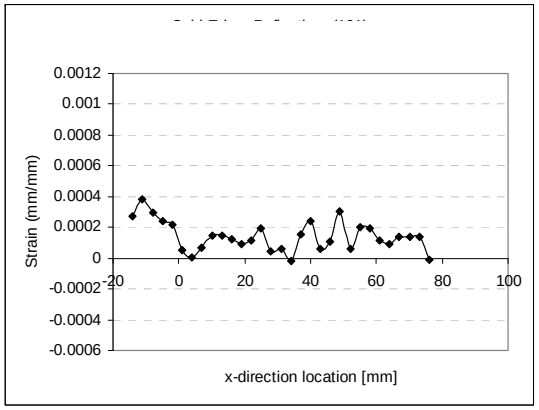

(g) Bottom edge; Reflection: $(10\bar{1}1)$

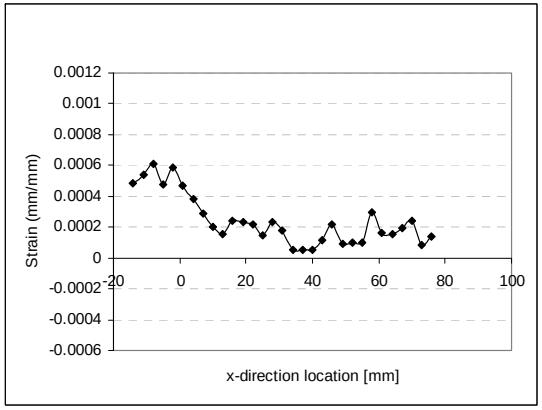

(h) Centerline; Reflection: $(10\bar{1}1)$

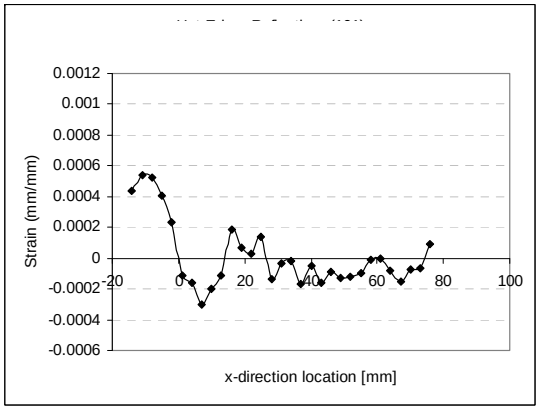

(i) Top edge; Reflection: $(10\bar{1}1)$

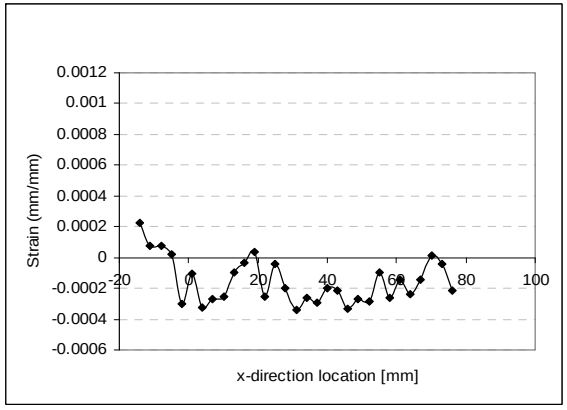

(j) Bottom edge; Reflection: $(10\bar{1}2)$

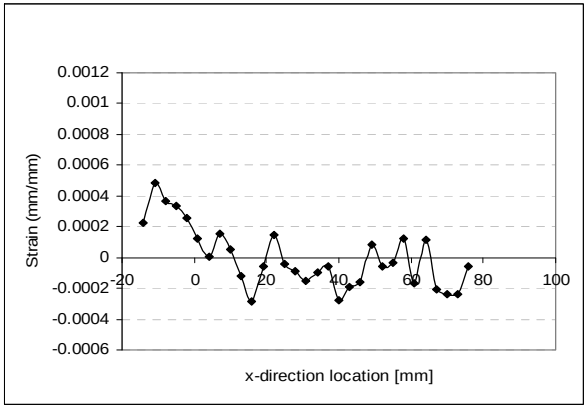

(k) Centerline; Reflection: $(10\bar{1}2)$

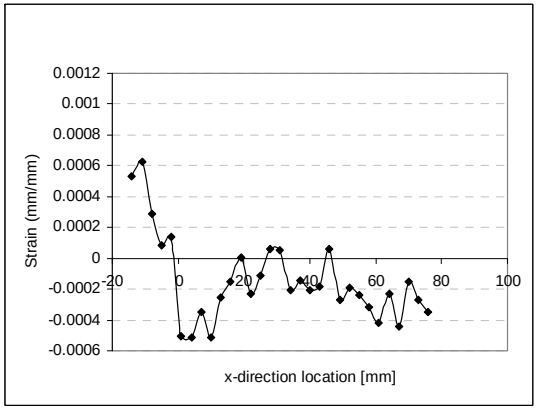

(l) Top edge; Reflection: $(10\bar{1}2)$

Figure A5. 5: ε_x profiles for bottom edge, centerline and top edge linescans for AZ91D casting at 210 °C mold temperature.

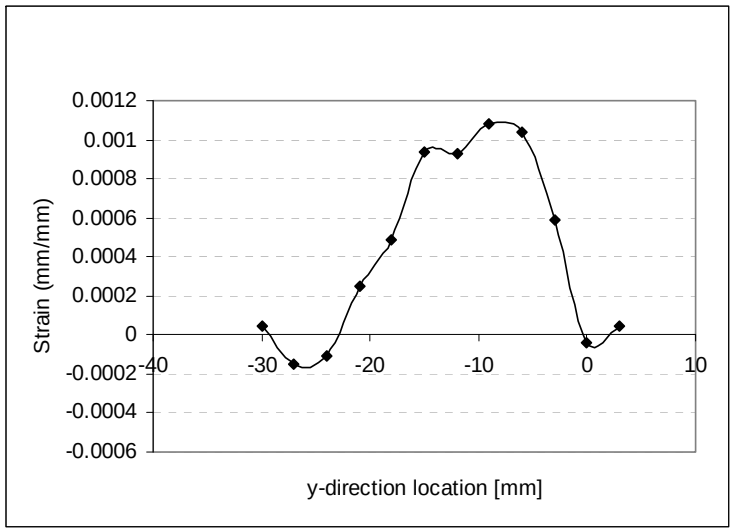

(a) Sprue cross-scan; Reflection: $(10\bar{1}0)$

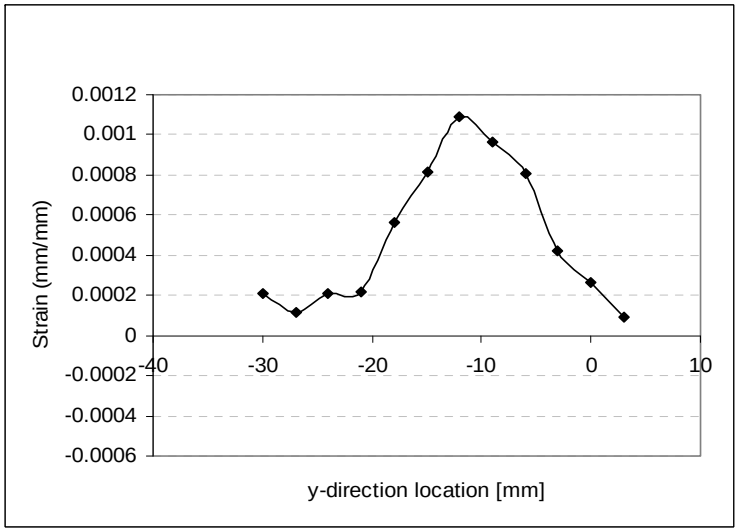

(b) Sprue cross-scan; Reflection: (0001)

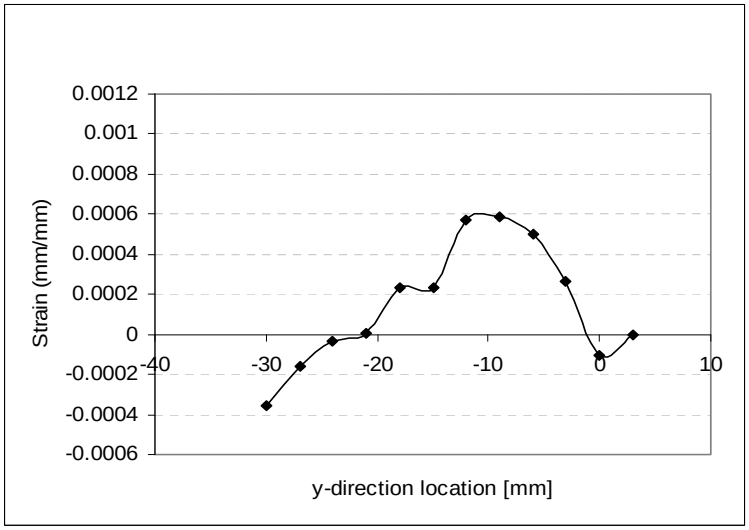

(c) Sprue cross-scan; Reflection: $(10\bar{1}1)$

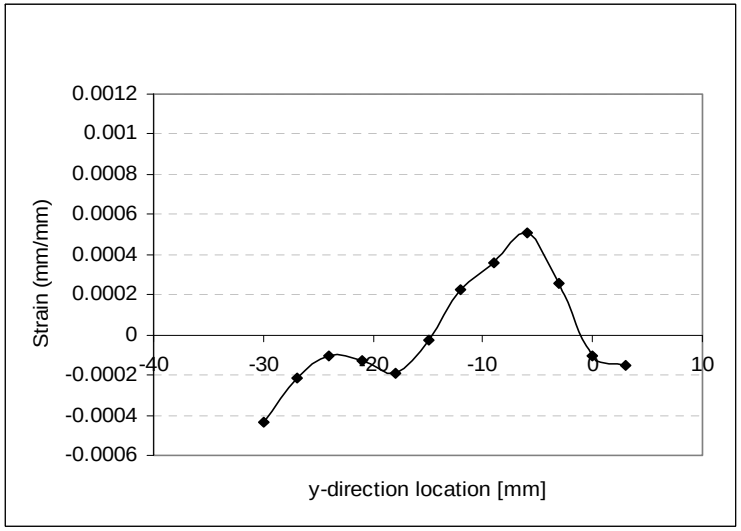

(d) Sprue cross-scan; Reflection: $(10\bar{1}2)$

Figure A5. 6: ε_x sprue cross-scan profile for AZ91D casting at 210 °C mold temperature.

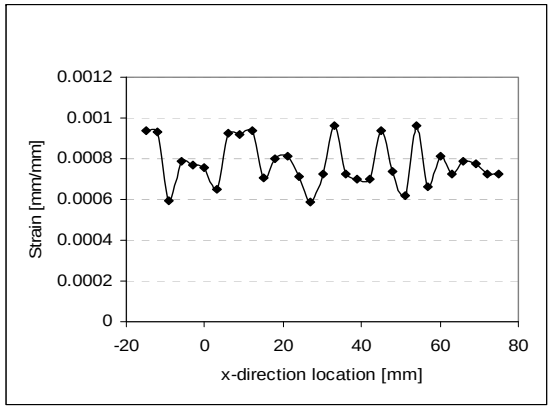

(a) Bottom edge; Reflection: $(10\bar{1}0)$

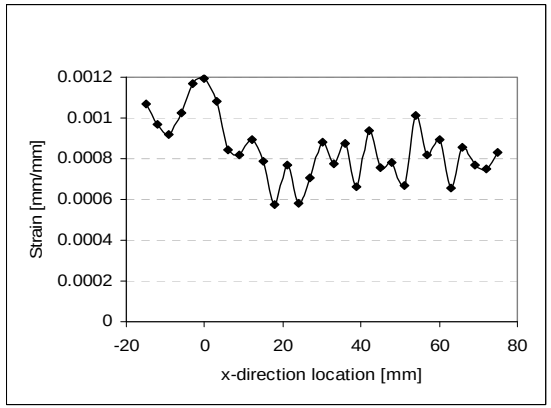

(b) Centerline; Reflection: $(10\bar{1}0)$

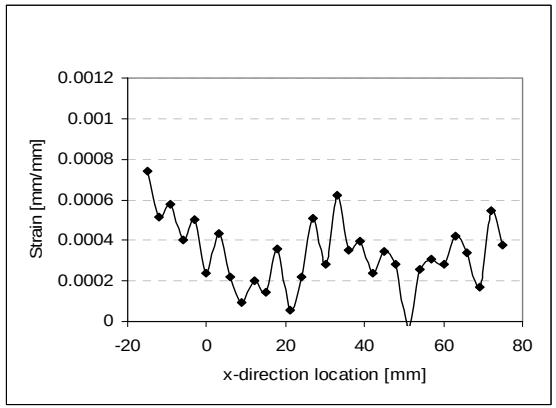

(c) Top edge; Reflection: $(10\bar{1}0)$

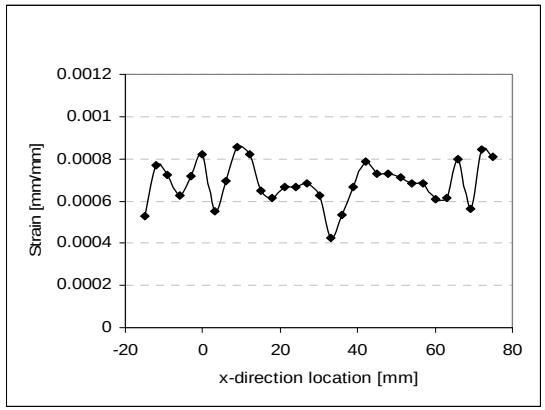

(d) Bottom edge; Reflection: (0001)

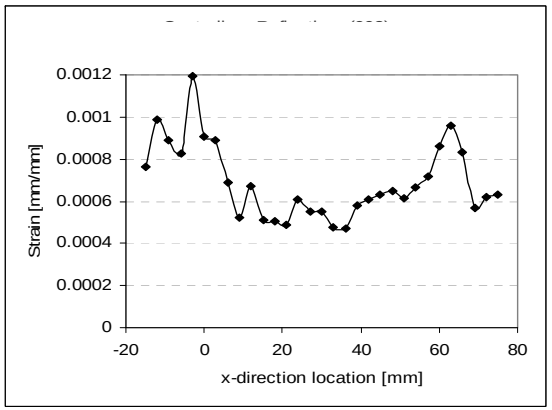

(e) Centerline; Reflection: (0001)

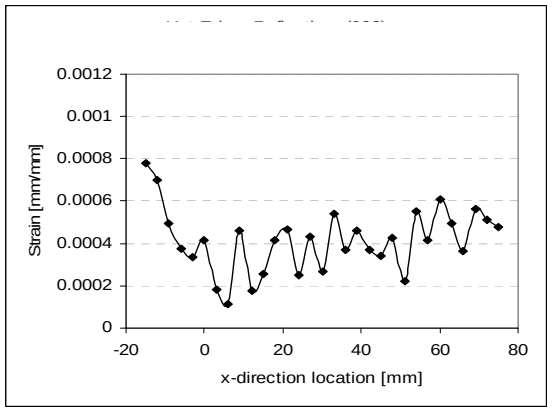

(f) Top edge; Reflection: (0001)

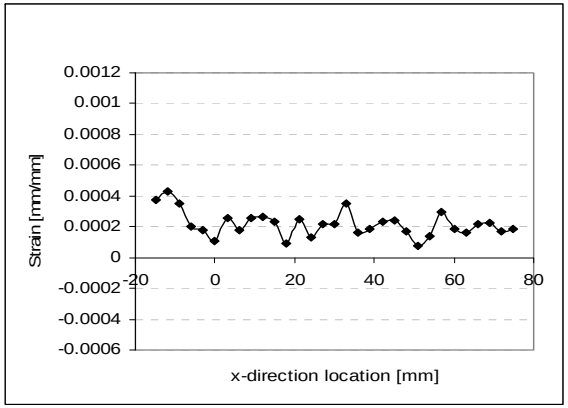

(g) Bottom edge; Reflection: $(10\bar{1}1)$

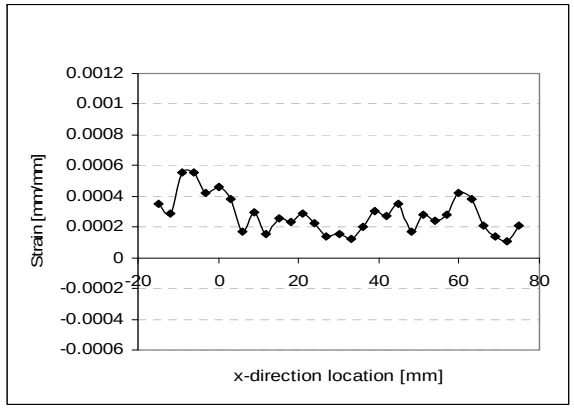

(h) Centerline; Reflection: $(10\bar{1}1)$

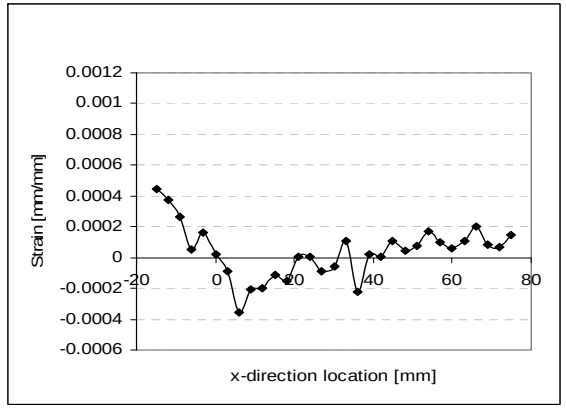

(i) Top edge; Reflection: $(10\bar{1}1)$

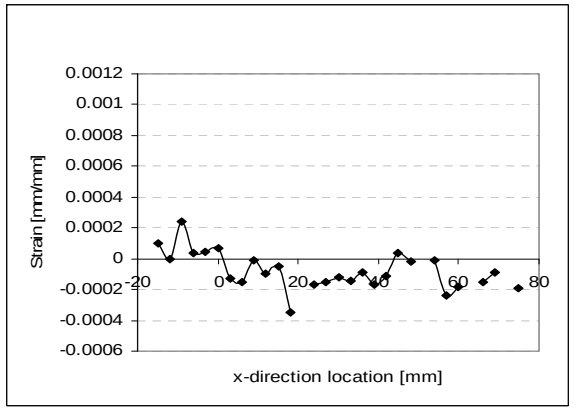

(j) Bottom edge; Reflection: $(10\bar{1}2)$

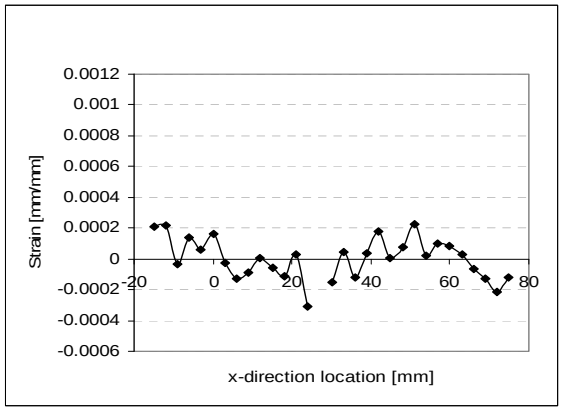

(k) Centerline; Reflection: $(10\bar{1}2)$

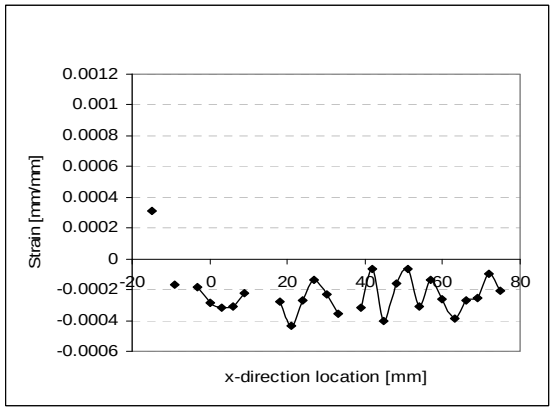

(l) Top edge; Reflection: $(10\bar{1}2)$

Figure A5. 7: ε_x profiles for bottom edge, centerline and top edge linescans for AZ91D casting at 250 °C mold temperature.

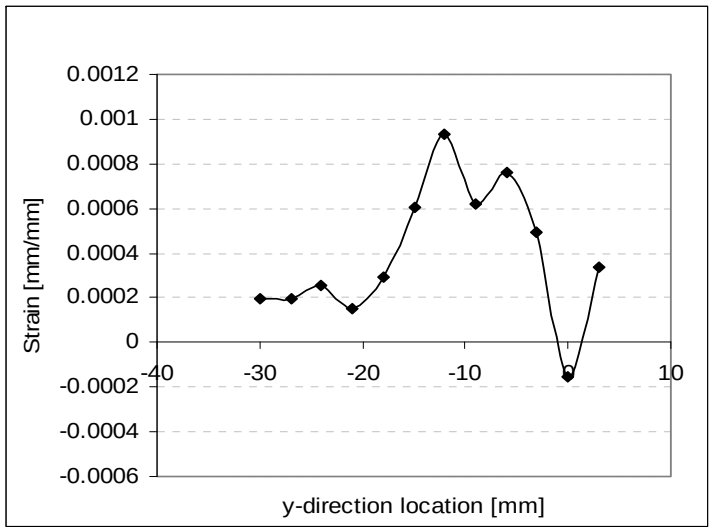

(a) Sprue cross-scan; Reflection: $(10\bar{1}0)$

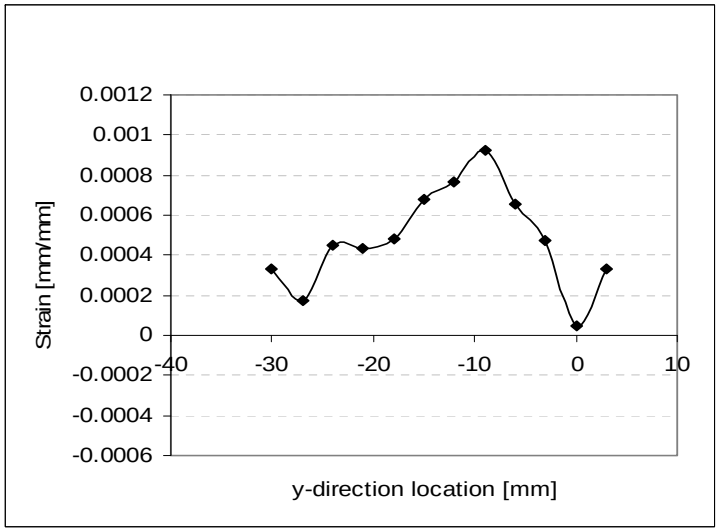

(b) Sprue cross-scan; Reflection: (0001)

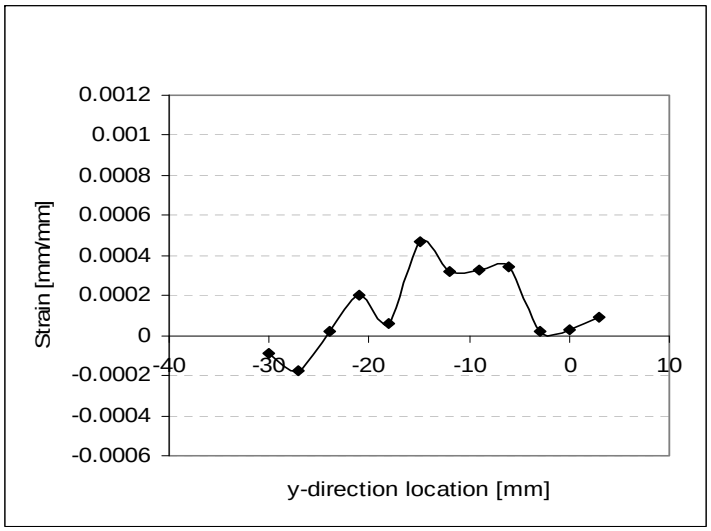

(c) Sprue cross-scan; Reflection: $(10\bar{1}1)$

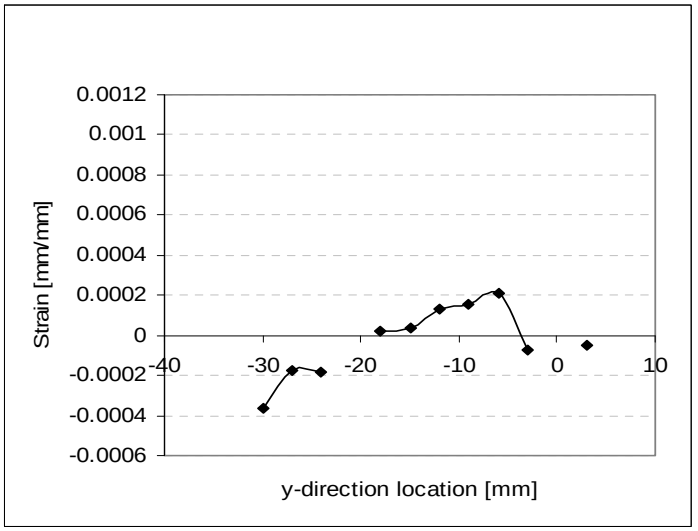

(d) Sprue cross-scan; Reflection: $(10\bar{1}2)$

Figure A5. 8: ε_x sprue cross-scan profile for AZ91D casting at 250 °C mold temperature.

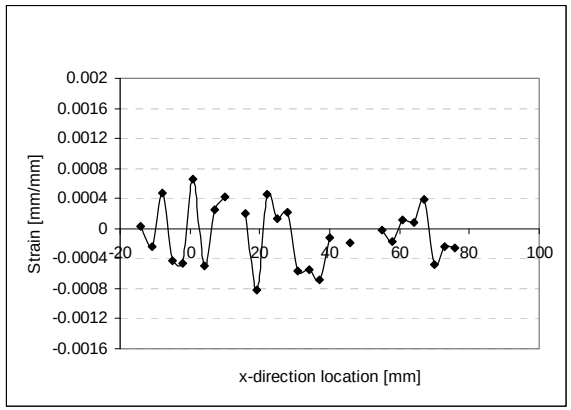

(a) Bottom edge; Reflection: $(10\bar{1}0)$

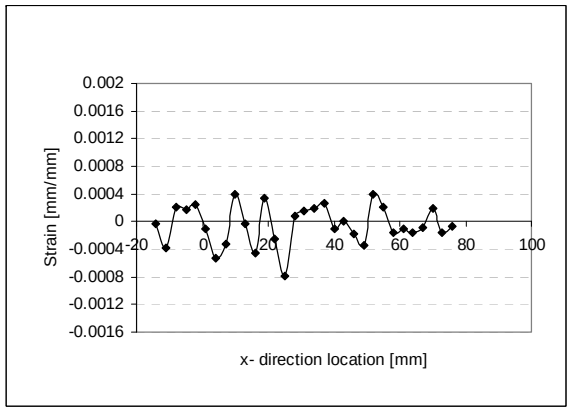

(b) Centerline; Reflection: $(10\bar{1}0)$

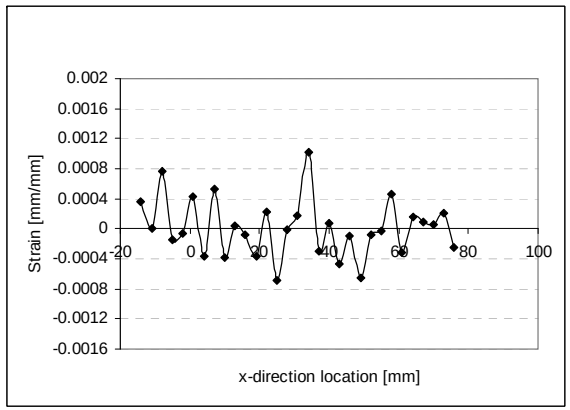

(c) Top edge; Reflection: $(10\bar{1}0)$

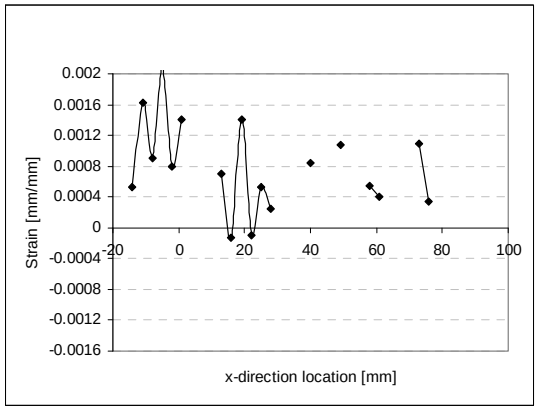

(d) Bottom edge; Reflection: (0001)

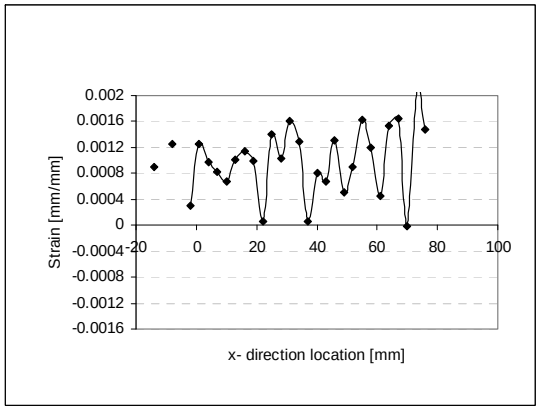

(e) Centerline; Reflection: (0001)

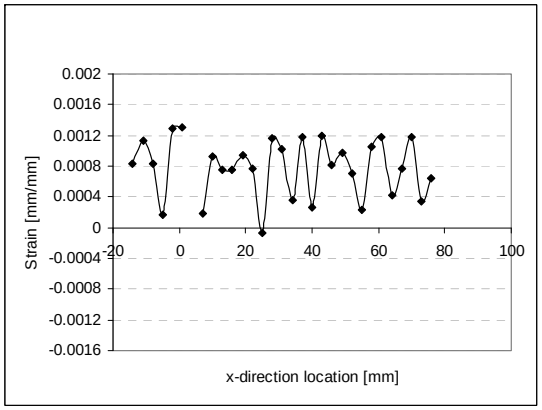

(f) Top edge; Reflection: (0001)

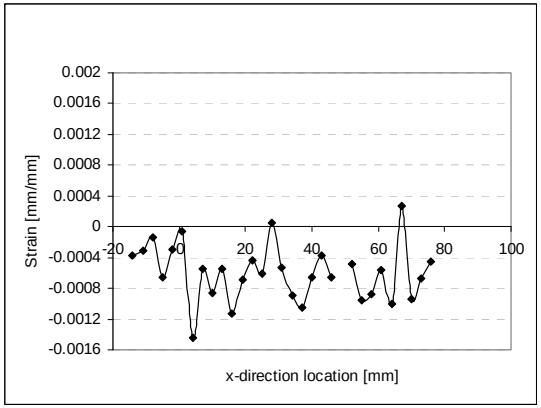

(g) Bottom edge; Reflection: $(10\bar{1}1)$

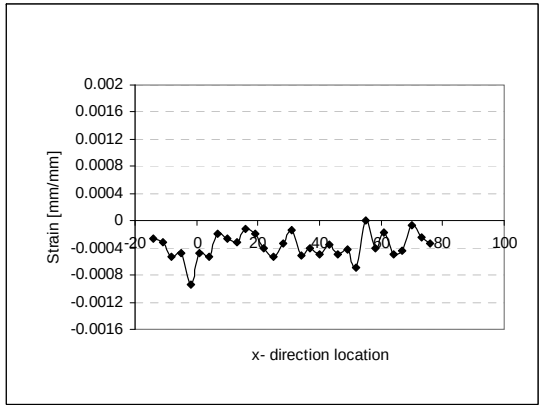

(h) Centerline; Reflection: $(10\bar{1}1)$

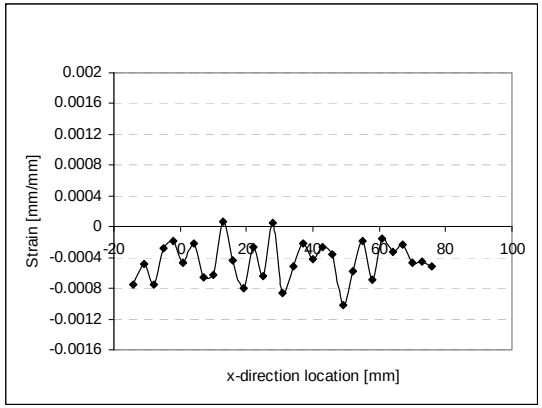

(i) Top edge; Reflection: $(10\bar{1}1)$

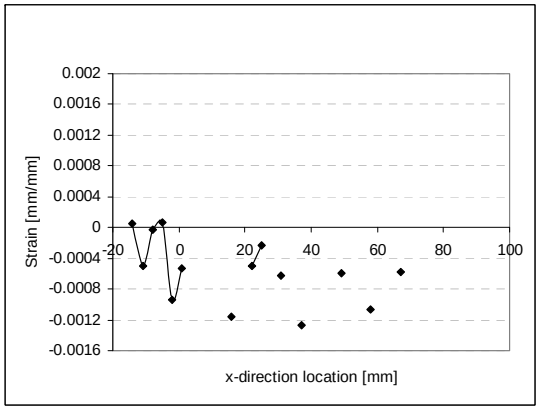

(j) Bottom edge; Reflection: $(10\bar{1}2)$

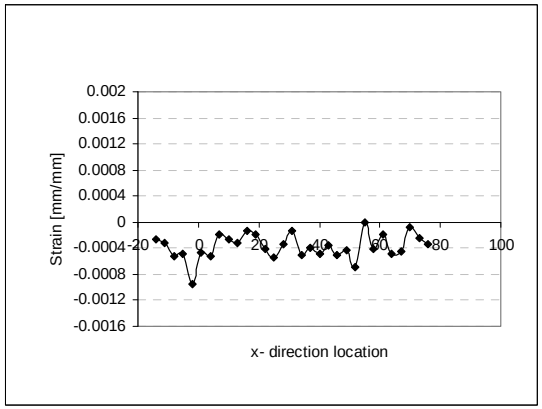

(k) Centerline; Reflection: $(10\bar{1}2)$

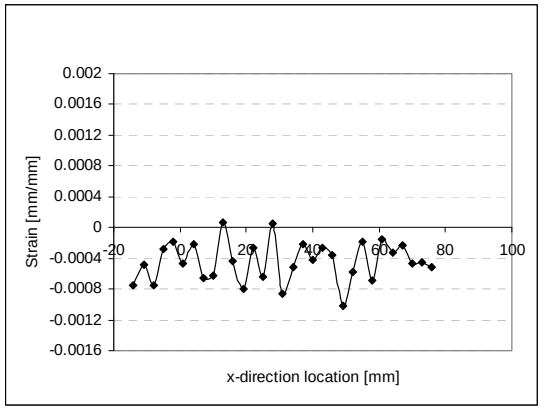

(l) Top edge; Reflection: $(10\bar{1}2)$

Figure A5. 9: ε_x profiles for bottom edge, centerline and top edge linescans for AE42 casting at 340 °C mold temperature.

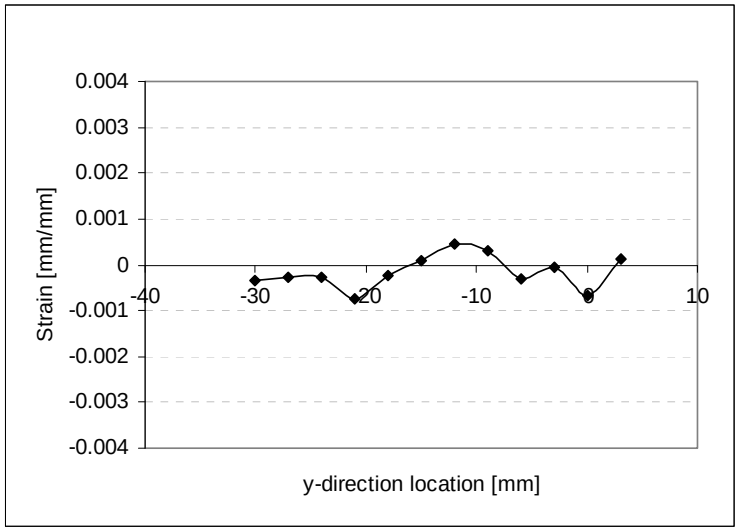

(a) Sprue cross-scan; Reflection: $(10\bar{1}0)$

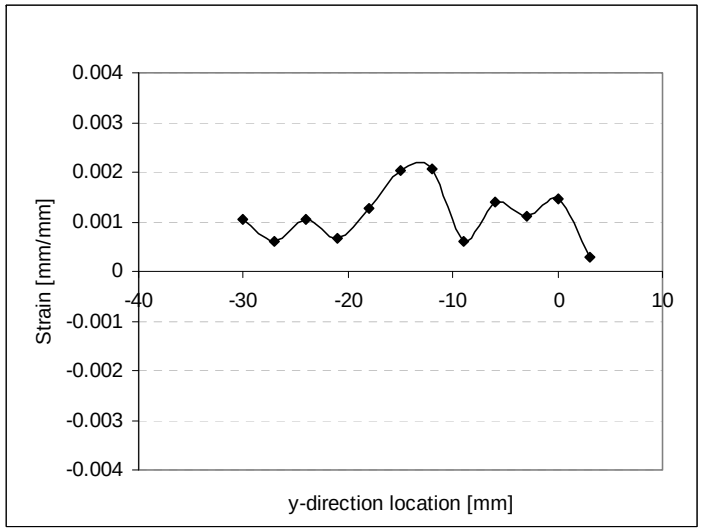

(b) Sprue cross-scan; Reflection: (0001)

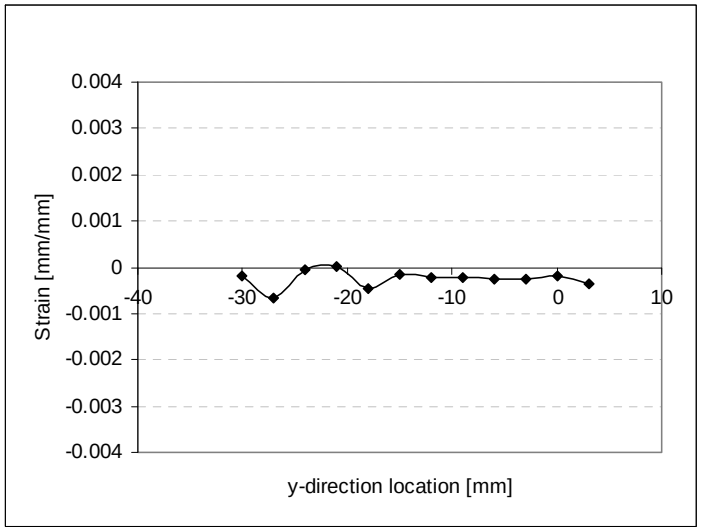

(c) Sprue cross-scan; Reflection: $(10\bar{1}1)$

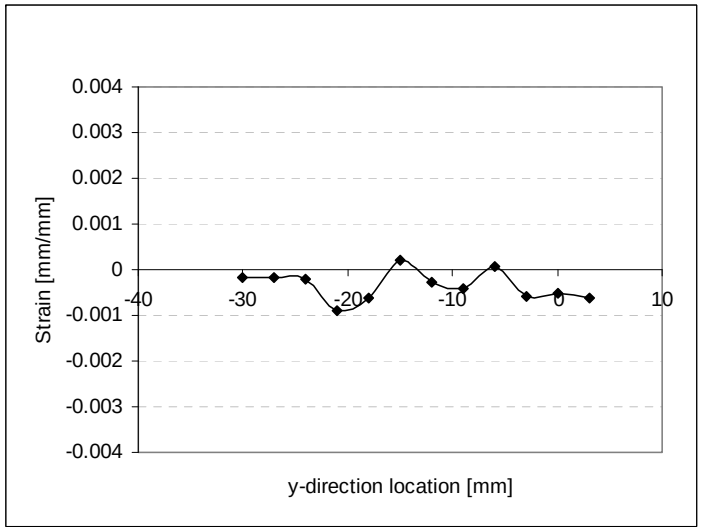

(d) Sprue cross-scan; Reflection: $(10\bar{1}2)$

Figure A5. 10: ε_x sprue cross-scan profile for AE42 casting at 340 °C mold temperature.

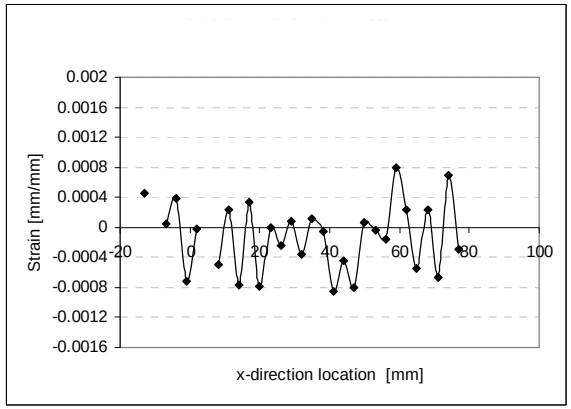

(a) Bottom edge; Reflection: $(10\bar{1}0)$

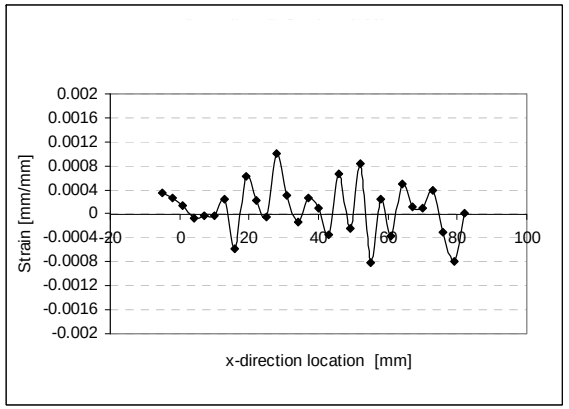

(b) Centerline; Reflection: $(10\bar{1}0)$

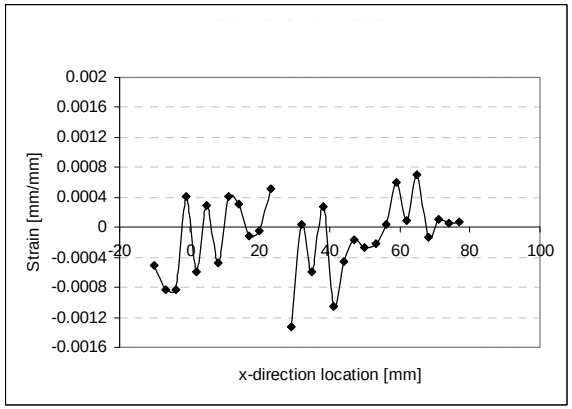

(c) Top edge; Reflection: $(10\bar{1}0)$

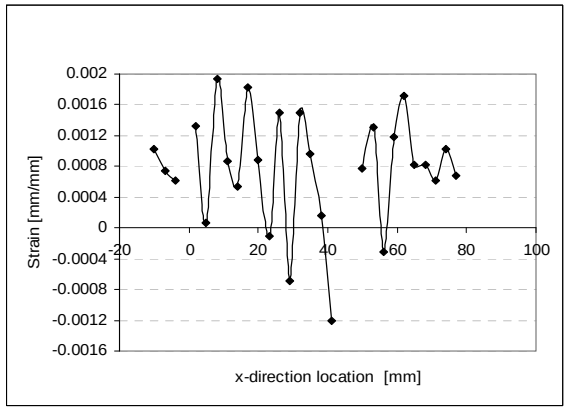

(d) Bottom edge; Reflection: (0001)

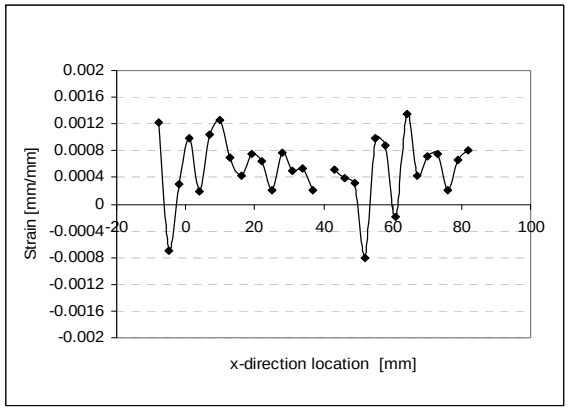

(e) Centerline; Reflection: (0001)

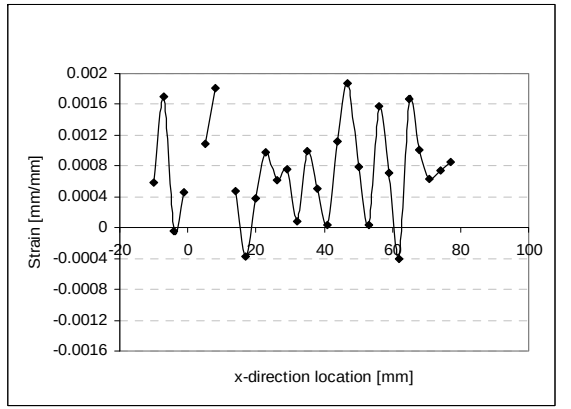

(f) Top edge; Reflection: (0001)

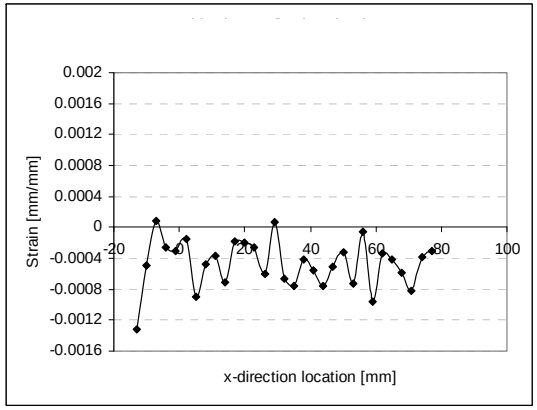

(g) Bottom edge; Reflection: $(10\bar{1}1)$

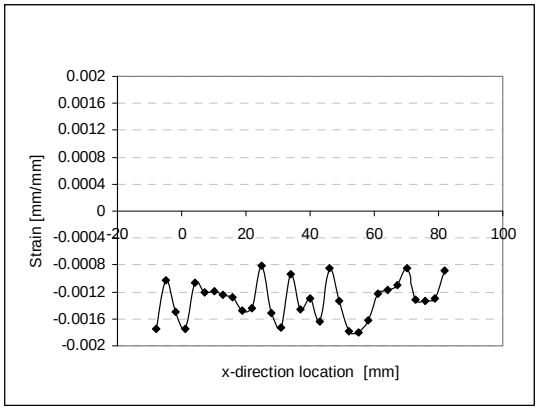

(h) Centerline; Reflection: $(10\bar{1}1)$

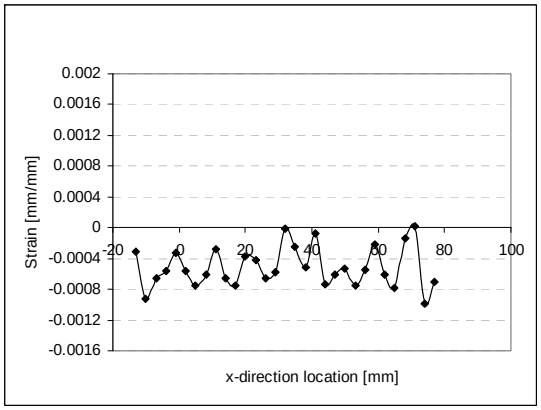

(i) Top edge; Reflection: $(10\bar{1}1)$

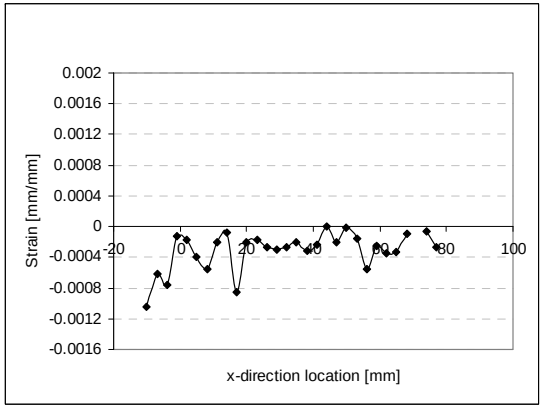

(j) Bottom edge; Reflection: $(10\bar{1}2)$

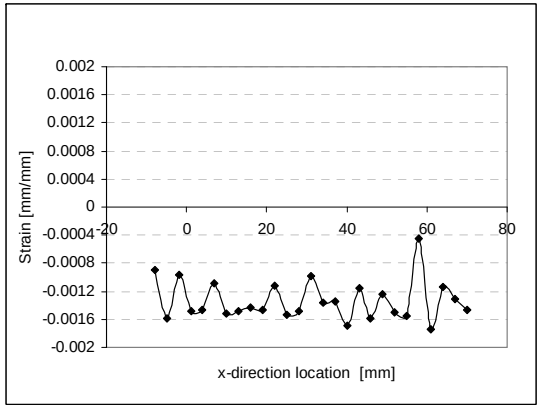

(k) Centerline; Reflection: $(10\bar{1}2)$

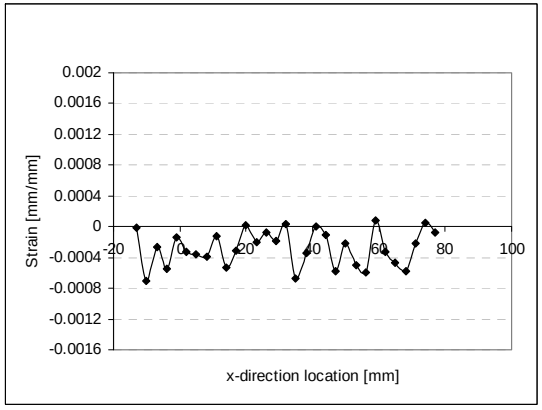

(l) Top edge; Reflection: $(10\bar{1}2)$

Figure A5. 11: ε_x profiles for bottom edge, centerline and top edge linescans for AE42 casting at 390 °C mold temperature.

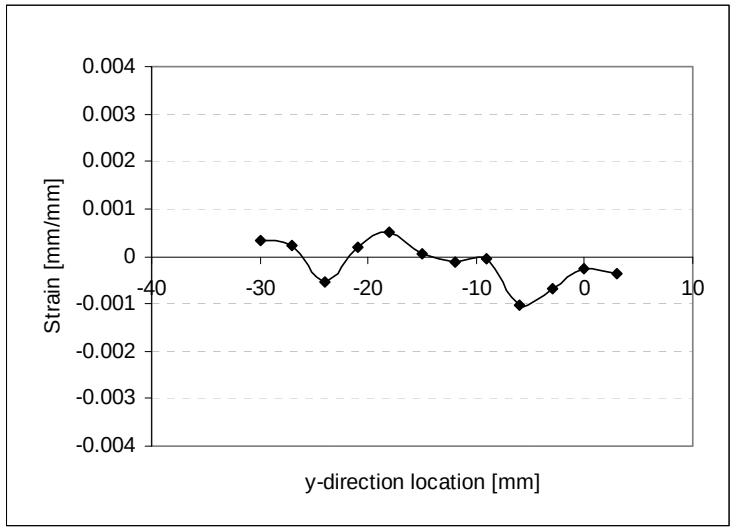

(a) Sprue cross-scan; Reflection: $(10\bar{1}0)$

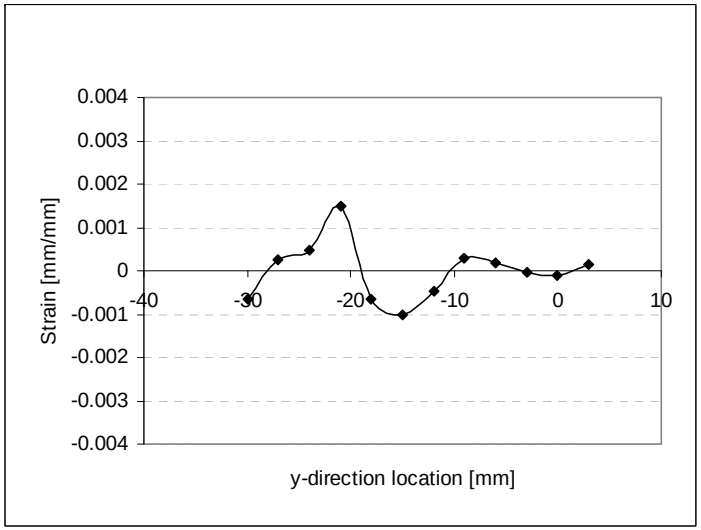

(b) Sprue cross-scan; Reflection: (0001)

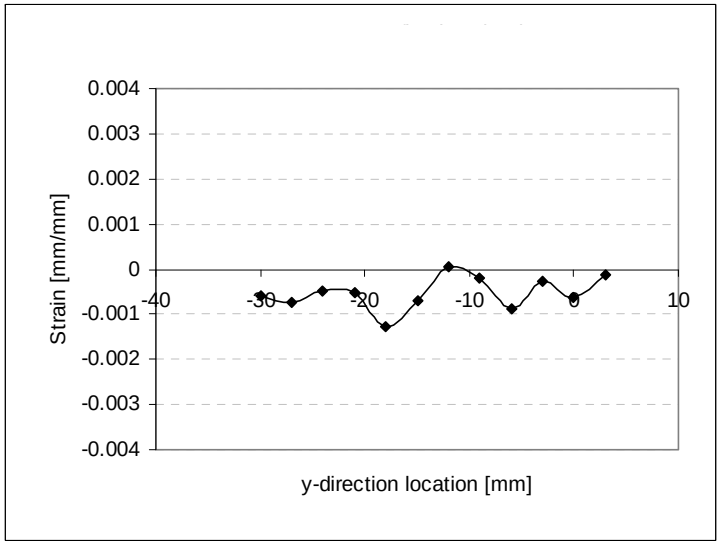

(c) Sprue cross-scan; Reflection: $(10\bar{1}1)$

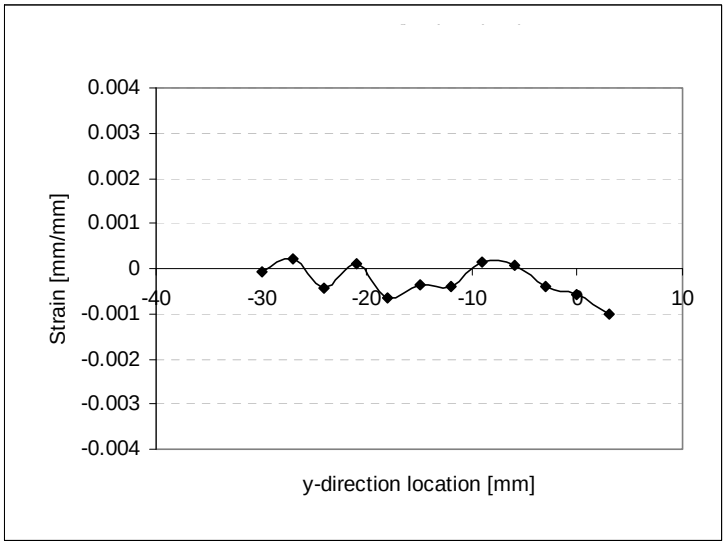

(d) Sprue cross-scan; Reflection: $(10\bar{1}2)$

Figure A5. 12: ε_x sprue cross-scan profile for AE42 casting at 390 °C mold temperature.

A5.3 Residual Strain in y-Direction

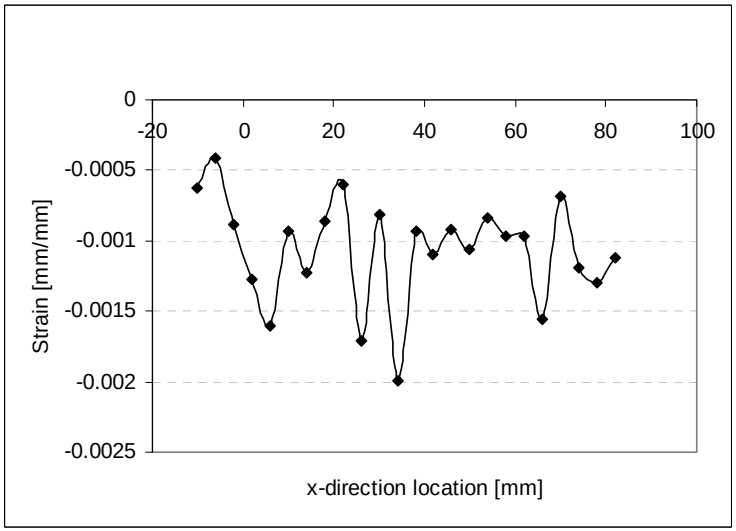

(a) Top edge; Reflection: $(10\bar{1}0)$

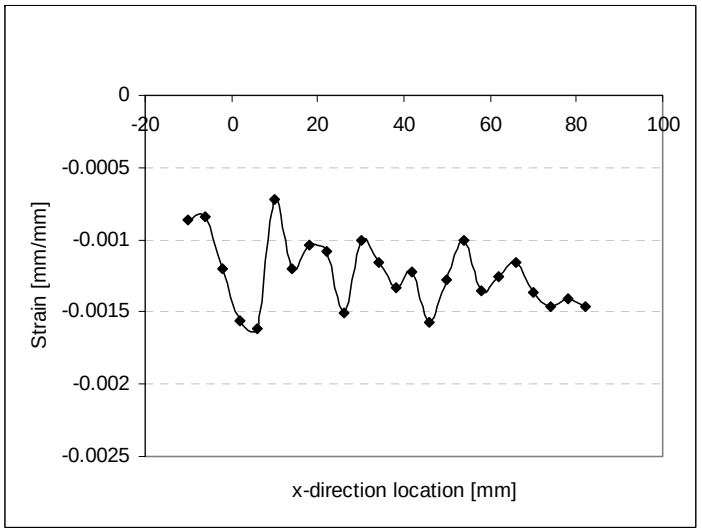

(b) Top edge; Reflection: (0001)

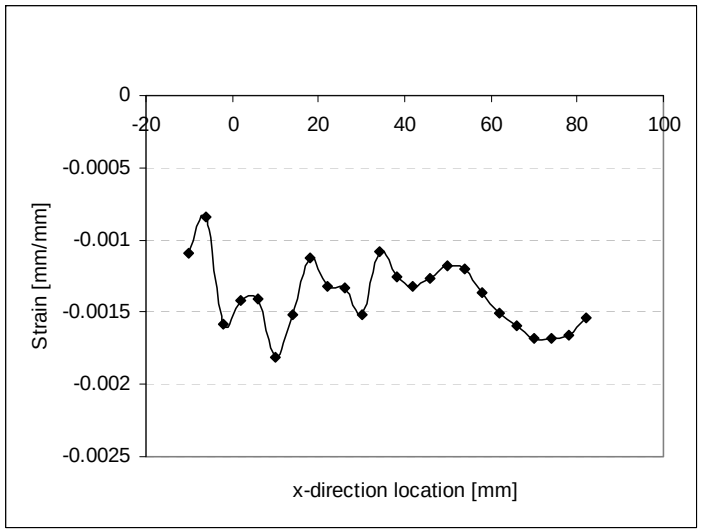

(c) Top edge; Reflection: $(10\bar{1}1)$

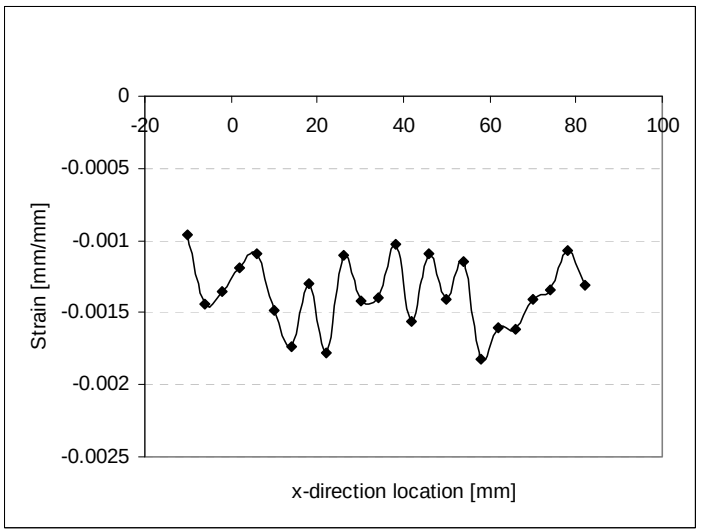

(d) Top edge; Reflection: $(10\bar{1}2)$

Figure A5. 13: ε_y profiles for top edge linescan for AZ91D casting at 210 °C mold temperature.

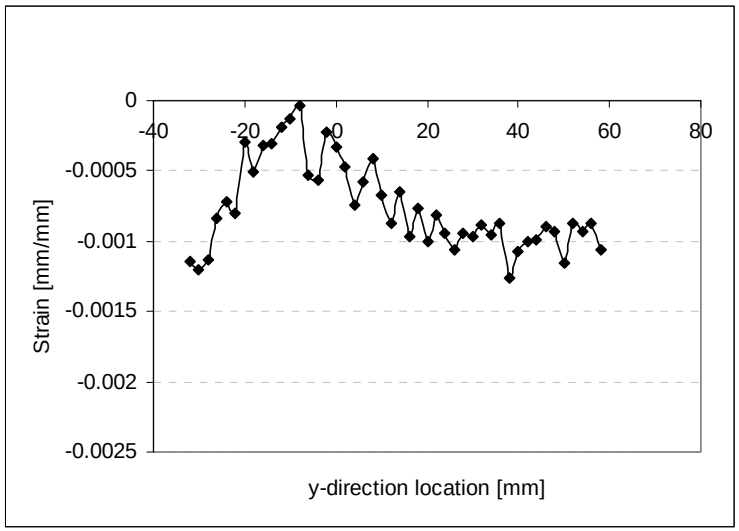

(a) Sprue cross-scan; Reflection: $(10\bar{1}0)$

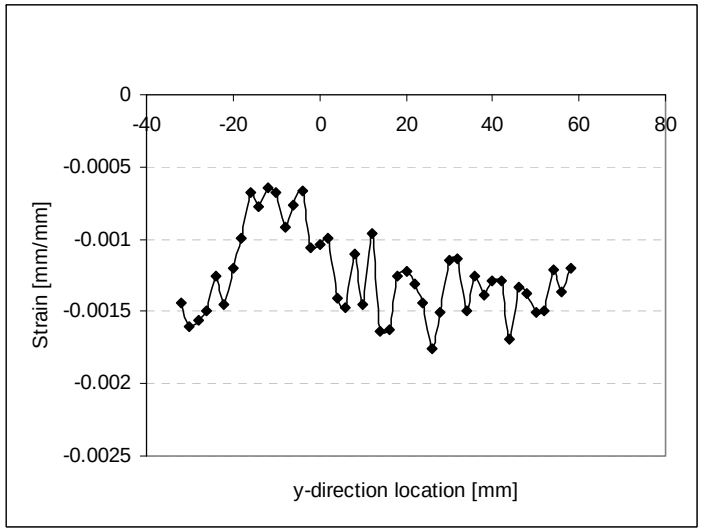

(b) Sprue cross-scan; Reflection: (0001)

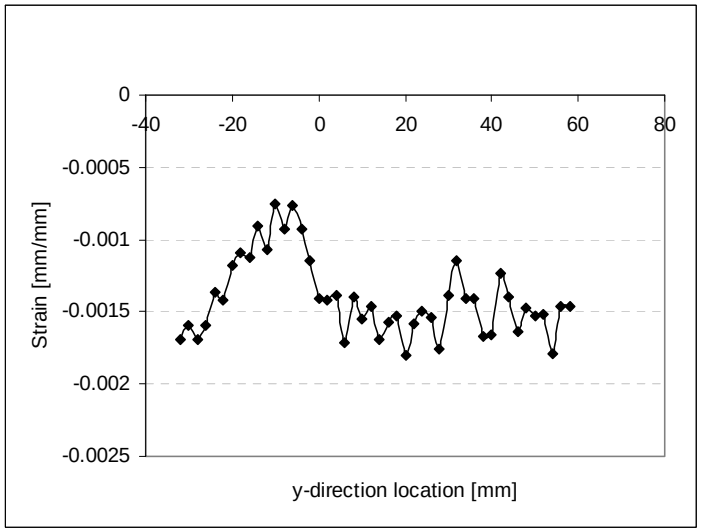

(c) Sprue cross-scan; Reflection: $(10\bar{1}1)$

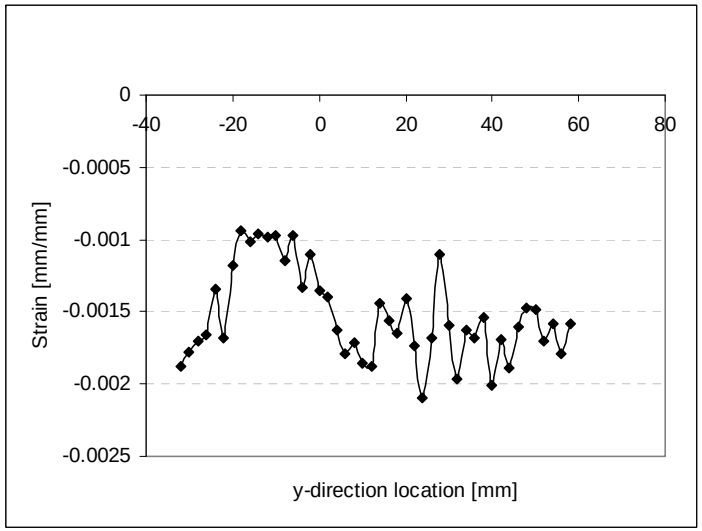

(d) Sprue cross-scan; Reflection: $(10\bar{1}2)$

Figure A5. 14: ε_y profiles for sprue cross-scan for AZ91D casting at 210 °C mold temperature.

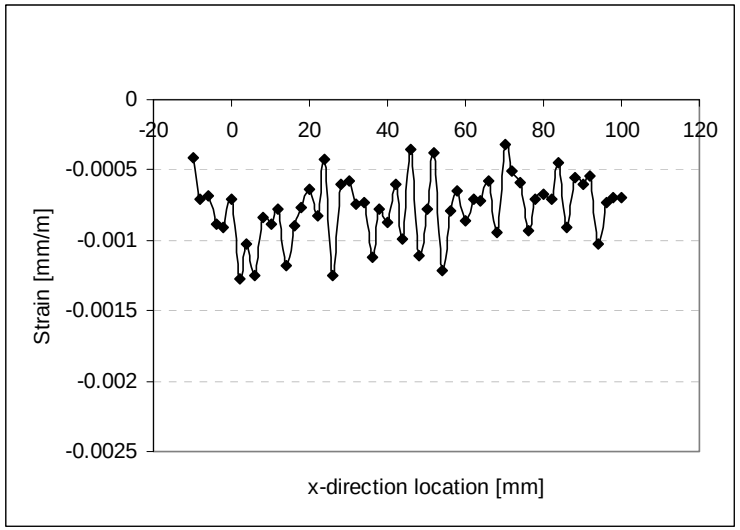

(a) Top edge; Reflection: $(10\bar{1}0)$

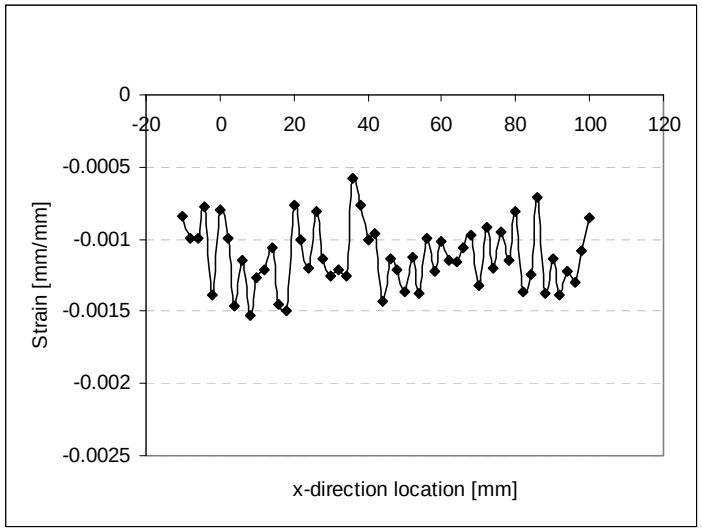

(b) Top edge; Reflection: (0001)

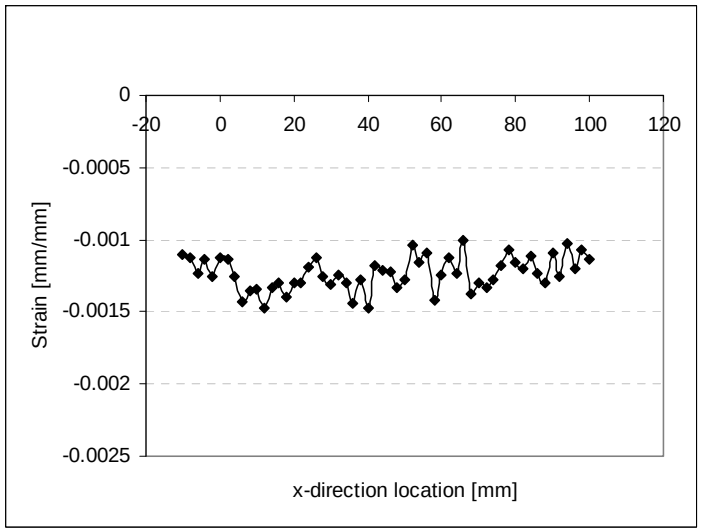

(c) Top edge; Reflection: $(10\bar{1}1)$

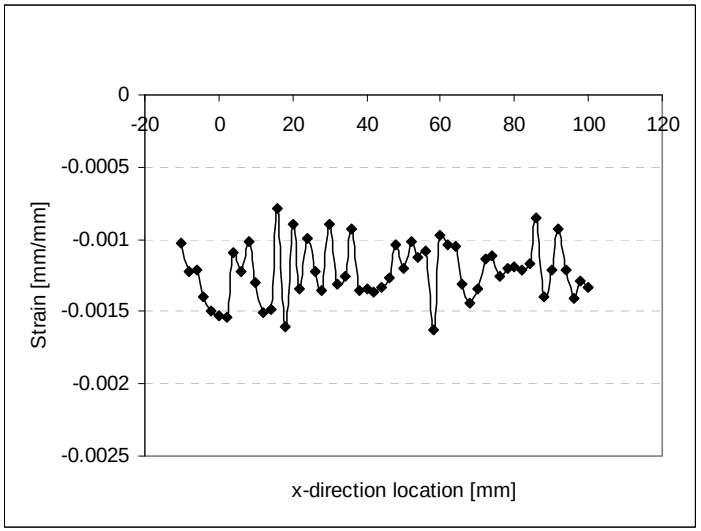

(d) Top edge; Reflection: $(10\bar{1}2)$

Figure A5. 15: ε_y profiles for top edge linescan for AZ91D casting at 250 °C mold temperature.

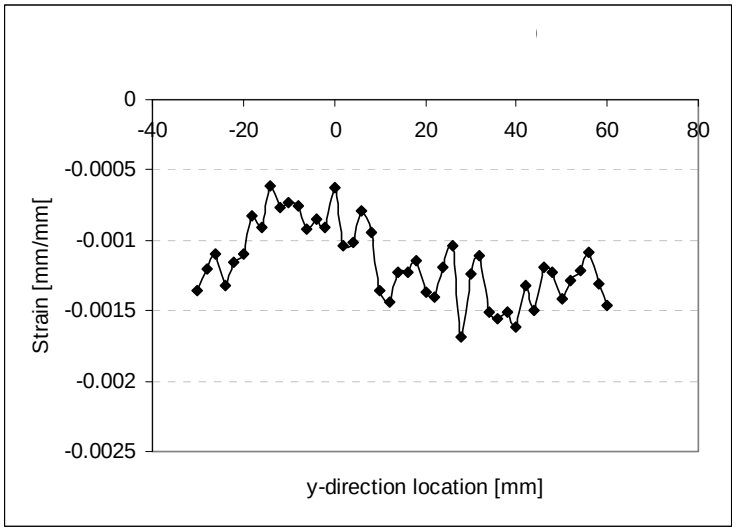

(a) Sprue cross-scan; Reflection: $(10\bar{1}0)$

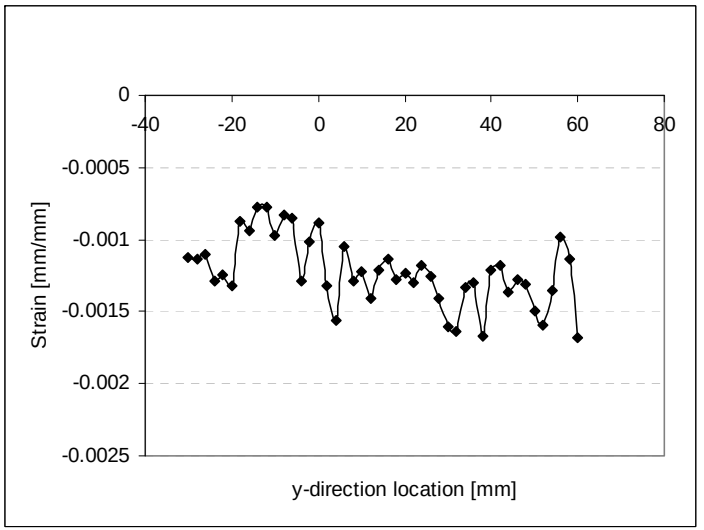

(b) Sprue cross-scan; Reflection: (0001)

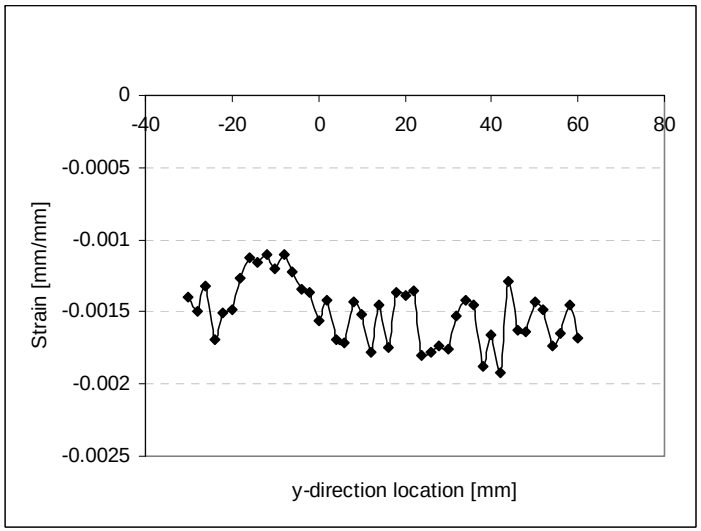

(c) Sprue cross-scan; Reflection: $(10\bar{1}1)$

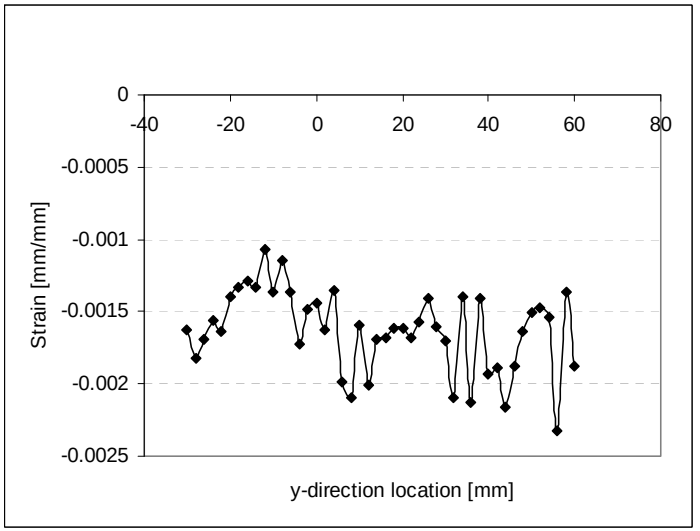

(d) Sprue cross-scan; Reflection: $(10\bar{1}2)$

Figure A5. 16: ε_y profiles for sprue cross-scan for AZ91D casting at 250 °C mold temperature.

A5.4 Residual Strain in z-Direction

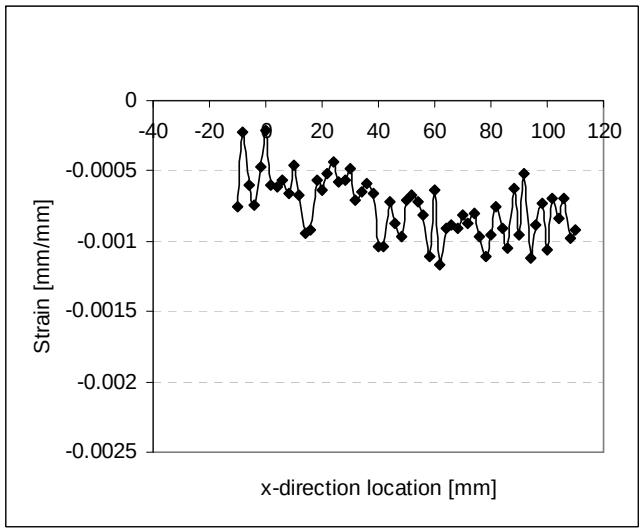

(a) Top edge; Reflection: $(10\bar{1}0)$

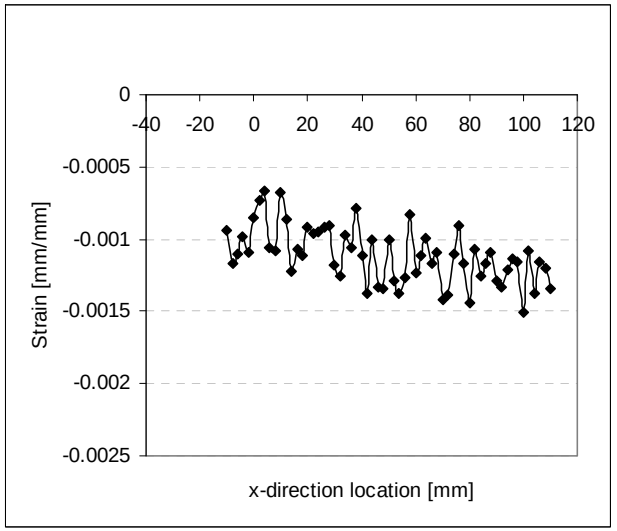

(b) Top edge; Reflection: (0001)

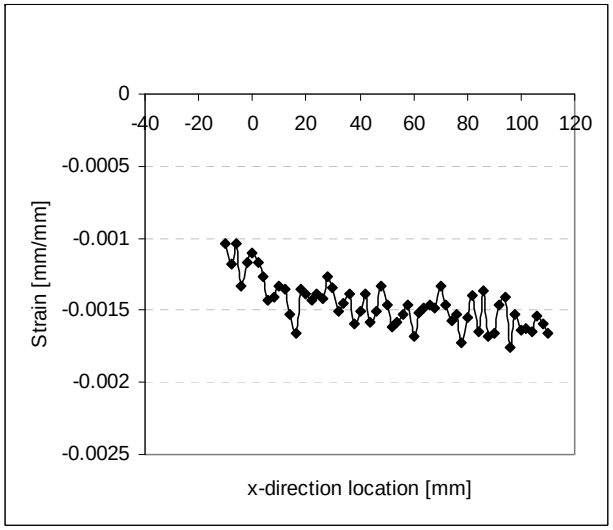

(c) Top edge; Reflection: $(10\bar{1}1)$

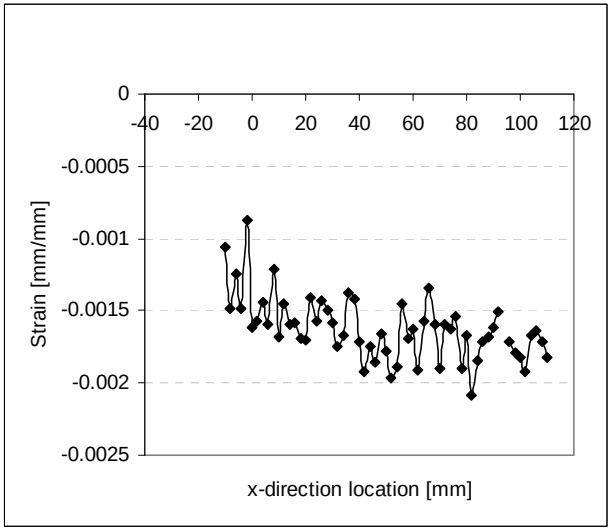

(d) Top edge; Reflection: $(10\bar{1}2)$

Figure A5. 17: ε_z profiles for top edge linescan for AZ91D casting at 210 °C mold temperature.

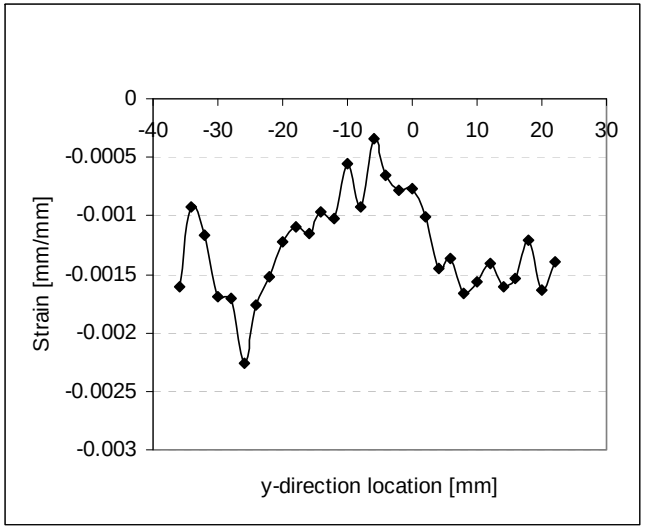

(a) Sprue cross-scan; Reflection: $(10\bar{1}0)$

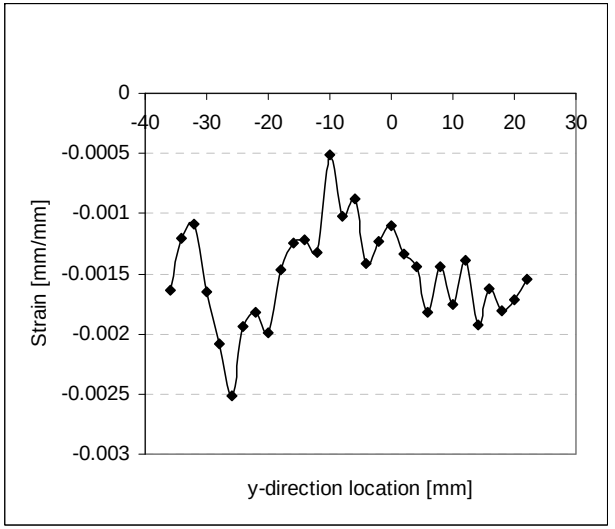

(b) Sprue cross-scan; Reflection: (0001)

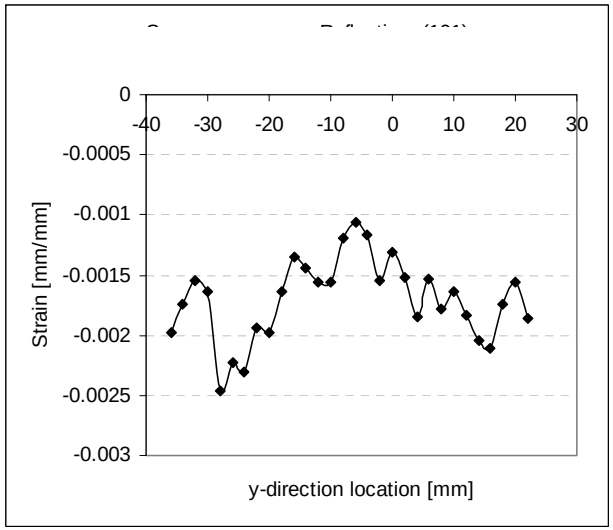

(c) Sprue cross-scan; Reflection: $(10\bar{1}1)$

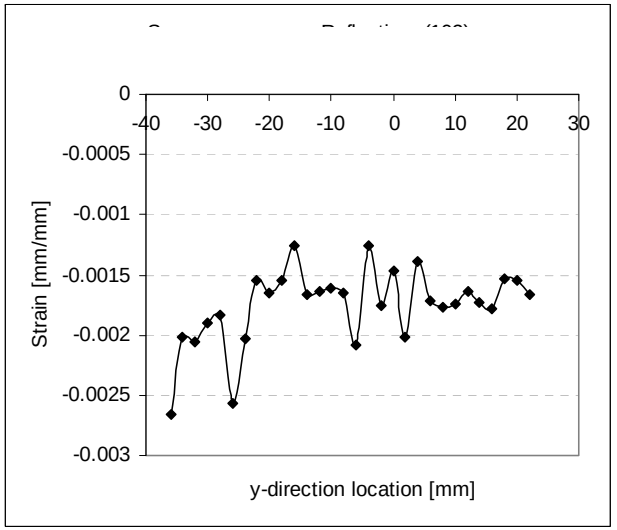

(d) Sprue cross-scan; Reflection: $(10\bar{1}2)$

Figure A5. 18: ε_z profiles for sprue cross-scan for AZ91D casting at 210 °C mold temperature.

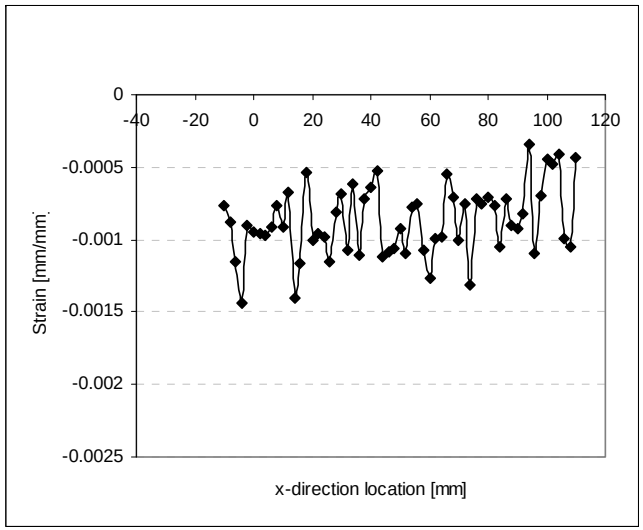

(a) Top edge; Reflection: $(10\bar{1}0)$

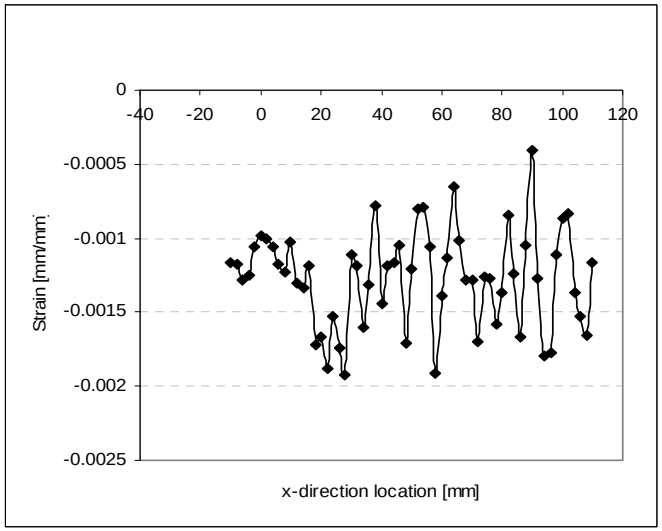

(b) Top edge; Reflection: (0001)

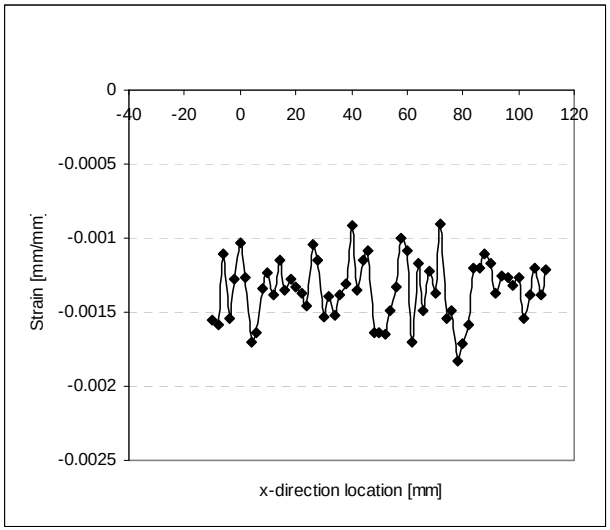

(c) Top edge; Reflection: $(10\bar{1}1)$

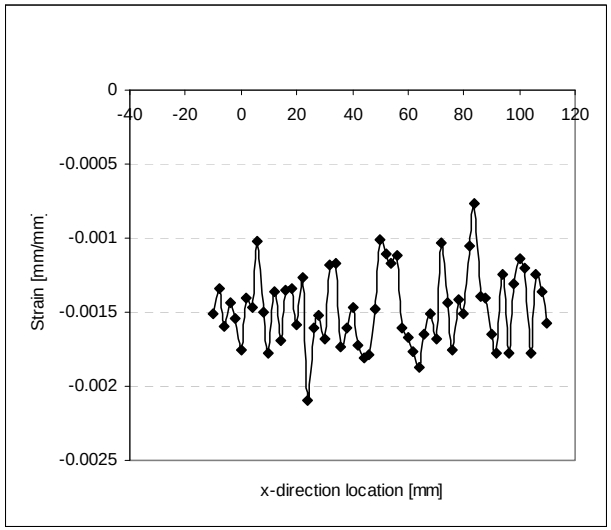

(d) Top edge; Reflection: $(10\bar{1}2)$

Figure A5. 19: ε_z profiles for top edge linescan for AZ91D casting at 250 °C mold temperature.

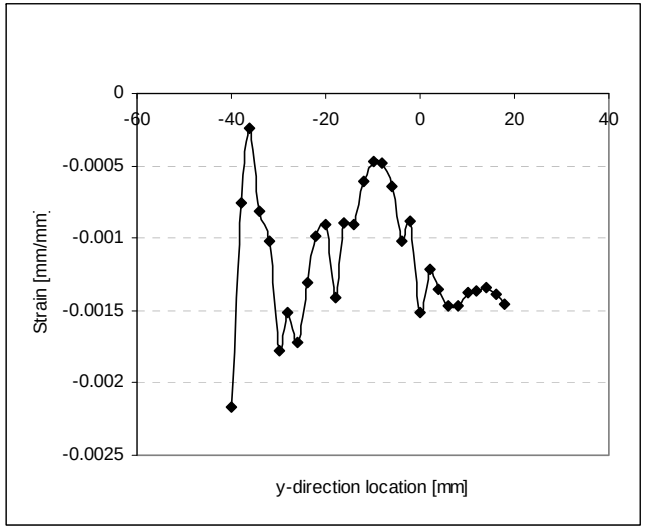

(a) Sprue cross-scan; Reflection: $(10\bar{1}0)$

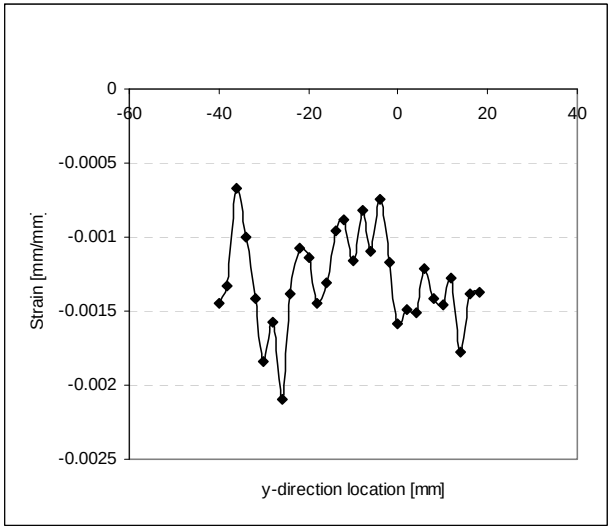

(b) Sprue cross-scan; Reflection: (0001)

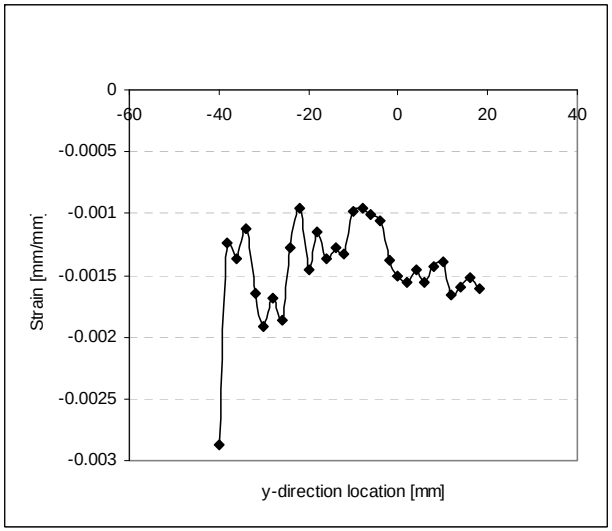

(c) Sprue cross-scan; Reflection: $(10\bar{1}1)$

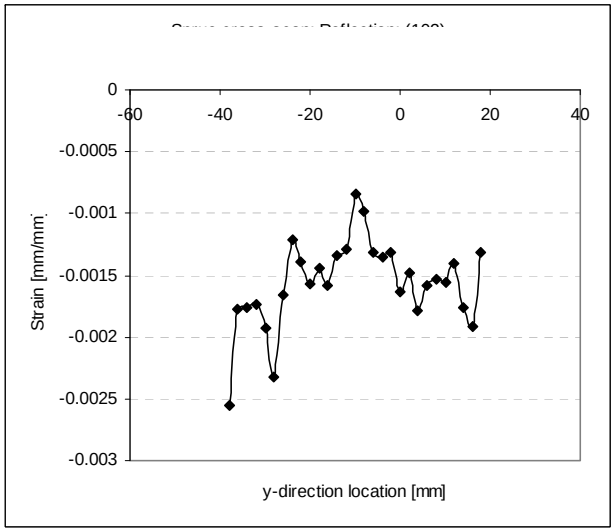

(d) Sprue cross-scan; Reflection: $(10\bar{1}2)$

Figure A5. 20: ε_y profiles for sprue cross-scan for AZ91D casting at 250 °C mold temperature.

A5.5 Texture Analysis

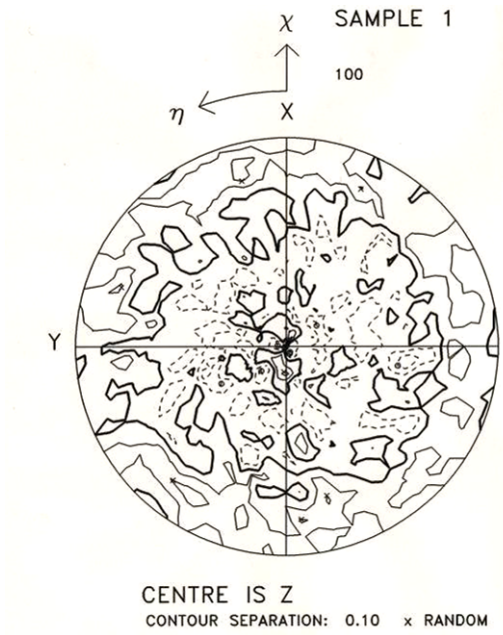

(a) Reflection: $(10\bar{1}0)$

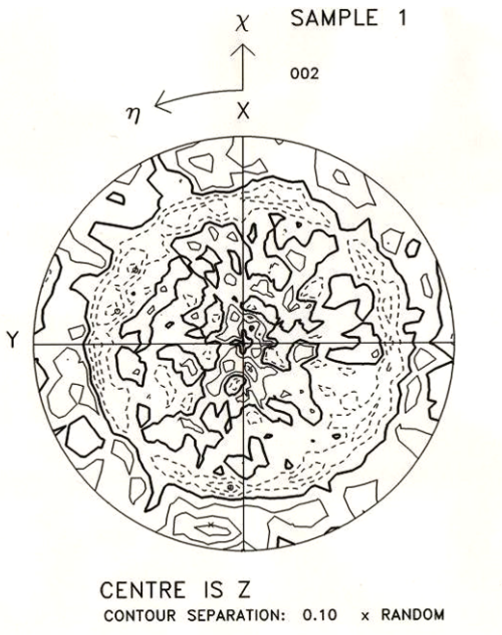

(b) Reflection: (0001)

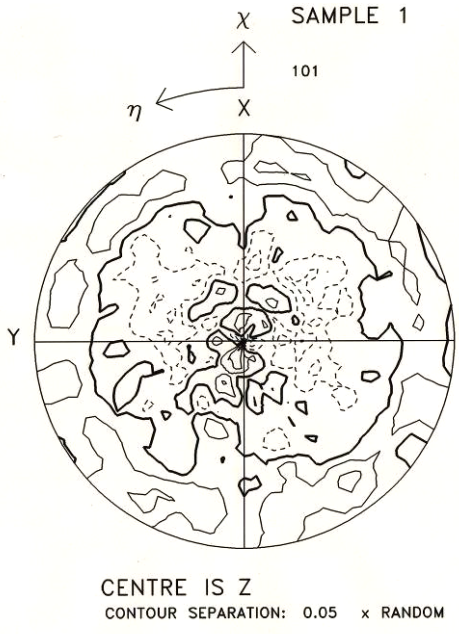

(c) Reflection: $(10\bar{1}1)$

(d) Reflection: $(10\bar{1}2)$

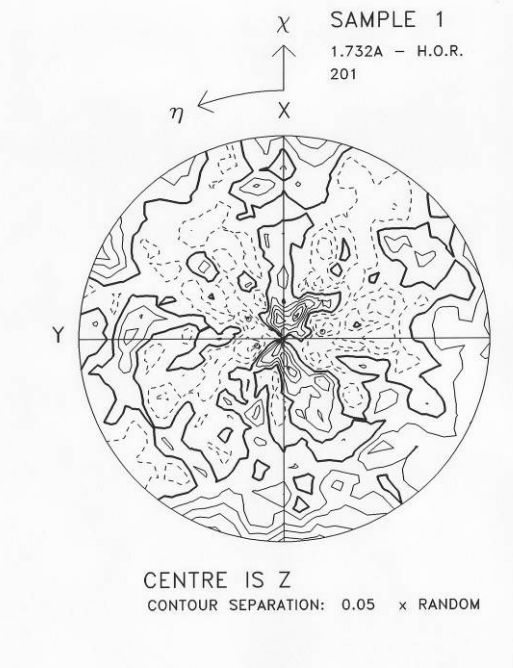

(e) Reflection: $(20\bar{2}1)$

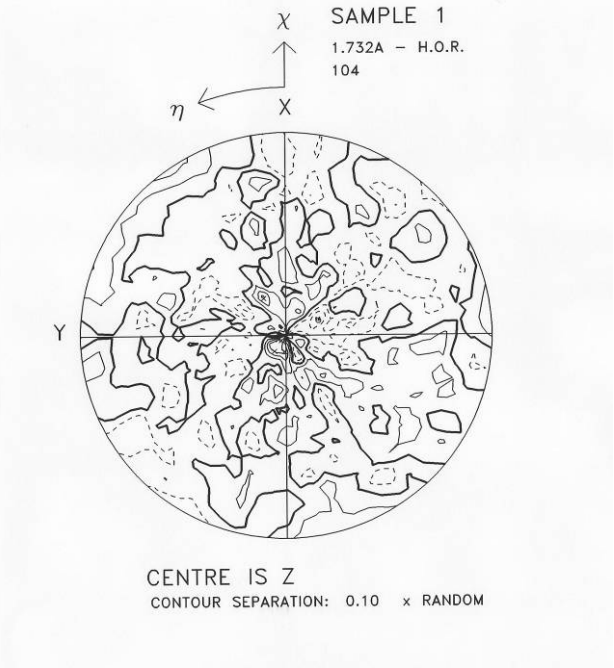

(f) Reflection: $(10\bar{1}4)$

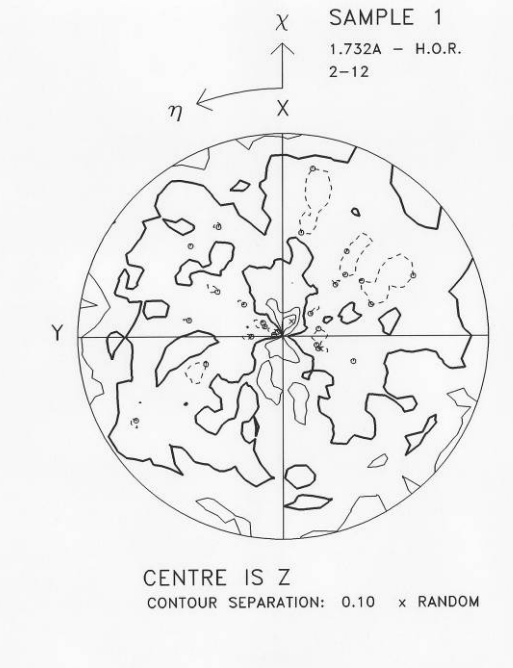

(g) Reflection: $(2\bar{1}12)$

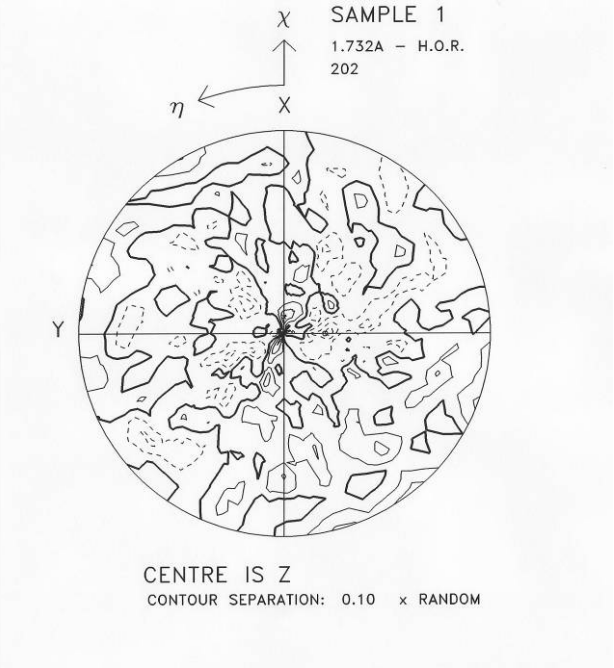

(h) Reflection: $(20\bar{2}2)$

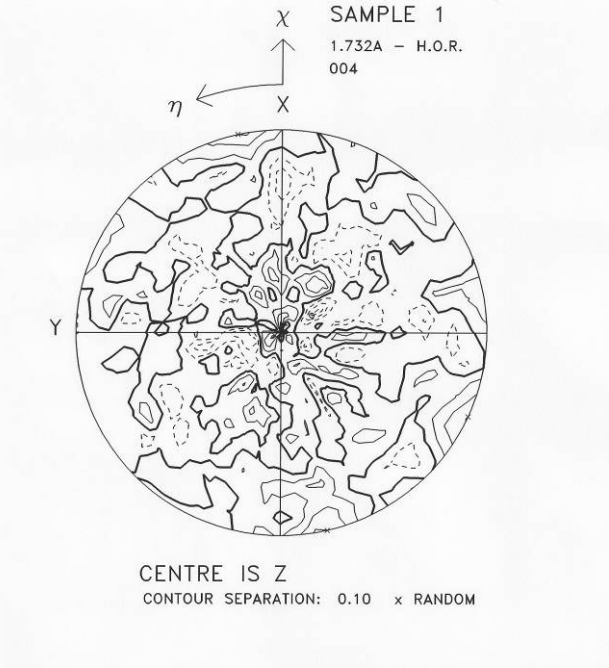

(i) Reflection: (0002)

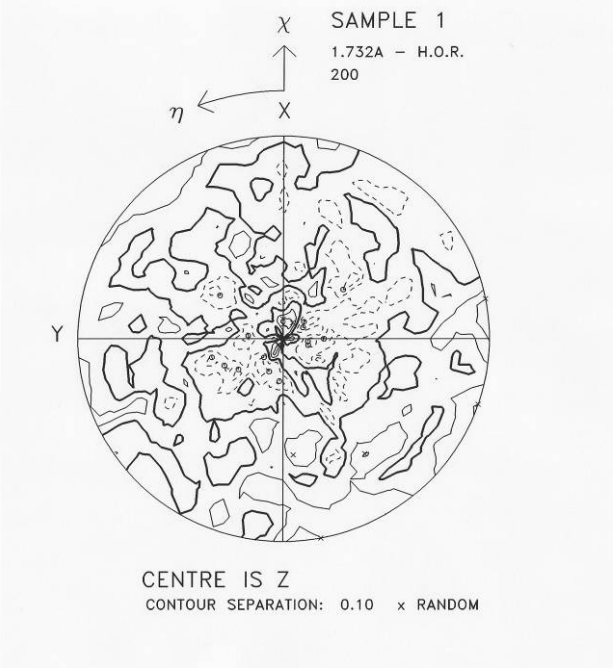

(j) Reflection: $(20\bar{2}0)$

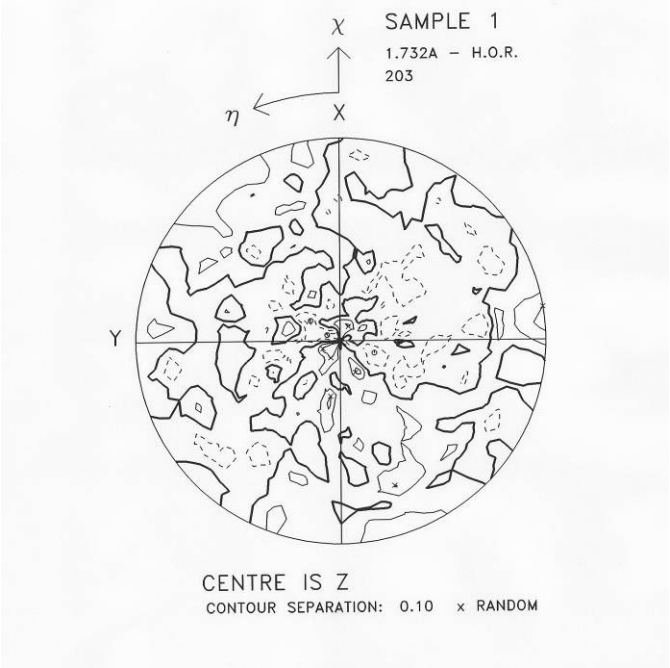

(k) Reflection: $(20\bar{2}3)$

Figure A5. 21: Pole figures for AZ91D / 220 texture specimen.

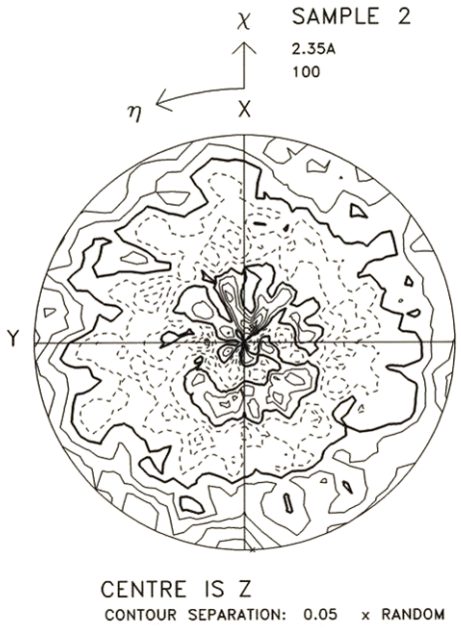

(a) Reflection: $(10\bar{1}0)$

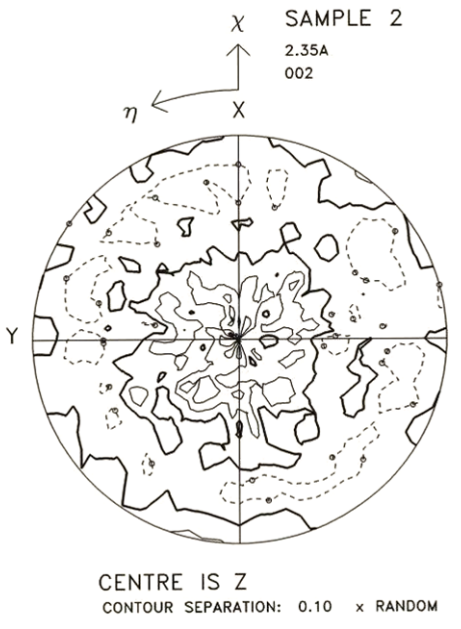

(b) Reflection: (0001)

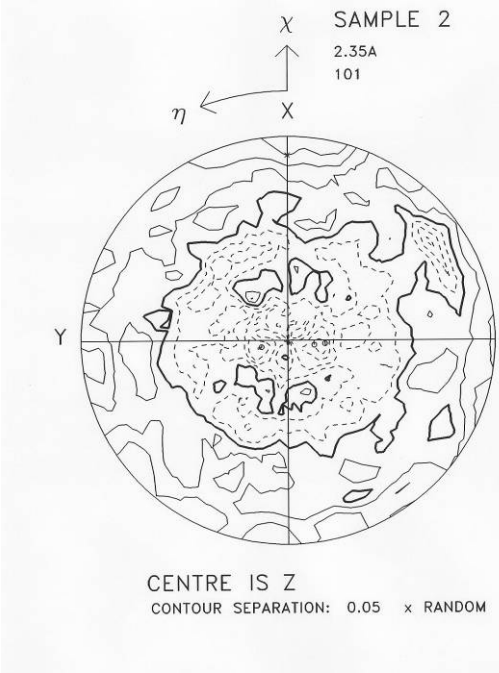

(c) Reflection: $(10\bar{1}1)$

(d) Reflection: $(10\bar{1}2)$

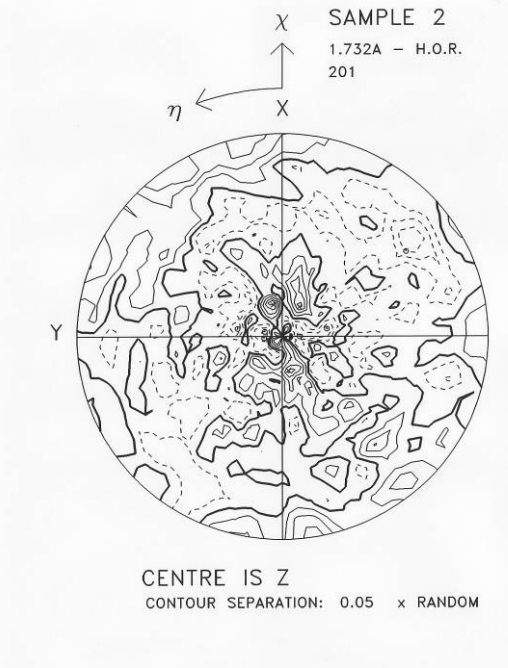

(e) Reflection: $(20\bar{2}1)$

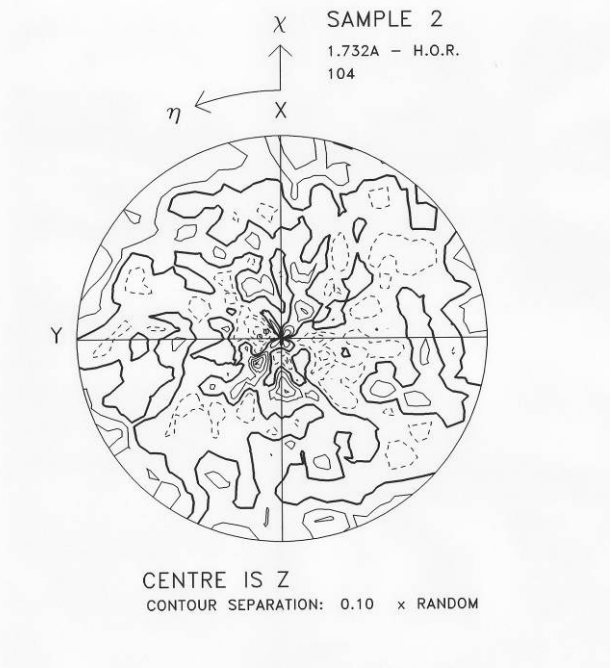

(f) Reflection: $(10\bar{1}4)$

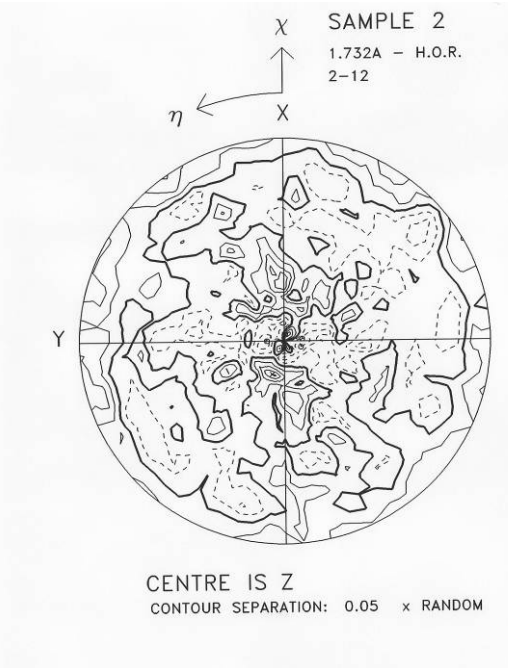

(g) Reflection: $(2\bar{1}12)$

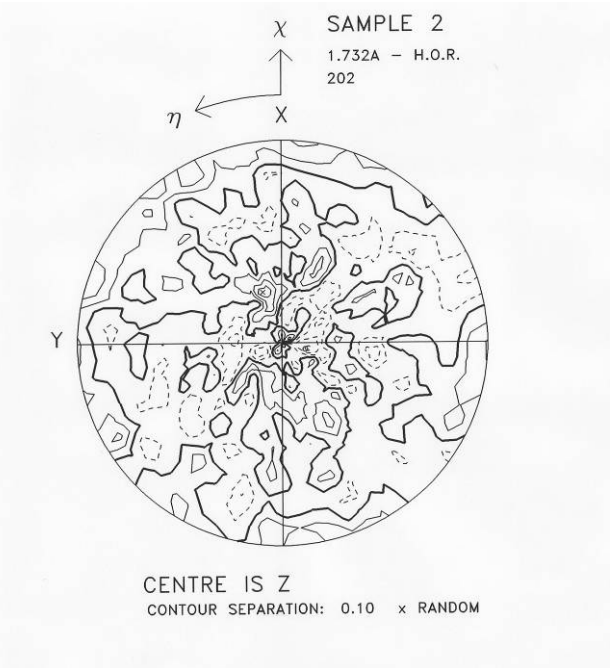

(h) Reflection: $(20\bar{2}2)$

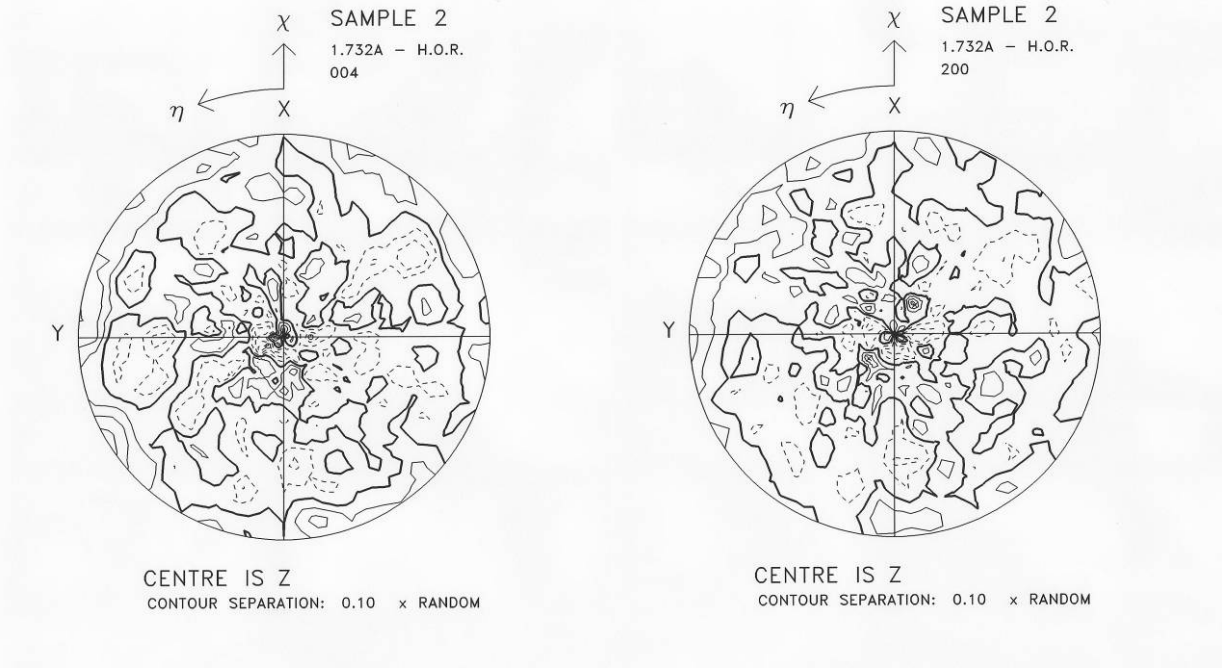

(i) Reflection: (0002) *(j) Reflection:* $(20\bar{2}0)$

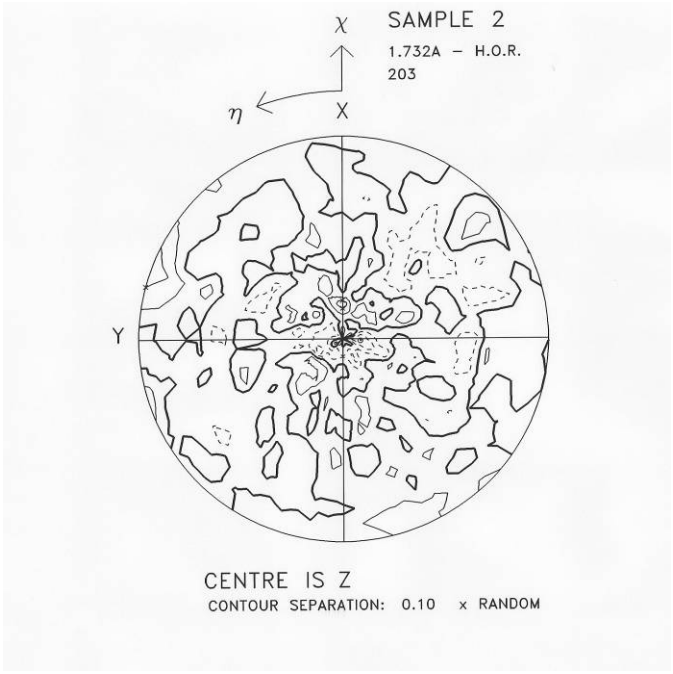

(k) Reflection: $(20\bar{2}3)$

Figure A5. 22: Pole figures for AZ91D / 320 texture specimen.

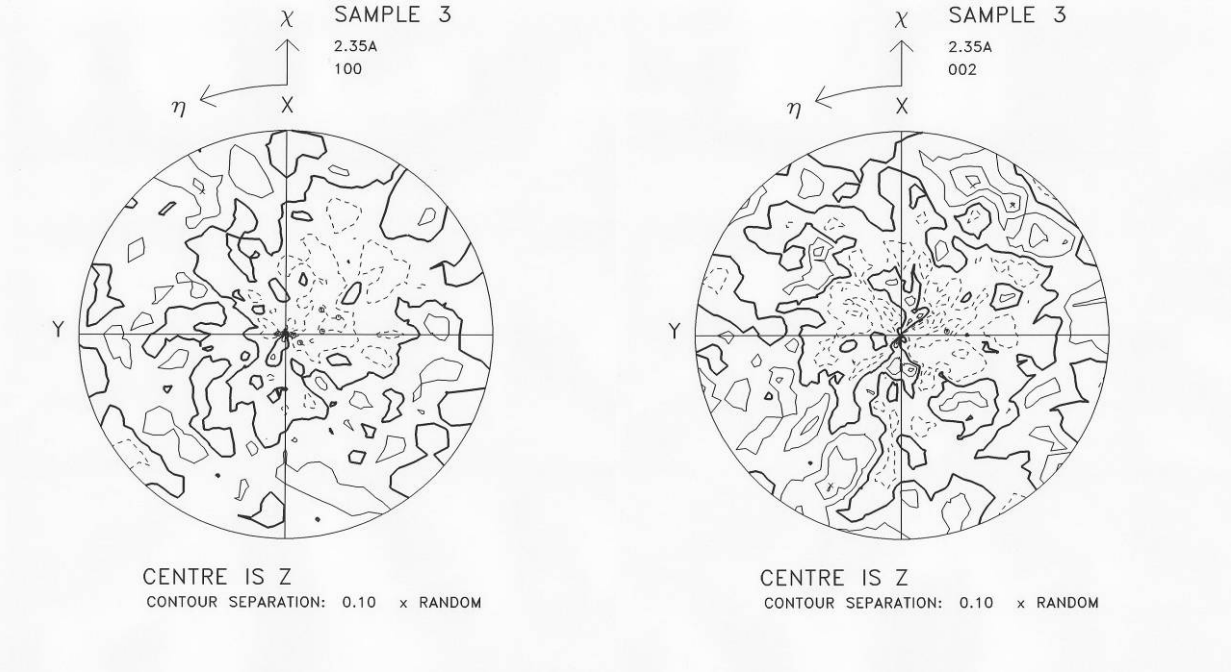

(a) Reflection: $(10\bar{1}0)$ *(b) Reflection:* (0001)

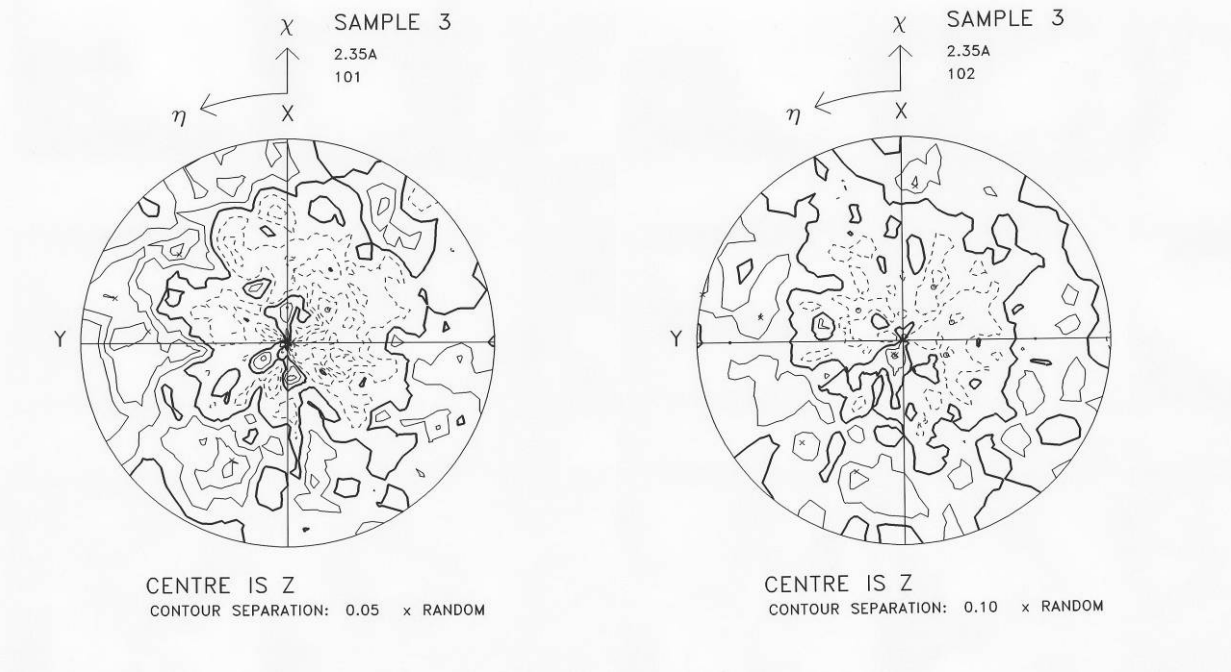

(c) Reflection: $(10\bar{1}1)$ *(d) Reflection:* $(10\bar{1}2)$

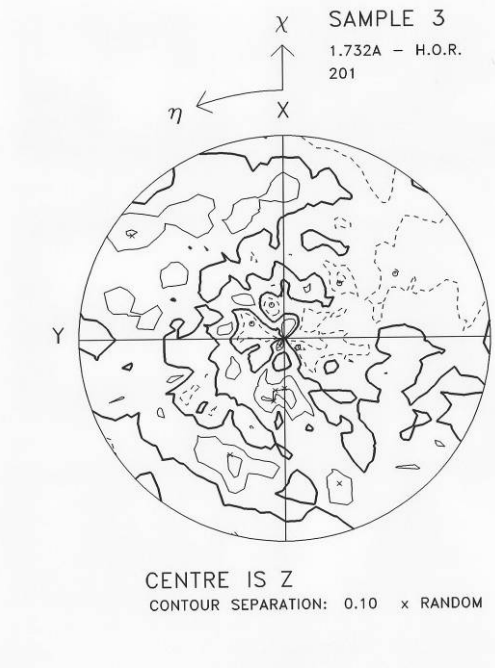

(e) Reflection: $(20\bar{2}1)$

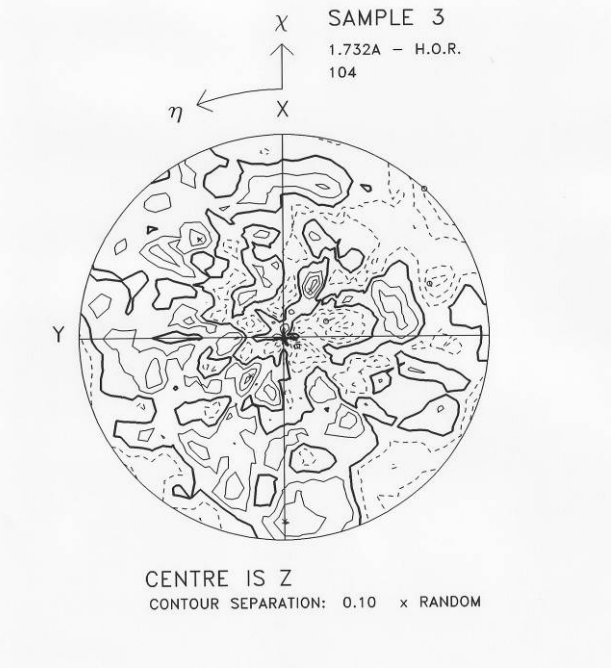

(f) Reflection: $(10\bar{1}4)$

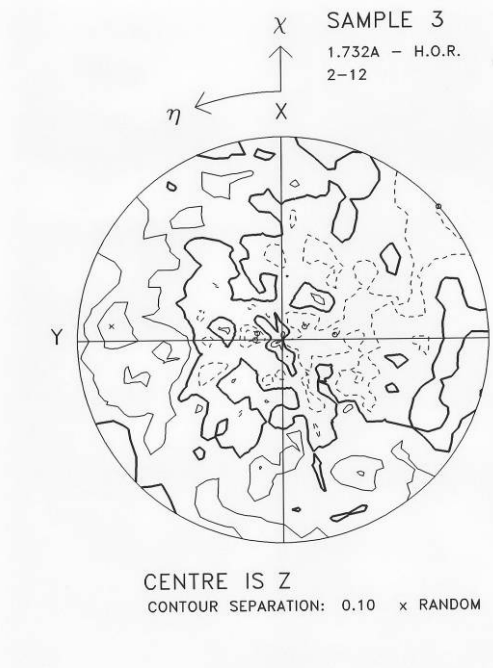

(g) Reflection: $(2\bar{1}12)$

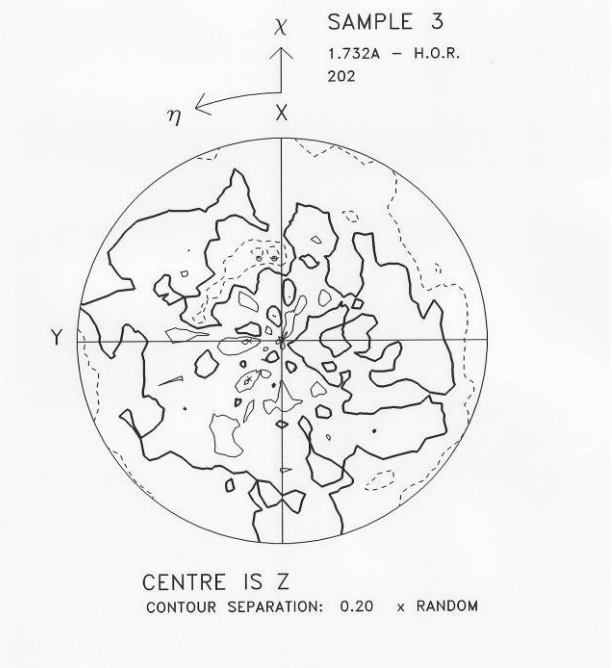

(h) Reflection: $(20\bar{2}2)$

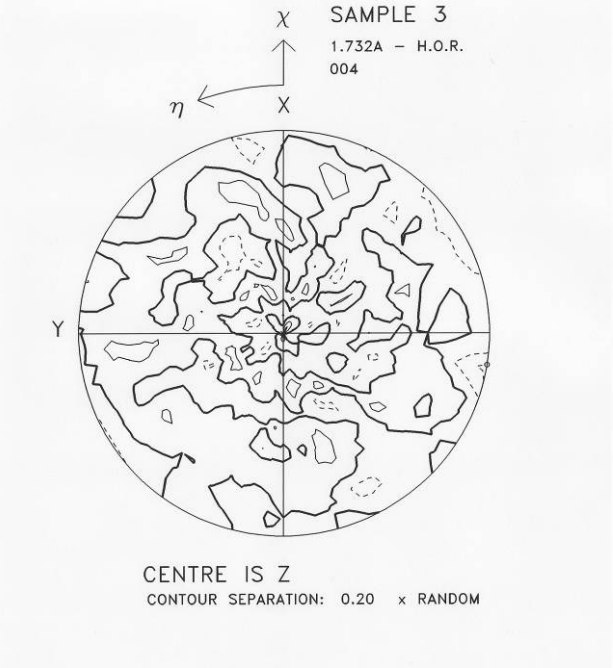

(i) Reflection: (0002)

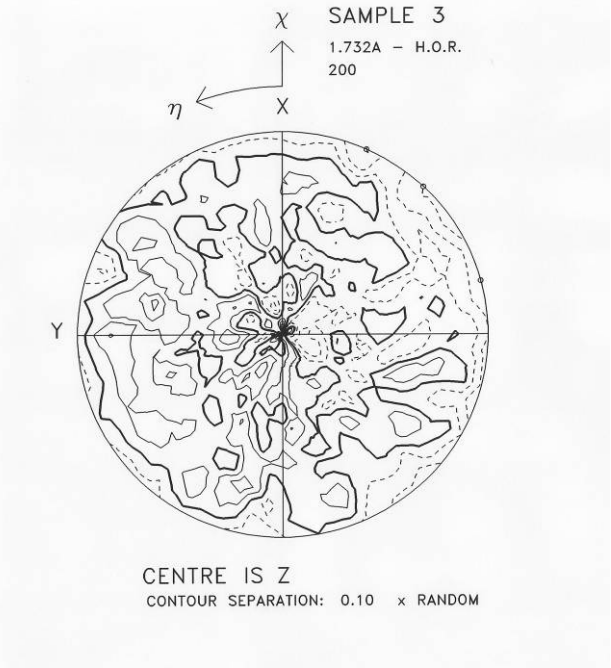

(j) Reflection: $(20\bar{2}0)$

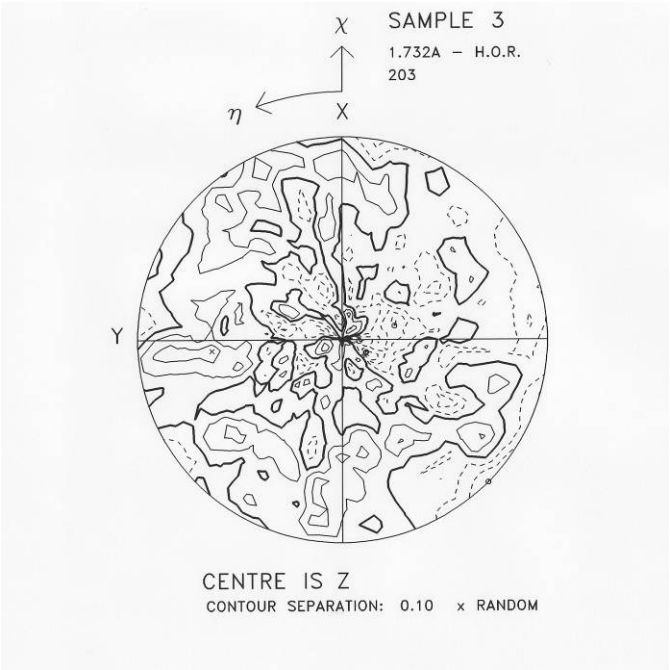

(k) Reflection: $(20\bar{2}3)$

Figure A5. 23: Pole figures for AZ91D / 340 texture specimen.

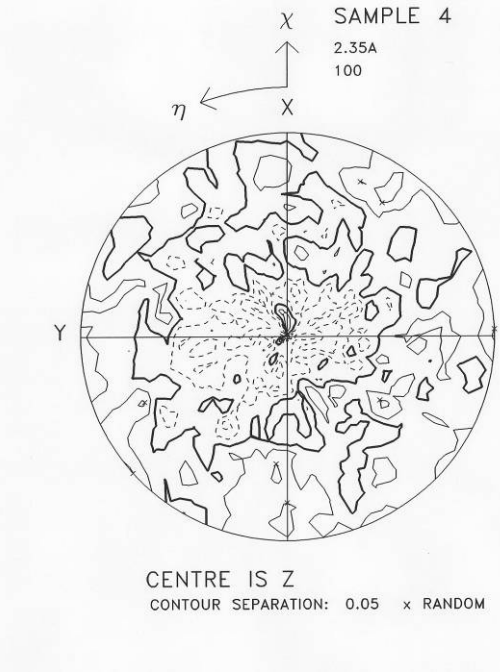

(a) Reflection: $(10\bar{1}0)$

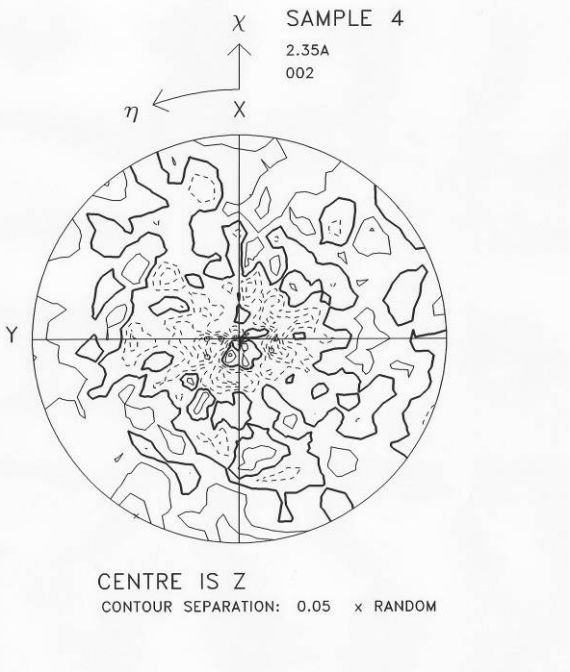

(b) Reflection: (0001)

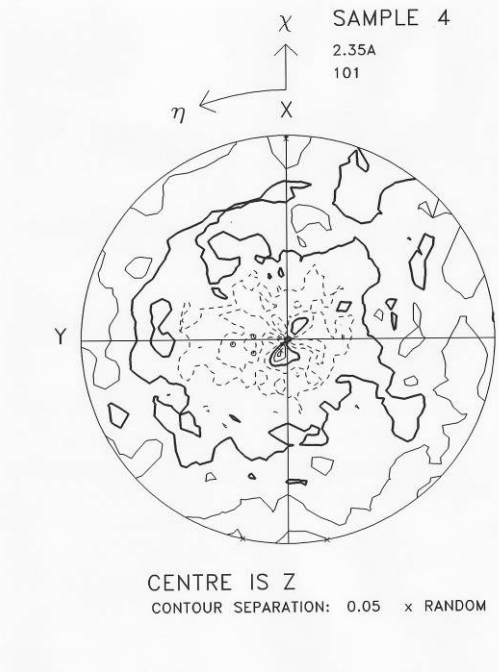

(c) Reflection: $(10\bar{1}1)$

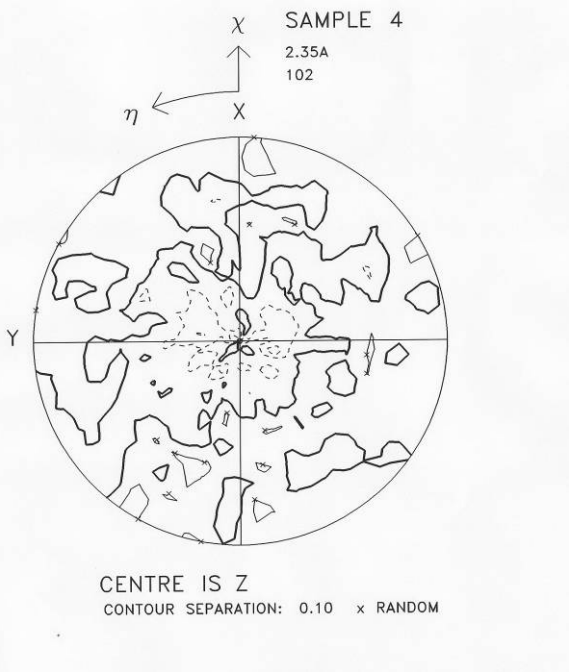

(d) Reflection: $(10\bar{1}2)$

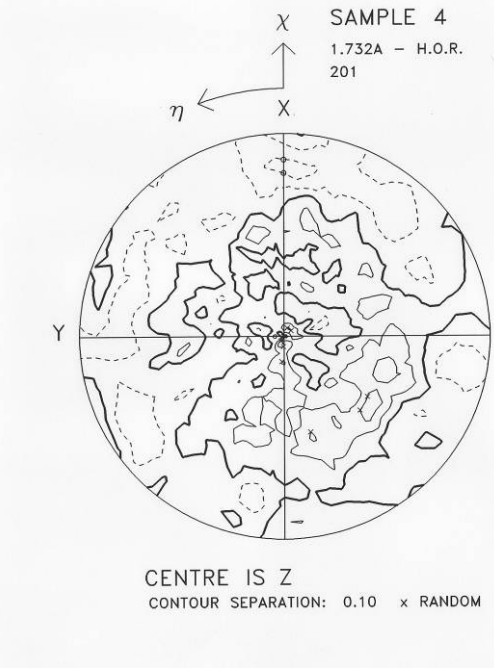

(e) Reflection: $(20\bar{2}1)$

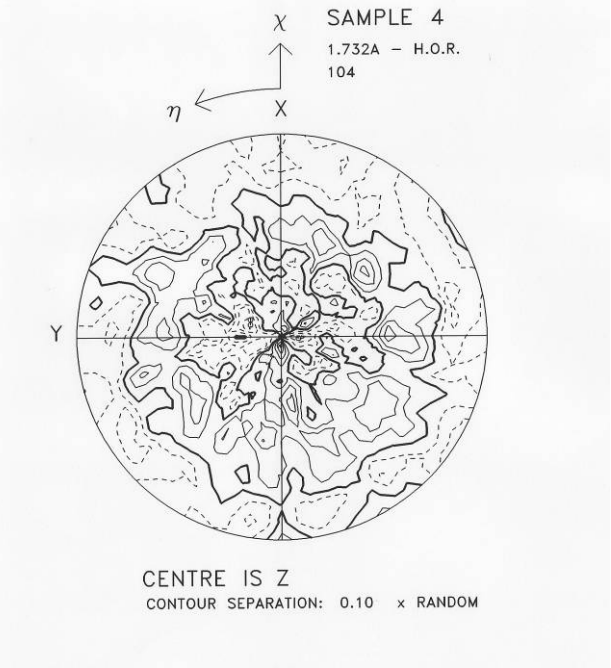

(f) Reflection: $(10\bar{1}4)$

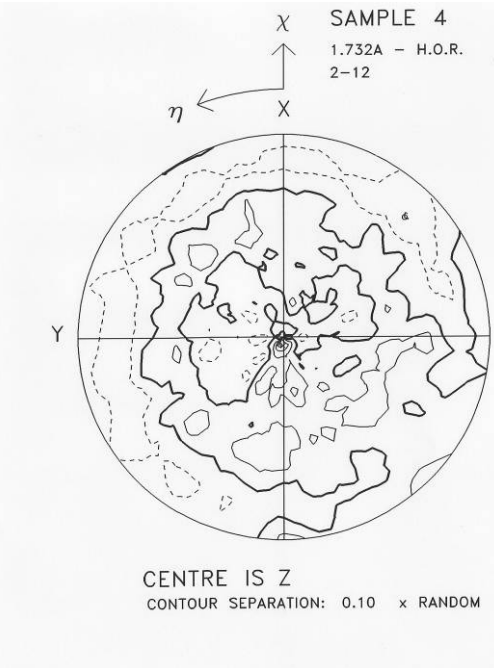

(g) Reflection: $(2\bar{1}12)$

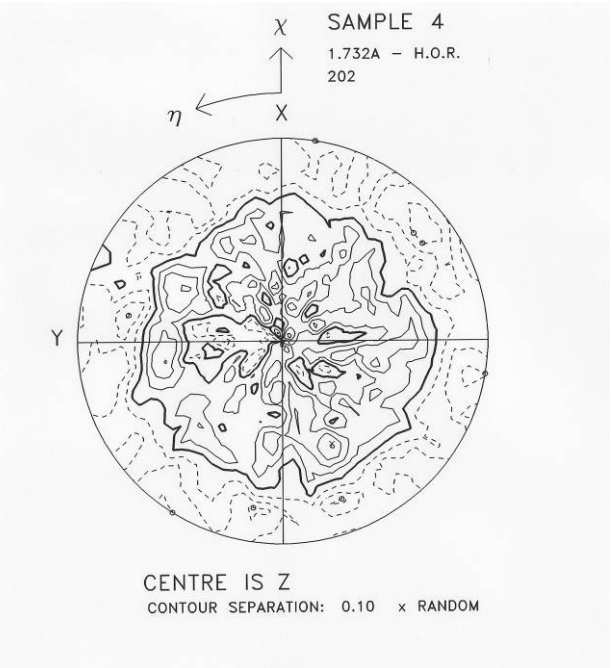

(h) Reflection: $(20\bar{2}2)$

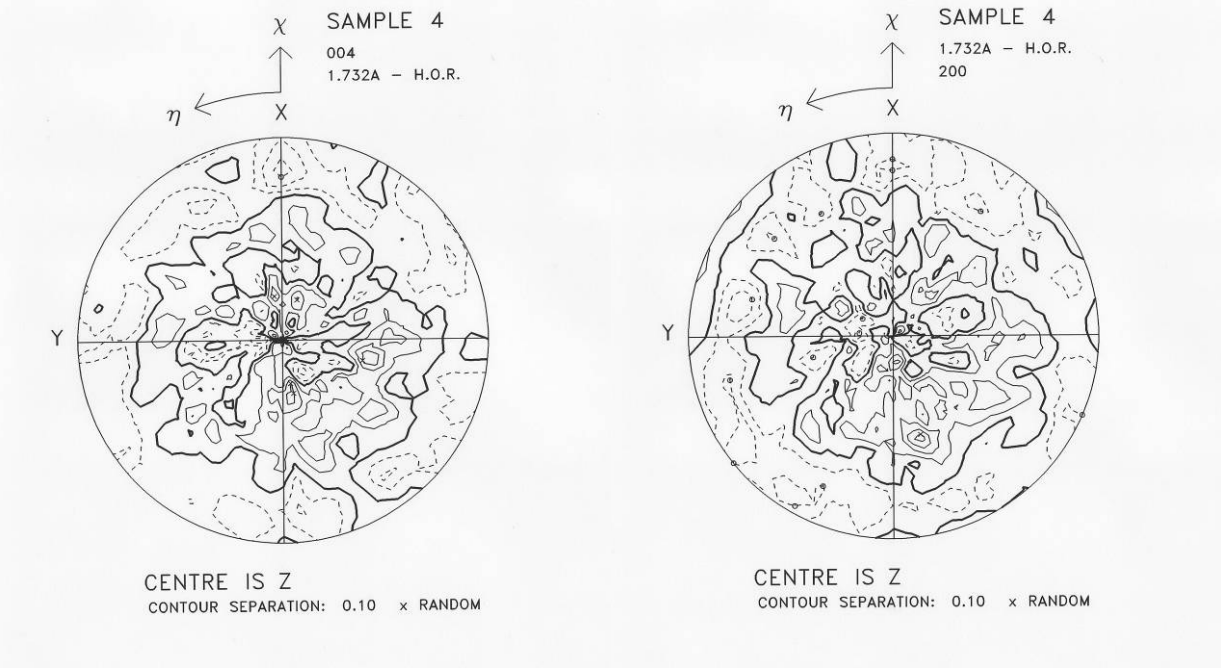

(i) Reflection: (0002) *(j) Reflection:* $(20\bar{2}0)$

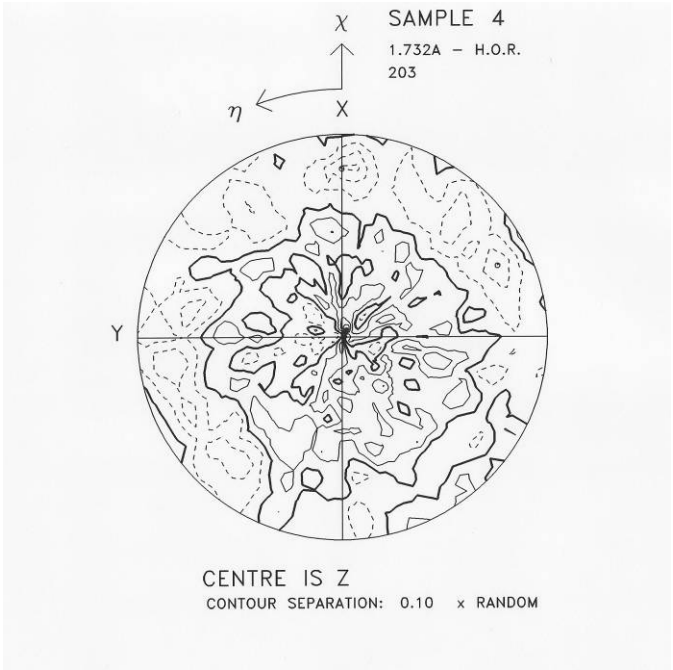

(k) Reflection: $(20\bar{2}3)$

Figure A5. 24: Pole figures for AZ91D / 380 texture specimen.

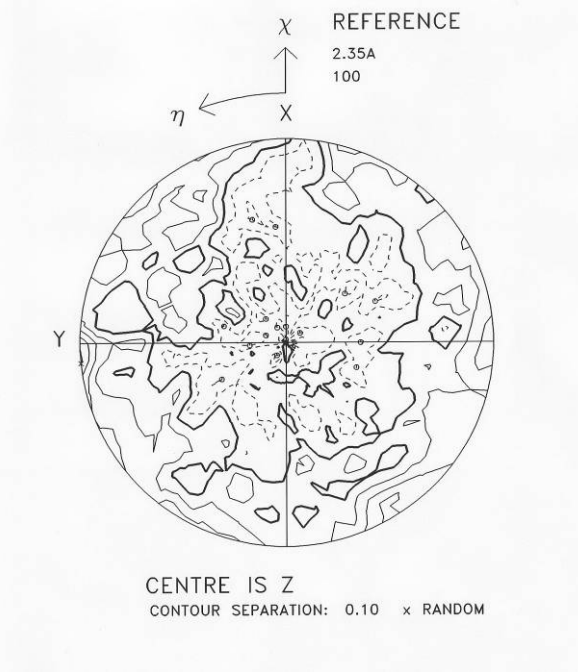

(a) Reflection: $(10\bar{1}0)$

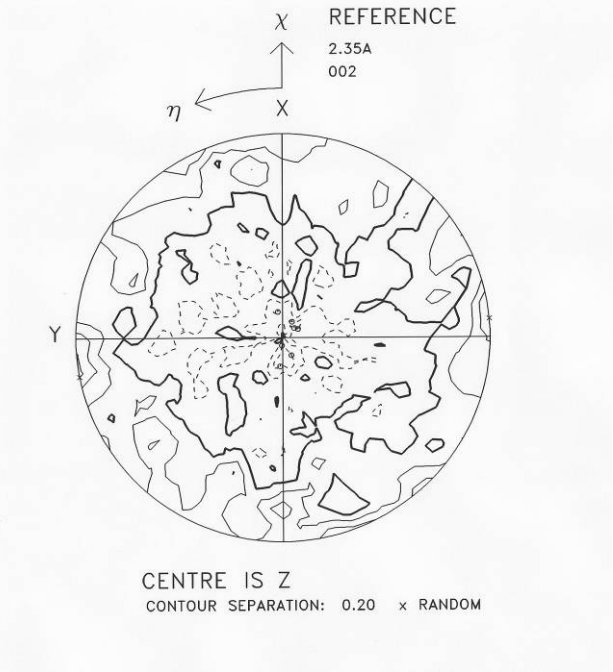

(b) Reflection: (0001)

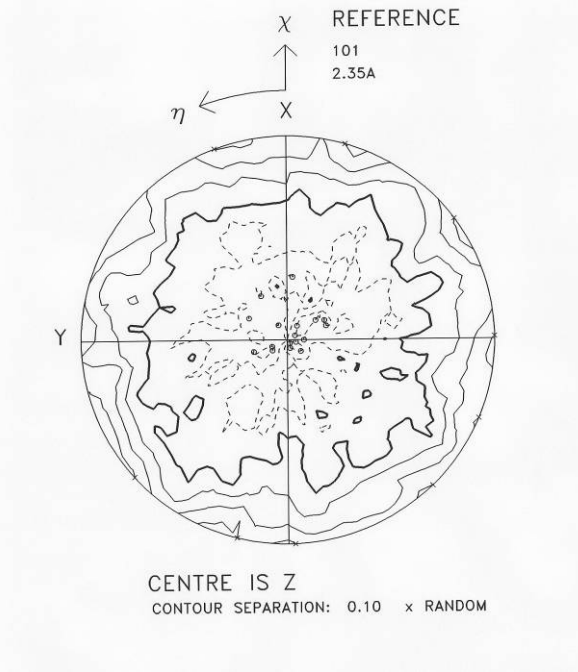

(c) Reflection: $(10\bar{1}1)$

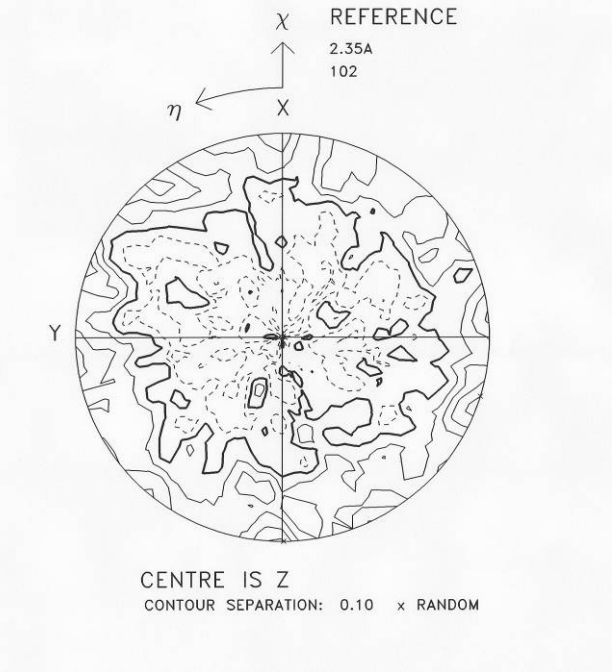

(d) Reflection: $(10\bar{1}2)$

(e) Reflection: $(20\bar{2}1)$

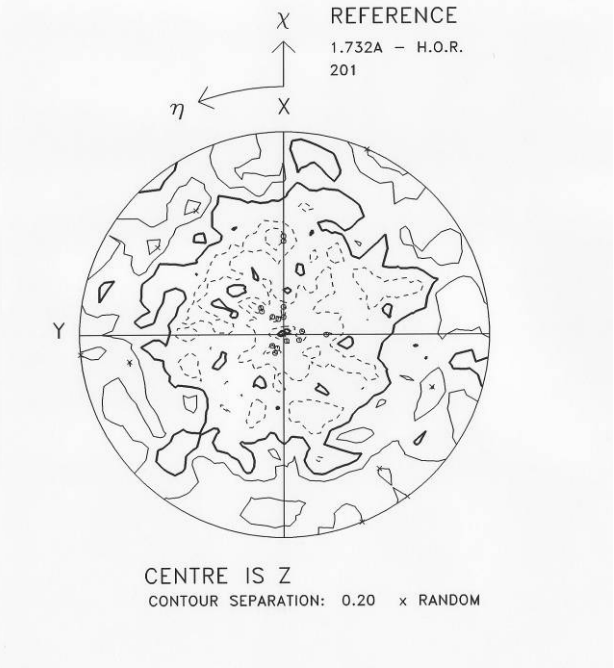

(f) Reflection: $(10\bar{1}4)$

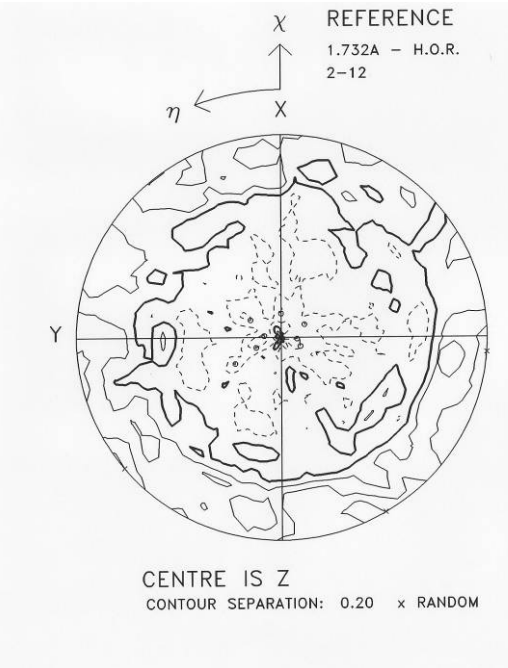

(g) Reflection: $(2\bar{1}12)$

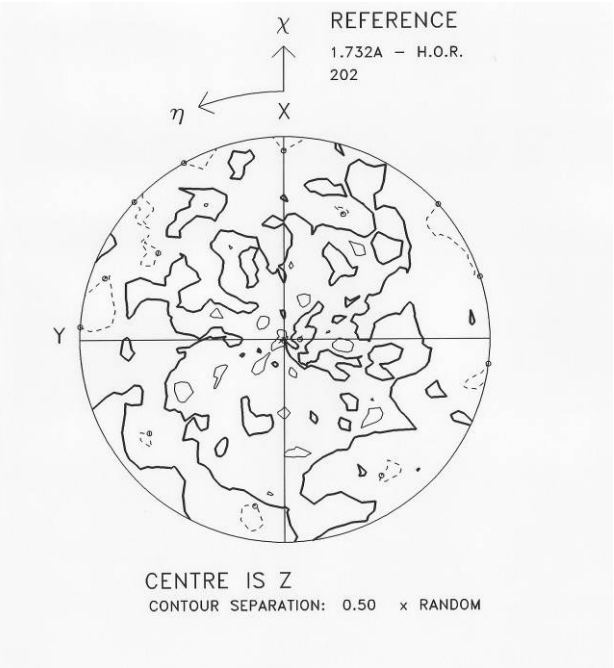

(h) Reflection: $(20\bar{2}2)$

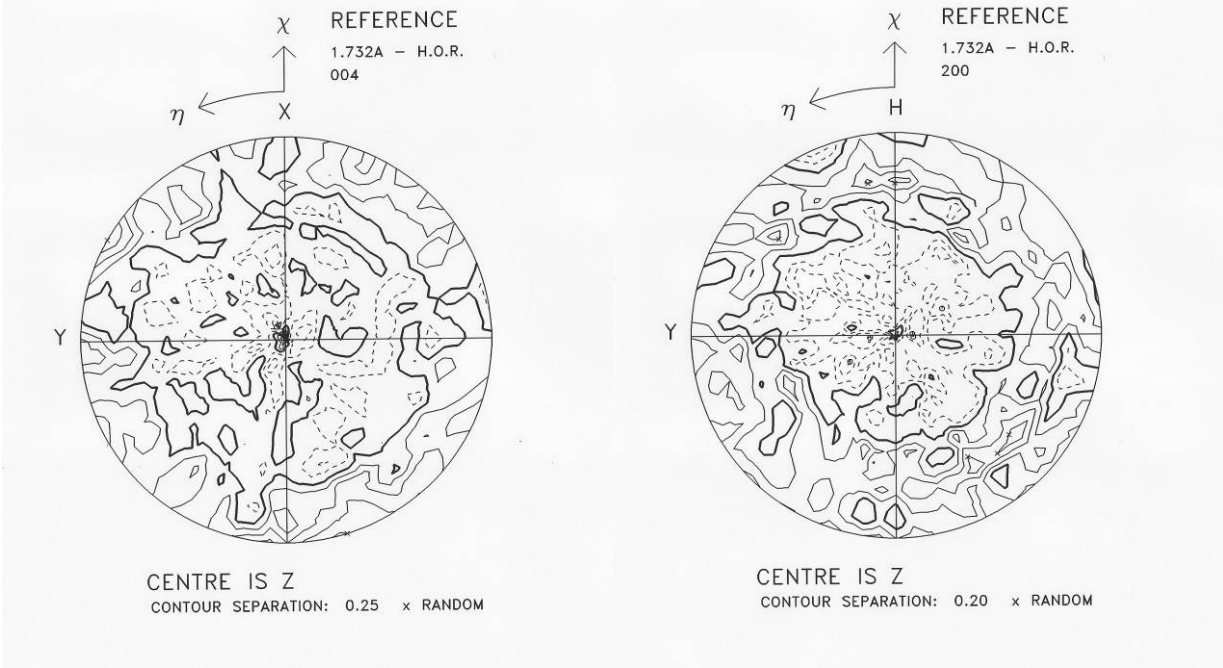

(i) Reflection: (0002) *(j) Reflection:* $(20\bar{2}0)$

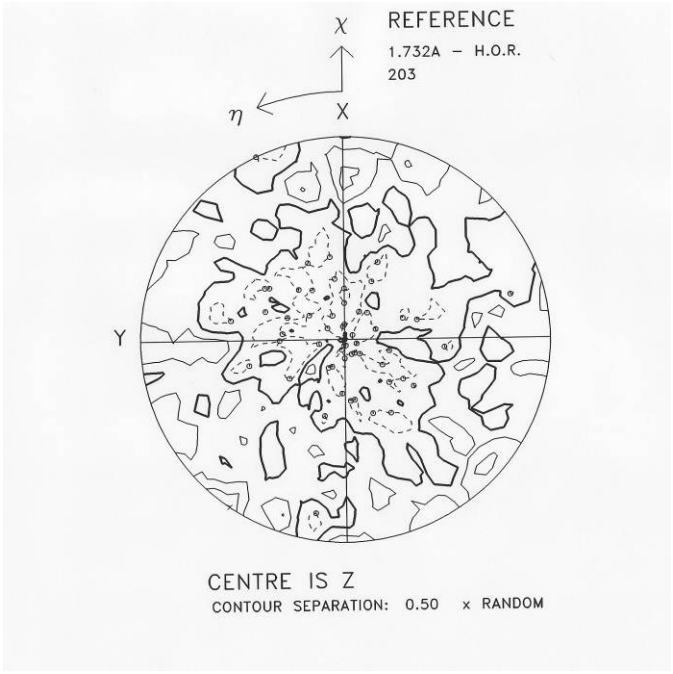

(k) Reflection: $(20\bar{2}3)$

Figure A5. 25: Pole figures for stress free (reference) AZ91D texture specimen.